

Determination of the local structure of NbO_6 octahedra in the orthorhombic phase of a KNbO_3 crystal using EXAFS

L. A. Bugaev, V. A. Shuvaeva, I. B. Alekseenko, K. N. Zhuchkov, and R. V. Vedrinskiĭ

Rostov-on-Don State University, 344090 Rostov-on-Don, Russia
(Submitted November 20, 1997)

Fiz. Tverd. Tela (St. Petersburg) **40**, 1097–1101 (June 1998)

A new method proposed by us to determine the displacement direction of B atoms from centrosymmetric positions in ABO_3 crystals is used to study the local atomic structure of KNbO_3 in the orthorhombic phase. It is shown that the conventional treatment of the EXAFS yields serious errors in determinations of the local distortions of NbO_6 octahedrons. To eliminate these errors, it is suggested that diffraction data on the average atomic displacements should be combined with the results of direct calculations of the Nb *K*-EXAFS of KNbO_3 in the orthorhombic phase. This approach was used to establish that the preferential direction of displacement of Nb in the orthorhombic phase of KNbO_3 is in the direction of the polar two-fold axis. © 1998 American Institute of Physics. [S1063-7834(98)02806-8]

In Ref. 1 we proposed a new method to determine the displacement of B atoms from centrosymmetric positions in perovskite structures of ABO_3 binary oxides. This method is based on the qualitative difference observed in Ref. 1 in the behavior of the Fourier transforms of the EXAFS of polycrystalline samples for various possible types of displacement of the B atom. We use the results obtained in Ref. 1 to study the local atomic structure of a KNbO_3 crystal. It has now been established that like BaTiO_3 , this crystal exhibits significant structural disorder, which has been studied in numerous publications (see, for example, Refs. 2–5). Experimental data^{2,3} indicate that local distortions of ideal NbO_6 octahedra in these crystals are even found in the highly symmetric cubic phase. Similar conclusions were recently drawn for the PbTiO_3 crystal.⁵ Since the atomic displacements responsible for local disorder do not possess long-range order, these are difficult to determine by conventional diffraction methods and, as will be shown subsequently, information on the required local atomic structure can only be obtained by using EXAFS spectroscopic data in conjunction with data obtained by conventional structure analysis.

It should be noted that the problem of determining small atomic displacements in perovskite crystals by EXAFS is highly complex. In view of the complex splitting of the first coordination sphere of the Nb atom caused by small displacements of this atom from the center of the NbO_6 octahedron, formal implementation of the conventional procedure for fitting the experimental spectra may yield errors in the determination of the magnitude and the directions of displacement. For instance, the similarity between the Nb *K*-EXAFS in the rhombohedral and orthorhombic phases of the KNbO_3 crystal would appear to indicate that the local distortions of the NbO_6 octahedra in the orthorhombic phase are of a rhombohedral nature.⁶ However, as will be shown subsequently, the combined use of EXAFS and results of diffraction structure analysis reliably indicates that these distortions are orthorhombic, where the Nb atoms are displaced

from the centers of NbO_6 octahedra along the two-fold axis. An analysis of the EXAFS spectra obtained for a single-crystal sample⁷ confirms this conclusion.

1. EXPERIMENTAL

EXAFS spectra above the *K* absorption edge of the Nb atom in a KNbO_3 polycrystal in the rhombohedral and orthorhombic phases at temperatures $T=270$ and 300 K were kindly supplied by the authors of Ref. 6, and for the orthorhombic phase these spectra were recorded by one of the authors (V. A. Shuvaeva) using a laboratory EXAFS spectrometer at $T=300$ K. The absorption spectra of the samples were measured in the energy range between $18\,700$ and $19\,800$ eV at intervals of around 3.5 eV. The radiation intensity at each point in the spectrum was measured by a fixed count of 10^6 pulses. The energy resolution was better than 9 eV.

2. RESULTS AND DISCUSSION

There are two possible models of phase transitions in a KNbO_3 crystal: the displacement-type transition model and the order–disorder transition model. The first model assumes that, as a result of lattice anharmonicity at a certain temperature, which is the same as the phase transition temperature, the crystal symmetry changes spontaneously and is accompanied by displacement of Nb atoms along the four-fold axis for a transition from the cubic to the tetragonal phase ($T=693$ K), along the two-fold axis for a transition to the orthorhombic phase ($T=488$ K), and along the three-fold axis for a transition to the rhombohedral phase ($T=238$ K), as shown schematically in Fig. 1. In this case, the amplitudes of the thermal vibrations about the appropriate sites are not anomalously high in any of the phases. On the other hand, the order–disorder transition model assumes that the local structure of the NbO_6 octahedra in almost all phases is the same and is similar to the structure of these octahedra in the

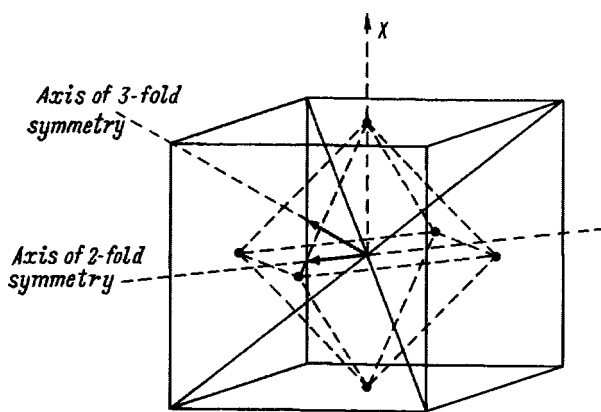


FIG. 1. Possible directions of displacements of Nb atoms in the orthorhombic phase of a KNbO_3 crystal.

rhombohedral phase, where the Nb atoms are displaced relative to the centers of the octahedra along their axes of three-fold symmetry. Only in the rhombohedral phase are all the octahedra translationally equivalent at given instant. In the high-temperature phases they are only equivalent on average, while at any instant the directions of displacement of the Nb atoms in different octahedra are different. Thus, it may be roughly assumed that in the orthorhombic phase, there are two types of instantaneous displacement of Nb atoms along the two local axes of three-fold symmetry closest to the direction of average displacement of these atoms, which is determined by the direction of electric polarization of the crystal oriented along one of the axes of two-fold symmetry, frequently called the polar axis. Thus, in the tetragonal phase, there are four possible directions of displacement of Nb atoms along the axes of three-fold symmetry of the octahedra so that, on average, the displacement takes place along the polar axis of four-fold symmetry, situated between these axes. Finally, in the cubic phase, the Nb atoms have an equal probability of being displaced in all eight possible directions from the centers of the octahedra along their axes of three-fold symmetry. This model of the atomic structure of a KNbO_3 crystal, which assumes extremely strong anharmonicity, was first proposed by Comes, Lambert, and Guinier² and will subsequently be called the CLG model. The results of recent diffraction analyses⁸ do not agree with the CLG model, but they do not yield any definitive conclusion on the nature of the local distortions of KNbO_3 octahedra. We used EXAFS data to obtain additional information which would allow us to establish beyond doubt the nature of these distortions in a KNbO_3 crystal. However, if a comparative analysis of the Nb K -EXAFS spectra in the rhombohedral and orthorhombic phases of KNbO_3 is confined to the conventional procedure for the analysis of experimental spectra, based on Fourier transformation followed by fitting, the similarity between the Fourier transforms of the Nb K -EXAFS spectra in the rhombohedral and orthorhombic phases of KNbO_3 shown in Fig. 2 would most likely yield the conclusion that the directions and magnitudes of the Nb atomic displacements in these phases are identical, as has been noted. On this basis, the authors of Ref. 6 concluded that EXAFS spectroscopy directly confirms the CLG model.

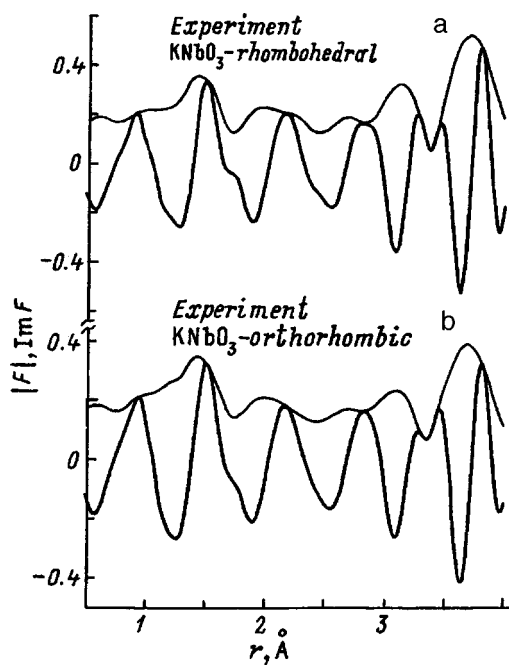


FIG. 2. Moduli $|F|$ (fine lines) and imaginary parts $\text{Im } F$ (thick lines) of Fourier transforms of experimental Nb K -EXAFS spectra of a KNbO_3 crystal in the rhombohedral phase at $T=270$ K (a) and in the orthorhombic phase at $T=300$ K (b).

In order to obtain a better understanding of the similarity between the Nb K -EXAFS spectra in the rhombohedral and orthorhombic phases, we made direct calculations of these spectra for two models of local distortion of the NbO_6 octahedra in a KNbO_3 crystal: rhombohedral and orthorhombic. The results showed that the experimental spectra obtained for a polycrystalline KNbO_3 sample can be explained equally well by either model if we use different values for the displacements of the Nb atom from the center of the NbO_6 octahedron along the axes of two-fold and three-fold symmetry, respectively. For the calculations we used methods developed earlier which, as was shown in Refs. 9 and 10, give good results for crystals known to exhibit no local disorder. Data on the atomic positions given in Ref. 11 were used to calculate the spectrum of the rhombohedral phase. Apart from $E_{\text{MT}}=18\,965.0$ eV, which was determined as in Ref. 10 and then fixed, the other parameters characterizing the EXAFS spectra¹² used in the calculations, were determined by the conventional procedure from the best agreement between the calculated and experimental spectra. These parameters were $2\sigma^2=0.004$ Å², $\Gamma=3$ eV, and $S_0^2=0.9$. It should be stressed that the spectrum does not depend very strongly on the parameter Γ , which determines the rate of decay of electron-hole excitation in the crystal, but the calculated spectrum depends considerably more strongly on the thermal parameter σ^2 in the Debye-Waller factor. It can be seen that the Fourier transform of the calculated EXAFS spectrum for a rhombohedral KNbO_3 polycrystal plotted in Fig. 3 shows good agreement with the experimental spectrum, which further confirms the accuracy of the results obtained in Ref. 11, especially the displacement of the Nb atom from the center of the oxygen octahedron by 0.19 Å along

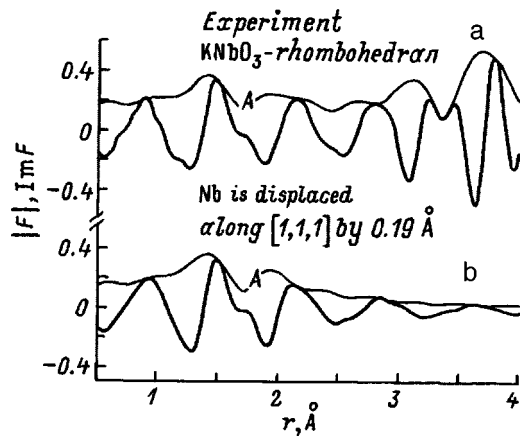


FIG. 3. Moduli $|F|$ (fine lines) and imaginary parts $\text{Im } F$ (thick lines) of Fourier transforms: a — of the function $k\chi^{\text{exp}}(k)$ of the experimental Nb K -EXAFS spectrum of a rhombohedral KNbO_3 crystal at $T=270$ K; b — of the function $k\chi_1^{\text{th}}(k)$ of the theoretical Nb K -EXAFS-spectrum calculated for displacement of the Nb atom along the axis of three-fold symmetry by 0.19 \AA .

the three-fold axis. At this point, it is appropriate to note that neither the results of the structure analysis nor the data on the diffuse scattering of x-rays by the KNbO_3 crystal in the rhombohedral phase give any reason to assume local disorder in different NbO_6 octahedra, so that no doubts are cast on the assumption that the Nb atoms in all octahedra are displaced along the axis of three-fold symmetry. However, in principle, the magnitude of this displacement can be refined. It was shown in Ref. 1 that the intensity of the additional peak A in the imaginary part of the Fourier transform of the EXAFS spectrum is highly sensitive to the displacement of the Nb atom along the three-fold axis. Thus, good agreement between the imaginary parts of the Fourier transforms of the calculated and experimental EXAFS spectra provides excellent confirmation of the displacement of the Nb atom from the center of the oxygen octahedron along the axis of three-fold symmetry, obtained in Ref. 11 by an analysis of neutron-diffraction data from a powder sample. At the same time, this agreement further confirms the high accuracy of the calculation method used.

We shall examine the results of the calculations for the orthorhombic phase, in which there is reason to expect some differences in the local structure of different NbO_6 octahedra. We initially disregarded this possibility and used information on the atomic positions obtained by diffraction techniques,^{8,11} assuming that the local structure of all the NbO_6 octahedra in the orthorhombic phase is identical, as in the rhombohedral phase. Other parameters of the EXAFS spectrum were the same as in the rhombohedral phase, assuming that the spectra were recorded at similar temperatures. Thus, we assumed that Nb atoms in all NbO_6 octahedra are displaced from the centers of the octahedra by 0.21 \AA along the axis of two-fold symmetry (model of orthorhombic distortion of octahedra). The results of the calculations plotted in Fig. 4 (curve b) show that in this model of the local atomic structure of a KNbO_3 crystal in the orthorhombic phase, the agreement between the Fourier transform of the calculated EXAFS spectrum and that of the experimental

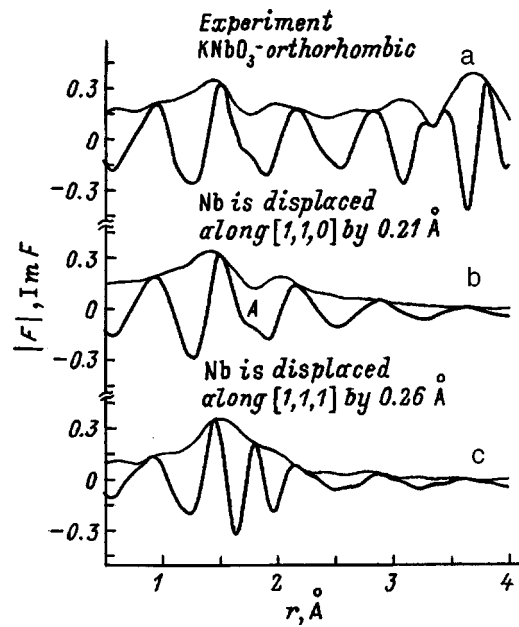


FIG. 4. Moduli $|F|$ (fine lines) and imaginary parts $\text{Im } F$ (thick lines) of Fourier transforms: the function $k\chi^{\text{exp}}(k)$ of the experimental Nb K -EXAFS-spectrum of an orthorhombic KNbO_3 crystal at $T=300$ K (a), the function $k\chi_1^{\text{th}}(k)$ of the theoretical Nb K -EXAFS-spectra calculated for displacements of the Nb atom along the axis of two-fold symmetry by 0.21 \AA (b) and along the axis of three-fold symmetry by 0.26 \AA (c).

spectrum is as good as that in the rhombohedral phase. This result is important in its own right, since it indicates that the similarity between the EXAFS spectra in different phases is not a sufficient basis for concluding that the nearest-neighbor structures of the ionizable atoms in these phases are identical. This result also indicates that the model of a displacement-type of transition for a phase transition from the rhombohedral to the orthorhombic phase in a KNbO_3 crystal does not contradict the EXAFS spectroscopic data. In order to determine whether these results are consistent with the CLG model, we turned our attention to the fact that this model should give the same average displacement of an Nb atom from the center of the oxygen octahedron along the polar axis of two-fold symmetry as the displacement model. In other words, if we wish to reconcile the CLG model (the model of local rhombohedral distortion) with the diffraction data, we must assume that the Nb atom is displaced from the center of the oxygen octahedron along the axis of three-fold symmetry by the distance $\tilde{\Delta}$, whose projection on the polar axis of two-fold symmetry is $\Delta=0.21 \text{ \AA}$ (Fig. 1). It is easy to see that this requires $\tilde{\Delta}=0.26 \text{ \AA}$. Calculations of the EXAFS spectrum for this displacement of the Nb atom along the axis of three-fold symmetry give the Fourier transform of the spectrum shown in Fig. 4 (curve c). This clearly shows that the calculated spectrum differs abruptly from the experimental one, this difference being qualitative.

In order to investigate the sensitivity of the calculated results to the model parameters, we also calculated the spectra for various intermediate models with different displacements of the Nb atom from the nodal point along the x axis, shown in Fig. 1. The results of these calculations made for displacements of 0.04 , 0.06 , and 0.08 \AA together with the

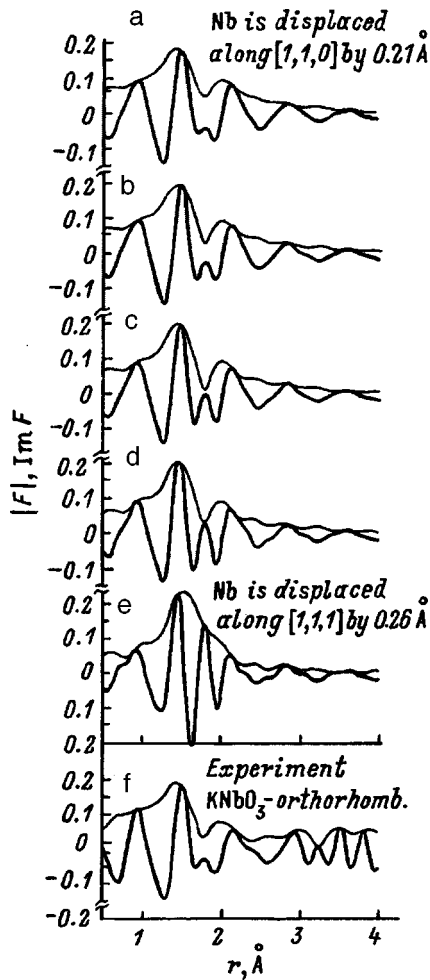


FIG. 5. Moduli $|F|$ (fine lines) and imaginary part $\text{Im } F$ (thick lines) of the Fourier transforms of the function $k\chi_1^{\text{th}}(k)$ of the theoretical Nb K -EXAFS spectra calculated with $\Gamma=8$ eV for displacement of an Nb atom from the nodal point along the x axis by 0 (a), 0.04 (b), 0.06 (c), 0.08 (d), and 0.15 Å (e), compared with the experimental data for orthorhombic KNbO_3 (f) at $T=300$ K.

results obtained in the absence of any displacement along the x axis (the Nb atom lies on the polar axes of twofold symmetry), and also for a displacement of 0.15 Å (displacement along the axis of three-fold symmetry) made for $\Gamma=8$ eV are plotted in Fig. 5 together with the Fourier transform of the experimental spectrum of an orthorhombic KNbO_3 crystal. The results of the calculations made using a fairly wide range of values of the parameters σ^2 and Γ ($\sigma^2=0-0.008$ Å², $\Gamma=0-15$ eV) indicate that the characteristics of the function $\text{Im } F(r)$ remain stable ($F(r)$ is the Fourier transform of the normalized EXAFS function $\chi(k)$) and a comparison of these Fourier transforms with each other and with the experiment shows that the model of local orthorhombic distortion of NbO_6 octahedra gives the best results for moderate values of the parameters σ^2 and Γ obtained by fitting for the orthorhombic phase.

These results suggest that the combined use of data obtained by conventional structure analysis and EXAFS eliminates the possibility of using the pure form of the CLG model to describe the local structure of NbO_6 octahedra in a KNbO_3 crystal. In order to make this model consistent with

the EXAFS data, it would be necessary to assume that the conventional structure analysis gives a highly exaggerated average displacement of the Nb atom from the center of the oxygen octahedron along the polar two-fold axis in the orthorhombic phases of a KNbO_3 crystal (agreement would be achieved for a displacement of 0.15 Å). Since the value of 0.21 Å used by us was obtained by several authors^{6,11} by analyzing x-ray diffraction and neutron diffraction data, there is no serious basis for reexamining this value. Thus, the combined use of conventional structure analysis and EXAFS data suggests that the CLG model cannot be used to describe the phase transitions in a KNbO_3 crystal. This conclusion is consistent with the observation that the values of the thermal parameters determined by neutron diffraction for the orthorhombic and tetragonal phases of the KNbO_3 crystal are considerably lower¹¹ than those which should be observed if the CLG model accurately described the local structure of the high-temperature phases in this crystal. However, a perceptible increase in the thermal parameters on transition from the rhombohedral to the orthorhombic phase, as evidenced by neutron diffraction data,¹¹ indicates that the pure displacement-type transition model also does not accurately describe the experimental data for the transition from the rhombohedral to the orthorhombic phase. Data on the diffuse scattering of x-rays² also indicate that specific local disorder exists in the high-temperature phases of a KNbO_3 crystal. All this evidence suggests that the crystal lattice in a KNbO_3 crystal exhibits complex dynamics which have by no means been exhaustively studied and which will require considerable effort to understand.

Thus, the following conclusions can be drawn on the basis of this study:

1) The conventional method of analyzing EXAFS spectra to study distortions accompanying phase transitions in the local atomic structure of perovskite binary oxides may yield serious errors because the experimental EXAFS spectra can be explained with almost the same accuracy using different assumptions as to the nature of the local distortions in the crystal.

2) Additional information is required to eliminate the ambiguity of the results of analyses of the EXAFS spectra, particularly information on the average coordinates of the atoms in the lattice which can be provided by conventional methods of diffraction structure analysis.

3) The combined use of Nb K -EXAFS spectra and diffraction data for a KNbO_3 crystal in the orthorhombic phase indicates that the local distortions of the NbO_6 octahedrons in the orthorhombic phase are orthorhombic distortions with preferential displacements of Nb atoms along the polar axis of two-fold symmetry.

4) The assumption that the local distortions of the NbO_6 octahedra in an orthorhombic KNbO_3 crystal are rhombohedral, which follows logically from the similarity between the Nb K -EXAFS spectra in the rhombohedral and orthorhombic phases, gives displacements of the Nb atoms along the axes of three-fold symmetry at variance with the diffraction data on the average positions of the Nb atoms in the lattice of an orthorhombic KNbO_3 crystal.

This work was supported by the Russian Fund for Fundamental Research (Grant 95-02-05716-a).

- ¹L. A. Bugaev, V. A. Shuvaeva, and I. B. Alekseenko *Opt. Spektrosk.* **81**, 258 (1996) [*Opt. Spectrosc.* **81**, 231 (1996)].
- ²R. Comes, M. Lambert, and A. Guinier, *Solid State Commun.* **6**, 715 (1968).
- ³G. Kwei, S. Billinge, S. Cheong, and J. Saxton, *Ferroelectrics* **164**, 57 (1995).
- ⁴P. Dougherty, G. Wiederrecht, and K. Nelson, *Ferroelectrics* **164**, 253 (1995).
- ⁵E. A. Stern and Y. Yacoby, *J. Phys. Chem. Solids* **57**, 1449 (1996).
- ⁶N. de Mathan, E. Prouzet, E. Husson, and H. Dezpert, *J. Phys.: Condens. Matter* **5**, 1261 (1993).
- ⁷V. A. Shuvaeva, K. Yanagi, K. Sakaue, and H. Terauchi, *J. Phys. Soc. Jpn.* **66**, 1351 (1997).
- ⁸V. A. Shuvaeva and M. Yu. Antipin, *Kristallografiya* **40**, 511 (1995) [*Crystallogr. Rep.* **40**, 466 (1995)].
- ⁹L. A. Bugaev, V. A. Shuvaeva, I. B. Alekseenko, and R. V. Vedrinskii, *Physica B* **208&209**, 169 (1995).
- ¹⁰L. A. Bugaev, R. V. Vedrinskii, I. G. Levin, and V. M. Airapetian, *J. Phys.: Condens. Matter* **3**, 8967 (1991).
- ¹¹A. W. Hewat, *J. Phys. C.: Solid State Phys.* **5**, 2559 (1973).
- ¹²I. B. Borovskiĭ, R. V. Vedrinskiĭ, V. L. Kraĭzman, and V. P. Sachenko, *Usp. Fiz. Nuak* **149**, 275 (1986) [*Sov. Phys. Usp.* **29**, 539 (1986)].

Translated by R. M. Durham

EPR of the ferroelectric phase transition in $\text{Li}_2\text{Ge}_7\text{O}_{15}:\text{Cr}^{3+}$ crystals

M. P. Trubitsyn, M. D. Volnyanskiĭ, and I. A. Busoul

Dnepropetrovsk State University, 320625 Dnepropetrovsk, Ukraine

(Submitted December 1, 1997)

Fiz. Tverd. Tela (St. Petersburg) **40**, 1102–1105 (June 1998)

A Cr^{3+} EPR study of lithium heptagermanate crystals, $\text{Li}_2\text{Ge}_7\text{O}_{15}$ (LHG), close to the phase transition is reported. Orientation dependences of the spectra in the paraelectric phase of LHG have been measured. An anomalous broadening of the resonant lines accompanied by a crossover in their shape was found in the vicinity of the transition point. Doublet splitting of the EPR lines was observed to occur below T_C as a result of emergence of two structurally nonequivalent positions for Cr^{3+} ions. © 1998 American Institute of Physics. [S1063-7834(98)02906-2]

In the paraelectric phase, the structure of $\text{Li}_2\text{Ge}_7\text{O}_{15}$ crystals belongs to space group D_{2h}^{14} and contains four formula units per unit cell.¹ When cooled below $T_C=283.5$ K, lithium heptagermanate (LHG) crystals transform to the ferroelectric phase^{2,3} with orthorhombic symmetry⁴ C_{2v}^5 . In the vicinity of the phase transition, a soft mode with an anomalously small effective charge was observed by optical⁵ and submillimeter-wave⁶ spectroscopy. The estimated contribution of the soft mode to dielectric permittivity is not more than 10% of the maximum value of ϵ at the transition point.⁶ A study of dielectric dispersion showed the anomaly in ϵ in the vicinity of T_C to be dominated by a relaxation-type mode.⁷ Neutron diffraction measurements contributed to understanding on the microscopic scale.^{8,9} These data^{8,9} permitted one to assign the oscillator mode to rotational vibrations of the $[\text{GeO}_4]^{4-}$ tetrahedra, and the relaxation mode, to the motion of Li^+ ions, which are located in channels of the LHG structure and are only weakly bonded to its germanium-oxygen framework.

Of main interest in EPR studies of structural phase transitions are paramagnetic centers of various nature, which occupy structurally nonequivalent lattice positions.¹⁰ Our earlier EPR study¹¹ dealt with Mn^{2+} centers substituting for Li^+ ions with double oxygen coordination^{8,9} in the LHG lattice. In view of different dynamic properties assigned to the Ge-O framework in the structure and to the sublattice of weakly bonded Li^+ ions, it appeared expedient to study the paramagnetic centers substituting for Ge^{4+} ions in the LHG lattice.

This work deals with EPR spectra of LHG crystals activated with Cr^{3+} ions (0.01 wt %). The spectra were obtained in the X range on a Radiopan SE/X 2547 spectrometer.

Figure 1 shows magnetic-field scans of the spectra in paraelectric phase ($T=298$ K) made in the [010], [100], and [001] planes. One observes spectra of Cr^{3+} ions ($S=3/2$) corresponding to the four magnetically nonequivalent positions of paramagnetic centers in the LHG paraphase structure. The **H** scans reveal two conjugate spectra for each plane, which exhibit the same angular patterns and are shifted by a certain angle ($\pm\alpha$) relative to the crystallographic axes. These spectra are characterized by strongly an-

isotropic resonant-line width and clearly pronounced low-symmetry effects.¹²

The multiplicity $k_m=4$ and the orientation of the magnetic axes of conjugate spectra indicate that Cr^{3+} centers are localized in either C_i or C_1 positions. Taking into account the relative magnitude of the ionic charges and radii of the Cr^{3+} paramagnetic centers and Ge^{4+} and Li^+ ions in the LHG lattice, substitution of the centers for germanium ions appears to be the most likely possibility. According to x-ray diffraction data,¹ the framework of the LHG unit cell is made up of 24 $[\text{GeO}_4]^{4-}$ tetrahedra sharing corners with one another and with four $[\text{GeO}_6]^{8-}$ octahedra. The octahedrally coordinated Ge1 ions occupy positions with local symmetry C_2 and magnetic multiplicity $k_m=2$. The germanium ions located at the centers of the oxygen tetrahedra are localized in three structurally nonequivalent positions Ge2, Ge3, and Ge4 with monoclinic symmetry C_1 and multiplicity $k_m=4$. Our results indicate that local symmetry of the Cr^{3+} paramagnetic centers corresponds to that of the Ge2, Ge3, and Ge4 positions. Allowing Cr^{3+} centers to be surrounded by oxygen tetrahedra, we have to assume equally probable occupation by chromium of all three structurally nonequivalent positions. In this case one should observe three groups of structurally nonequivalent Cr^{3+} spectra, with each consisting of four conjugate spectra; this is, however, at odds with the data of Fig. 1. The multiplicity of the observed spectra ($k_m=4$) suggests that Cr^{3+} ions substitute for Ge1 in the oxygen octahedra, and that the lowering of point symmetry from monoclinic C_2 to triclinic C_1 occurs as a result of local charge compensation of the impurity ion.

EPR spectra of Cr^{3+} centers in LHG crystals were studied before.¹³ A detailed calculation of the principal values and determination of the tensor axis orientation of the Cr^{3+} spin Hamiltonian provided a basis for a model,¹³ by which the effective negative charge of the Cr^{3+} center in the octahedral position Ge1 is compensated by an "excess" interstitial ion Li^+ . Investigation of optical electronic spectra of $\text{LHG}:\text{Cr}^{3+}$ confirmed the model of the pair-dipole center $\text{Cr}^{3+}-\text{Li}^+$ and showed that the excess Li^+ ion lies in the direction of the **a** axis relative to the Cr^{3+} position.

The pattern of the angular scans displayed in Fig. 1 is in

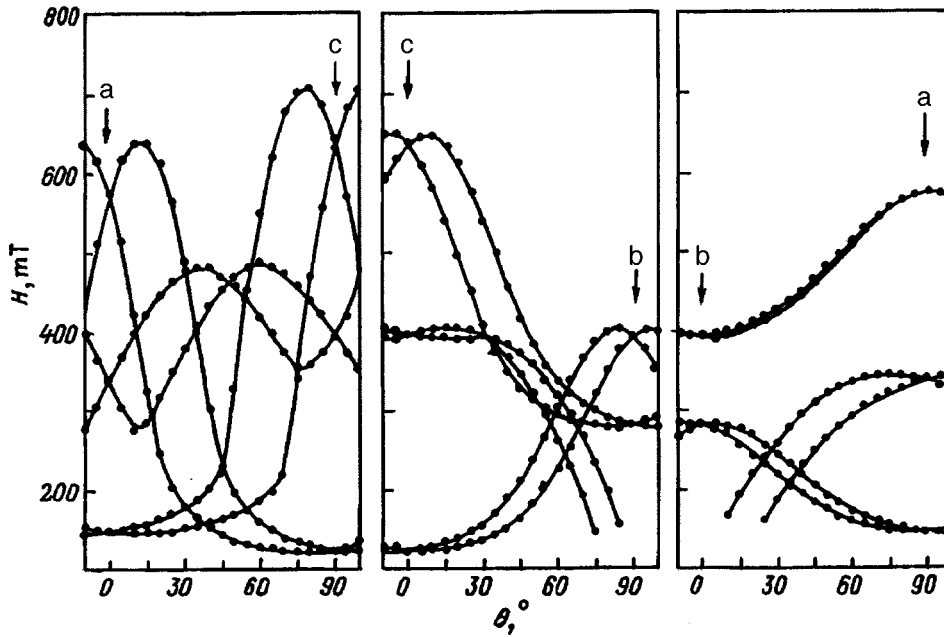


FIG. 1. Magnetic field scans of Cr³⁺ EPR spectra in LHG crystals in crystallographic planes. T = 298 K.

agreement with the EPR angular plots obtained¹³ in the Q range. One may conclude that paramagnetic ions in the LHG:Cr³⁺ single crystals studied by us sit in the same positions, and that the model of the Cr³⁺ centers substantiated in Refs. 13–15 is in accord with our present experimental data.

We studied the temperature dependence of Cr³⁺ spectra close to the main orientations of a dc magnetic field in the vicinity of the ferroelectric transition in LHG crystals. Figure 2a shows the transformation of the low-field resonant line $|M_S| = 1/2 \leftrightarrow 3/2$ for the $\mathbf{H} \parallel \mathbf{a}$ orientation. For the chosen magnetic field direction, the conjugate spectra are indistinguishable in the paraphase, and the given electronic transition produces a single line. As seen from Fig. 2a, as one approaches T_C from above, the line shifts slightly toward high fields and exhibits considerable broadening in the vicinity of the transition point. The temperature dependence of the linewidth, $\delta H(T)$, measured as the distance between the extrema of the first derivative of the absorption line, is shown in Fig. 3. The graph looks as a characteristic λ -shaped anomaly, the linewidth far from T_C is ~ 0.48 mT and increases to ~ 1.15 mT near the transition point.

The increase in width δH is accompanied by a change in the resonant-line shape. At $T = 297$ K (Fig. 2b), the experimental resonant-line profile is close to a Lorentzian. Near T_C the line increases in width, and its shape approaches a Gaussian (Fig. 2b). These data indicate that the anomalous broadening of the EPR lines in the vicinity of the transition is caused by inhomogeneous mechanisms.

As evident from Fig. 2a, at $T_C \approx 283$ K the line splits into two components, which shift under further cooling. The temperature dependence of the positions of the line above T_C and of the split components below T_C is shown in the inset to Fig. 3. Note that for arbitrary orientations of the external magnetic field the transition results in doubling of each of the four spectra which are conjugate in the paraphase. In accordance with Ref. 13, in the polar phase one observes two

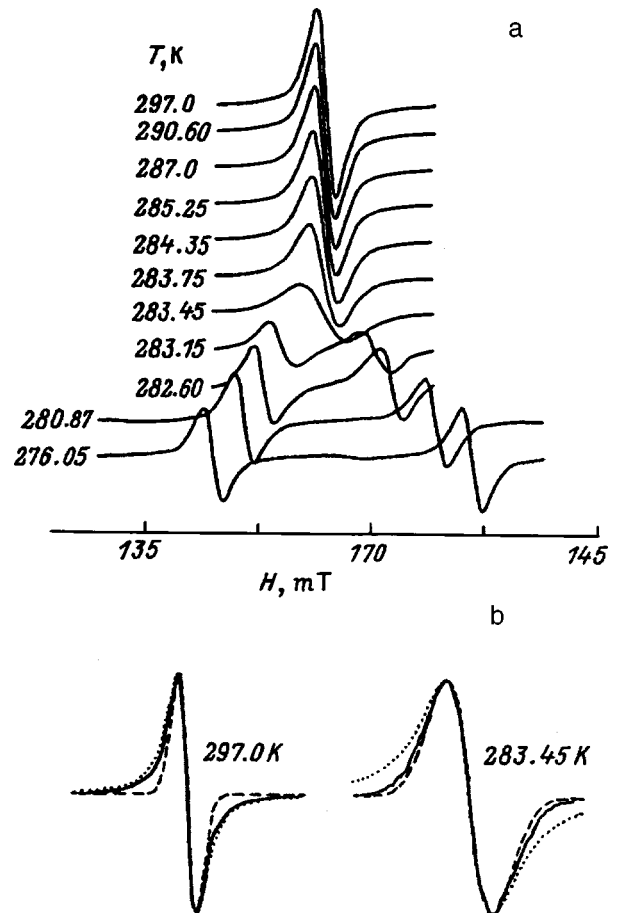


FIG. 2. (a) Temperature-induced transformation of the low-field line $|M_S| = 1/2 \leftrightarrow 3/2$ in the vicinity of the phase transition. $\mathbf{H} \parallel \mathbf{a}$; (b) Resonant-line shape far from the transition and in the vicinity of T_C . Solid line - experiment. Also shown is a Lorentzian (dotted line) and a Gaussian (dashed line) calculated using the experimental width parameters δH . The line intensity at $T = 283.45$ K is magnified 3.2 times.

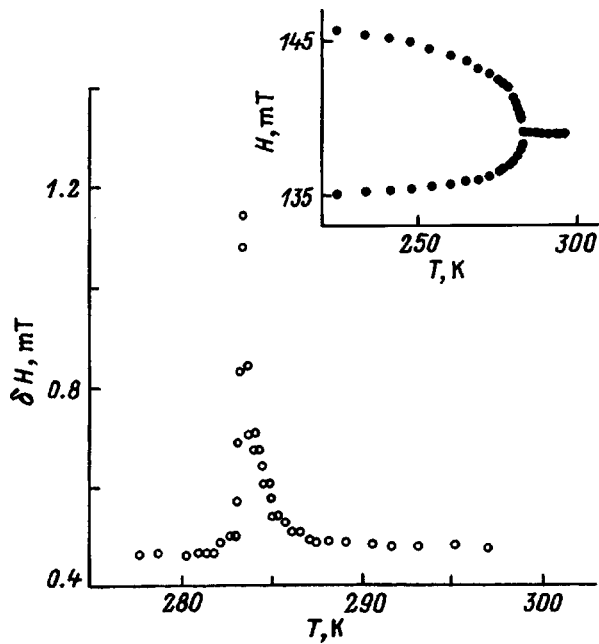


FIG. 3. Temperature behavior of the width of the $|M_S|=1/2 \leftrightarrow 3/2$ line. The inset shows the behavior with temperature of the line position above T_C and of the split components below T_C .

groups of structurally nonequivalent spectra, with each consisting of four conjugate spectra.

It is known that temperature transformation of EPR spectra can result from the following main reasons: 1) local paramagnetic-center vibrations, 2) thermal expansion of the lattice, and 3) squared displacement of paramagnetic centers from their equilibrium positions averaged over all lattice vibrations. The first two factors are not capable of changing the center symmetry and produce any anomalies near a phase transition. Hence the observed inhomogeneous broadening of the EPR lines and their doublet splitting below T_C result from correlated atomic displacements in the local environment of the paramagnetic probe during in the phase transition.

An EPR study of Mn^{2+} ions substituting for Li^+ ions in channels of the LHG lattice showed that the temperature dependences of the local order parameter and of the rms value of fluctuations exhibit an Ising-type critical behavior within a

broad region around the transition point.^{16,17} Mn^{2+} paramagnetic centers are sensitive to structural ordering-type changes, which, according to neutron diffraction data,^{8,9} are assigned to the lithium sublattice of the LHG structure. Cr^{3+} impurity centers are incorporated into the Ge-O framework of the LHG lattice, which is associated with displacement-type structural distortions. The data presented in Fig. 3 suggest that Cr^{3+} ions may serve as an effective probe in studying the ferroelectric transition in LHG. An analysis of the temperature dependence of Cr^{3+} EPR spectra may provide additional information on the critical properties of LHG crystals.

- ¹H. Vollenkle, F. Wittman, and H. Nowotny, *Monatsh. Chem.* **101**, 46 (1970).
- ²S. Haussühl, F. Wallrafen, K. Recker, and J. Eckstein, *Z. Kristallogr.* **153**, 329 (1980).
- ³M. Wada, A. Sawada, and Y. Ishibashi, *J. Phys. Soc. Jpn.* **50**, 1811 (1981).
- ⁴H. Terauchi, S. Iida, Y. Nishihata, M. Wada, A. Sawada, and Y. Ishibashi, *J. Phys. Soc. Jpn.* **52**, 2312 (1983).
- ⁵H. Orihara, M. Wada, and Y. Ishibashi, *J. Phys. Soc. Jpn.* **52**, 1478 (1983).
- ⁶A. A. Volkov, G. V. Kozlov, Yu. G. Goncharov, M. Wada, A. Sawada, and Y. Ishibashi, *J. Phys. Soc. Jpn.* **54**, 818 (1985).
- ⁷M. Horioka, A. Sawada, and M. Wada, *J. Phys. Soc. Jpn.* **58**, 3793 (1989).
- ⁸Y. Iwata, N. Koyana, and I. Shibuya, *Ann. Rep. Res. React. Inst. Kyoto Univ.* **19**, 11 (1986).
- ⁹Y. Iwata, I. Shibuya, M. Wada, A. Sawada, and Y. Ishibashi, *J. Phys. Soc. Jpn.* **56**, 2420 (1987).
- ¹⁰K. A. Müller and J. C. Fayet, in *Structural Phase Transitions II*, edited by K. A. Müller and H. Thomas [Springer-Verlag, Berlin-N.Y., Vol. 45, 1991, p. 1.].
- ¹¹M. P. Trubitsyn, M. D. Volnyanskiĭ, and A. Yu. Kudzin, *Kristallografiya* **36**, 1472 (1991) [*Sov. Phys. Crystallogr.* **36**, 835 (1991)].
- ¹²M. L. Meil'man and M. I. Samoĭlovich, *Introduction into the EPR Spectroscopy of Activated Single Crystals* [in Russian], Atomizdat, Moscow, 1977, 270 pp.
- ¹³A. A. Galeev, N. M. Khasanova, A. V. Bykov, V. M. Vinokurov, N. M. Nizamutdinov, and G. R. Bulka, in *Spectroscopy, Crystal Chemistry, and Real Structure of Minerals and their Analogs* [in Russian], KGU, Kazan, 1990, p. 77.
- ¹⁴S. A. Basun, A. A. Kaplyanskiĭ, and S. P. Feofilov, *Fiz. Tverd. Tela (Leningrad)* **34**, 3377 (1992) [*Sov. Phys. Solid State* **34**, 1807 (1992)].
- ¹⁵S. A. Basun, A. A. Kaplyanskiĭ, and S. P. Feofilov, *Fiz. Tverd. Tela (St. Petersburg)* **36**, 3429 (1994) [*Phys. Solid State* **36**, 1821 (1994)].
- ¹⁶M. P. Trubitsyn, *Fiz. Tverd. Tela (St. Petersburg)* **40**, 114 (1998) [*Phys. Solid State* **40**, 101 (1998)].
- ¹⁷M. P. Trubitsyn, *Fiz. Tverd. Tela (St. Petersburg)* (in press).

Translated by G. Skrebtsov

Effect of γ irradiation on the heat capacity of Rb_2ZnBr_4 in the vicinity of phase transitions

A. U. Sheleg, T. I. Dekola, and N. P. Tekhanovich

Institute of Solid-State and Semiconductor Physics, National Academy of Sciences of Belarus, 220072 Minsk, Belarus

(Submitted July 28, 1997; resubmitted December 8, 1997)

Fiz. Tverd. Tela (St. Petersburg) **40**, 1106–1108 (June 1998)

Heat capacity of Rb_2ZnBr_4 as a function of γ irradiation dose has been measured within the 85–300 K range by the adiabatic calorimeter technique. It is shown that, as the irradiation dose increases, the heat capacity peak in the vicinity of the incommensurate-commensurate first-order phase transition (PT) decreases, and the transition temperature T_c increases. The heat capacity peak in the region of the second-order PT at $T_3=112$ K does not depend on γ irradiation, both in magnitude and in position, just as the heat capacity throughout the remainder of the temperature range studied. © 1998 American Institute of Physics.

[S1063-7834(98)03006-8]

Rb_2ZnBr_4 crystals belong to a large group of water-soluble A_2BX_4 compounds, which exhibit a sequence of phase transitions (PT) with variation of temperature. When cooled, Rb_2ZnBr_4 crystals undergo a second-order transition from paraelectric to incommensurate phase with a modulation wave vector $q_i=(\frac{1}{3}-\delta)c^*$, followed by a first-order transition at $T_c=194$ K from the incommensurate to ferroelectric commensurate phase with a tripling of the unit-cell period along the c axis ($q_c=\frac{1}{3}c^*$).^{1–3} In the low-temperature domain one observes three more PTs at $T_3=112$ K, $T_4=77$ K, and $T_5=50$ K.^{2,3} The PT at $T_3=112$ K is a second-order transition from the ferroelectric to antiferroelectric phase along the b axis, which persists down to $T_4=77$ K.³

It is known that interaction of the modulation wave with

impurities and various lattice defects in crystals with incommensurate phases results in a change of the temperature behavior of some physical properties, a phenomenon becoming particularly manifest in the vicinity of PTs. Among them, heat capacity is the most sensitive among them to a PT in a crystal.

This work reports on a study of the effect of γ irradiation on the heat capacity of Rb_2ZnBr_4 in the vicinity of the first- and second-order PTs ($T_c=194$ K and $T_3=112$ K, respectively). The heat capacity measurements were carried out on an UNTO setup providing automatic temperature control in adiabatic vacuum adiabatic calorimeter during discrete heat supply to the sample. The sample mass was 16.594 g. The sample heating rate was 0.1–0.07 K/min, and was slowed down to 0.03–0.04 K/min in the region of a PT. The

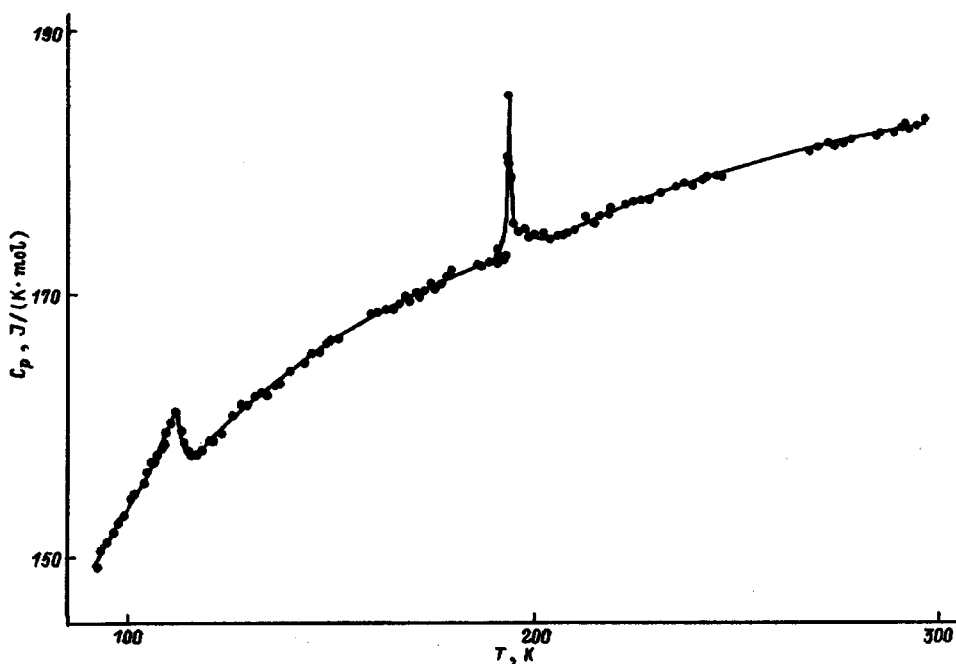


FIG. 1. Temperature dependence of the heat capacity of unirradiated Rb_2ZnBr_4 .

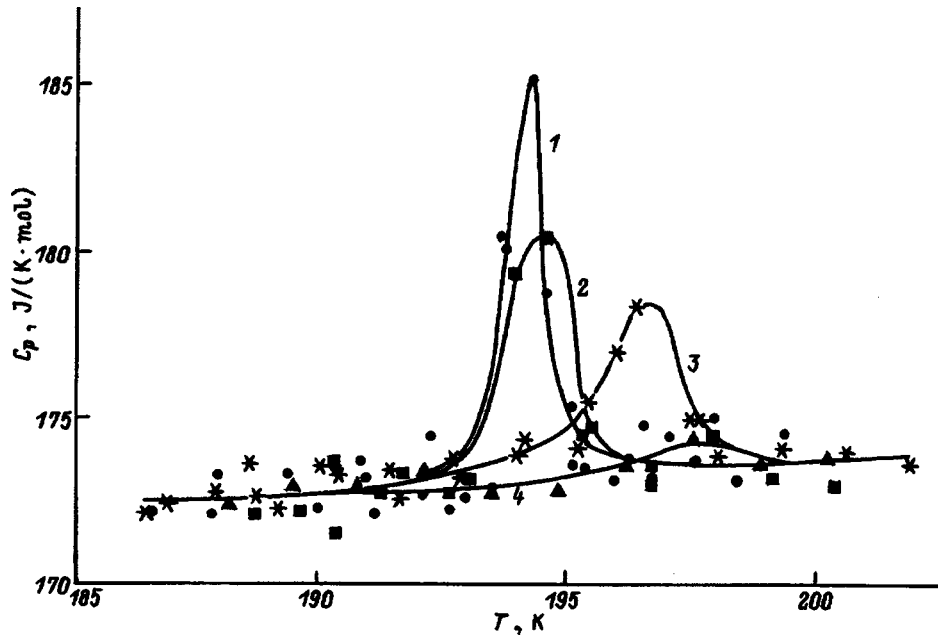


FIG. 2. Variation of the heat capacity of Rb_2ZnBr_4 in the vicinity of the incommensurate-commensurate phase transition vs temperature and γ irradiation dose. 1 — unirradiated Rb_2ZnBr_4 crystal; dose (R): 2 — 10^7 , 3 — 10^8 , 4 — 3×10^8 .

heat capacity was measured in steps of 1.3–2 K, and in the region of a PT, every 0.3–0.4 K. The setup is capable of measuring the heat capacity to within 0.3%. The crystals were irradiated at room temperature with γ rays from a Co^{60} source with an intensity of ≈ 300 R/s.

The results of heat capacity measurements made on unirradiated samples are presented in Fig. 1. Figures 2 and 3 plot the heat capacity as a function of temperature and γ irradiation dose in the vicinity of the first- and second-order PTs, respectively. The temperature dependences of heat capacity are seen to have anomalies in the form of maxima in the vicinity of the incommensurate–commensurate-ferroelectric PT at $T_c = 194$ K, and at $T_3 = 112$ K, where the ferroelectric phase becomes antiferroelectric along the b axis. As the γ irradiation dose increases, the heat capacity decreases in the region of the incommensurate-commensurate phase transition down to a practically complete disappearance of the maximum in the $C_p(T)$ curve at a dose of 3×10^8 R. Be-

sides, the phase-transition point is seen to shift noticeably toward higher temperatures. As evident from Fig. 3, in the region of the second-order PT at $T_3 = 112$ K γ irradiation practically does not affect either the heat capacity or the PT temperature. It should be pointed out that between the PT temperatures the heat capacity does not change under γ irradiation within experimental error.

The experimental data obtained were used to calculate the entropy and enthalpy of the transitions for unirradiated Rb_2ZnBr_4 crystals, which are, respectively, $\Delta S = 0.06$ J/K · mol and $\Delta H = 11.8$ J/mol at $T_c = 194$ K, and $\Delta S = 0.13$ J/K · mol and $\Delta H = 14.2$ J/mol at $T_3 = 112$ K.

To conclude, we have established that γ irradiation depresses the peak in the region of the incommensurate-commensurate PT and increases the transition temperature T_c , whereas, as follows from published data,^{4,5} the transition points of ferroelectrics, as a rule, decrease with increasing irradiation dose. Note that low-temperature x-ray diffraction

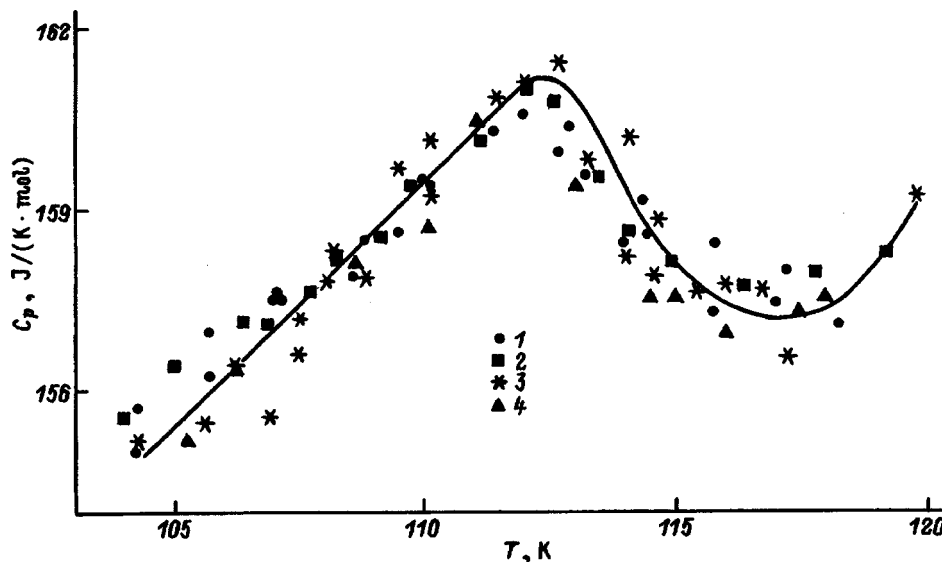


FIG. 3. Temperature dependence of the heat capacity in the vicinity of the second-order phase transition of a Rb_2ZnBr_4 crystal subjected to various γ ray doses. Notation same as in Fig. 2.

data⁶ and acoustic measurements⁷ made on γ irradiated Rb_2ZnBr_4 crystals showed that T_c increases with irradiation dose, which is in agreement with heat capacity data. Such an anomalous behavior of T_c is possibly due to the fact that within the $T_c - (T_c + 10 \text{ K})$ range one observes in Rb_2ZnBr_4 three superstructural modulation waves with different parameters.¹ The mechanism of interaction of these waves both with one another and with radiation defects, as well as the reason for the increase of T_c with γ irradiation dose, remain, however, unclear.

Support of the Fundamental Research Foundation of the Republic of Belarus is gratefully acknowledged.

¹M. Iizumi and K. Gesi, *J. Phys. Soc. Jpn.* **52**, 2526 (1983).

²T. Ueda, S. Iida, and H. Terauchi, *J. Phys. Soc. Jpn.* **51**, 3953 (1982).

³K. Nomoto, T. Atake, B. K. Chaudhuri, and H. Chihara, *J. Phys. Soc. Jpn.* **52**, 3475 (1983).

⁴T. R. Volk, I. T. Rakhimov, V. M. Sarnatskiĭ, E. V. Charnaya, L. A. Shuvalov, and V. A. Shutilov, *Fiz. Tverd. Tela (Leningrad)* **27**, 3613 (1985) [*Sov. Phys. Solid State* **27**, 2176 (1985)].

⁵B. A. Strukov, K. A. Minaeva, and T. P. Spiridonov, *Fiz. Tverd. Tela (Leningrad)* **31**, 288 (1989) [*Sov. Phys. Solid State* **31**, 515 (1989)].

⁶A. U. Sheleg and E. M. Zub, *Fiz. Tverd. Tela (St. Petersburg)* **37**, 3354 (1995) [*Phys. Solid State* **37**, 1843 (1995)].

⁷A. U. Sheleg and E. V. Shesholko, *Inorg. Mater. Inorg. Mater.* **31**, 975 (1995).

Translated by G. Skrebtsov

Electronic structure of deep centers in LiNbO_3

I. Sh. Akhmadullin, V. A. Golenishchev-Kutuzov, and S. A. Migachev

Kazan Physicotechnical Institute, Russian Academy of Sciences, 420029 Kazan, Russia

(Submitted December 19, 1997)

Fiz. Tverd. Tela (St. Petersburg) **40**, 1109–1116 (June 1998)

A model is proposed for photo- and thermally induced processes in lithium niobate crystals. The model is based on the presence of structural defects formed as a result of departure of the crystal composition from stoichiometry. Defects of the type $\text{Nb}_{\text{Li}}-\text{Nb}_{\text{Li}}$ are introduced and the influence of oxidation-reduction heat treatment on the optical characteristics of the crystals is analyzed. © 1998 American Institute of Physics. [S1063-7834(98)03106-2]

Lithium niobate, LiNbO_3 , is one of the most widely used materials in modern solid-state devices for processing and transferring optical information. The possibility of achieving lasing followed by frequency conversion in a single working crystal has also attracted considerable interest. A knowledge of the characteristic features of its optical properties is essential for any applications of lithium niobate, so that numerous studies have examined this aspect.^{1–13} Particular attention has been paid to photo-induced changes in the absorption coefficient and refractive index and to the possibility of specifically varying these. In the course of the investigations, it was established that changes in the optical properties may be controlled by heat treatment under oxidation-reduction conditions.

It was established that after prolonged exposure in an oxygen-deficient atmosphere at $T > 800$ K, the crystals undergo intense darkening in the visible and near ultraviolet. Subsequent heat treatment of the crystals in an oxidizing environment (oxygen or air) at a suitable temperature almost completely bleached the light absorption induced by the reduction annealing. Thermal annealing also significantly alters the photoinduced change in the refractive index.

The authors of Ref. 13 investigated the change in the absorption of light in lithium niobate induced by ionizing radiation. It was established that the induced absorption spectra predominantly contain the same components as under reduction annealing.

Since the thermally and photoinduced changes in the optical characteristics of lithium niobate are highly complex, interest is still being shown in structural and defect centers and their role in the formation of the optical properties of lithium niobate.

An important characteristic of lithium niobate crystals which determines their optical properties to a significant degree, is that the $\text{O}^{2-}-\text{Nb}^{5+}$ bond is predominantly covalent and considerably stronger than the $\text{O}^{2-}-\text{Li}^+$ bond, which is purely ionic. The radii of the Li^+ and Nb^{5+} ions are almost the same. This factor has the result that the composition of an LiNbO_3 crystal can be appreciably deficient in lithium compared with stoichiometric. The crystals possessing the most uniform optical properties have a so-called congruent composition, for which the melt ($\text{Li}_2\text{O}-\text{Nb}_2\text{O}_5$) has the

highest crystallization temperature and the ratio of the ionic concentrations of the cations is $[\text{Li}]/[\text{Nb}]=0.94$. It was also established^{13,14} that any change in the composition toward stoichiometry reduces the thermally and photoinduced effects.

It is well-established that any departure from stoichiometry leads to a high degree of structural disorder in a lithium niobate crystal. Thus, the thermally and photoinduced changes in the absorption are assumed to be mainly caused by the formation of Nb_{Li} substitutional defects (antisite defect), which are deep electron traps.⁹ These defects comprise a pair of niobium ions distributed along the c_3 axis (z axis) at a distance of ~ 3 Å. These $\text{Nb}_{\text{Li}}-\text{Nb}_{\text{Nb}}$ pairs form small-radius polarons with one trapped electron and Heitler–London bipolarons with two trapped electrons.

However, despite the abundance of experimental data, existing models of structural defects (polarons, bipolarons) cannot systematically describe the processes of thermally and photoinduced changes in the optical properties of lithium niobate. The aim of the present paper is to develop a model which also includes new structural defects but can provide a more adequate description of the thermally and photoinduced processes in lithium niobate crystals.

1. METHOD AND RESULTS

We used single crystals of lithium niobate, grown by the Czochralski method, of near-congruent composition. The samples were rectangular parallelepipeds, measuring $6 \times 4 \times 0.7$ mm, with optically polished faces.

From ESR data, the nominally pure crystals also contained other paramagnetic impurities, predominantly Fe^{3+} ($\sim 3 \times 10^{16} \text{ cm}^{-3}$), Mn^{2+} , Cr^{3+} , and Ti^{3+} ($< 10^{15} \text{ cm}^{-3}$).

The method involved a series of oxidation-reduction annealing processes at different temperatures and the use of different media, exposure of the crystals to light at various wavelengths filtered through a large-aperture MDR-12 monochromator, and measurement of the optical absorption and ESR spectra after each thermal or optical treatment. The radiation intensity was monitored using an IMO-2 detector and was of the order of 1 W/cm^2 . The crystals were oxidized in air or oxygen and reduction annealing was carried out in vacuum at a pressure of $\sim 10^{-2}$ Torr.

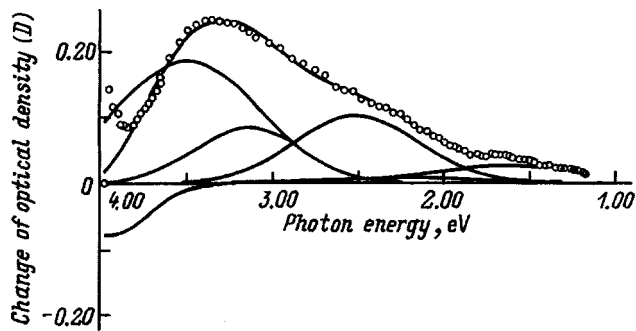


FIG. 1. Optical absorption spectrum of lithium niobate crystals ($T=77$ K) induced by reduction annealing at $T_{\text{ann}}=720$ K. Circles — experimental data, solid curves — results of an expansion in terms of Gaussian components.

The optical absorption spectra were recorded using an SF-46 spectrophotometer for unpolarized light propagating in the direction of the crystal optic axis (z axis) at room temperature ($T\sim 290$ K) and liquid-nitrogen temperature (77 K). The spectral differences induced by the external influences were analyzed by computer.

To obtain the initial data, all the samples were first subjected to long-term ($t\sim 10$ h) annealing in an oxidizing environment at $T_{\text{ann}}=870$ K. All the induced changes were measured from these values since, under this annealing, the optical absorption in the visible range is minimal.

Figure 1 shows the change in the optical density of the lithium niobate crystals at $T_{\text{ann}}=720$ K. The appearance of optical bands with centers at 4.05, 3.48, 3.15, 2.49, and 1.64 eV should be noted in the induced absorption spectra. The 4.05, 3.15, and 2.49 eV bands are attributed to the presence of iron ions and their charge transfer $\text{Fe}^{3+}\rightarrow\text{Fe}^{2+}$ (Ref. 12). After annealing at $T_{\text{ann}}=720$ K for more than 5–6 h, the ESR data indicate that the iron ions almost completely change their valence, which significantly slows the growth of the bands attributed to the iron.

Increasing the reduction annealing temperature to 870 K increases the absorption over the entire range observed (Fig. 2) with the formation of new optical bands centered at ~ 2.3 , 2.9, 3.3, and 4.0 eV. To simplify the following analysis, we give the difference spectrum for $T_{\text{ann}}=870$ and 720 K. This

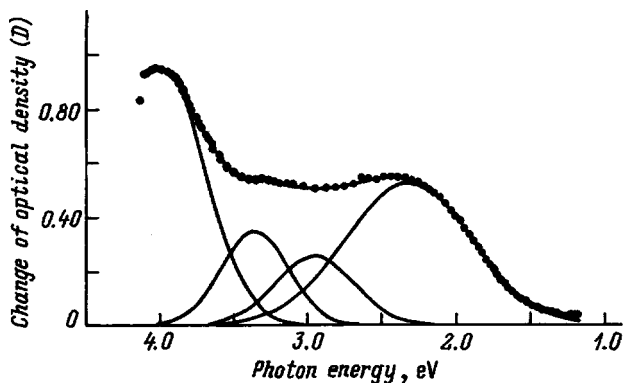


FIG. 2. Optical absorption spectrum of lithium niobate crystals ($T=77$ K) induced by reduction annealing at $T_{\text{ann}}=870$ K.

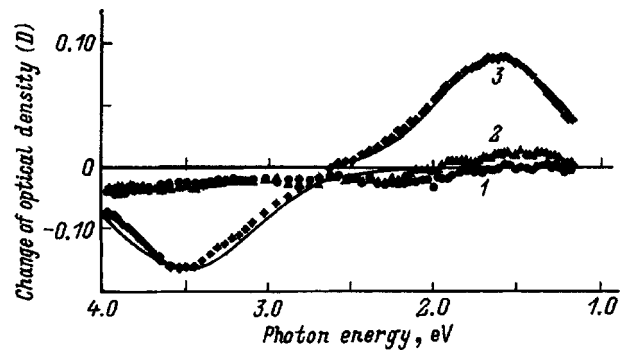


FIG. 3. Change in the absorption of light for lithium niobate samples reduced at $T_{\text{ann}}=720$ K under exposure to optical radiation (77 K): $\lambda_{\text{irrad}}=760$ (1), 546 (2), and 365 nm (3).

removes the absorption assigned to Fe impurities and the 3.48 eV band.

Figure 3 illustrates the changes in the absorption induced in a sample reduced at $T_{\text{ann}}=720$ K by light at different wavelengths. It can be seen that 546 and 760 nm light induces hardly any changes in the absorption whereas exposure to 365 nm (3.4 eV) light causes appreciable bleaching in the 3.48 eV band accompanied by increased absorption in the 1.64 eV band.

The change in the absorption of lithium niobate samples reduced at $T_{\text{ann}}=870$ K induced by exposure to light at different wavelengths is complex (Fig. 4). The light-induced changes in the absorption broadly correlate with those induced by thermal annealing. A more important observation is that exposure to longer-wavelength light also has a significant influence. Note that the appearance of photoinduced absorption in the 1.64 eV band is accompanied by the formation of a ten-component ESR signal ($g_{\parallel}\approx 1.9$) assigned to Nb^{4+} ($4d^1$) ions.

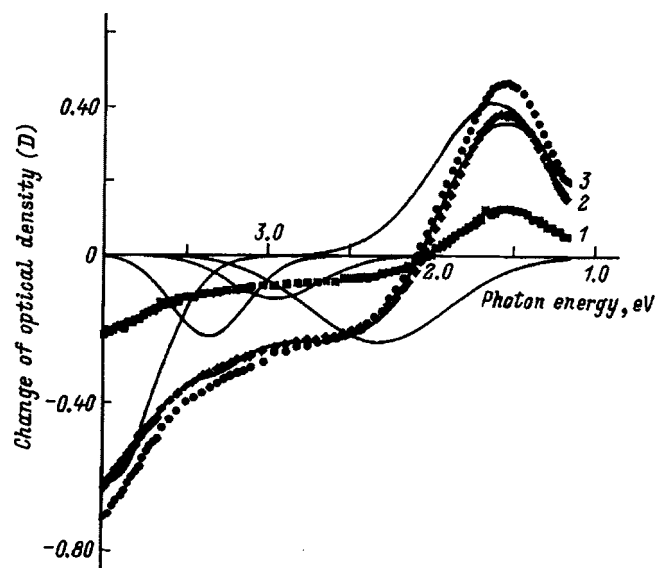


FIG. 4. Change in the absorption of light for lithium niobate samples reduced at $T_{\text{ann}}=870$ K under exposure to optical radiation (77 K): $\lambda_{\text{irrad}}=760$ (1), 546 (2), and 365 nm (3).

An increase in the reduction annealing temperature to 1000 K also has the result that the induced changes cease to be irreversible during subsequent oxidation–reduction cycles. For the investigations we used a lithium niobate sample which had been additionally reduced in vacuum for 8 h at 1150 K prior to the primary oxidation annealing. The following heat treatment conditions were identical to those for the samples reduced at 720 K. As a result, we observed an appreciable (~ 1.5 -fold) increase in the absorption in the 3.48 eV band with the optical absorption bands for the iron impurities still identified.

2. MODEL. DISCUSSION OF RESULTS

The proposed model of photo- and thermally induced processes is based on the existence of structural defects formed in lithium niobate crystals as a result of their nonstoichiometry.⁹ The results of studies of x-ray irradiation of lithium niobate crystals¹³ confirm that the crystal elements responsible for the formation of optical absorption in the range under study are initially present even in oxidized crystals.

An x-ray structural analysis of lithium niobate crystals, reported in Ref. 15, showed that the composition of congruent LiNbO_3 crystals may be described by the formula $(\text{Li}_{1-5x}\text{Nb}_{5x})\text{Nb}_{1-4x}\text{O}_3$, where $x=0.0118$. The need to allow for electrical neutrality leads us to the following composition: $(\text{LiNbO}_3)_{0.941}(\text{Nb}_{\text{Li}}\text{Nb}_{\text{Nb}}\text{O}_3)_{0.0118}(\text{V}_c\text{NbO}_3)_{0.0472}$.

The first component is lithium niobate having the usual composition, the second are fragments which include so-called antisite defects, and the third includes cationic vacancies V_c . An important factor for the proposed model is that the crystals contain around 1% of Nb_{Li} ions in the neighborhood of Nb_{Nb} with a high V_c concentration (around 4.7% of the cation positions). This corresponds to a concentration of $\text{Nb}_{\text{Li}}\text{--Nb}_{\text{Nb}}$ defects (b defect) of around $2 \times 10^{20} \text{ cm}^{-3}$. For the cationic vacancies we therefore find $[V_c] \sim 8 \times 10^{20} \text{ cm}^{-3}$.

According to Ref. 9, the reduction annealing of lithium niobate is accompanied by loss of oxygen by the sample and the released electrons are captured by existing traps. It is also assumed that the cations formed by dissociation of surface LiNbO_3 molecules diffuse into the bulk of the crystal and fill existing cationic vacancies V_c . Capture of an electron from the conduction band by a b defect results in the formation of a small polaron (P) $\text{Nb}_{\text{Li}}^{4+}\text{--Nb}_{\text{Nb}}^{5+}$ which has an optical absorption band of 1.64 eV. Accordingly, the capture of two electrons by a b -defect results in the formation of a bipolaron (B) with a broad optical band in the absorption spectra in the range 1.7–4 eV.

In our proposed model we also introduce defects associated with interaction of Nb ions occupying Li positions ($\text{Nb}_{\text{Li}}\text{--Nb}_{\text{Li}}$) to obtain a more comprehensive description of the experimental observations. The minimum distance between the positions of the Li ions in the LiNbO_3 structure is 3.76 Å (Fig. 5) with three nearest neighbors. Assuming that the Nb_{Li} defects are distributed randomly, we obtain the number of Nb_{Li} ions having nearest neighbors other than Nb_{Li} , which is 3×10^{-4} or 0.03% of the total number of

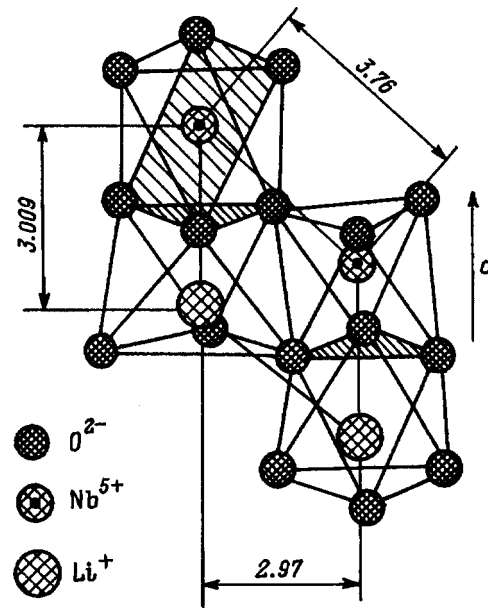


FIG. 5. Structure of lithium niobate crystal.

lithium sites. We call the $\text{Nb}_{\text{Li}}\text{--Nb}_{\text{Li}}$ structural defects q -type defects and their concentration is $[q] \sim 6 \times 10^{18} \text{ cm}^{-3}$.

In the initial (oxidized) state, the crystals contain a certain concentration of b - and q -type structural defects, depending on the degree of stoichiometry. The concentration of free electrons in oxidized lithium niobate is low, only the deepest (q -type) traps are partly filled, and the defects have a minimal influence on the optical properties.

Let us consider the processes accompanying reduction annealing. In the first range of annealing temperatures (700–800 K), the dominant process after cooling is electron filling of deeper traps — q -type structural defects, which is accompanied by increased optical absorption centered at 3.48 eV (Fig. 1).

The second range of annealing temperatures (850–1000 K) is characterized by increased structural rearrangement of the crystal which gives a slightly increased concentration of structural defects (b and q types). Appreciable filling of q -type defects takes place and electrons begin to be captured by b -type defects, which is accompanied by the appearance of optical absorption in the visible and ultraviolet ranges (Fig. 2).

An increase in the reduction anneal temperature to 1000 K and above increases the lithium ion deficit. Some of the resulting cationic vacancies are filled with Nb ions, which increases the concentrations of b - and q -type structural defects. This factor explains the observed increase in the 3.48 eV band in samples which have undergone further reduction at 1150 K.

We shall now analyze the electronic structure of the centers which determine the optical properties of lithium niobate.

3. $[\text{NBO}_3]^{7-}$ CLUSTER

In order to construct a systematic model of the electronic defects in an LiNbO_3 crystal, we need to construct the initial

single-electron states of the valence band and the conduction band. For the general case, this problem was solved numerically in Ref. 16. The qualitative characteristics of the electronic states of a lithium niobate crystal can be described using a simplified model which, however, includes the three most important features of the crystal: the dominant role of the $[\text{NbO}_6]^{7-}$ niobium octahedron in the formation of the actual electronic states,¹⁷ the ferroelectric displacement of the Nb ion from the central (paraelectric) position of the oxygen octahedron, and the crystal symmetry, which we approximate by the C_{3v} group.

In the state basis we include five $4d$ orbitals of niobium and eighteen $2p$ orbitals of oxygen and we neglect O–O interaction. Subject to these simplifying assumptions, the eigenvectors and eigenvalues of the $[\text{NbO}_6]^{7-}$ cluster can be determined accurately, in analytic form. The results of the calculations will not be given in full because of their cumbersome nature. We merely note two consequences of direct relevance to the following analysis: 1) the lowest antibonding state of the cluster (the bottom of the conduction band is associated with this state in the calculations) is a doublet; 2) this doublet is a combination of $4d$ states of niobium and $2p$ states of oxygen as given by

$$\begin{aligned} \Psi_1 = & D_1(E_1)|x^2 - y^2\rangle + D_1(E_2)|xz\rangle + \sum_{n=\pm} [P_1^n(E_1)\Psi_1^n(E_1) \\ & + P_2^n(E_2)\Psi_2^n(E_2) + P_1^n(E_3)\Psi_1^n(E_3)], \\ \Psi_2 = & D_2(E_1)|xy\rangle + D_2(E_2)|yz\rangle + \sum_{n=\pm} [P_2^n(E_1)\Psi_2^n(E_1) \\ & + P_1^n(E_2)\Psi_1^n(E_2) + P_2^n(E_3)\Psi_2^n(E_3)], \end{aligned} \quad (1)$$

where $|x^2 - y^2\rangle, |xy\rangle, \dots$ are the basis $4d$ orbitals of the niobium ion, $\Psi_{1,2}^\pm(E_{1,2,3})$ are linear combinations of the basis $|p_\alpha\rangle$ ($\alpha = x, y, z$) orbitals of oxygen which transform by the irreducible representation E_1, E_2 , or E_3 of the C_{3v} group, $D_{1,2}(E_{1,2})$ and $P_{1,2}^\pm$ are the amplitudes of the appropriate basis states of niobium and oxygen, normalized to unity, and \pm denote the states of the lower and upper oxygen planes of the octahedron to which the C optic axis of the crystal is normal. The random Coulomb fields of the charge compensators present in the crystal lift the orbital degeneracy of the states (1), which will be assumed subsequently.

4. BIPOLARON

It was noted in Ref. 9 that a bipolaron in a lithium niobate crystal is a singlet Heitler–London pair $\text{Nb}_{\text{Li}}^{4+} - \text{Nb}_{\text{Nb}}^{4+}$ of nearest Nb ions whose electronic states are stabilized by local deformation of the lattice. To calculate the spectrum of this system, we consider a simplified model in which two electrons are positioned at two lattice sites: a and b . We write the Hamiltonian of the system in the form

$$\begin{aligned} H = & \sum_{i\sigma} \varepsilon_i n_{i\sigma} + \sum_{ij\sigma} T_{ij}(c_{i\sigma}^+ c_{j\sigma} + c_{j\sigma}^+ c_{i\sigma}) + \sum_i U_{ii} n_{i\downarrow} n_{i\uparrow} \\ & + \sum_{ij\sigma} V_{ij} n_{i\sigma} n_{j\sigma} - \sum_{ij} J_{ij} n_{i\sigma} n_{j\sigma} + \frac{1}{2} \beta \sum_{ij} x_{ij}^2 \\ & + \lambda \sum_{ij\sigma} (n_{i\sigma} + n_{j\sigma}) x_{ij}, \end{aligned} \quad (2)$$

where $n_{i\sigma} = c_{i\sigma}^+ c_{i\sigma}$ is the number of electrons at site i with spin σ , $c_{i\sigma}^+, c_{i\sigma}$ are the creation and annihilation operators of an electron at site i with spin σ , T_{ij} is the hopping integral between sites $i(=a, c)$ and $j(=b, d)$, V_{ij} and J_{ij} are the Coulomb and exchange interactions between them, and U_{ii} is the Mott–Hubbard parameter. The last two terms in Eq. (2) describe the elastic energy of the lattice and the electron–lattice interaction, respectively. The Hamiltonian (2) is a generalization of the Hamiltonian given in Ref. 18 in terms of three aspects: a) the exchange interaction J_{ij} is added, which partially lifts the spin degeneracy and is important for correct allowance for the bipolaron triplet state; b) the single-electron unperturbed energies ε_i and ε_j differ — this is acknowledged to model the inequality of the atomic energies at sites $\text{Nb}_{\text{Li}}^{5+}$ and $\text{Nb}_{\text{Nb}}^{5+}$; c) the number of unperturbed levels at each site is two. This is because, as was shown in the previous section, the lowest antibonding state of the $[\text{NbO}_6]^{7-}$ cluster is a doublet which transforms by the E representation of group C_{3v} . Performing a standard¹⁸ procedure for eliminating of electron–phonon interaction in Eq. (2), we obtain the polaron Hamiltonian

$$\begin{aligned} H = & \sum_{i\sigma} \varepsilon_i^{\text{ef}} n_{i\sigma} + \sum_{ij\sigma} T_{ij}^{\text{ef}} (c_{i\sigma}^+ c_{j\sigma} + c_{j\sigma}^+ c_{i\sigma}) \\ & + \sum_i U_{ii}^{\text{ef}} n_{i\downarrow} n_{i\uparrow} + \sum_{ij\sigma} V_{ij}^{\text{ef}} n_{i\sigma} n_{j\sigma} - \sum_{ij} J_{ij} n_{i\sigma} n_{j\sigma} \end{aligned} \quad (3)$$

with the renormalized parameters^{19,20}

$$\begin{aligned} \varepsilon_i^{\text{ef}} = & \varepsilon_i - \lambda^2 / \beta, \quad U_{ii}^{\text{ef}} = U_{ii} - 2\lambda^2 / \beta, \\ V_i^{\text{ef}} = & V_{ij} - 2\lambda^2 / \beta, \quad T_{ij}^{\text{ef}} = T_{ij} \exp(-\lambda^2 / 2\beta\omega_0), \end{aligned} \quad (4)$$

where ω_0 is the atomic vibration frequency ($\omega_0^2 = \beta/m$).

The electron spectrum described by the polaron Hamiltonian (3) with the parameters (4) was calculated numerically using a two-electron basis. Since the experimental values of the parameters (4) are unknown, their values were chosen for the numerical analyses on the basis of the following reasoning.

The initial value of the parameter $\varepsilon_i^{\text{ef}}$ which includes the chemical potential of the system, may be determined for $\text{Nb}_{\text{Li}}^{4+}$ ions by equating its activation energy W to the electrical conductivity $\sigma(T) = \sigma_0 \exp(-W/kT)$, measured in LiNbO_3 by Nagels.²¹ We then obtain an estimate for $\varepsilon_i^{\text{ef}} \approx -(0.6 - 0.7)$ eV. For $\text{Nb}_{\text{Li}}^{5+}$ ions we shall assume that the ground-state energy is higher than that for an $\text{Nb}_{\text{Nb}}^{5+}$ defect and is in the range 0.05–0.2 eV. This assumption is made because, although the ground state of an Nb_{Li} defect lies in the band gap (i.e., lower than the Nb_{Nb} states), no $\text{O}(2p) \rightarrow \text{Nb}_{\text{Li}}(4d)$ optical charge transfer band is observed with the

TABLE I. Initial values of the parameters of the Hamiltonian (3) (energy in electron volts).

U_{ii}^{ef}	V_{ij}^{ef}	J_{ij}	J_{ii}	T_{ij}^{ef}	$\varepsilon_i^{\text{ef}}$	$\varepsilon_j^{\text{ef}}$
2–3	-0.5–0.0	$< V_{ij} $	$\ll U_{ii}^{\text{ef}}$	0.1–0.2	0.6–0.7	0.4–0.5

energy $h\omega < E_{\text{gap}}$, which should exist in an oxidized crystal. Thus, the parameter $\varepsilon_j^{\text{ef}}$ of a regular $\text{Nb}_{\text{Nb}}^{4+}$ polaron may be estimated as 0.4–0.5 eV, which gives an estimate for the polaron reduction factor $\lambda^2/\beta \approx 0.4–0.5$ eV.

The initial values of the parameters V_{ij}^{ef} , U_{ii}^{ef} , J_{ij}^{ef} , and T_{ij}^{ef} are more difficult to ascertain and thus we used rough estimates for our numerical analyses (although the results seemed to be more sensitive to the values of $\varepsilon_i^{\text{ef}}$). For instance, the typical value of the parameter U_{ii} for free ions is ~ 10 eV or higher.²² However, the covalence and electron polarization appreciably reduce its value to a negative value which stabilizes the Anderson bipolarons.¹⁹ Thus, for Nb ions in an LiNbO_3 crystal the initial value U_{ii}^{ef} was selected in the range 3–4 eV. The interionic Coulomb interaction V_{ij} of two electrons at the distance 3 \AA in the crystal is ~ 1 eV which gives the initial value $V_{ij}^{\text{ef}} \sim 0 - (-0.05)$ eV. This value is reasonable since the condition for bipolaron formation is either polaron attraction (which is typical of crystals with a narrow conduction band¹⁸) or smallness of V_{ij}^{ef} compared with the superexchange interaction which is typically $\sim 0.02–0.1$ eV (Ref. 22). The exchange interaction J_{ij} was varied so that $J_{ij} < V_{ij} \ll U_{ii}$. For high exchange values the bipolaron singlet state was destroyed and converted to a triplet state with spin $S=1$. The resonance integral T_{ij} can be estimated for the $\text{Nb}_{\text{Li}}^{4+} \rightarrow \text{Nb}_{\text{Nb}}^{4+}$ pair by the Harrison method,²³ which gives $T_{ij} \approx 1$ eV for the $4d$ wave functions $|3z^2 - r^2\rangle$ of Nb ions oriented along the bipolaron axis parallel to the C optic axis of the crystal. It then follows from Eq. (4) that T_{ij}^{ef} lies in the range 0.1–0.15 eV ($\omega_0 \sim 0.1$ eV, which corresponds to an atomic vibration frequency of $\sim 10^{13}$ Hz). These estimated initial parameters (4) are given in Table I.

Numerical modeling of the spectrum of the $\text{Nb}_{\text{Li}}^{4+} - \text{Nb}_{\text{Nb}}^{4+}$ pair showed that a singlet bipolaron is stable for the model parameters (3) given in Table II, where a and c are the two components of the E split doublet of the $\text{Nb}_{\text{Li}}^{4+}$ ion and b and d are the two components of the E split doublet of the $\text{Nb}_{\text{Nb}}^{4+}$ ion. We attribute this splitting to the electric fields of compensating defects in the crystal. The numerical analysis showed that, if this splitting is zero, the bipolaron ground state will be a spin triplet which disagrees with the experimental data in Ref. 9. The spectrum of bipolaron energies is given in Table III for the values of the parameters (4) from Table II. This spectrum may be divided into three groups of

TABLE II. Optimized values of the parameters of the Hamiltonian (3) (energy in electron volts).

U_{ii}^{ef}	V_{ab}^{ef}	V_{ac}^{ef}	J_{ab}	J_{ac}	$\varepsilon_a^{\text{ef}}$	$\varepsilon_b^{\text{ef}}$	$\varepsilon_c^{\text{ef}}$	$\varepsilon_d^{\text{ef}}$	T_{ab}
3.0	-0.5	1.5	0.01	0.05	-0.7	-0.55	-0.2	-0.05	0.2

TABLE III. Eigenvalues of the polaron Hamiltonian (3) (energy in electron volts).

l	E_l	l	E_l	l	E_l	l	E_l
0	-1.35	7	-0.88	14	-0.31	21	0.93
1	-1.31	8	-0.82	15	-0.30	22	0.95
2	-1.31	9	-0.81	16	0.59	23	0.95
3	-1.30	10	-0.80	17	0.60	24	1.62
4	-0.93	11	-0.80	18	0.65	25	1.93
5	-0.90	12	-0.35	19	0.65	26	2.62
6	-0.90	13	-0.31	20	0.88	27	2.93

levels. The first includes bipolaron bound states whose energy is lower than the ground state energy $\varepsilon_a + \varepsilon_b = -1.25$ eV of the two polarons. The second group includes those states whose energy E is higher than $\varepsilon_a + \varepsilon_b$, but lower than $\varepsilon_c + \varepsilon_d = -0.25$ eV — the excited state energies of the two polarons. The third group includes the remaining bipolaron states with the energy $E > \varepsilon_c + \varepsilon_d$. Transitions between the first and second groups of levels lie in the infrared while those between the first and third groups lie in the visible. This aspect is discussed in greater detail subsequently.

The wave function of the ground ($E_0 = -1.35$ eV) state is given by the combination

$$\Psi_0 = -0.7|\uparrow_a \downarrow_b\rangle + 0.7|\downarrow_a \uparrow_b\rangle + 0.1|\uparrow_a \downarrow_a\rangle + 0.1|\uparrow_b \downarrow_b\rangle, \quad (5)$$

where the arrows indicate the electron spins in states a and b (the ground states of the $\text{Nb}_{\text{Li}}^{4+}$ and $\text{Nb}_{\text{Nb}}^{4+}$ ions, respectively), and $|\downarrow_a \uparrow_b\rangle \dots$ are the two-electron wave functions. It can be seen from Eq. (4) that ψ_0 is a combination of Heitler–London $\{|\uparrow_a \downarrow_b\rangle, |\downarrow_a \uparrow_b\rangle\}$ and Anderson $\{|\uparrow_a \downarrow_a\rangle, |\uparrow_b \downarrow_b\rangle\}$ bipolarons: the relative amplitudes of these states are determined by the Mott–Hubbard repulsion U_{ii}^{ef} and for negative U_{ii}^{ef} , the ground state is determined by the Anderson bipolarons (negative- U center).

The first excited state ($E_{1,2} = 1.31$ eV, doubly degenerate) is a spin triplet with the wave functions

$$\Psi_1 = |\uparrow_a \uparrow_b\rangle, \quad \Psi_2 = -|\downarrow_a \downarrow_b\rangle. \quad (6)$$

Since the spin triplet (6) is a non-Kramers one, it must be recorded using unconventional methods such as acoustic ESR. However, the population of the triplet (6) at $T = 4$ K (typical temperature of an acoustic ESR experiment) is negligible.

The second excited state E_3 is a singlet with the wave function

$$\Psi_3 = -0.7|\uparrow_a \downarrow_b\rangle + 0.7|\downarrow_a \uparrow_b\rangle. \quad (7)$$

5. Q-POLARON

It has been noted that the concentration of $(\text{Nb}_{\text{Li}}^{5+} - \text{Nb}_{\text{Li}}^{5+})^q$ pairs, where $q = +8$ is the charge of the pair relative to the lattice, in a congruent lithium niobate crystal is $\approx 10^{18} \text{ cm}^{-3}$. Thus, the filling of these traps by electrons should influence the optical spectrum of lithium niobate crystals, at energies higher than the optical dissociation energy of the $\text{Nb}_{\text{Li}}^{4+} - \text{Nb}_{\text{Nb}}^{4+}$ singlet bipolaron with an optical

TABLE IV. Eigenvalues of the polaron Hamiltonian (3) for the four-polaron problem (energy in electron volts).

l	E_l	l	E_l	l	E_l	l	E_l
0	-2.67	16	-0.17	32	0.26	48	0.57
1	-2.65	17	-0.13	33	0.28	49	0.62
2	-2.65	18	-0.11	34	0.33	50	0.63
3	-2.63	19	-0.10	35	0.34	51	0.68
4	-2.63	20	-0.09	36	0.37	52	0.70
5	-2.62	21	-0.03	37	0.40	53	0.71
6	-2.62	22	-0.01	38	0.41	54	0.73
7	-2.60	23	0.03	39	0.42	55	0.75
8	-2.60	24	0.12	40	0.45	56	0.79
9	-2.58	25	0.19	41	0.46	57	0.80
10	-2.58	26	0.20	42	0.47	58	0.83
11	-2.58	27	0.21	43	0.52	59	0.84
12	-2.58	28	0.21	44	0.53	60	0.89
13	-2.58	29	0.22	45	0.54	61	0.94
14	-2.57	30	0.23	46	0.56	62	0.96
15	-2.55	31	0.24	47	0.57	63	0.99

absorption band around 2.33 eV. Numerical modeling of the $\text{Nb}_{\text{Li}}^{4+} - \text{Nb}_{\text{Li}}^{4+}$ bipolaron state using the method described in the previous section revealed that this defect makes no contribution to the optical spectrum of the crystal in the energy range $E > 2.3$ eV. Thus, we analyzed the four-electron defect

$$\text{Nb}_{\text{Nb}}^{4+} - \text{Nb}_{\text{Nb}}^{4+} \\ \text{Nb}_{\text{Li}}^{4+} - \text{Nb}_{\text{Li}}^{4+}, \quad (8)$$

in which, however, for each Nb ion there is only one degenerate level. Thus, this defect is also described by the ‘‘four-site’’ Hamiltonian (2) and (3) but on a four-electron basis. From the set of basis states we excluded states of the type $|\uparrow_a \downarrow_b \uparrow_b \downarrow_c 0_c 0_d\rangle \dots$ with two Anderson bipolarons since their energy is of the order $2U$ and lies above the conduction band. Since the defect (8), whose geometry is shown in Fig. 5, may be considered to be a combination of two $\text{Nb}_{\text{Li}}^{4+} - \text{Nb}_{\text{Nb}}^{4+}$ bipolarons considered above, the results of the previous section can be used for a numerical modeling of the spectrum of this defect. We assumed that since $T_{ij} \sim r^{-5}$ (Ref. 23), where r is the distance between the nearest Nb ions, the resonance integral between a pair of bipolarons is approximately $(3 \text{ \AA})^5 / (3.76 \text{ \AA})^5 \cong 3$ times smaller than the corresponding value for a bipolaron. The results of numerical modeling of the four-electron spectrum are given in Table IV.

The spectrum of Q -polaron states given in Table IV can be divided into two groups of levels. The first group includes bound states of the Q polaron whose energy is lower than the ground-state energy $\varepsilon_a + \varepsilon_b + \varepsilon_c + \varepsilon_d = -2.5$ eV of the four polarons. The second group contains the remaining Q -polaron states with the energy $E > \varepsilon_a + \varepsilon_b + \varepsilon_c + \varepsilon_d$. It can be seen from Tables III and IV that the ground state of the Q polaron is lower than the energy of four polarons (first group) but higher than the energy of two bipolarons $= (-1.35) \times 2 = -2.7$ eV. Thus, the Q -polaron modeled here is four bound polarons.

The wave function of the E_0 ground state of the Q polaron is a combination of singlet four-electron basis functions

$$\Psi_0 \approx -0.47|\uparrow_a \uparrow_b \downarrow_c \downarrow_d\rangle - 0.48|\downarrow_a \downarrow_b \uparrow_c \uparrow_d\rangle \\ - 0.5|\uparrow_a \downarrow_b \downarrow_c \uparrow_d\rangle - 0.5|\downarrow_a \uparrow_b \uparrow_c \downarrow_d\rangle. \quad (9)$$

Here and subsequently we omitted terms with amplitudes < 0.1 for simplicity. The first excited state in the first group is doubly degenerate in terms of energy and is described by the wave functions

$$\Psi_1 \approx -0.28|\downarrow_a \uparrow_b \uparrow_c \uparrow_d\rangle - 0.59|\uparrow_a \downarrow_b \uparrow_c \uparrow_d\rangle - 0.61|\uparrow_a \uparrow_b \downarrow_c \uparrow_d\rangle \\ - 0.28|\uparrow_a \uparrow_b \uparrow_c \downarrow_d\rangle + 0.1|\uparrow_a \downarrow_b \downarrow_c \downarrow_d\rangle + 0.2|\downarrow_a \uparrow_b \downarrow_c \downarrow_d\rangle \\ + 0.21|\downarrow_a \downarrow_b \uparrow_c \downarrow_d\rangle + 0.1|\downarrow_a \downarrow_b \downarrow_c \uparrow_d\rangle \quad (10)$$

and is 0.02 eV higher than the ground state. Since the state (10) is not a Kramers one, it is difficult to observe for the same reasons as the triplet bipolaron (6). A remarkable feature of this spectrum is the wide (~ 2.5 eV) gap in the spectrum between the first and second group of levels. Consequences of this will be analyzed subsequently.

6. OPTICAL PROPERTIES

The optical properties of a bipolaron in this model will merely be discussed qualitatively since quantitative estimates require a knowledge of the parameters of the Hamiltonian (2). An optical transition from the bipolaron ground state to the conduction band is parity-favored. For this we must assume that the conduction-band states, according to the cluster calculations, are linear combinations of $4d$ niobium states and $2p$ oxygen states

$$\Psi_{\text{cond}} = a\Psi_{4d} + b\Psi_{2p}. \quad (11)$$

The wave function of the bipolaron ground state is a Slater determinant, generally constructed from single-electron antibonding states of the $[\text{NbO}_6]$ cluster having the form as in Eqs. (1) and (11). Thus, the matrix element of the dipole moment will be nonzero and is determined by the matrix elements of the parity-favored $4d \rightarrow 2p$ transitions. In comparisons with the experimental data, it should be borne in mind that the maximum of the imaginary part of the permittivity $\varepsilon_2(\omega)$ in LiNbO_3 is shifted up from the bottom of the conduction band by around 1 eV (Ref. 17). This factor is clearly a property common to perovskites.^{24,25} With this in mind, the optical absorption band centered at around 2.3 eV may be interpreted using the proposed model as an optical transition from the ground state of a singlet bipolaron to the conduction band.

In the proposed bipolaron model the distance between the first and third group of levels (Table III) lies in the optical range. From this set we identify transitions with $\Delta S = 0$, where S is the bipolaron spin. We then find that at $T = 0$ optical transitions can take place from the ground state with energy E_0 to states with energies $E_{22} = E_{23}$ (photon energy $h\nu = 2.3$ eV) and $E_{18} = E_{19}$ ($h\nu = 2.0$ eV). Transitions from the bipolaron ground state to the Anderson bipolaron states E_{24} ($h\nu = 2.97$ eV), E_{25} ($h\nu = 3.28$ eV), E_{26} ($h\nu = 3.97$ eV), and E_{27} ($h\nu = 4.28$ eV) are not parity- and spin-forbidden.

These values are similar to the expansions of the experimental spectra (Figs. 2 and 4). The density of these states is half that of the $E_{22}=E_{23}$ and $E_{18}=E_{19}$ states.

It should be noted that, as can be seen from Table 3, the minimum threshold for optical dissociation of a bipolaron to give two polarons lies in the infrared. This corresponds to the optical transition ($\Delta M=1$, $\Delta S=0$) $E_0 \rightarrow E_5$ with $h\nu=0.45$ eV, which is consistent with our data.

Similar reasoning was also applied to analyze the spectrum of a Q polaron. The transition from the Q -polaron ground state corresponds to a broad optical absorption band around 3.5 eV, which was first identified in Ref. 12. A characteristic feature of this absorption band is that it is only bleached for a photon energy $h\nu > 2.5$ eV. In our model this characteristic is attributed to a gap of the order of $E_{16}-E_{15} \approx 2.5$ eV in the Q -polaron spectrum (Table IV).

Thus, qualitative agreement is achieved between the data obtained using the proposed model and the experimental observations.

The authors would like to thank B. M. Khabibullin for useful discussions and S. P. Mironov for assistance with the experiments and analysis of the results.

¹P. J. Jorgensen and R. W. Bartlett, *J. Phys. Chem. Solids* **30**, 2639 (1969).

²W. Phillips and D. L. Staebler, *J. Electron. Mater.* **3**, 601 (1974).

³M. G. Clark, F. J. DiSalvo, A. M. Glass, and G. E. Peterson, *J. Chem. Phys.* **59**, 6209 (1973).

⁴O. F. Schirmer and D. von der Linde, *Appl. Phys. Lett.* **33**, 35 (1978).

⁵Y. Ketchum, K. Sweeney, and L. Halliburton, *Phys. Lett. A* **94**, 450 (1983).

⁶D. M. Smyth, *Ferroelectrics* **50**, 93 (1983).

⁷G. G. De Leo, G. L. Dobson, M. E. Masters, and L. H. Bonjack, *Phys. Rev. B* **37**, 8394 (1988).

⁸H. Donnerberg, S. M. Tomlinson, C. R. A. Catlow, and O. F. Schirmer, *Phys. Rev. B* **40**, 909 (1989).

⁹O. F. Schirmer, O. Thieman, and M. Wohlecke, *J. Phys. Chem. Solids* **52**, 185 (1991).

¹⁰I. Sh. Akhmadullin, V. A. Golenishchev-Kutuzov, S. A. Migachev, and S. P. Mironov, *Fiz. Tverd. Tela (Leningrad)* **32**, 1854 (1990) [*Sov. Phys. Solid State* **32**, 1080 (1990)].

¹¹I. Sh. Akhmadullin, S. A. Migachev, and S. P. Mironov, *Nucl. Instrum. Methods Phys. Res.* **65**, 260 (1992).

¹²I. Sh. Akhmadullin, V. A. Golenishchev-Kutuzov, S. A. Migachev, and S. P. Mironov, *Fiz. Tverd. Tela (St. Petersburg)* **37**, 415 (1995) [*Phys. Solid State* **37**, 224 (1995)].

¹³A. García-Cabanes, J. A. Sanz-García, J. M. Cabrera, F. Agullo-López, C. Saldo, P. Pareja, K. Polgar, K. Raksanyi, and I. Foldvari, *Phys. Rev. B* **37**, 6085 (1988).

¹⁴A. García-Cabanes, E. Dieguez, J. M. Cabrera, and F. Agullo-López, *J. Phys. Condens. Matter* **1**, 6453 (1989).

¹⁵S. C. Abrahams and P. Marsh, *Acta Crystallogr. B* **42**, 61 (1986).

¹⁶W. Y. Ching, Zong-Quan Gu, and Y. N. Xu, *Phys. Rev. B* **50**, 1992 (1994).

¹⁷B. K. Chakraverty, M. Sienko, and J. Bonnerot, *Phys. Rev. B* **17**, 3781 (1978).

¹⁸Zheng Hang, *Solid State Commun.* **65**, 731 (1988).

¹⁹P. W. Anderson, *Phys. Rev. Lett.* **34**, 953 (1975).

²⁰L. Hafid and F. M. Michel-Calendini, *J. Phys. C* **19**, 2907 (1986).

²¹P. Nagels, in *The Hall Effect and its Applications*, edited by C. L. Chien and C. R. Westlake [Plenum Press, New York, 1980, 253 pp.].

²²P. W. Anderson, *Phys. Rev.* **115**, 2 (1959).

²³W. A. Harrison, *Electronic Structure and the Properties of Solids* (Freeman, San Francisco, 1980).

²⁴F. M. Michel-Calendini, H. Chermette, and J. Weber, *J. Phys. C* **13**, 1427 (1980).

²⁵S. A. Prosadeev, *Electronic Structure and Physical Properties of Ionic Covalent Crystals*, [in Russian], Rostov, 1990, 189 pp.

Translated by R. M. Durham

LOW-DIMENSIONAL SYSTEMS AND SURFACE PHYSICS**Self-consistent calculation of Landau levels of a quasi-two-dimensional hole gas at a GaAs/AlGaAs *p*-type heterojunction**

O. V. Volkov

Institute of Solid-State Physics, Russian Academy of Sciences, 142432 Chernogolovka, Moscow Region, Russia

(Submitted June 21, 1997; resubmitted October 29, 1997)

Fiz. Tverd. Tela (St. Petersburg) **40**, 1117–1125 (June 1998)

An efficient method is proposed for the self-consistent calculation of Landau levels of a quasi-two-dimensional hole gas at a GaAs/AlGaAs heterostructure in a perpendicular magnetic field. The method is based on transforming the Schroedinger and Poisson equations to a system of nonlinear differential equations which are then spatially discretized and solved by the method of relaxation. The method proposed is used to model the optical spectra for recombination of the quasi-two-dimensional hole gas with electrons localized at a δ layer of donors in an isolated *p*-type heterojunction. Particular attention is paid to effects associated with the dependence of the wave functions and shape of the potential well on the magnetic field, which have not been considered before. © 1998 American Institute of Physics. [S1063-7834(98)03206-7]

In the course of the last few decades, there has been intense interest in fundamental physical phenomena observed in systems with low dimensionality. However, whereas the properties of quasi-two-dimensional (2D) electronic systems have been extensively studied using various experimental techniques, much less information has been obtained regarding the properties of 2D-hole systems. In essence this is because the effective mass of holes is considerably larger than that of electrons, and the nonparabolicity and anisotropy of the degenerate valence band leads to a complicated structure for the energy spectrum under size-quantization conditions. Despite the fact that a theoretical model for the valence band was constructed almost 40 years ago,^{1,2} the fundamental implications of this model for a system of low dimensionality have been derived and understood only recently.^{3–7} Thus, it was shown in Ref. 5 that Landau levels of a 2D-hole gas are not equidistant and in fact are quite nonlinearly spaced. Nevertheless, it is only recently that this complicated behavior has been observed directly in experiment, due to the smallness of the energy splittings between these levels. For the case of 2D electrons, study of the recombination of the electron gas with holes localized in a δ layer of acceptors located a certain distance from the heterojunction boundary has turned out to be an extremely useful way to probe the system physics.⁸ In this case the luminescence spectrum is determined by the product of the density of states of the 2D-electron gas and the amplitude of the wave function in the δ layer, which determines the matrix element for the transition. Recently, analogous structures were obtained for a *p*-type heterojunction with a δ layer of donors. Studies of the recombination of 2D holes with electrons localized in the δ layer of donors make it possible to

observe directly Landau levels of a hole gas for the first time.⁹ The primary purpose of the analysis given below is to describe such a situation.

The problem of computing the energy spectrum of a 2D-hole gas in a perpendicular magnetic field has been studied by many authors.^{4–7} All the numerical calculations to date have been made using matrix methods based on diagonalizing a Hamiltonian written in a basis made up of a certain set of functions which usually have a simple analytic form. The accuracy of this method depends on the number of basis functions and on the degree of completeness of the set chosen. The problem is especially complicated for the case of an isolated *p*-type heterojunction, since here the quantizing potential itself is determined by the quantities we want to solve for, i.e., the hole wave functions. This makes it necessary to repeat the diagonalization procedure iteratively many times, a procedure that converges very slowly. For this reason, authors usually do not discuss any effects connected with self-consistent calculations, nor do they treat the dependence of the potential shape on the magnetic field. In this paper a computational method is proposed that practically eliminates these inadequacies. The method is based on spatial discretization of the problem by first reducing it to a system of first-order nonlinear differential equations and then to a system of difference equations. This method makes it possible to solve the Schroedinger and Poisson equations simultaneously, thereby obtaining a self-consistent solution without additional iterations. In the sections that follow we will describe this method of solution, derive the starting system of equations, and address the problem of choosing boundary conditions. Then we will discuss the basic results of the calculation within this model and their connection with the observed recombination spectrum in a heterojunction with δ doping.

1. COMPUTATIONAL MODEL

Assume that we have already obtained a system of first-order differential equations corresponding to our physical system. Let us write it in the most general form

$$\mathbf{Y}' - \mathbf{F}(\mathbf{Y}) = \mathbf{0}, \quad (1)$$

where \mathbf{Y} is an N -component solution vector. Let us pick out M equally spaced points z_k a distance h from one another within the spatial interval of interest (where z is the independent variable). Then we can approximate our system of differential equations by an equivalent system of difference equations for the \mathbf{Y}_k values of the function we are looking for at the points z_k :

$$\mathbf{E}_k = \mathbf{Y}_k - \mathbf{Y}_{k-1} - \frac{h}{2}(\mathbf{F}(\mathbf{Y}_k) + \mathbf{F}(\mathbf{Y}_{k-1})) = \mathbf{0}. \quad (2)$$

Let us now define a new $N \times M$ -component solution vector \mathbf{Y} containing all the components of the vectors \mathbf{Y}_k ; then we can write our system in the following simple form: $\mathbf{E}(\mathbf{Y}) = \mathbf{0}$. The general method for solving such a system (the relaxation method) is based on iterating Newton's method. Let us define an error vector $\mathbf{\Delta}_s = \mathbf{E}(\mathbf{Y}_s)$ after the s -th iteration. Then the next solution vector can be written based on the expression

$$\mathbf{Y}_{s+1} = \mathbf{Y}_s - \left[\frac{\delta \mathbf{E}}{\delta \mathbf{Y}} \right]^{-1} \mathbf{\Delta}_s. \quad (3)$$

The Jacobi matrix $\hat{\mathbf{S}} = \delta \mathbf{E} / \delta \mathbf{Y}$ for this problem is block-diagonal in form. We used the efficient algorithm described in Ref. 10 to invert this matrix. The advantages of this approach become more palpable when the problem is not limited to solution of the Schroedinger equation alone, since any other equations in the original system (1) that must be solved in combination with the Schroedinger equation can be incorporated as well. Furthermore, the eigenvalue problem is also solvable by simply including the additional equation $\lambda' = 0$ in the original system, where the eigenvalue λ (the energy in our case) is regarded as a function of the independence variable z . The procedure of iterating the solution of system Eq. (2) using Eq. (3), requires specification of a certain initial approximation. In our case we require a whole series of solutions with different physical properties, each of which should start from a different initial approximation. These are trivial to obtain in the limit of zero magnetic field and a planar quantizing potential with infinite barriers. We then change the parameters step by step so as to approach the limit we want, using the solution obtained at the previous step as an initial approximation for the next step. This procedure ensures that our solution will be continuous and that we can track its properties.

Following Ref. 5, we start from the 4×4 Luttinger Hamiltonian² with an external magnetic field B parallel to the z axis, neglecting terms linear in the quasimomentum⁴:

$$\mathbf{H} = \begin{pmatrix} X^+ - 3Z & S^+ & R^+ & 0 \\ S & X^- - Z & 0 & R^+ \\ R & 0 & X^- + Z & -S^+ \\ 0 & R & -S & X^+ + 3Z \end{pmatrix}, \quad (4)$$

where

$$X^+ = P + Q, \quad X^- = P - Q, \quad Z = \frac{e}{2c} KB,$$

$$P = \frac{\gamma_1}{2}(k_z^2 + k^2), \quad k_{\pm} = k_x \pm ik_y,$$

$$Q = \frac{\gamma_2}{2}(-2k_z^2 + k^2), \quad k^2 = k_x^2 + k_y^2,$$

$$R = -\frac{\sqrt{3}}{2}\bar{\gamma}k_-^2 + \frac{\sqrt{3}}{2}\mu k_+^2, \quad \bar{\gamma} = \frac{1}{2}(\gamma_3 + \gamma_2),$$

$$S = \sqrt{3}\gamma_3 k_z k_-, \quad \mu = \frac{1}{2}(\gamma_3 - \gamma_2).$$

In this case, the wave function vector has the following form (the subscripts denote projections of the spin on the z axis):

$$\Phi = \begin{pmatrix} \phi_{-3/2} \\ \phi_{-1/2} \\ \phi_{+1/2} \\ \phi_{+3/2} \end{pmatrix}. \quad (5)$$

When an external magnetic field B is applied along the direction z , the components of the quasimomentum in the plane no longer commute: $[k_x, k_y] = -ieB/(\hbar c) = -il^{-2}$, where $l = (\hbar c/eB)^{1/2}$ is the magnetic length. Let us introduce ladder operators according to the expressions

$$a^+ = \frac{l}{\sqrt{2}}k_+, \quad a = \frac{l}{\sqrt{2}}k_-, \quad N = a^+ a.$$

It is not difficult to show that these satisfy the relations $[a, a^+] = il^2[k_x, k_y] = 1$. From this it follows that the operator N has eigenvalues $0, 1, 2, \dots$. Let us denote the corresponding eigenfunctions by $\zeta_0, \zeta_1, \zeta_2, \dots$; then these functions satisfy the following relations:

$$a^+ \zeta_{n-1} = \sqrt{n} \zeta_n, \quad a \zeta_n = \sqrt{n} \zeta_{n-1}. \quad (6)$$

Let us now rewrite the Hamiltonian (4) in terms of these ladder operators, neglecting the anisotropic term in R (which contains μ), which allows us to write the solution vector in a finite basis in what follows. As was shown in Ref. 5, inclusion of the anisotropy leads to the appearance of anticrossings among Landau levels with labels that differ by 4. Using the relation $N = (1/2)(l^2 k^2 - 1)$, we can write the Hamiltonian (4) in the following form:

$$\mathbf{H} = \begin{pmatrix} \Phi_n - 3q & b^+ & -d^+ & 0 \\ b & \Phi_l - q & 0 & -d^+ \\ -d & 0 & \Phi_l + q & -b^+ \\ 0 & -d & -b & \Phi_n + 3q \end{pmatrix}, \quad (7)$$

where we have introduced the notation

$$\Phi_h = \frac{k_z^2}{m_h} + \frac{A}{l^2} \left(N + \frac{1}{2} \right), \quad \Phi_l = \frac{k_z^2}{m_l} + \frac{B}{l^2} \left(N + \frac{1}{2} \right),$$

$$q = \frac{K}{2l^2}, \quad b = \frac{2s}{l} k_z a, \quad b^+ = \frac{2s}{l} k_z a^+,$$

$$d = \frac{r}{l^2} a^2, \quad d^+ = \frac{r}{l^2} a^{+2},$$

$$m_h = \left(\frac{\gamma_1}{2} - \gamma_2 \right)^{-1}, \quad m_l = \left(\frac{\gamma_1}{2} + \gamma_2 \right)^{-1},$$

$$A = \gamma_1 + \gamma_2, \quad B = \gamma_1 - \gamma_2,$$

$$r = \sqrt{3} \bar{\gamma}, \quad s = \sqrt{\frac{3}{2}} \gamma_3.$$

Here, m_h and m_l are the doubled effective masses of light and heavy holes. We will look for a solution in the form

$$\Phi = \begin{pmatrix} \zeta_n(x,y) \psi_1(z) \\ -i \zeta_{n-1}(x,y) \psi_2(z) \\ -\zeta_{n-2}(x,y) \psi_3(z) \\ i \zeta_{n-3}(x,y) \psi_4(z) \end{pmatrix}, \quad (8)$$

where ζ_n are functions of the coordinates in the (x,y) plane corresponding to the Landau level with label n (eigenfunctions of the operator N), and ψ_i are functions of z alone that correspond to the various spin projections. This description corresponds to conservation of the sum of the spin and orbital angular momenta [compare with (5)], which holds in the presence of the spin-orbit interaction. Using Eq. (6), we can rewrite the Hamiltonian (7) in the form of a matrix that acts only on the columns of the function $\psi_i(z)$:

$$\mathbf{H} = \begin{pmatrix} \mathcal{E}_0 & -\frac{2Q}{l} \frac{\partial}{\partial z} & N/l^2 & 0 \\ \frac{2Q}{l} \frac{\partial}{\partial z} & \mathcal{E}_1 & 0 & \frac{M}{l^2} \\ \frac{N}{l^2} & 0 & \mathcal{E}_2 & \frac{2P}{l} \frac{\partial}{\partial z} \\ 0 & \frac{M}{l^2} & -\frac{2P}{l} \frac{\partial}{\partial z} & \mathcal{E}_3 \end{pmatrix}, \quad (9)$$

where we have made the substitution $k_z \rightarrow -i(\partial/\partial z)$ and used the notation

$$M = r \sqrt{(n-1)(n-2)}, \quad N = r \sqrt{n(n-1)},$$

$$P = s \sqrt{n-2}, \quad Q = s \sqrt{n},$$

$$E_0 = \frac{A}{l^2} \left(n + \frac{1}{2} \right) - \frac{3K}{2l^2}, \quad E_1 = \frac{B}{l^2} \left(n - \frac{1}{2} \right) - \frac{1K}{2l^2},$$

$$E_2 = \frac{B}{l^2} \left(n - \frac{3}{2} \right) + \frac{1K}{2l^2}, \quad E_3 = \frac{A}{l^2} \left(n - \frac{5}{2} \right) + \frac{3K}{2l^2},$$

$$\mathcal{E}_0 = -\frac{1}{m_h} \frac{\partial^2}{\partial z^2} + E_0, \quad \mathcal{E}_1 = -\frac{1}{m_l} \frac{\partial^2}{\partial z^2} + E_1,$$

$$\mathcal{E}_2 = -\frac{1}{m_l} \frac{\partial^2}{\partial z^2} + E_2, \quad \mathcal{E}_3 = -\frac{1}{m_h} \frac{\partial^2}{\partial z^2} + E_3.$$

Now our problem is to obtain a system of first-order differential equations from this second-order differential operator. The easiest method, i.e., treating the first derivatives ψ'_i as unknown functions, is somewhat inconvenient here since these functions will not be continuous at the boundary between GaAs and AlGaAs. In order to satisfy the requirement of continuity, let us construct new unknown functions by operating on the vector ψ with the velocity operator $v_z = (i/\hbar)(\mathbf{H}z - z\mathbf{H})$. The continuity of the functions v_z will be a consequence of the law of conservation of particle number. Substituting the Hamiltonian of the form

$$\mathbf{H} = A \frac{\partial^2}{\partial z^2} + B \frac{\partial}{\partial z} + C,$$

into the velocity operator, we obtain by analogy with Ref. 11

$$v_z = \frac{i}{\hbar} \left(2A \frac{\partial}{\partial z} + B \right). \quad (10)$$

Now we can write the complete system of first-order differential equations for the functions ψ and $\tilde{\psi} = v_z \psi$. The first four equations are obtained directly from Eq. (10), while the next four are obtained by differentiating the first and substituting the expressions obtained for the second derivatives ψ''

into the original operator (9):

$$\begin{cases} \psi'_1 - m_h (\tilde{\psi}_1 - \frac{Q}{l} \psi_2) = 0, \\ \psi'_2 - m_l (\tilde{\psi}_2 + \frac{Q}{l} \psi_1) = 0, \\ \psi'_3 - m_l (\tilde{\psi}_3 + \frac{P}{l} \psi_4) = 0, \\ \psi'_4 - m_h (\tilde{\psi}_4 - \frac{P}{l} \psi_3) = 0, \\ \tilde{\psi}'_1 - \left[\left(A(n + \frac{1}{2}) - m_l Q^2 - \frac{3}{2} K \right) \frac{1}{l^2} + u - \epsilon \right] \\ \quad \times \psi_1 + m_l \frac{Q}{l} \tilde{\psi}_2 - \frac{N}{l^2} \psi_3 = 0, \\ \tilde{\psi}'_2 - \left[\left(B(n - \frac{1}{2}) - m_h Q^2 - \frac{1}{2} K \right) \frac{1}{l^2} + u - \epsilon \right] \\ \quad \times \psi_2 - m_h \frac{Q}{l} \tilde{\psi}_1 - \frac{M}{l^2} \psi_4 = 0, \\ \tilde{\psi}'_3 - \left[\left(B(n - \frac{3}{2}) - m_h P^2 + \frac{1}{2} K \right) \frac{1}{l^2} + u - \epsilon \right] \\ \quad \times \psi_3 - m_h \frac{P}{l} \tilde{\psi}_4 - \frac{N}{l^2} \psi_1 = 0, \\ \tilde{\psi}'_4 - \left[\left(A(n - \frac{5}{2}) - m_l P^2 + \frac{3}{2} K \right) \frac{1}{l^2} + u - \epsilon \right] \\ \quad \times \psi_4 + m_l \frac{P}{l} \tilde{\psi}_3 - \frac{M}{l^2} \psi_2 = 0, \end{cases} \quad (11)$$

where u is the electrostatic potential and ϵ is the energy eigenvalue. For the case $n=0$, all the components of the wave function (8) except those with spin $-3/2$ equal zero. In this case, only the first and fifth equations remain in the system (11), and the state is a pure spin state. For $n=1$, there are two, and for $n=2$ there are three nonzero spin components, and system (11) contains four and six equations, respectively. These have two or three solutions, corresponding to different spin sublevels. All the remaining states have four nonzero spin components in all, and the system (11) admits four different solutions. Nevertheless, in the limit $B=0$ all the solutions become pure with respect to spin. The spin projection corresponding to the nonzero component of the wave function that remains in this limit can also be assigned to a Landau level. In this case, the solutions with spin $\pm 3/2$ will correspond to heavy holes, while those with spin $\pm 1/2$ correspond to light holes. Following Ref. 12, we will use, along with the Landau level label N , an additional label i for the component $\zeta_i(x,y)$ that dominates the solution vector (8) in the limit $B \rightarrow 0$, i.e., $n, n-1, n-2, n-3$ for states with spin $-3/2, -1/2, +1/2, +3/2$ respectively. In this system of notation, all the Landau levels have four spin sublevels apiece, with two corresponding to heavy and two to light holes.

In order to obtain a complete system of equations that describe the problem under study, we should include in the system the Poisson equation for the potential u , which is a second-order equation. We can transform it to a first-order equation by integrating over the coordinate z . The integral of the square of the wave function which enters into this equation will be used as yet another unknown function χ which satisfies the equation $\chi' = |\psi|^2$. Finally, the last equation is for the eigenvalue ϵ . Thus, we obtain

$$\begin{cases} u' + 4\pi \frac{e^2}{\epsilon} [n_s(p_l \chi + \rho_l - 1) + N_i z - N_s] = 0, \\ \chi' - \psi_1^2 - \psi_2^2 - \psi_3^2 - \psi_4^2 = 0, \\ \epsilon' = 0. \end{cases} \quad (12)$$

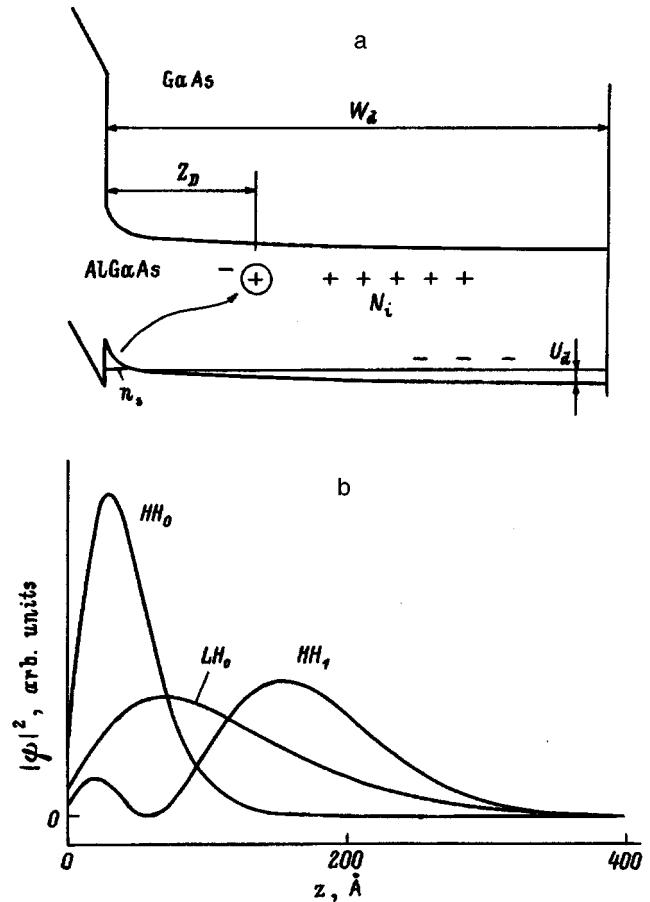


FIG. 1. a) Structure of bands near the heterojunction and basic model parameters. b) Square of the wave function in zero magnetic field plotted versus distance to the heterojunction for the size-quantized subbands HH_0 , LH_0 and HH_1 .

Here we have introduced the following notations: n_s is the density (per unit surface area) of the hole gas, ϵ is the dielectric permittivity, l is a label that enumerates a given energy level, p_l is the fraction of the overall number of holes that belongs to the l -th energy level ($\sum p_l = 1$), χ is the integral of the wave function density ($\chi(z \rightarrow -\infty) = 0$, $\chi(z \rightarrow +\infty) = 1$) and ρ_l is the integral of the wave function density averaged over all the remaining levels, i.e., $\rho_l = \sum_{i \neq l} p_i \chi_i$, N_i is the bulk density of charged impurities in the depletion layer, and N_s is the total number of charged impurities in the depletion layer per unit heterojunction area. For this we have $N_s = W_d N_i$, where W_d is the width of the depletion region.

As is well-known, under conditions of steady-state photoexcitation the potential behind the heterojunction very rapidly becomes flat due to neutralization of the depletion layer charge.¹³ In this case, the quasi-Fermi level of the holes measured from the top of the valence band will equal half the binding energy of an acceptor: $U_d \approx 15$ meV (Fig. 1a). The width of the depletion layer can be estimated from the first equation in (12) if we do not include the hole charge and impose the equation $u(W_d) = U_d$. Thus, we obtain $W_d = (U_d \epsilon / 2\pi e^2 N_i)^{1/2}$. For $N_i \approx 10^{15} \text{ cm}^{-3}$ this gives $W_d \approx 1500 \text{ \AA}$.

It is possible to solve Eqs. (11) and (12) using the relaxation method described above only along a finite segment of

the z axis. It is convenient to pick as this segment the region of width W_d between the heterojunction boundary and the region of constant potential. As we shall show below, for a constant potential there exists a simple algorithm for constructing boundary conditions for the wave function that takes into account its penetration of the barrier. In this case, for the left-hand boundary, i.e., in AlGaAs, we also shall assume the potential is a constant, since the interval over which it varies considerably exceeds the penetration depth of the wave function. In this approximation the wave function $\mathbf{y} = \{\psi, \bar{\psi}\}$ is a solution to the differential equation $\mathbf{y}' + A\mathbf{y} = \mathbf{0}$ with a matrix A that is independent of z . The boundary conditions required to solve Eqs. (11) and (12) on the interval $[0, W_d]$ are made up to two parts. First of all we should guarantee that the wave function attenuates at the barrier. For this we must obtain matrix projection operators onto the subspaces of eigenvectors of the matrix A whose eigenvalues have positive and negative real parts. It is easy to obtain a matrix \tilde{A} (as the solution to the equation $\tilde{A}^2 = A^2$) that differs from A only by the sign of certain eigenvalues. Let us choose these signs such that the real parts of all the eigenvalues will be positive. Then the matrix projection operators are obtained according to the expression $A^\pm = A \pm \tilde{A}$. The second boundary condition includes the integral of the wave function density χ . At the right edge of the integral we can set this integral equal to unity, since the amplitude of the wave function is negligibly small there. However, for the right-hand boundary we require an exact computation. In the most general case $\chi = \int y^T D y dz$, where D is a quadratic form. The problem reduces to calculating the integral

$$\int_0^\infty y^T D y dz = y_0^T I_0^\infty(A, D) y_0,$$

where I_0^∞ is the matrix of the unknown quadratic form. When the matrix A is z independent, we can write the solution vector y with the help of a matrix exponential, by which we understand the sum of the corresponding series, as follows: $y(z) = e^{-Az} y_0$. Then $I = \int e^{-ATz} D e^{-Az} dz$. Integrating by parts and taking into account that during the integration we have $e^{-Az} \rightarrow 0$ at the infinite limit, we obtain the following recursion relation that allows us to compute I_0^∞ to any pre-specified accuracy:

$$I_0^\infty(A, D) = \frac{1}{2} D A^{-1} + \frac{1}{2} I_0^\infty(A, D - A^T D A^{-1}). \quad (13)$$

Now we can write the necessary boundary conditions at the left and right boundaries in the following form:

$$\begin{cases} A_0^+ y_0 = 0, \\ \chi_0 - y_0^T I_0 y_0 = 0, \\ u_0 = 0, \end{cases} \quad \begin{cases} A_1^- y_1 = 0, \\ \chi_1 = 1, \end{cases} \quad (14)$$

where the labels 0, 1 denote parameters that are computed at the left- and right-hand boundaries respectively. The procedure for self-consistent calculation of the shape of the potential requires computation of the integrated density function $\rho_l(z)$ and the occupation numbers p_l at each magnetic field

step. The occupation numbers should be calculated from the capacity of the Landau levels, which depends on magnetic field. In this case it is understood that the occupation factor ν is smaller than the total number of levels M involved in the calculation. In the range of magnetic fields where this condition is not satisfied, we can set all the p_l equal to M^{-1} as a first approximation. However, this approach leads us to a completely incorrect result in the limit of zero magnetic field, since in this case all the holes will have $\mathbf{k} = 0$. In order to resolve this problem, we make use of the following concept. At a certain magnetic field B_x , where $\nu < M$, let us fix the factor $(2N+1)/(2l^2)$ in the Hamiltonian and decrease the magnetic field while keeping all the occupation numbers p_l constant. In the limit $B \rightarrow 0$ this corresponds to $N \rightarrow \infty$, where the level N transforms into a state with $(k^2/2) = (2N+1)(eB_x)/(2\hbar c)$. The two spin sublevels transform into two spin dispersion branches.^{4,6} Equal occupation numbers of Landau levels will correspond to equal fractions of states that are equidistant with respect to k^2 . In this case we will not necessarily obtain the exact value of the Fermi energy in zero field, but the approximate shape of the potential well will be entirely satisfactory. The shape of the potential well in the range $0 < B < B_x$ can be kept in memory and used for the next calculation of energy levels.

In order to compare the results of this calculation with data from optical experiments, it is necessary to obtain expressions for the quantities observed in these experiments, i.e., the intensity and degree of polarization of the recombination light. We shall ignore the actual shape of the wave function of an electron bound to a donor, which is similar to the ground state of a hydrogen atom, and approximate it by an inverse-exponential dependence in the z direction: $|e_D\rangle = \exp(-|z - z_D|/a_D)$, where z_D is the coordinate of the δ -layer and a_D is the Bohr radius. To accuracy up to a numerical factor, the intensity of luminescence in the $\sigma+$ and $\sigma-$ polarizations for a level with label l can be written in the form

$$\begin{cases} I_l^+ = p_l \left[\frac{3}{4} \langle \psi_1 | e_D^- \rangle + \frac{1}{4} \langle \psi_2 | e_D^+ \rangle \right], \\ I_l^- = p_l \left[\frac{3}{4} \langle \psi_4 | e_D^+ \rangle + \frac{1}{4} \langle \psi_3 | e_D^- \rangle \right], \end{cases} \quad (15)$$

where $|e_D^\pm\rangle$ are wave functions of an electron in the z direction with two directions of spin; the matrix elements $\langle \psi_i | e_D^\pm \rangle$ are understood to be integrals over the variable z . Here we have taken into account that the optical transition matrix element connected with the spin is three times larger for heavy holes than it is for light holes.¹⁴ In this case the selection rule for the spins is the following: the difference between spins of an electron and hole should equal ± 1 [compare Eqs. (8) and (5)]. Neglecting the spin splitting of the electron and its polarization, we can set $|e_D^\pm\rangle = |e_D\rangle$, and then the total intensity of circularly polarized light will equal

$$I_l^\sigma = \frac{p_l}{4} [3 \langle \psi_1 | e_D \rangle + \langle \psi_2 | e_D \rangle + \langle \psi_3 | e_D \rangle + 3 \langle \psi_4 | e_D \rangle], \quad (16)$$

while the degree of polarization is

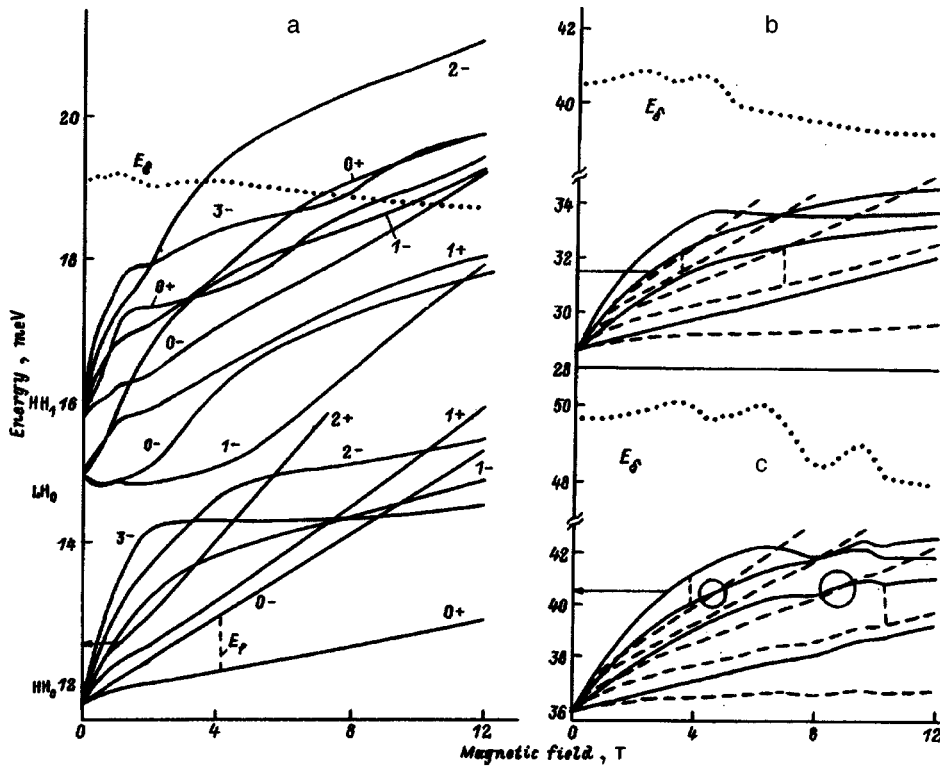


FIG. 2. a—Energy levels of a 2D hole gas plotted versus magnitude of the magnetic field for three size-quantized subbands at a concentration of $1 \times 10^{11} \text{ cm}^{-2}$. Also shown is the position of the Fermi level E_f and the magnitude of the electrostatic potential at the δ layer U_δ . The position of the Fermi level in zero magnetic field is denoted by arrows. b, c—Energy levels of the ground-state heavy-hole subband at concentrations of 5×10^{11} and $7.5 \times 10^{11} \text{ cm}^{-2}$ respectively. Also shown is the dependence of U_δ on magnetic field, which reflects the filling and emptying of levels with different spins, denoted by solid (–) and dotted (+) curves. The circles denote the pinning region of the energy levels.

$$\rho_l = \frac{I_l^+ - I_l^-}{I_l^+ + I_l^-} = \frac{3\langle\psi_1|e_D\rangle + \langle\psi_2|e_D\rangle - \langle\psi_3|e_D\rangle - 3\langle\psi_4|e_D\rangle}{3\langle\psi_1|e_D\rangle + \langle\psi_2|e_D\rangle + \langle\psi_3|e_D\rangle + 3\langle\psi_4|e_D\rangle}. \quad (17)$$

For linearly polarized light, the difference in spins should be zero, and the spin matrix element should equal $1/2$.¹⁴ Accordingly, we obtain for the intensity $I_l^\pi = (p_l/2)[\langle\psi_2|e_D\rangle + \langle\psi_3|e_D\rangle]$. In these calculations we start from the following choice of parameters⁶: $\gamma_1 = 6.85$, $\gamma_2 = 2.1$, $\gamma_3 = 2.9$, $K = 1.2$, and $\varepsilon = 12.5$.

2. RESULTS AND DISCUSSION

The calculations show that for the chosen values $U_d = 15 \text{ meV}$ and $N_i = 10^{15} \text{ cm}^{-3}$ (Fig. 1a) three size-quantized levels are present in the potential well: a lower heavy-hole level HH_0 , a lower light-hole level LH_0 , and the first size-quantized heavy-hole level HH_1 . Figure 1b shows the dependence of the square of the wave function $|\psi|^2 = \psi_1^2 + \psi_2^2 + \psi_3^2 + \psi_4^2$ on the coordinate z for zero magnetic field. The Landau levels for these three size-quantized subbands in the range of magnetic fields from 0 to 12T at a concentration of $n_s = 1 \times 10^{11} \text{ cm}^{-2}$ are shown in Fig. 2a. This figure shows the position of the Fermi level E_f . It is clear from the figure that the pure-spin Landau level $0-$ in the HH_0 subband is not the lowest in energy, since the level $0+$ is located considerably below it. Out of the entire set of levels only $0-$ remains more or less linear over the entire range of magnetic fields: its deviation from linearity is due only to changes in the shape of the potential well. The largest nonlinearity in the HH_0 subband is for level $N-$ (for $N > 0$), which increases

with increasing N . In Fig. 3 we show the dependence of the square of the wave function $|\psi|^2$ on coordinate z for Landau levels $H_0 3-$, $L_0 0+$ and $H_1 3-$, i.e., the three subbands, in fields 1, 5, and 12T. It is clear from this figure that the nonlinearity of the $N-$ level in the HH_0 subband is unambiguously associated with the strong dependence of the wave function on magnetic field. Conversely, the level $N+$ behaves practically linearly with respect to field. Its wave functions differ only slightly from the wave function $0-$ over the entire range of magnetic fields.

The light-hole Landau levels of the subband LH_0 differ by a still larger nonlinearity even in the range of small fields. Qualitatively this is explained by the presence in the Hamiltonian (9) of terms proportional to $l^{-1} = \sqrt{B}$, which act on the wave function component with spin $\pm 1/2$ and are dominant in the small-field range. In this case, even the sign of the g factor for light holes turns out to be opposite the sign of the g factor for heavy holes: levels with negative projection of the spin lie lower in energy. Furthermore, levels $0-$ and $0+$ have larger energy than $1-$ and $1+$ (although for higher labels this is no longer true). This anomaly is probably explained by the fact that these levels have an incomplete set of spin components. As is clear from Fig. 3, the wave function for level $0+$ changes significantly with increasing magnetic field, its maximum shifts to the right, which also causes an increase in energy. The other levels behave analogously. The figure reveals the nonmonotonic character of the change in shape of the wave function as well, connected with the appearance of new zeros as the magnetic field increases. This feature, which is characteristic of all the hole levels except the few with an incomplete set of spin components, can be described as follows: the number of zeros of the wave function increases continuously with increasing magnetic field

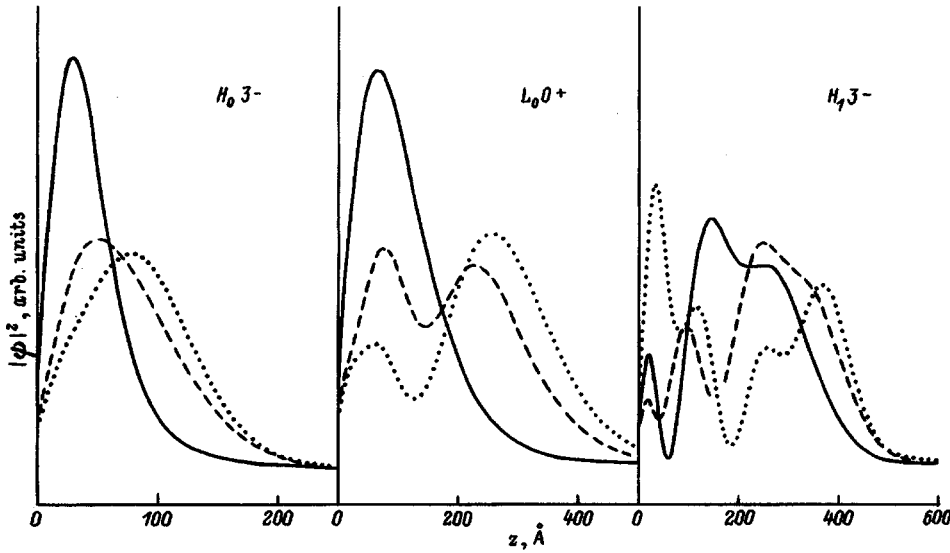


FIG. 3. Square of the wave function plotted against distance to the hetero-junction for Landau levels of three size-quantized subbands in magnetic fields of 1T (solid curve), 5 T (dashed curve), and 12 T (dotted curve) at a concentration of $5 \times 10^{11} \text{ cm}^{-2}$.

roughly as \sqrt{B} , with a coefficient that depends on the label of the level. This is explained qualitatively by the presence of a term with $S \sim k_z k_-$ in the Hamiltonian (4), which mixes the motion in the plane of the potential well with the motion normal to it. If, however, we revert to the dispersion law for zero magnetic field,³ then the behavior of the new zeros will be connected with the appearance of anticrossings of various size-quantized subbands. The Landau levels are constructed out of states with $k^2 \sim B$, while the energy of the size-quantized subbands is proportional to n^2 . Accordingly, the anticrossings appear for $k^2 \sim n^2$, from which it is clear that the number of zeros should increase like k and \sqrt{B} . The Landau levels of the HH_1 subband have a still more complicated structure. Here the g factor again has a reversed sign, but it does not depend as strongly on magnetic field as for the case of the light holes. This phenomenon is apparently explained by the interaction with the low-lying subband of light holes. Although essentially the Landau levels of various subbands do not have sharply expressed anticrossings and can intersect each other, the overall character of their field dependence reflects anticrossings that existed in the dispersion. The wave functions of Landau levels of this subband begin to depend strongly on magnetic field even at fields of 1T (Fig. 3). This probably reflects the increasing importance of the cross term $S \sim k_z k_-$ in the Hamiltonian (4) as k_z increases.

As the concentration of the hole gas increases, the change in the shape of the wave functions in a magnetic field begins to affect the shape of the potential well more and more strongly, since levels turn out to be occupied with larger and larger labels for the same field. In order to estimate the scale of this shape change of the potential, in Fig. 2 we show the magnetic field dependence of the potential for the δ -layer $U_\delta = u(z_D)$ by a dotted curve. At a concentration of $5 \times 10^{11} \text{ cm}^{-2}$ (Fig. 2b), the occupation of level $N-$ of the subband HH_0 is found to have a strong effect on the shape of the potential well in the range of fields where its wave functions begin to shift to the right due to the appearance of new zeros. Occupation of this level turns out to leads

to broadening of the potential well and to an increase in U_δ and the energy of the higher-lying size-quantized subbands due to the overall increase in the difference of potentials between the left and right edges of the potential well. When the Fermi level eventually passes through this level, its emptying is accompanied by an abrupt change in the shape of the well and a corresponding decrease in the energy of the higher-lying levels. It is clear from Fig. 2b that the oscillations in fields of 2.5 and 4.5T are unambiguously related to emptying of Landau levels $2-$ and $1-$ respectively. The subsequent smooth falloff in U_δ at large fields is apparently connected with the fact that the wave function of level $0+$ has a tendency to be compressed with increasing magnetic field. One more interesting phenomenon connected with changes in the shape of the potential well takes place when levels $N-$ and $M+$ intersect while the Fermi level lies within one of the two. At a concentration of $7.5 \times 10^{11} \text{ cm}^{-2}$ (Fig. 2c) this happens twice: in a field of 4.7T, where levels $2-$ and $4+$ intersect, and in a field of 9T, where levels $1-$ and $2+$ intersect. As the hole levels intersect, their populations begins to redistribute. As a result, the occupation of level $N-$ increases, while that of $M+$ decreases. However, since the wave function of level $N-$ is considerably broader than that of $M+$, this leads to a change in the shape of the potential well, which is apparent in the increase in U_δ . However, because the wave function of level $N-$ is considerably broader, it reacts strongly to this change, and its energy increases. The feedback that arises decreases the occupation of this level, and as a result a pinning of these two levels takes place: within a certain interval of magnetic field they remain very close to one another, and only the occupation of the levels changes. All of this is accompanied by the appearance of distinctive features in U_δ and in the energy of the higher-lying levels. Of course, a correct calculation of this situation requires choice of a specific hole temperature. The scheme described above for calculating the occupation numbers p_l is implicitly zero-temperature, and leads to computational instability in the case of pinning. The simplest method of removing this instability was used, i.e., introducing a linear

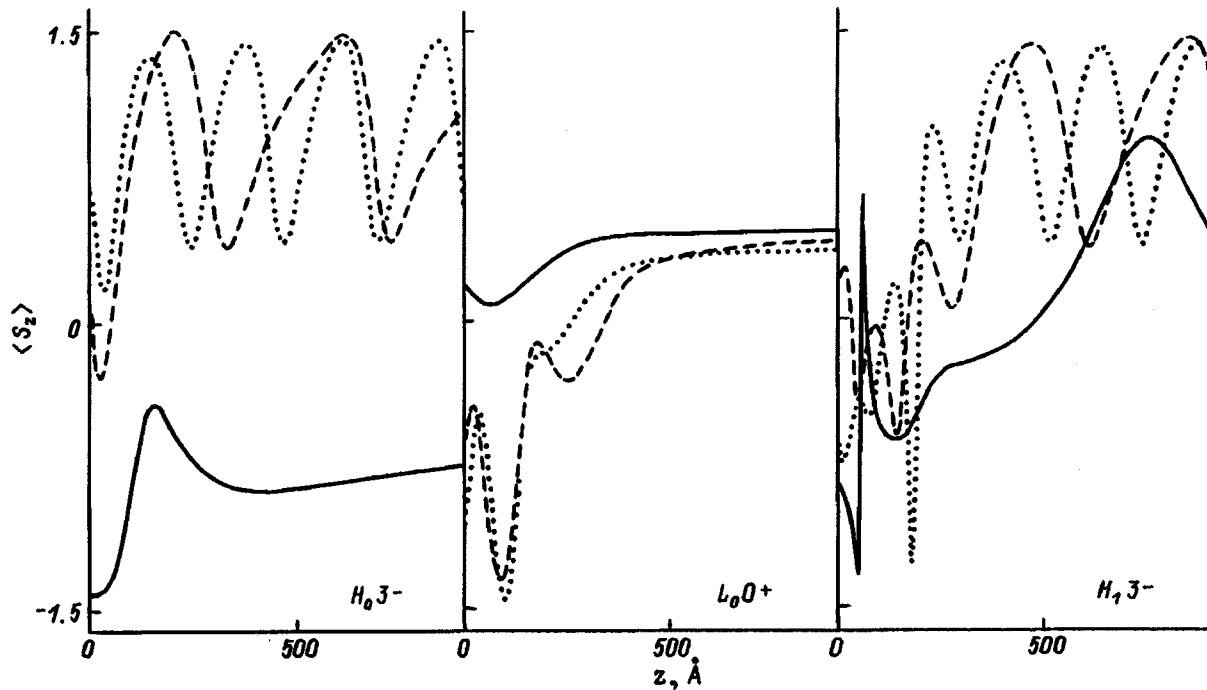


FIG. 4. Dependence of the average spin on the distance to the heterojunction for the levels shown in Fig. 3.

washing-out of the Fermi level over a fixed energy interval.

Figure 4 shows the dependence of the average spin $\langle S_z \rangle$ on coordinate z for the Landau levels shown in Fig. 3, which were calculated from the expression

$$\langle S_z \rangle = \frac{-\frac{3}{2}\psi_1^2 - \frac{1}{2}\psi_2^2 + \frac{1}{2}\psi_3^2 + \frac{3}{2}\psi_4^2}{\psi_1^2 + \psi_2^2 + \psi_3^2 + \psi_4^2}.$$

As is clear from this figure, the average spin of all the levels (except for the pure-spin level 0^- for heavy holes) exhibits a strong dependence both on the magnitude of the magnetic field and on coordinates. The spin of level 3^- undergoes nonattenuating oscillations in both subbands, which spread with unchanged period even into the region of the potential barrier where the wave functions are strongly attenuated. Here is yet another interesting property of the hole wave functions: they can attenuate in the barrier in an oscillatory manner, and the period of these oscillations depends only weakly on the potential energy. This is explained qualitatively by the presence of the cross term $S \sim k_z k_-$ in the Hamiltonian (4), which adds a real part that is potential-independent to the imaginary part of k_z in the below-barrier region.

The phenomena discussed above should be directly visible in the optical properties of this system, i.e., the intensities and polarizations of the luminescence lines. The dependence of the intensity of recombination light on magnetic field for the two ground-state heavy-hole levels 0^- and 0^+ is shown in Fig. 5a. For this calculation we use Eq. (16) and the following parameters of the electron wave function at the donor: $z_D = 500 \text{ \AA}$, $a_D = 80 \text{ \AA}$. As is clear from the figure, the intensity of the luminescence of the pure spin level 0^- behaves quite trivially: first it increases linearly

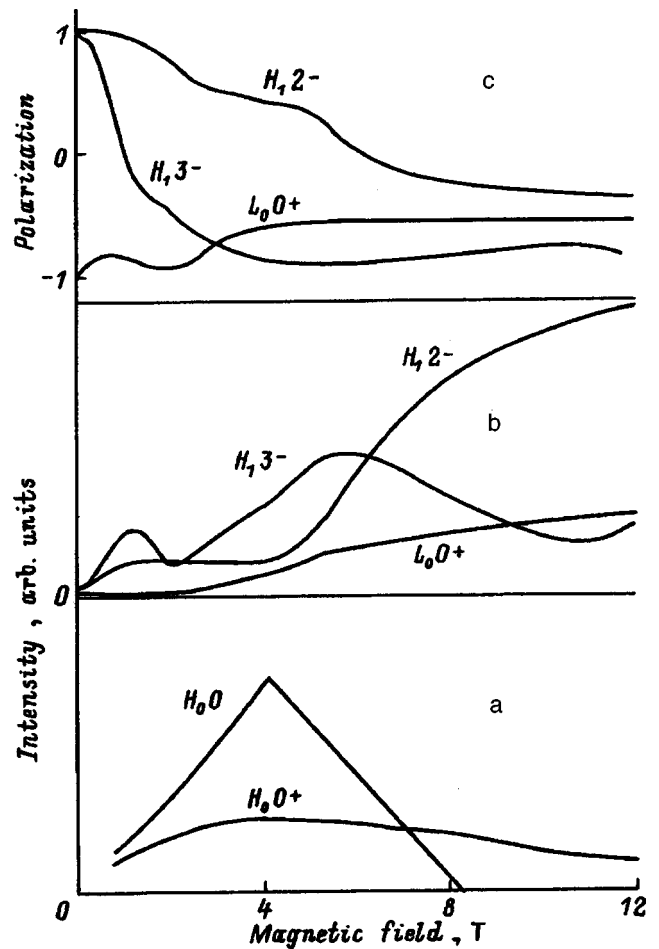


FIG. 5. a—Dependence of the luminescence intensity from the ground-state subband level HH_0 on the magnitude of the magnetic field at a concentration of $2 \times 10^{11} \text{ cm}^{-2}$. b, c—Dependence of the intensity and degree of polarization of the luminescence from Landau levels of the upper size-quantized subband that are most active in recombination on the magnitude of the magnetic field for a concentration of $5 \times 10^{11} \text{ cm}^{-2}$.

with field, proportional to the increase in capacity of the level, and then falls off, also linearly, proportional to its emptying. The intensity of the luminescence from level $0+$ depends on field in a more complicated way. Here the increase due to the increased capacity of the level competes with the falloff due to the weak compression of the level with increasing magnetic field. However, the effects described above are manifested in the most dramatic way in the intensity and polarization of luminescence from nonequilibrium occupied levels of the higher-lying subbands. Figures 5b and 5c show the field dependences of the intensity and degree of polarization of recombination light from the most luminescence-active Landau levels of the excited subbands at a concentration of $5 \times 10^{11} \text{ cm}^{-2}$. These oscillations in intensity and degree of polarization are connected with changes in the shape of the wave functions and the potential well, and also with the oscillations of the average spin discussed above. Reference 9 gives a more detailed comparison of the calculations with experimental results.

Thus, the method given here is a very effective instrument for calculating hole wave functions, especially when this requires a self-consistent calculation of the shape of the potential well caused by the holes themselves. It was used to calculate energy levels and wave functions for 2D holes in an isolated p -type heterojunction in a perpendicular magnetic field at various 2D hole concentrations. We have shown that the wave functions corresponding to different hole quantized states exhibit a strong dependence on magnetic field, which is enhanced with increasing level energy and depends appreciably on the level spins. We have demonstrated that at high hole-gas concentrations effects of occupation and emptying of different-spin levels of the ground-state heavy-hole subband lead to a change in the shape of the potential well and pinning of the energy levels. We have discussed the pro-

cesses of recombination of 2D holes with electrons bound to a δ layer of donors near the heterojunction. We have shown that the change in shape of the wave functions of holes in a magnetic field is accompanied by an increase in the number of zeroes of the wave function and oscillations in the average spin, leading to oscillations in the intensity and polarization of the recombination light.

The author is grateful to V. E. Bisti, and also to I. V. Kukushkin and V. E. Zhitomirskii for fruitful discussions in connection with the theoretical model and the results obtained using it.

This work was carried out with the support of the Russian Fund for Fundamental Research (Grant 96-02-16177) and INTAS (Grant 95-IN/RU-675).

- ¹J. M. Luttinger and W. Kohn, Phys. Rev. **97**, 869 (1955).
- ²J. M. Luttinger, Phys. Rev. **102**, 1030 (1956).
- ³M. I. D'yakonov and A. V. Khaetskii, Zh. Éksp. Teor. Fiz. **82**, 1584 (1982) [Sov. Phys. JETP **55**, 917 (1982)].
- ⁴D. A. Broido and L. J. Sham, Phys. Rev. B **31**, 888 (1985).
- ⁵S.-R. Eric Yang, D. A. Broido, and L. J. Sham, Phys. Rev. B **32**, 6630 (1985).
- ⁶U. Ekenberg and M. Altarelli, Phys. Rev. B **32**, 3712 (1985).
- ⁷E. Bangert and G. Landwehr, Surf. Sci. **170**, 593 (1986).
- ⁸I. V. Kukushkin and V. B. Timofeev, Adv. Phys. **45**, 147 (1996).
- ⁹O. V. Volkov, V. E. Zhitomirskii, I. V. Kukushkin, W. Dietsche, K. V. Klitzing, A. Fischer, and K. Eberl, Phys. Rev. B **56**, 7541 (1997).
- ¹⁰W. H. Press, S. A. Teukolsky, W. T. Vetterling, and B. P. Flannery, in *Numerical Recipes in C* (Cambridge Univ. Press, 1992).
- ¹¹R. Eppenga, M. F. H. Schuurmans, and S. Golak, Phys. Rev. B **36**, 1554 (1987).
- ¹²B. B. Goldberg, D. Heiman, M. J. Graf, D. A. Broido, A. Pinczuk, C. W. Tu, J. H. English, and A. C. Gossard, Phys. Rev. B **38**, 10 131 (1988).
- ¹³I. V. Kukushkin and V. B. Timofeev, Zh. Éksp. Teor. Fiz. **92**, 258 (1987) [Sov. Phys. JETP **65**, 146 (1987)].
- ¹⁴C. R. Pidgeon and R. N. Brown, Phys. Rev. **146**, 575 (1966).

Translated by Frank J. Crowne

Multiphonon capture of carriers in parabolic quantum wells in a constant electric field

É. P. Sinyavskii and A. M. Rusanov

Institute of Applied Physics, Moldavian Academy of Sciences, MD-2028, Kishinev, Moldavia
(Submitted October 31, 1997)

Fiz. Tverd. Tela (St. Petersburg) **40**, 1126–1129 (June 1998)

The zero-radius potential model is used to investigate multiphonon (radiationless) transitions between bound states of a parabolic quantum well (PQW) in a constant electric field whose intensity vector is perpendicular to the PQW surface. It is shown that thermal-capture thicknesses depend significantly on the magnitude and direction of the electric field and on the position of the impurity in the spatially bounded system. © 1998 American Institute of Physics. [S1063-7834(98)03306-1]

1. In crystals, the capture of carriers by deep defect centers increases exponentially as the defect approaches the surface. As shown in Ref. 1, recombination rates are greatly increased for impurity centers whose distance from the surface R is less than 10–20 Å. In a number of cases, electron capture is increased when $R < 200$ Å. An analogous effect occurs in spatially bounded systems (quantized layers or isolated quantum wells). A first-principles theory of multiphonon capture of carriers by deep centers in rectangular quantum wells was discussed in Ref. 2, where it was shown that multiphonon capture depends significantly on the impurity location. In a parabolic quantum well (PQW) in a constant electric field, the energies of the bound states (in the zero-radius potential model of Ref. 3) of a deep impurity center depend on the position of the defect z_0 and the magnitude of the electric field intensity \mathbf{F} directed along the axis Oz of spatial quantization⁴,

$$\varepsilon = -E_0 + \frac{m_c \omega^2}{2} (z_0 + d_0)^2. \quad (1)$$

Here $\hbar \omega = [8\hbar^2 E_c / m_c d^2]^{1/2}$ is the spatial quantization energy, E_c is the energy depth of a quantum well of width d , $d_0 = (|e|Fd^2/8E_c)$ determines the shift of the minimum of the PQW potential $V(z)$ in an electric field ($V(z) = 4E_c/d^2 z^2 + |e|Fz$), and E_0 is the energy depth into the band gap of the impurity state for the three-dimensional crystal. In the calculations that follow we use the Huang–Rhys model, in which adiabatic terms for bound and free electronic states are represented by the same parabolas shifted relative to one another. The range of applicability of this model was discussed in Ref. 5.

The effect of the impurity location and the magnitude of the constant electric field intensity on multiphonon processes in a spatially bounded system can be qualitatively understood by analyzing the behavior of the adiabatic potentials (Fig. 1). The calculations that follow were made under the assumption that the size-quantization energies in the PQW are considerably smaller than the activation energy of the defect. In this approximation, we are justified in discussing the behavior of the adiabatic potentials in terms of normal coordinates.² If there is no field ($F=0$), and the impurity is

located at the center of the quantum well ($z_0=0$), then the capture of an electron from the conduction band (adiabatic potential 1) to the ground state of the impurity center (adiabatic potential 2) at high temperatures is activated in character, with an activation energy Δ (Fig. 1). In the presence of a constant electric field the energy distance of the impurity state to the conduction band decreases at $z_0=0$ by an amount $(m_c \omega^2/2) d_0^2$ [according to Eq. (1)], and the recombination processes take place with activation energy $\Delta_1 < \Delta$. This should lead to a considerable increase in multiphonon recombination processes. The decrease in the tunneling path length ($a_1 b_1 < ab$) in the presence of an electric field can explain why an external field can significantly stimulate radiationless capture of carriers on deep-lying bound states at low temperatures as well.

2. Let us calculate the multiphonon capture thickness for an impurity center using the model of a zero-radius potential,³ whose wave functions and bound state energies are known for a parabolic quantum well in a constant electric field.⁴ Within a quasiclassical description of vibrations of the crystal lattice that takes into account non-Kondo effects, the probability of an electron making a multiphonon transition from the conduction band (nk_{\perp}) to a bound state of a local center (s) is determined by the expression⁶

$$W_{k_{\perp}, n, s} = \frac{1}{2\hbar} \left[\frac{\pi}{ak_0 T} \right]^{1/2} \sum_{\mathcal{N}} |V_{\mathcal{N}nk_{\perp}, s}|^2 \times (2N_{\mathcal{N}} + 1) \exp \left\{ - \frac{(I_{k_{\perp}ns} - a)^2}{4k_0 T a} \right\},$$

$$a = \frac{1}{2} \sum_{\mathcal{N}} \frac{|V_{\mathcal{N}ss}|^2}{\hbar \omega_{\mathcal{N}}},$$

$$I_{k_{\perp}, n, s} = \frac{\hbar^2 k_{\perp}^2}{2m_c} + n\hbar \omega + I_s^0 - \frac{m_c \omega^2}{2} (z_0 + d_0)^2, \quad (2)$$

where $V_{\mathcal{N}ss}$ is the electron-phonon interaction matrix element for wave functions of a localized state of the PQW in a constant electric field, $\hbar \omega_{\mathcal{N}}$ is the energy of an acoustic phonon with wave vector \mathcal{N} , $N_{\mathcal{N}}$ is the distribution of phonons at a temperature T , $\hbar k_{\perp}$ is the quasimomentum of an electron of mass m_c in the plane perpendicular to the axis of spatial

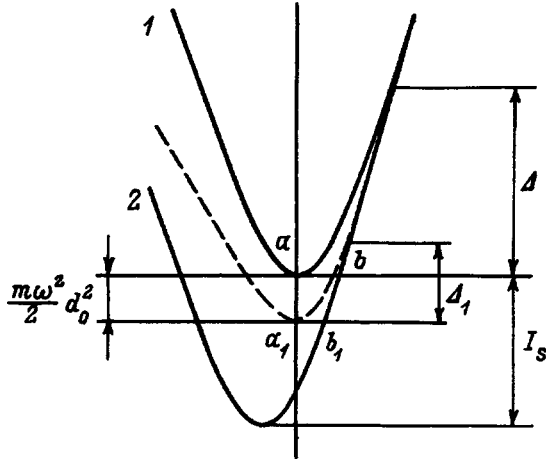


FIG. 1. Adiabatic potentials (1 and 2) for the continuous spectrum and localized state in a spatially bounded system. The dashed curves illustrate the adiabatic potential of a band electron in an electric field.

quantization ($k_{\perp} = \sqrt{k_x^2 + k_y^2}$), n labels the size-quantized conduction band Q , and I_s is the distance between minima of the adiabatic potentials (Fig. 1).

A PQW exhibits size quantization even at rather large thicknesses (for example, when $d = 10^3$ Å, $\hbar\omega = 14.5$ meV); therefore, we may treat the electron as interacting with bulk oscillations of the crystal lattice. Let us calculate the heat-release parameter a taking into account the interaction of an electron with acoustic phonons of the lattice, when $\hbar\omega/E_0 \ll 1$. In this approximation

$$a = \frac{E_1^2 m_c \mathcal{N}_D}{4\rho v^2 \hbar^2} E, \quad (3)$$

where E_1 is the deformation potential constant, \mathcal{N}_D is the Debye value of the phonon wave vector, ρ is the density of the crystal, v is the velocity of sound in the crystal, and $E = E_0 - (m_c \omega^2/2)(z_0 + d_0)^2 ((\hbar\omega/4E_0))^2$. The heat-release parameter depends on the electric field intensity and impurity position through E ; however, for $\hbar\omega/E_0 \ll 1$ this dependence can be neglected.

In what follows we shall consider the case where electrons are found in the lowest size-quantized conduction band ($n=0$). This approximation is valid if $\hbar\omega/k_0 T > 1$, and for typical parameters of the PQW ($m_c = 0.06m_0$, $E_0 = 0.255$ eV, $\hbar\omega = (14.5/\tilde{d}_0)$ (eV) (where \tilde{d}_0 is the size of the quantum well in angstroms) this latter inequality is fulfilled when $d_0 = 10^3$ Å at a temperature $T = 100$ K.

Let us calculate the matrix element $V_{\mathcal{N}0k_{\perp},s}$ for the electron-phonon interaction, which mixes the initial and final electronic states, assuming the following inequalities:

$$\frac{eFd}{8E_c} \ll 1, \quad \sqrt{\frac{m_c \omega d}{\hbar}} > 1, \quad \frac{e^2 F^2 d^2}{E_c} < |E_0|. \quad (4)$$

The first inequality implies that we are considering those values of electric field intensity for which there are still rather many size-quantized levels in the displaced quadratic potential of the quantum well. When the second inequality is fulfilled, we can use the wave functions of a quantized har-

monic oscillator in a constant electric field in subsequent calculations. When the last inequality holds, it implies that tunneling processes from a bound state to the continuous spectrum in an electric field are absent. As a result ($N_{\mathcal{N}} \approx (k_0 T / \hbar \omega_{\mathcal{N}})$),

$$\sum_{\mathcal{N}} \frac{|V_{\mathcal{N}0k_{\perp},s}|^2}{\hbar \omega_{\mathcal{N}}} \approx \frac{E_1^2 d \mathcal{N}_D}{v 2\pi^4 \sqrt{\pi} \rho v^2 \sqrt{2}} \sqrt{\frac{E_0}{\hbar \omega}} e^{-\xi^2}, \quad (5)$$

$$\xi^2 = \frac{m_c \omega}{\hbar} (z_0 - d_0)^2, \quad (6)$$

where v is the volume of the spatially bounded system.

The cross section for nonradiative capture is determined from the relation

$$\sigma = \frac{v \sum_{k_{\perp}} W_{k_{\perp}0,s} e^{-\beta \varepsilon_{k_{\perp}}}}{\frac{\hbar}{m_c} \sum_{k_{\perp}} k_{\perp} e^{-\beta \varepsilon_{k_{\perp}}}}, \quad \beta = \frac{1}{k_0 T}, \quad \varepsilon_{k_{\perp}} = \frac{\hbar^2 k_{\perp}^2}{2m_c}. \quad (7)$$

In the case under discussion, where \mathbf{F} is directed perpendicular to the surface of the quantum well, the energy of a band electron equals⁴

$$E_{nk_{\perp}} = \frac{\hbar^2 k_{\perp}^2}{2m_c} + \hbar \omega (n + 1/2) - \frac{F^2 e^2 d^2}{16E_c}.$$

Consequently, an external field only shifts the size-quantized bands, and therefore there is no heating.

Including Eqs. (2), (3), and (5) we finally obtain

$$\sigma(F) = \sigma_0 e^{-\xi^2} \exp\{-\beta(\Delta - \Delta_0)\},$$

$$\Delta = \frac{1}{4a} \left[I_s^0 - \frac{\hbar \omega}{2} \xi^2 \right]^2, \quad \Delta_0 = \frac{1}{4a} (I_s^0)^2,$$

$$\sigma_0 = \left[\frac{d^2 \mathcal{N}_D \hbar \omega}{\pi E_0 \rho v^2} \right]^{1/2} \frac{E_1}{\pi^4} e^{-\beta \Delta_0} \equiv \sigma(0) e^{-\beta \Delta_0}, \quad (8)$$

where σ_0 is the multiphonon capture thickness in the PQW when the impurity is located at the center of the quantum well ($z_0 = 0$) and $F = 0$.

With increasing electric field intensity the minimum of the quantum well potential moves away from the impurity center, and the overlap of the wave functions of the continuous spectrum and the bound state decreases, which leads to slowing of the multiphonon capture processes. The appearance of the factor $\exp(-\xi^2)$ in Eq. (8) is connected with this fact. For the PQW parameters listed above and $E_1 = 5$ eV, $E_0 = 0.1$ eV, $\rho = 5$ g/cm³, $v = 5 \times 10^5$ m/s, $d \approx 10^3$ Å we obtain $\sigma(0) = 4 \times 10^{-11}$ cm². If the impurity is located at the center of the quantum well ($z_0 = 0$), then the multiphonon recombination processes are activated with increasing F . Figure 2 shows the dependence of σ/σ_0 on F for $z_0 = 0$ (curve 1).

Note that the change of σ as a function of F is largely determined by the decrease in activation energy in an external field, and not by $\exp(-\xi^2)$. The primary dependences of this process on the impurity position and electric field intensity are determined by the parameter ξ^2 in Eq. (6). If the

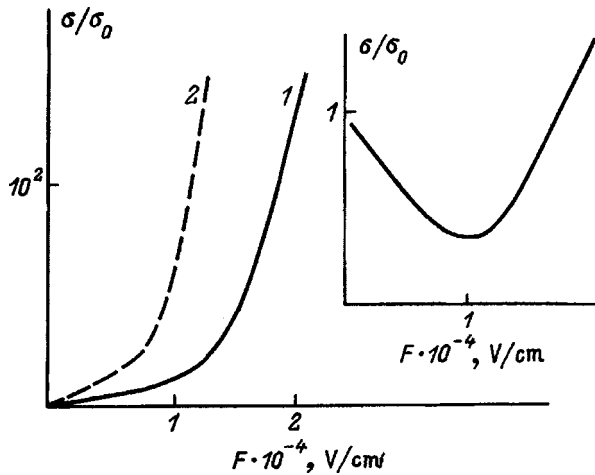


FIG. 2. Dependence of the multiphonon capture thickness (in relative units) on the electric field intensity. Curve 1 was obtained for $z_0=0$, curve 2 for $z_0=100 \text{ \AA}$. The inset shows the dependence of the radiationless capture thickness on the electric field intensity for $z_0=-100 \text{ \AA}$.

impurity is located at the point $-z_0$, then ξ^2 depends non-monotonically on F : $\xi^2 = (m\omega/\hbar)(z_0 - (|e|Fd^2/8E_c))^2$. With increasing F , ξ^2 decreases, becoming equal to zero at $z_0 = (|e|Fd^2/8E_c)$ (the minimum in the PQW potential energy is at the point where the impurity is located), and then increases (the minimum of the potential energy moves away from the defect). This behavior of ξ^2 leads to a nonmonotonic dependence of the thermal capture thickness on F (the inset to Fig. 2 shows the dependence of σ/σ_0 on F for $z_0 = -100 \text{ \AA}$). If the electric field intensity is directed opposite to the axis of spatial quantization (the impurity is located at a point $z = -z_0$ and $\xi^2 = (m\omega/\hbar)(z_0 + |e|Fd^2/E_c)^2$), then σ increases with increasing F . In this case [within the customary approximation (4)] the multiphonon capture thickness increases with increasing F more rapidly than at $z_0=0$. Curve 2 in Fig. 2 is shown for $z_0=100 \text{ \AA}$.

Thus, the rate of multiphonon recombination processes in a PQW depends significantly on the position of the impurity in an isolated quantum well, and on the magnitude and direction of the external electric field intensity.

Let us consider the low-temperature case, when electrons interact with optical vibrations of the lattice. The heat-release parameter for $E_0/\hbar\omega \gg 1$ is easily calculated:

$$a = \frac{1}{2} \sum_N \frac{|V_{Ns}|^2}{\hbar\omega_0} \approx \frac{2\sqrt{2}(\ln 2)E_0 c_0 e^2}{\hbar} \left[\frac{m_c}{E_0 - \hbar\omega\xi^2/2} \right]^{1/2}, \quad (9)$$

where $c_0 = (1/\varepsilon_0) - (1/\varepsilon_\infty)$ and $\hbar\omega_0$ is the energy of the highest-frequency optical phonon. It follows directly from Eq. (9) that a depends on the electric field intensity and the position of the impurity in the quantum well, but for $E_0/\hbar\omega \gg \xi^2/2$ this dependence can be neglected. For parameters of a crystal like GaAs ($c_0 = 1.4 \times 10^{-2}$) when $E_0 = 0.3 \text{ eV}$, $a = 10^{-2} \text{ eV}$, i.e., for $\hbar\omega_0 = 0.02 \text{ eV}$ we obtain $a/\hbar\omega_0 \approx 0.5$.

The probability of a radiationless transition of a carrier to a localized state in the Einstein model (weak dispersion of the optical vibration frequencies is neglected) is determined by the usual methods of the theory of multiphonon transitions⁷:

$$W_{k_\perp, n, s} = \frac{2\pi}{\hbar^2} \sum_{Nm=-\infty}^{\infty} |V_{Nk_\perp, s}|^2 I_m(z) \left[\frac{1+N}{N} \right]^{m/2} e^{\frac{a}{\hbar\omega_0}(1+2N)} \times \delta \left\{ -I_s + \frac{\hbar\omega\xi^2}{2} + (m-1)\hbar\omega_0 \right\},$$

$$z = 2\sqrt{N(N+1)}a_0, \quad a_0 = \frac{1}{2} \sum_N \frac{|V_{Ns}|^2}{(\hbar\omega_0)^2}. \quad (10)$$

Here N is the equilibrium distribution of optical phonons and $I_m(z)$ is a modified Bessel function. At low temperatures $N \ll 1$ ($z \ll 1$); taking Eqs. (10) and (7) into account, the thickness for radiationless capture is determined by the relation

$$\sigma(F) = \sigma(0) \frac{\langle l-1 \rangle!}{\langle l_F-1 \rangle!} (a_0)^{\langle l_F-1 \rangle - \langle l-1 \rangle} e^{-\xi^2}. \quad (11)$$

Here $l_F = (I_s - (\hbar\omega/2)\xi^2/\hbar\omega_0)$, $l = (I_s/\hbar\omega_0)$, $\langle l \rangle$ is the integer part of l , $\sigma(0)$ is the multiphonon capture thickness in a parabolic quantum well in the absence of an electric field, the impurities are located at the center of the spatially bounded system ($\xi=0$),

$$\sigma(0) = \sigma^0 (a_0)^{\langle l-1 \rangle} \frac{1}{\langle l-1 \rangle!}, \quad \sigma^0 \equiv \frac{4e^2 \hbar \omega_0 c_0 d}{\pi} \left(\frac{\beta}{2E_s} \right)^{1/2},$$

for $E_s = 0.4 \text{ eV}$, $d = 10^3 \text{ \AA}$, $T = 4 \text{ K}$ $\sigma^0 = 2.3 \times 10^{-14} \text{ cm}^2$. If $a_0 = 1$, then for $E_s = 0.4 \text{ eV}$ ($l = 20$) and $F = 2.8 \times 10^4 \text{ cm/V}$ ($l_F = 19$) $\sigma(F)/\sigma(0) = 19$. If $a_0 < 1$, the increase in the multiphonon capture thickness in an electric field is still more pronounced. The nonmonotonic behavior of the change in ξ^2 with increasing field leads to the same features in the behavior of $\sigma(F)$ that were characteristic of radiationless capture thicknesses calculated within the quasiclassical description of the phonons given above.

According to the principle of detailed balance for thermal transitions,⁷ the probability of ionization $W_{s, k_\perp, n}$ is simply related to the probability of multiphonon capture $W_{k_\perp, n, s}$:

$$W_{s, k_\perp, n} = W_{k_\perp, n, s} \exp(-\beta I_{k_\perp, n, s}). \quad (12)$$

Relation (12) holds since there is no heating in a longitudinal electric field for a PQW and (in contrast to the three-dimensional case⁸) when the last inequality in Eq. (4) holds the direct tunnel ionization of deep levels is impossible. According to Eq. (12), multiphonon ionization in a PQW, as well as the rate of thermal capture, depends on the position of the impurity in the quantum well, and the magnitude and direction of the electric field intensity.

- ¹A. A. Pakhomov and I. N. Yassievich, *Fiz. Tekh. Poluprovodn.* **27**, 482 (1993) [*Semiconductors* **27**, 270 (1993)].
- ²A. A. Pakhomov and I. N. Yassievich, *Fiz. Tekh. Poluprovodn.* **29**, 511 (1995) [*Semiconductors* **29**, 265 (1995)].
- ³Yu. N. Demkov and V. N. Ostrovskii, *The Zero-Radius Potential Method in Atomic Physics* (Leningrad, 1975, 240 pp.).
- ⁴E. P. Sinyavskii and E. Yu. Kanarovskii, *Fiz. Tverd. Tela* (St. Petersburg) **35**, 1641 (1993) [*Phys. Solid State* **35**, 826 (1993)].
- ⁵V. N. Abakumov, I. A. Merkulov, V. I. Perel', and I. N. Yassievich, *Zh. Éksp. Teor. Fiz.* **89**, 1472 (1985) [*Sov. Phys. JETP* **62**, 853 (1985)].
- ⁶E. P. Sinyavskii and V. A. Kovarskii, *Fiz. Tverd. Tela* (Leningrad) **9**, 1464 (1967) [*Sov. Phys. Solid State* **9**, 1142 (1967)].
- ⁷V. A. Kovarskii, *Multiphoton Transitions* [in Russian], ShTIINTsA, Kishinev, 1974, 228 pp.
- ⁸V. Karpus and V. I. Perel', *Zh. Éksp. Teor. Fiz.* **91**, 2319 (1986) [*Sov. Phys. JETP* **64**, 1376 (1986)].

Translated by Frank J. Crowne

Effect of free electron-hole pairs on the saturation of excitonic absorption in GaAs/AlGaAs quantum wells

K. L. Litvinenko and V. G. Lysenko

Institute for Problems in Microelectronics and Ultrapure Materials Technology, Russian Academy of Sciences, 142432 Chernogolovka, Moscow Region, Russia

I. M. Hvam

Mikroelektronik Centret, DTU, DK-2800 Lyngby, Denmark

(Submitted June 11, 1997; resubmitted November 10, 1997)

Fiz. Tverd. Tela (St. Petersburg) **40**, 1130–1133 (June 1998)

The pump-probe experimental method is used to investigate the effect of photoexcited carriers on the dynamics of the exciton absorption spectra of GaAs / Al_xGa_{1-x}As-multilayer quantum wells. Use of the method of moment analysis for processing the results makes it possible to identify the simultaneous contribution of changes in oscillator strength and width of the exciton lines in the saturation of exciton absorption. It was found that the oscillator strength recovers its initial value in the course of the first 100–130 ps, whereas broadening and energy-shift of the exciton lines is observed for 700–800 ps. These are the first experimental measurements of the excitation densities at which the oscillator strength of the excitonic state saturates when the latter is perturbed only by free-electron-hole pairs, and when it is perturbed only by other excitons. © 1998 American Institute of Physics. [S1063-7834(98)03406-6]

Saturation of exciton absorption in multilayer quantum wells is determined both by changes in the oscillator strength f of the exciton transition and by broadening of the exciton lines.¹ The question of what type of particle (free-electron-hole pairs or the excitons themselves) is more effective in causing f to decrease has remained open for a long time. In the first experimental papers,^{2,3} in which the effect of broadening of the exciton lines was not fully taken into account, the authors were led to the conclusion that excitons had a stronger effect on the change in f at room temperature than free carriers. In the course of their own theoretical investigations, the authors of Ref. 4 were led to the opposite conclusion. They showed that free-electron-hole pairs are more effective by a factor of at least 2 in decreasing the oscillator strength than excitons. In another theoretical study,⁵ it was established that, at low temperatures, excitons should have a stronger effect on f than free carriers, whereas, at temperatures above 25 K, their effects becomes practically the same.⁵ Despite the fact that free-electron-hole pairs actually saturate the exciton absorption more strongly than excitons at low temperatures,⁶ their effect on f is quite difficult to isolate due to the simultaneous broadening of the exciton lines, which also leads to a decrease in the exciton absorption. If we recall that free-electron-hole pairs are several times more effective in broadening the exciton absorption line than the exciton gas itself, which was unambiguously demonstrated in the four-wave mixing experiments of Ref. 7, it becomes quite unclear which type of particle has the dominant influence in changing f . The subject of this paper will be the resolution of this question.

We investigated the nonlinear-optics properties of mul-

ti-quantum wells grown by molecular-beam epitaxy and consisting of 20 periods of GaAs layers of width 80 Å and AlGaAs layers of width 100 Å. For this we used the pump-probe method.¹ As a source of laser light we used a titanium-sapphire tunable laser with a pulse duration of 120 fs, and a repetition rate of 76 MHz. In order to study the effect of electron-hole plasmas we used resonant and nonresonant exciton excitation. During all of these experiments the sample was held in an optical helium cryostat and its temperature was kept at 5 K.

In Fig. 1 we show the line spectrum of exciton absorption and the spectra of the laser light used in the nonlinear experiment. In order to process the absorption spectra we used the method of moment analysis,⁸ whose essence is the determination of all the exciton parameters at once. The use of this method does not require knowledge of the exact form of the absorption spectrum and allows us to treat the latter as an arbitrary statistical distribution (for more details on this method of analysis of absorption spectra see Ref. 1). In Fig. 2 we show the results of applying this method to absorption spectra obtained under nonresonant excitation of the sample under study. The initial density of photoexcited carriers in this case was approximately $9 \times 10^{10} \text{ cm}^{-2}$. It is clear from Fig. 2 that f , the broadening and, consequently, the maximum in the exciton absorption all change simultaneously with the arrival of the pump pulse ($\tau=0$), whereas the blue shift of the exciton line reaches its maximum value only after $\sim 110\text{--}130$ ps. This behavior of the resonance position of the exciton line is easily explained by the fact that, as we

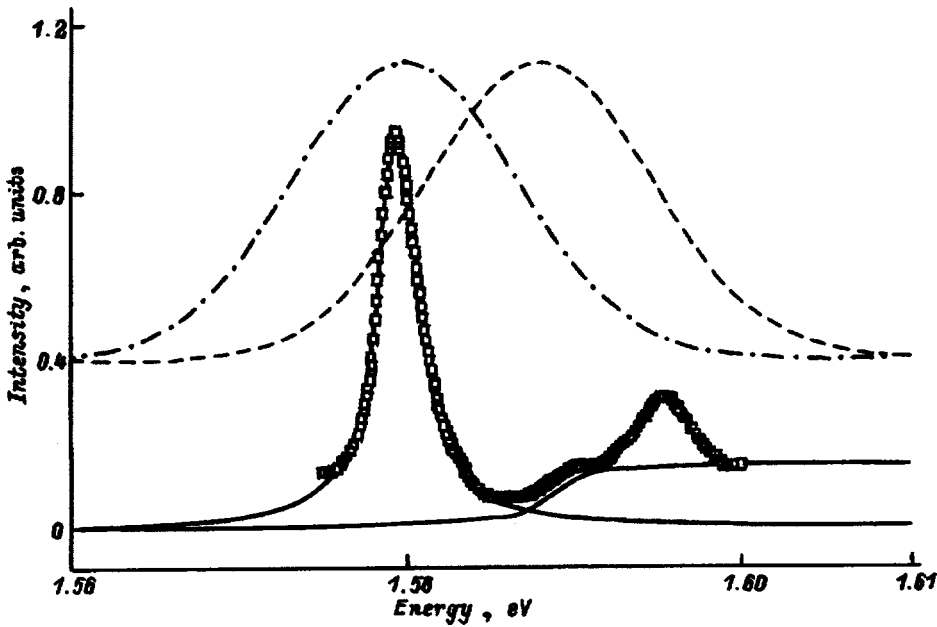


FIG. 1. Experimental (squares) and theoretical (solid curves) absorption spectra for ground-state heavy-hole excitons and an electron-hole plasma. The dashed and dotted-dashed curves show the spectra of the excitation laser light.

showed in Ref. 1, free-electron-hole pairs whose presence leads to an additional red shift of the exciton line⁹ disappear from the system during this time period, forming excitons. For delays longer than 130 ps, the energy shift and broadening of the exciton lines decreases exponentially with the same characteristic time. Within the limits of error, this time coincides with the lifetime of free excitons $T_1^{\text{exc}} = 410$ ps obtained under resonant excitation.¹ This also confirms the assertion that free particles are no longer affecting the dynamics of the exciton state. Under resonance excitation, we observe qualitatively the same behavior of the exciton parameters as shown in Fig. 2, with the only difference that the

energy shift reaches its maximum value at the initial time ($\tau=0$) and that the initial changes in the broadening and f are decreased by almost a factor of 2 compared to nonresonant excitation for the same density of photoexcited carriers.

In order to determine the partial contributions of free-electron-hole pairs and excitons to the change in f , we investigated the dependence of the relative change in this quantity ($\Delta f/f$) on the density of photoexcited particles at time $\tau \approx 20$ ps. The cases of resonant and nonresonant excitation are shown in Fig. 3. In both cases, we used a linear dependence to approximate the experimental results, which can be expressed by the following equations:

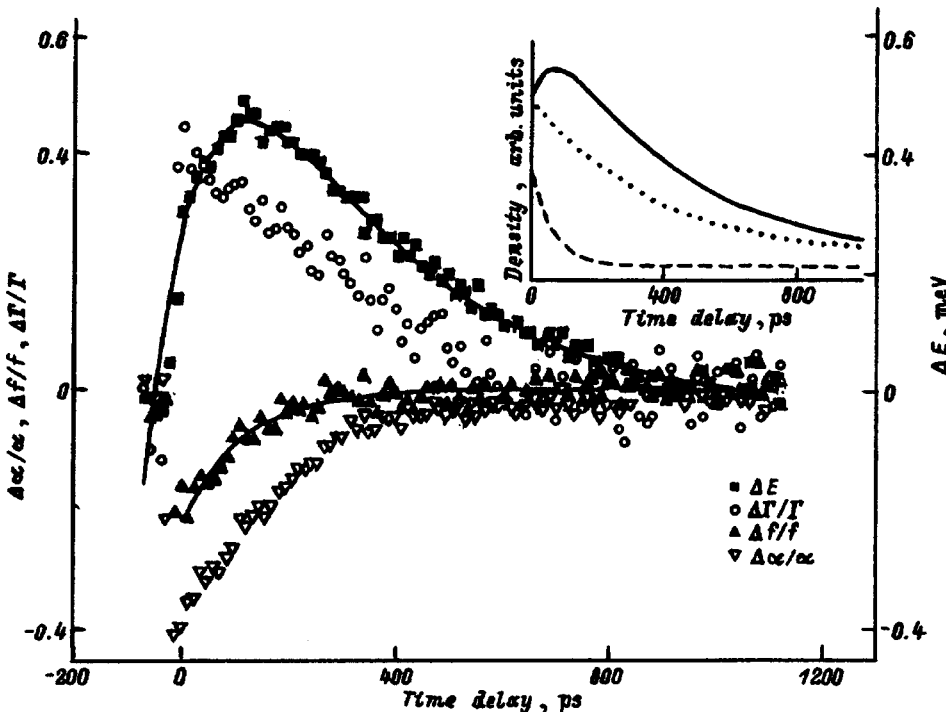


FIG. 2. Dependence of the relative change in oscillator strength ($\Delta f/f$), the maximum in the absorption coefficient ($\Delta\alpha/\alpha$), the broadening ($\Delta\Gamma/\Gamma$), and the energy shift (ΔE) of the exciton absorption line on delay time for the case of nonresonant excitation. The inset shows the change in the density of exciton states (solid curve) and free-electron-hole pairs (dashed curve) as a function of delay time. For comparison, we show the behavior of the density of exciton states in the absence of free carriers (the dotted curve).

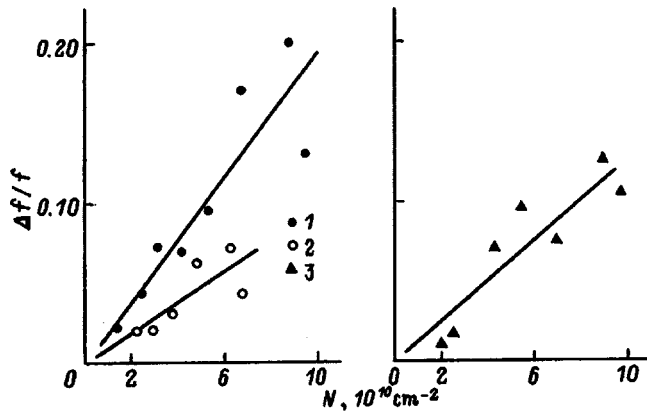


FIG. 3. Dependence of the relative change in oscillator strength of the exciton transition on the density of particles for nonresonant (1, 2) and resonant (3) excitation.

$$\frac{\Delta f^{(res)}}{f} = C^{(res)} N^{(res)} = \frac{N_{exc}^{(res)}}{N_{s,exc}} + \frac{N_{pl}^{(res)}}{N_{s,pl}},$$

$$\frac{\Delta f^{(non)}}{f} = C^{(non)} N^{(non)} = \frac{N_{exc}^{(non)}}{N_{s,exc}} + \frac{N_{pl}^{(non)}}{N_{s,pl}},$$

$$N^{(i)} = N_{exc}^{(i)} + N_{pl}^{(i)}, \quad i = res, non, \quad (1)$$

where $N_{exc}^{(i)}$, $N_{pl}^{(i)}$, and $N^{(i)}$ are the exciton density, the density of the electron-hole plasma, and the total densities under resonant ($i=res$) and nonresonant ($i=non$) conditions of excitation respectively, $N_{s,exc}$ and $N_{s,pl}$ are the saturation densities in cases where only excitons or only free carriers act on f , and $C^{(i)}$ ($i=res, non$) are coefficients of proportionality measured experimentally. From Fig. 3 we obtain $C^{(res)} = 1.2 \times 10^{-12} \text{ cm}^2$ and $C^{(non)} = 2 \times 10^{-12} \text{ cm}^2$.

In order to determine $N_{s,exc}$ and $N_{s,pl}$ it is necessary to know what portion of the overall density consists of free carriers, and what part consists of excitons under both conditions of excitation. The density of photoexcited particles is proportional to the integral of the absorption coefficients of these particles multiplied by the intensity of the excitation laser light. The laser-light spectra, and also the theoretical absorption spectra of ground-state heavy-hole excitons and of free-electron-hole pairs, are shown in Fig. 1. In order to obtain the latter we used the generalized Elliot equation.¹⁰ In this way we find that $N_{exc}^{(res)}/N_{pl}^{(res)} \approx 10.5$ and $N_{exc}^{(non)}/N_{pl}^{(non)} \approx 1.7$. Knowing the ratio of densities and also the quantities $C^{(res)}$ and $C^{(non)}$, we obtain from Eq. (1) $N_{s,exc} = 1 \times 10^{12} \text{ cm}^{-2}$ and $N_{s,pl} = 2.5 \times 10^{11} \text{ cm}^{-2}$. The values of saturation density turn out to be almost an order of magnitude larger than the values predicted in Refs. 4 and 5; however, their ratio is in good agreement with the conclusions of Ref. 4.

Within 130 ps after the passage of the pump pulse the density of free-electron-hole pairs becomes negligibly small, and the change in f is determined by the excitons alone. Let us determine $N_{s,exc}$ from the dependence of $\Delta f/f$ on density for $\tau = 135$ ps. The exciton density for this delay time is determined from the following relations:

$$\begin{cases} \frac{dN_{exc}}{dt} = -\frac{N_{exc}}{T_{l,exc}} + \frac{N_{pl}}{T_{l,pl}}, \\ \frac{dN_{pl}}{dt} = -\frac{N_{pl}}{T_{pl}} \end{cases}, \quad (2)$$

where $T_{l,exc}$ and $T_{l,pl}$ are lifetimes of excitons and free electron-hole pairs respectively ($T_{l,pl} \approx 65$ ps, see Ref. 1). At time $t = 0$ the exciton and electron-hole pair densities equal $N_{pl}^{(0)}$ and $N_{exc}^{(0)}$. These quantities are easy to obtain once we know their ratio (see above) and their total value. For larger τ the densities of both types of quasiparticles reduce to zero. The solution to the system of equations (2) is shown in the inset to Fig. 2 by the solid curve. For comparison we show in this inset the change in the density of free-electron-hole pairs (the dashed curve) and the density of excitons in the absence of free carriers (the dotted curve).

Figure 3 shows the dependence of the relative change in f on the exciton density for $\tau = 135$ ps. The best linear approximation for this function, which is obtained when the value of the proportionality coefficient $C = 9.6 \times 10^{-13} \text{ cm}^2$, is shown in Fig. 3 by the solid curve. Knowing C , we obtain from Eq. (1) $N_{s,exc} = 1 \times 10^{12} \text{ cm}^{-2}$. Despite the fact that the accuracy in determining $N_{s,exc}$ is roughly 10 %, the values of $N_{s,exc}$ obtained for $\tau \approx 20$ and ≈ 135 ps are in striking agreement with one another.

Thus, in this paper, we have measured saturation densities for the oscillator strength of the exciton transition for the first time in two cases: when free-electron-hole pairs perturb the transition ($N_{s,exc} = 1 \times 10^{12} \text{ cm}^{-2}$) and when excitons perturb it ($N_{s,pl} = 2.5 \times 10^{11} \text{ cm}^{-2}$). In this way we show that, for the multiquantum well we used, the cold electron-hole plasma has a larger effect on the oscillator strength than the exciton gas in the range of low to average densities of photoexcited carriers.

This work was carried out with the support of the following funds: Russian Fund for Fundamental Research Grants 95-02-05046 and 97-02-16833, INTAS-94-0324 and INTAS-RFBR-95-0576.

¹K. L. Litvinenko, A. Gorshunov, I. M. Hvam, and V. G. Lysenko, JETP Lett. (in press).

²N. Peyghambarian and H. M. Gibbs, Phys. Rev. Lett. **53**, 2433 (1984).

³W. H. Koch, R. L. Fork, M. C. Downer *et al.*, Phys. Rev. Lett. **54**, 1306 (1985).

⁴S. Schmitt-Rink, D. S. Chemla, and D. A. B. Miller, Phys. Rev. B **32**, 6601 (1985).

⁵R. Zimmermann, Phys. Status Solidi B **146**, 371 (1988).

⁶P. C. Becker, D. Lee, A. M. Johnson *et al.* Phys. Rev. Lett. **68**, 1876 (1992).

⁷L. Schultheis, J. Kuhl, A. Honold *et al.*, Phys. Rev. Lett. **57**, 1635 (1986).

⁸G. Korn and T. Korn, *Mathematics handbook* [in Russian], Nauka, Moscow, 1970.

⁹D. R. Wake, H. W. Yoon, J. P. Wolfe *et al.*, Phys. Rev. B **46**, 13 452 (1992).

¹⁰P. Lefebvre, P. Cristol, and M. Mathieu, Phys. Rev. B **48**, 17 308 (1993).

Electron states in quantum-dot and antidot arrays placed in a strong magnetic field

V. Ya. Demikhovskii and A. A. Perov

Lobachevskii Nizhni-Novgorod State University, 603600 Nizhni Novgorod, Russia
(Submitted November 10, 1997)

Fiz. Tverd. Tela (St. Petersburg) **40**, 1134–1139 (June 1998)

Quantum electronic states in a dot (antidot) array in the presence of a dc magnetic field are studied. A new method of numerical calculation of the electron spectrum and wave functions in a two-dimensional periodic potential and perpendicular magnetic field is proposed. The magnetic-subband energies, density of electron states, and electron density $|\psi(x,y)|^2$, as well as the amplitude of the potential, and lattice period and degree of anisotropy for different magnetic fields have been found. The calculations were performed for quantum dots in the $\text{In}_{0.2}\text{Ga}_{0.8}\text{As}$ –GaAs and GaAs– $\text{Al}_{0.3}\text{Ga}_{0.7}\text{As}$ systems. The rearrangement of the spectrum with variation of magnetic field and with transition from the tight-binding ($\hbar\omega_c/V_0 \ll 1$) to weak-binding ($\hbar\omega_c/V_0 \gg 1$) approximation is studied (ω_c is the cyclotron frequency, and V_0 is the periodic-potential amplitude). The calculations show that the two-dimensional lattices epitaxially grown presently on semiconductor surfaces permit observation of quantum effects associated with rearrangement of the spectrum (electron transport and optical absorption) in magnetic fields $H \leq 1$ MG. © 1998 American Institute of Physics. [S1063-7834(98)03506-0]

The behavior of a Bloch electron in an external magnetic field has been invariably attracting the interest of physicists. The main ideas bearing on the structure of the corresponding electron states can be found in Refs. 1–8. Numerical methods for calculation of the electron energy spectrum and wave functions in a two-dimensional periodic and uniform perpendicular magnetic field were also developed. In Refs. 9 and 10, the solution of the Schrödinger equation for a periodic potential, invariant to within a phase factor under magnetic translations, was presented in the form of an expansion in eigenfunctions of the electron in a uniform magnetic field, which was calculated in symmetric vector-potential gauge $\mathbf{A}(-Hy/2, Hx/2, 0)$. Such functions satisfying the generalized Bloch conditions (zero-approximation functions) were constructed by Ferrari.¹¹ The Ferrari-function basis was used in the first numerical calculation⁹ of the electron states of a square dot and antidot array (with a period $a = 500$ nm and amplitude of the potential $V_0 = 5$ meV) obtained by high-resolution electron lithography, in the presence of a magnetic field.

Despite the continuing interest in the problem and a wealth of relevant theoretical papers, no effects associated with rearrangement of the Bloch electron spectrum in a magnetic field have regrettably thus far been observed.¹²

Considerable progress has been reached recently in preparation of two-dimensional lattice structures made up of quantum dots.¹³ Such structures form in the course of epitaxial growth through spontaneous self-organization. Preparation of (In,Ga)As structures on a GaAs substrate with a characteristic period of 15–30 nm was reported.¹⁴ We are going to present here the results of a calculation of spectra, wave functions, and density of electronic states for a two-dimensional array consisting of quantum dots and antidots with parameters similar to those quoted in Ref. 14 in a perpendicular field \mathbf{H} . It is shown that the effects of radical

spectrum rearrangement, which govern the transport and magneto-optics of such structures, should be observable experimentally in magnetic fields $H \leq 1$ MG. The methods of electrical and optical measurements in magnetic fields of the order of and above 1 MG were developed by the Sarov group (see, e.g., Refs. 15–17).

1. MAIN EQUATIONS. METHOD OF CALCULATION

The Schrödinger equation for a two-dimensional electron moving in a periodic field of a two-dimensional rectangular array in the (x,y) plane in a uniform magnetic field directed along the z axis can be written

$$(\hat{H} - E)\psi = \left\{ \frac{(\mathbf{p} - e\mathbf{A}/c)^2}{2m^*} + V(x,y) - E \right\} \psi = 0, \quad (1)$$

where m^* is the effective mass, e is the electronic charge, c is the velocity of light, and \mathbf{p} is the generalized momentum. The vector potential will be presented subsequently in Landau gauge, $\mathbf{A} = (0, Hx, 0)$. The potential of the two-dimensional array in Eq. (1) will be given by a periodic function

$$V(x,y) = -V_0 \cos^2(\pi x/a) \cos^2(\pi y/b). \quad (2)$$

Here the plus sign refers to a system of quantum dots, and the minus, to an antidot system. The array periods in x and y are a and b , respectively. We shall assume that the electron motion is confined in the z direction, and that the electron resides in the lowest quantized subband.

If the number of magnetic flux quanta throughout the unit cell given by vectors $\mathbf{a}_1(a,0)$ and $\mathbf{a}_2(0,b)$ is a rational number p/q (p and q are coprime numbers), the solutions to the steady-state Schrödinger equation (1) should satisfy the generalized Bloch conditions

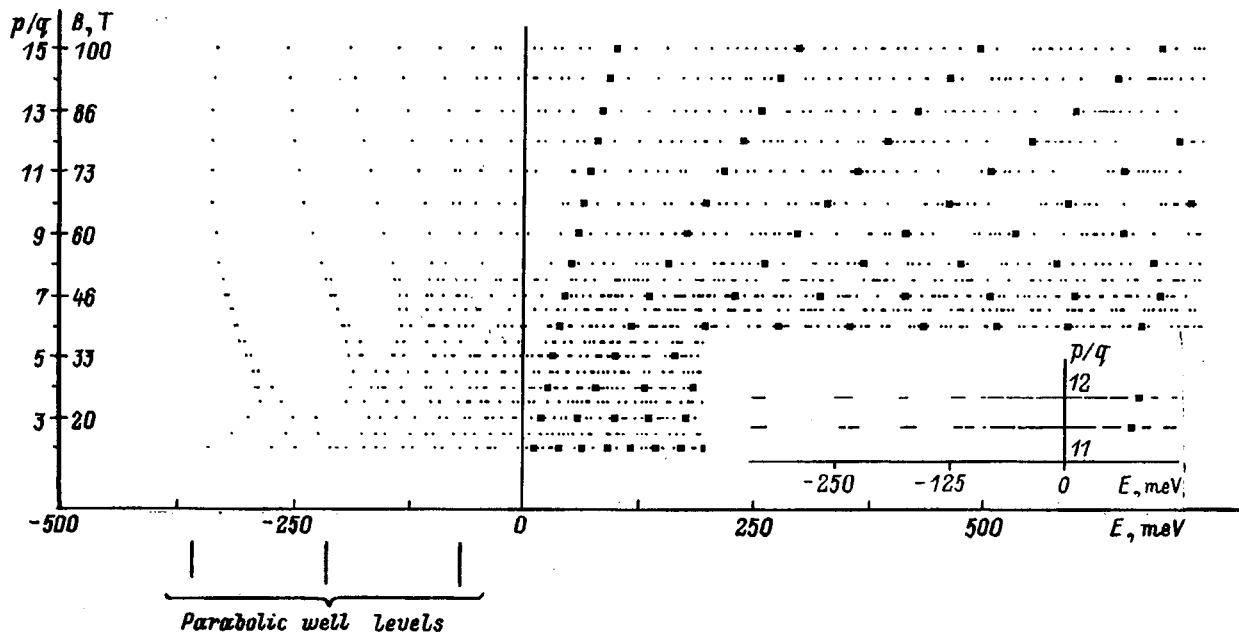


FIG. 1. Energy spectrum of an $\text{In}_{0.2}\text{Ga}_{0.8}\text{As}$ square quantum-dot array ($a=b=25$ nm, $V_0=500$ meV) placed in a magnetic field for $k_x=k_y=0$. Inset shows magnetic subband structure for $p/q=11$ and 12 .

$$\begin{aligned} \psi_{k_x, k_y}(x, y) = & \psi_{k_x, k_y}(x + qa, y + b) \exp(-ik_x qa) \\ & \times \exp(-ik_y b) \exp(-2\pi i p y / b). \end{aligned} \quad (3)$$

If the magnetic translation vectors are chosen in the form $\mathbf{a}_n = n_1 q \mathbf{a}_1 + n_2 \mathbf{a}_2$, where n_1 and n_2 are any integers, then translation of a wave function by vector \mathbf{a}_n will transfer it into a function with the same quasi-momentum $\mathbf{k}(k_x, k_y)$.

We shall look for a solution to Eq. (1) satisfying boundary conditions (3) in the form of an expansion in eigenfunctions of the zero Hamiltonian $H_0 = (\mathbf{p} - e\mathbf{A}/c)^2 / 2m^*$, which correspond to eigenvalues $E_N^0 = \hbar \omega_c (N + 1/2)$, where N is the number of the Landau level. Because in Landau gauge the functions corresponding to the energy E_N^0 are plane waves propagating along the y axis and eigenfunctions of a harmonic oscillator in the x direction, the solution to Eq. (1) can be presented as an expansion¹⁸

$$\begin{aligned} \psi_{k_x, k_y}(x, y) = & \sum_{N=0}^{\infty} \sum_{n=1}^p C_{Nn} \sum_{s=-\infty}^{+\infty} \chi_N \left(\frac{x - x_0 - sqa - nqa/p}{l_H} \right) \\ & \times \exp \left[ik_x \left(sqa + \frac{nqa}{p} \right) \right] \\ & \times \exp \left(2\pi i y \frac{sp+n}{b} \right) \exp(ik_y y), \end{aligned} \quad (4)$$

where $x_0 = c\hbar k_y / eH$, $\chi_N(x)$ is the harmonic-oscillator eigenfunction, and $l_H^2 = \hbar c / eH$ is the square of the magnetic length. The quasi-momentum components k_x and k_y vary within the magnetic Brillouin zone. We shall see later that despite different dependence on coordinates x and y of the functions used in expansion (4) the calculated density of probability has the full symmetry of Hamiltonian \hat{H} .

Substituting Eq. (4) into (1) yields a system of algebraic equations, which determines the electron energy spectrum $E(k_x, k_y)$ and the Hamiltonian eigenvectors C_{Nn}

$$\begin{aligned} \sum_{N'n'} H_{Nn}^{N'n'} C_{N'n'} = & \sum_{N'n'} (E_N^0 \delta_{N'n} \delta_{N'n}) \\ & + V_{Nn}^{N'n'}(p/q, k_x, k_y) C_{N'n'} = EC_{Nn}. \end{aligned} \quad (5)$$

Here $V_{Nn}^{N'n'}$ are matrix elements of periodic potential (2) calculated in basis (4). They are expressed through associated Laguerre polynomials $L_i^j(l_H^2/a^2)$.¹⁹ The scheme used to calculate the matrix elements is discussed in Ref. 18. Matrix $H_{Nn}^{N'n'}$ has a block structure. Each block is labeled with numbers N' and N . The number of blocks is determined by that of Landau levels taken into account in expansion (4). Each block is a square three-diagonal matrix with dimension $p \times p$, with the elements of a block being given by indices n and n' . Thus the dimension of complete matrix is $Np \times Np$. The number of Landau levels (i.e., the number of blocks of matrix $H_{Nn}^{N'n'}$) in numerical calculations was determined experimentally so as to make the spectrum within the desired energy interval and the corresponding wave functions independent of the number N . Incidentally, the structure of the matrix elements of $V_{Nn}^{N'n'}$ and Eqs. (5) appear to us to be simpler than the system used in Ref. 9. At the same time our method gives the same results for the array parameters specified in Ref. 9.

2. RESULTS AND THEIR DISCUSSION

We performed calculation of spectra, wave functions, and density of states for different typical parameters of two-

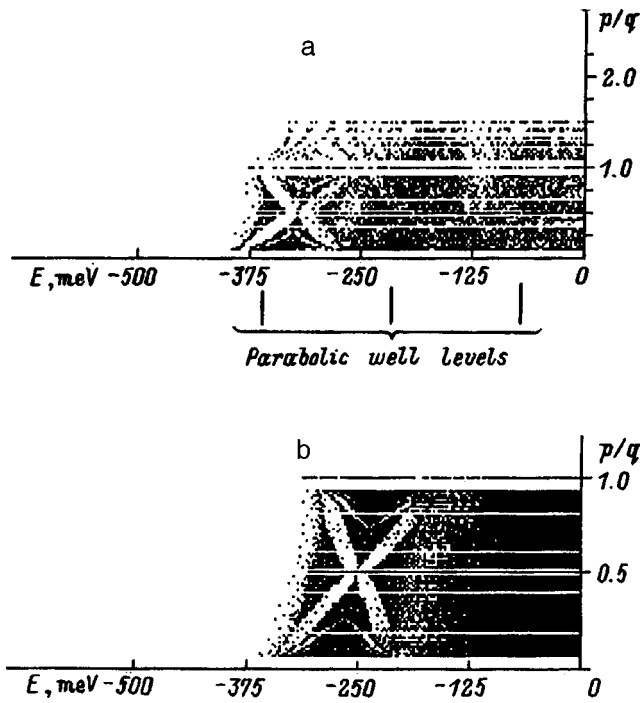


FIG. 2. Electron spectrum of an $\text{In}_{0.2}\text{Ga}_{0.8}\text{As}$ square quantum-dot array ($V_0=500$ meV). (a) isotropic array ($a=b=25$ nm), (b) anisotropic array ($a=25$ nm, $b=20$ nm). Shown below are levels of a parabolic well approximating the potential $V(x,y)$ for $x \rightarrow 0, y \rightarrow 0$.

dimensional arrays of quantum dots and antidots. Figures 1 and 2 present calculated energy spectra for quantum-dot arrays in the $\text{In}_x\text{Ga}_{1-x}\text{As}-\text{GaAs}$ system placed in GaAs for different values of H . The calculations assumed the solid-solution concentration to be $x=0.2$. The jump of the potential at the $\text{In}_{0.2}\text{Ga}_{0.8}\text{As}-\text{GaAs}$ interface had a typical value $V_0=500$ meV, the effective mass $m^*=0.0582m_e$, which corresponds to $\text{In}_{0.2}\text{Ga}_{0.8}\text{As}$ and differs by not more than 10% from $m_{\text{GaAs}}^*=0.067m_e$.

Consider the band evolution with variation of the magnetic field. Figure 1 shows the level position at the center of the magnetic subbands ($k_x=k_y=0$) for a quantum-dot system with periods $a=b=25$ nm as a function of applied magnetic field. Plotted along the vertical axis is the number of magnetic flux quanta passing through the unit cell ($p/q \geq 2$). We readily see that both at negative and positive energies the levels show a tendency of crowding around the unperturbed Landau levels. The positions of the latter are identified with filled circles. Taking into account the $E(k_x, k_y)$ relation spreads the levels into magnetic subbands which can overlap. This is illustrated by the inset in Fig. 1 showing magnetic subbands for $p/q=11, 12$. Several subbands form under each Landau level, and the subband separation grows with increasing magnetic field, so that for $p/q \geq 10$ the number of nonoverlapping subbands is p . These data suggest that the separation between magnetic subbands in magnetic fields of the order of 1 MG can exceed substantially the natural level width $\Delta E \sim \hbar/\tau_{\text{rel}}$ for typical values $\tau_{\text{rel}} \sim 10^{-12}$ s. Therefore, under these conditions one can observe experimentally effects (transport, optical absorption

etc.) connected with rearrangement of the superlattice spectrum in a field H .

In the low-field domain, where $p/q \leq 2$, the spectrum has a different structure (Figs. 2a and 2b). For negative energies, and with no magnetic field present, levels of each well spread to form an energy band, and if the minimum separation between the dots $a=25$ nm, the wave functions are strongly localized, which corresponds to strong-binding conditions. The position of three degenerate levels in a single well is shown in the lower part of Fig. 2a. Each of these bands splits in a magnetic field into q subbands to form spectra of the type of Hofstadter's "butterflies".⁶ One such butterfly derived from the ground level of the potential well is clearly seen in the left-hand part of Fig. 2a. The second and third levels of the potential well are degenerate, and therefore application of magnetic field makes the corresponding butterflies overlap. It should be pointed out that equations (5) do not have the property of periodicity in p/q , and therefore the pattern of the levels does not repeat with increasing magnetic field (increasing p/q); within the $1 \leq p/q \leq 2$ interval the butterfly is already not so clearly pronounced.

Figure 2b presents the energy spectrum for an anisotropic rectangular quantum-dot array. The existence of open electronic orbits in an anisotropic array is reflected in the structure of the spectrum as well. In low magnetic fields, open trajectories correspond to a continuum spectrum. Therefore in the case of an anisotropic array the butterfly appears more crowded. This is illustrated by Fig. 2b. Calculations show that in strong magnetic fields (for $p/q \geq 5$), where coupling between various magnetic levels in magnetic field is not very significant (matrix $V_{Nn}^{N'n'}$ breaks up into independent blocks corresponding to different N), the energy spectrum, similar to the case of an isotropic array, consists of narrow subbands derived from unperturbed Landau levels.

Because the levels of a single well and the overlap integrals determining the band width in the strong-binding approximation depend on the applied magnetic field, the band edges shift with variation of the latter. As H increases, the band derived from the electron ground-state level (Fig. 2b) moves toward higher energies (the butterfly is tilted). In an anisotropic array, where $b < a$, these effects are more pronounced than those in an isotropic one.

Figure 3 presents an electron-energy spectrum in a quantum-antidot system ($a=b=10$ nm) as a function of magnetic field. The parameters chosen correspond to the $\text{Al}_x\text{Ga}_{1-x}\text{As}-\text{GaAs}$ system. In the region of strong magnetic fields ($p/q \geq 5$) the energy spectrum is seen to consist of narrow subbands lying above the unperturbed Landau levels. The positions of the latter are shown with filled circles. For a magnetic field corresponding to $p/q=10$ the parameter $V_0/\hbar\omega_c=0.4$. Therefore the energy spectrum has here the same pattern as that obtained in the weak-binding approximation. The number of subbands under each Landau level is p .

The method used in this work also permits calculation of electron wave functions. Figure 4a and 4b displays the distribution of electron density $|\psi(x,y)|^2$ in the lowest band for

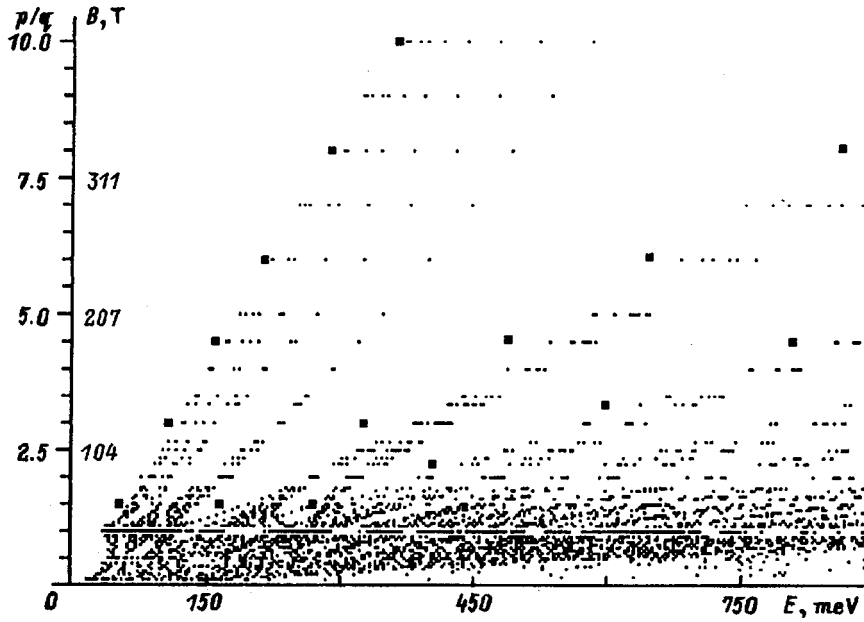


FIG. 3. Magnetic subbands in a square quantum-antidot array placed in a magnetic field ($a=b=10$ nm, $V_0=-300$ meV).

quantum dot and antidot arrays. The probability density distribution is seen to be essentially nonzero either in the region of the potential well (quantum dots) or between antidots. The electron density has translational symmetry. Although the calculation was not performed in a symmetric gauge, the probability density has the necessary symmetry.

A calculated density of electron states $g(E)$ in quantum dot and antidot arrays placed in a magnetic field is shown in Fig. 5. The number of magnetic flux quanta per unit cell was $p/q=4$. For an array with a period $a=b=10$ nm this corresponds to a magnetic field $H \approx 1.6$ MG. In such strong magnetic fields (Fig. 5a) the dependence of the density of states

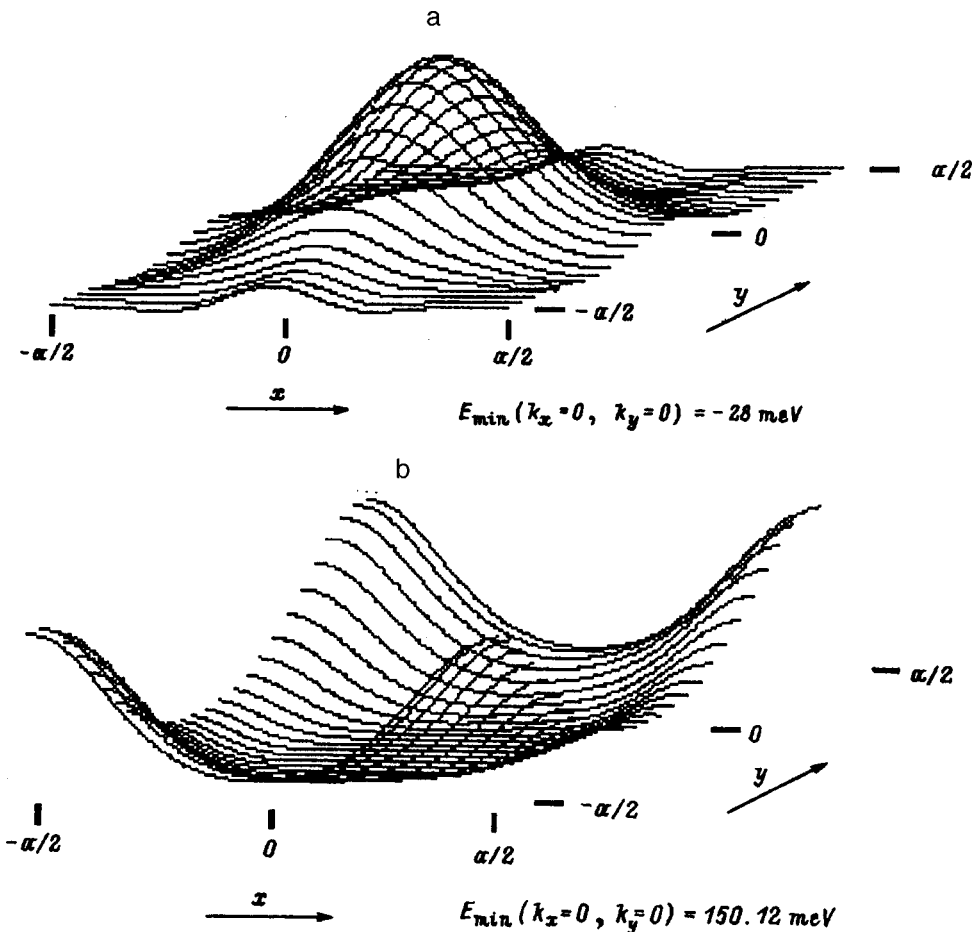


FIG. 4. Electron-density distribution for the $k_x=k_y=0$ state in the first (lowest) subband in square arrays: (a) quantum dots, (b) quantum antidots, in a magnetic field corresponding to $p/q=4$ ($a=b=10$ nm, $|V_0|=300$ meV).

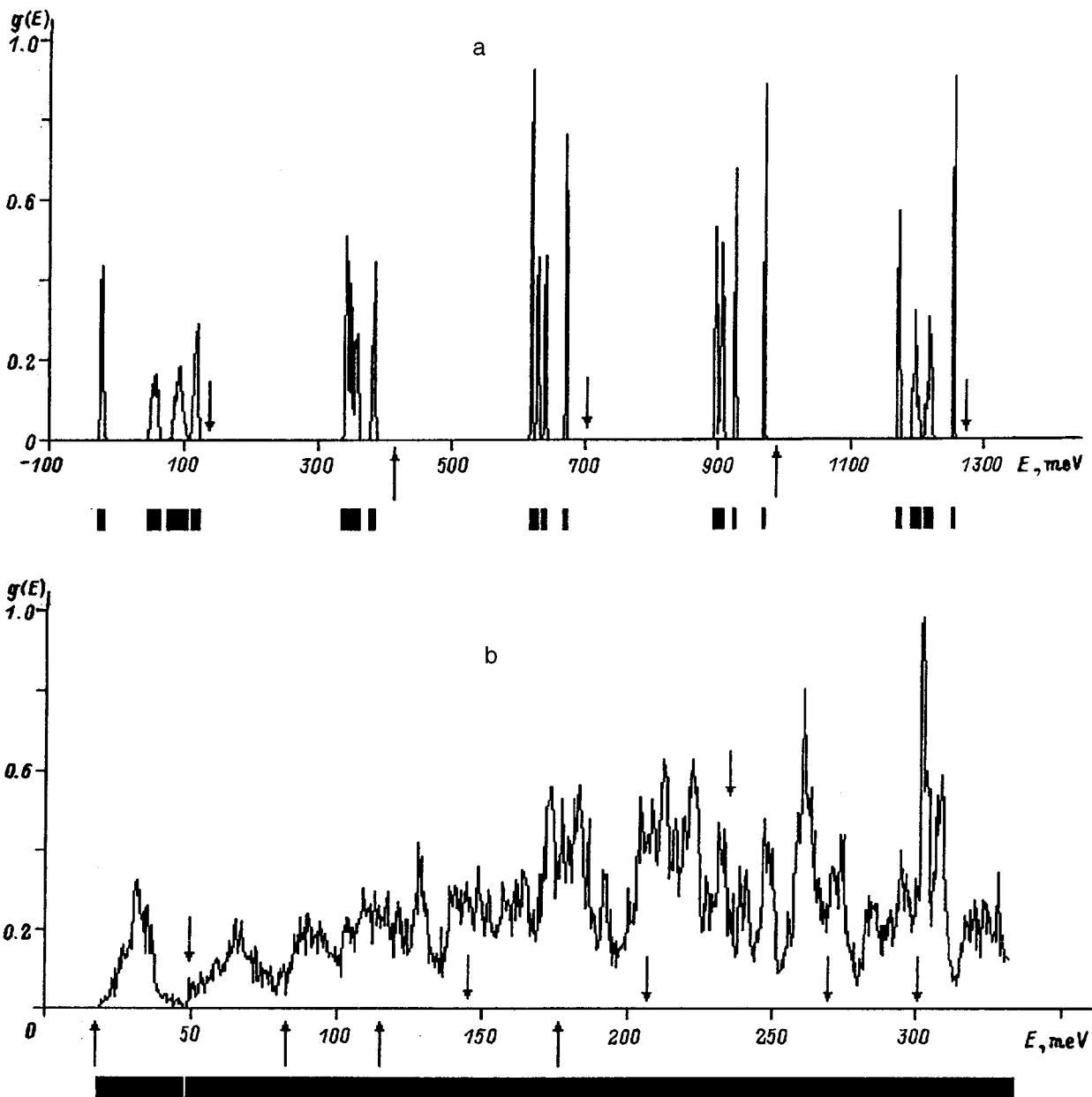


FIG. 5. Electron density of states for arrays of (a) quantum dots ($p/q=4$, $a=b=10$ nm, $V_0=300$ meV) and (b) quantum antidots ($p/q=4$, $a=b=30$ nm, $V_0=-300$ meV) placed in a magnetic field.

on energy in each subband has the shape of a pagoda because of the existence of van Hove singularities. The magnetic subbands are well resolved, and one sees four peaks in the density of states near each Landau level. The position of the energy subbands is shown in the lower part of the figures. The character of the $g(E)$ function changes with increasing array period. Fig. 5b presents the density of electron states for an antidot array. The magnetic field, chosen here to be $H \approx 185$ kG, cannot be considered strong, because the ratio $V_0/\hbar\omega_c \approx 10$. As a result, the Landau level splitting is large, and singularities in the density of states are not so clearly pronounced.

To conclude, the numerical method proposed in this work offers a possibility of studying electron states of a two-dimensional Bloch electron in a magnetic field over a broad range of parameters, including the strong- and weak-binding

regions. Our calculations permit determination of the regions of magnetic fields and of parameters of surface arrays made up of quantum dots or antidots (period, surface potential etc.) within which one can experimentally observe the quantum effects associated with electron transport and optical absorption in such systems.

Support of the Russian Fund for Fundamental Research (Grant 96-02-18067a) and of the State Committee on Higher Education (Grant 95-0-5.5-63) is gratefully acknowledged.

¹G. E. Zil'berman, Zh. Éksp. Teor. Fiz. **23**, 49 (1952); *ibid.* **30**, 1092 (1956); *ibid.* **32**, 296 (1957) [Sov. Phys. JETP **3**, 835 (1956) *[sic]*].

²J. Zak, Phys. Rev. **134**, A1602, A1607 (1964).

³M. Ya. Azbel', Zh. Éksp. Teor. Fiz. **46**, 929 (1964) [Sov. Phys. JETP **19**, 634 (1964)].

⁴A. Rauh, Phys. Status Solidi B **65**, K131 (1974); *ibid.* **69**, K9 (1975).

⁵G. H. Wannier, Phys. Status Solidi B **88**, 757 (1978).

- ⁶D. R. Hofstadter, Phys. Rev. B **14**, 2239 (1976).
- ⁷Y. Hasegawa, Y. Hatsugai, M. Kohmoto, and G. Montambaux, Phys. Rev. B **41**, 9174 (1990).
- ⁸A. Barelli and R. Fleckinger, Phys. Rev. B **46**, 11559 (1992).
- ⁹H. Silberbauer, J. Phys. Condens. Matter **4**, 7355 (1992).
- ¹⁰H. Silberbauer, P. Rotter, U. Rössler, and M. Suhrke, Europhys. Lett. **31**, 393 (1995).
- ¹¹R. Ferrari, Phys. Rev. B **42**, 4598 (1990).
- ¹²T. Schlösser, K. Ensslin, J. P. Kotthaus, and M. Holland, Semicond. Sci. Technol. **11**, 1582 (1996).
- ¹³Zh. I. Alferov, D. Bimberg, A. Yu. Egorov, A. E. Zhukov, P. S. Kop'ev, N. N. Ledentsov, S. S. Ruvimov, V. M. Ustinov, and J. Heydenreich, Esp. Fiz. Nauk **165**, 224 (1995).
- ¹⁴S. Ruvimov, P. Werner, K. Scheerschmidt, U. Gösele, J. Heydenreich, U. Richter, N. N. Ledentsov, M. Grundmann, D. Bimberg, V. M. Ustinov, A. Yu. Egorov, P. S. Kop'ev, and Zh. I. Alferov, Phys. Rev. B **51**, 14776 (1995).
- ¹⁵V. D. Selemir, A. E. Dubinov, I. V. Makarov, *Abstracts of the 7th International Conference Generation of "MG-Range Magnetic Fields and Related Experiments"* (Sarov, 1996), p. 23.
- ¹⁶M. I. Dolotenko, A. S. Obchinnikov, V. V. Platonov, V. I. Plis, A. I. Popov, O. M. Tatsenko, and A. K. Zvezdin, *ibid.*, p. 100.
- ¹⁷A. E. Dubinov, K. E. Mikheev, and V. D. Selemir, *ibid.*, p. 103.
- ¹⁸V. Ya. Demikhovskii and A. A. Perov, in *Megagauss and Megampere Technology and Applications* [in Russian] (VNIIEF, Sarov, 1997).
- ¹⁹I. S. Gradshteyn and I. M. Ryzhik (Eds.), *Tables of Integrals, Series, and Products* (Academic Press, New York, 1965; Nauka, Moscow, 1971).

Translated by G. Skrebtsov

Temperature-induced delocalization of excitations in GaAs/AlAs type-II superlattices

I. Ya. Gerlovin, Yu. K. Dolgikh, and V. V. Ovsyankin

S. I. Vavilov State Optics Institute, 199034 St. Petersburg, Russia

Yu. P. Efimov, I. V. Ignat'ev, and E. E. Novitskaya

St. Petersburg State University Scientific Institute for Physics Research, 198904 Petrodvorets, Russia

(Submitted June 26, 1997; resubmitted November 28, 1997)

Fiz. Tverd. Tela (St. Petersburg) **40**, 1140–1146 (June 1998)

This paper describes investigations of the photoluminescence spectra of heterostructures containing short-period type-II GaAs/AlAs superlattices grown both within the regime where the heterojunction is smoothed, and in a regime where it is not smoothed, in the temperature range 10–40 K. A quantitative analysis of the experimental data shows that the quenching of exciton luminescence in the majority of cases is characterized by a single value of the activation energy $E_2 = 8 \pm 1$ meV which coincides with the value of the binding energy of an $X-\Gamma$ exciton. It is concluded that the primary reason for quenching in this temperature interval is thermal dissociation of the exciton into a pair of free carriers whose delocalization is accompanied by nonradiative recombination at traps. It is observed that smoothing the heterojunction leads to an increase in the probability of quenching by 1–2 orders of magnitude on the average. [S1063-7834(98)03606-5]

Short-period GaAs/AlAs superlattices are type-II structures as a rule, in which the lowest excited state is an indirect $X-\Gamma$ exciton.¹ The relatively small probability of a radiative transition hinders its competition with nonradiative processes, which should lead to quenching of the $X-\Gamma$ luminescence. Nevertheless, the results of many experiments show^{2–4} that luminescence for type-II GaAs/AlAs superlattices at low temperatures (less than 10 K) is in practice no less bright than luminescence from type-I superlattices, in which radiative transitions are completely allowed. The presence of a bright exciton luminescence indicates a small probability for nonradiative decay of the $X-\Gamma$ excitons at low temperatures. It is customary to assume that the principal reason for the high quantum yield of $X-\Gamma$ exciton luminescence is the localization of these excitons, which prevents spatial diffusion and annihilation by quenching centers (deep traps, structural defects, etc.). As the temperature increases to 30–40 K, an abrupt (by more than 2 orders of magnitude) falloff in the intensity of the exciton luminescence is observed,² along with an equally abrupt decrease in its attenuation time.³ This radically distinguishes the behavior of $X-\Gamma$ excitons from the behavior of direct $\Gamma-\Gamma$ excitons whose kinetics and luminescent intensity do not undergo any important changes in this temperature interval. As a rule, thermal liberation of $X-\Gamma$ excitons from localized states is considered to be the mechanism for the rapid temperature-induced quenching of luminescence in type II superlattices, which leads to their spatial diffusion and annihilation by quenching centers.⁴ Although the effect of thermally stimulated diffusion of excitations in type-II GaAs/AlAs superlattices actually was detected experimentally in Ref. 3, the lack of systematic experimental data on the dynamics of temperature-induced quenching prevents us from identifying unambiguously the reason for localization of $X-\Gamma$ excitons

or the mechanism for their thermal delocalization. However, there is an alternative mechanism for delocalization of these excitations, which has not been examined so far—thermally stimulated dissociation of an exciton with the formation of a pair of free carriers and subsequent delocalization of at least one of them. The capture of the delocalized carrier by a trap, which prevents reverse recombination with the formation of an exciton, can also serve to explain the quenching of the exciton luminescence.

In this paper we present the results of a systematic experimental study of the mechanism of temperature quenching of $X-\Gamma$ excitons in short-period type-II GaAs/AlAs superlattices. We used samples in these experiments having similar size parameters but significantly different heterojunction profiles, whose nonuniformity is generally viewed as the primary reason for localization of excitons in quasi-two-dimensional heterostructures. Qualitative analysis of temperature changes in the luminescent spectra allow us to conclude that the high brightness of low-temperature luminescence in the superlattices under study was caused not by energy localization but rather an initially small mobility of free $X-\Gamma$ excitons. The primary mechanism for delocalization of the excitations leading to temperature quenching is the dissociation of $X-\Gamma$ excitons into pairs of free carriers in this case.

1. EXPERIMENT

As objects of study we used a *NMSL1* heterostructure grown at the Center for Optical Research at Arizona State University (USA),⁵ and two heterostructures (*e119* and *e129*) grown at the St. Petersburg State University Scientific Institute for Physics Research. Each heterostructure contained a short-period GaAs/AlAs-superlattice. The nominal

TABLE I. Nominal superlattice parameters

Parameter	Sample		
	<i>NMSL1</i>	<i>e119</i>	<i>e129</i>
GaAs thickness, monolayers	7	8	8
AlAs thickness, monolayers	5	5	4

size parameters of the superlattices in these structures are listed in Table I. All the heterostructures were grown by molecular-beam epitaxy. In growing the *NMSL1* structure, the growth was interrupted at each boundary in order to smooth the heterojunctions, whereas structures *e119* and *e129* were grown without interruption. All the structures were grown without rotating the substrate, as a result of which the superlattices had a significant gradient in the size of the period in the plane (approximately 0.5 monolayer/cm). This allowed us to obtain a set of superlattices in each sample with smoothly varying period.

Luminescence in the sample was excited by the light from a He-Ne laser. The intensity of the excitation light was chosen to be rather low, so that the spectra would not exhibit any nonlinear distortion. The luminescence was recorded with a double spectrometer made by Jobin-Yvon, using a cooled photomultiplier operating in the photon counting regime. The sample was placed on a cold finger in the vacuum cavity of a helium cryostat, which was part of a Laybold-Heraeus setup. The construction of the cryostat allowed us to smoothly vary the temperature of the sample in the range 10–100 K. The temperature was monitored according to the ratio of intensities of the *R* luminescence line from a thin film of crystal ruby attached to the same cold finger Q in the immediate vicinity of the sample.

Luminescence spectra recorded at a temperature of 10 K are shown in Fig. 1. Spectra from the *NMSL1* structure grown with smoothed heterojunctions (Fig. 1a) contained two distinctly resolved peaks as a rule, each of which had its own system of phonon replicas, a characteristic of $X-\Gamma$ excitons in GaAs/AlAs superlattices.¹ According to data from a detailed spectroscopic study,⁵ these peaks can be assigned to excitons localized in planar islands where the GaAs and AlAs layer thicknesses are integer numbers of monatomic layers. The transformation of the spectrum shown in Fig. 1a as we move along the surface of the sample is due to changes in the statistical weights of islands of different thicknesses as the average value of the period changes.

The spectrum of low-temperature luminescence from sample *e119* (Fig. 1b) contained only one bright exciton line, whose energy position varied smoothly as we moved along the sample surface in the direction of the gradient of the superlattice period. Such behavior is characteristic for structures in which the scale of nonuniformity of the heterojunction is significantly smaller than the exciton radius.⁶ Further motion in the direction of increasing period eventually led to a distinct transformation of the luminescence spectrum of sample *e119*: the ground-state line was somewhat broadened and the phonon satellites that are characteristic of luminescence from $X-\Gamma$ excitons disappeared (curve 3 in Fig. 1b).

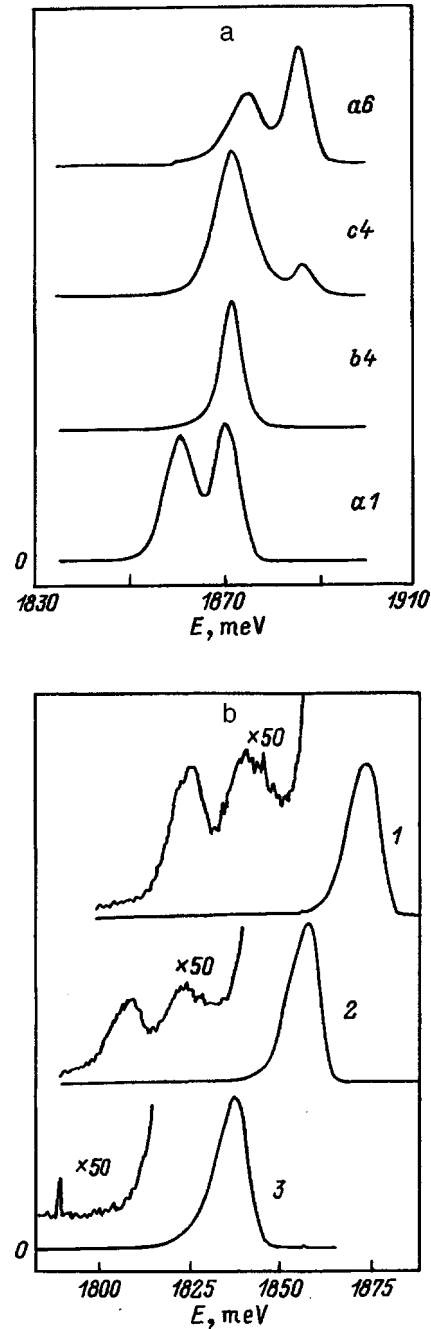


FIG. 1. Spectrum of low-temperature luminescence measured at various points on sample *NMSL1* (a) and *e119* (b).

This change in the spectrum corresponds to entering a region where the structure has become a type-I superlattice. In this case it is significant that the transition from a type-II superlattice to a type-I superlattice is not accompanied by an abrupt change in the luminescence intensity, despite the fact that the probability of a radiative transition increases by at least 3 orders of magnitude.⁷ This fact is evidence of the high quantum yield of exciton luminescence in the samples under study. The spectroscopic characteristics of sample *e129* are similar to the characteristics of sample *e119*. Increasing the temperature is generally accompanied by a rapid falloff in the total luminescence intensity of the structure under study, which indicates the presence of thermal quenching. Further-

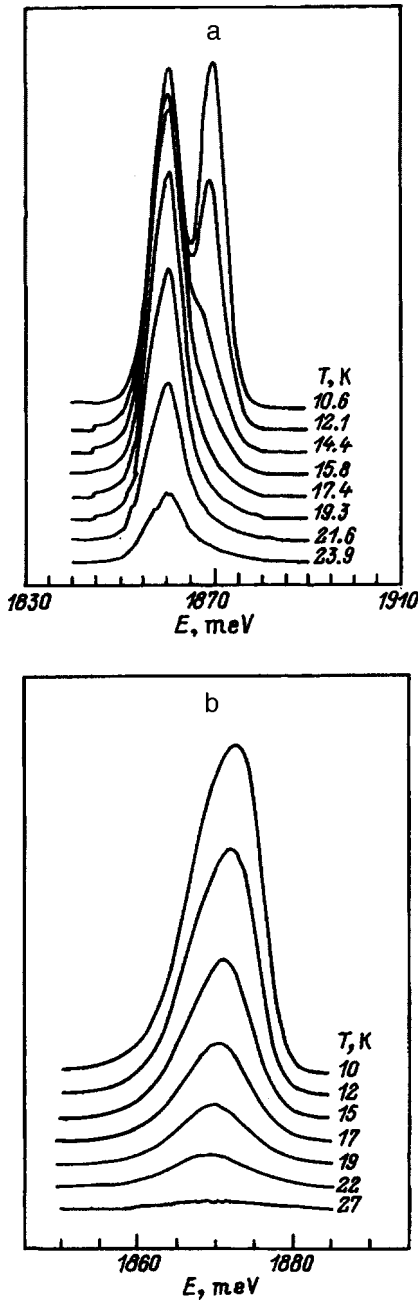


FIG. 2. Temperature induced change in the luminescence spectra of sample NMSL1 at point a1 (a) and sample e119 at point 2 (b).

more, as the temperature increases we observe a redistribution of the intensity of doublet lines from the NMSL1 sample (Fig. 2a). The experimental data were analyzed quantitatively by mathematically decomposing the recorded spectra into sums of line shapes described in general by the Voigt function. The intensity of each peak is defined to be the integral under the line shape. The results of this processing are partially shown in Fig. 3.

2. ANALYSIS AND DISCUSSION OF RESULTS

The high brightness of low-temperature $X-\Gamma$ luminescence observed in experiments and the practically linear dependence of the intensity of the exciton peaks on the excita-

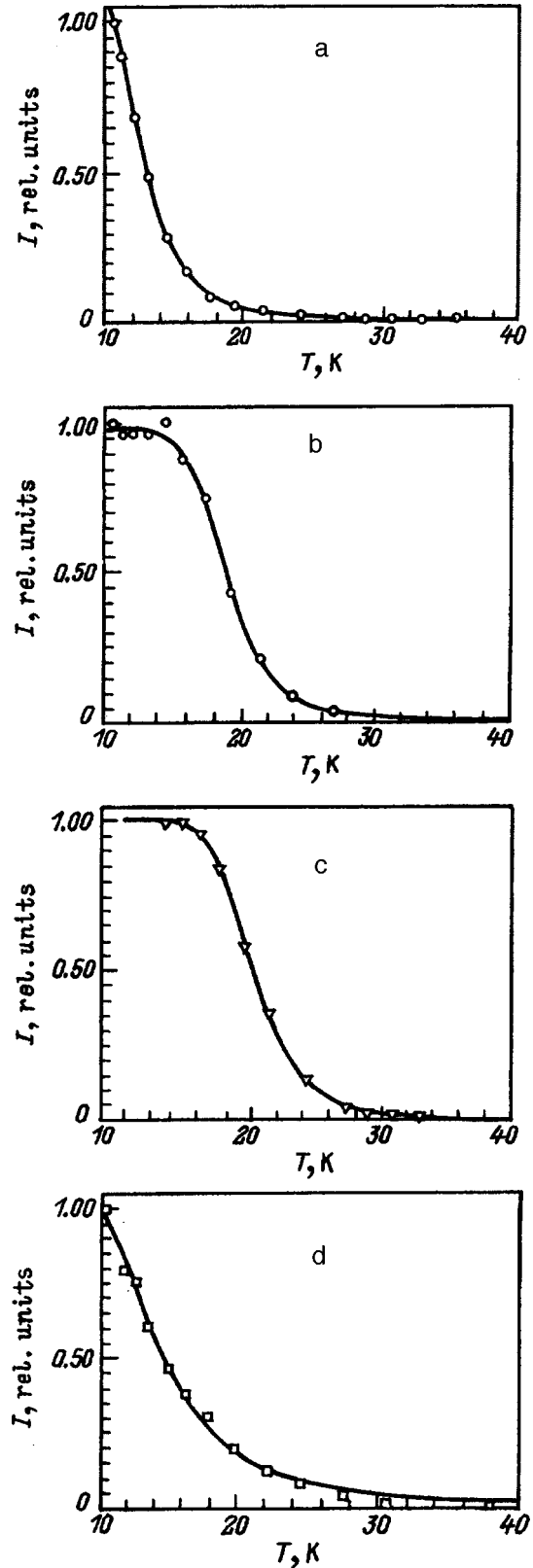


FIG. 3. Dependence of the intensity of exciton lines on temperature. Dots—experimental data; solid curves—results of calculations using Eq. (5). a—sample NMSL1, point a1, photon emission energy 1870 meV; b—NMSL1, point a6, 1875 meV; c—NMSL1, point a1, 1860 meV; d—e119, point 1, 1874 meV.

tion density attest to low nonradiative losses at all stages that precede the formation of the $X-\Gamma$ exciton. From this it fol-

lows that temperature quenching takes place primarily by a nonradiative loss of excitations directly from the exciton level. As we already mentioned above, nonradiative losses arise as a result of thermally stimulated delocalization of the excitations, which facilitates their encounter with quenching centers.

Generally speaking, we stimulate two alternative processes by increasing the temperature: increase of the exciton energy as a whole with a transition to higher-lying delocalized states, and dissociation of the exciton into a pair of free carriers. Since the low-temperature mobility of a $X-\Gamma$ exciton is small according to theoretical estimates,⁸ the second process can make delocalization of the excitations significantly easier. The thermal activation energy for this process is given by the binding energy of the $X-\Gamma$ exciton, which for short-period GaAs/AlAs superlattices is 8–10 meV.⁹

The parameters of the delocalization process for the exciton as a whole should be determined by the mechanism for initial localization of the $X-\Gamma$ exciton. The mechanisms that are regarded as most effective in spatially localizing a quasi-two-dimensional $X-\Gamma$ exciton in a type-II superlattice are localization at point defects with the formation of a bound exciton state^{10,11} and localization by nonplanar boundaries between heterojunction layers.¹² In the first case, the size of the localization region coincides with the Bohr radius of the exciton, and the localization energy is of order 3–5 meV.

In the second case, the character of exciton localization depends significantly on the profile of the heterojunction. For high-quality structures grown on well-oriented substrates using continuous growth regimes, the heterojunctions consist of a combination of planar sections (islands) that differ in width by the thickness of a single monolayer (for GaAs this is 2.83 Å). The difference in exciton energy for superlattices that differ in their GaAs or AlAs layer thicknesses by a single monolayer is 10–20 meV.⁵ This quantity should also give the depth of energy localization of the excitons in thick monolayer islands.

In superlattices grown without smoothing of the heterojunctions, the size of a planar island is considerably smaller than the exciton radius. In such structures the energy of an exciton is given by the average position of the heterojunction, and its fluctuations lead to inhomogeneous broadening of the exciton line shape. In this case, the low-frequency wing of the line shape is generated by exciton states that are localized at large-scale fluctuations of the heterojunction barrier, while the high-frequency wing is due to delocalized exciton states. Thus, the energy of localization of an exciton in these structures is not a constant, but rather varies smoothly over the inhomogeneous line shape.

The discussion above implies very different spectroscopic manifestations of thermally stimulated delocalization of an exciton, as a whole, in superlattices having different heterojunction structures. In lattices with smoothed boundaries, the lowest exciton state is generated either in planar layers of large transverse spatial extent or in relatively thick islands of small transverse spatial extent (comparable to the exciton radius). Motion in planar layers does not require thermal activation, generally speaking, while thermal ejection of an exciton from a thick island into a spatially ex-

tended layer containing quenching centers is characterized by fixed values of the activation energy equal to the difference between the corresponding exciton energies. In lattices with fine-scale fluctuations of the heterojunction barrier the activation energy is not fixed, but rather varies over the inhomogeneously broadened line shape.

In contrast to processes of exciton delocalization, dissociation of the exciton into a pair of free carriers is characterized by a single value of the activation energy which is practically independent of the shape of the heterojunction. The difference in values of activation energy for different delocalization processes of the excitations allows us to identify the dominant process based on the results of temperature measurements.

The customary framework used to describe the process of temperature-induced quenching of the luminescence is an elementary three-level scheme. In this scheme, in addition to the ground state 0 and radiative exciton state 1 there is another state 2 located above state 1 and characterized by a large probability for nonradiative relaxation. As the temperature increases, transitions from level 1 to level 2 become possible with the absorption of a phonon, “switching on” a “2–0” channel for quenching. If states 1 and 2 are localized and thermal equilibrium is established between them, then the populations of levels 1 and 2 should be related by the Boltzmann relation

$$n_2 = n_1(g_2/g_1)\exp(-E_{12}/kT). \quad (1)$$

Here g_i is the statistical weight of the level, and E_{12} is the energy gap. The total occupation of levels 1 and 2 is determined in this case by the steady-state solution to the balance equation

$$d(n_1 + n_2)/dt = -a_{10}n_1 - b_{20}n_2 + P, \quad (2)$$

where a_{10} is the probability for radiative, and b_{20} for nonradiative transitions, and P is the pump.

Expressions (1) and (2) are not difficult to generalize within the framework of a more realistic model that takes into account the presence of a continuous spectrum (bands) of delocalized states. In this case

$$n_2/n_1 = (g_2/g_1) \int f_2(E)\exp(-(E_{12}+E)/kT)dE, \quad (3)$$

where $f_2(E)$ is the normalized spectral density of delocalized states. Since near the bottom of the band the spectral density of quasi-two-dimensional exciton states is practically constant, integration of Eq. (3) over energy gives

$$n_2/n_1 = (g_2/g_1)A_1 \exp(-E_{12}/kT). \quad (4)$$

Here A_1 is a normalization constant.

The combined solution of Eqs. (2) and (4) allows us to obtain an expression for the temperature dependence of the intensity of exciton luminescence

$$I(T) = n_1 a_{10} = I(0)/(1 + AT \exp(-E_{21}/kT)), \quad (5)$$

$$A = A_1(b_{20}/a_{10}),$$

where $I(0)$ is the intensity of low-temperature luminescence. By using Eq. (5) to analyze the temperature dependence of

TABLE II. Parameters of quenching process

Sample	Point	Superlattice	Energy	A	E_{12} , meV
		Period, monolayers	Peak, meV		
NMSL1	a1	12.6	1860	950	18.0
			1870	120	8.1
	b4	12.2	1871	20	8.4
	a6	12.1	1875	2250	18.5
			1886	44	8.4
	c4	12.0	1871	170	12.4
1886			1800	10.0	
e119			1856	2.8	7.3
e129			1889	33	8.1

the luminescence intensity, we can establish the value of the energy gap between states 1 and 2 and thereby determine the basic mechanism for delocalization of the excitations.

Figure 3 shows a comparison of calculated curves based on Eq. (5) and the results of experiments. It is clear from this figure that in the temperature range 10–25 K the theoretical curves are in quite satisfactory agreement with the experimental data for all the samples under study. At higher temperatures we observe an additional increase in the probability of quenching caused probably by occupation of delocalized high-energy band states.

The computed values of the pre-exponential factors and activation energy are listed in Table II.

Analysis of the data presented in Table II, taking into account the picture we have at the present time of the structure of the heterojunctions in the samples under study, allows us to draw certain definite conclusions about the basic mechanisms for thermal delocalization of excitations in type-II GaAs/AlAs superlattices.

Under these circumstances it is most informative to analyze data obtained at various points on sample NMSL1, whose microstructure was investigated in considerable detail in Ref. 5. An especially noteworthy feature, which draws our attention to temperature-induced luminescence quenching, is the presence of high-frequency peaks assigned to excitons located in planar islands with large spatial extent. The conditions for energy localization are not satisfied for these excitons; however, experimental results show that the process that quenches them nevertheless requires thermal activation. The value of the activation energy for quenching of these high-frequency peaks turns out to be practically the same at all sample points. Furthermore, as is clear from Table II, it coincides within limits of error with the activation energy for temperature-induced quenching of luminescence in samples e119 and e129, which have fundamentally different heterojunction structures. To this we can add the results of our analysis of literature data (Fig. 3 in Ref. 3), which shows that, in the temperature range 10–30 K, the temperature induced change in the kinetics of $X-\Gamma$ luminescence in analogous superlattices is also characterized by an activation energy close to our value of E_{12} . Starting from this, we may conclude that a universal process exists for thermal delocalization of excitations in type-II GaAs/AlAs superlattices.

The fact that the luminescence quenching process for excitons located in spatially extended portions of the planar

heterojunctions must be thermally activated has essentially two possible explanations. According to the first, free excitons in such regions are delocalized and their luminescence is quenched even at low temperatures. In this case, the spectrum of low-temperature luminescence is generated by excitons bound at point defects (for example, carbon-containing acceptor centers), which are present in the form of uncontrolled impurities in all epitaxial structures. Increasing the temperature leads to liberation of the bound excitons and a decrease in the intensity of their luminescence. The activation energy for this process equals the binding energy at the acceptor centers, which as we mentioned above comes to 3–5 meV. Using the data listed in Table II, it is not difficult to see that all the experimentally obtained values of E_{21} are considerably larger than this quantity. Furthermore, in accordance with Eq. (4) heat should lead to the appearance of a luminescence line for free excitons in the high-frequency wing of the exciton peak, which is not observed in experiments.

The second explanation for the necessity of thermal activation follows from the assumption that $X-\Gamma$ excitons have very low mobility, caused by scattering by micro-inhomogeneities of the heterojunction (such micro-inhomogeneities, whose dimensions are significantly smaller than the exciton radius, may exist even in regions that are planar on the average). As a result of this, the radius for exciton diffusion turns out to be smaller than the average distance between quenching centers, which abruptly lowers the probability of quenching.

As the temperature increases, the possibility arises that the exciton can dissociate (ionize) into a pair of free carriers that can move much more rapidly than their parent particle. The trapping of delocalized carriers leads to quenching of the exciton luminescence. The primary evidence in favor of this model is the constant value of the activation energy E_{12} mentioned above, obtained for various structures, and the agreement of this value within limits of error with the value of the binding energy of a $X-\Gamma$ exciton. Within the framework of this model, the absence of a buildup of the high-frequency wing of the exciton line during heating is explained without contradiction by the relatively small probability (compared to the excitons) of radiative recombination of the free carriers.

The temperature behavior of the low-frequency components of the doublets at points a1 and a6 of sample NMSL1 is characterized by certain other regularities. On the initial segment (10–15 K) an insignificant (in the range 10–15%) but quite perceptible growth in the intensity of these components is observed. Further increases in the temperature are accompanied by a falloff in this intensity. Just as for the high-frequency components, the falloff in intensity is well described by Eq. (5) (Fig. 3), but the activation energy in this case turns out to be considerably larger. According to Ref. 5, the low-frequency components are emitted by excitons localized in spatially bounded planar islands formed by monolayer fluctuations of one of the heterojunctions. During the dissociation of such excitons only one of the carriers is freed, while the other carrier remains localized in the island. Complete delocalization of an excitation will occur only after the

transition of the second carrier to a more spatially confined layer. The additional energy required for this process equals the change in energy of the $X-\Gamma$ exciton during a monolayer change in the thickness of the corresponding well. Using the data of Table II, it is not difficult to convince oneself that for points *a1* and *a6* this pattern is well obeyed. The difference in values of E_a for the two peaks at each of the points coincides within limits of error with the difference in frequency of these peaks. The initial buildup of the intensity of low-frequency components mentioned above indicates the presence of a thermally stimulated exchange of energy between excitons located in layers of different thickness. Identifying the mechanism for energy exchange and its dependence on the structure parameters requires additional research.

As we already mentioned above, the temperature quenching of luminescence in samples *e119* and *e129* having inhomogeneous heterojunctions is characterized by the same value of activation energy as for quenching of the high-frequency peaks in sample *NMSL1*. At the same time, the relative probability for quenching (coefficient *A* in Table II) turns out to be considerably smaller in these samples. The latter implies that the degradation in the quality of the heterojunctions caused by the change in growth technology (i.e., the absence of smoothing) leads to a decrease in the mobility of the free carriers formed as a result of thermal dissociation of an exciton.

Thus, the comparative experimental investigations described here of temperature variations in the luminescence spectra of type-II GaAs/AlAs superlattices with significantly different structures of their heterojunction boundaries lead us to the following conclusions. We may consider it established that the high brightness of the low-temperature luminescence of such superlattices is caused by the fundamentally small mobility of $X-\Gamma$ excitons, and not by their energy localization on structural defects. The primary reason for luminescence quenching in the temperature range 10–30 K is ther-

mally stimulated dissociation of the exciton into a pair of free carriers having higher mobilities than the exciton, and efficient trapping centers. This process is universal for type-II GaAs/AlAs superlattices, independent of their preparation method. At the same time, the efficiency of quenching, which is determined by the degree of delocalization of the carriers, depends strongly on the structure of the superlattice layers formed, as specified by the heterojunction relief. For superlattices grown in the regime of smoothing of the heterobarrier, the probability of quenching is on the average 1–2 orders of magnitude higher than for superlattices grown in the usual regime.

The authors are grateful to H. M. Gibbs and G. Khitrov for kindly providing the samples and to M. V. Belousov for discussing the results obtained.

This work was supported by the Russian Fund for Fundamental Research (Grants Nos. 97-02-18163 and 9702-18339).

¹P. Dawson, Opt. Quantum Electron. **22**, S231 (1990).

²D. V. Korbutyak, A. I. Bercha, L. A. Demchina, V. G. Litovchenko, and A. V. Troshchenko, Fiz. Tverd. Tela (Leningrad) **34**, 3350 (1992) [Sov. Phys. Solid State **34**, 1793 (1992)].

³G. D. Gilliland, A. Antonelli, D. J. Wolford, K. K. Bajaj, J. Klem, and J. A. Bradley, Phys. Rev. Lett. **71**, 3717 (1993).

⁴J. Ihm, Appl. Phys. Lett. **50**, 1068 (1987).

⁵M. V. Belousov, I. Ya. Gerlovin, H. M. Gibbs, I. V. Ignatev, A. V. Kavokin, G. Khitrova, and I. E. Kozin, Inst. Phys. Conf. Ser. (IOP Publishing Ltd, 1997) N155, Ch. 12, p. 885.

⁶D. Gammon, B. V. Shanabrook, and D. S. Katzer, Appl. Phys. Lett. **57**, 2710 (1990).

⁷M. Nakayama, K. Imazawa, K. Suyama, I. Tanaka, and M. Mishimura, Phys. Rev. B **49**, 13 564 (1994).

⁸A. B. Dzyubenko and G. E. W. Bauer, Phys. Rev. B **51**, 14 524 (1995).

⁹C. P. Chang and Y.-T. Lu, Phys. Rev. B **49**, 5438 (1994).

¹⁰C. I. Harris, B. Monemar, H. Kalt, P. O. Holtz, M. Sundaram, J. L. Merz, and A. C. Gossard, Phys. Rev. B **51**, 13 221 (1995).

¹¹R. Klann, H. T. Grahn, and K. Fujiwara, Phys. Rev. B **51**, 10 232 (1995).

¹²M. Kohl, D. Heitmann, S. Tarucha, K. Leo, and K. Ploog, Phys. Rev. B **39**, 7736 (1989).

Translated by Frank J. Crowne

Coulomb interaction controlled room temperature oscillation of tunnel current in porous Si

V. V. Afonin and V. L. Gurevich

Wihuri Physical Laboratory, University of Turku, FIN-20014 Turku, Finland;

A. F. Ioffe Physicotechnical Institute, Solid State Physics Division, 194921 St. Petersburg, Russia

R. Laiho, A. Pavlov, and Y. Pavlova

Wihuri Physical Laboratory, University of Turku, FIN-20014 Turku, Finland

(Submitted December 15, 1997)

Fiz. Tverd. Tela (St. Petersburg) **40**, 1147–1150 (June 1998)

A novel phenomenon of regular oscillations is observed in I – V characteristics of porous silicon under illumination by visible light. The measurements are performed at room temperature using a scanning tunneling microscope. The heights of the oscillation peaks appear to be a linear function of the oscillation number. The experimental value of the Coulomb energy determined from the oscillation period is much smaller than $k_B T$. The oscillations are attributed to a Coulomb effect, i.e., to the periodic trapping of a multielectron level in a quantum well within a Si nanocrystal under the combined influence of the voltage variation at the STM tip and the Coulomb interaction among the carriers. © 1998 American Institute of Physics. [S1063-7834(98)03706-X]

We have observed periodic oscillations in I – V characteristics of porous Si illuminated by visible light. The experiment is performed at room temperature using a scanning tunneling microscope (STM). The relative amplitude of the oscillating part is about 10%. At the same time, the Coulomb energy determined from the distance between the adjacent oscillation peaks is smaller than the thermal energy $k_B T$ at room temperature so that within the framework of the standard theory of Coulomb blockade the oscillation amplitude should be exponentially small.

Ours is a typical charge transport experiment in which a voltage difference is applied to a source (a metallic tip) and a sink (silicon, see Fig. 1) separated by an insulating gap. In the middle of the gap lies a third electrode (porous Si nanocrystal). Under illumination the electrons are excited to the conduction band whereas the holes are in the valence band. Part of the excited electrons annihilate with holes, another part is localized on traps while some electrons are left in the conduction band taking part in the charge transport. As the electron-phonon scattering is intensive, the electrons will be in a partial thermodynamic equilibrium, i.e., they have an equilibrium distribution function. However, their chemical potential μ is determined by the illumination. Under the action of the voltage, the electrons in the nanocrystal create a current from the conduction band into the semiconductor sink. The neutrality is maintained by the flow of electrons between the metal tip and the valence band of the nanocrystal.

Porous Si specimens were prepared by ordinary method using electro-chemical anodizing of p -Si(100) wafers of resistivity $5 \Omega/\text{cm}$ for 5 minutes at the current $25 \text{ mA}/\text{cm}^2$. Before measurements, the samples were stored for several days in the ambient to reach a quasi-steady-state regime of natural oxidation.¹ As shown in Fig. 1, the tunnel junction

for STM investigations was formed between the tip of the microscope and the porous Si layer grown on a wafer. To increase the number of free carriers, and the tunneling current I , the specimens were illuminated with light from a Xe lamp or a Kr/Ar laser working at $\lambda=514$ or 647 nm (with power density up to $P_{\text{max}} \approx 10 \text{ mW}/\text{mm}^2$). STM images of our samples show clusters (with size about 100 nm) of prolonged particles (columns) of 3 to 5 nm width and about 20 nm height on the top of the porous Si layer. The distance between the particles is 3–5 nm. The total thickness of the porous layer is about $3 \mu\text{m}$. These structures are similar to

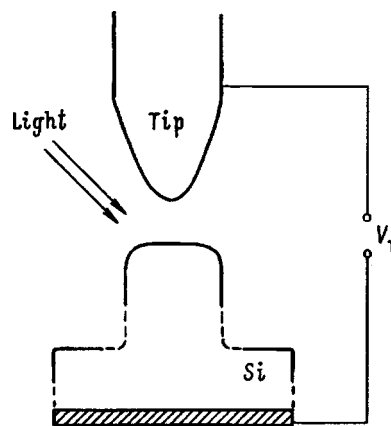


FIG. 1. Schematic representation of a tungsten tip of a scanning tunneling microscope placed above an illuminated nanoparticle (column) of porous Si. The top of a nanoparticle, covered with an oxide layer, is separated from the bulk Si by a poorly conducting region of porous Si. Below the nanoparticle the bulk of the specimen with aluminumized back side (shaded) is schematically depicted. V_T is the external voltage applied between the tip and the aluminumized back side.

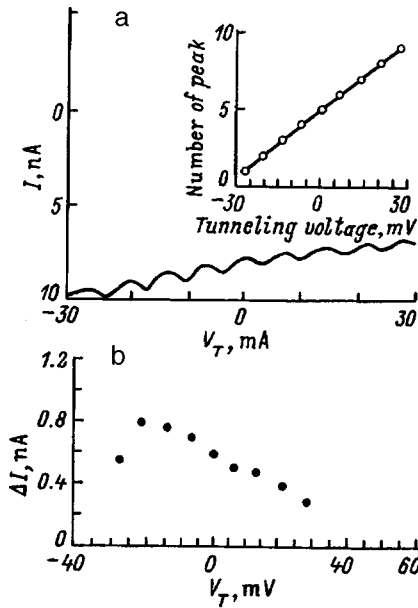


FIG. 2. a) Oscillation of the tunneling current I between the STM tip and porous Si surface illuminated at $\lambda=647$ nm from the Kr/Ar laser, when the value of V_T is changed. b) Dependence of the amplitude ΔI of the current modulation on the voltage V_T .

the surface features of porous Si observed previously by AFM and STM.²

Porous Si can capture injected carriers,³ exhibits both the surface photovoltaic effect with photoinduced trapping of charge in the oxide on the surface⁴ and shows persistent photoconductivity.⁵ These phenomena are usually observed in structures with built-in potential barriers where the excess carriers are injected optically into the vicinity of such a barrier. In the presence of the surface photovoltaic effect it is possible to get a tunneling current, I , sufficient to operate STM at values of the applied tunneling voltage $V_T=0$. The $I-V$ curves obtained in this way have shapes similar to those observed under illumination (i.e., photoconductivity) using a thin metal film electrode on porous Si.⁶ The enhancement of the carrier density by light may be 2–3 orders of magnitude⁷ although the actual current value varies strongly in different experiments.^{6,7} Furthermore, metal electrodes evaporated on Si usually introduce interface states⁸ which may seriously influence the transfer of charge. Such defects are not present in transport experiments by vacuum tunneling like ours.

At small V_T (up to few tens of mV) a regular modulation of the $I-V$ curve as shown in Fig. 2a is observed when V_T is swept slowly (within 20 s) from -30 to $+30$ mV at a randomly selected point of the tip above the sample surface, irrespective of the light source or the wavelength of the Kr/Ar laser. As is evident from the inset of the figure, the oscillations are periodic in V_T with an average period $\Delta V_T = 6.7$ mV. The current steps shown in Fig. 2b vary from 0.3 to 0.8 nA. When V_T is swept from the negative towards positive values the size of ΔI increases at first steeply and then slowly decreases in a linear way after a kink in the ΔI versus V_T plot.

The shape of the $I-V$ curves and the current oscillations observed on different places of the sample surface are gen-

erally similar to the pattern shown in Fig. 2. However, the number of such clearly discernible oscillations of I may vary from point to point and values of ΔV_T between 2.5–6.7 mV have been observed in different experiments and different samples. It means variation of $\Delta V_T/k_B T$ between 0.1–0.25. Points of the sample surface showing small modulation of the $I-V_T$ curve could be found relatively easy. But only a small fraction of them (10–15%) had amplitude comparable with the plot in Fig. 2a. We attribute these oscillations to a Coulomb effect that will be described below.

Electron tunneling in correlation with charging effects was extensively investigated during recent years (see, for instance, Ref. 9) and were clearly demonstrated in multi-junction normal-conducting devices¹⁰ at rather low temperatures T . Quite recently, however, they were observed at room temperatures.^{11,12} The high-temperature experiments were made on very small samples. In the present paper we propose and investigate a different way to reach the high-temperature limit in charging effects.

To begin with discussion of the origin of this oscillation we shall start with the simplest possible example comprising, however, all the relevant features of the phenomenon (as we understand it). We shall consider electrostatic interaction of a gate electrode (the STM tip in our case) with a nanocrystal of a good conductor.

We start with the equation for the electrostatic energy \mathcal{U} of the relevant part of the system (gate electrode + nanocrystal). Assume that the gate electrode is at a constant potential ϕ while the nanocrystal is characterized by the charge variable q . We subtract from the total electrostatic energy the work of the source maintaining the potential constant (cf with Landau and Lifshitz,¹³ Sec. 5) so that

$$\mathcal{U} = (q - C_{12}\phi)^2 / 2C_{11} - C_{22}\phi^2 / 2. \quad (1)$$

Here C_{ik} is the capacitance matrix (where index 1 denotes the conductor while index 2 denotes the gate electrode). One can rewrite the first term as $(1/2)C_{11}\Phi^2(q, \phi)$, Φ being the potential of the nanocrystal which can be considered as a function of two variables, q and ϕ . This is an electrostatic energy of the nanocrystal in the field of the gate electrode. The equations are valid provided that all the charges are situated on the sample surface. Here we imply that, in addition to the electrostatic forces, there are also sufficiently large forces of a different origin ensuring the overall stability of the Coulomb system. For the energy stabilizing the system we introduce notation W . In our present example this is an electron work function at the metal's surface.

Let us discuss the first term on the right-hand side of Eq. (1). Term $q^2/2C_{11}$ describes the mutual repulsion of the excess charges. Term $C_{12}^2\phi^2/2C_{11}$ represents the repulsion of the polarization charges induced by the gate voltage. Finally, term $-C_{12}q\phi/C_{11}$ describes the interaction between these two types of charges.

Now we will turn to a more realistic situation in regard to our experiment. Consider a conductor with a small number of carriers (electrons and holes), so that they cannot screen out the gate field in the whole nanocrystal. Let us assume presence of a potential well inside the conductor, so that the conductor is nonhomogeneous. Were the well suffi-

ciently deep and wide, all the electrons would be trapped in the well, so that the system could be looked upon as a small piece of metal in a dielectric matrix. For the mechanic energy of such a metal droplet one can also use Eq. (1). Let us now assume that the potential well is shallow. In this situation one can expect that W will be sufficiently small (see below). If W is smaller than $(1/2)C_{11}\phi_1^2$ the electrons could not be trapped in the well. For $W=0$ only a state of indifferent equilibrium where $q_1=C_{12}\phi_2$ can exist. This is a manifestation of the Earnshaw theorem (according to which a classical system where only electrostatic interaction cannot be stable).

Further in the present paper we shall be interested in the case where $W < E_C$ (here $E_C = e_0^2/2C_{11}$, e_0 being the electron charge). Such states can be stable only if the energy of repulsion of the excess charge as well as of the polarization charge is almost compensated by the energy of their interaction. Stability the limits of such a state are very narrow, i.e., the states with the charge that differs from $C_{12}\phi_2$ by $\pm e_0$, i.e., by a single elementary charge, would be unstable [see below—Eq. (2)]. It means that the multielectron state consisting of the excess charge and polarization cloud will be distributed as a whole over the entire volume of the nanocrystal. These considerations permit one to define W in our case. It will be equal to the distance between the uppermost level within the well and the bottom of the conduction band.

Thus we postulate existence of a multielectron state characterized by a multielectron charge q and existing for those values of the gate voltage where $C_{12}\phi/e_0$ is very close to an integer. Such a state cannot take part in the current transport (the electrons bound within the well cannot move along the potential drop). Due to the same condition $W < E_C$, this state is unstable for such values of the gate potential when $C_{12}\phi/e_0$ deviates sufficiently from an integer. This physical picture is self-consistent as the state of indifferent equilibrium is stabilized by a small potential of non-electrostatic origin. Formally we could just state that the electrostatic energy \mathcal{U} is diagonalized by introduction of a variable $q' = q_1 - C_{12}\phi$.

Now we can calculate the probability of realizing the n -electron state for finite temperatures T . Besides electrons in an ordinary conduction band, an n -electron state discussed above can also be excited provided that

$$E_n = E_C(n - N)^2 < W. \tag{2}$$

Here $N = C_{12}\phi/e$. This state may not be excited at all, then $n = 0$. If it is excited then $n = [N]$ where by $[N]$ we denote the integer part of N . Thus the existence and spectrum of the bound-electron state depends on the voltage at the gate electrode.

Let the number of one-electron levels in the well be g . The number of ways for n electrons to occupy g levels is C_g^n (cf with Ref. 14). For simplicity, we assume that the distance between energy levels in the well is the smallest energy scale. Then the additional part of the thermodynamic potential due to multielectron excitation is

$$\Omega_n = -k_B T \ln \left(1 + C_g^n \exp \frac{\mu n - E_n}{k_B T} \right). \tag{3}$$

Thus the average number of electrons bound within a well is

$$\bar{n} = -k_B T \frac{\partial \Omega}{\partial \mu} = \frac{n C_g^n \exp[(\mu n - E_n)/k_B T]}{1 + C_g^n \exp[(\mu n - E_n)/k_B T]}. \tag{4}$$

We are interested in the case where

$$E_n \approx W < E_C \ll k_B T. \tag{5}$$

One can see that the oscillation amplitude is not exponentially small provided that

$$C_g^n \exp(\mu n/k_B T) \gg 1. \tag{6}$$

In our case of an illuminated nanocrystal, the number of electrons N_p rather than the chemical potential is fixed. The chemical potential should be calculated from equation $N_p = N_b \exp(\mu/k_B T) + n$ where

$$N_b = \mathcal{V} \int d\epsilon \nu(\epsilon) \exp(-\epsilon/k_B T). \tag{7}$$

Here \mathcal{V} is the volume of the nanocrystal while $\nu(\epsilon)$ is the density of electron states. Here we assume that the electrons in the conduction band are nondegenerate. One can see that this is the case if $(N_p - n)/N_b \ll 1$.

For $n \ll g$ one can use the following approximate equation $g! = (g - n)! g^n$. Then Eq. (6) can be rewritten

$$\frac{1}{n! N_b^n} g^n (N_p - n)^n \gg 1. \tag{8}$$

This is a product of big and small parameters. When the product is small the oscillation amplitude goes down. In the case we are interested for which Eq. (6) is valid there are n electrons in the well in spite of the fact that the chemical potential is negative and its absolute value is bigger than $k_B T$. This is due to a large statistical weight of the states in the well. As a result, we have for the current $I = GV(1 - n/N_p)$ where V is the voltage applied across the nanocrystal, including the potential barriers at its surfaces, G is the conductance of the nanocrystal for $V \rightarrow 0$. Here we made use of the fact that the electron distribution function for Boltzmann statistics has a factor $\exp(\mu/k_B T)$. The ratio of the oscillatory part of the current, ΔI , to the non-oscillating part for $[N] < n_0$ is given by $|\Delta I|/I = n/N_p$.

When inequality Eq. (6) is reversed the oscillation amplitude goes to zero as this small parameter, i.e., exponentially. The case $g - n \ll g$ can be treated in the same manner as above with replacement $n \rightarrow g - n$. When $g - n$ goes down, so that inequality (6) is reversed, the oscillation amplitude is again exponentially small.

In some sense the phenomenon discussed and Coulomb blockade have opposite physical meaning. In our situation the state where n electrons have the lowest energy is pinned to the potential well under the combined influence of the Coulomb interaction among the carriers and the gate voltage variation. As a result, the electrons are excluded from the conduction process provided that $W < E_C$. This means that for a particular value of ϕ only one multielectron state with corresponding number n can be bounded. To the contrary, the manifestation of the Coulomb blockade is that for $k_B T < E_C$ only such a state conducts the current.

Let us discuss possible origin of the well in our experiment. In principle any relatively shallow potential well with a small interlevel distance can bring about the oscillatory behavior. We feel, however, that in a systems like porous Si there is a special reason for existence of such wells. We mean that the inhomogeneity of the nanocrystal surface and its oxidations can be responsible for the well formation. Due to the oxidation of the surface (and maybe also illumination) the bands are bent upward near the surface. One may expect that the scale of the bands' bending due to a poor screening may be even comparable to the size of the nanocrystal itself. The bending is in general different in different points of the nanocrystal surface. The band bendings should result in formation of potential wells for the conduction electrons or holes. Some of these wells would not let the carriers reach the regions from which they can tunnel out of the nanocrystal. Thus the band bendings can be centres of multielectron state pinning.

Comparing the data in Fig. 2 with Eq. (1) we come to the conclusion that the holes (rather than electrons) are localized in the well ($C_{12} < 0$). If one linearly extrapolates the current-voltage characteristic in Fig. 2 it crosses the abscissa axis at $V = -60$ mV. This is a typical value of the surface photovoltage for Si.¹⁵

The oscillation pattern is sinusoidal rather than a system of sharp peaks. This may be due to the fact that W is of the order of E_C [see Eq.(2)], so that the effect is due to the levels within a stripe of the width E_C in a rather deep well.

The oscillation we discuss has a period of several mV. Oscillation of dI/dV (at a constant tunnel current I) with the period of several V have been observed on some metals—see¹⁶ and the references therein. The oscillation is ascribed to the resonances between the de Broglie wavelength of electron and the distance between the tip and the metal's surface. Such interpretation cannot be varied in our case as it would demand enhancement of the distance between the metal tip and the porous Si surface to ~ 1000 Å.

It is possible to pick out the amplitude of the oscillating current from the total current (see Fig. 2b). The accuracy of the amplitude measurement is about 15% of the amplitude. The oscillation pattern ceases not abruptly but in a gradual way (see the left points in Fig. 2b). The states with large values of n can be achieved only if the highest levels in the well are filled. If the electron lifetime on the highest levels is finite (as the uppermost levels can be hybridized between the well and conduction band) it may provide an explanation for the behavior of this sort.

The following estimates are given for the least favorable case where the degeneracy parameter is of the order of 1, i.e., $N_b \sim N_p$. For a $5 \times 10 \times 30$ nm nanocrystal we have $N_p \approx 150$. As one can see in Fig. 2a, $|\Delta I|/I \approx 0.1$. Thus it is sufficient to have 5–10 levels in the well to explain the observed phenomenon. Such numbers demand rather high concentrations of electrons within the nanocrystal. We believe that such concentrations can be achieved because the probability for an electron to tunnel out of the nanocrystal is very low. We remind that we assume existence of continuous conduction and valence bands in the nanocrystal but not in the

sample as a whole. Thus one can expect accumulation of the carriers in the nanocrystal.

Let us estimate the numbers of electrons involved so that the oscillation could be observable. Eq. (6) gives

$$\left(\frac{egN_p}{nN_b} \right)^n \gg 1 \quad (9)$$

(where $e = 2.72$) for $N_p \gg n \gg 1$. This inequality is fulfilled due to the high power n in Eq. (9).

In summary, we have observed for the first time room-temperature periodic oscillations in the I - V characteristics of STM current tunneling into porous Si which is illuminated by visible light. The heights of the oscillation peaks appear to be a linear function of the oscillation number. The oscillations are attributed to the periodic trapping of a multielectron level in a quantum well (situated in a Si nanocrystal) under the combined influence of the gate voltage variation and the Coulomb interaction among the carriers. We believe that, in the future, regular nanostructures possessing the properties necessary for observation of this effect can be tailored.

Valuable discussions with Y. Galperin and G. E. Pikus are gratefully acknowledged.

V. V. A. and V. L. G. are grateful to Wihuri Foundation and the Russian Fund Fundamental Research (Grant N 97-02-18286-a) for supporting this work.

¹F. Kozlowski and W. Lang, *J. Appl. Phys.* **72**, 5401 (1992).

²T. George *et al.*, *Appl. Phys. Lett.* **60**, 2359 (1992); G. B. Amisola *et al.*, *Appl. Phys. Lett.* **61**, 2595 (1992); R. M. Sanaki *et al.*, *J. Vac. Sci. Technol. B* **14**, 2432 (1996).

³A. V. Petrov and A. G. Petrukhin, *Fiz. Tekh. Poluprovodn.* **28**, 82 (1994) [*Semiconductors* **28**, 49 (1994)].

⁴A. B. Matveeva *et al.*, *Fiz. Tekh. Poluprovodn.* **29**, 2190 (1995) [*Semiconductors* **29**, 1142 (1995)].

⁵R. Laiho, A. Pavlov, and Y. Pavlova, E-MRS 1996 Spring Meeting (Strasbourg, France); *Thin Solid Films* **297**, 138 (1997).

⁶G. Giebel and L. Panesi, *Phys. Status Solidi A* **151**, 335 (1995); D. B. Dimitrov, *Phys. Rev. B* **51**, 1562 (1995).

⁷T. Ozaki *et al.*, *J. Appl. Phys.* **76**, 1986 (1994).

⁸C. Barret and J. Vapaille, *J. Appl. Phys.* **50**, 4217 (1979).

⁹H. van Houten *et al.*, *Single Charge Tunneling*, edited by M. H. Devoret and H. Grabert (Plenum, New York, 1992).

¹⁰D. V. Averin and K. K. Likharev, in *Mesoscopic Phenomena in Solids*, edited by B. L. Altshuler, P. A. Lee, and R. A. Webb (Elsevier, Amsterdam, 1991).

¹¹K. Bock, *Phantoms* (Newsletter), 12 October 1996.

¹²E. S. Soldatov *et al.*, *JETP Lett.* **64**, 556 (1996).

¹³L. D. Landau and E. M. Lifshitz, *Electrodynamics of Continuous Media*, Pergamon (1993).

¹⁴G. E. Pikus, *Principles of the Theory of Semiconductor Devices* [in Russian], Nauka, 1965.

¹⁵R. J. Hamers, in *Scanning Tunneling Microscopy I*, edited by H.-J. Güntherodt and R. Wiesendanger (Springer, Berlin, 1994).

¹⁶Y. Kuk, *ibid.*

Inelastic resonant tunneling

L. S. Braginskiĭ and É. M. Baskin

Institute of Semiconductor Physics, Siberian Branch of the Russian Academy of Sciences, 630090 Novosibirsk, Russia; Novosibirsk State University, 630090 Novosibirsk, Russia
(Submitted December 23, 1997)

Fiz. Tverd. Tela (St. Petersburg) **40**, 1151–1155 (June 1998)

A general expression for the resonant contribution to a tunneling current has been obtained and analyzed in the tunneling Hamiltonian approximation. Two types of resonant tunneling structures are considered: structures with a random impurity distribution and double-barrier structures, where the resonant level results from size quantization. The effect of temperature on the current-voltage curves of tunneling structures is discussed. The study of the effect of potential barrier profile on the d^2I/dV^2 line shape is of interest for experiments in inelastic tunneling spectroscopy. Various experimental situations where the inelastic component of the tunneling current can become comparable to the elastic one are discussed. © 1998 American Institute of Physics. [S1063-7834(98)03806-4]

The problem of resonant tunneling mediated by electron-phonon coupling was solved in Ref. 1. It allows exact solution only under the assumption that only electrons localized at an impurity can interact with phonons. As this could be expected, electron-phonon coupling broadens the resonant peak. At the same time, however, the wave-function phase of the tunneling electron can be conserved. This is indeed so, provided the potential barrier is such that the time the electron resides at the impurity is substantially shorter than the characteristic phase relaxation time.

This work considers another limiting case. It is assumed that the electron residence time at an impurity is substantially longer than the phase relaxation time. While this makes exact solution of the problem impossible, it permits one to introduce the electron distribution function at the impurity.

Second-order approximation in the electron-phonon coupling constant takes fully into account the effect of lattice vibrations on the resonant tunneling current. It is shown that interaction with phonons in the course of tunneling provides a dominant contribution to the inelastic resonant current if the barrier width is much larger than the localization length.

Expressions for the elastic and inelastic components of the tunneling current are obtained. Possible experimental conditions in which the inelastic tunneling-current component may become comparable to the elastic one are discussed. It is shown that the shape of the peaks in experimental plots of the second derivative of resonant tunneling current vs voltage varies with increasing temperature. For low temperatures, I'' has the shape of the first derivative of δ function, and for high temperatures, that of the second derivative.

1. INELASTIC RESONANT TUNNELING THROUGH A BARRIER WITH IMPURITIES

Consider electron tunneling through a barrier with impurities which have a localized state with energy E_0 . The analysis carried in Ref. 2 permits us to limit ourselves to

taking into account electron-phonon coupling only for electrons tunneling to a resonant impurity. We write the Hamiltonian in the form

$$\begin{aligned}
 H = & \sum_p \varepsilon_1(p) a_p^+ a_p + \sum_p \varepsilon_2(p) b_p^+ b_p + E_0 \sum_i c_i^+ c_i \\
 & + \sum_q \omega(q) \left(f_q^+ f_q + \frac{1}{2} \right) 1/\sqrt{V} \sum_{i,p} t_{1i} (a_p^+ c_i e^{ipR_i} + \text{h.c.}) \\
 & + 1/\sqrt{V} \sum_{i,p} t_{2i} (b_p^+ c_i e^{ipR_i} + \text{h.c.}) \\
 & \times \sum_{p,i,q} T_{1i} [a_p^+ c_i (f_q^+ - f_{-q}) e^{ipR_i} + \text{h.c.}] \\
 & + \sum_{p,i,q} T_{2i} [b_p^+ c_i (f_q^+ - f_{-q}) e^{ipR_i} + \text{h.c.}]. \quad (1)
 \end{aligned}$$

Here a_p^+ and b_p^+ are free-electron creation operators to the left and right of the barrier, c_i^+ creates an electron at the impurity at point R_i , and f_q^+ creates a phonon. The first two terms in Eq. (1) describe the kinetic energy of electrons on different sides of the barrier, the third one, the electron at impurity, the fourth, phonons with dispersion $\omega(q)$ (for the sake of simplicity, only one phonon branch is assumed to exist), the fifth and sixth terms relate to elastic electron tunneling from the electrodes to the impurity, and the seventh and eighth, to phonon-assisted tunneling to the impurity. The quantities t_1 , t_2 , T_1 , and T_2 depending on the impurity coordinates are defined by Eqs. (5) and (9) of Ref. 2, respectively. Besides, Eq. (1) does not contain the term associated with direct tunneling between impurities in the barrier. The latter assumption is valid if the characteristic separation between impurities is of the order of or exceeds the barrier width.

We define the current operator as the derivative with

respect to time of the operator of the number of particles to the left of the barrier, i.e.,

$$\hat{I} = e\hat{N} = -e \sum_p [a_p^+ a_p, H] = -eIm \left\{ 1/\sqrt{V} \sum_{p,i} t_{1i} a_p^+ c_i e^{ipR_i} + \sum_{p,i} T_{1i} a_p^+ c_i (f_q^+ - f_{-q}) e^{ipR_i} \right\}.$$

Then for the current we obtain

$$I = -eIm \left\{ 1/\sqrt{V} \sum_{p,i} t_{1i} \langle a_p^+ c_i \rangle e^{ipR_i} + \sum_{p,i} T_{1i} \langle a_p^+ c_i (f_q^+ - f_{-q}) \rangle e^{ipR_i} \right\}. \tag{2}$$

The angular brackets $\langle \rangle$ denote here the thermodynamic mean. In first order of perturbation theory, Eq. (2) yields

$$I = I_1 + I_2, \quad I_1 = -eIm\Pi_1, \quad I_2 = -eIm\Pi_2,$$

$$\Pi_1 = -\frac{2T}{(2\pi)^3} \sum_{n,i} \int |t_{1i}|^2 G_1(p, \omega_n) D_0(\omega_n) d^3p,$$

$$\Pi_2 = \frac{2T^2}{(2\pi)^6} \sum_{n,l,i} \int |T_{1i}|^2 G_1(p, \omega_n) \times D_0(\omega_l) F(q-p, \omega_l - \omega_n) d^3p d^3q. \tag{3}$$

Here

$$G_{1,2} = \frac{1}{i\omega_n - \varepsilon_{1,2}(p) + \mu_{1,2}}, \quad D_0 = \frac{1}{i\omega_n - E_0 + \mu_i},$$

$$F(q, \omega_n) = -\frac{\omega(q)}{\omega_n^2 + \omega^2(q)}$$

are Green's functions for electrons to the right of the barrier, electrons to the left of it, electrons at the impurity, and phonons, respectively, $\varepsilon_{1,2}(p)$ and $\mu_{1,2}$ are the energies and Fermi levels of electrons to the left and right of the barrier, μ_i is the Fermi level of electrons at impurity, $\omega_n = \pi T(2n + 1)$, ($n=0, \pm 1, \pm 2, \dots$), and T is the temperature.

We shall assume in what follows the electron-phonon coupling to be weak. Then the correction to D_0 in higher orders of perturbation theory will be connected only with the possibility of direct electron tunneling from the impurity into the band. This means that D_0 in Eq. (3) should be replaced by the complete Green's function of the impurity electron determined from the equation

$$D_{ii'} = D_0 \delta_{ii'} + 1/V \sum_{i''} \int t_{1i''} t_{1i'}^* G_1(p) e^{ip(R_i - R_{i''})} \times D_{i''i'} D_0 d^3p + 1/V \sum_{i''} \int t_{2i''} t_{2i'}^* G_2(p) e^{ip(R_i - R_{i''})} \times D_{i''i'} D_0 d^3p. \tag{4}$$

This equation can be solved assuming the nondiagonal terms in $D_{ii'}$ to be small. This assumption is valid for low impurity concentrations ($N \ll d^{-2} \sqrt{2mE_0}$, where d is the barrier width) and is certainly satisfied in our model. Indeed, the starting Hamiltonian (1) does not include interimpurity transitions, which is possible only if a still more rigorous condition on the impurity concentration is upheld ($Nd^3 \ll 1$).

Dropping the i 's, we obtain

$$D = D_0 + 1/V \left[\int |t_{1i}|^2 G_1(p) d^3p + \int |t_{2i}|^2 G_2(p) d^3p \right] D_0 D,$$

$$D = \frac{1}{i\omega - E_0 + \mu_i + i\Gamma_i}, \tag{5}$$

where Γ_i is the imaginary part of the bracketed expression; the possibility for electrons to tunnel into the band results in a broadening of the impurity level. The real part of the bracketed expression gives the shift of the impurity level E_0 relative to the Fermi levels to the right and left of the barrier, which is inessential for us. The quantity Γ_i for the case of a single impurity was determined in Ref. 3. After straightforward but cumbersome manipulations we obtain from Eq. (3)

$$I_1 = -\frac{4e}{(2\pi)^3} \sum_i \int \frac{\Gamma_i [f_1(\varepsilon_1) - f_i] |t_{1i}|^2}{(\varepsilon_1 - E_0 + \mu_i - \mu_1)^2 + \Gamma_i^2} \frac{d\varepsilon_1}{V_\perp} d^2p_\parallel,$$

$$I_2 = -\frac{2e}{(2\pi)^6} \sum_i \int \frac{|T_{1i}|^2}{V_\perp} \times \left\{ \frac{\Gamma_i [(1+N)f_i(1-f_i) - Nf_1(1-f_i)]}{[\varepsilon_1 - E_0 + \omega(q) - \mu_1 + \mu_i]^2 + \Gamma_i^2} - \frac{\Gamma_i [(1+N)f_1(1-f_i) - Nf_i(1-f_1)]}{[\varepsilon_1 - E_0 - \omega(q) - \mu_1 + \mu_i]^2 + \Gamma_i^2} \right\} d\varepsilon_1 d^2p_\parallel d^3q. \tag{6}$$

Here $V_\perp = 1/m_1 \sqrt{2m_1 \varepsilon_1 - p_\parallel}$, N is the number of phonons in the system (the Bose function), f_1 is the Fermi function for electrons to the left of the barrier, and f_i is the average number of electrons at the impurity. For $\Gamma_i \neq 0$, f_i is not the Fermi function. It can be found by numerical summation of the series

$$f_i = \frac{1}{2} + T \sum_n \frac{1}{i\omega_n - E_0 + \mu_i + i\Gamma_i}. \tag{7}$$

f_i plotted vs $E_0 - \mu_i$ has the form of a diffuse step, with the diffused width equal to $\max(T, \Gamma_i)$.

The tunneling current $I = I_1 + I_2$ determined in this way corresponds to that between the left electrode and the impurities. The current between the impurities and the right electrode can be found in the same way. By equating the tunneling currents, one can obtain the continuity equation determining the Fermi level of electrons at impurities. This procedure of tunneling current calculation is valid only for low-transmission barriers. In this case the residence time of electrons at impurities is long enough, first, to result in phase relaxation of their wave function, and second, for quasi-

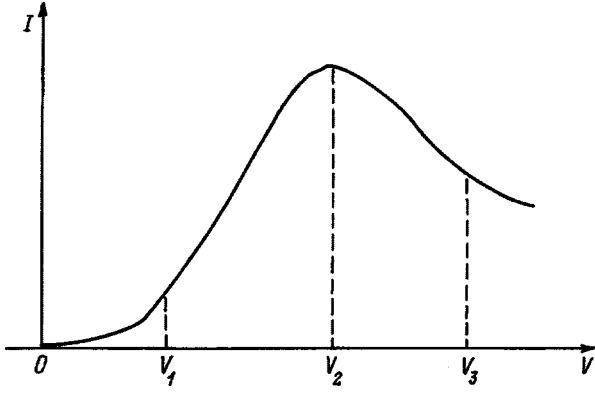


FIG. 1. Current-voltage characteristic of a barrier with a resonant level.

equilibrium to set in. This justifies the use of equilibrium temperature diagrammatic techniques in tunneling current determination.

Consider possible manifestations of resonant tunneling effects in experiments. These effects are seen, as a rule, in the current-voltage characteristics of structures, as well as in tunneling spectroscopy experiments, where one measures the second derivative of tunneling current with respect to voltage. Equations (6) permit one to obtain the current-voltage characteristic of a structure where both elastic (I_1) and inelastic (I_2) resonant tunneling take place.

To analyze Eqs. (6), we first assume that there is no electron-phonon coupling, and that the temperature is zero. Consider the contribution to Eq. (6) due to one impurity located, in accordance with the resonance condition, inside the barrier, so that $t_{1i} = t_{2i}^*$. The first integral in Eq. (6) contains the Lorentzian term $\Gamma / [(\varepsilon - E_0 + \mu_i - \mu_1)^2 + \Gamma^2]$. This means that if the Fermi level to the left of the barrier, μ_1 , is below the impurity level, then the resonant current through the barrier is zero. A rise of the Fermi level results in the appearance of an elastic component in the resonant tunneling current. If $t_{1i} = t_{2i}^*$, then, dropping I_2 in the continuity equation, we find $\mu_i = (\mu_1 + \mu_2)/2$. The condition for the elastic component of the current to appear is $eV > E_0$.

Figure 1 shows the $I(V)$ plot in the region $eV \approx E_0$. The rise of the current results from the appearance of I_1 , so that $e(V_2 - V_1) \sim \Gamma$. The falloff within the region $V_2 - V_3$ is connected, first, with the decrease in the barrier transmission t_1 for electrons tunneling with an energy $E = E_0$ because of its becoming higher. Besides, the different changes in the barrier tunneling transmissions, t_1 and t_2 , breaks the resonant tunneling condition if the bias is increased still more. The quantity $V_3 - V_2$ can be estimated by assuming that under such a bias the barrier transmission changes by an amount of the order of the transmission itself, in which case

$$e(V_3 - V_2) \sim \frac{2k}{md},$$

where $k = \sqrt{2mU_0}$, and U_0 is the characteristic barrier height. As a rule, $\Gamma \ll k/md$, so that $|V_2 - V_1| \ll |V_3 - V_2|$, i.e. the current-voltage characteristic of resonant current through a single impurity has the shape of a step.

Consider the current-voltage characteristic of a structure with randomly distributed impurities. Let resonant tunneling through some impurity set in at a certain bias eV . This means that the Fermi energy of the tunneling electron is equal to the impurity level energy, and, besides, that the condition $t_{1i} = t_{2i}^*$ is upheld. A change in bias voltage drives this impurity out of resonance. But the condition of resonance in energy will now be satisfied for some other impurity whose z coordinate differs from that of the first (resonant) impurity. This implies that resonant tunneling can involve impurities confined in a layer whose thickness is of the order of the under-barrier electron wavelength. Summation over all impurities in this layer results in an effective broadening of the step in the current-voltage characteristic. In order of magnitude, the width of the rise region

$$e|V_2 - V_1| \sim \frac{eV}{kd} \sim \frac{k}{md},$$

so that the extent of the rise region turns out to be of the same order of magnitude as that of the falloff, $|V_3 - V_2|$. In other words, the current-voltage characteristic of a barrier with randomly distributed impurities is bell-shaped, with a width of order $2k/md$.

2. INELASTIC RESONANT TUNNELING THROUGH A DOUBLE-BARRIER STRUCTURE

To consider tunneling through multibarrier structures, one has to take into account the possibility of longitudinal electron motion in the quantum well between barriers. This results in the appearance of an additional quantum number characterizing electron states in the well, viz. electron momentum directed parallel to the barrier plane, and the lateral confinement level E_0 broadens to become a band. Including the conservation of the longitudinal component of the tunneling-electron quasi-momentum, Hamiltonian (1) takes on the form

$$\begin{aligned} H = & \sum_p \varepsilon_1(p) a_p^+ a_p + \sum_p \varepsilon_2(p) b_p^+ b_p + \sum_i E_0(p_{\parallel}) c_{p_{\parallel}}^+ c_{p_{\parallel}} \\ & + \sum_q \omega(q) \left(f_q^+ f_q + \frac{1}{2} \right) + \sum_p t_{1p} (a_{p_{\perp}, p_{\parallel}}^+ c_{p_{\parallel}} + \text{h.c.}) \\ & + \sum_p t_{2p} (b_{p_{\perp}, p_{\parallel}}^+ c_{p_{\parallel}} + \text{h.c.}) \\ & + \sum_{p,q} T_{1p} [a_{p_{\perp}, p_{\parallel}}^+ c_{p_{\parallel}+q_{\parallel}} (f_{q_{\perp}, q_{\parallel}}^+ - f_{-q_{\perp}, -q_{\parallel}}) + \text{h.c.}] \\ & + \sum_{p,q} T_{2p} [b_{p_{\perp}, p_{\parallel}}^+ c_{p_{\parallel}+q_{\parallel}} (f_{q_{\perp}, q_{\parallel}}^+ - f_{-q_{\perp}, -q_{\parallel}}) + \text{h.c.}], \end{aligned} \quad (8)$$

and the expressions for the current (6) become, accordingly,

$$I_1 = - \frac{4e}{(2\pi)^3} \int \frac{\Gamma [f_1(\varepsilon_1) - f] |t_{1p}|^2}{[\varepsilon_1 - E_0(p_{\parallel}) + \mu - \mu_1]^2 + \Gamma^2} \frac{d\varepsilon_1}{V_{\perp}} d^2 p_{\parallel},$$

$$I_2 = -\frac{2e}{(2\pi)^6} \int \frac{|T_{1p}|^2}{V_{\perp}} \times \left\{ \frac{\Gamma[(1+N)f(1-f_1) - Nf_1(1-f)]}{[\varepsilon_1 - E_0(p_{\parallel}) + \omega(q) - \mu_1 + \mu_i]^2 + \Gamma_i^2} - \frac{\Gamma[(1+N)f_1(1-f) - Nf_i(1-f_1)]}{[\varepsilon_1 - E_0(p_{\parallel}) - \omega(q) - \mu_1 + \mu]^2 + \Gamma^2} \right\} d\varepsilon_1 d^2 p_{\parallel} d^3 q. \quad (9)$$

Here Γ , f , and μ are, respectively, the spread of the lateral confinement level, average number of particles, and Fermi level for electrons in the quantum well. They are determined by Eqs. (5) and (7), and the continuity equation for the current, respectively.

We shall assume for simplicity that the lateral confinement level is broadened by longitudinal motion into a parabolic band with an effective mass equal to that of the electron in the left-hand semiconductor. Resonant tunneling will start in this case at bias voltages where the electron Fermi level at the left contact coincides with the bottom of the lateral confinement band, $E = E_0(0)$. Further increase of the bias leads to an increase in the resonant tunneling current. In this case conservation of the energy of the tunneling electron should be complemented by that of the longitudinal component of its momentum, p_{\parallel} . In other words, electrons with a transverse momentum component $p_{\perp}^2 = 2mE_0$ and longitudinal component $p_{\parallel}^2 < 2meV$ will now take part in resonant tunneling. The current will stop to grow at a bias $eV \sim k/md$, where the effective increase of barrier height for resonant tunneling electrons becomes essential. Thus the peaks in the current-voltage characteristics of the two structures turn out to have similar shapes. Current-voltage curves of the type shown in Fig. 1 were observed in many experiments (see, for instance, Ref. 4), as well as are obtained⁵ in numerical simulation.

3. SHORT-WAVELENGTH PHONONS IN RESONANT TUNNELING

We have been considering thus far situations where the inelastic current I_2 was only a small addition to the resonant elastic current. Strictly speaking, inelastic effects are noticeable in this case only in inelastic tunneling spectroscopy (see Sec. 4).

There are, however, conditions in which I_2 is of the order of or even slightly larger than I_1 . This can occur when resonant tunneling requires emission of a short-wavelength phonon. Then the effects of inelasticity will be directly seen in the current-voltage characteristics.

We assume tunneling to proceed through an impurity level associated with a side valley of an indirect semiconductor. The electron wave function at the impurity can be written

$$y_i(\mathbf{r}) = e^{-\sqrt{2M[U(z_0) - E]}|\mathbf{r} - \mathbf{r}_0| + i\mathbf{k}_0 \mathbf{r}_0},$$

and for the electron wave function in the barrier we have

$$\varphi_p(\mathbf{r}) = \sqrt{\frac{2}{\pi|p|}} e^{-\int_0^z |p| dz + i\mathbf{p}_{\parallel} p}.$$

Here $\mathbf{r}_0 = \{\rho_0, z_0\}$ are the impurity coordinates, \mathbf{k}_0 is the position of the side-valley bottom in k space ($|\mathbf{k}_0| \sim \pi/a$), \mathbf{p}_{\parallel} is the electron momentum component parallel to the barrier plane, $\boldsymbol{\rho} = \{x, y\}$ are coordinates in this direction, $|p| = \sqrt{2m[U(z) - E] + p_{\parallel}^2}$, and m and M are the effective masses in the central and side valleys, respectively. Using Eq. (5) from Ref. 2, we obtain

$$t_1 = \frac{1}{4m} \sqrt{\frac{2}{\pi|p(z_0)|}} [|p(z_0)| + ik_{0z}] \times \frac{k}{[k^2 + (p_{\parallel} - k_{0\parallel})^2]^{3/2}} e^{-\int_0^{z_0} |p| dz},$$

$$k = \sqrt{2M[U(z_0) - E]}.$$

Here $\mathbf{k}_{0\parallel}$ and k_{0z} are the components of vector \mathbf{k}_0 parallel and perpendicular to the barrier plane, respectively. Compared to the $|\mathbf{k}_0| = 0$ case, t_1 contains a parameter $(k/k_0)^3$, and for the current we have $I_1 \propto (k/k_0)^6$. For a relatively shallow resonant level, $k/k_0 \ll 1$.

The small parameter k/k_0 does not appear in calculation of the inelastic resonant current T_1 . If the small parameter associated with the inelasticity of electron-phonon coupling is larger than $(k/k_0)^3$, then $|t_1| < |T_1|$, and $I_2 > I_1$.

4. DISCUSSION. TUNNELING SPECTROSCOPY

The peak of the second derivative of tunneling current with respect to voltage in the case of a single impurity is similar in shape to that of the first derivative of δ function, and its width is equal to that of the impurity level Γ . Structures with substitutional impurities distributed randomly over lattice sites should exhibit a series of such peaks, with each of these peaks being due to resonant tunneling through impurities located in the corresponding crystallographic planes parallel to the barrier plane. In order of magnitude, the number of peaks is equal to the ratio of the electron under-barrier wavelength to the lattice constant.

The characteristic separation between these peaks is determined by the slope of the potential barrier and is of the order of $\Delta \sim Ea_0$, where E is the field in the barrier, and a_0 is the lattice constant. Thus for $\Delta > \Gamma$, tunneling spectroscopy experiments permit observation of resonant tunneling through impurities lying in different planes, as confirmed in Ref. 6.

The tunneling peaks should change substantially in shape with increasing temperature T . Indeed, the characteristic size of the rise region, $V_2 - V_1$, for a single impurity is in this case of order $T \gg \Gamma$. If at the same time $T < k/md$, the peak retains its shape. As the temperature increases still more ($T > k/md$), the current-voltage characteristic of a single impurity becomes bell shaped, and the corresponding line in the tunneling spectrum I'' has the shape of the second derivative of δ function. Now the condition for resolution of the tunneling spectral lines corresponding to impurities located in adjacent crystallographic planes, $T < \Delta$, becomes compatible

with the inequality $T > k/md$, provided $ka_0 > 1$. Actually, this implies a possibility of resonant tunneling only through impurities lying in the same plane. This variation of spectral shape with temperature permits certain qualitative conclusions on the barrier shape or on position of the impurities involved in resonant tunneling. Indeed, consider two barriers with the same tunneling transmission, $k'd' = k''d''$. The first of them is high but narrow, whereas the second is low and broad. Then there obviously should exist an intermediate temperature region $k'/m'd' > T > k''/m''d''$, within which the shape of I'' will be different for different barriers. The same relates to various types of impurities in the same barrier. Namely, there should exist a temperature interval within which the tunneling spectrum will feature resonant peaks of different shape.

The influence of electron-phonon coupling can be analyzed using the expressions for I_2 [(6) and (9)]. We see that besides resonant tunneling features one can observe their phonon replicas. The conditions for their observation are $eV/kd > \omega_0 \gg \Gamma$, where ω_0 is the characteristic phonon frequency, and $eV = E_0$ is the bias corresponding to the main resonant peak. Such phonon replicas were observed experimentally.⁷

The authors express their gratitude to M. V. Éntin for numerous fruitful discussions, and to A. P. Kovchavtsev, who drew our attention to the variety of peak shapes in tunneling spectra.

Partial support of the Russian Fund for Fundamental Research (Grant 96-02-19028) and of the Program "Universities of Russia" (Grant 95-0-7.2-151) is gratefully acknowledged.

¹L. I. Glazman and R. I. Shekhter, Zh. Éksp. Teor. Fiz. **94**, No. 1, 292 (1988) [Sov. Phys. JETP **67**, 163 (1988)].

²L. S. Braginskii and É. M. Baskin, Fiz. Tverd. Tela (St. Petersburg) **40**, 1151 (1998) [Phys. Solid State **40**, 1051 (1998)].

³A. V. Chaplik and M. V. Éntin, Zh. Éksp. Teor. Fiz. **67**, 208 (1974) [Sov. Phys. JETP **40**, 106 (1974)].

⁴H. Fukuyama, T. Waho, and T. Mizutani, J. Appl. Phys. **79**, 1801 (1996).

⁵V. F. Elesin, D. V. Mel'nikov, and A. I. Podlivaev, Fiz. Tekh. Poluprovodn. **30**, 620 (1996) [Semiconductors **30**, 337 (1996)].

⁶A. P. Kovchavtsev, G. L. Kuryshev, K. O. Postnikov, I. M. Subbotin, and Zh. I. Khorvat, Fiz. Tekh. Poluprovodn. **21**, 1944 (1987) [Sov. Phys. Semicond. **21**, 1178 (1987)].

⁷U. Lutz, M. Keim, G. Reuscher, F. Fischer, K. Schüll, A. Waag, and G. Landwehr, J. Appl. Phys. **80**, 6329 (1996).

Translated by G. Skrebtsov

Study of the local atomic structure of a silver aluminum alloy by the method of extended electron energy loss fine structure (EELFS)

V. A. Shamin, A. Kh. Kadikova, A. N. Deev, and Yu. V. Rats

Physicotechnical Institute, Ural Branch of the Russian Academy of Sciences, 426001 Izhevsk, Russia
(Submitted June 27, 1997; resubmitted November 28, 1997)
Fiz. Tverd. Tela (St. Petersburg) **40**, 1156–1161 (June 1998)

Extended energy loss fine structure spectra are obtained for electrons at the Al K and Ag $M_{4,5}$ edges for an Al–20 wt %Ag solid solution after high-temperature aging, as well as for the pure alloy components. The analysis layer depth was ~ 20 Å. Radial distribution functions for the atoms are determined by Fourier transforming these spectra with a correction for the phase shift and the method of regularization. For pure aluminum and silver it is found that the position of the first coordinate spheres does not differ from bulk interatomic distances. For the binary alloy it was shown that the state of the sample corresponds to a decomposed solid solution with inclusions of a phase enriched with silver against an aluminum host background. The interatomic Al–Al distances in the binary alloy correspond to the length of a pure aluminum bond. The partial distances to the first two coordination spheres for the pairs Ag–Ag, Ag–Al are the same and equal the interatomic distances of the γ -phase Ag_2Al . © 1998 American Institute of Physics. [S1063-7834(98)03906-9]

Recently, extended electron energy loss fine structure (whose international abbreviation is EELFS) has been used to determine the structural parameters associated with the local atomic environment in near-surface layers.¹ The EELFS method, like EXAFS,² is sensitive to the local region around atoms of a specific kind. However, the traditional use of the Fourier transform to extract structural information from EELFS allows us to obtain only the total atomic radial distribution function (ARDF). Obtaining partial ARDF is impossible using Fourier transforms, in contrast to the method of regularization. It has been shown^{3,4} that the latter can be used to obtain qualitative information about interatomic distances and coordination numbers⁵ for one-component materials. The problem of obtaining partial ARDF for multicomponent materials remains unsolved in EELFS, although it has been solved for EXAFS.^{6–8} It is necessary to exhaustively test this method of determining the partial ARDF on materials that have been well studied by other methods. Binary materials, the simplest kind of multicomponent materials, can be used for this purpose. In our opinion, a particularly well-studied test material is the binary alloy Al–20 wt %Ag after high-temperature aging.

The goal of this work is to determine the local atomic structure using EELFS with respect to atoms of a given type for the Al–20 wt %Ag alloy after high-temperature aging. The depth of the analysis layer was chosen to be sufficiently large to decrease the influence of surface effects and the possibility of comparing results with bulk values obtained by other methods.

1. EXPERIMENT

The specimens used were polycrystalline samples of high-purity (99.99%) silver and aluminum and a sample of the solid solution Al–20 wt %Ag after gradual high-temperature aging to $t=350$ °C.

First, the surfaces of all the samples were mechanically polished. In order to remove the layer damaged during this mechanical processing, the samples of polycrystalline aluminum and silver were polished electrochemically for 4–5 minutes. For the Al–20 wt %Ag alloy, no electrochemical polishing was used. Subsequent preparation steps were the same for all the samples. Before loading into the analysis chamber, the samples were washed in acetone and alcohol in an ultrasonic bath in order to remove grease from the prepared surfaces. The remaining contaminants were removed in the sample chamber by ion etching (Ar^+ , $I=20$ mA). The energy of the argon ions was 0.5 kV for silver, while for the samples of polycrystalline aluminum and the binary alloy they were 1 kV for a first cleaning and 0.5 kV for cyclic cleaning. The purity of the surface was monitored by Auger-electron methods. The level of contaminants of the surface did not exceed 1 atomic %.

EELFS spectra were obtained for the K edges of aluminum and the $M_{4,5}$ edges of silver by a standard JAMP-10S Auger-electron spectrometer. The vacuum level in the analysis chamber was 5×10^{-7} Pa. The excitation electron beam was directed at normal incidence. The beam current was ~ 1 μA . The energy of the primary electron beam was 2500 eV for the K edges of aluminum and the $M_{4,5}$ edges of pure silver, while for the $M_{4,5}$ edge of silver in the binary alloy it was 1200 eV. This allowed us to obtain extended fine structure spectra for pure aluminum and the solid solution to a depth of ~ 20 Å.⁹ The extended fine structure spectra were obtained at room temperature in the first-derivative regime with an amplitude modulation of 10 V. By obtaining spectra cyclically, combined with ion etching and Auger-electron monitoring of the cleanliness of the surface, we were able to accumulate good statistics for the spectra, which were accu-

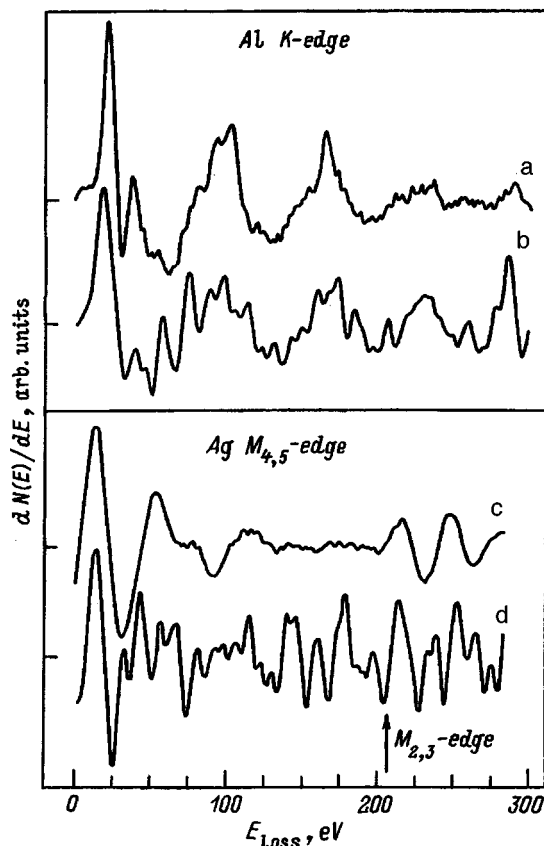


FIG. 1. Extended fine structure spectra obtained in the first-derivative regime. a—K-edge of pure polycrystalline Al, b—K edge of Al in the binary compound Al-20 wt %Ag, c— $M_{4,5}$ edge of pure polycrystalline Ag, d— $M_{4,5}$ edge of Ag in the binary compound Al-20 wt %Ag.

mulated after 1500 passes with steps of 1 eV and 10,000 counts at each point.

2. PRELIMINARY PROCESSING OF THE SPECTRA

Preliminary processing of the experimental EELFS spectra in order to separate out the oscillatory part $\chi(k)$ was done in the standard way for all the experiments.

The background was calculated using cubic splines and partitioning into 5–6 equal sized intervals such that the energy interval was 50–60 eV per division. Figure 1 shows the spectra after subtracting the background and transforming to the energy loss scale. The numerically integrated data are translated into a dependence on wave number in accordance with the quadratic dispersion law.

As a result of this preliminary processing, we separated out the oscillatory parts of the experimental spectra $\chi(k)$ (Figs. 2 and 3).

1) *Pure components of the alloy.* The extracted experimental oscillatory parts are shown in Figs. 2b and 3a for pure aluminum and silver respectively. A detailed description of the mathematical processing used to determine interatomic distances from these experimental data was given in Ref. 10. Here we present only the final results of the processing. Figure 4 shows the Fourier transforms of the oscillatory parts for aluminum and the solution obtained by the method of regularization. It is clear from Fig. 4 that the maximum of the

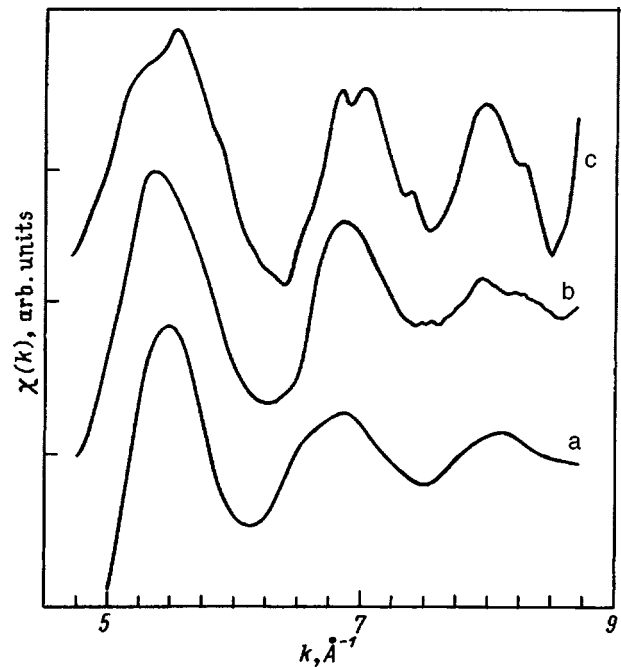


FIG. 2. Oscillatory parts for Al. a—model obtained for two bulk coordination spheres using the theoretical phase functions, b—experimental for pure polycrystal, c—experimental for the binary compound.

first peak in the method of regularizing coincides (within error bars of $\pm 0.02 \text{ \AA}$) with the position of the first coordination sphere for the model ARDF of aluminum. By Fourier transforming with a correction for the phase shift for ten atomic layers of aluminum, we obtained the average value of the first coordination sphere, which corresponds to the crystallographic bulk distance. The phase-shift correction for the

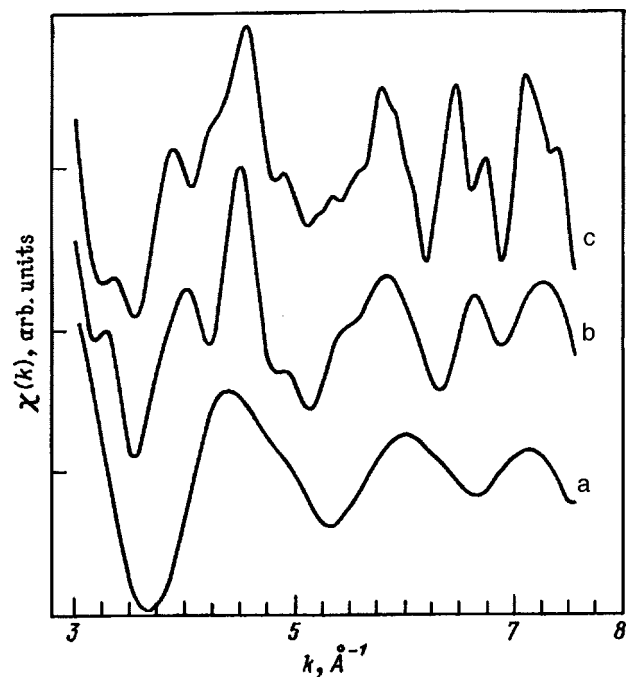


FIG. 3. Oscillatory part for Ag. a—experimental for pure polycrystal, b—model obtained for seven bulk coordination spheres of the γ phase, c—experimental for the binary compound.

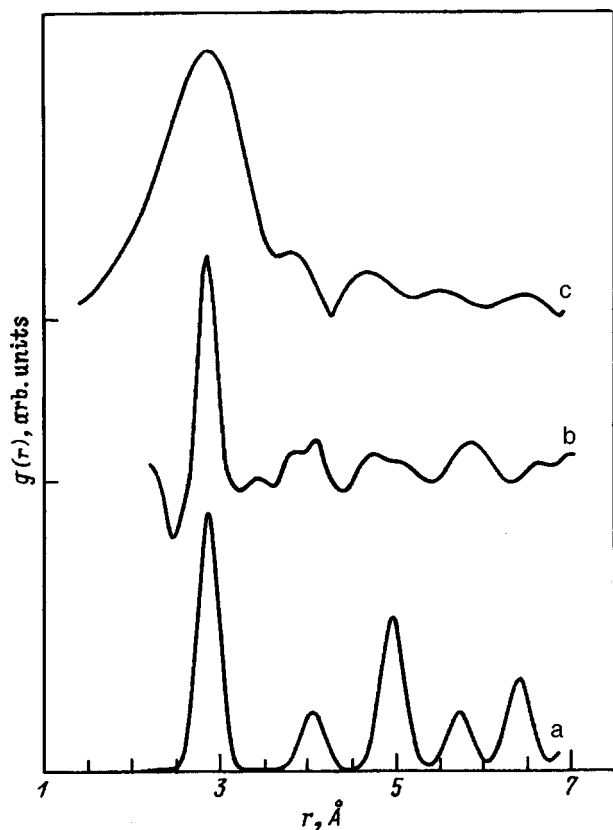


FIG. 4. ARDF for pure Al. a—bulk model of five coordination spheres, b—solution obtained by the method of regularization, c—Fourier transform with phase shift.

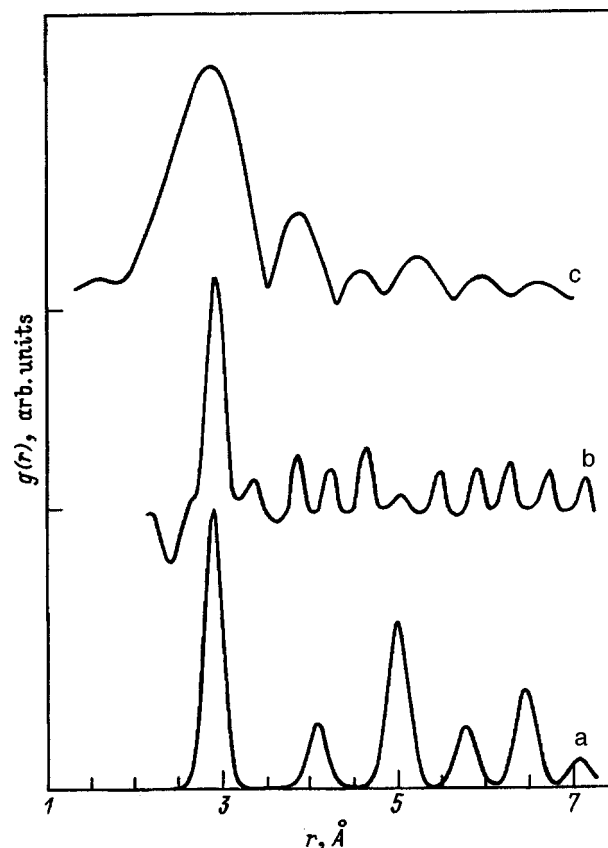


FIG. 5. ARDF for pure Ag. a—bulk model of five coordination spheres, b—solution obtained by the method of regularization, c—Fourier transform with phase shift.

Fourier transform is set equal to half the linear coefficient of the overall theoretical phase function taken with opposite sign. The Fourier transform of the oscillatory part for silver, and also the result of solving the inverse problem by the method of regularization is shown in Fig. 5. In this case we also can see that the maxima of the first peaks of both the Fourier transform with corrections for the phase shift and the regularized solution correspond within limits of error to the bulk values of the interatomic distance for the first coordination sphere in polycrystalline silver.

2) *The binary system Al–20 wt %Ag.* Starting from the proposition that the binary system is a decomposed solid solution, and taking into account the concentration ratios of the components (~ 95 at. % Al and ~ 5 at. % Ag), we can postulate the following model for the atomic structure.¹¹ All the silver atoms are located at nodes of a γ phase, whose stoichiometric composition is close to Ag_2Al . The crystal structure of the γ phase has an HCP lattice with equiprobable occupation of the sites by silver and aluminum atoms (the lattice parameters are $a=2.885$ Å, $c=4.582$ Å.) The fundamental host consists of pure aluminum with FCC structure.

3) *Al K edge of the binary compound.* Figure 1b shows the experimental EELFS spectrum correspond to the K edge of aluminum in the binary compound. The oscillations after the K edge were observed over a range of ~ 300 eV. Comparison of the extracted oscillating part for aluminum in the binary compound (Fig. 2c) and the experimental $\chi(k)$ for

pure aluminum (Fig. 2b) show good agreement between the basic envelopes on the interval of $4.7-8.7$ Å⁻¹. In the range $k > 8.0$ Å⁻¹ the intensity of the oscillatory portion for aluminum in the binary compound is somewhat larger. Furthermore, the presence of an additional component other than pure aluminum in the spectrum is obvious; however, the amplitude of this component is considerably smaller than the fundamental features.

After the Al–20 wt %Ag solid solution decomposes, according to the assumptions of our model, only a small fraction of the aluminum atoms should enter into the composition of the γ phase. Therefore, the primary contribution to the oscillatory part of the aluminum comes from scattering by aluminum atoms that belong to the host, in which case the contribution from Al–Ag pairs to the oscillatory part is negligibly small. For this reason we treat the problem as one-component. The Fourier transform corrected for the total phase shift corresponding to the Al–Al pair ($+0.66 \pm 0.06$ Å) is shown in Fig. 6c. The form of the double intense peak located in the region $2-4$ Å is in good agreement with the analogous peak in the Fourier transform of the oscillatory part for pure aluminum, which confirms our assumption that the contribution from Al–Ag pairs is small. For the solution obtained by the method of regularization shown in Fig. 6b we observe an intense peak whose position corresponds to the bulk interatomic distance of pure aluminum.

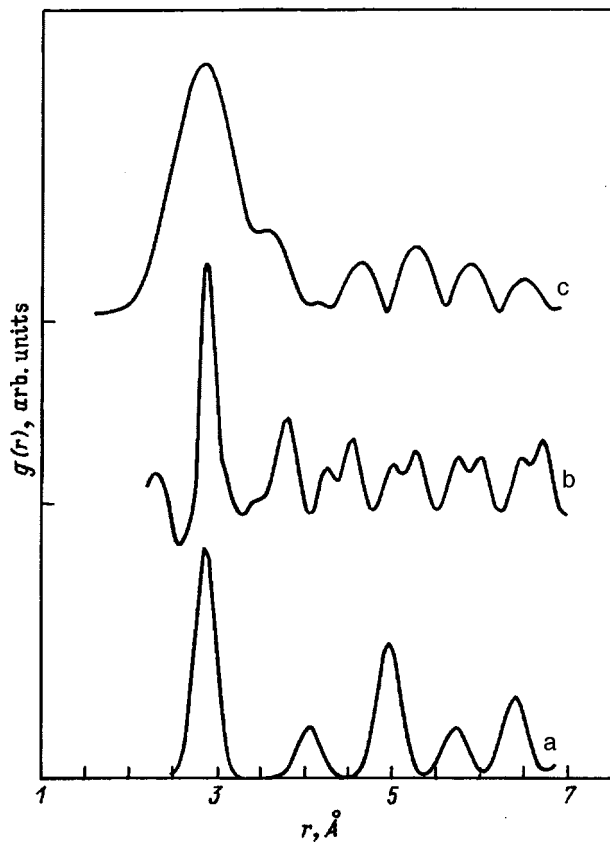


FIG. 6. ARDF for Al in the binary compound. a—bulk model of five coordination spheres, b—solution obtained by the method of regularization, c—Fourier transform with phase shift.

The instability of the problem of determining interatomic distances by the method of regularization does not yield us reliable information for more than the first coordination sphere. The reasons for this instability are, first of all, the small extent of the experimental oscillatory part (of order 4 \AA^{-1}), and secondly the relatively weak contribution to the oscillatory part coming even from the second coordination sphere. Therefore, as in the cases of pure aluminum and silver, we limit ourselves here to discussing only the first coordination sphere.

4) *Ag $M_{4,5}$ edge of the binary compound.* In Fig. 1d we show the experimental EELFS spectrum for the $M_{4,5}$ edge of silver in the binary compound. The extracted oscillatory part is shown in Fig. 3c. Comparison with the oscillatory part for pure silver (Fig. 3a) shows that the behavior of these $\chi(k)$ functions differ considerably.

Five intense peaks appear in the Fourier transform of the oscillatory part of the $M_{4,5}$ edge of Ag (Fig. 7c). The first and second peaks in the Fourier transform have split maxima, associated with the presence of aluminum atoms in the immediate neighborhood of the silver. Since the phase shift functions for backward scattering of aluminum and silver behave so differently, the Fourier transforms of the aluminum and silver peaks are shifted relative to one another. Thus, in solving the problem by the method of regularization it is necessary to take into account the contribution from the two types of atoms. In this case the equation for determining

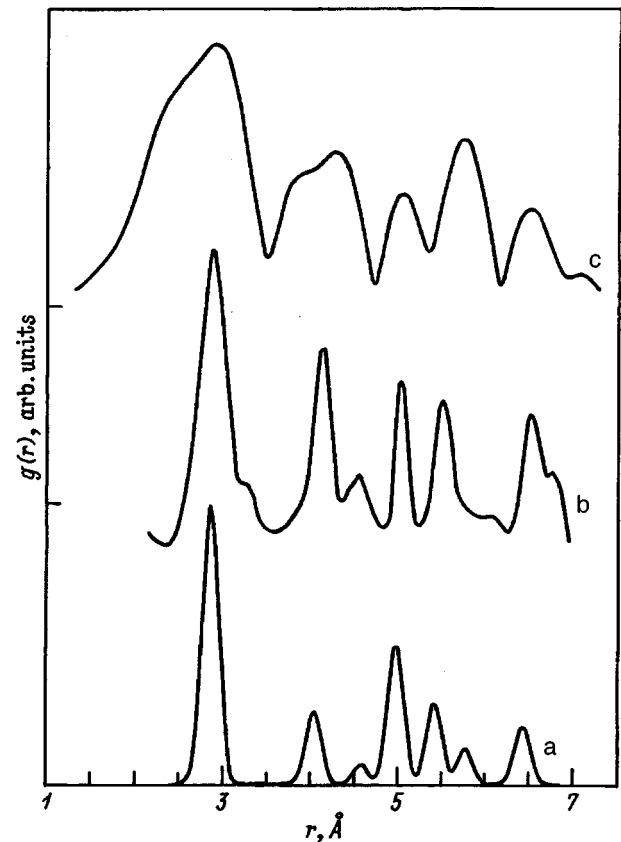


FIG. 7. ARDF for Ag in the binary compound. a—bulk model of seven coordination spheres, b—solution obtained by the method of regularization, c—Fourier transform with phase shift.

partial ARDF for Ag–Ag and Ag–Al atomic pairs is written as a sum of two terms:

$$\begin{aligned} \chi_{\text{Ag}}(k) = & (4\pi\rho_0 c_{\text{Ag}}/k) \int_a^\infty f_{\text{Ag}}(k,r) g_{\text{Ag}-\text{Ag}}(r) \\ & \times \exp(-2r/\lambda(k)) \sin(2kr + 2\delta_{\text{Ag}}(k) \\ & + \varphi_{\text{Ag}}(k,r)) dr + (4\pi\rho_0 c_{\text{Al}}/k) \\ & \times \int_a^\infty f_{\text{Al}}(k,r) g_{\text{Ag}-\text{Al}}(r) \exp(-2r/\lambda(k)) \\ & \times \sin(2kr + 2\delta_{\text{Ag}}(k) + \varphi_{\text{Al}}(k,r)) dr, \end{aligned} \quad (1)$$

where the first term describes scattering from the immediate neighborhood of silver atoms, and the second term scattering from that of aluminum atoms.

The problem of finding two partial ARDF from a single experiment is highly unstable, and can be solved only in a limited number of cases. The small extent of the experimental structure in our case (5 \AA^{-1}) prevents us from obtaining a qualitative solution to the problem. Nevertheless, in this case we can use another approach. For an equiprobable distribution of atoms of different kinds,¹¹ the partial ARDF of Ag–Ag and Ag–Al are the same to accuracy up to different Debye–Waller factors. However, the difference in the Debye–Waller factors $2\sigma_1^2$ for atoms of Ag and Al at a temperature $T=293 \text{ }^\circ\text{C}$ (0.021 and 0.029 respectively¹²) is not large in our case, and does not significantly distinguish the

partial ARDF of Ag–Ag and Ag–Al. In the approximation of equal partial ARDF for the cell of the γ phase $\{g_{\text{Ag–Ag}}(r) = g_{\text{Ag–Al}}(r) = g(r)\}$ we can transform Eq. (1) to a single component equation introducing the concept of a compound amplitude and compound phase-shift function

$$\chi_{\text{Ag}}(k) = (4\pi\rho_0/k) \int_a^\infty f_{\text{com}}(k,r)g(r)\exp(2r/\lambda(k)) \times \sin(2kr + 2\delta_{\text{Ag}}(k) + \varphi_{\text{com}}(k,r))dr, \quad (2)$$

where the compound amplitude is defined as

$$[f_{\text{com}}(k,r)]^2 = [c_{\text{Ag}}f_{\text{Ag}}(k,r)\sin(\varphi_{\text{Ag}}(k,r)) + c_{\text{Al}}f_{\text{Al}}(k,r)\sin(\varphi_{\text{Al}}(k,r))]^2 + [c_{\text{Ag}}f_{\text{Ag}}(k,r)\cos(\varphi_{\text{Ag}}(k,r)) + c_{\text{Al}}f_{\text{Al}}(k,r)\cos(\varphi_{\text{Al}}(k,r))]^2, \quad (3)$$

and the compound phase shift function

$$\varphi_{\text{com}}(k,r) = \arctan\left[\frac{A+B}{C+D}\right], \quad (4)$$

where

$$\begin{aligned} A &= c_{\text{Ag}}f_{\text{Ag}}(k,r)\sin(\varphi_{\text{Ag}}(k,r)), \\ B &= c_{\text{Al}}f_{\text{Al}}(k,r)\sin(\varphi_{\text{Al}}(k,r)), \\ C &= c_{\text{Ag}}f_{\text{Ag}}(k,r)\cos(\varphi_{\text{Ag}}(k,r)), \\ D &= c_{\text{Al}}f_{\text{Al}}(k,r)\cos(\varphi_{\text{Al}}(k,r)). \end{aligned}$$

Figure 3b shows the model oscillatory part for the $M_{4,5}$ edge of silver in the binary compound, calculated using Eqs. (2)–(4). In constructing the model oscillatory part we used seven coordination spheres for the HCP structure of the γ phase with the Debye–Waller factor of silver (Fig. 7a). In these calculations we used the theoretical amplitude and phase for the scattering,¹³ which led to a rather successful description of the experimental oscillatory parts of the EELFS spectra. Since there are no data for the M edges in Ref. 13, the phase shift function at the central silver atom $2\delta_{\text{Ag}}^{\prime=3}(k)$ was determined from experiments for pure silver.¹⁰ The best agreement between the model and experimental oscillatory parts was obtained for concentration coefficients $c_{\text{Ag}} = 0.8$, $c_{\text{Al}} = 0.2$. These values differ slightly from the concentration coefficients for the compound Ag_2Al ; however, the accuracy of determining the concentration coefficients by this method is rather nominal in the absence of normalization of the oscillatory structures. Nevertheless, these values qualitatively show that the phase identified when the solid solution decomposes is enriched by silver atoms. A comparison of the curves in Figs. 3b and 3c shows good agreement between the model $\chi(k)$ and the experimental oscillatory part over the entire interval shown.

The solution to Eq. (2) by the method of regularization is shown in Fig. 7b. The solution obtained contains four peaks corresponding to positions of the coordination spheres for the γ phase Ag_2Al . In this case the maxima of the first two peaks coincide with the positions of the first two coordination spheres for the model ARDF. The peaks of the fourth

and fifth coordination spheres are found at distances that differ by one grid step (0.025 Å) from the corresponding coordination spheres of the model ARDF. However, in determining quantitative values from a regularized solution one should rely on only the first two coordination spheres, since peaks of the regularized solution corresponding to coordination spheres higher than the second are in only qualitative agreement with the model ARDF. We were unable to obtain the correct positions of even the second coordination spheres for the pure components; however, in our view this result is no accident. This is confirmed by examining the Fourier transform, which shows the presence of an additional contribution to the oscillatory structure from distant coordination spheres. We were able to obtain a symmetric form for the first two peaks of the regularized solution, thanks to our inclusion of aluminum atoms in the immediate vicinity of the silver atoms. This fact confirms our *a priori* assertion that the partial distances to the first two coordination spheres for Ag–Ag and Ag–Al pairs are the same.

Thus, the radial distribution functions we have obtained around the silver and aluminum atoms allow us to conclude that the alloy state is that of a completely decomposed solid solution in the near surface layers. In this case, the immediate neighborhood of an aluminum atom will contain only other aluminum atoms, whereas silver atoms can have both silver and aluminum atoms as neighbors. We can predict with high reliability that an equiprobable distribution of atoms of various kinds is present in the alloy that matches the crystal lattice of the γ phase.

Thus, by using methods for studying the structure of solid surfaces with the help of standard electron-probe instrumentation we were able to obtain information about near surface layers of solids. In this paper we have obtained experimental electron energy-loss spectra for the K edge of aluminum and the $M_{4,5}$ edge of silver in the decomposed solid solution Al–20 wt % Ag, and also for the same edges in pure polycrystalline samples of aluminum and silver. The oscillatory parts were extracted and the problem of determining the ARDF in the near surface layers was solved to a depth of 20 Å in the layer.

We have determined that the positions of the first coordination spheres of pure aluminum and silver do not differ from bulk interatomic distances in a layer of order 20 Å. For the case of the complex binary compound, we used the ARDF around atoms of different kinds to show that the state of the sample in the near-surface layer corresponds totally to a decomposed solid solution, with a phase whose composition close to Ag_2Al appearing against an aluminum host background.

¹M. De Crescenzi, Surf. Sci. **21**, 89 (1995).

²M. De Crescenzi, L. Papagno, G. Chiarello, R. Scarmozzino, E. Colavita, E. Rosei, and S. Mobilio, Solid State Commun. **40**, 616 (1981).

³A. H. Kadikova, N. V. Ershov, A. L. Ageev, Yu. V. Ruts, and S. P. Sentemov, Phys. Status Solidi A **122**, K143 (1990).

⁴A. H. Kadikova, Yu. V. Ruts, N. V. Ershov, and A. L. Ageev, Solid State Commun. **82**, 871 (1992).

⁵D. V. Surnin, A. E. Denisov, and Yu. V. Ruts, J. de Phys. IV **7**, C2-577 (1997).

- ⁶Yu. A. Babanov and V. R. Shvetsov, *Phys. Status Solidi B* **131**, K1 (1985).
- ⁷Yu. A. Babanov and V. R. Shvetsov, *J. de Phys. IV* **47**, C8-37 (1986).
- ⁸Yu. A. Babanov, N. V. Ershov, V. R. Shvetsov, A. V. Serikov, A. L. Ageev, and V. V. Vasin, *J. Non-Cryst. Solids* **79**, 1 (1986).
- ⁹D. R. Penn, *Phys. Rev. B* **35**, 2, 482 (1987).
- ¹⁰V. A. Shamin, A. Kh. Kadikova, and Yu. V. Ruts, *Fiz. Met. Metalloved.* **83**(5), 47 (1997) [in Russian].
- ¹¹L. F. Mondelfo, *Structure and Properties of Aluminum Alloys* (Metallurgiya, Moscow, 1979).
- ¹²G. Schulz, *Metal Physics* (in German) [Russ. trans., Mir, Moscow, 1971, 503 pp.].
- ¹³A. G. McKale, B. W. Veal, A. P. Paulikas, S.-K. Chan, and G. S. Knapp, *J. Am. Chem. Soc.* **110**, 3763 (1988).

Translated by Frank J. Crowne

POLYMERS. LIQUID CRYSTALS**Changes in the optical properties of conducting polydiacetylene THD brought on by doping**

E. G. Guk, M. E. Levinshhteĭn, V. A. Marikhin, and L. P. Myasnikova

A. I. Ioffe Physicotechnical Institute, Russian Academy of Sciences, 194021 St. Petersburg, Russia
(Submitted October 8, 1997)Fiz. Tverd. Tela (St. Petersburg) **40**, 1162–1166 (June 1998)

Changes in the optical properties of conducting polydiacetylene THD (poly-1,1,6,6-tetraphenylhexadiindiamine) brought on by doping are investigated for the first time. Spectral dependences of the extinction coefficients were studied in the range $400\text{--}25\,000\text{ cm}^{-1}$ both for the undoped polymer ($\sigma < 10^{-9}\text{ S/cm}$) and at various doping levels (up to $\sigma \sim 5 \times 10^{-3}\text{ S/cm}$). The results obtained attest to the appearance of high carrier concentrations in polydiacetylene THD with conductivities $\sigma \geq 10^{-4}\text{ S/cm}$. The relatively low observed macroscopic conductivity is explained by the complex hierarchy of structural formations that are intrinsic to polymers. The results obtained are compared with the corresponding data for conducting polyacetylene. © 1998 American Institute of Physics.
[S1063-7834(98)04006-4]

Recently, we proposed a new approach¹ to the doping of polydiacetylenes, a unique class of conjugate polymers capable of forming large-scale single crystals. Within the framework of this approach, we demonstrated for the first time that it is fundamentally possible to dope polydiacetylene THD, a polymer with lateral bridges of considerable geometric size. Moreover, within the framework of this approach we obtained values of $\sigma = 3 \times 10^{-2}\text{ S/cm}$ for polydiacetylene THD, which are record breaking for the polydiacetylenes.

We investigated the electrical properties of the doped polymer THD for the first time in Ref. 2. The results of these studies indicated that the conductivity of doped polydiacetylene THD has a complex percolation-like character that is characteristic of all conjugated polymers. A multiyear study of other doped polymers (c.f. Ref. 3) has shown that investigating only the electrical properties of a conducting polymer does not provide enough information to estimate the true carrier concentration induced by doping. Even at very high carrier concentrations, the macroscopic conductivity can have relatively low values, since near the percolation threshold only a small number of free carriers take part in the current transport. Furthermore, in contrast to classical metals and semiconductors, conducting polymers typically exhibit a macroscopic current transport that is multistage in character. Flow of current “from contact to contact” requires transport of carriers along the polymer molecules over the conjugation length, transport from molecule to molecule within fibers, and interfiber transport.³ As we will show later, for polydiacetylene there is yet another complicated scheme for current flow, due to the presence of microcrystalline boundaries.

Under these conditions the study of extinction near the intrinsic absorption edge can give independent information

about the carrier concentration as a function of the doping conditions.⁴

By studying absorption spectra in the infrared region ($\nu \leq 5000\text{ cm}^{-1}$) and comparing the data obtained with known spectra for conducting polyacetylene (see, e.g., Ref. 5), we can also obtain additional information about the concentration of free carriers. Moreover, such studies allow us to track changes in the vibrational spectrum of the original polymer during doping.

In this paper we describe first-ever investigations of the optical properties of doped conducting polydiacetylene THD, both near the intrinsic absorption edge and in the infrared region of the spectrum.

1. EXPERIMENTAL CONDITIONS

The optical properties of undoped polydiacetylene THD have been investigated in a number of papers (see, e.g., Refs. 6 and 7). Interest in these types of investigations stems from the high third-order nonlinear-optics susceptibility $\chi^{(3)}$ of this polymer. Because of the high absorption coefficient of polydiacetylene in the spectral range of interest, solid transparent films are prepared (see Refs. 6 and 7) based on polymethylmethacrylate (PMMA) with a thickness $d \sim 10\text{--}15\ \mu\text{m}$, in which the content of polydiacetylene crystals was $\sim 3\text{ wt}\%$.⁷ Crystals of polydiacetylene are “suspended” in the transparent host with optically smooth walls (Fig. 1a).

Unfortunately, this experimental geometry cannot be used to measure the extinction in doped polydiacetylene, since the key issue is how to measure extinction in the same sample at different doping levels.

The microcrystals of polydiacetylene THD intended for measurement were prepared according to the method described in Ref. 1. Initially needle-shaped polydiacetylene

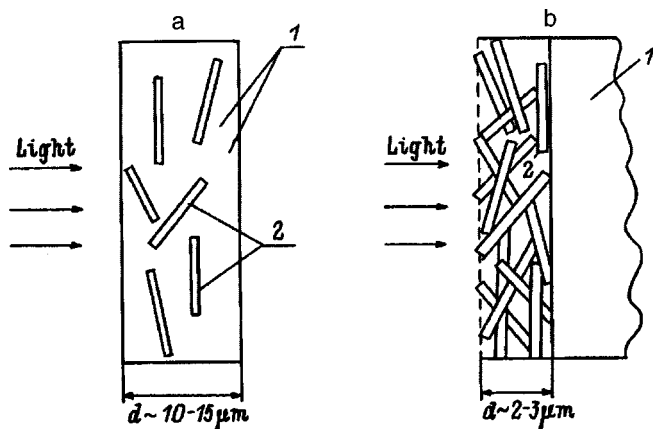


FIG. 1. Samples for measuring extinction. a) Sample for measuring extinction coefficient of undoped polydiacetylene THD (see Refs. 6 and 7). 1—film of polymethylmethacrylate (PMMA), 2—crystals of polydiacetylene THD. The crystals are $\sim 3-5 \mu\text{m}$ in length, with diameters $d \leq 1 \mu\text{m}$. b) Sample for measuring extinction coefficient of doped polydiacetylene THD. The sizes of the crystals are the same as in Fig. 1a.

single crystals of length $l \sim 3-5 \text{ mm}$ and diameter $d \sim 0.3-0.5 \text{ mm}$ were twice subjected to mechanical grinding in an electric mill. The microcrystals obtained from this processing were typically $l \sim 30-50 \mu\text{m}$ in length and $d \sim 3-5 \mu\text{m}$ in diameter. Using ultrasound, a suspension of microcrystallites in acetone was obtained. The suspension was painted on either a glass plate (for measuring extinction in the range $5000 \leq \nu \leq 25000 \text{ cm}^{-1}$) or a polished plate of n -germanium with carrier concentration close to intrinsic (for measuring extinction in the range $400 \leq \nu \leq 5000 \text{ cm}^{-1}$). After the acetone evaporated away, a friable opaque matted film formed on the substrate, with a saturated red color. The density of this film was $\sim 0.1 \text{ g/cm}^3$, which is approximately ten times less than the density of the single-crystal modification of polydiacetylene THD. The structure of the film, which is easily distinguished with the help of an ordinary optical microscope, is qualitatively illustrated in Fig. 1b.

The film that forms on the substrate was doped in iodine vapor at 70°C for 40 minutes. After doping the electrical conductivity and optical extinction coefficient were measured. Then the film was once more subjected to doping. The process was repeated until changes in the absorption spectrum indicated that the polydiacetylene was being destroyed by "overdoping." The maximum achievable value of electrical conductivity σ was $5 \times 10^{-3} - 10^{-2} \text{ S/cm}$, which corresponded to a total doping time of about 48 hours.

The optical extinction coefficient was measured on an SF-20 spectrophotometer, while the electrical conductivity was measured by the four-probe method.

2. MEASUREMENT RESULTS AND DISCUSSION

Figure 2a shows the spectral dependence of the extinction coefficient α for polydiacetylene THD in the range $5000-25000 \text{ cm}^{-1}$ under various doping conditions. The solid curve 1 corresponds to the spectrum of the undoped

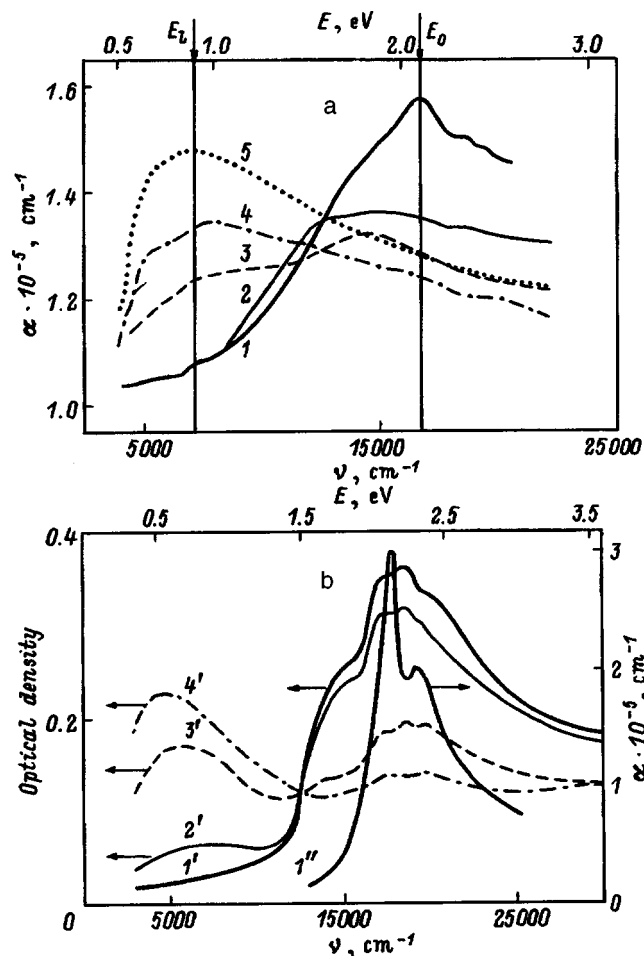


FIG. 2. a) Spectral dependence of the extinction coefficient for polydiacetylene THD at various doping levels. 1—undoped sample. σ (S/cm): 2 — $\sim 10^{-6}$, 3 — $\sim 10^{-5}$, 4 — $\sim 10^{-4}$, 5 — $\sim 10^{-3}$. b) Spectral dependence of extinction coefficient for undoped polydiacetylene THD measured in the geometry corresponding to Fig. 1a (curve 1'') and the analogous dependences for polyacetylene under various doping conditions (see Ref. 5). 1'—undoped sample. σ (S/cm): 2' — 20, 3' — 50, 4' — 100.

original polymer. The numerical value of the extinction coefficient is computed taking into account the density of single-crystal polydiacetylene THD.

Comparison of curve 1 with curve 1'' (Fig. 2b), which corresponds to the spectrum for extinction of undoped polydiacetylene given in Refs. 6 and 7, shows the qualitative similarity of both curves. The maximum of the extinction is located at $\nu \approx 17000 \text{ cm}^{-1}$ ($E_0 \approx 2.1 \text{ eV}$ on curve 1 and $E_0 \approx 2.28 \text{ eV}$ on curve 1''). Note that the maximum of the extinction (curve 1' in Fig. 2b) for the spectrum of undoped polyacetylene⁵ corresponds to the value $\nu \approx 18500 \text{ cm}^{-1}$ ($E_0 \approx 2.29 \text{ eV}$). It is well known that the average conjugation length in a polymer can be deduced from the value of the energy at the extinction maximum: the energy corresponding to the absorption maximum decreases with increasing conjugation length and tends towards the limiting value of $\sim 2 \text{ eV}$ for a sufficiently long conjugation length. For polyacetylene, for example, a value of the energy $E_0 \approx 2.1 \text{ eV}$ was observed in Ref. 4. Thus, we can conclude that in our polydiacetylene THD, which was subjected to intense mechanical grinding, the average conjugation length remains very high, i.e., grind-

ing the sample is not accompanied by mechanical destruction of the polymer, and this initial high value is maintained. The slight increase in E_0 for curve I'' (Fig. 2b) is perhaps explainable by arguing that microcrystals of polydiacetylene THD undergo a slight nonuniform distortion within the PMMA film.

The qualitative differences in the functions $\alpha(\nu)$ for curves I and I'' are very significant. The function $\alpha(\nu)$ corresponding to curve I is characterized by less absorption at the maximum ($\alpha_{\max} \sim 1.6 \times 10^5 \text{ cm}^{-1}$) than for curve I'' ($\alpha_{\max} \sim 3 \times 10^5 \text{ cm}^{-1}$), and a notable broadening. This difference can be entirely accounted for by the different experimental geometry (Fig. 1).⁸

It is clear from Fig. 2a that as the doping level increases a long-wavelength maximum appears on the curve $\alpha(\nu)$ in the near IR region for values of $E_1 \approx E_0/2$. With increasing doping levels, the amplitude of this maximum increases. Conversely, the amplitude of the maximum at an energy $E = E_0$ corresponding to the maximum for the undoped material decreases monotonically with increasing doping levels. Qualitatively the picture is entirely analogous to the often-observed change in the extinction spectrum when polydiacetylene is doped (Fig. 2b). Comparison of these spectra indicates that the mechanisms for doping polydiacetylene and polyacetylene are qualitatively analogous.

However, one important fact worth noting is that in polyacetylene at relatively low doping levels, when the absorption at $E = E_0$ is still considerably larger than at $E = E_1$, we observe a very large scatter (over many orders of magnitude) in the level of macroscopic conductivity (compare, e.g., the data from Refs. 4 and 5) as a function of the dopant, doping regime, etc. However, at high doping levels, when conversely the absorption at $E = E_1$ considerably exceeds the absorption at $E = E_0$, the macroscopic conductivity always turns out to be high ($\sigma \sim 10 - 100 \text{ S/cm}$).

For curve 5 in Fig. 2a, the absorption at $E = E_1$ is practically equal to the original absorption at $E = E_0$ in undoped polydiacetylene THD, while the absorption peak at $E = E_0$ is almost entirely suppressed. Nevertheless, the value of the macroscopic conductivity σ in polydiacetylene turns out to be 4–5 orders of magnitude smaller than in polyacetylene.

Within the framework of band theory, the absorption at photon energies of $E \sim E_0$ is viewed as absorption by a direct-gap one-dimensional semiconductor (see, e.g., Ref. 9). In this case the width of the semiconductor band gap corresponds to energies somewhat smaller than E_0 . The effect of doping is to create an “impurity” level at the center of the forbidden gap ($E_1 \approx E_0/2$). In the language of chemical bonds, the absorption at $E = E_0$ is viewed as excitation of a double π -bond in the conjugated chain (in this case the excitation energy of π -electrons depends on the conjugation length). The absorption at $E_1 = E_0/2$ is connected with “absorption by free carriers” (solitons or bipolarons). It is reasonable to infer things about the carrier concentration, and to choose between the two approaches, based on the ratio of absorptions at the maxima corresponding to energies E_1 and E_0 . For curve 5 (Fig. 2a) the ratio $\alpha(E_1)/\alpha(E_0)$ is ~ 1.6 . For curve 4', $\alpha(E_1)/\alpha(E_0) \approx 1.43$. Thus, for polydiacetylene with its maximum attainable electrical conductivity

$\sigma \sim 10^{-3} \text{ S/cm}$, this ratio is actually slightly larger than the value of $\alpha(E_1)/\alpha(E_0)$ for polyacetylene with an electrical conductivity of only $\sigma \sim 10^2 \text{ S/cm}$.

Of course, even for the same material (polyacetylene) the scatter in values of σ can be several orders of magnitude for the same values of $\alpha(E_1)/\alpha(E_0)$. Depending on the orientation of the fibers in the material, the density of the “fiber net,”¹⁰ the mutual position of polymer chains and chains of donor ions, etc. can very strongly (exponentially) change the relative number of free carriers that participate in the macroscopic conductivity. For equal total concentrations of carriers, depending on the structural properties of the material different populations of carriers can be concentrated in isolated clusters and “dead ends” on the one hand and in conducting chains of the infinite cluster type that provides the macroscopic conductivity on the other.

The data given above show that in polydiacetylene THD the total carrier concentration at attainable doping levels is probably no less than the carrier concentration in polyacetylene with a conductivity level of $\sim 10 - 100 \text{ S/cm}$ (which already corresponds to “metallic” conductivity^{5,9,10}). Nevertheless, the record value of conductivity for doped polydiacetylene THD is still $\sigma \sim 3 \times 10^{-2} \text{ S/cm}$, i.e., considerably smaller than for polyacetylene.

It is interesting to discuss the question of just what structural features of polydiacetylene determine this considerable difference in electrical conductivity. Analysis of scanning electron microphotographs of the needle-like single crystals of polydiacetylene THD^{1,2} show that within each single crystal the position of the fiber is very ordered. The level of ordering is considerably higher than in the “nonoriented” polyacetylene (compare, e.g., with the corresponding electron microphotographs shown in Fig. 3 in Ref. 10). However, we must take into account two facts. First of all, the single crystals that make up a macroscopic sample were oriented completely randomly in Refs. 1 and 2. Secondly, as our preliminary investigations showed, the boundary between single crystals, even when oriented parallel to one another, is a potential barrier which prevents the exchange of charge carriers between neighboring fibers belonging to different single crystals. Thus, to the three mechanisms for transport listed above that are characteristic for polyacetylene, we probably must add a fourth in the case of polydiacetylene—intercrystalline transport between neighboring fibers belonging to neighboring crystals. We can hope that in the future a more ordered arrangement of microcrystals and a successful method for “disrupting” the intercrystalline boundaries will allow us to greatly increase the conductivity of polydiacetylene THD for the same amount of doping.

Figure 3a shows the spectral dependence of the extinction coefficient of polydiacetylene THD in the infrared region ($400 - 4000 \text{ cm}^{-1}$). Curve I in Fig. 3a is the extinction spectrum for the original undoped polymer. In contrast to the spectrum of undoped polyacetylene (see, e.g., Ref. 5), the spectrum of polydiacetylene THD contains a relatively small number of characteristic maxima with rather small intensities: many types of vibrational transitions that are allowed in polyacetylene are forbidden in polydiacetylenes by selection rules (see, e.g., Ref. 11).

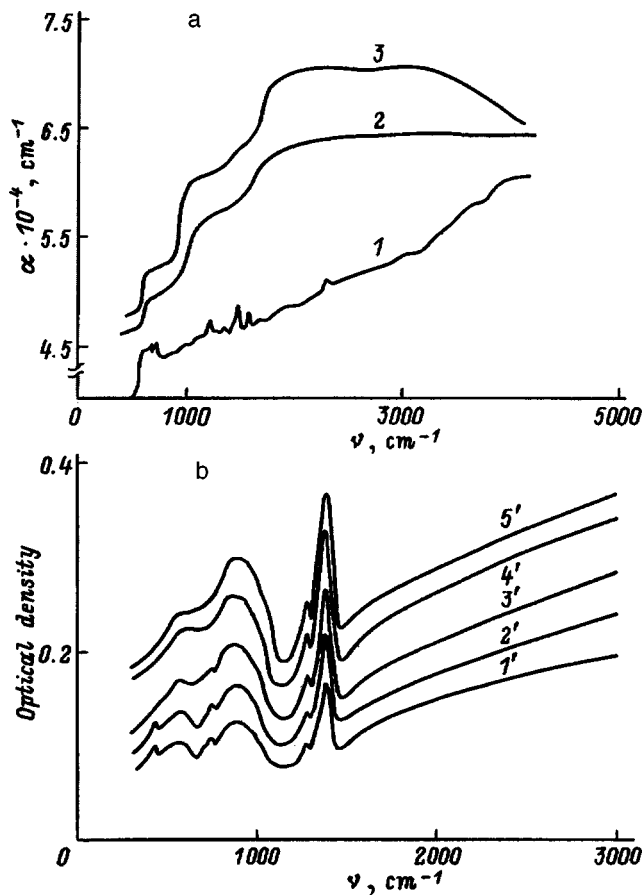


FIG. 3. a) Spectral dependence of the extinction coefficient for polydiacetylene THD in the long-wavelength region for various doping levels. 1—undoped sample ($\sigma < 10^{-9}$ S/cm), $\sigma \sim 10^{-4}$ (2) and $\sim 10^{-3}$ S/cm (3). b) Spectral dependence of optical density for polyacetylene at various doping levels (see Ref. 5). σ (S/cm): 1' — 1, 2' — 6, 3' — 15, 4' — 30, 5' — 40.

In the doped material (curves 2 and 3 in Fig. 3a) the absorption bands characteristic of the original polydiacetylene THD are not observed. In contrast to polyacetylene, doping does not lead to the appearance of a new absorption band in the spectrum (compare with curves 1'–5' in Fig. 3b).

In the spectrum of doped polydiacetylene THD we observe distinct “steps” in the regions $\nu \sim 625$, ~ 1000 and $\sim 1800 \text{ cm}^{-1}$. An abrupt increase in the extinction when ν exceeds $\sim 625 \text{ cm}^{-1}$ is clearly observed in the spectrum of undoped polydiacetylene THD as well (curve 1 in Fig. 3a). The corresponding features in the spectrum of undoped material for $\nu \sim 1000$ and $\sim 1800 \text{ cm}^{-1}$ are practically invisible. The nature of these features is unclear at the present time.

The increase in the long-wavelength absorption coefficient with increasing doping level is usually associated with

free-carrier absorption. Actually, the absorption in the long-wavelength region increases monotonically with increasing conductivity of the material both for polyacetylene and for polydiacetylene THD (Fig. 3a). It is clear from Fig. 3b that the functions $\alpha(\nu)$ for doped polyacetylene are, to good accuracy, parallel over a very wide range $400 \leq \nu \leq 3000 \text{ cm}^{-1}$, which is also characteristic of free-carrier absorption. However, this absorption differs qualitatively from absorption in “classical” semiconductors, in that the absorption α in normal semiconductors (Si, Ge, GaAs, etc.) increases with increasing wavelength λ of the incident light ($\alpha \sim \lambda^2$). This feature arises for quite fundamental reasons: the smaller the photon energy, the smaller the momentum a “free carrier” must obtain from the lattice (phonons) or from impurities in order to absorb the light photon. It is clear from Fig. 3b that for polyacetylene the opposite situation obtains: if we exclude individual bands, the absorption decreases with increasing wavelength (see also Ref. 12). It is clear from Fig. 3a that for polydiacetylene THD this tendency is still more sharply expressed. This fact also argues in favor of the assumption that the overwhelming number of carriers created as a result of doping are concentrated in isolated clusters and “dead ends.”

This work was supported by the Russian Fund for Fundamental Research (Grant No. 96-03-32462-a).

- ¹V. A. Marikhin, E. G. Guk, and L. P. Myasnikova, *Fiz. Tverd. Tela* (St. Petersburg) **39**, 774 (1997) [*Phys. Solid State* **39**, 686 (1997)].
- ²E. G. Guk, M. E. Levinshtein, V. A. Marikhin, L. P. Myasnikova, and S. L. Rumyantsev, *Fiz. Tverd. Tela* (St. Petersburg) **39**, 778 (1997) [*Phys. Solid State* **39**, 690 (1997)].
- ³*Handbook of Conducting Polymers*, T. A. Skotheim (Ed.) (Marcel Dekker, N. Y.–Basel, 1986), Vol. 2.
- ⁴C. R. Fincher, Jr., M. Ozaki, M. Tanaka, D. Reebles, L. Lauchlan, and J. Heeger, *Phys. Rev. B* **20**, 1589 (1979).
- ⁵J. Tanaka and M. Tanaka, in *Handbook of Conducting Polymers*, T. A. Skotheim (Ed.) (Marcel Dekker, N. Y.–Basel, 1986), Vol. 2, p. 1269.
- ⁶N. V. Agrinskaya, E. G. Guk, L. A. Remizova, and I. N. Khakhaev, *Fiz. Tverd. Tela* (St. Petersburg) **37**, 546 (1995) [*Phys. Solid State* **37**, 296 (1995)].
- ⁷N. V. Agrinskaya, E. G. Guk, I. A. Kudryavtsev, and O. G. Lublinskaya, *Nonlinear Opt.* **12**, 301 (1995).
- ⁸C. F. Bohren and D. R. Huffman, *Absorption and Scattering of Light by Small Particles* [Wiley, New York, 1983; Mir, Moscow, 1986, 660 pp.].
- ⁹R. R. Chance, D. S. Boudreaux, J. L. Bredas, and R. Sibey, in *Handbook of Conducting Polymers*, T. A. Skotheim (Ed.) (Marcel Dekker, N. Y.–Basel, 1986), Vol. 2, p. 825.
- ¹⁰A. I. Heeger, in *Handbook of Conducting Polymers*, T. A. Skotheim (Ed.) (Marcel Dekker, N. Y.–Basel, 1986), Vol. 2, p. 729.
- ¹¹R. H. Boughman and K. C. Jee, *Macromolec. Rev.* **12**, 219 (1978).
- ¹²J. F. Rabolt, T. C. Clarke, and G. B. Street, *J. Chem. Phys.* **71**, 6414 (1979).

Translated by Frank J. Crowne

Negative space charge and electric field intensity in polymeric insulators at low temperatures

V. A. Zakrevskii and N. T. Sudar'

A. I. Ioffe Physicotechnical Institute, Russian Academy of Sciences, 194021 St. Petersburg, Russia

(Submitted November 13, 1997)

Fiz. Tverd. Tela (St. Petersburg) **40**, 1167–1172 (June 1998)

The effect of negative space charge accumulation due to injection of electrons from cathode microprotrusions on the steady-state and transient electric field distributions in polymer dielectrics is discussed. An isolated microprotrusion is modeled by a spherical capacitor in which an electrode of smaller radius is the cathode. The calculations include the fact that the distribution of negative space charge depends on the rate of capture and liberation of electrons by traps, while the activation energy of this process depends on the electric field intensity. An exponential energy distribution is proposed for the traps. It is shown that significant electrical overvoltages can only appear near the cathode microtips immediately after switching on the voltage. In the course of 10^{-6} – 10^{-5} s, the coefficient of electrical overvoltage drops to a few units and approaches its steady-state value. The region of significant electrical overvoltage is localized, and is the same order as the dimensions of the microtip. © 1998 American Institute of Physics. [S1063-7834(98)04106-9]

There has always been great interest in the study of the processes of space charge accumulation in polymer dielectrics and the distribution of electric fields within them. The reason for this is that these field intensities determine the rate of electrical damage of the polymers, and the point where the electrical overvoltage is localized determines the region in which the damage is most intense.

In strong electric fields, a negative space charge in polymers accumulates due to field emission of electrons from the cathode. Tunneling of electrons takes place not from the entire electrode surface but only from individual microtips located on it, at which the value of the electric field intensity exceeds its average value. Injected electrons captured by traps form the negative space charge. We can assume that effects due to negative space charge will be most evident at low temperatures, where the emptying of traps is hindered. A distinguishing feature of polymer dielectrics is their high concentrations of neutral traps. The dominant type of trap in polymers is the intermolecular cavity, i.e., a trap of structural type.¹ Such traps are classified in a rather nominal way as deep or shallow. It is assumed that, at room temperature, traps with a depth of more than 0.5 eV belong to the "deep" class, since most of the negative space charge will accumulate in them. The concentration of deep traps is estimated to be 10^{18} cm⁻³.²

The calculations published in the literature of the distribution of fields and charges in polymers are based on simplified models of the polymer dielectrics. Specifically, the presence of traps in these materials is taken into account either by introducing a drift mobility³ or by assuming that only single-energy traps are present.⁴ However, in real polymers the traps are distributed with respect to "depth," i.e., energy. It is this circumstance that we shall discuss in this paper. It is assumed that polymer dielectrics are character-

ized by an exponential distribution of traps with respect to depth:⁵

$$M(U) = n(kT_0)^{-1} \exp[-U/(kT_0)]. \quad (1)$$

Here $M(U)$ is the density of the trap distribution with respect to energy, n is the total trap concentration ($n \approx 10^{20}$ cm⁻³), U is the depth of the trap, k is the Boltzmann constant, and T_0 is a parameter of the distribution with the units of temperature. The value of the parameter T_0 is determined from the relation

$$n_1 \approx n(kT_0)^{-1} \int_{U_1}^{\infty} \exp[-U/(kT_0)] dU,$$

where n_1 is the concentration of deep traps at room temperature and $U_1 = 0.5$ eV. A value of $T_0 \approx 1000$ K is obtained.

At low temperatures, the molecular motion in the polymer is hindered and electrons can only be liberated from the traps by thermally activated ejection. That is, electrons are released from those traps whose barriers equal its thermal depth.⁴ If we take the shape of the trap to be rectangular, the escape frequency of an electron $P(U, E)$ from the trap can be written

$$P(U, E) = \nu_0 \exp[-(U - eaE)/(kT)], \quad (2)$$

where $\nu_0 \approx 10^{13}$ s⁻¹, e is the electron charge, a is the half-width of the trap ($a = 2 \times 10^{-8}$ cm), E is the local field intensity, which is a function of time and coordinates, and T is the temperature. Electrons that have left the trap drift in the intermolecular space of the polymer with a velocity determined by the microscopic mobility μ_0 , whose value is estimated to be roughly equal to 1 cm²/(V·s).²

In accordance with the statements made above, the kinetics of capture and liberation of electrons from traps of depth U will be determined by the relation

$$d[n_{tr}^u(t,r)]/dt = v\sigma[M(U) - n_{tr}^u(t,r)] \times n_0(t,r) - n_{tr}^u(t,r)P(U,E), \quad (3)$$

where $n_{tr}^u(t,r)$ and $n_0(t,r)$ are the energy distribution density for traps occupied by electrons, which depends on time and the coordinates, and the concentration of quasi-free electrons respectively, v is the velocity of the electrons, and σ is the capture cross section for an electron by a structural trap ($\sigma \approx 10^{-15} \text{cm}^2$).

A convenient model for the nonuniform field associated with a microprotrusion is the field of a spherical capacitor. For $r_0 \ll R$ (where r_0 is the radius of the smaller-diameter electrode, i.e., the cathode, and R is the radius of the anode), emission from a spherical cathode is approximated satisfactorily by injection from a point contact.⁶ It should be noted that the model of a spherical capacitor probably matches real conditions only at distances for which $E(r) \geq E_{mid}$, where by E_{mid} we mean the field intensity in a sample with planar geometry and thickness $d = R - r_0$.

The system of equations that describes the field and charge distributions includes the Poisson equation and the continuity equation along with Eq. (3), which can be written in a spherical system of coordinates

$$d[r^2 E(t,r)]/dr = -e(\epsilon\epsilon_0)^{-1}[n_{tr}(t,r) + n_0(t,r)], \quad (4)$$

$$d[r^2 I(t,r)]/dt = ed\{[n_{tr}(t,r) + n_0(t,r)]\}/dt, \quad (5)$$

where $n_{tr}(t,r)$ is the total concentration of trapped electrons, ϵ is the dielectric permittivity of the polymer dielectric, ϵ_0 is the dielectric constant, and $I(t,r)$ is the conduction current density, which equals $I(t,r) = e\mu_0 n_0(t,r)E(t,r)$, since in strong electric fields the diffusion component of the current can be neglected. To this system of equations we must add the equation that determines the current density for autoelectron emission I_c . The density of this emission current is given by an equation like that of Fowler–Nordheim.⁷ In accordance with Eqs. (8), (9) it can be written in the form

$$I_c = 1.55 \times 10^{-10} E_c^2 W^{-1} \exp[-6.86 \times 10^9 W^{3/2} s(y)/E_c], \quad (6)$$

where I_c is given in A/m², E_c is the field intensity at the cathode (in V/m), $s(y)$ is a function that takes into account the effect of the image force on the height of the potential barrier, and W is the height of the barrier at the metal-polymer boundary through which the electrons tunnel, which is estimated to be roughly 3.5 eV.⁴

1) *Steady-state case.* For $d[n_{tr}^u(t,r)]/dt = 0$ we have

$$n_{tr}^u(r) = v\sigma M(U)/[v\sigma n_0(r) + P(U,E)]. \quad (7)$$

In order to calculate the total concentration of electrons in traps, Eq. (7) must be integrated with respect to energy. Introducing a new variable of integration $x = \exp[-U/(kT_0)]$ we obtain

$$n_{tr}(r) \approx v\sigma\nu_0^{-1} n_0(r) n \int_0^1 dx/[v\sigma n_0(r) + x^p], \quad (8)$$

where $p = T_0/T$. Since at low temperatures we have $p \gg 1$, while the concentration of quasifree electrons is not large,

$[v\sigma\nu_0^{-1} n_0(r)]^{1/p} \ll 1$ and the integral in Eq. (8) can be reduced to tabular form (Ref. 10, Eq. 856.05). Then

$$n_{tr}(r) \approx n\{v\sigma\nu_0^{-1} n_0(r) \exp[-(eaE)/(kT)]\}^{1/p}. \quad (9)$$

When the field and charge distributions are stationary, Eq. (5) implies that

$$n_0(r) = I_c r_0^2 / [e\mu_0 r^2 E(r)]. \quad (10)$$

The combined solution to Eqs. (4), (9), and (10) allows us to compute $E(r)$ and $n_{tr}(r)$ within the model system under discussion. The boundary condition is that $E(r_0) = E_c$. By applying a voltage V to the sample and varying E_c , we can choose a function $E(r)$ that satisfies the condition $\int_{r_0}^R E(r) dr = -V$, which will be the field distribution we seek.

2) *Transient case.* The dynamics of negative space charge accumulation were analyzed for this model with a step voltage applied to the sample. We assume that initially there is no charge in the sample, and the field distribution in it is determined by the geometry of the electrodes. After switching on the voltage, injection of electrons begins and a negative space charge accumulates in the traps. It affects the field distribution in the sample and limits the injection current.

The algorithm used to solve this problem was the following. A certain time discretization Δt was chosen during which the field and charge distributions are assumed to be unvarying within the entire interelectrode space. The distance between the large and small spheres was divided up into N segments of length $\Delta r = (R - r_0)/N$, where $\Delta r \ll r_0$. Each segment corresponds to a spherical shell of volume V_i , in which the field intensity is assumed to be constant and changes discontinuously when we go from one shell to another. We assume that at time t_j a field distribution is set up in the sample such that the field intensity equals $E_{i,j}$ in each i -th shell (here and in what follows the first subscript i labels the shell, while the second j labels the time interval). This field intensity is calculated using data on the distribution $n_{tr}^{i,(j-1)}$ of the trapped electron concentration over the spherical shell obtained from the previous time interval. After a time Δt charge is injected into the sample equal to $\Delta Q = 4\pi r_0^2 I_c(t_j) \Delta t$. The density of the autoelectron current is calculated from Eq. (6), in which we set $E_c = E(r_0, t_j)$. The injected electrons are treated as quasifree. As they drift from anode to cathode, they could be captured at traps. We assume that electrons are captured only by that set of traps whose retention time exceeds Δt . The minimum depth of the ‘‘active’’ traps for which this condition is satisfied, using Eq. (2) is given by

$$U_{min}^{i,j} = eaE_{i,j} + kT \ln(\nu_0 \Delta t). \quad (11)$$

Since the quantities $E_{i,j}$ are different in each shell, the concentrations of ‘‘active’’ traps $n_a^{i,(j-1)}$ should differ as well. The value of $n_a^{i,j}$ can be calculated by integrating Eq. (1) over energy in the limits from $U_{min}^{i,j}$ to infinity. We find that $n_a^{i,j} = n \exp[-U_{min}^{i,j}/(kT_0)]$.

Let us assume that $N_0^{(i-1),j}$ quasi-free electrons drift from layer $i - 1$ to layer i . If the concentration of ‘‘active’’

traps $n_a^{i,j}$ turns out to be larger than the concentration of electrons on traps $n_{tr}^{i,(j-1)}$, then a portion of the drifting electrons are captured at these traps. The number of electrons captured at traps in the i -th layer at time t_j is given by

$$\Delta N_{tr}^{i,j} = \{1 - \exp[-\sigma \Delta r (n_a^{i,j} - n_{tr}^{i,(j-1)})]\} N_0^{(i-1),j}. \quad (12)$$

The capture of some of the electrons increases their concentration at the traps up to a value $n_{tr}^{i,j} = n_{tr}^{i,(j-1)} + \Delta N_{tr}^{i,j}/V_i$, while the number of electrons capable of drifting into layer $i+1$ decreases by an amount $\Delta N_{tr}^{i,j}$.

If the concentration of "active" traps at time t_j turns out to be smaller than the concentration of electrons that accumulate in the "active" traps at time t_{j-1} , i.e., $n_a^{i,j} < n_{tr}^{i,(j-1)}$, then we assume that some of the electrons leave the traps and the condition $n_{tr}^{i,j} = n_a^{i,j}$ is satisfied. A decrease in the number of "active" traps implies an increase in the number of free electrons capable of drifting into the next layer. The total number of electrons drifting into layer $i+1$ is in this case determined by $N_0^{(i+1),j} = N_0^{(i-1),j} + [n_{tr}^{i,(j-1)} - n_{tr}^{i,j}]V_i$.

In what follows, we shall use an analogous approach to calculate the electron concentration in layer $i+1$ at time t_j , etc. from layer to layer, as long as the total injected charge ΔQ is not exhausted or the electrons do not reach the anode, where they are neutralized, i.e., we use the value $N_0^{R,j} = 0$.

Thus, we determine the charge distribution in the interelectrode space, and based on it we can undertake to calculate the field distribution in the sample.

The solution to the Poisson equation (4) for the microprotrusion model under discussion can be written in the form³

$$E(t,r) = (r_0/r)^2 [E_c(t) + q(r,t)/(4\pi\epsilon\epsilon_0 r_0)], \quad (13)$$

where

$$q(r,t) = 4\pi \int_{r_0}^r \rho(x,t) x^2 dx,$$

and $\rho(x,t)$ is the space charge density and $E_c(t)$ is the time-dependent field intensity of the cathode, which equals

$$E_c(t) = (RE_{mid})/r_0 - R[4\pi\epsilon\epsilon_0 r_0(R-r_0)]^{-1} \times \int_{r_0}^r x^{-2} q(x,t) dx. \quad (14)$$

The function $q(r,t)$ describes how the negative space charge changes in the polymer as r increases from r_0 to R . Since the concentration of electrons at traps is constant in each spherical shell, we set $\rho(x,t) = en_{tr}^{i,j}$ in these calculations, and the integral in Eq. (14) is calculated in explicit form. The expressions given above allow us to compute the charge distribution in the interelectrode space at time t_{j+1} .

3) *Results of calculations.* All the calculations were done for $R = 2.5 \mu\text{m}$ and $r_0 = 0.25 \mu\text{m}$. Since experiment shows that the breakdown voltage for the majority of polymer films of thickness $2-3 \mu\text{m}$ is around 2 kV, in these calculations we set $V = 2000 \text{ V}$, which corresponds to an average electric field intensity $E_{mid} = 889 \text{ MV/m}$. For the transient regime we pick $\Delta t = 10^{-9} \text{ s}$, $N = 225$.

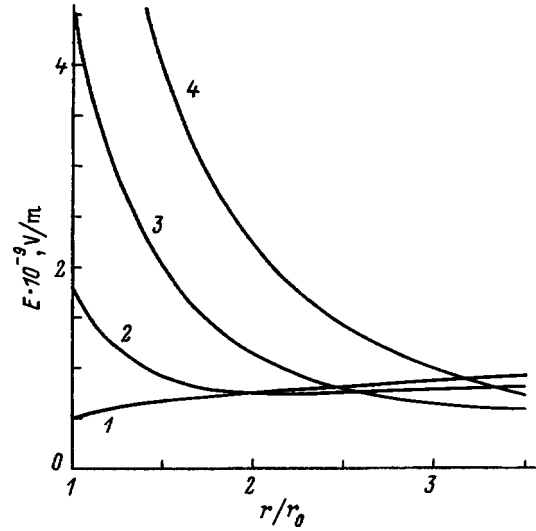


FIG. 1. Steady-state distribution of electric field with respect to depth into the sample at various temperatures. T (K): 1—30, 2—77, 3—150, 4—no negative space charge.

Figure 1 shows the results of a calculation of the steady-state distribution of field intensity in the sample at temperatures of 30, 77, and 150 K (curves 1—3). This figure shows the field distribution in the absence of bulk space charge (curve 4). It is clear that as the temperature decreases the degree of boundedness of the negative space-charge field increases. Thus, at $T = 150 \text{ K}$ the coefficient of electric overvoltage at the cathode $k_{el} \approx 5$ ($k_{el} = E(r)/E_{mid}$), at $T = 77 \text{ K}$ $k_{el} \approx 2$, while for $T = 30 \text{ K}$ the negative space charge limits the field at the cathode to a value smaller than E_{mid} , i.e., $k_{el} < 1$. The region of electric overvoltage is localized to the immediate vicinity of the cathode, with a linear size $\sim r_0$. If we compare the results of this calculation of the electric field distribution with the calculations given in Ref. 4 for an analogous microprotrusion model but for a polymer with single-energy traps, we note that in the latter case the limiting of the field turns out to be stronger. In fact, for single-energy traps of depth 1 eV (with a trap concentration 10^{19} cm^{-3}) the field at the cathode becomes bounded by a value $\sim E_{mid}$ at $T = 100 \text{ K}$, while for traps with an exponential energy distribution this happens only at $T = 30 \text{ K}$. At higher temperatures ($T = 150 \text{ K}$) for a model with single-energy traps of depth 0.5 eV the value of k_{el} at the cathode turns out to be ~ 2.3 , whereas for a model with an exponential distribution of traps this value increases to 5, i.e., by more than a factor of 2.

The form of the function $E(r)$ and the degree of limiting of the negative space-charge field in the near-cathode region are determined by the magnitude and distribution of charge in the sample. In Fig. 2 we show the function $n_{tr}(r)$ calculated for temperatures of 30 (curve 1), 77 (curve 2), and 150 K (curve 3). At $T = 30 \text{ K}$ the maximum concentration of trapped electrodes ($n_{tr,max}$) is reached at the cathode. At this temperature, the limiting of the field is most apparent at the cathode (the field intensity is close to average), and consequently the effect of the electric field on the probability of ejection of electrons from the traps is not as marked as it is at

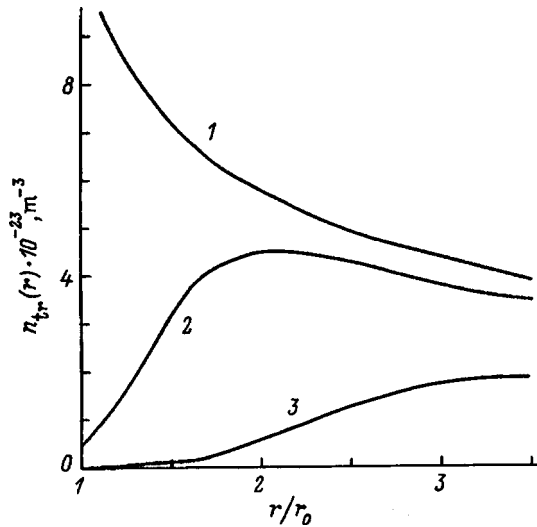


FIG. 2. Steady-state distribution of the concentration of electrons at traps with respect to depth into the sample at various temperatures. T (K): 1—30, 2—77, 3—150.

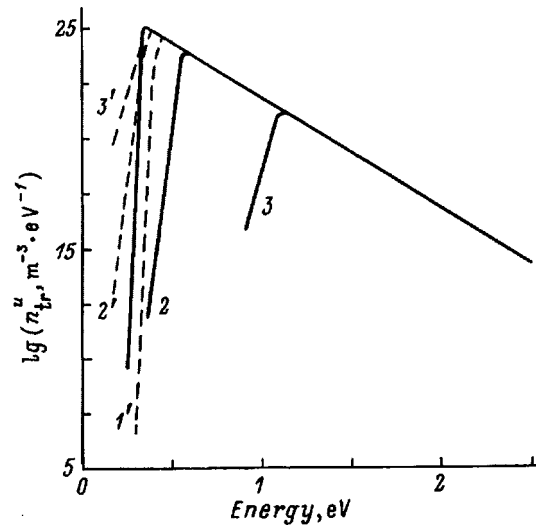


FIG. 3. Distribution density for traps occupied by electrons versus energy at various points in the sample and at various temperatures for $r=r_0$ (1–3) and $2r_0$ (1'–3'). T (K): 1,1'—30, 2,2'—77, 3,3'—150.

higher temperatures. As the temperature decreases, the shape of the function $n_{tr}(r)$ changes. This is because the probability of emptying a trap increases with increasing temperature, a lower charge accumulates in the sample, and the degree of field limiting at the cathode decreases. The rising field intensity in this region of the sample increases the probability of ejection of electrons from the traps even more. Eventually, so many traps in the near-cathode region are emptied that the concentration of electrons becomes less than the bulk concentration.

As the negative space charge forms, electrons are captured at traps lying at different depths. Since the traps are distributed with respect to energy and the rate of liberation of electrons from them depends on the trap depth and electric-field intensity, the energy density of traps occupied by electrons will be different in different regions of the polymer. In steady state, the value of $n_{tr}^u(r)$ was calculated from Eq. (7) for different temperatures and different points of the sample. Functions 1–3 in Fig. 3 were obtained for $r=r_0$ at 30, 77, and 150 K respectively. It is clear that as the temperature increases, and the electric field at the cathode connected with it increases, the maximum of the distribution density ($n_{tr,max}^u$) shifts to deeper trap levels, and the quantity $n_{tr,max}^u$ rapidly decreases. It should be noted that as the temperature increases the number of traps at which electrons are captured decreases, since capture can take place only for traps that are sufficiently deep. The minimum depth for such traps at the cathode can be calculated from the condition $U_{min} - eaE_c = 0$. It is found that for $T=30$ K $U_{min}=0.1$ eV, for $T=77$ K $U_{min}=0.358$ eV, while for $T=150$ K $U_{min}=0.9$ eV.

Curves 1'–3' of this figure were calculated for $r=2r_0$ at 30, 77, and 150 K respectively. For this region of the polymer, along with the dependence on temperature we have $E(r) \approx E_{mid}$ (Fig. 1). It is clear that the quantity $n_{tr,max}^u$ and its position are practically temperature independent. Increasing the temperature leads only to a decrease in the slope of the left-hand portion of the resulting distribution.

Thus, the energy spectrum of traps occupied by electrons, and the way it changes under heating or cooling of the polymer, differ significantly as we go from deep in the sample to the near-cathode region. On the whole, however, based on these calculations of the steady-state field distribution and charge distribution, we can assert that when an electric field acts for a long period on the sample the bulk negative charge injected into it is incorporated to a considerable depth (even at cryogenic temperatures). The negative space charge that forms limits the field near the cathode so that electric overvoltages at the cathode practically disappear at $T=30$ K. However, as the temperature increases, the values of k_{el} increase to values of order one.

There is interest in thoroughly analyzing the dynamics of negative space charge accumulation in polymers and the change in the character of the field distribution in a sample with time. To this end, we calculated the transient field distribution and charge distribution in a model sample. Figure 4 shows the dependence of the transient distribution $E(r)$ near the cathode at $T=77$ K at various times while the voltage is applied: 0.1, 1, 10, 100, and 1000 μ s (curves 1–5 respectively). In all cases the maximum field intensity (E_{max}) is reached at the cathode-polymer boundary ($r=r_0$), whereas the value of E_{max} decreases with increasing time during which the electric field acts on the sample. All the transient functions $E(r)$ are monotonically decreasing, so that for $r \geq 3r_0$ we have $E(r,t) \approx E_{mid}$. Analysis of changes in the values of the electrical overvoltage at the cathode with time show that they are nonuniform. Within a time $\sim 10^{-5}$ s, after switching on the voltage, the value of k_{el} decreases from 10 at $t=0$ to 4.37 at $t=10^{-5}$ s, and differs from the value of k_{el} for a steady-state distribution by more than a factor of 2. Subsequent decreases in k_{el} occur quite slowly, so that at times $\sim 10^{-3}$ s k_{el} has only decreased from 4.37 to 3.36, i.e., by a factor of 1.3 in all, and still differs from the steady-state value by a factor of 1.68. Extrapolation of this function to the long-time region (direct calculation of the field and charge

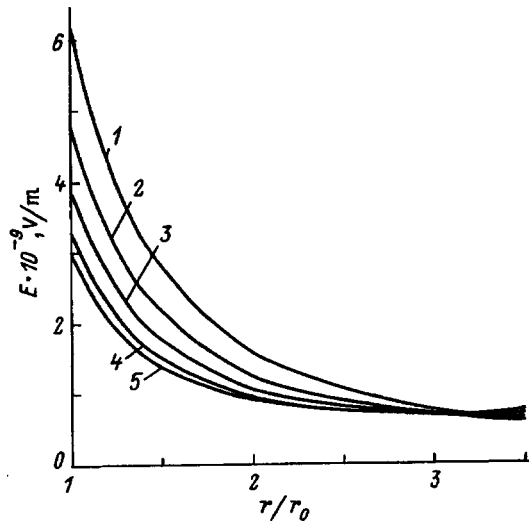


FIG. 4. Electric field distribution versus depth in the sample at $T=77$ K and at various times after voltage is switched on. t (μ s): 1—0.1, 2—1, 3—10, 4—100, 5—1000.

distributions for $t > 10^{-3}$ s are hindered by an unacceptably large expenditure of computer time) shows that the value of $k_{\text{el.max}}$ differs from its steady-state value by 10% after 0.1 s.

Figure 5 shows the results of calculating the distribution density for negative space charge captured by traps with respect to depth into the sample at $T=77$ K at different times: 0.1, 1, 10, 100, and 1000 μ s (curves 1–5). A maximum in the negative space charge density forms at a certain distance from the cathode and, as the time in which the electric field acts on the sample increases, it drifts towards the cathode. However, the value of $n_{\text{tr.max}}$ obtained for the steady-state distribution of charge is somewhat smaller than for the tran-

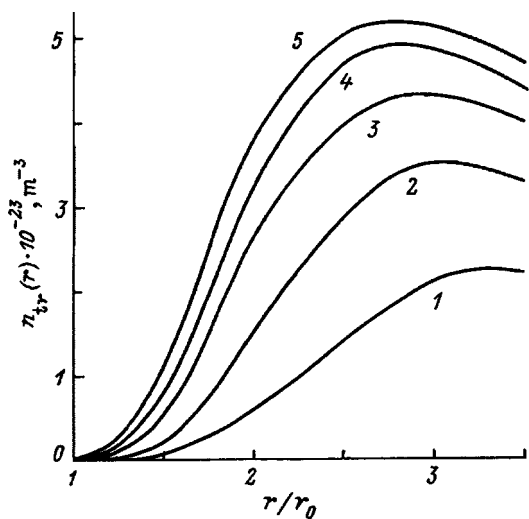


FIG. 5. Distribution of the concentration of electrons at traps versus depth into the sample at $T=77$ K and at various times after switching the voltage on. t (μ s): 1—0.1, 2—1, 3—10, 4—100, 5—1000.

sient case. The reason for this is that in calculating the transient charge distribution the ejection of electrons from traps was only calculated approximately.

Comparing the transient field and charge distributions shown in Figs. 4 and 5, we note that initially the field distribution near the cathode is close to $E(r)$ determined for no negative space charge. Under these conditions, electrons are practically incapable of remaining in the traps near the cathode, where the field is high. As they drift toward the anode, some are captured by traps in the sample bulk and some reach the anode. The long range of electrons in the sample is caused by the small capture cross section of electrons by neutral structural traps in the polymer, and consequently their low capture probability at these traps, and also the increased probability for liberating electrons from the traps in strong electric fields. The charge accumulated in a short time still weakly limits the field at the cathode. As time passes the concentration of electrons increases and the limiting of the field becomes more and more effective.

Thus, our discussion of the dynamics of negative space charge accumulation in polymers and the changes in the electric field distribution in the sample associated with this accumulation allow us to conclude that significant electrical overvoltages near a microprotrusion at the cathode can only arise immediately after switching on the voltage, and that very soon thereafter, in the course of $10^{-6} - 10^{-5}$ s, the coefficient of electrical overvoltage decreases to a quantity of order one. Then the rate of change decreases, so that the process of establishing a steady-state field and charge distribution occupies a considerably longer time (of order 10^{-1} s); during this period, the electric field near the cathode decreases slowly, while the maximum of the electron density in the traps gradually drifts from deep in the sample to the cathode.

This work was supported by the Russian Fund for Fundamental Research (Grant No. 95-03-08144).

¹V. A. Zakrevskii and V. A. Pakhotin, *High Molecular Weight Compounds* **A23**, 3, 658 (1981) [in Russian].

²A. P. Tyutnev, A. V. Vannikov, G. S. Mingaleev, and V. S. Saenko, *Electrical Phenomena in Illuminated Polymers* [in Russian], Energoatomizdat, 1985, 176 pp.

³V. B. Berezanskii, V. M. Bykov, V. V. Gorodov, V. A. Zakrevskii, and N. T. Sudar', *High Molecular Weight Compounds* **B21**, 4, 275 (1989) [in Russian].

⁴V. A. Zakrevskii, and N. T. Sudar', *Zh. Tekh. Fiz.* **60**, 66 (1990) [*Sov. Phys. Tech. Phys.* **35**, 175 (1990)].

⁵*Radiation Chemistry of Polymers*, V. L. Karpova (Ed.) [in Russian], Nauka, Moscow, 1973, 369 pp.

⁶M. Lampert and P. Mark, *Current Injection in Solids* [Academic Press, New York, 1970; Nauka, Moscow, 1973, 416 pp.].

⁷A. Chaïnovet, *Usp. Fiz. Nauk* **75**, 169 (1961).

⁸O'Dwyer, in *Proceedings of the 2nd International Conference on Conduction and Breakdown in Solid Dielectrics* (N.Y., 1986), p. 31.

⁹A. Modinos, *Auto, Thermo, and Secondary Electron Emission Spectroscopy* [in Russian], Nauka, Moscow, 1990, 320 pp.

¹⁰H. B. Dwight, *Tables of Integrals and Other Mathematical Data*, 4th ed. [Macmillan, London, 1961; Nauka, Moscow, 1973, p. 184].

Molecular motion and distinctive features of the strength of thermotropic liquid-crystal oriented polymers^{*})

E. A. Egorov, A. V. Savitskiĭ, V. V. Zhizhenkov, and I. A. Gorshkova

A. F. Ioffe Physicotechnical Institute, Russian Academy of Sciences, 194021 St. Petersburg, Russia

(Submitted November 18, 1997)

Fiz. Tverd. Tela (St. Petersburg) **40**, 1173–1177 (June 1998)

Nuclear magnetic resonance (NMR) is used to study molecular motion in two fully aromatic oriented liquid-crystal (LC) polymers (the copolymer with the brand name Vectra and poly-para-phenylphenyleneterephthalate) at high temperatures up to 610 K. Above the temperature of the thermotropic transition, a fine structure is observed in the NMR spectra analogous to structures seen previously only in studies of low-molecular-weight LC materials. Analysis of the results indicates that macromolecules in the LC state participate in cooperative types of motion. The relation between structural rearrangements and hardening during thermal processing is discussed, along with the role of distinctive features in the molecular motion in the mesophase.

© 1998 American Institute of Physics. [S1063-7834(98)04206-3]

According to the concepts advanced by S. N. Zhurkov,¹⁻³ the failure of solid bodies is an activated process which develops in time and depends on the temperature T . The lifetime of a sample τ subjected to a mechanical stress σ is given by the expression

$$\tau = \tau_0 \exp((U_0 - \gamma\sigma)/kT), \quad (1)$$

where $\tau_0 \approx 10^{-13}$ s is the period of atomic vibrations in the solid, U_0 is the activation energy for the failure process, and γ is a coefficient that takes into account the structure of the solid and especially the nonuniformity of the distribution of local stresses in it. Thus, the tensile strength σ_τ is physically meaningful for the specified time τ during which the sample is under load:

$$\sigma_\tau = (1/\gamma)(U_0 - kT \ln(\tau/\tau_0)). \quad (2)$$

During active loading an effective value of σ_τ can be computed.³

According to Ref. 2, hardening of solids can occur essentially as a result of either a decrease in the local stress concentration (decreasing γ) or an increase in the net energy barrier U_0 .

For bent-chain polymers, the primary method of hardening is orientational drawing, in which the increased hardness is due only to a considerable decrease in the coefficient γ (by factors of 10 or more).³ Orientational drawing is effective above the glass forming temperature, when some of the amorphous regions are carried along by an intense motion of segments. As the hardness increases, the segment mobility is braked, i.e., mechanical glass forming takes place,^{4,5} which imposes a limit on the process of structural rearrangement. In general outline, this is the interrelation between molecular dynamics and the strength of bent-chain polymers.

Thermotropic fully-aromatic liquid-crystal (LC) polymers with mesogens in the primary chain constitute a special class. Their chains are so rigid that true segment (micro-brownian) motion, which is connected with the almost free reorientation of individual units in space, is impossible in

them. The patterns of their hardening are also fundamentally different. A high degree of orientation of the macromolecules of the LC polymers can be achieved even during the process of forming fibers, and further hardening (an increase of σ_τ by several times) takes place as a result of thermal processing, specifically, heating the polymer for a certain time at a temperature close to the thermotropic transition temperature. In this case the coefficient γ changes negligibly or not at all, and lengthening of the sample practically does not occur,⁶ instead, the increase in hardness is connected with an increase in the energy U_0 .

In the literature there are data on the increase in degree of crystallinity and changes in the crystal modifications during thermal processing of thermotropic LC polymers; it is observed that the dynamic elasticity modulus falls sharply as we approach the transition temperature to the LC phase, and then once more increases as the structure is rearranged.^{7,8} We do not exclude the possibility of chemical conversions and cross linking of macromolecules at high temperatures.⁹ All of these effects can be related to hardening. In order to produce appreciable collective rearrangements during thermal processing it is necessary to invoke a specific type of molecular motion. The experimental study of this issue is the goal of the present paper.

As the basic method for investigation we used broad-line NMR. We knew that low-molecular-weight thermotropic liquid crystals have wide spectra, like solids, but with a characteristic fine structure that reflects the makeup of individual molecules.¹⁰ The fine structure results from averaging the dipole-dipole intermolecular interactions caused by the increased molecular motion in the LC phase.

We know of no NMR spectra for the LC phase of thermotropic polymers given in the literature.

1. METHOD

A NMR spectrometer, which was made at the Ioffe Physicotechnical Institute, allowed us to record both the first

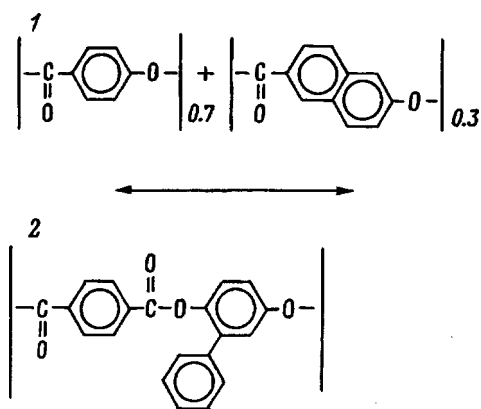


FIG. 1. Structural formulae of objects of study. 1—Vectra A950, 2—PPT. The arrow denotes the direction of the axis of orientation for the sample.

derivative of the absorption spectrum and the original spectrum directly at temperatures up to 610 K; the latter measurements used magnetic field modulation by large rectangular pulses.⁴ For monitoring we also used differential thermal analysis and measurement of the sound velocity in the samples at various temperatures. Our basic investigations were carried out in highly oriented fibers of the LC-copolymer with the industrial brand name Vectra A950, which contained 70 mole% of fragments of 4-hydroxybenzoic acid and 30 mole% of 6-hydroxy-2-naphthoic acid. The fibers were obtained by forming of original material from the Hoechst–Celanese Corporation. We also conducted trials on oriented fibers of poly-paraphenylphenyleneterephthalate (PPT). The polymer was synthesized in the laboratory of A. Yu. Bilibin (Institute of High Molecular Weight Compounds of the Russian Academy of Sciences), and fibers were fabricated and tested on laboratory apparatus of the Ioffe Physicotechnical Institute.

The structural formulas for these samples are shown in Fig. 1. In macromolecules of Vectra, the phenylene and naphthalene units are distributed statistically. In PPT, the lateral phenyls can be joined to any of four carbon atoms of the phenylene ring within the main backbone. A distinctive feature of these LC polymers is the fact that mesogenic groups in them are located in the primary backbone and are not separated by bent “decoupling” units, i.e., spacers. This gives the macromolecules a high rigidity, and their molecular motion is considerably restricted. The mechanical characteristics of the samples (initial and after thermal processing) are listed in Table I. Here the tensile strength corresponds to a

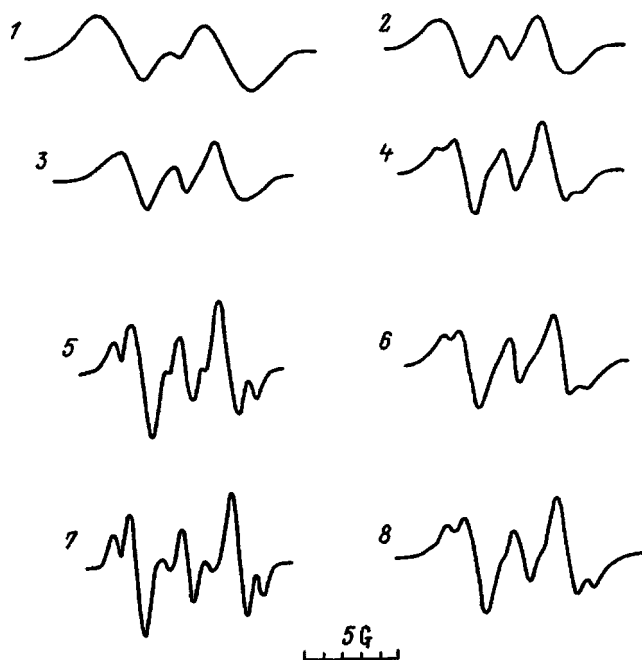


FIG. 2. NMR spectra of Vectra copolymer. Experimental spectra before thermal processing (1–5) and after thermal processing (6) are at various temperatures. T (K): 1—293, 2—423, 3—473, 4—543, 5, 6—573. 7— theoretical calculation, 8—results of superimposing spectra 2 and 5 in the ratio 60%:40%. The axis of orientation of the samples is parallel to the magnetic field of the spectrometer.

lifetime under load of $\tau \approx 0.1$ s. The parameters γ and U_0 were determined from mechanical trials based on the method described in Ref. 11.

2. RESULTS

Previously, NMR was used by Allen *et al.*,^{12,13} to investigate an orienting material close in composition to Vectra, but only up to a temperature of 423 K; it was shown that (nearly free) rotation of the phenylene groups can occur at 373 K, and that the naphthalene units can rotate at 423 K. Thus, below 423 K the polymer admits only local forms of molecular motion that are characteristic of solids. We are interested in much higher temperatures.

Figure 2 shows NMR spectra (first derivative) for samples of Vectra at various temperatures. The axis of fiber orientation coincides with the direction of the magnetic field of the spectrometer. The samples were first heated to 423 K in order to remove traces of moisture. Spectra 1–5 refer to the original sample; as they were plotted, the sample was

TABLE I. Sample characteristics.

Polymer	Original Sample			After thermal processing			
	σ , GPa	γ , cm ³ /mol	U_0 , kJ/mol	Thermal processing conditions	σ , GPa	γ , cm ³ /mol	U_0 , kJ/mol
Vectra	1.35	45.3	130	Three-step process: 523, 543, 560 K, Overall time — 8 h	2.75	39.0	176
PPT	1.0	51.1	120	593 K, 4 h	3.0	50.4	220

kept at high temperature for no more than 7–10 minutes, after which the thermal processing was interrupted. However, when the sample in the spectrometer was kept at 573 K for long periods and its spectrum was periodically recorded, it was observed that the shape of the spectra changed with time. After three hours, the spectrum 6 (Fig. 2) was recorded, with considerably poorer resolution.

As reported in Ref. 12, for not-too-high temperatures the spectra of the Vectra copolymer consist of triplets, whose resolution improves with increasing temperature. The triplet structure is a result of superposition of a doublet from the protons of the phenylene ring (proton pairs) on a more complicated trace with a central component of its spectrum, coming from groups of the three nearest protons in the naphthalene fragment. The structure is easy to see because of the considerable separation of the groups from one another and the rather low overall proton concentration. A fundamental change in the spectrum takes place above 423 K. At 423 K a fine structure takes shape and evolves against the background of an overall broad spectrum that is characteristic of solids. In spectrum 5 seven components are visible. We claim that that this spectrum is characteristic of LC states of the solid, despite the fact that the solid is high-molecular weight. Such ‘‘liquid-crystal’’ spectra were also observed for other orientations of the sample in the magnetic field of the spectrometer at 573 K. Consequently, the chain structure of the polymer does not prevent certain cooperative types of molecular motion which lead to considerable averaging of the intergroup magnetic dipole-dipole interactions.

Fine structure was also observed in the NMR spectrum of PPT (Fig. 3) above the thermotropic transition temperature (600 K), which was monitored by differential thermal analysis.

3. DISCUSSION OF RESULTS

Analysis of the results in terms of second moments of the spectra is not very effective in describing the fine structure, because this integral characteristic is only slightly sensitive to the changes in shape that occur near the center of the spectrum, while the overall width does not change. Therefore, in order to extract additional information about the mo-

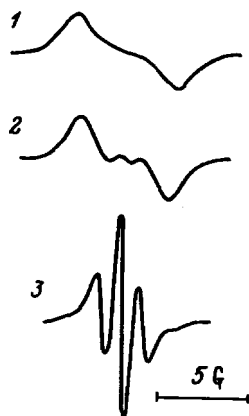


FIG. 3. NMR spectra of PPT copolymer for various temperatures. T (K): 1—293, 2—423, 3—605. The axis of orientation is perpendicular to the magnetic field.

lecular motion we attempted to calculate the shape of the spectrum of a Vectra sample oriented along the magnetic field (this case is the most convenient for calculation). The spectrum of the copolymer should consist of a superposition of two spectra: a doublet from the pair of nearby protons in phenylene rings, and a more complicated system consisting of seven components and the spectrum from the group of three closest-in protons in the naphthalene fragments. If there were no intergroup interactions at all, these spectra should consist of infinitely narrow lines whose intensity and positions can be exactly calculated (Refs. 14 and 15 for a pair and trio of protons respectively). In order to obtain the necessary data on the interproton distance within groups and the orientations of the internuclear vectors relative to the magnetic field of the spectrometer, we used the results of x -ray structural investigations.^{16,17} It was assumed that the macromolecules were completely oriented relative to the fiber axis, and that the existing intergroup dipole-dipole interaction would actually lead to broadening of the spectral lines into a Gaussian. Thus, the computed spectra should consist of a convolution of two functions: the line shape spectrum and a Gaussian curve. By selecting individual values of the dispersions of the Gaussian curves for the phenylene and naphthalene fragments alone (β_{ph}^2 and β_n^2 respectively) we obtain the spectrum 7, which is closest in form to the experimental spectrum 5 (Fig. 2). In computing this spectrum we assumed that $\beta_{ph}^2 = 0.18 \text{ G}^2$, $\beta_n^2 = 0.09 \text{ G}^2$.

The value of the dispersion characterizes the spectral width of groups of protons caused by dipole-dipole interactions with all the neighboring protons that do not belong to the given group. The fact that β_{ph}^2 is larger than β_n^2 is understandable: motion of the cumbersome naphthalene fragments requires a larger free volume. Agreement between the calculated and experimental spectra appear to be good to us, especially since we are discussing a derivative for which any change in the shape is indicated much more sharply. Therefore, the values of the dispersion can be treated as real quantitative characteristics of the intergroup interaction. These values turn out to be so small that we cannot explain them by averaging only the interchain dipole-dipole interaction: the action of two groups of protons on one another within a single fragment of the macromolecule should lead to a large broadening of the components of the spectrum. When the macromolecules are oriented along the magnetic field of the spectrometer the intermolecular interaction should be averaged only when the motion of fragments of the chain is more complicated than a rotation around fixed axes; the orientation of these axes, and thus the configuration of the chain itself, should be continuously changing in space. Thus, the good resolution of the spectral components in the original polymer at 573 K allows us to draw conclusions about the character of the molecular motion in the LC phase: the chains execute cooperative motions connected with random changes of their configuration. Such motions can be modeled by repeated motions of the chain in a de Gennes ‘‘tube.’’¹⁸ However, for the LC phase, these tubes should be almost completely straightened out and oriented along the fiber axis, which is unlike a true melt. As a result of reptation, ‘‘successful’’ positions of fragments of neighboring chains can arise, leading to the

formation of crystals. According to Ref. 7, during thermal processing the degree of crystallinity of Vectra polymer reaches 30%. The nature of the LC state is such that we do not need to apply a tensile force to maintain the straightened state of macromolecules (as occurs in bent-chain polymers). The structural rearrangement during thermal processing takes place in the absence of a directed mechanical field and probably is determined by random approaches of the chains. Therefore, the process of structural rearrangement takes place slowly; this is also due to the irregular (statistical) structure of the macromolecules. The thermal processing lasts for tens of minutes or hours. The crystallites that appear during thermal processing may be treated as nodes (AC or DC) that join neighboring macromolecules,⁷ which should lead to restriction in the molecular motion. Obviously, the resolution of the NMR spectra should be worse after prolonged heating if this is true (compare spectra 5 and 6 in Fig. 2). Here we also can identify an analogy with bent-chain polymers: in order to rearrange the structure and harden it, specific cooperative motions of the macromolecules are needed, so that this motion is suppressed as the structure becomes more perfect. For the point of view of molecular dynamics the state of the LC phase can be regarded as a unique "quasi-highly-elastic" state and can be compared with the true highly elastic state of bent chain polymers. For the latter, the fraction of units that participate in segment motion can be quantitatively determined by NMR as the fraction of narrow components in the spectrum.⁵ We propose to introduce an analogous quantitative characteristic for LC polymers. Let us assume that in a polymer that has not been thermally processed all the chains participate in cooperative motion above the temperature of the LC transition, and that this "liquidlike" L -state corresponds to spectra like 5 (Fig. 2). After thermal processing a portion of the material enters the rigid R state. Let the R state correspond to spectra like 2 (Fig. 2), i.e., only rotational motion of the fragments can occur, while the configuration of the chains is fixed. Then the spectra of a thermally processed sample can be regarded as a superposition of these two spectra taken with weights α_L and α_R respectively. The dynamic state of the LC phase can be characterized by the figure of merit $K = \alpha_L / \alpha_R$. When the spectra 2 and 5 are superimposed, the best agreement with the experimental spectrum 6 is obtained for $\alpha_L = 0.4$ and $\alpha_R = 0.6$ (spectrum 8 in Fig. 2). Thus, as a result of the thermal processing, 60% of the sample appears as rigid regions. This value is higher than the degree of crystallinity determined in Ref. 7. Obviously, the node-crystallites decrease the mobility of neighboring segments of macromolecules that do not belong to them. The parameter K can be used to estimate the effectiveness of the thermal processing.

Thus, complex structural changes take place during thermal processing that require mutual translation of macromolecules, a consequence of which is significant hardening of the material. The slight decrease in the coefficient γ in Eq. (1) is not difficult to understand: hardening of the structure leads to a more uniform loading of the macromolecules, and perhaps local defects that remain after formation are "healed." Similar effects were observed previously in the thermal processing of the lyotropic LC polymer poly-

amidobenzimidazole.¹⁹ Our explanation for the increase of U_0 during thermal processing goes as follows: before thermal processing the macromolecules take up the load as individual chains, and are broken along their weakest links.³ After thermal processing, due to the increase in rigidity of the material at the microlevel (the formation of a rigid skeleton) elementary failure events become more cooperative: loading is taken up by "microblocks," in which the weakest link can turn out to be shunted (shielded). The decreased probability of failure at a weak link should lead to an increase in the net activation energy for damage.

Note that hardening has also been observed previously in nonliquid crystal polymers. The reason for this specific increase in rigidity of highly oriented polymer systems is an increase in U_0 . Thus, the quantity U_0 increases by a factor of 1.6 when the orienting fibers of acetylcellulose are converted into hydrated cellulose by chemical modification in the solid phase.¹¹ Perhaps this principle reflects a quite general regularity.

The authors are grateful to A. Yu. Bilibin for providing the PPT polymer.

This work was carried out with the financial support of the Russian Fund for Fundamental Research (Code 97-03-32624).

*The authors dedicate this article to the memory of S. N. Zhurkov.

¹ S. N. Zhurkov, Bull. USSR Acad. Sci. **11**, 78 (1957) [in Russian].

² S. N. Zhurkov Int. J. Fract. Mech. **1**, 311 (1965).

³ V. R. Perel', A. I. Slutsker, and E. E. Tomashevskii, *The Kinetic Nature of the Strength of Solids* [in Russian], Nauka, Moscow, 1974, 560 pp.

⁴ E. A. Egorov and V. V. Zhizhenkov, J. Polym. Sci., Polym. Phys. Ed. **20**, 7, 1089 (1982).

⁵ E. A. Egorov and V. V. Zhizhenkov, Int. J. Polym. Mater. **22**, 41 (1993).

⁶ K. E. Perepelkin, *Structure and Properties of Fibers* [in Russian], Khimiya, Moscow, 1985.

⁷ E. M. Antonov, S. D. Artamonova, I. A. Volegova, and Yu. K. Golovskii, High Molecular Weight Compounds **A37**, 5, 800 (1995) [in Russian].

⁸ M. J. Troughton, G. R. Davies, and I. M. Ward, Polymer **30**, 1, 58 (1989).

⁹ H. R. Kricheldorf, F. Ruhser, and G. Schwartz, Macromolecules **24**, 18, 4990 (1991).

¹⁰ A. Lösche, *Kerninduktion* (in German) [Deutsche Verlag der Wissenschaften, Berlin, 1957; IL, Moscow, 1963, p. 376.].

¹¹ A. V. Savitskii, B. Ya. Levin, I. A. Gorshkova, L. E. Utevskaia, and L. P. Zosin, High Molecular Weight Compounds **B16**, 11, 810 (1974) [in Russian].

¹² R. A. Allen and I. M. Ward, Polymer **32**, 2, 202 (1991).

¹³ R. A. Allen and I. M. Ward, Polymer **33**, 24, 5191 (1992).

¹⁴ G. E. Pake, J. Chem. Phys. **16**, 4, 327 (1948).

¹⁵ E. A. Andrew and R. Bersohn, J. Chem. Phys. **18**, 2, 159 (1950).

¹⁶ A. Biswas and J. Blackwell, Macromolecules **21**, 11, 3146 (1988).

¹⁷ Sung Kwon Hong and J. Blackwell, Polymer **30**, 2, 225 (1989).

¹⁸ P. G. de Gennes, J. Chem. Phys. **55**, 572 (1971).

¹⁹ E. A. Egorov, M. N. Shuster, V. V. Zhizhenkov, and I. P. Dobrovol'skaya, High Molecular Weight Compounds **A38**, 2, 246 (1996) [in Russian].

FULLERENES AND ATOMIC CLUSTERS

A disclination-based approach to describing the structure of fullerenes

A. L. Kolesnikova

Institute for Problems in Computer Science, Russian Academy of Sciences, 199178 St. Petersburg, Russia

A. E. Romanov

A. F. Ioffe Physicotechnical Institute, Russian Academy of Sciences, 194021 St. Petersburg, Russia

(Submitted November 3, 1997)

Fiz. Tverd. Tela (St. Petersburg) **40**, 1178–1180 (June 1998)

The possibility of using a disclination approach to describe the structure and properties of fullerenes is discussed. It is shown that the conversion of a planar carbon monolayer into a spherical macromolecule can be viewed as the result of introducing 12 disclinations with power $\pi/3$ into the original layer. © 1998 American Institute of Physics.
[S1063-7834(98)04306-8]

Disclinations are, by definition, line defects of a solid, associated with the rotation of regions of a material as it grows.¹ Usually disclinations are used to describe the structures and properties of crystals (for example, metals²), amorphous solids,³ and liquid crystals,⁴ i.e., three-dimensional objects. Examples of experimentally observed disclinations in such systems are well known. However, even during the earliest period of development of the disclination approach it was demonstrated that disclinations could appear in two-dimensional crystals.⁵ This idea was formulated to explain observations of distinctive features in the structures of viruses and biological membranes.⁶ In two-dimensional crystals disclinations turn out to be point defects, in whose nucleus the rotational symmetry characteristic of these crystals is disrupted. For example, in crystals with a square lattice, three- and five-fold disclination axes can pass through the nucleus, while in crystals with a triangular lattice five- and seven-fold axes can occur.^{1,6}

In analyzing the structure of fullerenes,⁷ the pentagonal rings in the carbon lattice can be treated as local disruptions of the symmetry of the original hexagonal graphite lattice. This allows us to regard the pentagonal rings as defects (as we show below, positive wedge disclinations) in the two-dimensional graphite crystal. In this paper we discuss the possibility of using the disclination approach to describe the structure and properties of fullerenes.

Let us consider a graphite monolayer in which each carbon atom is covalently bonded by sp^3 bonds to its three neighbors. The atoms form a hexagonal grid (Fig. 1a). An individual localized pentagonal ring in such a monolayer can be obtained by the following procedure: 1) Make an imaginary cut in the monolayer along a ray starting from the center of one of the hexagonal rings; 2) Remove a sector of the monolayer, one of whose sides coincides with the cut, while the angle at the vertex equals $\pi/3$ (Fig. 1b); 3) Combine the opposite sides of the wedge cutout so that recovery of the covalent bonds takes place along the cut (for this it is neces-

sary for us to elastically deform the entire grid in a special way). As a result, the central hexagonal ring is converted into a pentagon (Fig. 1c). In this case other pentagonal rings in the monolayer do not arise, although hexagonal rings turn out to be elastically distorted.

The procedure described above unambiguously corresponds to the process of forming a positive wedge disclination with power $\omega = \pi/3$ in the continuum. Therefore, the distortion near the localized pentagonal ring in the graphite layer plane can be computed using the results of disclination theory.¹ From this theory it follows that introduction of disclinations into a solid leads to an extremely high density of latent (elastic) energy $W \sim G\omega^2$, where G is the characteristic elastic modulus of the material. In three-dimensional solids the latent energy can be lowered only by introducing additional screening defects, for example, disclinations of opposite sign. In a two-dimensional crystal there is an additional possibility of decreasing the latent energy of the disclinations through loss of stability of the elastically deformed thin layer. In this case the graphite layer buckles and a conical surface forms (Fig. 1d).

The appearance of heptagonal rings in the hexagonal monolayer corresponds to introducing a negative wedge disclination by the procedure described above (Fig. 2a). Relaxation of the elastic energy of the negative disclination takes place in this case by transforming the planar monolayer into a saddle shape (Fig. 2b). We can propose introduce more powerful positive and negative disclinations into the graphite layer with $\omega = +2\pi/3$, $\omega = +\pi$, $\omega = -2\pi/3$, $\omega = -\pi$, leading to the appearance of four-, three-, eight-, and ten-fold rings respectively. Note that polygonal carbon rings are often discussed in the modeling of nucleation processes for fullerenes.⁸

From Fig. 1 it follows that the introduction of positive disclinations (pentagonal rings) causes a warping (positive Gaussian curvature) of the carbon layer. For a certain number of disclinations, the layer surface becomes closed. In this

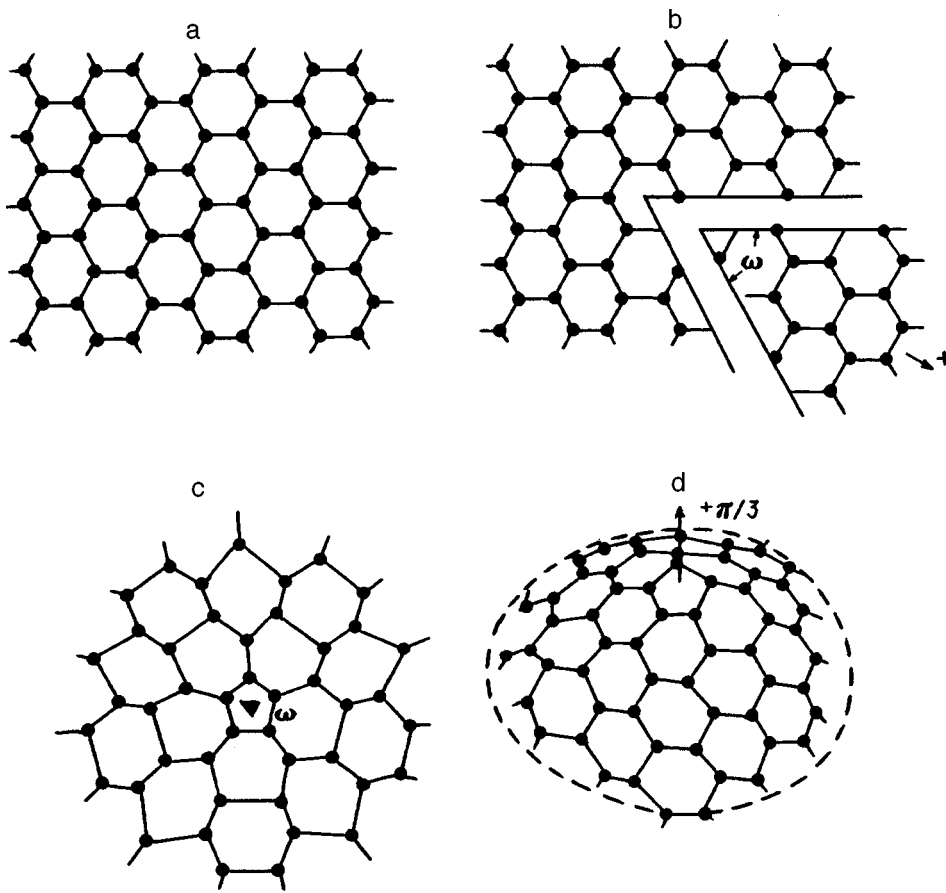


FIG. 1. Formation of a positive disclination in a graphite monolayer. a—hexagonal monolayer, b—formation of a positive disclination in the monolayer, c—a disclination with power $\omega = +\pi/3$ in a hexagonal lattice, d—formation of a conical surface.

case we can use the following relations for the total disclination power of a closed surface:

$$\sum_1^N \omega_i = 2\pi\chi, \tag{1}$$

where ω_i is the power of the i th disclination, N is the number of disclinations, and χ is the Euler characteristic of the surface: for the topology of a sphere $\chi = 2$, for that of a torus $\chi = 0$. It is obvious that the number of hexagonal rings that do not carry a disclination charge can be arbitrary in the closed surface. For a topological sphere (this, for example, is the case for the best known fullerene macromolecules C_{60} and C_{70}) the minimum possible number of disclinations with

power $\omega = +\pi/3$ equals 12, which exactly corresponds to the number of pentagonal rings in the absence of rings other than hexagonal. The disclination model of the fullerene macromolecule C_{60} is shown in Fig. 3a: in the graphite monolayer we introduce twelve disclinations, which are located at equal distances relative to one another as dictated by the symmetry of the problem and the requirement of minimum energy of long-range interactions between disclinations. The existence of a short-range (chemical) interaction between disclination nuclei implies a need for intervening hexagonal rings, which, however, do not change the topological sphericity of the simplest fullerenes.

Within the framework of the disclination model, we can

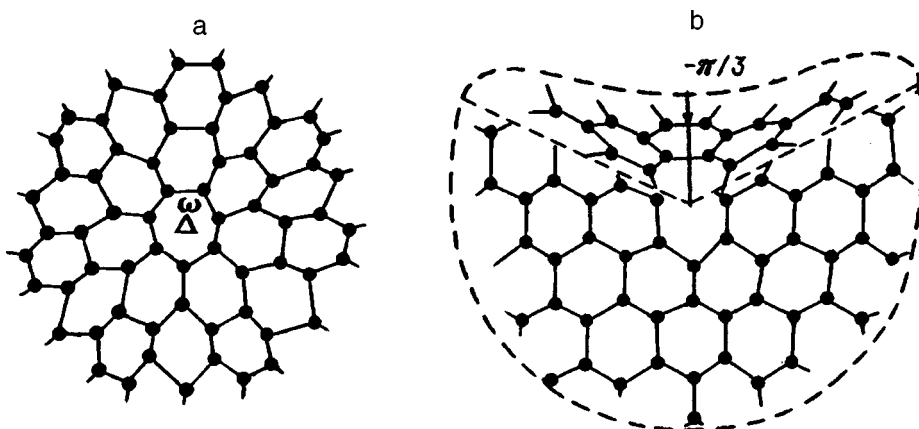


FIG. 2. Negative disclination in a graphite monolayer. a—a disclination with power $\omega = -\pi/3$ in a hexagonal lattice, b—formation of a saddle-shaped surface.

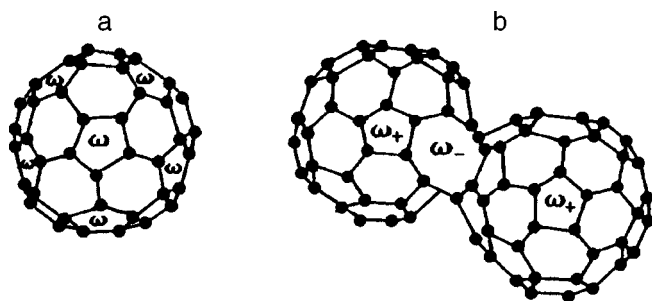


FIG. 3. Disclinations in fullerenes. a—disclination with power $\omega = -\pi/3$ in the macromolecule C_{60} , b—disclinations with powers $\omega_+ = +\pi/3$ and $\omega_- = -2\pi/3$ in the fullerene dimer C_{116} .

explain various geometric changes in the structure of simple fullerenes, and also construct more complicated fullerenes, for example, toroidal and carbon nanotubes. The process of degradation of fullerenes turns out to be connected with changes in the number N and power ω of the disclinations. For example, an external force can lead to transformation of two neighboring hexagonal rings into a pair consisting of a heptagonal and a pentagonal ring, which in the language of disclinations implies creation of a “defect-antidefect pair,” i.e., a positive and a negative disclination. Another example, shown in Fig. 3b, illustrates the change in disclination content during the formation of strongly covalent bonds between macromolecules. This process is possible if an external force partially disrupts the C_{60} molecules, which lose several carbon atoms each.^{9,10} The dimer C_{116} that forms already contains twenty positive disclinations with $\omega = +\pi/3$ (twenty pentagonal rings). In addition, another four negative disclinations are created with $\omega = -2\pi/3$, which model the octagonal ring in the location where the macromolecules join. It is obvious that Eq. (1) for the total disclination power remains valid as before.

The geometric considerations discussed in this paper for disclinations in fullerenes should doubtless be augmented by analysis of their energetic characteristics. For this we must use the theory of shells, in which the original graphite monolayer is modeled as a thin elastic shell with a given bending rigidity. Such an energy analysis will allow us to solve the problems mentioned above regarding stability of a carbon layer with a single disclination. One outgrowth of this approach will be computation of the interaction force between disclinations in the shell, and also investigation of the interaction of impurity atoms with disclination nuclei.

This work was carried out within the framework of the Russian Science and Engineering Program “Fullerenes and Atomic Clusters.”

¹V. I. Vladimirov and A. E. Romanov, *Disclinations in Crystals* [Leningrad, 1986], 224 pp.

²V. V. Rybin, *Large Plastic Deformations and Fracture of Metals* [Moscow, 1986], 224 pp.

³V. A. Likharev, A. E. Volkov, and V. E. Shudegov, *Continuum Theory of Defects* [Leningrad, 1986], 232 pp.

⁴I. A. Ovid'ko, *Defects in Condensed Media* [Leningrad, 1991], 247 pp.

⁵F. R. N. Nabarro, in *Fundamental Aspects of Dislocation Theory*, J. A. Simmons de Wit, and R. Bullough (Eds.) (U. S. Nat. Bur. Stand., Spec. Publ., 1970), 317. 1. 593.

⁶W. F. Harris, *Surf. Def. Prop. Sol.* **3**, 1, 57 (1974).

⁷D. Koruga, S. Hameroff, J. Wither, R. Loutfy, and M. Sundareshan, *Fullerene C₆₀: History, Physics, Nanobiology, Nanotechnology* (North-Holland, 1993), 379 pp.

⁸Yu. E. Lozovik and A. M. Popov, *Usp. Fiz. Nauk* **167**, 751 (1997).

⁹A. M. Rao, P. C. Eklund, V. D. Venkatesvaran, J. Tucker, M. A. Duncan, G. M. Bendele, P. W. Stepheer, J.-L. Hodeau, L. Marques, M. Nunez-Regueiro, I. O. Bashkin, P. G. Ponyatovsky, and A. P. Morovsky, *Appl. Phys.* **64**, 2, 231 (1997).

¹⁰D. Porezag, G. Jungnickel, Th. Frauenheim, G. Seifert, A. Ayuela, and M. R. Pederson, *Appl. Phys.* **64**, 3, 321 (1997).

Translated by Frank J. Crowne

BORIS PETROVICH ZAKHARCHENYA (ON HIS 70TH BIRTHDAY)

Fiz. Tverd. Tela (St. Petersburg) **40**, 953–956 (June 1998)

[S1063-7834(98)00106-3]

Academician Boris Petrovich Zakharchenya, prominent solid-state physicist, Director of the Division of Solid-State Physics at the A. F. Ioffe Physicotechnical Institute of the Russian Academy of Sciences, and chief editor of the journal ‘‘Physics of the Solid State,’’ celebrated his 70th birthday on May 1, 1998.

B. P. Zakharchenya was born in the Byelorussian city of Orsha into the family of a military engineer. The family soon moved to Leningrad, where Boris Petrovich completed secondary school in 1947 and matriculated in the Department of Physics at Leningrad State University.

After graduating in 1952 he was accepted for graduate studies at the Leningrad Physicotechnical Institute and began working as an experimental physicist under the supervision of an outstanding scientist in the field of optical spectroscopy, Corresponding Member of the Soviet Academy of Sciences E. F. Gross. This work involved a new and extremely interesting direction in solid-state physics that just been discovered in the experimental observation by E. F. Gross and

H. A. Karryev in 1951 of the hydrogen-like optical spectrum of an exciton — a quasiparticle predicted theoretically in 1937 by Ya. I. Frenkel’ for Cu_2O crystals.

Boris Petrovich’s investigations were conducted in an intensely productive environment characteristic of work in a new direction. The scientific results obtained made a major contribution to the establishment of the physics of excitons and optical spectroscopy of semiconductors. The observation in 1952 of two hydrogen-like series of exciton absorption was the first experimental evidence of spin-orbit splitting of the valence band in semiconductors. The first experiments on the effect of external electric and magnetic fields on the optical spectra of semiconductors were experiments performed in 1954 in which the Zeeman effect in exciton lines and the Stark effect were observed for the first time, demonstrating ionization of an exciton as a weakly-bound electron-hole system.

After successfully defending his Candidate’s Dissertation (1955), Boris Petrovich together with E. F. Gross performed a series of pioneering investigations in the spectroscopy of semiconductors in an external magnetic field. In 1956 a giant diamagnetic shift of the levels of an exciton, bound with a large orbital radius of the hydrogen-like states, was observed for the first time. In 1957 oscillations of the magnetoabsorption beyond the limit of the excitonic series in the spectra of cuprous oxide crystals were discovered. The observation of this basic magneto-optic effect due to the appearance of Landau levels in Cu_2O spectra (just as independent observations of magnetoabsorption oscillations in Ge by Lax and Zwerdling and in InSb by Burshtein and Paikus) marks the beginning of modern magneto-optics of semiconductors.

In the 1960s, B. P. Zakharchenya continued to develop exciton magneto-optics. Together with R. P. Seisyan he proved by means of many experiments the existence of quasi-one-dimensional excitons (magnetic excitons).

In 1961 B. P. Zakharchenya observed (independently but simultaneously with Thomas and Hopfield) in a certain experimental geometry a reversal of the magnetic field in the absorption spectrum of excitons in CdS crystals, which do not have a center of inversion. The discovery of magnetic field reversal, due to the fact that an exciton possesses momentum, i.e. due to exciton motion, had a large impact on the development of exciton optics with spatial dispersion.

B. P. Zakharchenya’s contribution to investigations of excitons in semiconductors was highly regarded. For this research, he was awarded (together with other authors) the 1966 Lenin Prize. In the same year he also successfully defended his doctoral dissertation.

In 1970 active investigations of the optical orientation of



electron and nuclear spins in semiconductors under pumping with circularly polarized light were begun at the initiative and with the participation of B. P. Zakharchenya. The appearance and development of this new direction in semiconductor physics played a very large role in the understanding of dynamic electronic and electron-nuclear spin processes in semiconductors. B. P. Zakharchenya together with V. G. Fleisher discovered a number of new phenomena: optical cooling of nuclear spin systems (down to 10^{-6} K), multi-quantum nuclear resonances under optical orientation conditions, optical orientation of holes, and others.

In 1976 the work performed by B. P. Zakharchenya and others at the Physicotechnical Institute on optical orientation in semiconductors was awarded the State Prize of the USSR. The collective monograph "Optical Orientation," published in English and edited by B. P. Zakharchenya and F. Maier, summarized the achievements of world science in this field.

In 1976 B. P. Zakharchenya together with D. N. Mirlin and others were the first to observe the luminescence of hot photoelectrons in semiconductors and photoelectron momentum alignment under excitation with linearly polarized light. The development of experimental and theoretical (V. I. Perel' and M. I. D'yakonov) research on hot luminescence, including in semiconductors, led to the development of a new direction in semiconductor physics. It was found that under the conditions of steady-state measurements of hot luminescence, including in a magnetic field, it is possible to study electronic relaxational processes in bulk semiconductors and in semiconductor structures, including extremely short femtosecond processes, and to obtain accurate values of the band parameters of semiconductors. The works on hot luminescence of semiconductors performed by scientists at the Physicotechnical Institute have elicited broad interest and have found followers in laboratories abroad.

At the present time B. P. Zakharchenya is investigating quantum-size structures, including quantum dots, by the methods of polarization optics and spectroscopy.

B. P. Zakharchenya's contribution to the development of optical spectroscopy and magneto-optics of semiconductors has won wide acclaim.

In 1976 B. P. Zakharchenya was elected Corresponding Member of the USSR Academy of Sciences and in 1992 to active membership in the Russian Academy of Sciences.

In 1996 the Russian Academy of Sciences recognized B. P. Zakharchenya's achievements in the development of the optics of semiconductors by awarding him the P. N. Lebedev Great Gold Medal. B. P. Zakharchenya's work on the optical orientation of carriers in semiconductors was recog-

nized with the Hanle Prize, which is awarded in Germany.

Speaking about the B. P. Zakharchenya's enormous scientific-organizational work, his work in the important job as Director of the Division of Solid-State Physics at the A. F. Ioffe Physicotechnical Institute of the Russian Academy of Sciences must be mentioned first. In a difficult time for science Boris Petrovich is expending a great deal of effort and energy on organizing the work of a large group in the Division and on supporting in this group new and promising directions of research.

As a professor at the St. Petersburg State Electrotechnical University, B. P. Zakharchenya lectures to students in the Department of Optoelectronics.

For many years B. P. Zakharchenya has been the chief editor of the journal "Physics of the Solid State." His role in organizing journal work under the new conditions and in the simultaneous and high-quality publication of the English language version of the journal is inestimable.

B. P. Zakharchenya is performing great organization work on the international level. For many years he has been a member of the Commission on Semiconductors of the European Union of Pure and Applied Physics.

In 1997 an International Conference on the Optics of Excitons in Condensed Media, dedicated to the 100th anniversary of the birthday of E. F. Gross, was successfully held in St. Petersburg under the direction of B. P. Zakharchenya. By actively participating in the organization of this conference Boris Petrovich paid a tribute of respect to the memory of his teacher E. F. Gross.

The number of scientific papers published by B. P. Zakharchenya in leading physics journals around the world can hardly be accurately counted. Boris Petrovich also writes for literary journals. In publications such as "Our Heritage," "Aurora," and others he has published essays on A. S. Pushkin and sketches of friends and close acquaintances, and not only from the world of science. These publications show Boris Petrovich to be a versatile, educated man with wide interests.

All who associate with him know him as a very interesting and lively conversationalist, talented story teller, a man of unique individuality, an intellectual in the full sense of the word.

We wish Boris Petrovich, on his 70th birthday, good health and continued success to the good of science.

Editorial Board of "Physics of the Solid State"

Translated by M. E. Alferieff

METALS. SUPERCONDUCTORS

Luminescence of metals excited by fast nondestructive loading

K. B. Abramova, A. I. Rusakov, A. A. Semenov, and I. P. Shcherbakov

A. F. Ioffe Physicotechnical Institute, Russian Academy of Sciences, 194021 St. Petersburg, Russia

(Submitted July 17, 1997; resubmitted October 28, 1997)

Fiz. Tverd. Tela (St. Petersburg) **40**, 957–965 (June 1998)

The paper reports a study of the luminescence excited on the back side of metal targets irradiated with laser pulses of energy substantially below the plasma-flare formation threshold, and calculation of the temporal and spatial distributions of temperature, thermal stresses, and rate of thermal-stress variation in a sample. The evolution of the luminescence pulse is compared with that of the laser pulse, sample temperature, thermal stresses, and rate of thermal-stress variation. It has been established that the luminescence is excited as soon as the stresses at the sample surface become approximately equal to the yield point of the sample material, its intensity grows as long as the rate of stress rise increases, after which the process decays. The temporal and spatial distributions of temperature, thermal stresses, and rate of thermal-stress variation have also been calculated for the experiments, in which anomalous electron emission from the back side of laser-pulse irradiated metal targets was detected, and which were described in the literature but not appropriately explained. The dynamics of experimental and calculated relations have been compared. A correlation closely similar to that found for mechanoluminescence has been established. © 1998 American Institute of Physics. [S1063-7834(98)00206-8]

The luminescence of metals is a well-known, however, little studied phenomenon. Luminescence from nearly 20 different metals and alloys has been experimentally detected. Light-excited photoluminescence,^{1,2} cathodoluminescence,^{3,4} and mechanoluminescence generated by fracture and deformation^{5–7} are widely known. Mechanisms for excitation of photo- and mechanoluminescence in noble metals have been proposed.^{1,2,8,9}

Using laser pulses to probe the emission phenomena (in particular, mechanoluminescence) excited on the back side of an irradiated sample is experimentally convenient and provides a wealth of information. Interaction of a laser pulse with the surface of metal targets at pulse energies below the plasma-flare onset threshold was studied, for instance, in Refs. 10 and 11. One can calculate quite accurately the temporal and spatial distributions of temperature and stresses in an irradiated target in absolute magnitude and compare them with the onset of the luminescence pulse excited on the target's back side, establish the minimum stresses able to excite luminescence, and confirm or establish correlation between the loading and emission. This is the objective of the first part of the present work.

The second part of the work deals with the possible relation between exoemission and mechanoluminescence excited by fast deformation of metal samples. Deformation and fracture of dielectrics, semiconductors, and metals gives rise to a number of nonequilibrium processes, including the emission of electrons and photons. It was convincingly demonstrated^{12,13} that deformation of alkali halide crystals LiF and NaF is accompanied by simultaneous excitation of

luminescence and electron emission, which result from the same dislocation processes.

Mechanical stressing of metals was also shown to be accompanied by electron emission.¹⁴ We are not aware of any simultaneous measurements of mechanoluminescence and electron emission from metals. There are, however, at least two groups of studies which established the existence of a burst of nonthermal electron emission from metal samples. Experiments were described in which a metal sample was irradiated with a laser pulse, electron emission from its back side was measured, and the temperature $T = T(t)$ of the back side was calculated.^{15,16} Two electron pulses, well spaced in time, were found to be initiated. The first pulse, short and strong, was detected from the cold surface, and the second pulse, identified as due to thermionic emission, escaped from the heated surface. A review paper¹⁷ sums up a number of experiments in which high-density electric currents were passed through metals to investigate the processes developing under fast heating. In all cases where the corresponding measurements were made electron emission was detected, which the authors call anomalous because of its magnitude and temporal characteristics. The electron emission current close to the melting point exceeds 10–100 times the steady-state thermal-emission level. After the current has been turned off, i.e., after the heating has been stopped, the electron emission decays in a time interval during which the cooling of the conductor is negligible.

A qualitative explanation of the observed phenomena was proposed. According to Ref. 17 and the physical model proposed in Ref. 18, the burst of electron emission is due to

the nonequilibrium defect concentration created in the bulk of the metal under fast heating as a result of the low diffusion rate of the vacancies produced at the surface. Thus some characteristics of the mechanoluminescence and mechanoemission of electrons from metals may be considered established. The objective of the second part of this work is to compare these processes.

1. CALCULATION

A single laser pulse striking a metal plate, whose surface dimensions exceed by far its thickness and the light spot diameter, excites luminescence from the back side of the target. The laser pulse energy, high enough for luminescence excitation, $P_{\text{las}} \geq 0.1 P_{\text{thr}}$, is much less than the energy P_{thr} required for destruction of the irradiated surface.¹⁹⁻²¹ To understand the processes occurring in the sample, one has to calculate its heating, i.e., the spatial and temporal distribution of the temperature and the heating-induced stresses, in other words, the distribution of thermal stresses in space and time.

A. Temperature distribution

The duration of the processes considered in this work is much shorter than the time required for heat to propagate to sample boundaries and, therefore, the sample is assumed to be infinite in width and length. The absorbed fraction of laser radiation is equated to the heat flux q_0 entering the sample through the illuminated spot on its surface, $r = r_0$, during the laser pulse length t_0 . We assume that there is neither heat emission through the sample surfaces into the surrounding medium nor heat exchange with the latter. The problem is considered in a cylindrical coordinate frame, whose axis z is perpendicular to sample plane and passes through the center of the laser-illuminated spot. The sample occupies space within $0 \leq z \leq a$. We assume the heat conductivity coefficient k , heat capacity c , and sample material density ρ to be temperature independent. Under these assumptions, the heat conductivity equation and its boundary conditions can be written

$$\Delta T = \frac{\partial T}{\partial \tau}, \quad \tau = \frac{kt}{c\rho}, \tag{1}$$

$$\left. \frac{\partial T}{\partial z} \right|_{z=0} = \begin{cases} \begin{cases} -\frac{q_0}{k} f(\tau), & \tau < \tau_0 = \frac{kt_0}{c\rho}, \\ 0, & \tau > \tau_0 \end{cases} & r \leq r_0, \\ 0, & r > r_0, \end{cases} \tag{2}$$

[$f(\tau)$ is the laser pulse shape]

$$\left. \frac{\partial T}{\partial z} \right|_{z=a} = 0. \tag{3}$$

Equation (1) with boundary conditions (2) and (3) was solved by applying Laplace transform in τ and Hankel transform in r .

The laser pulse shape was approximated with a function

$$f(\tau) = \begin{cases} \sin \frac{\pi \tau}{\tau_0}, & \tau \leq \tau_0, \\ 0, & \tau > \tau_0. \end{cases} \tag{4}$$

The expressions obtained for the temperature distribution in the sample are as follows: for $\tau < \tau_0$

$$T(r, z, \tau) = \frac{q_0 r_0}{k} \int_0^\infty J_1 \left(\lambda \frac{r_0}{a} \right) J_0 \left(\lambda \frac{r}{a} \right) \times \left\{ \frac{\lambda^2 \sin \frac{\pi \tau}{\tau_0} - \frac{\pi a^2}{\tau_0} \left[\cos \frac{\pi \tau}{\tau_0} - \exp \left(-\lambda^2 \frac{\tau}{a^2} \right) \right]}{\lambda^4 + \frac{\pi a^4}{\tau_0^2}} + 2 \sum_{n=1}^\infty \frac{\cos \frac{n \pi z}{a}}{(n^2 \pi^2 + \lambda^2)^2} \left\{ (n^2 \pi^2 + \lambda^2) \times \sin \frac{\pi \tau}{\tau_0} - \frac{\pi a^2}{\tau_0} \left[\cos \frac{\pi \tau}{\tau_0} - \exp \left(-(n^2 \pi^2 + \lambda^2) \frac{\tau}{a^2} \right) \right] \right\} \right\} d\lambda, \tag{5}$$

for $\tau > \tau_0$

$$T(r, z, \tau) = \frac{q_0 r_0}{k} \frac{\pi a^2}{\tau_0} \int_0^\infty J_1 \left(\lambda \frac{r_0}{a} \right) J_0 \left(\lambda \frac{r}{a} \right) \times \left\{ \frac{\exp \left(-\lambda^2 \frac{\tau}{a^2} \right) \left[\exp \left(\lambda^2 \frac{\tau_0}{a^2} \right) + 1 \right]}{\lambda^4 + \frac{\pi a^4}{\tau_0^2}} + 2 \sum_0^\infty \frac{\cos \left(\frac{n \pi z}{a} \right)}{(n^2 \pi^2 + \lambda^2)^2 + \frac{\pi a^4}{\tau_0^2}} \exp \left[-(n^2 \pi^2 + \lambda^2) \frac{\tau}{a^2} \right] \left[\exp \left((n^2 \pi^2 + \lambda^2) \frac{\tau_0}{a^2} \right) + 1 \right] \right\} d\lambda. \tag{6}$$

These relations permit one to calculate and plot temperature vs time graphs for different r and z , as well as to plot temperature as a function of time for a given absorbed energy and different r and z .

B. Quasi-static thermal stresses

An abrupt increase of temperature on one surface of the plate ("heat shock") can generate in it a compression wave

propagating with a velocity $c = \sqrt{2(1-\mu)G/(1-2\mu)\rho}$, where μ is the Poisson coefficient, $G = E/2(1+\mu)$ is the shear modulus, E is the Young modulus, and ρ is the density of plate material. The propagation of the wave is described by displacement equations including the inertia term $\rho \partial^2 \mathbf{U} / \partial t^2$, where \mathbf{U} is the displacement vector. If the temperature varies relatively slowly, the inertia may be neglected, and the motion considered as a sequence of equilibrium states (the hypothesis of Duhamel²²). This approach is called quasi-static.

As already mentioned, one of the objectives pursued in this work is an attempt at establishing the minimum stresses capable of exciting mechanoluminescence. We used in the experiments laser pulses of the lowest power at which one still can detect reliably luminescence from the irradiated sample. In these conditions, the luminescence pulse excited at the back side of the sample lagged behind the beginning of the laser pulse by a time more than two orders of magnitude longer than that required for a compression wave to travel through the sample. This means that no compression wave was generated in our experiment. This permitted us to use the quasi-static approach to the solution of the problem. (Analytic evaluation of the region where this approach is valid is a very complex physical problem, which could hardly be resolved within the study described here.)

The equations describing axially symmetric quasi-static thermoelastic displacement, in a cylindrical coordinate frame, can be written²²

$$\begin{cases} \Delta U_r - \frac{U_r}{r^2} + \frac{1}{1-2\mu} \frac{\partial}{\partial z} (\text{div } \mathbf{U}) = \frac{2(1+\mu)}{1-2\mu} \frac{\partial(\alpha T)}{\partial r}, \\ U_z + \frac{1}{1-2\mu} \frac{\partial}{\partial r} (\text{div } \mathbf{U}) = \frac{2(1+\mu)}{1-2\mu} \frac{\partial(\alpha T)}{\partial r}. \end{cases} \quad (7)$$

Here α is the thermal expansion coefficient, which is assumed to be constant.

Since no external forces act on the sample surfaces (we neglect here the laser light pressure), one should take the following boundary conditions

$$\sigma_{ik} n_k = 0, \quad (8)$$

which, in the small-strain approximation valid under our conditions, can be written in the following form:

$$\sigma_{zz} \Big|_{z=0;a} = 0, \quad (9)$$

$$\sigma_{rz} \Big|_{z=0;a} = 0. \quad (10)$$

Here σ_{ik} is the stress tensor, and \mathbf{n} are the normals to the sample surfaces.

The solution to Eqs. (7), subject to boundary conditions (9) and (10), was sought by means of the thermoelastic displacement potential and Love function.²² The relation between the displacements and the stress tensor will be used to obtain expressions for its components. We are interested here primarily in the stresses on the back surface of the sample,

i.e., for $z = a$. Here $\sigma_{rz} = \sigma_{zz} = 0$, and, as follows from numerical calculations, the dependences of σ_{rr} and $\sigma_{\varphi\varphi}$ on radius and time are the same, and therefore we are presenting one of the derived expressions:

$$\begin{aligned} \sigma_{rr} = -\beta \Bigg\{ & -\frac{1}{ar} \int_0^\infty J_1\left(\lambda \frac{r_0}{a}\right) J_0\left(\lambda \frac{r}{a}\right) F(\lambda, z, \tau) \lambda d\lambda \\ & + \int_0^\infty J_1\left(\lambda \frac{r_0}{a}\right) J_0\left(\lambda \frac{r}{a}\right) \frac{\partial^2 F(\lambda, z, \tau)}{\partial z^2} d\lambda + \frac{1}{ar} \\ & \times \int_0^\infty \frac{J_1\left(\lambda \frac{r_0}{a}\right) J_1\left(\lambda \frac{r}{a}\right)}{\sinh^2 \lambda - \lambda^2} \Bigg\{ (1-2\mu) \\ & \times \left(\lambda \sinh \lambda \frac{z}{a} - \sinh \lambda \sinh \lambda \left(1 - \frac{z}{a}\right) \right) \\ & - \lambda^2 \cosh \lambda \frac{z}{a} + \lambda \frac{z}{a} \left(\lambda \cosh \lambda \frac{z}{a} + \sinh \lambda \cosh \lambda \right. \\ & \left. \times \left(1 - \frac{z}{a}\right) \right) \Bigg\} F(\lambda, 0, \tau) - \Big\{ (1-2\mu) \\ & \times \left(\sinh \lambda \sinh \lambda \frac{z}{a} - \lambda \sinh \lambda \left(1 - \frac{z}{a}\right) \right) \\ & - \lambda \sinh \lambda \cosh \lambda \frac{z}{a} + \lambda \frac{z}{a} \left(\sinh \lambda \cosh \lambda \frac{z}{a} \right. \\ & \left. + \lambda \cosh \lambda \left(1 - \frac{z}{a}\right) \right) \Bigg\} \\ & \times F(\lambda, a, \tau) \Bigg] \lambda d\lambda - \frac{1}{a^2} \int_0^\infty \frac{J_1\left(\lambda \frac{r_0}{a}\right) J_0\left(\lambda \frac{r}{a}\right)}{\sinh^2 \lambda - \lambda^2} \\ & \times \Bigg\{ \left[\lambda \sinh \lambda \frac{z}{a} - \sinh \lambda \sinh \lambda \left(1 - \frac{z}{a}\right) - \lambda^2 \cosh \lambda \frac{z}{a} \right. \right. \\ & \left. \left. + \lambda \frac{z}{a} \left(\lambda \cosh \lambda \frac{z}{a} + \sinh \lambda \cosh \lambda \left(1 - \frac{z}{a}\right) \right) \right] F(\lambda, 0, \tau) \right. \\ & - \left[\sinh \lambda \sinh \lambda \frac{z}{a} - \lambda \sinh \lambda \left(1 - \frac{z}{a}\right) \right. \\ & \left. - \lambda \sinh \lambda \cosh \lambda \frac{z}{a} + \lambda \frac{z}{a} \left(\sinh \lambda \cosh \lambda \frac{z}{a} + \lambda \cosh \lambda \right. \right. \\ & \left. \left. \times \left(1 - \frac{z}{a}\right) \right) \right] F(\lambda, a, \tau) \Bigg] \lambda^2 d\lambda \Bigg\}. \quad (11) \end{aligned}$$

Here

$$\beta = 2G \frac{1+\mu}{1-\mu} \alpha \frac{q_0 r_0}{k} = \frac{\alpha E}{1-\mu} \frac{q_0 r_0}{k}; \quad \text{for } \tau < \tau_0,$$

$$F(\lambda, z, \tau) = a^2 \left\{ \frac{\lambda^2 \sin \frac{\pi \tau}{\tau_0} - \frac{\pi a^2}{\tau_0} \left[\cos \frac{\pi \tau}{\tau_0} - \exp \left(-\lambda^2 \frac{\tau}{a^2} \right) \right]}{\lambda^4 + \frac{\pi^2 a^4}{\tau_0^2}} + 2 \sum_{n=1}^{\infty} \cos \left(\frac{n \pi z}{a} \right) \frac{(n^2 \pi^2 + \lambda^2) \sin \frac{\pi \tau}{\tau_0} - \frac{\pi a^2}{\tau_0} \left[\cos \frac{\pi \tau}{\tau_0} - \exp \left(-(n^2 \pi^2 + \lambda^2) \frac{\tau}{a^2} \right) \right]}{(n^2 \pi^2 + \lambda^2)^2 + \frac{\pi^2 a^4}{\tau_0^2}} \right\}, \quad (12)$$

and for $\tau > \tau_0$

$$F(\lambda, z, \tau) = \frac{\pi a^4}{\tau_0} \left\{ \frac{\exp \left(-\lambda^2 \frac{\tau}{a^2} \right) \left[1 + \exp \left(\lambda^2 \frac{\tau_0}{a^2} \right) \right]}{\lambda^4 + \frac{\pi^2 a^4}{\tau_0^2}} + 2 \sum_{n=1}^{\infty} \cos \left(\frac{n \pi z}{a} \right) \frac{\exp \left[-(n^2 \pi^2 + \lambda^2) \frac{\tau}{a^2} \right] \left[1 + \exp \left((n^2 \pi^2 + \lambda^2) \frac{\tau_0}{a^2} \right) \right]}{(n^2 \pi^2 + \lambda^2)^2 + \frac{\pi^2 a^4}{\tau_0^2}} \right\}. \quad (13)$$

Thus the problem has been solved. The relations derived here permit calculation of the stress distributions we have been looking for.

2. EXPERIMENT

We studied experimentally the luminescence and thermal emission excited at the back side of a metal target irradiated by an incident laser pulse. The samples were 0.1–0.5-mm thick plates with a 30×30 mm surface area. One surface of the sample faced the entrance window of a FEU-136 PM tube sensitive to radiation within a broad spectral range of 300–800 nm and feeding the analog output into a digital storage oscillograph, or the window of an FSG-22-311 photoresistor sensitive within the 800–1500-nm region, whose signals were likewise fed into a digital storage oscillograph. The other side of the sample was illuminated with laser pulses having the following parameters: pulse length $t_{\text{las}} = 1.5$ ms, energy in the free-running mode $P = 24$ J, and wavelength 1.06 μm . The beam was focused to a spot with diameter $d_{\text{eff}} = 2$ –8 mm, and attenuated with neutral filters to the level P_{thr} corresponding to the threshold of destruction (or, which is the same, to the onset of laser-induced plasma-flare at the front side of the sample), or lower. The lowest laser-pulse energy was determined by the possibility of luminescence detection from the back side of the sample, and was 0.1–0.2 P_{thr} [for example, for copper $P_{\text{thr}} = 5 \times 10^5$ W/cm² (Ref. 10)].

We irradiated copper, aluminum, gold, silver, and platinum samples. The pulse energy P_{las} was monitored. Luminescence from the back side was excited, as a rule, for $P_{\text{las}} > 0.2 P_{\text{thr}}$. If the luminescence intensity was high enough for its reliable detection, the I_{lum} pulse for copper samples started 0.2–0.3 ms after the beginning of P_{las} , and ended, as a rule, before the end of P_{las} . Increasing the laser pulse intensity increased the luminescence intensity. If P_{las} was high enough, two time-resolved luminescence pulses, $I_{\text{lum}}^{(1)}$ and $I_{\text{lum}}^{(2)}$, were excited at the back side of the sample, with $I_{\text{lum}}^{(2)}$ appearing before $I_{\text{lum}}^{(1)}$. The luminescence-pulse de-

lay time relative to the beginning of the laser pulse and the energy P_{las} capable of exciting $I_{\text{lum}}^{(1)}$ and $I_{\text{lum}}^{(2)}$ permit a conclusion¹⁹ that while both pulses originate from mechanical stresses, $I_{\text{lum}}^{(2)}$ results from those caused by an acoustic wave or heat shock, and $I_{\text{lum}}^{(1)}$, from thermal stresses.

The experiments reported below were performed at laser energies $P_{\text{thr}} > P_{\text{las}} \geq 0.1$ –0.2 P_{thr} , i.e., where only $I_{\text{lum}}^{(1)}$ is excited, and it is for these conditions that the calculations were made.

The thermal radiation was measured, as already mentioned, with a photoresistor, which was calibrated beforehand. The surface of the sample facing the detector was protected with an opaque screen with a hole whose diameter equaled to that of the laser spot, after which the sample was heated with a stationary source to a fixed temperature determined by a thermocouple, and the photoresistor signal was measured. The measurements were made within the 25–120 °C interval in steps of 5 °C. These measurements were used to determine the vertical scale of the oscillographic traces obtained with the photoresistor.

3. RESULTS AND DISCUSSION

We measured in the experiments the luminescence emitted from the back side of the targets of platinum, silver, gold, cold-rolled and annealed copper, and aluminum irradiated with a laser pulse of energy $P_{\text{las}} < P_{\text{thr}}$. For such low excitation levels, no luminescence from aluminum and annealed copper was detected,²⁰ while in all the other cases it was reliably seen. For all metals, thermal emission was measured, and its evolution in time $I_T(t)$ was obtained with the photoresistor and oscillograph. Equations (5), (6), (11)–(13) were used to calculate the temporal and spatial dependences of

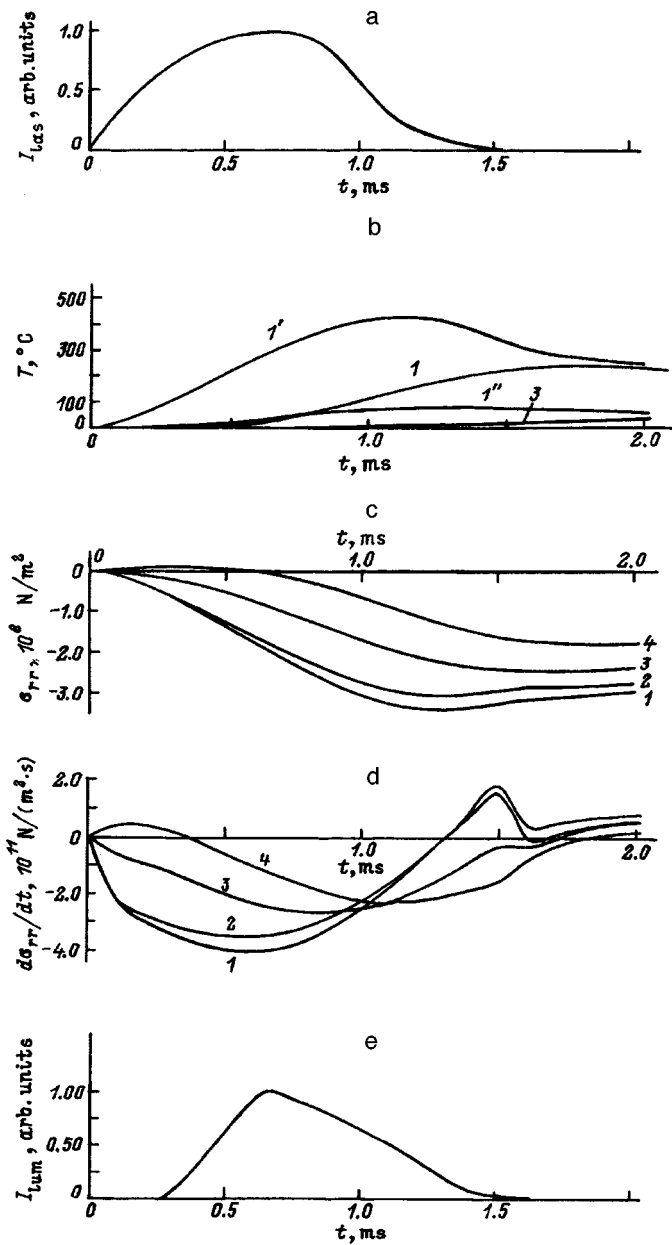


FIG. 1. Oscillographic traces of laser pulse (a), luminescence (e), thermal emission from the back side of a copper sample of thickness $z=0.5$ mm (b, curve I''), as well as calculated temperature (b, curves I , I' , I_3), thermal stresses (c), and thermal-stress variation rate (d). (b): I' — spot center on irradiated side ($z=0$, $r=0$); I_3 — back side ($z=0.5$ mm, center and edge of the heated spot, respectively). (c,d): back side ($z=0.5$ mm), r (mm): I — 0, 2 — 0.5, 3 — 1.0, 4 — 1.5. Energy input into the sample $E_{in}=1.6$ J, $\sigma_{0,2}=1.2 \times 10^8$ N/m².

temperature and thermal stresses in absolute magnitude. The calculations took into account that the absorbed radiation density is only a small fraction of the incident flux, for instance, for copper it is only 2–7%.²³

Figure 1 displays experimental and calculated dependences for irradiation of a copper sample made of a cold-rolled plate (yield point $\sigma_{0,2}=1.2 \times 10^8$ N/m²). We readily see that as the spot heats and the heating propagates through the sample after the beginning of the laser pulse (Fig. 1b), thermal stresses appear and grow in magnitude (Fig. 1c).

Figure 1e shows the mechanoluminescence pulse. The pulse is seen to appear after the thermal stresses in a region on the back side of the target have approached the yield point (Fig. 1c). Figure 1d plots the stress variation rate $\partial\sigma/\partial t$ in the sample with time. A comparison of the graphs in Fig. 1 suggests that the luminescence intensity I_{lum} correlates best of all with the stress variation rate $\partial\sigma/\partial t$. The larger is $\partial\sigma/\partial t$, the higher is the luminescence intensity, and when $\partial\sigma/\partial t$ decreases, I_{lum} decreases too, although the laser pulse is still on, and the thermal stresses and temperature are still growing. The maximum of the luminescence pulse lags in time slightly behind that of the stress variation rate at the center of the back side of the sample (curve I in Fig. 1d). This can be attributed to the fact that the PM tube measures the emission integrated over the whole loaded region, while the rate of stress variation at different points on the sample surface reaches a maximum at different instants of time (curves I – 4 in Fig. 1d). The temperature on the back side of the copper sample measured with the photoresistor (curve I'' in Fig. 1b) attains its highest level of 60–80 °C by the time the luminescence has decayed. The $T(t)$ graphs plotted in Fig. 1b require additional explanation. Curves I' , I , and I_3 are temperature variation curves calculated for different points on the front and back sides of the sample, I' is the center of the laser spot on the front surface, I is the center of the spot on the back side, I_3 is approximately the edge of the back-side spot, and I'' is the experimental curve, i.e., an oscillogram obtained with the photoresistor. This photoresistor was placed so as to intercept all of the radiation emitted from the heated back-side spot, and therefore curve I'' should be considered as an estimate, or a relation averaged over the area of the heated spot, which, however, fits fairly well to the calculation. All the metals studied exhibited (as, for instance, in Fig. 1) disagreement between the I_{lum} and $T(t)$ relations even for the hottest point within the heated spot.

Similar experiments were performed also on annealed copper samples with a yield point $\sigma_{0,2}=0.7 \times 10^8$ N/m². In these cases, however, no mechanoluminescence was detected. Studies are reported²⁰ of changes in the microstructure of copper samples following irradiation with similar laser pulses. In annealed samples, no changes in the microstructure were observed to occur. Mechanoluminescence was detected in the samples where such changes were revealed. In samples with a fine-grained microstructure the grains were observed to grow in size in the laser-irradiated region. It is known that the concentration of defects is the largest at grain boundaries. Therefore when grains change in size defects undergo redistribution in the bulk of the sample, which means that part of the defects were set in motion during laser irradiation.

We believe that the above analysis, based on a comparison of the calculated behavior of temperatures, stresses, and stress variation rate with a mechanoluminescence pulse, does not disagree with the dislocation mechanism of mechanoluminescence described in Refs.^{9,24}

As already mentioned, fast heating of metal conductors by an electric current¹⁷ or irradiation of metal targets with a laser pulse¹⁶ gives rise to a burst of electron emission, which is not of thermal origin and was termed¹⁷ anomalous. The

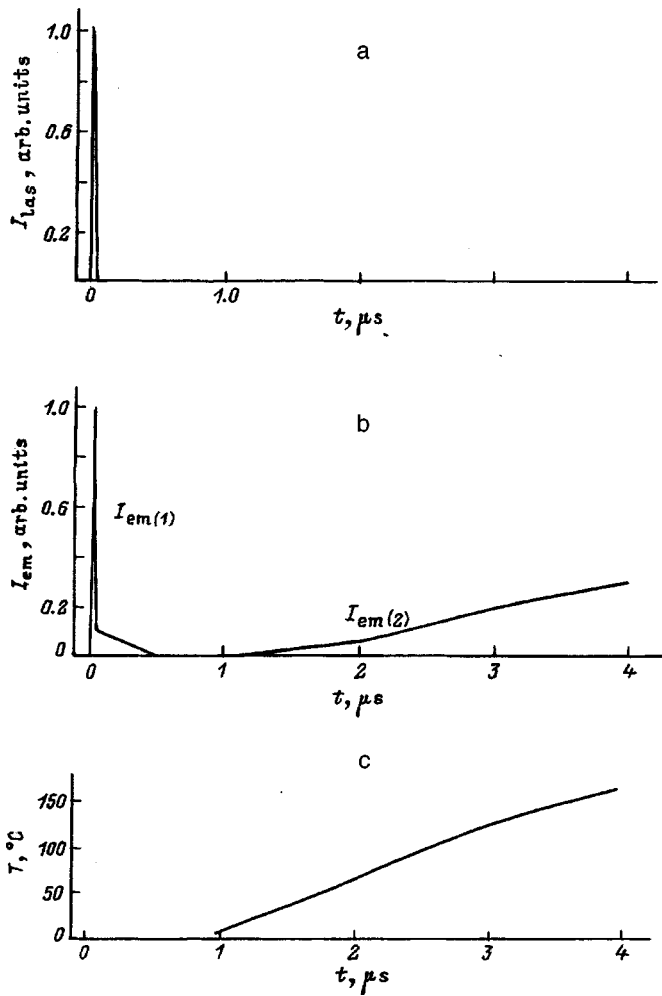


FIG. 2. Oscillographic traces¹⁶ of (a) laser pulse and (b) electron emission. (c) Temperature at spot center at the back side calculated in this work ($z = 0.05$ mm, $r = 0$ mm). Gold sample, $\sigma_{0.2} = 0.9 \times 10^8$ N/m², thickness 0.05 mm, $E_{in} = 0.002$ J.

anomaly of the electron emission observed under fast heating with electric current consists in that it exceeds by two–three orders of magnitude conventional thermionic emission, is excited at close to the melting temperature, and decays after the current is turned off for times during which the cooling of the sample may be neglected.

Irradiation of tungsten, tantalum, and gold samples with single laser pulses initiated electron emission from both the front and back sides of the sample.^{15,16} Two electron emission pulses were observed from each side, they were well resolved in time and had different duration, amplitudes, and electron energies. The later pulse is reliably identified as due to thermionic emission. The nature of the first pulse, which is shorter, larger in amplitude, and higher in particle energy by nearly an order of magnitude, is not clear, although some qualitative hypotheses can be put forward.

The available information^{15,16} is sufficient to make a calculation of the thermal stresses, rate of stress rise, and temperature growth. Figures 2 and 3 present the laser pulse intensity as a function of time, $I_{las}(t)$, and the temporal behavior of the electron emission intensity from the back side of a gold sample, $I_{em}(t)$,¹⁶ as well as our calculations of

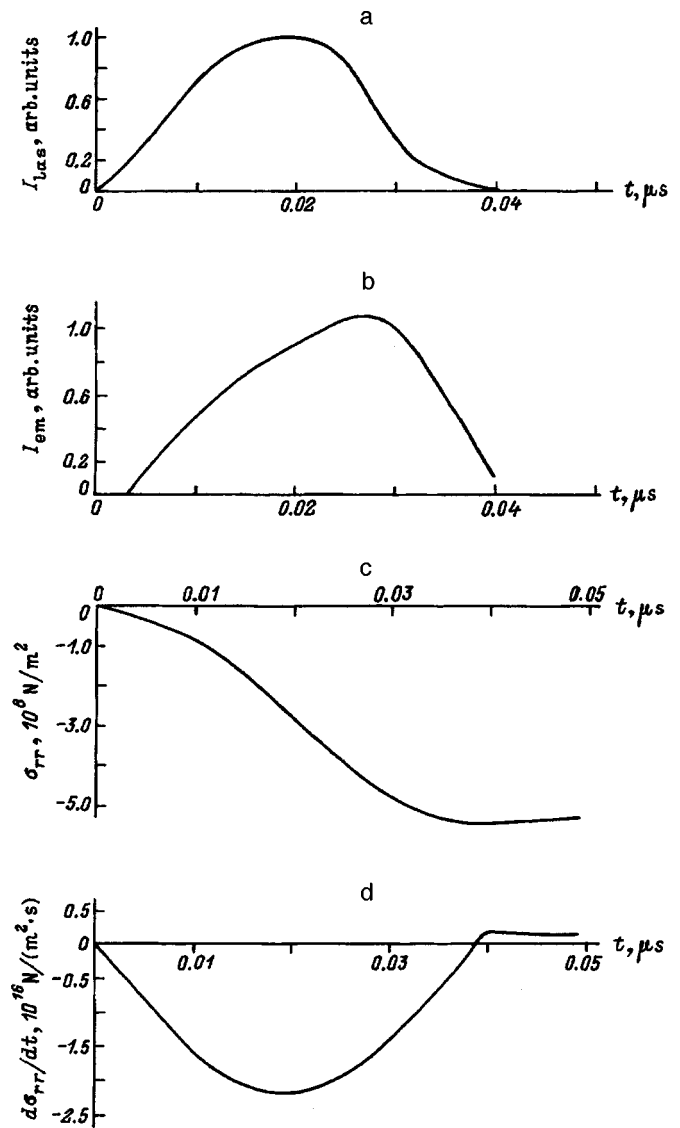


FIG. 3. Oscillographic traces¹⁶ of (a) laser pulse and (b) first electron emission pulse (a part of the oscillograms presented in Fig. 2a and 2b), as well as (c) thermal stresses and (d) rate of their variation on the back side of the sample referred to in Fig. 2 calculated in this work for $z = 0.05$ mm and $r = 0$.

$\sigma_{rr}(t)$, $\partial\sigma_{rr}(t)/\partial t$, and $T(t)$ made for the conditions specified in Ref. 16.

A comparison of the presented relations permits the same conclusions as those following from Fig. 1, with electron emission substituted for mechanoluminescence. As evident from Figs. 2 and 3, the first electron emission pulse correlates best of all with the $\partial\sigma_{rr}(t)/\partial t$ variation. The larger is $\partial\sigma_{rr}(t)/\partial t$, the higher is the electron emission intensity, and electron emission likewise decreases with decreasing $\partial\sigma_{rr}(t)/\partial t$. The slight lag of the emission maximum relative to the maximum of $\partial\sigma_{rr}(t)/\partial t$ by 0.005 μ s is apparently due to the same causes as in the case of mechanoluminescence in Fig. 1. The only difference is that in this case an electron multiplier was used as detector in place of the PM tube. The second pulse appears when the back side begins to heat, and the $I_{em(2)}(t)$ curve is similar to the $T(t)$ graph in Fig. 2.

Exoelectron emission was first observed in the fracture

of dielectrics.^{25,26} Studies of electron and photon exoemission occurring in deformation and destruction of alkali halide crystals are presently being actively pursued.^{12,13} In our opinion, there are grounds to believe that the anomalous electron emission observed under fast heating of conductors by an electric current and the first electron emission pulse from a laser-irradiated metal target result from the onset of thermal stresses in the metal sample.

A comparison of the magnitude, as well as of the temporal and spatial distributions of stresses and temperature with the temporal behavior of photon emission (mechanoluminescence) and electron emission (exoemission) from the back side of samples permits the following conclusions: (1) the dynamics of the emission processes are related to those of stresses, viz., the larger the stress variation rate, the higher is the intensity of mechanoluminescence and exoemission, and (2) mechanoluminescence starts when the stresses in the sample approach the yield point of the material.

Support of the Russian Fund for Fundamental Research (Grant 97-02-18097) is gratefully acknowledged.

¹A. Mooradian, Phys. Rev. Lett. **22**, 185 (1969).

²G. T. Boyd, Z. Yu, and Y. R. Shen, Phys. Rev. B **33**, 7923 (1986).

³A. Bannot, J. M. Debever, and J. Hanus, Solid State Commun. **10**, 173 (1972).

⁴P. G. Borzyak, I. P. Zapesochnyĭ, I. A. Konovalov, V. A. Kritskii, Yu. A. Kulyupin, K. N. Pilipchak, S. S. Pop, and P. M. Tomchuk, Izv. Akad. Nauk SSSR, Ser. Fiz. **40**, 1621 (1976).

⁵K. B. Abramova and I. P. Shcherbakov, Zh. Tekh. Fiz. **64**, No. 9, 75 (1994) [Tech. Phys. **39**, 901 (1994)].

⁶A. A. Tupik and N. P. Valuev, Pis'ma Zh. Tekh. Fiz. **6**, 82 (1980) [Sov. Tech. Phys. Lett. **6**, 37 (1980)].

⁷V. T. Sotnikov, V. A. Gritsan, and A. A. Nechiporenko, Pis'ma Zh. Tekh. Fiz. **13**, 1291 (1987) [Sov. Tech. Phys. Lett. **13**, 539 (1987)].

⁸P. Appel and R. Monreal, Phys. Scr. **38**, 174 (1988).

⁹M. I. Molotskii, Chem. Rev. (Soviet Sci. Rev. Section B) **13**, Pt. 3, 1 (1989).

¹⁰S. I. Anisimov, Ya. O. Imas, P. S. Solonov, and Yu. V. Khodyko, *Effects of High-Power Radiation on Metals* [in Russian], Nauka, Moscow, 1970.

¹¹J. F. Ready, *Effects of High-Power Laser Radiation* [Academic Press, Orlando, 1971; Mir, Moscow, 1974; 486 pp.].

¹²V. A. Zakrevskii and A. V. Shuldiner, Philos. Mag. B **71**, 127 (1995).

¹³A. A. Kusov, M. I. Klinger, and V. A. Zakrevskii, Fiz. Tverd. Tela (Leningrad) **32**, 1694 (1990) [Sov. Phys. Solid State **32**, 987 (1990)].

¹⁴*Exoelectron and Acoustic Emission Measurement Techniques* [in Russian], No. 215, edited by V. S. Kortov (UPI, Sverdlovsk, 1973), 188 pp.

¹⁵W. L. Knecht, Appl. Phys. Lett. **6**, No. 6, 99 (1965).

¹⁶W. L. Knecht, Appl. Phys. Lett. **8**, No. 10, 254 (1966).

¹⁷S. V. Lebedev and A. I. Savvatimskii, Usp. Fiz. Nauk **144**, 215 (1984) [sic].

¹⁸N. V. Stepanova, in *Proceedings of the XVII International Symposium Discharges and Electr. Insulation in Vacuum* (Berkeley, 1996), p. 770.

¹⁹A. M. Kondyrev, I. P. Shcherbakov, K. B. Abramova, and A. E. Chmel', Zh. Tekh. Fiz. **62**, No. 1, 206 (1992) [Sov. Phys. Tech. Phys. **37**, 110 (199)].

²⁰K. B. Abramova, I. P. Shcherbakov, I. Ya. Pukhonto, and A. M. Kondyrev, Zh. Tekh. Fiz. **66**, No. 5, 190 (1996) [Tech. Phys. **41**, 511 (1996)].

²¹K. B. Abramova, I. P. Shcherbakov, A. I. Rusakov, A. A. Semenov, I. Ya. Puchonto, and A. M. Kondyrev, in *Proceedings of the IX International Conference Nonresonant Laser-Matter Interaction* (Pushkin, Russia) SPIE No. 3093, 22 (1996).

²²H. Parkus, *Instantionäre Wärmespannungen* [Springer, Wien, 1959; GIFML, Moscow, 1963, 252 pp.].

²³*Physical Quantities: Handbook* [in Russian], edited by I. S. Grigor'ev and E. Z. Metlikhov (Énergoizdat, Moscow, 1991), 1231 pp.

²⁴B. P. Chandra, M. S. Khlan, S. R. Singh, and M. H. Ansari, Cryst. Res. Technol. **4**, 495 (1996).

²⁵N. A. Krotova and V. V. Karasev, Dokl. Akad. Nauk SSSR **92**, 607 (1953).

²⁶E. Rabinovich, Sci. Am. **236**, No. 1, 74 (1977) [Usp. Fiz. Nauk **127**, 163 (1977)].

Translated by G. Skrebtsov

Electromagnetic absorption of acoustic-wave packets in metals

V. A. Kukushkin and A. G. Kurbatova

Chuvash State Pedagogical Institute, 428000 Cheboksary, Russia
(Submitted October 29, 1997)

Fiz. Tverd. Tela (St. Petersburg) **40**, 966–973 (June 1998)

Damping of quasimonochromatic sound-wave packets in metals caused by the electromagnetic interaction of lattice vibrations with resonant current carriers is studied. It is assumed that the acoustic wavelength λ is much shorter than the electron mean free path length l but much longer than the characteristic damping depth σ of an electromagnetic wave in metals under anomalous-skin-effect conditions. It is also assumed that the transit time λ/\tilde{v} of a resonant particle through the region of field nonuniformity ($\sim\lambda$) is shorter than the electronic relaxation time τ_p ($a=\lambda/\tilde{v}\tau_p\ll 1$, where \tilde{v} is the characteristic velocity of the resonant electrons). The distribution of the potential of the eddy electromagnetic field accompanying an acoustic radiopulse with a prescribed shape is found by solving the kinetic equation and Maxwell's equations. The force exerted on the lattice by the resonant electrons is investigated, and the equation from the theory of elasticity that describes the evolution of a sound wave is solved. It is shown that a weak damping (of the order of the small parameter a) at the extrema of the deformation on the pulse edges as well as the appearance of high-frequency precursors near the pulse boundaries are characteristic for the evolution of a powerful transverse radiopulse. Such precursors were observed earlier by Fil' *et al.*, as components of a noise burst arising on the leading edge of a powerful transverse radiopulse propagating in ultrapure gallium. © 1998 American Institute of Physics. [S1063-7834(98)00306-2]

1. Absorption of spatially bounded wave packets is investigated in experiments on nonlinear acoustic damping in metals. In this connection it is of interest to solve the problem of the evolution of sound pulses interacting with conduction electrons. A theory of acoustic damping of pulses with longitudinal polarization in conductors has been constructed in Refs. 1–4. Nonlinear absorption of transverse video pulses in the form of a single “hump” and a “hump–well” of the deformation of a crystal was recently studied in Ref. 5.

Our objective in the present work is to study, following Ref. 5, the electromagnetic damping of quasimonochromatic packets (radiopulses) of transverse sound in a nonlinear regime. As is well known, damping of this type dominates in metals having a spherical Fermi surface under conditions such that the acoustic wavelength λ is much shorter than the electron mean-free-path length l but much longer than the characteristic penetration depth of the electromagnetic field in the anomalous skin effect regime $\sigma\approx(c^2v_F\lambda/w\omega_p^2)^{1/3}$

$$l\gg\lambda\gg\sigma. \quad (1)$$

Here w is the speed of sound, ω_p is the plasma frequency, and v_F is the electron velocity at the Fermi surface. The qualitative picture of the acoustoelectronic interaction in this case is as follows. The propagation of transverse sound in a metal is accompanied by the generation of an eddy electromagnetic field, which gives rise to compensation of the lattice current by the resonant-electron current over the thickness σ of the anomalous skin layer of the pulse.⁶ It is easy to show that the dynamics of resonant particles in the eddy field

is determined by the magnetic component of the field; the latter changes only the longitudinal (relative to the acoustic wave packet $\mathbf{q}\parallel 0x$) component v_x of the velocity of these particles and for this reason can be described by a “potential” field $U(x-wt)$.

If there is not enough time for an electron traversing the region of a characteristic nonuniformity of the field ($\sim\lambda$) to be scattered during the interaction time and in the process substantially change its velocity, i.e.

$$a=\lambda/\tilde{v}\tau_p\ll 1, \quad (2)$$

where \tilde{v} is the characteristic longitudinal velocity of the resonant particles and τ_p is the relaxation time, then a nonlinear damping regime operates. In this case the electron trajectories in the field $U(x-wt)$ can be described by the energy integral

$$\frac{mv_\xi^2}{2}+U(\xi)=\mathcal{E},$$

where $\xi=x-wt/\lambda$, $v_\xi=v_x-w$. Figure 1b shows a plot of the reduced “potential” $U_1(\xi)=U(\xi)/U_0$ obtained in the present work for the region corresponding to the leading edge of the acoustic radiopulse (see Fig. 1a). Here $U_0=\max U(\xi)$ and $U_k^{(\pm)}$ are the local extrema in the region of the k -th “period” of the function $U_1(\xi)$. The resonant electrons can be divided into three groups depending on the value of \mathcal{E} : electrons reflected from the magnetic barrier ($U_{k+1}^{(+)}<\mathcal{E}<U_k^{(+)}$), trapped electrons ($U_k^{(-)}<\mathcal{E}<U_k^{(+)}$), and transmitted electrons ($\mathcal{E}>U_0$). In a collisionless regime

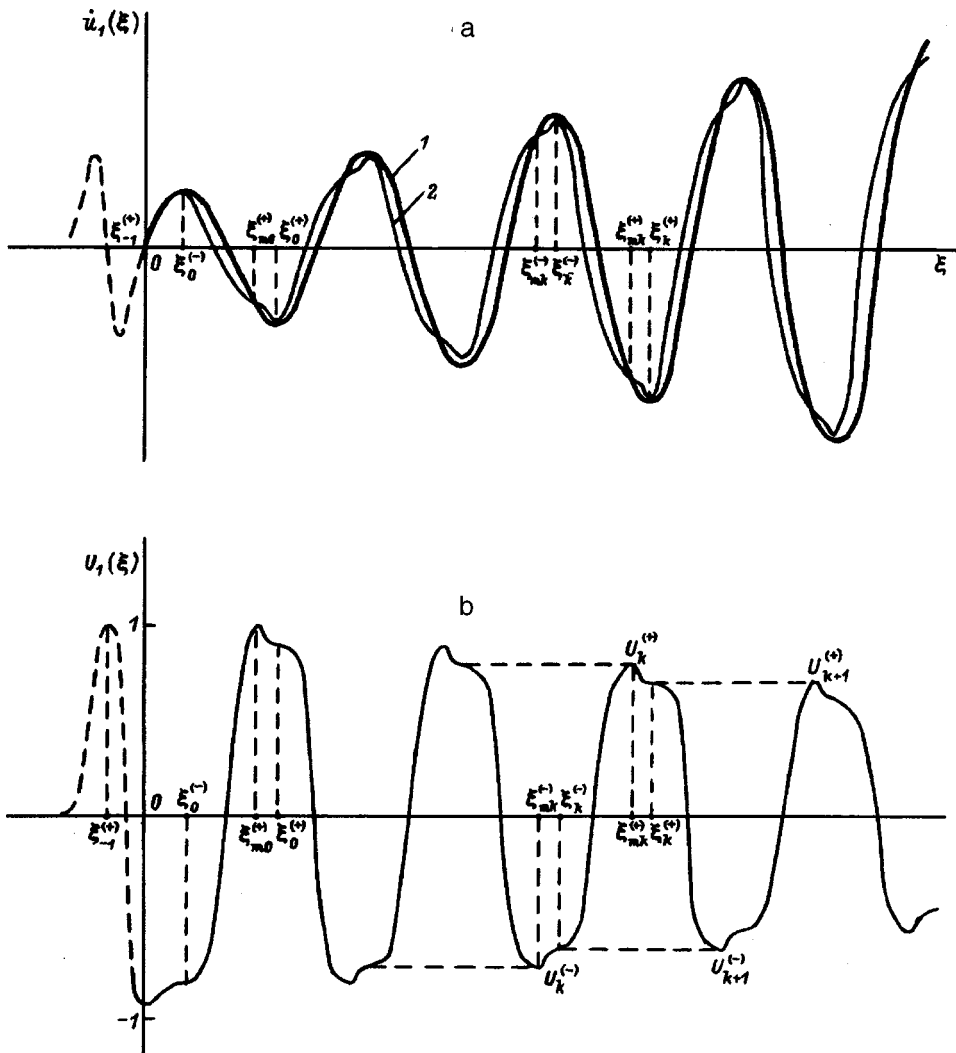


FIG. 1. a) Displacement velocity of the lattice in an acoustic radiopulse: 1 — Initially ($\tau=0$), 2 — for $\tau>0$. The dashed curve illustrates the characteristic deformation profile of the precursor. b) ‘Potential’ of the eddy electromagnetic field excited by the acoustic radiopulse.

($a \rightarrow 0$) the electron current in the metal is due only to the motion of the reflected particles (the contribution of trapped and transmitted electrons to the current is zero as a result of the antisymmetry of the nonequilibrium longitudinal-velocity distribution function of these particles). The work performed by the eddy field on the reflected particles increases their internal energy and, therefore, the latter is a functional of the lattice displacement so that it determines the force giving rise to damping of the acoustic pulse (nonlinear Landau damping).

It is shown in this paper that the extrema of the displacement velocity $\dot{u}(\xi)$ of the lattice in a radiopulse correspond to the points $\xi_k^{(\pm)}$ on the ‘potential’ energy profile $U(\xi)$, which are the limit points for the region of motion of the trapped particles (Fig. 1). As follows from the current compensation condition, the force exerted by the resonant electrons on the lattice vanishes at these points. This circumstance essentially determines the evolution of a powerful radiopulse of transverse sound in a metal: In the collisionless limit ($a \rightarrow 0$) the envelope of the leading edge of the radiopulse should not change in time.

An eddy electromagnetic field can be excited not only

inside but also outside the region of the sound pulse. In the latter case the electric component of the field leads to the appearance of an additional deformation of the crystal lattice — growth of acoustic precursors. In the present paper we investigate the shape of the growing precursor. It is shown that for times $t > (\sigma/k)^{1/3} \lambda/w v_F/w$ the precursor should evolve in accordance with a nonlinear theory which predicts the development of a series of powerful precursors with a quite complicated shape at the boundary of the main pulse.

The possibility of observing experimentally the effects described is considered in the concluding section of this paper. We note, specifically, that, in metals having a complicated Fermi surface, acoustic precursors can be detected in the form of a high-frequency burst of deformation, similarly to the burst observed earlier by Fil’ *et al.* in the spectrum of a noise signal arising at the edge of a powerful transverse pulse propagating in ultrapure gallium.⁷

2. The system of equations of the problem consists of a kinetic equation for the distribution function f of the resonant electrons, Maxwell’s equations, and the equations from the theory of elasticity:

$$\frac{\partial f}{\partial t} + v_x \frac{\partial f}{\partial x} - \frac{\partial U}{\partial x} \frac{\partial f}{\partial p_x} + \frac{f - f_0}{\tau_p} = 0, \quad (3)$$

$$\nabla \times \nabla \times \mathbf{A} = \frac{4\pi}{c} \mathbf{j}, \quad (4)$$

$$\mathbf{j} = \frac{2e}{(2\pi)^3} \int f \mathbf{v} d\mathbf{p}, \quad (5)$$

$$\rho \frac{\partial^2 u}{\partial t^2} - \rho w^2 \frac{\partial^2 u}{\partial x^2} = G(x, t) - \rho \nu' \frac{\partial^3 u}{\partial t \partial x^2}. \quad (6)$$

Here $G(x, t)$ is the force exerted by the resonant electrons on the lattice, ρ and ν' are, respectively, the density and viscosity of the crystal, $f_0(\varepsilon)$ is the equilibrium distribution function which depends on the Hamiltonian ε of the particles in a comoving coordinate system

$$\varepsilon(x, t, p) = \varepsilon_0(p) + D_{xy} \frac{\partial u}{\partial x} + U(x - wt, p),$$

$\mathbf{u}(0, u, 0)$ is the displacement of the lattice (it is assumed that the acoustic pulse propagates along the $0x$ axis and the polarization vector of the pulse is directed along the $0y$ axis), $D_{\alpha\beta}(p)$ is the deformation potential tensor. The particle spectrum $\varepsilon_0(p)$ in the unperturbed crystal is assumed to be isotropic and quadratic. In this case $D_{xy} = m_0 \Lambda(|\mathbf{p}|) v_x v_y$, $\Lambda \approx 1$, $U(\xi, \mathbf{p}) = -(e/c) \mathbf{A}(\xi) \cdot \mathbf{v}$, $\mathbf{A} = (0, A, 0)$ is the vector potential of the electromagnetic field accompanying the sound wave, and $\xi = (x - wt)/\lambda$. For resonant electrons whose transverse velocity v_y is of the order of v_F the function $U(\xi, \mathbf{p})$ plays the role of a "potential" energy: $U(\xi) = -(e/c) A(\xi) v_F \text{sign } v_y$. We note that the "potential" $U(\xi)$ describes uniquely the eddy electromagnetic field of the acoustic pulse as a result of the invariance of the pulse under a gradient transformation of the potential A .

We seek the particle distribution function in the form⁶

$$f(\mathbf{p}, x, t) = f_0(\varepsilon) + m_0 \Lambda v \dot{u} \frac{\partial f_0}{\partial \varepsilon} + g(\mathbf{p}, x, t). \quad (7)$$

Substituting the expression (7) into Eq. (3) and integrating Eq. (3) with the initial condition $g \rightarrow 0$ as $t \rightarrow -\infty$, we obtain for the nonequilibrium correction to the function $f_0(\varepsilon)$

$$g = w \text{sign } v_y \frac{\partial f_0}{\partial \varepsilon} \int_{-\infty}^t \frac{\partial U}{\partial x'} \exp\left(-\frac{t-t'}{\tau_p}\right) dt'. \quad (8)$$

In the nonlinear regime (2) the result of integrating over t' in Eq. (8) can be represented as⁵

$$g = -\frac{w}{v} U_0 \frac{\partial f_0}{\partial \varepsilon} [s - s_{-\infty} - a(\xi - s_{-\infty} \tau_1)]. \quad (9)$$

Here $\tilde{v} = (U_0/m)^{1/2}$, $U_0 = \max U(\xi)$; $s = (v_x - w)/\tilde{v}$ and $\tau_1 = \tilde{v}t/\lambda$ are, respectively, the dimensionless particle velocity and the time along a classical trajectory; $s_{-\infty} = (s^2 + 2U_1 \text{sign } v_y)^{1/2} \text{sign } s_{-\infty}$ is the velocity of the particles as they approach the pulse; $U_1(\xi) = U(\xi)/U_0$. The velocity interval $|s| \leq (2(1 - U_1 \text{sign } v_y))^{1/2}$ in Eq. (9) corresponds to the reflected electrons, while $|s| \geq (2(1 - U_1 \text{sign } v_y))^{1/2}$ cor-

responds to the transmitted electrons. For trapped particles $s_{-\infty} = 0$; they correspond to the velocity interval $|s| \leq (|U_1|)^{1/2}$.

Substituting the distribution function (7) and the expression (9) into the expression for the current density (5) and integrating we obtain

$$j_y(\xi) = C e n_0 \dot{u}(\xi) - j_y^e(\xi), \quad j_x = j_z = 0, \quad (10)$$

where

$$j_y^e(\xi) = \frac{3}{4\pi} e n_0 w \frac{U_0}{\varepsilon_F} [\Psi_+(U_1) + \Psi_-(U_1) + aF(\xi)], \quad (11)$$

$$\Psi_{\pm}(U_1) = \pm \int ds (s^2 \pm 2U_1)^{1/2} \text{sign } s_{-\infty}, \quad (12)$$

$|F|$, $C \approx 1$; n_0 is the equilibrium electron density; the + and - signs correspond to positive and negative signs of the velocity v_y of the resonant particles in the region of the pulse. The first term in Eq. (10) corresponds to the lattice current, while the second term is the current due to the resonant electrons. The collisionless current due to the reflected particles makes the main contribution to the current (11), which is of zeroth order in the small parameter a , while the collisional current due to the transmitted and trapped particles is proportional to a .

3. Let us transform Eq. (4), taking in account Eqs. (10) and (11), to the form

$$-\frac{\partial^2 U}{\partial \xi^2} = \frac{3}{4\pi} \delta^2 \left(-\frac{4\pi}{3} C \frac{\varepsilon_F}{w} \dot{u} - U_0 [\Psi(U_1) + aF(\xi)] \right), \quad (13)$$

where $\delta^2 = (\lambda/\sigma)^3$, $\Psi(U_1) = \Psi_+(U_1) + \Psi_-(U_1)$. In the region of the pulse, where the lattice deformation satisfies the inequality

$$|\dot{u}| \gg a w \frac{U_0}{\varepsilon_F}, \quad (14)$$

under the conditions (1) it is convenient to seek the solution of Eq. (13) in the form of a series in powers of the small parameter δ^{-2}

$$U(\xi) = U^{(0)}(\xi) + \delta^{-2} U^{(1)}(\xi) + \delta^{-4} U^{(2)}(\xi) + \dots$$

As a result, in the leading order approximation in the parameter $\max(\delta^{-2}, a) \ll 1$ we obtain

$$\frac{4\pi}{3} C \frac{\varepsilon_F}{w} \dot{u}(\xi) = U_0 \Psi(U_1). \quad (15)$$

Equation (15) is the condition for compensation of the lattice current $C e n_0 \dot{u}$ by the current $j_y^e(\xi)$ due to the resonant electrons in the region of the pulse. According to Eq. (15) the amplitude U_0 of the "potential" energy and the displacement velocity \dot{u}_0 of the lattice at the maximum are related to one another by the relation

$$U_0 = \frac{4\pi}{3} \frac{\varepsilon_F}{w} C \dot{u}_0.$$

Let us assume further that the acoustic pulse has the form of a quasimonochromatic packet, described by the function

$$\dot{u}_1(\xi) \equiv \frac{\dot{u}}{\dot{u}_0} = -(\tanh \alpha \xi + \beta) \sin \xi / (1 + \beta) \quad (16)$$

(Fig. 1). In the region of the leading edge of the pulse ($\alpha \xi \ll 1$) the constants α and β determine the amplitude difference $\Delta \dot{u}_{1k} = \dot{u}_1(\xi_{k+1}^{(-)}) - \dot{u}_1(\xi_k^{(-)})$ as well as the value of $\dot{u}_1(\xi_0^{(-)})$ at the first extremum of the function $\dot{u}_1(\xi)$. We shall assume that the quantities $\dot{u}_1(\xi_0^{(-)})$ and $\Delta \dot{u}_{1k}$ ($k=0, 1, 2, \dots, k_{\max}$) satisfy the inequality (14)

$$\min(|\dot{u}_1(\xi_0^{(-)})|, |\Delta \dot{u}_{1k}|) \gg a. \quad (17)$$

Here the index k enumerates the ‘‘period’’ of the wave ($k = [\xi/2\pi]$, where $[x]$ is the integer part of the number x).

We shall seek for equation Eq. (15) a solution $U_1(\xi)$ corresponding to this case in the form shown in Fig. 1b. The characteristic points on the curve $U_1(\xi)$ are $\xi_k^{(\pm)}$ and $\xi_{mk}^{(\pm)}$, which determine the limits of the region of motion of the trapped particles. Calculating next the integrals (12), we find for the chosen form of the ‘‘potential’’ $U_1(\xi)$ the stream function $\Psi(U_1) = \{\Psi_k(U_1)\}$ ($k=0, 1, 2, \dots$) of the reflected particles:

$$\Psi_k(U_1) = \begin{cases} -\varphi_1(U_1) + \varphi(-U_1) + U_k^{(+)} \varphi(U_1/U_k^{(+)}) \\ -|U_k^{(-)}| \leq U_1 \leq -|U_{k+1}^{(-)}|, \\ -\varphi_1(U_1) + \varphi(-U_1) - |U_{k+1}^{(-)}| \varphi\left(-\frac{U_1}{U_{k+1}^{(-)}}\right) \\ + U_k^{(+)} \varphi\left(\frac{U_1}{U_k^{(+)}}\right), \quad -|U_{k+1}^{(-)}| \leq U_1 \leq U_k^{(+)}, \\ -\varphi_1(U_1) + \varphi(-U_1) - |U_{k+1}^{(-)}| \varphi(-U_1/U_{k+1}^{(-)}) \\ U_{k+1}^{(+)} \leq U_1 \leq U_k^{(+)}, \\ -\varphi_1(U_1) + \varphi(-U_1) - |U_{k+1}^{(-)}| \varphi\left(-\frac{U_1}{U_{k+1}^{(-)}}\right) \\ + U_{k+1}^{(+)} \varphi\left(\frac{U_1}{U_{k+1}^{(+)}}\right), \quad -|U_{k+1}^{(-)}| \leq U_1 \leq U_{k+1}^{(+)}, \end{cases} \quad (18)$$

where $\varphi(\pm U_1) = \sqrt{1 \mp U_1} \pm U_1 \ln \frac{\sqrt{1 \mp U_1} + 1}{\sqrt{|U_1|}}$.

Now there is no difficulty in solving Eq. (15) and finding the function $U_1(\xi)$. Specifically, the positions of the singular points $\xi_{mk}^{(\pm)}$ as well as the corresponding extremal values $U_k^{(\pm)}$ of the ‘‘potential’’ that appear in the stream function (18) can be determined by solving the system of recurrence relations

$$\begin{aligned} \Psi_k(U_{k+1}^{(\mp)}) &= \dot{u}_1(\xi_k^{(\mp)}) \rightarrow U_{k+1}^{(\mp)}, \\ \Psi_k(U_k^{(\mp)}) &= \dot{u}_1(\xi) \rightarrow \xi_{mk}^{(\mp)} \end{aligned}$$

with the ‘‘initial’’ conditions $U_0^{(\mp)} = \mp 1$, $\xi_{m0}^{(-)} = 0$. Figure 2 shows a plot of the function $\Psi(U_1) = \{\Psi_k(U_1)\}$, obtained by

solving numerically Eq. (15) for the first four periods of the displacement velocity of the lattice (16) ($k=0, 1, 2, 3$). We call attention to the fact that at the limit points $U_k^{(\pm)}$ the stream function $\Psi_k(U_1)$ has a kink-type singularity. The behavior of the ‘‘potential’’ $U_1(\xi)$ near the points $\xi_{mk}^{(\mp)}$ and $\xi_k^{(\mp)}$, which is due to the singularities of the stream function $\Psi_k(U_1)$, can be represented in the analytical form

$$U_1(\xi) = \begin{cases} U_k^{(\mp)} \pm \kappa_k^{(\mp)} (\xi - \xi_{mk}^{(\mp)})^2, & \xi \leq \xi_{mk}^{(\mp)}, \quad k \neq 0, \\ U_k^{(\mp)} \pm \pi_k^{(\mp)} (\xi - \xi_{mk}^{(\mp)}), & \xi \geq \xi_{mk}^{(\mp)}, \quad k \neq 0, \\ U_{k+1}^{(\mp)} \pm \eta_k^{(\mp)} (\xi - \xi_k^{(\mp)})^2, & \xi \leq \xi_k^{(\mp)}, \\ U_{k+1}^{(\mp)} \pm \xi_k^{(\mp)} (\xi - \xi_k^{(\mp)})^4, & \xi \geq \xi_k^{(\mp)}, \end{cases} \quad (19)$$

$$U_1(\xi) = \begin{cases} -1 + \beta^2 \xi^2, & \xi \geq 0, \\ +1 - \left(\frac{\partial \dot{u}_1}{\partial \xi}\right)_{\xi_{m0}^{(+)}}^2 (\xi - \xi_{m0}^{(+)})^2, & \xi \geq \xi_{m0}^{(+)}. \end{cases} \quad (20)$$

Here

$$\begin{aligned} \kappa_k^{(\pm)} &= \left| \frac{\partial \dot{u}_1}{\partial \xi} \right|_{\xi_{mk}^{(\pm)}}, \quad \pi_k^{(\pm)} = \left| \frac{\partial \dot{u}_1}{\partial \xi} \right|_{\xi_{mk}^{(\pm)}} \left| \frac{\partial \Psi_k}{\partial U_1} \right|_{U_k^{(\mp)}}^{-1}, \\ \xi_k^{(\pm)} &= \frac{1}{4} \left| \frac{\partial^2 \dot{u}_1}{\partial \xi^2} \right|_{\xi_k^{(\pm)}}, \quad \eta_k^{(\pm)} = \frac{1}{2} \left| \frac{\partial^2 \dot{u}_1}{\partial \xi^2} \right|_{\xi_k^{(\pm)}} \left| \frac{\partial \Psi_k}{\partial U_1} \right|_{U_{k+1}^{(\mp)}}^{-1}. \end{aligned}$$

We note that the derivative $\partial U_1 / \partial \xi$ vanishes at the points $\xi_k^{(\pm)}$ corresponding to the extrema of the function \dot{u}_1 and has a discontinuity of the first kind at the points $\xi_{mk}^{(\pm)}$ ($k \neq 0$).

An eddy electromagnetic field can be excited not only inside but also outside (for $\xi \leq 0$) the region of the pulse. In the latter case it is determined by solving Eq. (13), where we must set $\dot{u}(\xi) = 0$:

$$\frac{\partial^2 U_1}{\partial \xi^2} = \frac{3}{4\pi} \delta^2 [\Psi_e(U_1) + aF(\xi)], \quad \xi \leq 0. \quad (21)$$

This equation must be solved under the condition of smooth joining of the ‘‘potential’’ U_1 with the function (20) at the point $\xi = 0$

$$U_1(0) = -1, \quad \frac{\partial U_1}{\partial \xi} \Big|_{\xi=0} = 0.$$

We note that the appearance of reflected particles outside the current pulse [described by the function $\Psi_e(U_1)$ in Eq. (21)] is largely due to the collisional component of the total current, which is proportional to a ; the significance of this component is that it generates an initial field U_1 playing the role of a magnetic barrier for the reflected electrons. Since the function $F(\xi)$ is complicated (an expression for this function is presented in Ref. 5), the procedure for solving Eq. (21) in the region $\xi \leq 0$ is very laborious, and we do not present it here.

The solution of Eq. (21) far from the boundaries of the pulse must be sought in the form shown in Fig. 1b by the dashed line. The stream function $\Psi_e(U_1)$ corresponding to this field is determined by the expression

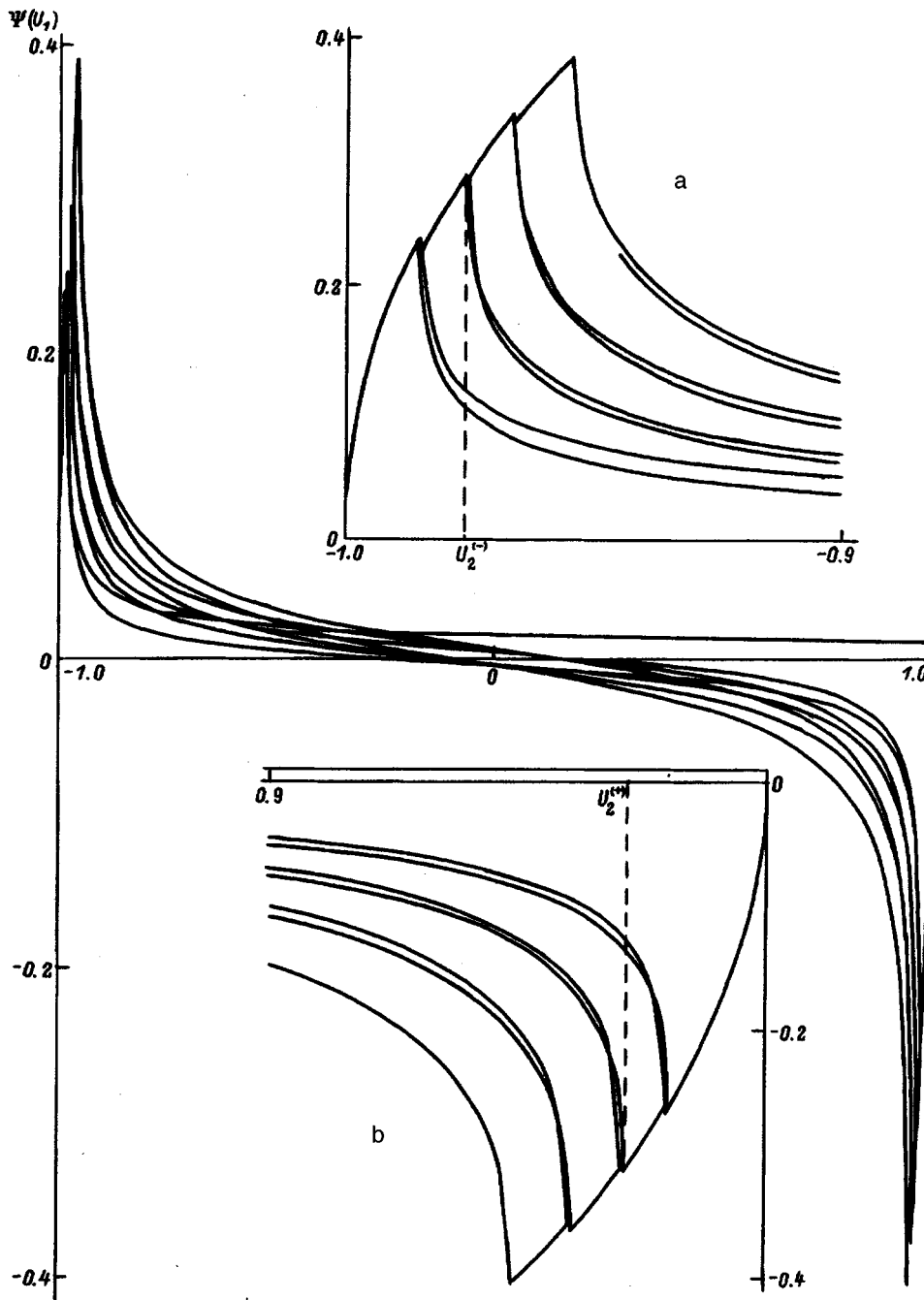


FIG. 2. Stream function of the reflected electrons. The regions of the maxima and minima corresponding to the first four branches of Ψ_k of the function $\Psi(U_1)$ (see Eq. (17), $k=0, 1, 2, 3$) are shown on a larger scale in the insets a and b, respectively.

$$\Psi_e(U_1) = \begin{cases} -\varphi(U_1), & -1 \leq U_1 \leq 1, \\ -\varphi(U_1) + \varphi(U_1), & 0 \leq U_1 \leq 1. \end{cases} \quad (22)$$

As analysis shows, the electromagnetic field outside the pulse can be excited on a characteristic scale $\Delta\xi \approx \delta^{-1}$ (in dimensionless units, it corresponds to the quantity $L\delta^{-1}$ which is of the order of the thickness σ of the anomalous skin layer of the metal). Near the maximum of the potential (at $\xi \approx \xi_{-1}^{(+)}$), as well as in the limit $\xi \rightarrow -\infty$, the solution of Eq. (21) has the form

$$U_1(\xi) = \begin{cases} 1 - \frac{3}{4} \pi \delta^2 \varphi(-1) (\xi - \xi_{-1}^{(+)})^2, & \xi \approx \xi_{-1}^{(+)}, \\ \exp\left(-\frac{3}{16\pi} \delta^2 \xi^2\right), & \xi \rightarrow -\infty. \end{cases} \quad (23)$$

4. In accord with Eq. (15), the electromagnetic damping of the acoustic pulses is determined by the force G , proportional to the derivative $\partial U / \partial x$,

$$G(x, t) = -\frac{C n_0 w}{v_F} \frac{\partial U}{\partial x}. \quad (24)$$

Using the slowly varying profile method, we transform Eq. (6) from the theory of elasticity in accord with the electronic force (24) to the form

$$\frac{\partial \dot{u}}{\partial \tau} = -\dot{u}_0 \frac{\partial U_1}{\partial \xi} - \nu \frac{\partial^2 \dot{u}}{\partial \xi^2}, \quad (25)$$

where $\tau = 2\pi C^2 n_0 \rho_F t' / 3\rho\lambda$, $\nu = 3\rho\nu' / 4\pi C^2 n_0 \rho_F \lambda$, and t' is the so-called "slow" time. The equation (25) together

with Maxwell's equation (15) solves the problem of electromagnetic damping of acoustic waves in metals.

It was noted above that at the points $\xi_{mk}^{(\pm)}$ ($k = 1, 2, \dots$) the derivative $\partial U_1 / \partial \xi$ and together with it the electronic force are discontinuous. Away from these points, where the force has no singularities, the viscous force, proportional to the small parameter ν , can be neglected in Eq. (25). In this case the solution of Eq. (25) can be written in the form⁵

$$\dot{u}(\xi, \tau) = \dot{u}_0(0) \Phi \left\{ \xi - \int_0^\tau \frac{d\tau'}{(\partial \Psi / \partial U_1)|_{\Psi = \dot{u}(\xi, \tau) / \dot{u}_0(\tau')}} \right\}. \quad (26)$$

Here the function $\Phi(\xi) = \dot{u}(\xi, 0) / \dot{u}_0(0)$ describes the initial profile of the pulse. According to Eq. (26), at the extrema $\xi_k^{(\pm)}$ of the function $\dot{u}(\xi)$, where according to Eqs. (18)–(20) the derivative $\partial U_1 / \partial \xi = 0$ while $|\partial \Psi / \partial U_1| \rightarrow \infty$, no changes occur in the deformation of the pulse (Fig. 1):

$$\dot{u}(\xi_k^{(\pm)}, \tau) = \dot{u}(\xi_k^{(\pm)}, 0). \quad (27)$$

This equation determines the characteristic feature of the evolution of a powerful radiopulse in the collisionless limit ($a \rightarrow 0$) — stability of the shape of the pulse envelope near the leading edge of the pulse. It must be underscored that the result (27) is a consequence of the potential distribution for the electromagnetic field, giving rise to compensation of the lattice current by the current of reflected particles, that is specific to packets of transverse sound. Indeed, the condition for such compensation requires that the derivative $\partial \Psi / \partial U_1$ change sign at the points $\xi_k^{(\pm)}$, undergoing in the process a discontinuity. Since, on the other hand

$$\frac{\partial \dot{u}}{\partial \xi} \Big|_{\xi_k^{(\pm)}} = \frac{\partial \Psi}{\partial U_1} \Big|_{U_{k+1}^{(\pm)}} \frac{\partial U_1}{\partial \xi} \Big|_{\xi_k^{(\pm)}} = 0,$$

for

$$\frac{\partial \Psi}{\partial U_1} \Big|_{U_k^{(\pm)}} \neq 0, \quad \frac{\partial U_1}{\partial \xi} \Big|_{\xi_k^{(\pm)}} = 0,$$

Eq. (27) follows.

Near the singular points $\xi_{mk}^{(\pm)}$ ($k \neq 0$), the solution of Eq. (25) describes the differential of the pulse deformation⁵ (Fig. 1)

$$\begin{aligned} \dot{u}(\eta) = & \dot{u}(\eta_{mk}^{(\pm)}) + [\dot{u} - \dot{u}(\eta_{mk}^{(\pm)})][1 - \exp((S + \gamma_k^{(\pm)}) \\ & \times (\eta_{mk}^{(\pm)} - \eta) / \nu)], \quad \eta \approx \eta_{mk}^{(\pm)}. \end{aligned}$$

Here $\eta = \xi - S\tau$, S is the rate of development of the difference in a coordinate system tied to the pulse, $\gamma_k^{(\pm)} = -1 / [\partial \Psi / \partial U_1]_{U_k^{(\pm)}}$, and the function \dot{u} describes the change in the pulse profile far from the singular points $\xi_{mk}^{(\pm)}$ (for $|\eta_{mk}^{(\pm)} - \eta| \gg \nu$) and satisfies the relation (26).

5. It was noted above that the potential of the electromagnetic field decreases rapidly over a distance $\sim \sigma$ at the boundary of a powerful sound pulse. This, in turn, leads to the appearance of a Lorentz force

$$\mathbf{G}_{\text{ion}} = e \mathbf{E} n_0 + \frac{e}{c} [\dot{\mathbf{u}}, \mathbf{H}] n_0, \quad (28)$$

acting on the ionic subsystem of the metal and giving rise to growth of additional signals — acoustic precursors. In addition to this, the precursors are damped by electrons which do not interact with the main pulse. It can be shown that the electronic damping force has the following form in an approximation linear in the deformation of the precursor:

$$G_L = - \frac{4}{3\pi} C \frac{\varepsilon_F n_0}{v_F \lambda} \frac{\partial}{\partial \xi} \int_{-\infty}^{\xi} \frac{\dot{u}(\xi')}{\xi - \xi'} d\xi'. \quad (29)$$

Compared with the first term, the second term on the right-hand side of Eq. (28), determining the Lorentz force exerted by the intrinsic magnetic field of the pulse, is small in the parameter $|\partial u / \partial x| \ll 1$ and can be neglected. Dropping also the viscous term in the force, the equation from the theory of elasticity for acoustic precursors can be represented in the form

$$\frac{\partial \dot{u}}{\partial \tau} = E(\xi) - \frac{\partial}{\partial \xi} \int_{-\infty}^{\xi} \frac{\dot{u}(\xi', \tau)}{\xi - \xi'} d\xi', \quad (30)$$

where

$$E(\xi) = \frac{3\pi}{4} \frac{e E_v v_F \lambda}{\varepsilon_F c} = \dot{u}_0 \frac{\partial U_1}{\partial \xi}.$$

The function $E(\xi)$ is assumed to be independent of the “slow” time τ in agreement with Eq. (27).

We write the solution of Eq. (30), obtained by the method of integral transformations, as follows:

$$\frac{\partial \dot{u}}{\partial \tau} = \frac{\tau}{\pi} \int_{-\infty}^{\infty} \frac{E(\xi')}{\tau^2 + (\xi - \xi')^2} d\xi' = \text{Re } E_{FL}(\tau + i\xi), \quad (31)$$

where $E_{FL}(p)$ is the Laplace transform of the Fourier component of the function $E(\xi)$. To estimate the rate of growth of the precursor we approximate the “potential” $U_1(\xi)$ near the point $\xi = \xi_{-1}^{(\pm)}$ by the function [compare Eq. (20)]

$$U_1(\xi) = \frac{\varepsilon^2}{\varepsilon^2 + (\xi - \xi_{-1}^{(\pm)})^2},$$

which has a characteristic width $\varepsilon \approx \delta^{-1} \ll 1$. Then we obtain from Eq. (31)

$$\dot{u}_1(z, \tau) = \frac{\varepsilon \tau z (\tau + 2\varepsilon)}{[(\tau + \varepsilon)^2 + z^2](z^2 + \varepsilon^2)}, \quad (32)$$

where $z = \xi - \xi_{-1}^{(\pm)}$. The characteristic deformation profile (32) of the precursor is shown in Fig. 1a (dashed line).

According to Eq. (32), the velocity of the precursor increases most strongly for $\tau < \varepsilon$. During this time, the maximum of the function $\dot{u}(z, \tau)$ (for $z \approx \varepsilon$) it grows up to values at which the inequality (14) becomes valid. The further evolution of the acoustic precursor (for $\tau > \varepsilon$) must now proceed in accordance with the nonlinear equations (15) and (25). However, the solution of the corresponding problem falls outside the scope of the present work, and we do not present it here. We note only that the conclusions drawn earlier, to

the effect that there is no damping at the extrema of the deformation of the main pulse and a high-frequency electric field is generated at the boundaries of the pulse, are also valid for a nonlinear precursor. Accordingly, the nonlinear precursor becomes a source of a series of later precursors, the length of each of which is $\delta \gg 1$ times smaller than the characteristic length of the preceding precursor.

6. The effects described in the present paper can be observed in alkali metals by the propagation of powerful radiopulses of transverse sound having a large slope of the envelope at the leading edge. We underscore that the amplitude difference $\Delta \dot{u}_{1k}$ between the neighboring maxima near the leading edge should satisfy the inequality (17), ensuring that the reflected particles make the dominant contribution to the electronic current (11). Near the top of the pulse (for $k > k_{\max}$) the neighboring maxima of $\dot{u}_1(\xi_{k+1}^{(-)})$ and $\dot{u}_1(\xi_k^{(-)})$ differ by an amount of the order of a and less, so that in the corresponding interval of the "potential" $\Delta U_k^{(+)} = U_k^{(+)} - U_{k+1}^{(+)}$ there is no collisionless current of reflected particles. Damping in this case, just as in the case of a monochromatic wave,⁶ is determined by the degree of screening of the lattice current by the collisional current of trapped and transmitted electrons and the strong nonlinearity regime is larger than the deformation damping (by a factor $\delta^4 \gg 1$) even in metals having an arbitrary carrier spectrum. Therefore, it should be expected that the acoustic signal should be substantially suppressed at the top of a powerful transverse radiopulse (compared to the edges of the pulse).¹⁾

In metals having a complicated Fermi surface, the electromagnetic absorption at the edges of the acoustic packets competes with deformation absorption; specifically, the latter gives rise to a finite damping at the local extrema of the deformation of the radiopulse.² Nonetheless, even in this case, electromagnetic effects should be expected to appear in the form of a powerful high-frequency burst of deformation at the boundary of the main pulse. This signal was apparently

observed earlier by Fil' *et al.*⁷ as a component of acoustic noise arising at the leading edge of a powerful radiopulse with transverse polarization propagating in ultrapure gallium. The electromagnetic nature of this noise was established in Ref. 7 from its suppression when the sample became superconducting.

For radiopulse frequencies ~ 100 MHz and pump power $\sim 10^2$ W/cm², the main parameters of the problem a and δ equal in order of magnitude 10^{-1} and 10, respectively. At the same time, the growth time of the precursor deformation is $\sim 10^{-7}$ s, while its extent $\sim 10^{-2}$ cm. The intensity H of the magnetic component of the eddy field of the pulse is of the order of 1 Oe, which corresponds to the estimates obtained in Ref. 8.

In closing, we thank S. L. Lebedev for a helpful discussion and V. I. Mikhaïlov for assisting in the numerical calculations.

¹⁾It is interesting to note that this suppression of the signal level near the top of a powerful acoustic radiopulse was described in Ref. 7.

¹V. Ya. Demikhovskii, G. M. Maksimova, and V. E. Sautkin, Zh. Éksp. Teor. Fiz. **86**, 1037 (1984) [Sov. Phys. JETP **59**, 605 (1984)].

²V. Ya. Demikhovskii, V. E. Sautkin, and O. V. Potapov, Fiz. Tverd. Tela (Leningrad) **27**, 1182 (1985) [Sov. Phys. Solid State **27**, 712 (1985)].

³V. Ya. Demikhovskii and V. A. Kukushkin, Fiz. Nizk. Temp. **14**, 141 (1988) [Sov. J. Low Temp. Phys. **14**, 77 (1988)].

⁴V. Ya. Demikhovskii and V. A. Kukushkin, Fiz. Tverd. Tela (Leningrad) **31**, 63 (1989) [Sov. Phys. Solid State **31**, 210 (1989)].

⁵V. A. Kukushkin, Fiz. Tverd. Tela (St. Petersburg) **35**, 899 (1993) [Phys. Solid State **35**, 464 (1993)].

⁶Yu. M. Gal'perin, Zh. Éksp. Teor. Fiz. **74**, 1126 (1978) [Sov. Phys. JETP **47**, 591 (1978)].

⁷V. D. Fil', A. L. Gaïduk, and V. I. Denisenko, Fiz. Nizk. Temp. **7**, 517 (1981) [Sov. J. Low Temp. Phys. **7**, 256 (1981)].

⁸A. A. Krokhin, N. M. Makarov, and V. A. Yampol'skii, Fiz. Nizk. Temp. **15**, 76 (1989) [Sov. J. Low Temp. Phys. **15**, 42 (1989)].

Magnetic susceptibility and inelastic electrical resistivity of $\text{GdZn}_x\text{Cu}_{1-x}$ alloys

Yu. P. Irkhin and N. I. Kourov

Institute of Metal Physics, Ural Branch of the Russian Academy of Sciences, 620219 Ekaterinburg, Russia
(Submitted December 8, 1997)

Fiz. Tverd. Tela (St. Petersburg) **40**, 974–979 (June 1998)

The deviation from the Nordheim–Kurnakov rule and the anomalous behavior of spin-disordered electrical resistivity in quasi-binary GdZn ($T_C=268$ K) – GdCu ($T_N=142$ K) solid solutions is explained in effective medium approximation within percolation theory for the case of three phases, viz., ferro-, antiferro-, and paramagnetic. The strong increase of ρ at zinc concentrations $x \sim 0.45$ is attributed to the closeness of the system to the percolation threshold. The phase volumes calculated for the random-distribution case fit well to the concentration dependence of magnetic susceptibility. © 1998 American Institute of Physics. [S1063-7834(98)00406-7]

1. MAIN CONCEPTS

The electrical and magnetic properties of the $\text{GdZn}_x\text{Cu}_{1-x}$ alloy system exhibit a number of interesting features which may even appear paradoxical when considered within universally accepted concepts. They were studied comprehensively in Refs. 1–6, where experiment revealed coexistence in alloys of intermediate concentrations ($0.2 \leq x \leq 0.8$) and in the low-temperature domain of ferro- (F) and antiferromagnetic (A) phases, and, possibly, of another phase of paramagnetic (P) or spin-glass type. This low-temperature magnetic state is usually called reentrant spin glass. Figure 1 presents a phase diagram of the magnetic state of $\text{GdZn}_x\text{Cu}_{1-x}$ alloys near the region of transition from A (for $x < 0.2$) to F (for $x > 0.8$) long-range order. At the same time even a qualitative explanation of the concentration and temperature dependences of electrical resistivity and magnetic susceptibility of these alloys meets with a number of difficulties which still have not been overcome.

The most essential of them are as follows:

1. The residual resistivity (measured at $T=4.2$ K) $\rho_0(x)$ of $\text{GdZn}_x\text{Cu}_{1-x}$ alloys does not obey the Nordheim–Kurnakov rule

$$\rho_{NK}(x) = 4\rho_{NK}^{\max}x(1-x), \quad (1)$$

by which $(1/4\rho)_{NK}^{\max} \cdot d\rho_{NK}/dx|_{x \rightarrow 0;1} = \pm 1$ and $(1/4\rho)_{NK}^{\max} \cdot d^2\rho_{NK}/dx^2|_{x \rightarrow 0;1} = -2$.⁷ As seen from Fig. 2, in actual fact $(1/4\rho)_{NK}^{\max} \cdot d\rho_0/dx|_{x \rightarrow 0;1} \sim \pm 2$, and $(1/4\rho)_{NK}^{\max} \cdot d^2\rho_0/dx^2|_{x \rightarrow 0;1} = 0$, which corresponds to a linear $\rho_0(x)$ relation with a large slope. And it is the absence of a negative quadratic-in- x term in Eq. (1) that results at $x=0.45$ in a giant residual resistivity $\rho_0^{\max} \sim 0.7 \mu\Omega$, which exceeds by nearly an order of magnitude the values $\rho_0 \sim 0.1 \mu\Omega$ typical of metal alloys.

2. The electrical resistivity in the paramagnetic temperature region (for $T \geq 300$ K) falls off linearly with decreasing zinc concentration for $x < 0.6$. It would seem that at $T=300$ K, $\rho(x)$ should be constant, because the resistivity is dominated primarily by the phonon, ρ_{ph} , and magnetic, ρ_m , contributions. Note that the phonon contribution does not

depend on x , which follows from practically the same slope of the $\rho(T)$ curves for $T > T_C, T_N$,^{4,5} and the magnetic contribution should be constant because scattering takes place only from spins of the Gd ions, whose magnitude and concentration in all $\text{GdZn}_x\text{Cu}_{1-x}$ alloys are the same.

3. Isolation of the spin-disordered component of resistivity by standard techniques (see, for instance, Ref. 8)

$$\rho_{mm} = \rho - (\rho_0 + \rho_{ph}) \quad (2)$$

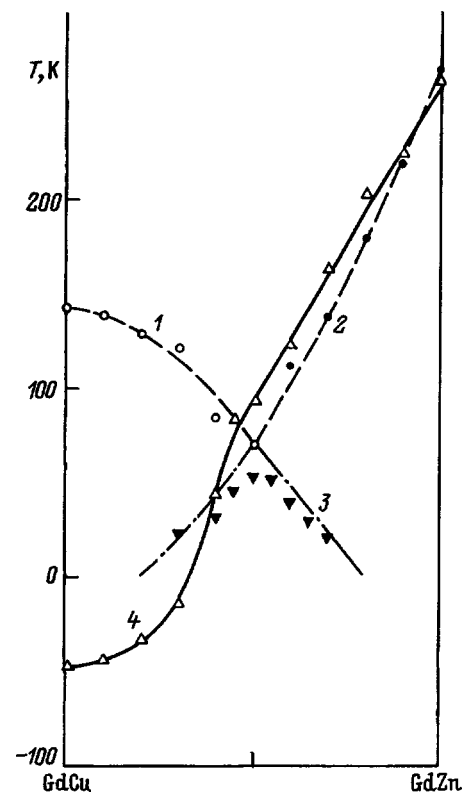


FIG. 1. Magnetic phase diagram of $\text{GdZn}_x\text{Cu}_{1-x}$ alloys. 1 — Néel points T_N ; 2 — Curie points T_C ; 3 — temperatures T_f corresponding to transition from collinear ferro- or antiferromagnetic states to reentrant-glass-type state; 4 — paramagnetic Curie temperatures Θ_p .

yields a fairly unusual result $\rho_{\text{mm}}(x)=0$ for $x<0.45$, i.e., in antiferromagnetic alloys (see Figs. 1 and 2).

Our explanation of the above features in $\rho(x)$ is based here on the following starting premises which are in accord with the current experimental data on $\text{GdZn}_x\text{Cu}_{1-x}$ alloys:

1) Alloys with $x\leq 0.5$ retain considerable spin disorder down to the lowest temperatures, which is evidenced by a strong paraprocess and the presence of a weak spontaneous moment at $T=4.2$ K even in $x<0.2$ alloys¹⁻³. This results in substantial spin scattering and, accordingly, in a large $\rho_0(x)$. It thus becomes clear that, when one enters the paramagnetic temperature region, the change in spin disorder is small and affects only weakly the behavior of $\rho(x, T)$. Therefore the usual method of isolation of the spin component yields an underestimate, in particular, a value close to zero for concentrations x where even at low temperatures the extent of spin disorder is large (i.e., for $x<0.5$).

2) Premise (1) is at odds, however, with the comparatively small low-temperature resistivity of antiferromagnetic alloys. For small $x\sim 0.1$, $\rho_0(x)\sim 0.1\ \mu\Omega$, while the maximum magnetic resistivity under total spin disorder $\rho_{\text{mm}}\sim 0.7\ \mu\Omega$. (This follows from ρ_{mm} measurements for the collinear ferromagnet GdZn , as well as from the value of ρ_0^{max} .)

We believe that one has to invoke the concepts of percolation theory for multiphase systems in order to explain this controversy. In accordance with experimental data,^{2,3} it is then assumed that samples with $0.2\leq x\leq 0.8$ contain A and F phases, with subsequent formation of a spin-glass-type spin-disordered phase P , which becomes dominant for $x\sim 0.5$. In this case the low-resistivity F and, possibly, part of the A phase with weak spin disorder shunt the high-resistivity P phase, thus reducing substantially the observed resistivity $\rho_0(x)$.

3) The $\rho(x)$ relation is affected also, through the mag-

netic component of resistivity, by the variation with zinc concentration of the sf exchange integral $I_{sf}(x)$.⁸ Since in the ‘‘clean’’ A phase ($x\leq 0.2$) $T_N=142$ K, and in the likewise ‘‘clean’’ F phase ($x=1$) $T_C=268$ K, the variation of $\rho_{\text{mm}}(x)$ due to this factor should be related to the T_N/T_C ratio. It would seem that this relation could be obtained in a more specific form from the $\rho(x)$ curve in the paramagnetic temperature region. Because all alloys at $T=300$ K are in the P state (see Fig. 1), one should expect $\rho(x)\equiv \text{const}$, if we disregard the $I_{sf}(x)$ dependence. As seen from Fig. 2, however, one observes a linear growth of $\rho(x)$ with x increasing from practically zero to 0.6. One could tentatively estimate the change in resistivity due to the concentration dependence of the quantity $I_{sf}^2(x)$ from the relation $\rho(x=0)/\rho(x>0.6)\sim T_N/T_C=142/268\sim 0.5$ [for $x>0.6$, $\rho(x)$ remains constant]. The experimental value $\rho(x=0)/\rho(x=1)\sim 0.4$ is slightly smaller. Note, however, that one cannot use in this estimation the $T_C(x)$ and $T_N(x)$ curves, as well as $\Theta_P(x)$, which vary strongly in the middle of the concentration range (for $x\sim 0.5$); this variation is caused by compensation of the positive and negative contributions due to the molecular fields which are generated by Cu and Zn ions surrounding Gd ions in the $\text{GdZn}_x\text{Cu}_{1-x}$ alloys.

2. SCHEME OF CALCULATION

In accordance with the preceding reasoning, we have to calculate the electrical resistivity of a three-phase system consisting of the A , F , and P phases. The resistivity of each of them is given by the relation

$$\rho_j = \rho_i^j + \rho_m^j + \rho_{\text{ph}}^j, \tag{3}$$

where $j=A, F, P$, ρ_i^j is the residual impurity resistivity of a phase, ρ_m^j is the magnetic component of resistivity associated with scattering from disordered spins through their exchange interaction with carriers, and ρ_{ph}^j is the phonon part of the resistivity. Experiments show that the ρ_{ph}^j component practically does not depend on concentration x and is described satisfactorily by standard theory. The resistivity ρ_i^j is apparently small compared to the other contributions. We shall therefore focus attention on $\rho_m^j(x)$.

We shall consider our system to consist of a continuous sequence of clusters of different $\text{GdZn}_x\text{Cu}_{1-x}$ species, where the number of Cu and Zn atoms surrounding Gd atoms varies from zero to eight for each species, with the probability of a certain $\text{Cu}_n\text{Zn}_{8-n}$ configuration depending on concentration x . These probabilities are given by binomial coefficients $C_n^8 = 8!/n!(8-n)!$, so that the probability for a given environment to become realized at a concentration x will be written

$$X_n(x) = C_n^8 x^n (1-x)^{8-n}. \tag{4}$$

As follows from Eq. (4), for any concentration x there is a finite probability $X_n(x)\neq 0$ for any type of environment $n, 8-n$ ($n=0, \dots, 8$). Applying this approach to the $\text{GdZn}_x\text{Cu}_{1-x}$ alloy system, one can consider all nine possible n states, and assume each of them to be a configuration possessing certain physical characteristics. Thus our alloys represent a microheterogeneous, but macrohomogeneous system which can be described in terms of percolation theory.

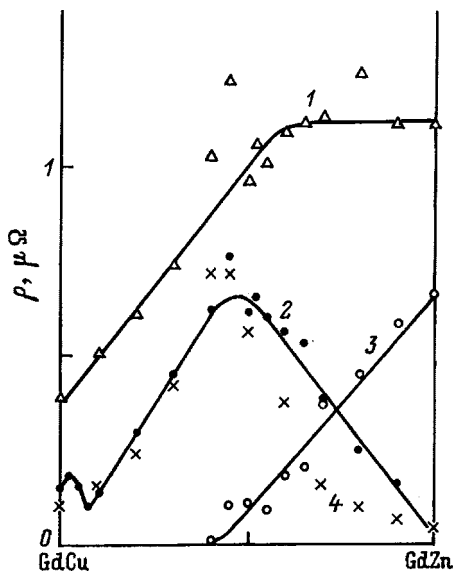


FIG. 2. Electrical resistivity of $\text{GdZn}_x\text{Cu}_{1-x}$ alloys. 1 — resistivity in paramagnetic temperature region for $T=300\text{ K}>T_C, T_N$; 2 — residual resistivity ρ_0 measured at $T=4.2$ K; 3 — spin-disorder resistivity ρ_{mm} calculated from Eq. (2); 4 — resistivity ρ^{th} calculated in accordance with Eq. (11).

TABLE I. Relative volume of magnetic phases in GdZn_xCu_{1-x} alloys calculated from Eq. (5).

X_j	x											
	0	0.1	0.2	0.3	0.4	0.45	0.5	0.6	0.7	0.8	0.9	1
X_F	0	0.0	0.01	0.058	0.173	0.258	0.359	0.583	0.781	0.902	0.947	1
X_A	1	0.962	0.797	0.552	0.316	0.222	0.148	0.061	0.036	0.043	0.048	0
X_P	0	0.038	0.193	0.390	0.511	0.520	0.492	0.356	0.183	0.055	0.005	0

To simplify the mathematic treatment of the problem, divide all possible values of n into three groups, which is in accord with the real physical situation. The phase corresponding to the values $n=0,1,2$ will be considered to be the A phase, that with $n=3,4$, the P phase (spin glass), and the phase with $n=5,6,7,8$, the F phase. Then for the volume of each X_j phase for a given x we can write

$$X_j = \sum_{n=n_j}^{n'_j} C_n^8 (1-x)^{8-n} x^n, \tag{5}$$

where n_j and n'_j are the initial and final values of n for the A , P , and F phases, respectively, with

$$\sum_j X_j = 1.$$

The values of $X_j(x)$ calculated using Eq. (5) are given in Table I.

Having an explicit expression (5) for the concentration dependence of phase volume, we can now calculate the dependence on concentration of the magnetic susceptibility $\chi_j(x)$ for each phase and the total susceptibility

$$\chi^{th} = \sum_j \chi_j(x). \tag{6}$$

We shall be interested in a relative quantity $\chi_j(x)/\chi_j(x_j)$, where $\chi_j(x_j)$ are the values of $\chi_j(x)$ at a reference point x_j chosen so as to make comparison with experiment convenient. Such points are obviously $x_j=x_A=0$ for the A phase, $x_j=x_F=1$ for the F phase, and $x_j=x_P=0.45$ for the P phase, where the experimental relation $\chi(x)$ passes through a maximum.

Then $\chi_j(x)$ can be written

$$\chi_j(x) = \chi_j(x_j) X_j(x) [X_j(x_j) t_j(x)]^{-1}, \tag{7}$$

where $t_j(x) = T_j(x)/T_j^{max}$, $T_j(x) = T_N(x)$ or $T_C(x)$, respectively, for the A or F phase, and $t_P(x) = 1$ for the P phase. Figure 1 shows $T_j(x)$ curves, with T_j^{max} being their maximum values. Introduction of the $t_j(x)$ factor in Eq. (7) takes

into account the exchange interaction in molecular-field approximation required to calculate the susceptibility. For the P phase the molecular field is zero, and therefore we drop factor $t_P(x)$ in Eq. (7).

The values of $\chi_j(x)$ and $\chi^{th}(x)$ calculated using Eqs. (6) and (7) are presented in Table II and Fig. 3. The agreement between the calculated, $\chi^{th}(x)$, and experimental, $\chi(x)$, values is seen to be quite satisfactory. Only within the $0.6 \leq x \leq 0.9$ interval do the values of $\chi^{th}(x)$ exceed somewhat those of $\chi(x)$. Remarkably, the maxima in $\chi^{th}(x)$ and $\chi(x)$ coincide, which is due exclusively to the existence of a maximum in the relative volume of the P phase at point $x_P=0.45$. This supports the validity of dividing individual atomic configurations into phases in Eq. (5) and offers a strong argument for the usefulness of the model proposed here.

Consider now the electrical resistivity. It is obvious from general considerations that there should exist a relation between the magnetic component of the resistivity and magnetic susceptibility. For the alloys dealt with here this follows also from experiment, when one considers the data presented in Figs. 2 and 3. In this case one can use the concentration dependences $\chi_j(x)$ to calculate $\rho_m^j(x)$. Direct proportionality between the magnetic contributions to χ and ρ exists, however, only for the P phase. We shall assume, therefore, the magnetic part of the resistivity of the P phase to be described by the relation

$$\rho_m^P(x) = r_P(x_P) (1 + \tau x) \chi_P(x) / X_P(x), \tag{8}$$

where $\chi_P(x)$ is calculated from Eq. (7).

Parameter $\tau = (T_C - T_N) / T_N = 0.89$ is introduced in Eq. (8) to take into account the concentration dependence of the exchange integral I_{sf} , which determines the amplitude of conduction electron scattering from Gd spins.

Parameter $r_P(x_P)$ in Eq. (8), similarly to the calculation of susceptibility using Eq. (7), is determined at the reference point.

From a theoretical standpoint, the relation between $\rho_m(x)$ and $\chi(x)$ is based on the well-known expressions⁹

TABLE II. Magnetic susceptibility χ (in EMU/g) calculated for GdZn_xCu_{1-x} alloys using Eqs. (4)–(7).

χ	x											
	0	0.1	0.2	0.3	0.4	0.45	0.5	0.6	0.7	0.8	0.9	1
χ_A	1.7	1.68	0.50	1.11	0.909	0.706	0.527	0.295	0.217	0.298	0.384	0
χ_F	0	0.003	0.035	0.097	0.193	0.248	0.301	0.356	0.387	0.340	0.292	0.25
χ_P	0	0.124	0.636	1.29	1.69	1.71	1.62	1.18	0.603	0.182	0.016	0
χ^{th}	1.70	1.81	2.17	2.49	2.79	2.67	2.45	1.83	1.21	0.82	0.693	0.25

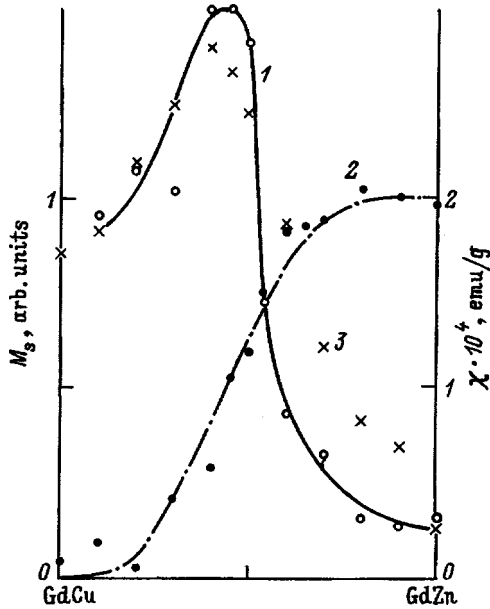


FIG. 3. (1) Magnetic susceptibility χ ; (2) spontaneous magnetization M_s of $\text{GdZn}_x\text{Cu}_{1-x}$ alloys determined at $T=4.2$ K; (3) susceptibility χ^{th} calculated in accordance with Eqs. (6) and (7).

$$\rho_m(x) = B(\overline{S^2} - \overline{S}^2), \quad \chi(x) = D(\overline{S^2} - \overline{S}^2). \quad (9)$$

Equation (9) for $\chi(x)$ can be derived, for instance, from the Ginzburg–Landau equation. Relations (9) are well applicable to the P state. For low temperatures and in a magnetically ordered state, however, they may be more complex. One should also bear in mind that spin flop on the magnetic sublattices of the A phase, which does not affect resistivity, can provide a considerable contribution to $\chi_A(x)$ at high fields. Therefore we shall use relations (9) only for the P phase.

Estimated $\rho_m(x)$ contributions in the A and F phases at $T=4.2$ K turn out to be considerably smaller (by about an order of magnitude) than that in the P phase. This permits us, as a first approximation, to neglect the components ρ_m^A and ρ_m^F at low temperatures. Taking into account the impurity resistivity ρ_i and the Nordheim–Kurnakov contribution $\rho_{NK}(x)$ connected with random substitution of Zn for Cu atoms in all phases, we come to

$$\rho_j(x) = \rho_{NK}(x) + \rho_{\text{ph}} + \rho_i^j(x) + \rho_m^j(x), \quad (10)$$

where components $\rho_{NK}(x)$ and $\rho_m^P(x)$ are found from relations (1) and (8), and $\rho_m^A(x)$ and $\rho_m^F(x)$ are ≈ 0 .

A. Low temperatures ($T=4.2$ K)

We note first of all that, for $T \rightarrow 0$ K, the magnetic component $\rho_m^P \neq 0$ because of the residual Gd spin disorder accompanying atomic disorder of Cu and Zn ions. Moreover, it is primarily the relation $\rho_m^P(x)|_{T \rightarrow 0}$ that determines the $\rho_0(x)$ curve in Fig. 2. Because the system has more than one phase, however, $\rho_m(x)|_{T \rightarrow 0}$ cannot be described in terms of the Nordheim–Kurnakov rule, but has a more complex form. The expression of Odelevskii–Kondorskii derived for the two-phase case was generalized in percolation theory.¹⁰ In

the effective-medium approximation an analytic expression was obtained¹⁰ for a three-phase system in which one phase is nonconducting:

$$\begin{aligned} \sigma_{\text{eff}} = 1/\rho^{\text{th}} = & [(3X_1 - 1)\sigma_1 + (3X_2 - 1)\sigma_2]/4 \\ & + \{[(3X_1 - 1)\sigma_1 + (3X_2 - 1)\sigma_2]^2/16 \\ & + (2 - 3X_3)\sigma_1\sigma_2/4\}^{1/2}. \end{aligned} \quad (11)$$

Here X_1 and X_2 are the volumes of conducting phases with electrical conductivities σ_1 and σ_2 , and X_3 is the volume of the nonconducting phase ($\sigma_3=0$). In the general case of $\sigma_3 \neq 0$, theory yields a more complex cubic equation. Assuming $\sigma_3 \ll \sigma_1, \sigma_2$, we shall consider Eq. (11) with index 1 referring to phase F , index 2 to phase A , and index 3 to phase P , to be approximately valid for the $\text{GdZn}_x\text{Cu}_{1-x}$ system. Besides, in contrast to the standard arrangement, we shall set, in accordance with Eq. (10), $\sigma_1 = \sigma_F(x)$, and $\sigma_2 = \sigma_A(x)$.

Prior to starting numerical calculation of σ_{eff} using Eq. (11) within the total concentration range, consider some analytical results obtained in the limiting case. The relative volume of the third phase in the percolation limit is $X_3^c = X_P^c = 2/3$. Then, as follows from Eq. (11), $\sigma_{\text{eff}} \rightarrow 0$, and, accordingly, $\rho^{\text{th}} = \sigma_{\text{eff}}^{-1} \rightarrow \infty$. Equation (5) yields 0.52 for the maximum value of X_P at $x=0.45$, i.e., $[X_P^c - X_P(x=0.45)] = \delta = 0.14 \ll 1$. This gives us grounds to make expansion in δ , which, in linear approximation and assuming $\sigma_1 = \sigma_2$, reduces Eq. (11) to a simple expression

$$\rho^{\text{th}} = \sigma_{\text{eff}}^{-1} = \frac{2}{3} \rho_P(x) \frac{1}{\delta(x)}. \quad (12)$$

Equation (12) provides a good fit to the concentration dependence of resistivity near the percolation threshold for a two-phase system and permits a crude estimate of the maximum $\rho^{\text{th}}(x)$. If, according to Eq. (10),

$$\begin{aligned} \rho_A(x) &= \rho_{NK}(x) + \rho_{\text{ph}} + \rho_i^A(x), \\ \rho_F(x) &= \rho_{NK}(x) + \rho_{\text{ph}} + \rho_i^F(x), \end{aligned} \quad (13)$$

as is true, for instance, in our case as well, and $\rho_{\text{ph}}|_{T \rightarrow 0} \sim 0$, and the impurity resistivities in the F and A phases do not differ very much, then $\rho^{\text{th}}(x)$ grows as $(2/3)1/\delta(x)$ near $x = 2/3$. Substituting a typical value $\rho_{NK}^{\text{max}} \sim 0.1 \mu\Omega$ into Eq. (1), we obtain using Eq. (12) $\sim 0.47 \mu\Omega$ for the maximum value of ρ^{th} , which means a nearly fivefold increase in resistivity near the percolation threshold compared to the Nordheim–Kurnakov contribution.

The main physical result of our calculation consists in that the presence of the high-temperature P phase at $x \sim 0.45$ brings about a considerable growth of $\rho^{\text{th}} \propto 1/\delta$ in the middle of the concentration interval. The applicability of Eq. (11) with $\sigma_3=0$ can be estimated using the relation of $\rho_m^P(x)$ to $\chi_P(x)$ given by Eq. (8). Table III lists the partial resistivities $\rho_A(x)$, $\rho_F(x)$, and $\rho_P(x)$ calculated by means of Eqs. (8) and (13). The parameter $r_P(x_P)$ was chosen so as to achieve a reasonable fit of $\rho_P(x)$ and $\chi_P(x)$ to the experimental values of $\rho_0(x)$ and $\chi(x)$ at $x=0.45$. As seen from

TABLE III. Electrical resistivity ρ (in $\mu\Omega$) calculated for $\text{GdZn}_x\text{Cu}_{1-x}$ alloys using Eqs. (8), (10), (11), (13)–(15).

ρ	x											
	0	0.1	0.2	0.3	0.4	0.45	0.5	0.6	0.7	0.8	0.9	1
ρ_A	0.16	0.22	0.26	0.25	0.25	0.23	0.21	0.17	0.15	0.15	0.15	0.025
ρ_F	0.025	0.06	0.09	0.11	0.13	0.13	0.14	0.14	0.13	0.11	0.08	0.04
ρ_P	0.52	0.60	0.67	0.73	0.79	0.82	0.84	0.88	0.91	0.94	0.95	0.96
$\rho_m^P \chi_P$	0	0.02	0.11	0.24	0.34	0.36	0.35	0.27	0.15	0.05	0.005	0
ρ^{th}	0.16	0.24	0.36	0.56	0.86	0.79	0.59	0.3	0.18	0.12	0.08	0.04
ρ_{mm}	0.08	0.01	0.08	0.18	0.45	0.63	0.49	0.51	0.57	0.73	0.59	0.52
ρ_m^{tot}	0	0.02	0.11	0.24	0.25	0.46	0.46	0.45	0.53	0.05	0.59	0.66

Table III, $\rho_P(x)$ exceeds considerably $\rho_A(x)$ and $\rho_F(x)$ throughout the concentration range covered. This justifies the $\sigma_3=0$ approximation in Eq. (11).

To obtain more accurate data for the whole x range than those given by Eq. (12), one should use Eq. (11) to calculate ρ^{th} . The results of this calculation are presented in Table III and Fig. 2. Figure 3 demonstrates a quite satisfactory agreement with experiment. In contrast to the estimates made with Eq. (12), this numerical calculation took into account also the impurity contributions $\rho_i^A(x)$ and $\rho_i^F(x)$, which were estimated from the experimentally determined residual resistivity at points $x=0$ and $x=1$. Being small, the value $\rho_i^F(x=1)=0.025 \mu\Omega$ affects very weakly the final result. The large value $\rho_i^A(x=0)=0.136 \mu\Omega$ is possibly due to the presence of an additional A phase with $T_N=40$ K in alloys based on the antiferromagnet GdCu .⁶ It remains, however, unclear, up to what value of x this additional phase persists, and how its volume depends on x . In our calculation we assumed that this phase is present for all x where the main A phase exists, i.e., we used the corresponding expression (10) for a constant $\rho_i^A(x)$. At the same time the final contribution due to $\rho_i^A(x)$ to the total resistivity ρ^{th} falls off with increasing x proportional to the decrease of the $X_A(x)$ volume for the A phase. A good agreement between $\rho^{\text{th}}(x)$ and the experimental value $\rho_0(x)$ at the maximum for $x=0.45$ is obtained for $\rho_i^A(x)=0.1 \mu\Omega$, which differs not by much from the experimentally found $\rho_i^A(x=0)=0.136 \mu\Omega$.

Thus a simple percolative model (11) permits one to achieve a satisfactory description of the $\rho_0(x)$ relation using only the experimental values of the residual resistivities $\rho_i^A(x=0)$ and $\rho_i^F(x=1)$, as well as the Nordheim–Kurnakov contribution $\rho_{NK}(x)$. This theory offers the following predictions for the behavior of $\rho^{\text{th}}(x)$. This quantity is most sensitive to the parameter $\delta(x)$ determining the closeness of the high-resistivity phase P to the percolation threshold. For $\text{GdZn}_x\text{Cu}_{1-x}$ alloys, $\delta(x=0.45)=0.14$. An increase in the volume of phase A can give rise to a considerable growth of $\rho^{\text{th}}(x)$. In connection with this, it appears reasonable to study $\text{RZn}_x\text{Cu}_{1-x}$ systems with $\text{R} = \text{Tb}, \text{Dy}$, and other REMs, for which pure R metals are antiferromagnets, so that one could expect an increase of the A phase in $\text{RZn}_x\text{Cu}_{1-x}$ compounds. Addition of impurities increasing the magnitude of $\rho_i^A(x)$ and $\rho_i^F(x)$ can also initiate a strong increase of $\rho^{\text{th}}(x)$.

B. High temperatures ($T > T_N, T_C$)

The concepts discussed in Sect. A offer an explanation for the behavior of $\rho(x)$ in the paramagnetic temperature region and, in particular, the apparent absence of the spin-disorder contribution ρ_{mm} in antiferromagnetic alloys. For $T > T_N$ and T_C , the alloy system under study becomes magnetically single phase, and, hence, $\rho(x)$ should be described by standard expressions.

One could again use, for quantitative determination of ρ_{mm} , the effective-medium approximation for multiphase systems, as we have done in Sec. A, but with a transition to the single-phase limit. One should then have to replace Eq. (11), describing the particular case of a three-phase system with $\sigma_3=\sigma_P=0$, with the corresponding expression for a finite $\sigma_3 \neq 0$. In this case one would, however, have to solve a cubic equation [see Ref. 10 and references therein]. Therefore, we shall restrict ourselves here to a simpler but no less revealing interpretation.

Considering that, for nearly all x with exception of the extreme ends of the interval, $x \cong 0$ and $x \cong 1$, the main contribution to the residual resistivity $\rho_0(x)$ comes from its magnetic part corresponding to its high-resistivity P phase (see Table III), we can use for crude estimation of ρ_{mm} the following relation

$$\rho_{\text{mm}}(x) = \rho(T > [T_N, T_C], x) - \rho_{NK}^{\text{max}} - \rho_i(x=1) - \rho_{\text{ph}}. \quad (14)$$

The values of $\rho_{\text{mm}}(x)$ calculated from Eq. (14) are present in Table III, where by $\rho(T > T_N, T_C)$ one understands the values of $\rho(x)$ measured at $T=300$ K, by ρ_{NK} —the quantity $4\rho_{NK}^{\text{max}}x(1-x)=0.4x(1-x)$, by $\rho_i(x=1)=0.025 \mu\Omega\text{m}$ — the residual resistivity of the ferromagnet GdZn , and for $\rho_{\text{ph}}(T=300 \text{ K})$ one took the same value $0.45 \mu\Omega$ for all x .

As seen from Table III, even in such a crude estimation the value $\rho_{\text{mm}} \sim 0.5 \mu\Omega\text{m}$ persists through most of the $x \geq 0.45$ interval. The above discussion suggests that for $x < 0.45$ one can assume the decrease of $\rho_{\text{mm}}(x)$ to result from a decrease in exchange interaction I_{sf} . Experiments exhibit a stronger decrease of $\rho(x)$ for $x < 0.3$. It should, however, be pointed out that the point at $x=0.3$ falls out markedly from the experimental $\chi(x)$ relation (see Fig. 3), and that starting with $x \leq 0.2$ the $\rho_0(x)$ curve in Fig. 2 and other properties of the $\text{GdZn}_x\text{Cu}_{1-x}$ alloys become distorted through formation

of the additional A phase, which is caused by the structural instability of the GdCu antiferromagnet (for more details, see Refs. 1–6).

It appears interesting to compare $\rho_{mm}(x)$ calculated from Eq. (14) with the magnetic component of resistivity $\rho_m^P(x)$ determined independently from Eq. (8) using its proportionality to the susceptibility. In essence, $\rho_m^P(x)$ is the magnetic resistivity component connected with spin disorder at $T = 4.2$ K. In this case, the total magnetic resistivity is obviously a sum of $\rho_m^P(x)X_P(x)$ and the high-temperature part ρ_{mm} obtained in a standard way from Eq. (2), i.e.

$$\rho_m^{\text{tot}}(x) = \rho_m^P(x)X_P(x) + \rho_{mm}. \quad (15)$$

Table III lists the values of $\rho_m^{\text{tot}}(x)$ obtained using Eqs. (2) and (15). The pattern here is similar to calculation of $\rho_{mm}(x)$ using Eq. (14).

To conclude, correct determination of the concentration dependence of the magnetic contribution to resistivity of a microinhomogeneous alloy should take into account both the behavior of the exchange interaction determining the amplitude of carrier scattering from disordered spins with concentration x and the shunting of high-resistivity phases by low-resistivity phases. The assumption of the persistence of spin disorder in the GdZn $_x$ Cu $_{1-x}$ alloy system at low temperatures ($T = 4.2$ K) offers an explanation for the concentration dependence of resistivity $\rho(x)$ and permits isolation of the magnetic component $\rho_m(x)$ from it. Quantitative description makes use of the correlation between $\rho(x)$ and magnetic

susceptibility $\chi(x)$ in the low-temperature domain and of percolation theory.

The authors are grateful to the staff of the Low-Temperatures Lab at the Institute of Metal Physics, Ural Branch, Academy of Sciences of Russia, for fruitful discussions, and to N. G. Bebenin and R. V. Pomortsev for valuable criticisms.

¹Yu. N. Tsioukin, N. I. Kourov, and I. I. Piratinskaya, *Fiz. Met. Metalloved.* **67**, 1097 (1989).

²N. I. Kourov, Yu. N. Tsioukin, and T. Mydlars, *Fiz. Nizk. Temp.* **16**, 1164 (1990) [*Sov. J. Low Temp. Phys.* **16**, 673 (1990)].

³Yu. N. Tsioukin and N. I. Kourov, *Fiz. Met. Metalloved.* **71**, No. 5, 91 (1990).

⁴N. I. Kourov and Yu. G. Karpov, *Fiz. Met. Metalloved.* **72**, No. 12, 50 (1991).

⁵N. I. Kourov and Yu. N. Tsioukin, *Fiz. Met. Metalloved.* **75**, No. 6, 62 (1993).

⁶N. I. Kourov, *Fiz. Nizk. Temp.* **16**, 749 (1990) [*Sov. J. Low Temp. Phys.* **16** 441 (1990)].

⁷Yu. P. Irkhin and V. Yu. Irkhin, *Electronic Structure and Physical Properties of Transition Metals* [in Russian], UrGU, Sverdlovsk, 1989, 115 pp.

⁸K. N. R. Taylor and M. I. Darby, *Physics of Rare-Earth Solids* [Chapman and Hall, London, 1972; Mir, Moscow, 1974, 374 pp.].

⁹S. V. Vonsovskii, *Magnetism* [Halsted, New York, 1975; Nauka, Moscow, 1971, p. 1032.].

¹⁰E. A. Mityushov, P. V. Gel'd, and G. A. Adamesku, *Generalized Conductivity and Elasticity of Macrohomogeneous Heterogeneous Materials* [in Russian], Metallurgiya, Moscow, 1992, 144 pp.

Translated by G. Skrebtsov

Nonphonon mechanism of superconductivity in compounds with quasi-two-dimensional complexes RuO₂

S. A. Karamov

Moscow Physicotechnical Institute, 141700 Dolgoprudnyĭ, Moscow District, Russia
(Submitted October 20, 1997)

Fiz. Tverd. Tela (St. Petersburg) **40**, 980–983 (June 1998)

The characteristics of nonphonon pairing of hybridized p and d electrons in planar complexes RuO₂ are studied in the presence of a strong short-range Hubbard repulsion. The phase diagram of superconductivity as a function of the degree of underfilling of the $2p^6$ and $4d^6$ shells in the RuO₂ complexes is calculated in a generalized Hubbard model. © 1998 American Institute of Physics. [S1063-7834(98)00506-1]

Compounds of the type Sr₂RuO₄,¹ including the planar RuO₂ structure, are studied. The description of such a structure assumes that hole excitations of the type $4d(xy)$ and $2p(x,y)$ in $4d^6\text{Ru}^{2+}$ and $2p^6\text{O}^{2-}$ shells are present in it. The crystal field splits the t_{2g} level of ruthenium into a singlet $4d(xy)$ and doublet $4d(xz,yz)$. The $4d(xz,yz)$ electronic levels are assumed to be completely filled.² The d and p electrons tunnel through the excited p (d) states of oxygen (ruthenium — depending on the ratio of the energies of the single-particle $2p$ and $4d$ states).

Strong internal correlations split the $4d(xy)$ and $2p(x,y)$ hole levels into Hubbard sublevels (two d and four p levels in accordance with the degrees of degeneracy of the single-particle atomic states), corresponding to certain single-particle energies ε_d and ε_p . The present paper examines the limiting case of infinitely high Hubbard energies, when only one Hubbard p level and one Hubbard d level are occupied simultaneously, $\varepsilon_p \sim \varepsilon_d$. The energy shift $r = \varepsilon_p - \varepsilon_d$ of the anionic levels relative to the cationic is the measurable parameter determining the phase properties of the compound.

When the tunneling interaction is taken into account, hybridization and simultaneous filling of the Hubbard hole levels ε_p and ε_d occur. As a result, the levels are collectivized into Hubbard bands.

1. GENERAL THEORY. EQUATIONS OF STATE AND CRITERIA FOR SUPERCONDUCTIVITY

The electronic structure of the complex RuO₂ is studied in a model that takes into account, together with the tunneling matrix elements $t_{p_\lambda;d}$ between the p and d states of the ruthenium and oxygen atoms (the Emery model³), the tunneling matrix elements $t_{d;d}$ between the d states of different ruthenium atoms (similarly to Ref. 4). The model assumes that these are the largest tunneling matrix elements and that, therefore, they play the main role in the formation of the elementary excitation spectrum. A numerical estimate of the matrix elements is given in the Appendix. The special case when the indicated matrix elements are equal for nearest-neighbor atoms — $t_{d_\lambda;d} = t_{d;d} = t$ is studied.

Neglecting the Coulomb interaction under the assumption that it is strongly screened leads to a generalized Hubbard model with the mean (self-consistent) field as the zeroth approximation with the Hamiltonian⁵

$$\hat{H} = \varepsilon_p \sum \hat{p}_{r\lambda}^+ \hat{p}_{r\lambda} + \varepsilon_d \sum \hat{d}_r^+ \hat{d}_r + \hat{V}, \quad (1)$$

$$\hat{V} = \sum t_{p_\lambda;d}(\mathbf{r}_1 - \mathbf{r}_2) (\hat{p}_{r_1\lambda}^+ \hat{d}_{r_2} + \hat{d}_{r_2}^+ \hat{p}_{r_1\lambda}) + \sum t_{d;d}(\mathbf{r}_1 - \mathbf{r}_2) \hat{d}_{r_1}^+ \hat{d}_{r_2}. \quad (2)$$

Here \hat{p}^+ , \hat{p} , \hat{d}^+ , and \hat{d} are creation and annihilation operators for the p and d hole states.

The following states are chosen as a basis for the atomic hole states in order to switch to the Hubbard representation:

For the oxygen atom O²⁻, $2p^6:|0\rangle$; single-hole O⁻, $2p^5:\hat{p}_{x\sigma}^+|0\rangle$, $\hat{p}_{y\sigma}^+|0\rangle$ (the level is four-fold degenerate), i.e., $\hat{p}_\lambda^+ = \hat{X}^{(\lambda|0)}$.

For the ruthenium atom, studying transitions between the states of Ru²⁺ and Ru³⁺: Ru²⁺, $4d^6|0\rangle$; single-hole states of Ru³⁺, $4d^5:\hat{d}_\sigma^+|0\rangle$ (the level is doubly degenerate), i.e., $\hat{d}_\sigma^+ = \hat{X}^{(\sigma/2|0)}$.

For the ruthenium atom, studying transitions between the states of Ru³⁺ and Ru⁴⁺: single-hole states of Ru³⁺, $4d^5:\hat{d}_\sigma^+|0\rangle$; two-hole states of Ru⁴⁺, $4d^4:\hat{d}_\uparrow^+ \hat{d}_\downarrow^+|0\rangle$, i.e., $\hat{d}_\sigma^+ = \hat{X}^{(\uparrow\downarrow-\sigma/2)}$.

The transition to the Hubbard representation transforms the Hamiltonian to the following form:

$$\hat{H} = \sum_{rk} \varepsilon_k \hat{X}_r^{kk} + \frac{1}{2} \sum_{\alpha\beta rr'} \hat{X}_r^\alpha \hat{X}_{r'}^\beta \hat{V}^{\alpha\beta}(\mathbf{r} - \mathbf{r}'), \quad (3)$$

where \hat{X}_r^α are Hubbard operators and α and β are the so-called root vectors, which identify transitions between cell states.⁶ This Hamiltonian corresponds to the following inverse virtual multicomponent single-particle Green's function for the no-loop Hubbard approximation:⁵

$$[G_\omega^{-1}(\mathbf{p})]_{\alpha\beta} = [\{G_\omega^{(0)}(\mathbf{p})\}^{-1}]_{\alpha\beta} - f_\alpha V_{\alpha\beta}(\mathbf{p}). \quad (4)$$

Here $G_{\omega}^{(0)}(\mathbf{p})$ is the diagonal atomic Green's function.

The tunneling interaction is taken into account in the nearest-neighbor approximation; f_p and f_d are the so-called terminal factors, which account for the existence of an infinite Hubbard energy and are fixed by the average numbers n_p and n_d characterizing the underfilling of the $2p^6$ and $4d^6$ electronic shells, respectively,

$$f_p = 1 - 3n_p/4, \tag{5}$$

$$f_d = \begin{cases} 1 - n_d/2, & 0 < n_d < 1, \\ n_d/2, & 1 < n_d < 2. \end{cases} \tag{6}$$

Together with the noncollectivized p branches $E = \varepsilon_p$, the single-particle Green's function (4) gives two branches

$$E_{1,2} = -\mu + f_d t F_{\mathbf{p}} \pm \sqrt{(r/2 - f_d t F_{\mathbf{p}})^2 + 2f_p f_d t^2 (2 - F_{\mathbf{p}})}. \tag{7}$$

Here $F_{\mathbf{p}} = \cos(p_x a) + \cos(p_y a)$, $\mu = -(\varepsilon_d + \varepsilon_p)/2$ is the chemical potential of the compound, $r = \varepsilon_p - \varepsilon_d$, t is the tunneling matrix element between the states of nearest atoms, and a is the modulus of the translational-symmetry vector.

The average occupation numbers n_p and n_d of the hole states can be expressed in terms of the matrix elements of the Green's function

$$[D_{\omega}(\mathbf{p})]_{\alpha\beta} = [G_{\omega}(\mathbf{p})]_{\alpha\beta} f_{\beta}, \tag{8}$$

thereby determining the equation of state of the system

$$n_p = f_p \left(3n_F(\varepsilon_p) + \sum_{\mathbf{p}'} B_j n_F(E_j) \right), \tag{9}$$

$$\sum_{\mathbf{p}'} A_j n_F(E_j) = \begin{cases} n_d / (2f_d), & 0 < n_d < 1, \\ (n_d - 1) / f_d, & 1 < n_d < 2, \end{cases} \tag{10}$$

where

$$A_1 = B_2 = \frac{1}{2} \left[1 - \frac{r - 2f_d t F_{\mathbf{p}}}{E_2 - E_1} \right],$$

$$A_2 = B_1 = \frac{1}{2} \left[1 + \frac{r - 2f_d t F_{\mathbf{p}}}{E_2 - E_1} \right]. \tag{11}$$

The appearance of superconductivity in the system is determined by the presence of a negative scattering amplitude at the Fermi surface. The condition for the appearance of a superconducting state is that a singularity appears in the two-particle multicomponent vertex part $\Gamma_{\alpha\beta}(\mathbf{p})$ with zero total energy, momentum, and spin.⁷ In the empty-lattice approximation (the gas approximation) it is given by the ladder series⁸

$$\Gamma_{\alpha\beta}(\mathbf{p}) = \Gamma_{\alpha\beta}^{(0)}(\mathbf{p}) - T \sum_{\omega \mathbf{p}'} \Gamma_{\alpha\beta\lambda\nu}^{(0)}(\mathbf{p}, \mathbf{p}') \times G_{\omega}^{\lambda\lambda'}(\mathbf{p}') G_{-\omega}^{\nu\nu'}(-\mathbf{p}') \Gamma_{\lambda'\nu'}(\mathbf{p}'). \tag{12}$$

Here $\Gamma_{\alpha\beta\lambda\nu}^{(0)}(\mathbf{p})$ is the two-particle vertex part, which is irreducible with respect to two lines with identical direction and which we find by the Dyson method.⁹

As a result, the superconductivity condition can be expressed by the conventional BCS formula $\lambda > 0$ with an effective constant λ

$$T_c \sim e^{-1/\lambda}, \quad \lambda = g\rho. \tag{13}$$

Here $\rho = \sum_{\mathbf{p}} \delta(E(\mathbf{p}))$ is the energy density of the states at the Fermi surface, g is an energy factor,

$$g = \frac{\pm 2\varepsilon_p^2 \varepsilon_d f_p - \varepsilon_p f_d (\varepsilon_d + L)^2}{f_p f_d (\varepsilon_p + \varepsilon_d + L)^2},$$

$$L = \frac{4f_p f_d t^2 - \varepsilon_p \varepsilon_d}{\varepsilon_p + f_p t}. \tag{14}$$

Here \pm correspond to the cases $0 < n_d < 1$ and $1 < n_d < 2$, respectively.

The density of states ρ is always positive, so that the existence of superconductivity in the system is determined by the condition $g > 0$.

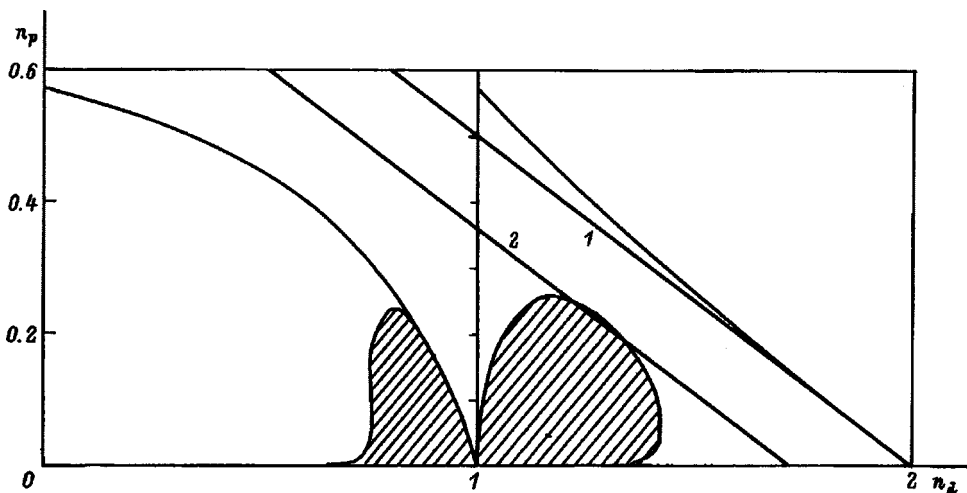


FIG. 1. Phase diagram of superconductivity for the complex RuO_2 . The regions of existence of superconductivity are hatched. 1, 2 — Lines of electrical neutrality (16) for $\delta = 0$ and 0.14.

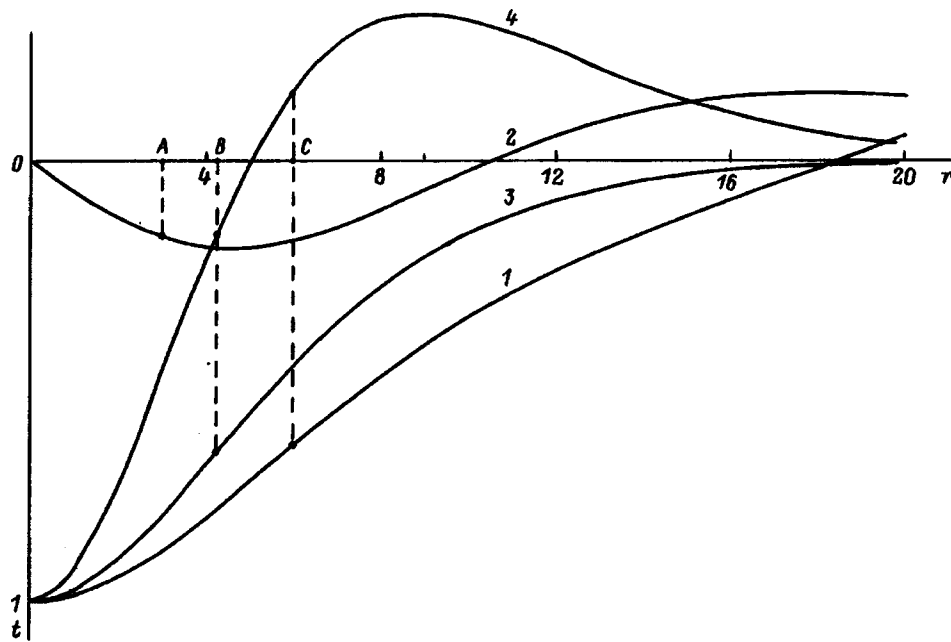


FIG. 2. Hopping integrals as a function of distance (in atomic units) between the centers of the orbitals. 1 — $t_{dd\pi}$, 2 — $t_{pd\pi}$, 3 — $t_{pp\pi}$, and 4 — $t_{pp\sigma}$. A, B, C — Distances between the nearest-neighbor atoms for the complex RuO_2 (lattice period $a \approx 6$).

2. CHARACTERISTIC FEATURES OF THE FILLING OF THE ELECTRONIC SPECTRUM. PHASE DIAGRAM

To each point of the phase plane (n_d, n_p) there corresponds a certain phase state that can be realized in a number of compounds of the type under study with the same value of T_c corresponding to this phase state. Each phase state (n_d, n_p) is in one-to-one correspondence with a pair of values (r, q) , where $q = 2n_p + n_d$ is the hole charge of the complex RuO_2 . In other words, (r, q) and (n_d, n_p) are alternative systems of phase coordinates. The ratio r/t is a parameter of the problem.

The parameter q is determined by the condition of electrical neutrality of the compound. The manifold of phase states (r, q) with the same value of q forms a line of electrical neutrality in the phase plane (n_d, n_p) (lines 1 and 2 in Fig. 1)

$$n_p = (q - n_d) / 2. \tag{15}$$

The position of the point corresponding to the phase state of the compound on this line is determined by the parameter r of the compound.

In the presence of a strong Hubbard repulsion, the existence of superconductivity is determined by the sign and magnitude of the amplitudes of both $d-d$ and $p-p$ scattering. The condition of superconductivity has the form (13). The numerical solution of the problem is presented in Fig. 1 (the regions of existence of the superconducting state are hatched).

The dependence of T_c on the parameters n_d and n_p forms a certain relief.¹⁰ It is obvious that T_c for the compound is all the lower, the closer the point of the phase state of the compound is to the boundary of the region of superconductivity. Beyond the limits of this boundary $T_c = 0$.

3. COMPARISON WITH EXPERIMENT AND CONCLUSIONS

In the present work it was assumed that the electron-phonon interaction in compounds of the type studied is negligibly small compared to the kinematic electron-electron interaction. Indeed, numerous experiments confirm that superconductivity in such compounds cannot be described by the BCS model. For example, calculations for high- T_c compounds taking account of only the kinematic interaction of the electrons¹⁰ describe the dependence of T_c on the charge carrier density in agreement with experiment,¹¹ while this dependence cannot be described in the BCS model.

The condition of electrical neutrality for the compounds studied has the form (15). A transition into the superconducting state has been observed for the compound Sr_2RuO_4 .¹ However, the stoichiometric coefficients of the experimentally investigated compounds are not known with sufficiently high accuracy. In reality, compounds of the type $\text{Sr}_2^+(\text{RuO}_2)\text{O}_{2+\delta}^-$ with small values of δ are investigated. For such a compound the electrical-neutrality condition (15) assumes the form

$$n_p = 1 - \delta - (n_d / 2). \tag{16}$$

Indeed, even for $\delta = 0.14$ the corresponding line of electrical neutrality intersects the region of superconductivity (line 2 in Fig. 1). Thus, a point of the phase state of such a compound on this line is determined by the parameter r of the compound and lies in the region of superconductivity in the square $1 < n_d < 2$. Since the point mentioned lies near the boundary of the region of superconductivity, the corresponding compound should have a quite low value of T_c . This is in good agreement with the experiment: $T_c = 0.93$ K.

In closing, I wish to thank R. O. Zaïtsev for exceeding

valuable recommendations and remarks concerning this work.

This work was supported by the State Program on High- T_c Superconductivity under the project No. 94011 "Ekstend II."

4. APPENDIX. ESTIMATE OF THE TUNNELING MATRIX ELEMENTS

It can be assumed that the tunneling matrix element $T_{ab} = \langle a|h|b \rangle$ between the atomic hole basis states $|a \rangle$ and $|b \rangle$ are approximately proportional to the quantity $(\varepsilon_a + \varepsilon_b)t_{ab}$. Here $t_{ab} = \langle a|b \rangle$ is the so-called hopping integral between the states $|a \rangle$ and $|b \rangle$ and ε_i is either the ionization potential of the cation, if $|i \rangle$ is the state of the cation, or the electron affinity of the anion, if $|i \rangle$ is the state of the anion.¹²

The numerically computed dependence of the hopping integrals $t_{dd\pi}$, $t_{pd\pi}$, $t_{pp\sigma}$, and $t_{pp\pi}$ on the distance between in the ions is given in Fig. 2 (the designations are taken from Ref. 12). One can see that for the complex RuO₂ studied the values of the hopping integrals are of the same order of magnitude (interatomic distances A , B , C in Fig. 2).

Since the O²⁻ ion has no bound states, which corresponds to the unknown negative electron affinity ε_p of the O⁻ ion, it can be assumed that this energy approximately equals in absolute magnitude the positive electron affinity of

a neutral oxygen atom: $\varepsilon_p \approx -1.46$ eV. Since the ionization potential of the Ru²⁺ ion equals 28.5 eV, it can be assumed that the ionization potentials of the Ru²⁺ and Ru³⁺ ions are much greater in absolute magnitude than the electron affinity mentioned: $|\varepsilon_p| \ll |\varepsilon_d|$.

In summary, the following tunneling matrix elements are found to be largest: $T_{dd\pi} \sim 2\varepsilon_d t_{dd\pi}$ and $T_{pd\pi} \sim \varepsilon_d t_{pd\pi}$. In the model studied it was assumed that they are equal.

¹Y. Maeno, H. Hashimoto, K. Yoshida, S. Nishizaki, T. Fujita, J. G. Bednorz, and F. Lichtenberg, *Nature (London)* **372**, 532 (1994).

²T. Oguchi, *Phys. Rev. B* **51**, 1385 (1995); D. J. Singh, *Phys. Rev. B* **52**, 1358 (1995).

³V. J. Emery, *Phys. Rev. Lett.* **58**, 2794 (1987).

⁴R. O. Zaitsev, *Fiz. Tverd. Tela (Leningrad)* **33**, 3183 (1991) [*Sov. Phys. Solid State* **33**, 1798 (1991)].

⁵J. Hubbard, *Proc. Roy. Soc. A* **276**, 238 (1963).

⁶R. O. Zaitsev, *Zh. Éksp. Teor. Fiz.* **70**, 1100 (1976) [*Sov. Phys. JETP* **43**, 574 (1976)].

⁷L. P. Gor'kov, *Zh. Éksp. Teor. Fiz.* **34**, 735 (1958) [*Sov. Phys. JETP* **7**, 505 (1958)].

⁸R. O. Zaitsev, *Phys. Lett. A* **134**, 199 (1988).

⁹F. Dyson, *Phys. Rev.* **102**, 1217 (1956).

¹⁰R. O. Zaitsev and S. A. Karamov, *SFKhT* **8**, 583 (1995).

¹¹C. C. Tsuei, D. M. Newns, C. C. Chi, and P. C. Pattnaik, *Phys. Rev. Lett.* **65**, 2724 (1990).

¹²W. Harrison, *Electronic Structure and the Properties of Solids* (Mir, Moscow, 1983).

Translated by M. E. Alferieff

Effect of vacancies and interstitials on the dynamic properties of the $\text{La}_{2-x}\text{Sr}_x\text{CuO}_4$ superconductor

V. G. Chudinov, A. G. Chirkov, and F. A. Sautin

Physicotechnical Institute, Ural Branch of the Russian Academy of Sciences, 426001 Izhevsk, Russia
(Submitted November 11, 1997)

Fiz. Tverd. Tela (St. Petersburg) **40**, 984–988 (June 1998)

The effect of vacancies and interstitials in the CuO_2 layer on the vibrational spectrum in the $\text{La}_{2-x}\text{Sr}_x\text{CuO}_4$ system has been calculated by molecular dynamics. It is shown that the excitation probability for local ~ 0.4 -eV high-frequency vibrations of nonphonon origin in the vicinity of Sr impurity atoms decreases if copper vacancies are introduced at a concentration $x=0.17$, which corresponds to the maximum superconducting transition temperature, this decrease being still more effective (by about ten times) if interstitial atoms are present. The appearance of interstitials makes a considerable region around them (five to six nearest neighbors) quasi-amorphous. A comparison with available experimental data is made. It is concluded that the behavior of the system under irradiation is accounted for primarily by interstitials, which bring about strong perturbation in the lattice (~ 1 nm) up to making it completely amorphous.

© 1998 American Institute of Physics. [S1063-7834(98)00606-6]

1. High- T_c superconductors are known to be much more sensitive to the presence of lattice defects than the low- T_c ones.^{1–4} The presence of defects results in a decrease of the superconducting transition temperature T_c , an increase of the superconducting transition width ΔT_c , an increase of electrical resistivity ρ , and a change in critical current density j_c .

Despite considerable effort devoted to studies of the nature of high- T_c superconductivity, the structure and the role of defects responsible for deviations from stoichiometry or produced by various radiations remain unclear. In our opinion, this is related, first, to the use of inadequate pair interaction potentials, which usually include tens of fitting parameters and do not take into account the screening of Coulomb interaction caused by the presence of metallic conduction.⁵ The second factor is the impossibility of separating the influence on the characteristics of high- T_c superconductors of many types of defects created simultaneously. Some properties of high- T_c superconductors however, can be considered to be presently established, namely: (1) degradation of the transition temperature is observed at doses one to two orders of magnitude lower than is the case with superconductors based on A-15 compounds, and three orders of magnitude lower than in metals, nitrides, and carbides;⁶ (2) all kinds of radiation behave qualitatively in a similar way in any ambient condition;³ (3) superconductivity can vanish completely, whereas in other superconductors T_c drops to a finite level;⁶ and (4) all kinds of irradiation applied up to a dose ~ 0.01 dpa result in an increase of the lattice parameters, while at 0.1 dpa the material becomes amorphous.⁴ Remarkably, isolated point defects produce regions with different superconducting properties having dimensions ~ 1 nm comparable to the coherence length. In this aspect, high- T_c materials differ from conventional superconductors. For instance, different compounds with the same A-15 structure may respond dif-

ferently to various kinds of irradiation.^{7,8} For instance, as a result of irradiation by fast reactor neutrons to the same dose, Nb_3Sn undergoes disordering with T_c decreasing from 17 to 1.5 K, Mo_3Si becomes amorphous with T_c increasing from 1.5 to 6 K, and V_3Si occupies an intermediate position. Irradiation of Nb_3Sn with α particles and oxygen ions does not produce disorder, although T_c decreases to 3.5 K. In other words, no complete degradation of T_c is observed. These differences are accounted for by the onset of fast cooling in small cascade regions without local melting, or by the formation of structures produced in collisional cascades (isolated vacancies and their clusters in high concentration, ~ 2 –5%). At the same time in large-cascade regions collisions may give rise to local melting with complete disappearance of the defect structure formed earlier, and directed motion of vacancies toward the center, and of interstitials to the periphery.⁹ It would seem that one should observe the same behavior in high- T_c superconductors. Since this is not so, one needs to look for other reasons for T_c degradation. We believe that this is a consequence of the different nature of the superconducting transition in high- T_c and conventional superconductors. From this standpoint, the La–Sr–Cu–O system is of particular interest, because it has a comparatively simple structure and the highest sensitivity to irradiation (a similar sensitivity was observed only for the Bi–Pb–Sr–Ca–Cu–O system). The upper boundary of the sensitivity lies between 2×10^{-5} and 8×10^{-5} dpa.⁴

Traditional concepts still have not offered an adequate understanding of the mechanism of high- T_c superconductivity.¹⁰ An attempt at solving this problem using a novel approach proposed by us within the anharmonic approximation has been made.^{11–14} In this attempt, the lattice dynamics of $\text{La}_{2-x}\text{Sr}_x\text{CuO}_4$ was studied by molecular dynamics simulation. It was shown that under certain conditions (strong anharmonicity and anisotropy of atomic inter-

TABLE I. Relative atomic displacements in $\text{La}_{1.83}\text{Sr}_{0.17}\text{CuO}_4$.

Near oxygen vacancy			Near copper vacancy		
Atom	$\Delta x/a_0$	$\Delta y/a_0$	Atom	$\Delta x/a_0$	$\Delta y/a_0$
2b	-0.001	0.000	2b	-0.001	-0.001
2d	0.001	0.000	2c	0.000	0.000
2f	0.000	0.000	2d	0.001	-0.005
3b	0.001	0.000	2e	0.000	0.000
3c	-0.002	-0.002	2f	-0.001	0.001
3d	0.000	-0.001	3b	-0.001	0.000
3e	0.003	-0.002	3d	0.001	-0.003
3f	0.000	0.000	3f	0.000	0.000
4b	0.001	0.000	4b	-0.004	0.000
4f	-0.002	0.000	4c	-0.002	0.000
5b	0.000	0.000	4e	0.003	-0.001
5c	-0.003	0.002	4f	0.005	-0.001
5d	0.000	0.001	5b	0.000	0.000
5e	0.003	0.002	5d	0.000	0.002
5f	0.000	0.000	5f	0.000	0.000
6b	-0.001	0.000	6b	0.000	0.000
6d	0.001	-0.004	6c	0.000	0.000
6f	0.000	0.000	6d	0.000	0.004
			6e	0.000	0.001
			6f	0.000	0.001

actions along and across the CuO_2 layer) there is a high probability for excitation of local high-frequency vibrations of a nonphonon origin (which possess both rotational and translational degrees of freedom and energy ~ 0.4 eV) of oxygen atoms in CuO_2 layers in the vicinity of Sr impurity atoms. Moreover, their average kinetic energy exceeds ~ 100 times the overall mean. This results in an effective cooling of the matrix, and it becomes capable, in principle, of supporting superconducting current. This approach allows any carrier pairing mechanism, including the conventional electron-phonon coupling. Obviously enough, in this case $T_{\text{cexp}} \gg T_{\text{cmat}}$ (here the experimentally measured sample temperature T_{cexp} is an averaged macroscopic quantity). It should be stressed that these vibrations are of nonphonon nature, and they are thus not subject to the limitations in the energy associated with phonon wavelength in a crystal lattice. This situation has a high probability of realization only in strongly anharmonic systems, where the canonic distribution is invalid (a nonperfect quasi-particle gas, phonons interact strongly with one another, and solitons are excited). It is possible that these local high-frequency vibrations are responsible for the peaks in Raman spectra in the region of ~ 0.4 eV, although they are currently assigned to excitations in the electronic subsystem, as well as to polarons; it thus appears that this observation has not received a commonly accepted explanation. Decisive evidence could come from neutron scattering experiments, which have not been performed in this energy region because of the associated technical difficulties.¹¹

The contribution of local high-frequency vibrations to the joint density of vibrational states was estimated with a model parameter S_{hf}/S_{lf} , where S_{hf} and S_{lf} are, respectively, the areas bounded by the curves describing the local high-frequency peaks and the low-frequency part of the vibrational density of states (DOS). Correlation between the

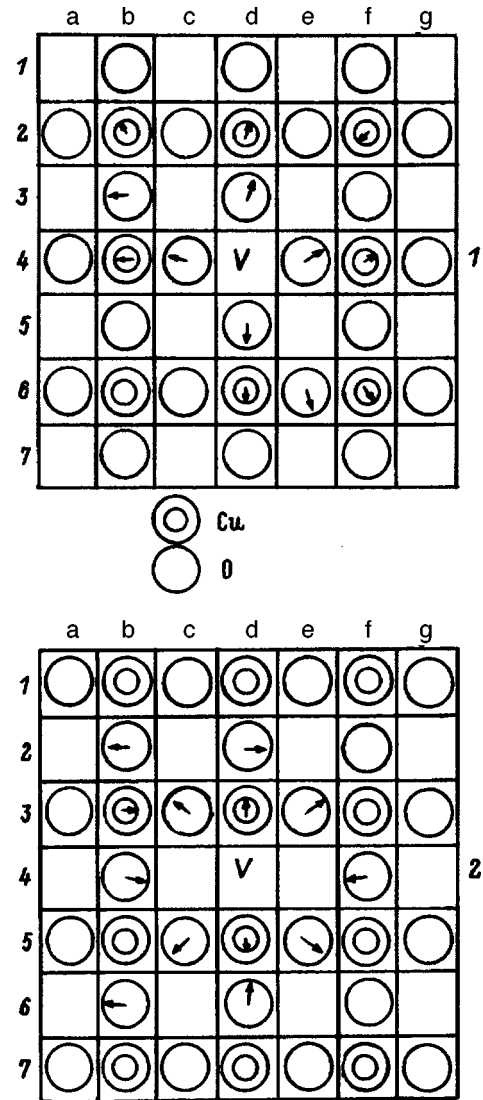


FIG. 1. Structure of vacancies in $\text{La}_{1.83}\text{Sr}_{0.17}\text{CuO}_4$. 1 — Cu vacancy, 2 — O vacancy; V — vacancy.

model parameter and T_c was established as a function of Sr concentration and external pressure.¹³ T_c was found to increase with this model parameter. Obviously enough, the higher the Sr concentration (within the low-concentration approximation), the larger is the number of such heated regions, the stronger is the matrix cooling for the same experimentally measured temperature, and the higher are the temperatures at which the superconducting transition can occur. At high Sr concentrations, however, the heated regions begin to overlap, thus suppressing superconductivity. In other high- T_c superconductors, such heated regions can be created, in principle, by defects of another type.

This work studies the influence of point defects on dynamic properties in the $\text{La}_{2-x}\text{Sr}_x\text{CuO}_4$ system.

2. The method of calculation was described in Ref. 11. We studied lattice dynamics for a Sr concentration $x=0.17$ and temperature $T=70$ K. The model crystallite consisted of three layers [La(Sr)-O, CuO_2 , La(Sr)-O] and contained ~ 2050 atoms. The atoms in the La(Sr)-O layers were fixed. The CuO_2 layer consisted of ~ 700 mobile atoms. Cyclic

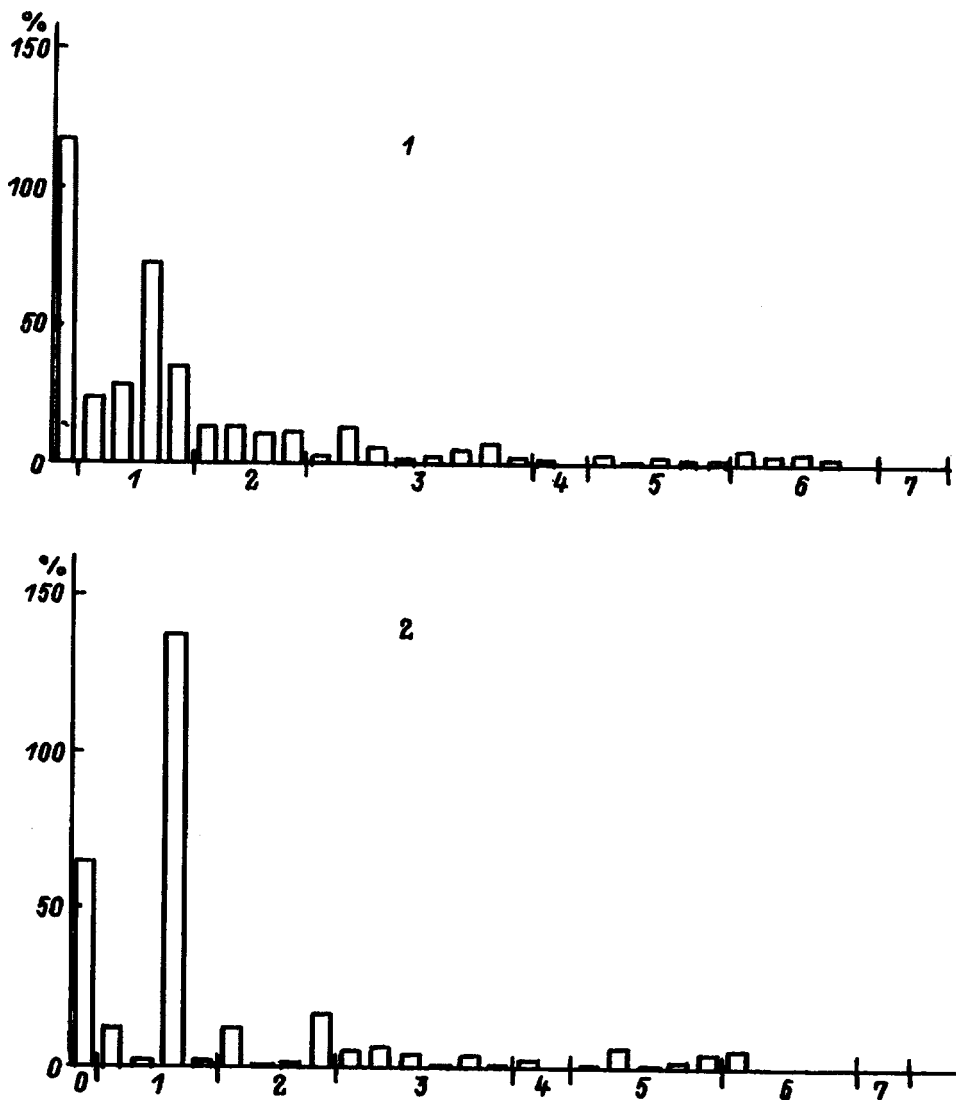


FIG. 2. Atomic displacements from the initial equilibrium position in unit-cell constants (vertical axis). Plotted on the horizontal axis are the numbers of the coordination spheres.

boundary conditions were prescribed along the CuO_2 layer. The vacancies and interstitials were created by removing or adding atoms to the CuO_2 layer with their subsequent relaxation. The pair interaction potentials were taken from Ref. 15. These potentials provided lattice stability, reproduced qualitatively the experimentally measured low-frequency part of the vibrational DOS, and, hence, the elastic constants. Defects were not allowed to interact. The concentration of vacancies was varied from zero to 3%, and that of interstitials, up to 1%. In all cases the lattice remained stable. Its parameters differed from the experimental values by not more than 5%.

Figure 1 presents the structure of isolated Cu and O vacancies in the CuO_2 layer calculated for $x=0.17$. Displacements up to $\sim 1\%$ extend over one to two nearest neighbors. The numerical estimates are given in Table I. Qualitatively similar results for the order-of-magnitude atomic displacements were obtained in calculations made for conventional superconductors.^{16,17} In this system, however, one observed noticeable symmetry distortions in relaxation of the surrounding atoms because of the presence of impurity Sr atoms.

The S_{hf}/S_{lf} parameter depends on the concentration of vacancies of various species. Copper vacancies present in concentrations of up to $\sim 1\%$ result in a drop of S_{hf}/S_{lf} by a factor 2–3, whereas oxygen vacancies practically do not produce any effect.

Interstitials (Sr, La, Cu, O) in the CuO_2 layer create a substantially stronger perturbation. Actually, their structure is impossible to determine. It appears more appropriate to speak about formation of a quasi-amorphous region $\sim 1 - 1.5$ nm in size. Displacements of atoms in the first coordination sphere amount to $\sim 100\%$, and in the fifth and sixth spheres, to $\sim 5\%$ (Fig. 2). Even a single interstitial ($c \sim 0.15\%$) affects very strongly the density of vibrational states. S_{hf}/S_{lf} decreases for Sr by a factor ~ 30 , for La and Cu, by ~ 20 times, and for O, ~ 15 times. For $c \sim 1\%$, local high-frequency vibrations are practically suppressed (Fig. 3), which means, if one recalls the correlation between S_{hf}/S_{lf} and T_c , that the superconducting transition in high- T_c superconductors should practically disappear at fairly low doses $\sim 10^{-3}$ dpa, which is in a good agreement with experiment.

3. The available experimental data regrettably, do not permit a well-substantiated discussion and comparison of the

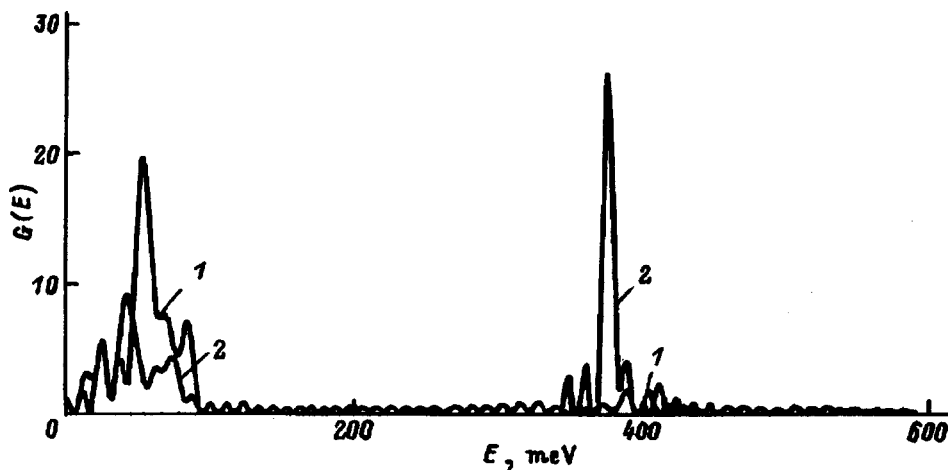


FIG. 3. Density of vibrational states of the $\text{La}_{1.83}\text{Sr}_{0.17}\text{CuO}_4$ system. 1 — with one interstitial La atom, 2 — without defects.

various details in the behavior of the $\text{La}_{2-x}\text{Sr}_x\text{CuO}_4$ system under irradiation. One can consider at present only parts of the general pattern. Our results suggest that interstitials and Cu vacancies should cause a decrease of T_c already at very low fluences.

Note also the correlation between the available experimental evidence for irradiation affecting stronger HTSC's with higher T_c for the same doses and the substantial decrease of the S_{hf}/S_{lf} parameter at $x=0.17$ (the concentration in $\text{La}_{2-x}\text{Sr}_x\text{CuO}_4$ corresponding to $T_{c\text{max}}$ in the experiment) compared to $x=0.03$.¹²

Our results suggest that vacancies can hardly be the main reason for suppression of high- T_c superconductivity, because the regions within which atoms undergo noticeable displacements ($\sim 1\%$) extend over two–three coordination spheres ($\sim 0.2\text{--}0.3$ nm) and do not differ qualitatively from those in A-15 compounds. The crystal lattice retains its initial symmetry. And although the density of vibrational states is distorted as a result of the decrease in local high-frequency vibration intensity, this distortion is not very strong.

The creation of interstitials should affect much more the properties of high- T_c superconductors under irradiation. Interstitials produce quasi-amorphous regions $\sim 1\text{--}1.5$ nm in size and suppress local high-frequency vibrations already at low doses. Such regions exhibiting dielectric properties are observed to appear under irradiation, including the case of formation of single defects under irradiation by fast electrons,⁴ which create single Frenkel pairs. Direct observation of pinning by electron microscopy provides supportive evidence for this conclusion.¹⁸

Now what is the physical explanation for this influence of defects? In our opinion, it is due to the large anharmonic contribution to atomic interactions. It was shown both theoretically¹⁴ and experimentally¹⁹ that only in this case can local high-frequency vibrations set in. We demonstrated earlier¹¹ that strong lateral atomic interactions are capable of maintaining atoms in the CuO_2 layer in nonequilibrium positions with respect to longitudinal directions, and this is what accounts for the anharmonic contribution. When vacancies are created, the nearest-neighbor atoms acquire a possibility of relaxing toward the minimum of the pair-interaction potential, i.e. toward decreasing anharmonicity. This reduces

the contribution of the local high-frequency vibrations to the joint DOS and to T_c .

Interstitials intensify this process through formation of substantially larger perturbed regions (by ~ 100 times), so that the actual species used in irradiation is not essential, provided it is capable of creating interstitials. This is in excellent agreement with the available experimental data discussed here.

Experimental results can naturally be seriously affected by changes in the density distribution of electronic states, which can give rise to considerable changes in electron density at the Fermi surface.

Regrettably, there are at present no direct neutron-diffraction data which would support the existence of local high-frequency vibrations in high- T_c superconductors; as for the peaks in IR scattering spectra observed in La–Sr–Cu–O (~ 0.4 eV), Y–Ba–Cu–O (~ 0.6 eV), and Bi–Sr–Ca–Cu–O (~ 1 eV), they cannot be unambiguously interpreted because of possible scattering from electrons. Interpretation of available experimental data within the above model will hopefully provide an impetus to a better understanding of the nature of high- T_c superconductivity.

The authors are grateful to E. I. Salamatov for fruitful discussions and valuable comments.

¹B. A. Aleksashin, V. I. Voronin, S. V. Verkhovskii, B. N. Goshchitskii, S. A. Davydov, Yu. I. Zhdanov, A. E. Kar'kin, V. L. Kozhevnikov, A. V. Mirmel'shtein, K. N. Mikhalev, M. V. Sadovskii, and S. M. Cheshnitskii, *Zh. Eksp. Teor. Fiz.* **95**, 678 (1989) [*Sov. Phys. JETP* **68**, 382 (1989)].

²K. Shiraishi, *J. Nucl. Mater.* **169**, 305 (1989).

³V. F. Elesin and I. A. Rudnev, *Sverkhprovodimost' (KIAE)* **4**, 2055 (1991).

⁴I. A. Abroyan and V. Ya. Velichko, *Izv. Akad. Nauk SSSR, Ser. Fiz.* **54**, 1396 (1990).

⁵M. S. Islam, M. Leslie, S. M. Tomlinson, and C. R. A. Catlow, *J. Phys. C* **21**, L109 (1988).

⁶J. Gerek, H. C. Li, G. Linker, O. Meyer, G. Politis, F. Ratzel, R. Smithey, B. Strehlau, X. X. Xi, and G. C. Xiong, in *Proceedings of the Symposium on Plasma and Ion Processing of High- T_c Superconductors* (Tokyo, 1987), p. 312.

⁷V. G. Chudinov, N. V. Moseev, B. N. Goshchitskii, and V. I. Protasov, *Phys. Status Solidi A* **55**, 109 (1979).

⁸V. G. Chudinov, N. V. Moseev, B. N. Goshchitskii, and V. I. Protasov, *Phys. Status Solidi A* **85**, 435 (1984).

⁹V. G. Chudinov, V. P. Gogolin, B. N. Goshchitskii, and V. I. Protasov, *Phys. Status Solidi A* **67**, 61 (1981).

- ¹⁰V. L. Ginzburg, *Sverkhprovodimost' (KIAE)* **5**, 1 (1992).
- ¹¹V. G. Chudinov, A. G. Chirkov, E. B. Dolgusheva, and V. M. Dyadin, *Sverkhprovodimost' (KIAE)* **6**, 205 (1993).
- ¹²V. G. Chudinov and A. G. Chirkov, *Sverkhprovodimost' (KIAE)* **8**, 243 (1995).
- ¹³A. G. Chirkov and V. G. Chudinov, *Sverkhprovodimost' (KIAE)* **7**, 800 (1994).
- ¹⁴E. I. Salamatov and V. G. Chudinov, *Fiz. Tverd. Tela (St. Petersburg)* **36**, 1392 (1994) [*Phys. Solid State* **36**, 761 (1994)].
- ¹⁵V. G. Chudinov, E. B. Dolgusheva, and A. A. Yur'ev, *Sverkhprovodimost' (KIAE)* **4**, 2086 (1991).
- ¹⁶V. G. Chudinov, N. V. Moseev, B. N. Goshchitskii, and V. I. Protasov, *Phys. Status Solidi A* **73**, 325 (1982).
- ¹⁷N. V. Moseev, V. G. Chudinov, B. N. Goshchitskii, and V. I. Protasov, *Phys. Status Solidi A* **94**, 147 (1986).
- ¹⁸T. I. Arbuzova, I. B. Smolyak, V. L. Arbuzov, A. É. Davletshin, S. V. Naumov, A. A. Samokhvalov, and W. Havalek, *Fiz. Nizk. Temp.* **19**, 244 (1993) [*Low Temp. Phys.* **19**, 169 (1993)].
- ¹⁹T. Timusk and D. B. Tanner, in *Physical Properties of High-Temperature Superconductors I*, edited by D. M. Ginsberg [World Scientific, Singapore, 1989; Mir, Moscow, 1990].

Translated by G. Skrebtsov

Scaling of the current–voltage characteristics of superconducting films in the flux creep model

A. N. Lykov and A. Yu. Tsvetkov

P. N. Lebedev Physical Institute, Russian Academy of Sciences, 117924 Moscow, Russia

(Submitted December 16, 1997)

Fiz. Tverd. Tela (St. Petersburg) **40**, 989–992 (June 1998)

On the basis of the magnetic flux creep model, taking viscous vortex motion and the spatial shape of the pinning potential into account, we have constructed a model explaining the shape of the current–voltage characteristics (CVC's) of high-temperature superconducting films and the sign change of the curvature of these characteristics with change in temperature. The model given also allows one to explain the scaling of these curves. © 1998 American Institute of Physics. [S1063-7834(98)00706-0]

The phenomenon of magnetic flux creep is determined by the effect of thermal fluctuations on the interaction of Abrikosov vortices with the pinning centers. A detailed analysis of this phenomenon would make it possible to obtain additional information clarifying its microscopic nature. For example, it would be possible to estimate the characteristic dimensions of the pinning centers and the spatial shape of the pinning potential (U_0). In addition, a study of the current–voltage characteristics (CVC's) would provide information about the magnetic flux dynamics in superconductors. In the one-dimensional flux creep model it has been shown¹ that the induced electric field in superconducting films is described well by the expression

$$E = Ba_f \omega \exp\left[\frac{-U(j)}{k_B T}\right] \left[1 - \exp\left(\frac{-\pi U_0 j}{k_B T}\right)\right], \quad (1)$$

where E is the electric field strength, B is the external magnetic field, a_f is the distance between vortices, $j = J/J_{c0}$ is the normalized current density in the sample, J_{c0} is the critical superconducting current density in the creep-free case, ω is the frequency of attempts of the vortices to escape from the potential well. This frequency is usually assumed to be equal the vibrational frequency of the vortex lattice inside this well and lies in the range $10^6 - 10^{11} \text{ s}^{-1}$. It follows from Eq. (1) that the voltage drop on the sample is not equal to zero even when the current density through the sample is less than J_{c0} . The present paper analyzes the CVC's of HTSC films.² The most interesting result of this work is the sign change of the curvature of the experimental CVC's in the temperature interval 70–90 K. Such behavior of the CVC's cannot be explained from the point of view of the usual Kim–Anderson flux creep model,³ in which the $\log V(\log I)$ curves have only positive curvature.

Several efforts have been made to explain the sign change of the curvature of the CVC's. For example, Ref. 2 explains it with the help of a vortex glass–vortex liquid phase transition. On the other hand, Brant⁴ and Coopersmith⁵ explain this change by taking magnetic flux creep into account by way of the method of Ambegaokar and Galperin,⁶ applied to a study of the effect of fluctuations in Josephson

junctions. In Ref. 7 this phenomenon is explained by taking into account the energy dissipation arising in the motion of vortices by the method of Bardeen and Stefan in the classical flux creep model. But each of these approaches possesses substantial shortcomings. Thus, for example, the vortex liquid–vortex glass phase transition model is valid for bulk superconductors, and its application to films, which is where the CVC measurements are usually made, leads to additional, challenging restrictions. In addition, this model is based on the theory of collective pinning, which is valid in the case of weak pinning centers, but weak pinning and the consequent small critical current are of little interest in practical applications. Use of the Ambegaokar–Galperin equation⁶ to describe the vortex motion is justified. The approach suggested in Ref. 7 does not explain scaling of the CVC's.⁸ Thus, the problem of explaining the sign change of the curvature of the CVC's of high-temperature superconductors remains real.

In the present paper we approach this phenomenon from the point of view of an independent interaction of isolated vortices with sinusoidal pinning potential within the framework of the one-dimensional model.^{9,10} In Refs. 10 and 11 it was shown that this model is useful in the study of flux creep and it allows one, in particular, to explain the anomalous character of the dependence of the effective pinning potential on the temperature. In the present study we consider a more complicated form of the pinning potential corresponding to a collection of inhomogeneities spread out over some distance. The effective pinning centers making the main contribution to vortex pinning have a characteristic size on the order of the coherence length $\xi(T)$. Thus we think that the distance between the sinusoidal pinning centers is significantly larger than $\xi(T)$. In other words, the product $N\xi(T)$, where N is the number of pinning centers, is much less than the film width w . In accordance with this, we can introduce a pinning potential $U(T)$ corresponding to the given type of inhomogeneities. Mathematically, this spatial dependence of the pinning potential is given by the following expression:

$$U(x) = \begin{cases} -U_0 \sin(2\pi(x - kw/N)/\xi), & x \in [kw/N; kw/N + \xi], \\ 0, & x \in [kw/N + \xi; (k+1)w/N], \end{cases} \quad (2)$$

where x is the coordinate of the X axis, and the x axis is located in the film plane and is directed perpendicular to the transport current, and k is an integer taking values in the range from 0 to $N - 1$. In addition, we think that the mean distance between the pinning centers is much less than the penetration depth of the magnetic field, $\lambda(T)$. If this is the case, the pinning centers have no effect on the distribution of the transport current density in the superconductor. This is the actual case in superconductors, where the most efficient pinning centers are grain boundaries whose thickness is significantly less than the size of the grains themselves. In other words, this form of the pinning potential is closer to the actual situation than the usual sinusoidal form.

As was shown in Ref. 10, the sinusoidal pinning centers create potential barriers which depend on the transport current in the following way:

$$U(j) = U_0[(1 - j^2)^{0.5} - j \cos^{-1}j]. \quad (3)$$

This relation is well approximated by the expression $U(j) \approx (1 - j)^{1.5}$ in the limit $j \rightarrow 1$. The time during which the vortex moves in the film consists of two parts: the residence time at the pinning centers, and the time of viscous motion away from them. The time of viscous motion of a vortex in that part of the film that is free from the influence of the pinning centers is given by the usual relation $\tau_f \approx w/\langle v \rangle$, where $\langle v \rangle$ is the mean speed of the vortices. As $j \rightarrow 1$, during which $U(j) \rightarrow 0$, this term begins to make a noticeable contribution to the total residence time of the vortices in the film. The model given allows us to take into account the viscous motion of the vortices, which has considerable influence on the shape of the CVC's. This influence is due to the fact that the appearance of a voltage on the sample implies a substantial decrease of the pinning potential $U(j)$ and, as a consequence, a substantial decrease in the role of flux creep. The residence time at the pinning centers according to the accepted model is given by

$$\tau_c = \omega^{-1} N \exp\left[\frac{U(j)}{k_B T}\right] \left[1 - \exp\left(\frac{-\pi U_0 j w \omega}{k_B T N \xi}\right)\right]^{-1}. \quad (4)$$

As a result, the CVC's can be found with the help of the relation

$$E = Bw/\tau = Bw \left\{ \omega^{-1} N \exp\left[\frac{U(j)}{k_B T}\right] \times \left[1 - \exp\left(\frac{-\pi U_0 j w \omega}{k_B T N \xi}\right)\right]^{-1} + w \eta/J\Phi_0 \right\}^{-1}, \quad (5)$$

where η is the viscosity coefficient of the vortex motion. Using this equation, we can calculate the CVC's for HTSC films at different temperatures, in particular in the interval of interest to us, 70–81 K, for the external magnetic field intensity equal to 4 T.

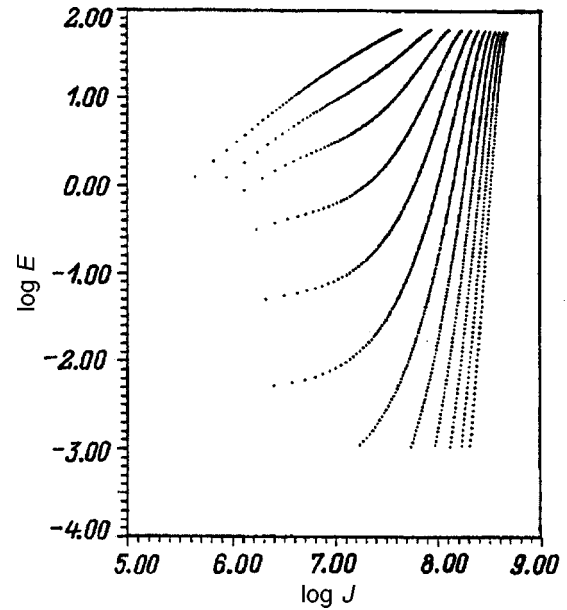


FIG. 1. Theoretical CVC's of a model HTSC sample for temperatures lying in the interval 70–90 K (with a step of 2 K), in an external magnetic field of 4 T.

RESULTS AND DISCUSSION

CVC's, calculated on the basis of Eq. (5) and using parameters of the samples in Ref. 2, are plotted in Fig. 1 on a log–log scale. Since our model is valid for the transport current J , varying within the range from 0 to $J_{c0}(T)$, the CVC's are plotted in this range. We have set $N = 10^2$, which corresponds to the distance between pinning centers, which is equal to $8 \times 10^{-2} \mu\text{m}$. Also, $\omega = 3 \times 10^8 \text{ s}^{-1}$, $J_{c0}(T) = J_{c0}(0)(1 - (T/T_c)^2)$, where $J_{c0}(0) = 10^8 \text{ A/m}^2$ and $T_c = 92 \text{ K}$, $U_0(T) = U_0(0)(1 - (T/T_c)^2)(1 - (T/T_c)^4)^{0.5}$, $U_0(0)/k_B = 25\,000 \text{ K}$. These are the parameter values that are usually given for $\text{YBa}_2\text{Cu}_3\text{O}_{7-x}$ (Refs. 12–14). It is clear from Fig. 1 that all the characteristics have both regions of positive (at low transport currents) and negative curvature (at high currents, at which $J \rightarrow J_{c0}$). The appearance of a segment of the CVC's with negative curvature is due to the decrease of the pinning potential [$U(j) \rightarrow 0$] as $j \rightarrow 1$. In this case the residence time on the pinning centers becomes small in comparison with τ_f . Note that such behavior of the pinning potential $U(j) \rightarrow 0$ as $j \rightarrow 1$ is universal and does not depend on the form of the pinning potential. Thus, the variation of the curvature of the CVC's can be obtained within the given approach not only for the sinusoidal potential, but also for any other potential.

To compare the theoretical characteristics with the experimental to it is necessary to choose a ‘‘window’’ in E and J , in which to carry out a specific experiment. Most often, this window is governed by the sensitivity of the experimental arrangement. To compare our model to experiment, we choose the ‘‘window’’ in conformity with Ref. 2, i.e., $-15 < \log E < 2$. Under such conditions, our CVC's divide into two families: those calculated for temperatures below $T_g = 77.5 \text{ K}$ have only negative curvature, and those calculated for temperatures above T_g have only positive curvature, in

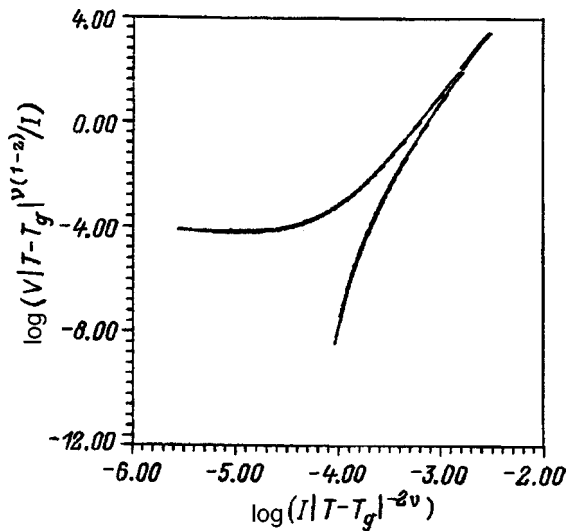


FIG. 2. Scaling of the theoretical CVC's in the temperature interval 70 – 90 K (with a step of 0.4 K) in an external magnetic field $H=4$ T. For the case $\nu=0.6$ and $z=8.5$.

good agreement with Ref. 2. In the vortex liquid–vortex glass phase transition model T_g is the phase transition temperature, while in our model it is the transition temperature from viscous vortex motion to flux creep in the chosen voltage interval. For a more graphic representation of our CVC's, let us transform to other coordinates. Along the ordinate axis we will plot $\log(V/|T-T_g|^{\nu(z-1)})$, and along the abscissa $\log(I/|T-T_g|^{2\nu})$. The coefficients z and ν used in these constructions are determined by the method proposed in Ref. 8. The CVC's are plotted on this scale in Fig. 2 for $z=8.5$ and $\nu=0.7$, the values of these parameters that provide maximum agreement with experiment for the HTSC films with the above-indicated parameters. It is easily seen from this figure that all the CVC's for $T < T_g$ for a curve having the characteristic positive curvature, while for $T > T_g$ they all form a curve having negative curvature. This result is in good qualitative agreement with the corresponding scaling of the CVC's obtained from the experimental data in Ref. 2. Moreover, with growth of the film temperature, the CVC's become quasilinear, which is also in good agreement with the experimental data.

The only difference from Ref. 2 is that the coefficients z and ν for the experimental CVC's are equal respectively to 4.8 and 1.7. In order to construct theoretical CVC's with such coefficients and try to scale them, it is necessary to choose new values for the parameters U_0 , N , and ω . In the given case only the value of N changes, to $N=200$. The characteristic scaling of the theoretical CVC's constructed with the altered parameters is shown in Fig. 3. In this case a somewhat greater degree of smearing is observed than in Fig. 2. Thus, using the experimental scaling coefficients z

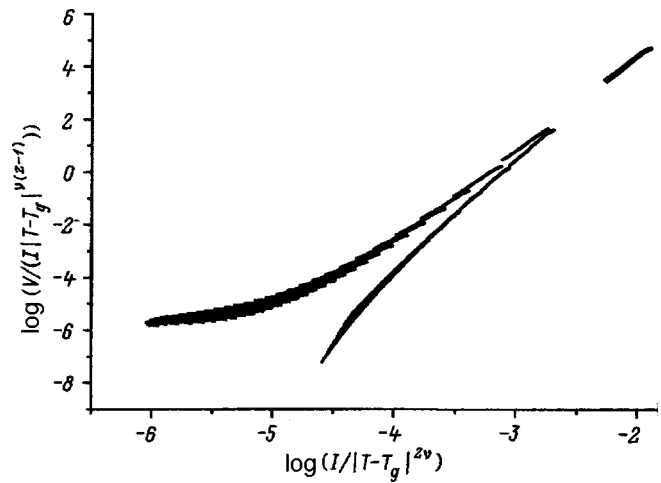


FIG. 3. Scaling of the theoretical CVC's in the temperature interval 70 – 81 K (with a step of 0.4 K) in an external magnetic field $H=4$ T. For the case $\nu=1.7$ and $z=4.8$.

and ν , we can judge the values of the parameters U_0 , N , and ω appropriate to a real sample. Consequently, within the framework of the improved flux creep model it is possible to qualitatively explain the behavior of the experimental CVC's for HTSC films, which is not possible within the usual flux creep model; specifically, the variation of the $\log V(\log I)$ curves with the temperature can be explained by taking the viscous vortex motion into account in the usual flux creep model.

This work was carried out with the financial support of the Scientific Committee of the State Program on Science and Technology (GNTP) ‘‘Current Topics in the Physics of Condensed Media’’ (Project No. 96041) and the Russian Fund for Fundamental Research (Grant No. 97-02-17545).

- ¹T. Matsushita, A. Matsuda, and K. Yanagi, *Physica C* **213**, 477 (1993).
- ²R. H. Koch, V. Foglietti, W. J. Gallagher, G. Koren, A. Gupta, and M. P. A. Fisher, *Phys. Rev. Lett.* **63**, 1151 (1989).
- ³P. W. Anderson and Y. B. Kim, *Rev. Mod. Phys.* **36**, 1, 39 (1964).
- ⁴E. H. Brandt, *Z. Phys. B* **80**, 2, 167 (1990).
- ⁵S. N. Coopersmith, M. Inui, and P. B. Littlewood, *Phys. Rev. Lett.* **64**, 2585 (1990).
- ⁶V. Ambegaokar and B. I. Galperin, *Phys. Rev. Lett.* **22**, 1364 (1969).
- ⁷J. Chen, D. L. Yin, C. Y. Li, and J. Tan, *Solid State Commun.* **89**, 775 (1994).
- ⁸R. H. Koch, V. Foglietti, and M. P. A. Fisher, *Phys. Rev. Lett.* **64**, 2586 (1990).
- ⁹M. R. Beasley, R. Labush, and W. W. Webb, *Phys. Rev.* **181**, 682 (1969).
- ¹⁰T. Matsushita and E. S. Otabe, *Jpn. J. Appl. Phys.* **31**, 1A/B, L33 (1992).
- ¹¹A. N. Lykov, L. Maritato, S. L. Prishpa, and S. V. Zhdanovitch, *J. Supercond.* **7**, 849 (1994).
- ¹²P. Chaudhari, R. H. Koch, R. B. Laibowitz, T. R. McGuire, and R. J. Gambino, *Phys. Rev. Lett.* **58**, 2684 (1987).
- ¹³Y. Yeshurun and A. P. Malozemoff, *Phys. Rev. Lett.* **60**, 2202 (1988).
- ¹⁴M. Tinkham, *Phys. Rev. Lett.* **61**, 1658 (1988).

Translated by Paul F. Schippnick

NMR line shape in anisotropic superconductors in a tilted magnetic field

S. A. Efremova, Yu. N. Proshin, and S. L. Tsarevskii

Kazan State University, 420008 Kazan, Russia

(Submitted August 11, 1997; resubmitted December 23, 1997)

Fiz. Tverd. Tela (St. Petersburg) **40**, 993–997 (June 1998)

NMR line shape has been constructed for anisotropic type-II superconductors in tilted magnetic fields, with inclusion of vortex-lattice magnetic-field nonuniformities and of the skin effect near the superconductor surface. The NMR line shape parameters are shown to change considerably when the external magnetic field changes direction. This makes it possible to obtain more detailed information about the characteristics of a superconductor, in particular, its anisotropy parameter. © 1998 American Institute of Physics. [S1063-7834(98)00806-5]

1. NMR is widely used in studies of the properties of high- T_c superconductors. Interpretation of the NMR line shape should take into account the following three essential factors: first, the homogeneous linewidth, second, the nonuniformity of local magnetic field $\mathbf{h}(\mathbf{r})$ in a superconductor, and third, the specific features of microwave magnetic field penetration a superconductor. Because an ac electromagnetic field penetrates a superconductor to a depth $\sim \lambda$ (λ is the magnetic-field penetration depth in a superconductor),¹ one should take into account the nonuniformity of the magnetic field $\mathbf{h}(\mathbf{r})$ within a narrow near-surface region in the superconductor. The nonuniformity of the vortex-lattice magnetic field in the near-surface layer of a type-II superconductor differs, however, substantially from that of $\mathbf{h}(\mathbf{r})$ in its bulk.² The NMR line shape in type-II superconductors was constructed³ with due account of the real variation of

nonuniformities in the vortex-lattice magnetic field near the superconductor surface, and it was shown that inclusion of these variations affects strongly the NMR line shape parameters. Taking into account surface effects³ may change substantially the conclusions concerning the vortex lattice type and the superconductor parameters which are usually extracted from an analysis of the NMR line shape⁴. The NMR line shape for superconductors was constructed in Ref. 3 with inclusion of surface effects for the case where external uniform magnetic field \mathbf{H} is normal to the superconductor surface and parallel to the c axis of the superconductor. Because high- T_c superconductors are strongly anisotropic, it appears of interest to study the variation of NMR line parameters in external magnetic fields tilted to the superconductor surface. This work presents a calculation of the NMR line shape with inclusion of surface effects as a function of the

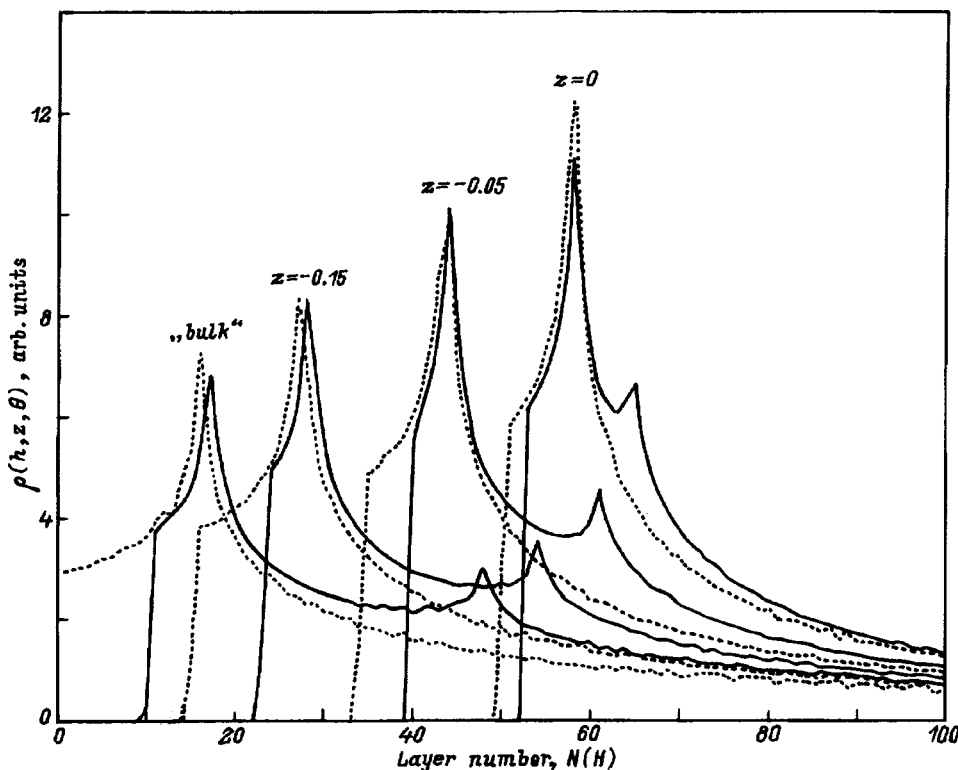


FIG. 1. Distribution function $\rho(h, z, \theta)$ of local magnetic field in a unit cell of the vortex lattice in the superconductor bulk (in arbitrary units). Dotted line corresponds to $\theta=0$. Solid line refers to the $\theta = \pi/6$ case. The bulk case is $z = -5.0$. The horizontal axis plots the field in units of $100(h - h_{\min}) / (H - h_{\min})$.

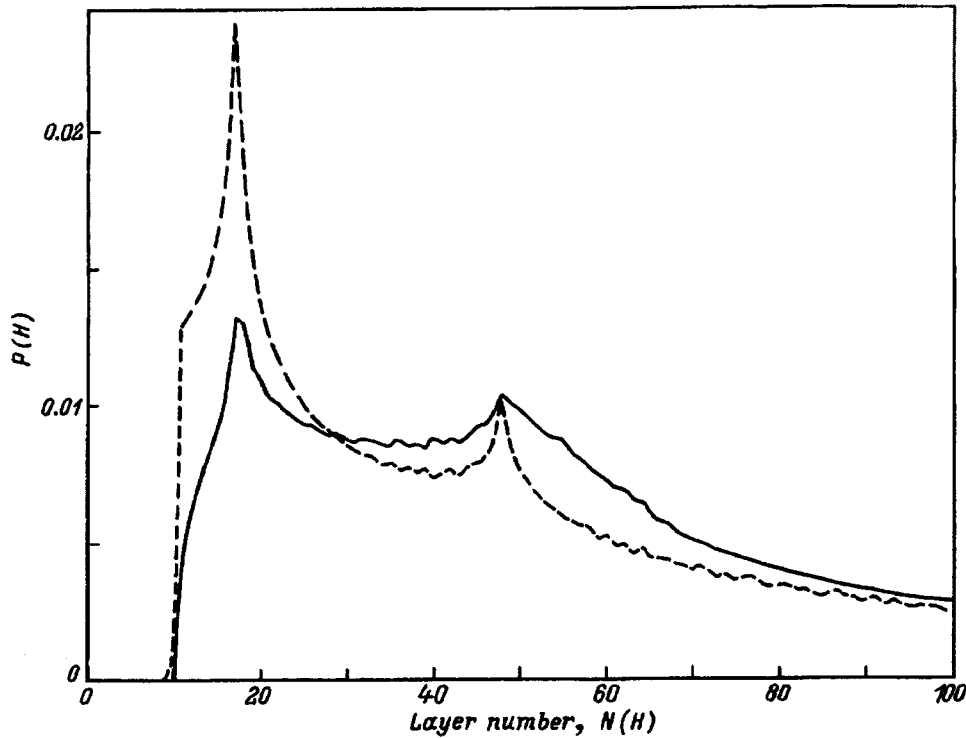


FIG. 2. Absorbed energy vs magnetic field for $\theta = \pi/6$. Dotted line corresponds to the bulk case without inclusion of surface effects. Solid line takes into account surface effects ($\delta = 1, \Delta = 1$). The notation on the horizontal axis is the same as in Fig. 1.

angle θ between the superconductor surface normal and the direction of the external magnetic field \mathbf{H} . It is shown that the line shape is essentially different for different θ .

2. Consider a type-II anisotropic superconductor which occupies a half-space $z < 0$ in an external magnetic field \mathbf{H} tilted at an angle θ between vector \mathbf{H} and the z axis. We assume also that the z axis is parallel to the superconductor axis c . If $H_{c1} < H < H_{c2}$ ($H_{c1, c2}$ are the first and second criti-

cal fields), then the local magnetic field $\mathbf{h}(\mathbf{r}, \theta)$ penetrates into the superconductor in the form of quantized Abrikosov vortices, becomes strongly nonuniform, and assumes short-range order in the case of an anisotropic vortex lattice, whose period is determined by the magnitude of H . The field $\mathbf{h}(\mathbf{r}, \theta)$ can be presented as a Fourier expansion in reciprocal lattice vectors \mathbf{G} . The London equations subject to the corresponding boundary conditions were solved⁵ to obtain ana-

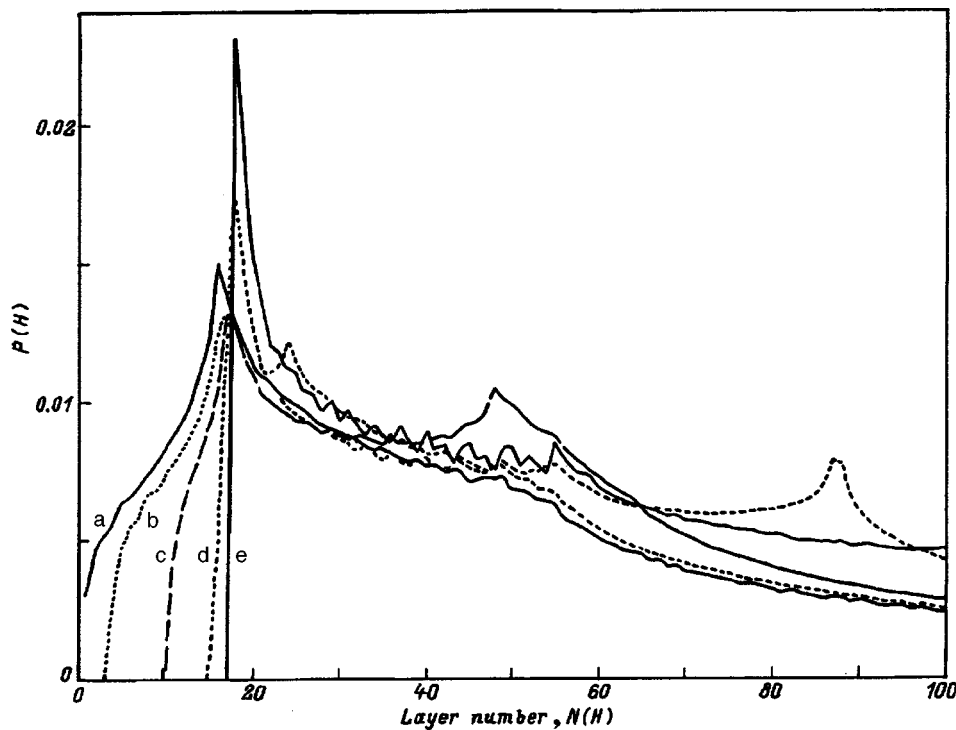


FIG. 3. Absorbed energy vs magnetic field for different angles θ calculated with inclusion of surface effects ($\delta = 1, \Delta = 1$, the skin case): θ : (a) 0, (b) $\pi/12$, (c) $\pi/6$, (d) $\pi/4$, (e) $\pi/3$ and $5\pi/12$. The notation on the horizontal axis is the same as in Fig. 1.

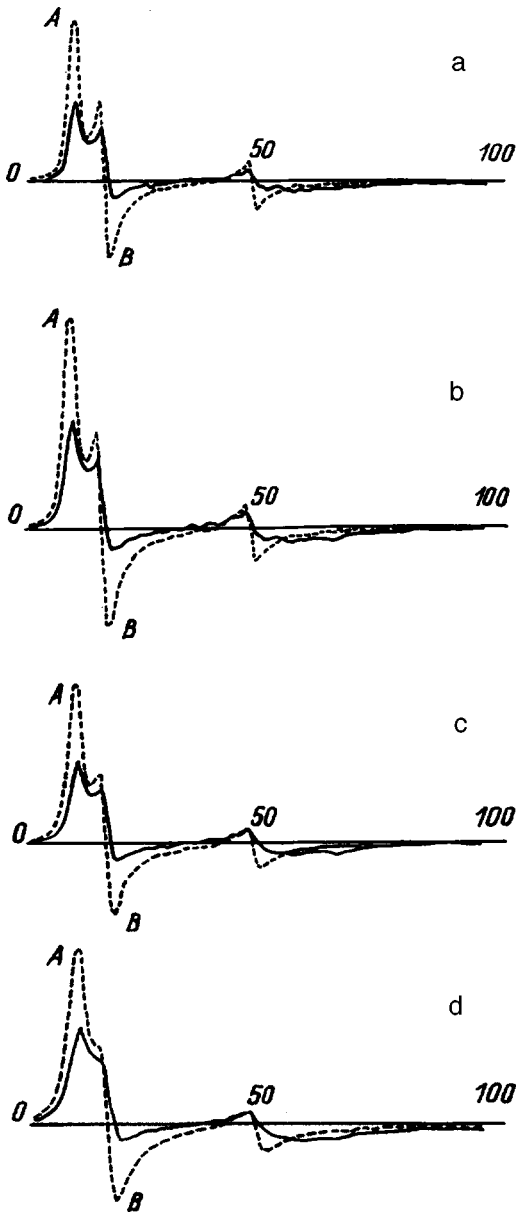


FIG. 4. dP/dH curve for the $\theta = \pi/6$ case. Horizontal line corresponds to $dP/dH=0$, its notation is the same as in Fig. 1. Dotted line is the bulk case. Solid line takes into account surface effects ($\delta=1$, the skin case). Δ : (a) 0.75, (b) 1, (c) 1.25, (d) 1.75. (a) bulk case $A/B=1.99$, skin case $A/B=4.08$; (b) bulk case $A/B=2.15$, skin case $A/B=4.54$; (c) bulk case $A/B=2.16$, skin case $A/B=4.92$; (d) bulk case $A/B=2.26$, skin case $A/B=5.53$.

lytic expressions for the Fourier components of local magnetic field as functions of z and θ , $\mathbf{h}_G(z, \theta)$. The magnetic field distribution $\mathbf{h}(\mathbf{r}, \theta)$ in $z = \text{const}$ sections for a given θ can be reconstructed by summing the Fourier series with the use of the values of $\mathbf{h}_G(z, \theta)$. The next step consists in determining the distribution function $\rho(h, z, \theta)$ of the local magnetic field $h = |\mathbf{h}|$ in a unit cell of the vortex lattice for a layer which is thin compared to λ and is located at a distance z from the superconductor surface. The function $\rho(h, z, \theta)$ was found by calculating the relative number of points in the (x, y) plane of the vortex lattice cell for which the local magnetic field is confined between h and $h + dh$ [$dh = (H - h_{\min})/100$, where $H=2$ is the external field, and the mini-

um field in the superconductor, $h_{\min} = 1.8767$, was determined at a depth $z = -5.0$ (i.e., in its bulk)]. The wings of the function correspond to the maximum of the magnetic field, which is at vortex center, and to the minimum in the valley of the field distribution relief, and the peaks of the function can be identified with the saddle points. The $\rho(h, z, \theta)$ function was analyzed using the magnetic-field distribution maps plotted for different distances from the surface z and different angles θ . The vortex lattice cell is divided into 512×512 points at which $\mathbf{h}(\mathbf{r}, \theta)$ is calculated. Figure 1 presents for illustration $\rho(h, z, \theta)$ curves calculated for some values of z and θ . Here and in what follows we shall be using dimensionless units, viz. distance is measured in units of λ , and magnetic field, in units of Φ_0/λ^2 , where Φ_0 is the magnetic flux quantum. The $\rho(h, z, \theta)$ functions were calculated for a superconductor with an anisotropy parameter $\Gamma = 25$ ($\Gamma = m_3/m_1$, $m_1 = m_2$, m_3 are the principal values of the "mass tensor" introduced to describe the kinetic energy density of superconducting electrons). $\Gamma = 25$ corresponds to the anisotropy of the high- T_c superconductor Y-Ba-Cu-O with $T_c = 90$ K. The local magnetic field distribution $\rho(h, z, \theta)$ was calculated with a step of $\Delta z = 0.05$ from the surface to $z = -0.7$, after which the step was increased, because at a depth of about $\lambda/2$ the $\rho(h, z, \theta)$ function approaches the magnetic field distribution in an unlimited (bulk) superconductor, and practically does not change from $z \leq -0.5$ to $z = -5.0$. As evident from Fig. 1, the local magnetic field distribution varies substantially not only with increasing distance from the superconductor surface but with the tilt angle θ as well. An additional peak appears in the $\rho(h, z, \theta)$ distribution function in the case of a tilted field. Its existence is a consequence of the appearance of saddle points of different height in the magnetic field distribution relief.

3. Our NMR line-shape analysis takes into account that an electromagnetic microwave field penetrating into a superconductor changes both in magnitude and in phase. Because of the screening by superconducting currents, ac field decreases in amplitude while penetrating into a type-II superconductor to a depth $\sim \lambda$, but its phase changes at a considerably larger depth.¹ As a result, when homogeneous broadening Δ is much smaller than the local field spread, a case typical of NMR in a type-II superconductor, the absorbed microwave power turns out to be proportional to the imaginary part of the microwave susceptibility χ'' so that the NMR line shape is dominated by specific features in the local magnetic-field distribution.⁶

Let us calculate the ac magnetic-field power absorbed by resonant nuclear spins confined within a narrow layer z , $z + dz$. Obviously enough, it will be $\propto \exp(2z/\delta)\rho(h, z)dz$. The exponential factor accounts for the exponential decay of the amplitude of the ac magnetic field with distance from the superconductor surface, with δ equal to the penetration depth of an ac magnetic field of frequency ω into a superconductor. We shall assume subsequently that the homogeneous broadening is described by a Lorentzian with a width Δ . The ac field power absorbed by all resonant spins with an isotropic g factor depends on external homogeneous magnetic field H as (see also Ref. 3)

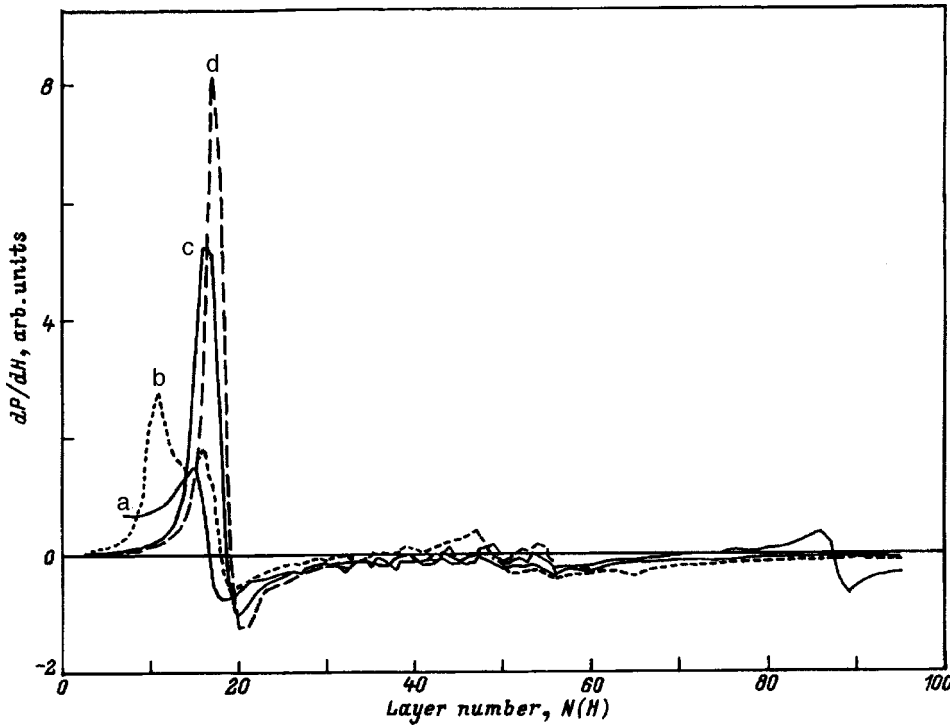


FIG. 5. dP/dH curves calculated for different θ with inclusion of surface effects ($\delta=1, \Delta=1$, skin case), θ : (a) 0, (b) $\pi/12$, (c) $\pi/6$, (d) $\pi/4$. Horizontal line corresponds to $dP/dH=0$, its notation is the same as in Fig. 1.

$$P(H, \theta) = C \int_{-\infty}^{\infty} dh \frac{\Delta}{\Delta^2 + (H-h)^2} \int_0^{\infty} dz \rho(h, z, \theta) \exp(2z/\delta). \quad (1)$$

The constant C is determined by the normalization condition $\int P(H, \theta) dH = 1$.

Figure 2 presents an NMR line shape [absorbed energy $P(H, \theta)$] calculated using Eq. (1) for an anisotropic superconductor with parameters $\Gamma=25, \Delta=1, \delta=1$ for the case of $\theta=\pi/6$. For comparison, the dashed curve shows the NMR line of a superconductor with the same parameters but obtained without taking into account the variation of the nonuniform field with distance from the superconductor surface, i.e., for the case of $\rho(h, z, \theta) = \rho(h, -\infty, \theta)$. We readily see that the inclusion of surface effects changes the NMR line shape for tilted fields similar to the case of a magnetic field H oriented parallel to the z axis. Figure 3 displays NMR lines calculated for different angles θ from 0 to $\pi/2$ with a step of $\pi/12$. We see here a relatively small shift of the high-field peak, and a larger one, of the low-field peak. Tilting the field has a marked effect on the line shape characteristics; indeed, one clearly sees an additional peak, which decreases with increasing θ , to practically disappear at $\theta = \pi/3$. Note that the absorption lines at $\theta = \pi/3$ and $\theta = 5\pi/12$ nearly coincide (i.e., when $\theta \rightarrow \pi/2$).

The changes in microwave absorption are particularly evident in the line shape of the derivative of absorbed energy with respect to magnetic field, dP/dH . Figure 4 shows this line shape, dP/dH , calculated using Eq. (1) for different Δ , both with and without inclusion of local-field variations near the superconductor surface, for instance, for the angle $\theta = \pi/6$. As the parameter Δ describing homogeneous broadening increases, the two narrow low-field lines merge to form a broader one, and the additional broad high-field peak

corresponding to magnetic-field energy absorption near the surface becomes more pronounced. A characteristic feature of all curves is that the NMR-line asymmetry parameter A/B (A/B is the ratio of the main low-field to main high-field peak in the magnetic-field derivative of absorbed energy) increases by about two times, if one takes into account the variation of magnetic field nonuniformities close to the superconductor surface.

Figure 5 shows for comparison NMR dP/dH curves for a superconductor with parameters $\Gamma=25, \Delta=1, \delta=1$ calculated for different angles θ . One clearly sees a sharp increase of the A/B parameter with increasing angle θ . Such pronounced changes in NMR line shape can affect noticeably the conclusions bearing on the vortex lattice type and superconductor parameters, which are usually derived from NMR line-shape analysis. The calculation shows that the nonuniformity in the magnetic field distribution varies noticeably with orientation of the external field \mathbf{H} with respect to the surface of an anisotropic superconductor, so that the NMR line parameters can change noticeably too. Thus NMR turns out to be quite sensitive to the magnetic field distribution in a type-II superconductor.

We note, in conclusion, that when analyzing NMR line shape in anisotropic high- T_c superconductors, one usually does not take into account magnetic field nonuniformities in the near-surface region of a superconductor and the specific features of ac magnetic field penetration into the bulk of the superconductor (e.g., Refs. 7,8); indeed, λ is traditionally obtained using the expression for the second moment of magnetic field distribution in a bulk isotropic superconductor for an equilateral triangular lattice.⁹ Such an analysis yields only an averaged depth of magnetic field penetration into the superconductor without taking into account its anisotropic properties. As seen from the above results (Figs. 3–5), the

experimentally measured NMR line-shape parameters should be essentially different if one includes the specific features of penetration of the nonuniform vortex-lattice magnetic field and the skin effect. Thus an analysis of experimental data for NMR in tilted magnetic fields made within our theory can yield useful information about the parameters of a superconductor ($\lambda, \Gamma, \delta, \Delta, \mathbf{G}$).

We note also that, since our calculations were carried out for a half-space occupied by a superconductor, the data obtained can be used for high- T_c samples representing platelets (films) whose thickness is much less than their length and width, and which are properly oriented in the external magnetic field.

- ¹L. P. Gor'kov and G. M. Éliashberg, *Zh. Éksp. Teor. Fiz.* **54**, 612 (1968) [*Sov. Phys. JETP* **27**, 328 (1968)].
- ²B. I. Kochelaev and E. P. Sharin, *Sverkhprovodimost': (KIAE)* **5**, 1982 (1992).
- ³B. I. Kochelaev, Yu. N. Proshin, and S. L. Tsarevskii, *Fiz. Tverd. Tela (St. Petersburg)* **38**, 3220 (1996) [*Phys. Solid State* **38**, 1758 (1996)].
- ⁴D. MacLaughlin, *Solid State Phys. (Tokyo)* **31**, 1 (1976).
- ⁵V. G. Kogan, A. Yu. Simonov, and M. Ledvij, *Phys. Rev. B* **48**, 392 (1993).
- ⁶B. I. Kochelaev and M. G. Khusainov, *Zh. Éksp. Teor. Fiz.* **80**, 1480 (1983) [*Sov. Phys. JETP* **53**, 759 (1983)].
- ⁷H. Niki, T. Suzuki, S. Tomiyoshi, H. Hentona, M. Omori, T. Kajitani, T. Kamiyama, and R. Igei, *Solid State Commun.* **69**, 547 (1989).
- ⁸M. Mehring, F. Hentsch, H. J. Mattausch, and A. Simon, *Solid State Commun.* **75**, 753 (1990).
- ⁹P. Pincus, A. C. Gossard, V. Jaccarino, and J. H. Wernick, *Phys. Lett.* **13**, 21 (1964).

Translated by G. Skrebtsov

Superconducting gap observed in Raman spectra of $\text{Bi}_2\text{Sr}_2\text{CaCu}_2\text{O}_{8+x}$

O. V. Misochko

Institute of Solid State Physics, Russian Academy of Sciences, 142432 Chernogolovka, Russia
(Submitted December 23, 1997)

Fiz. Tverd. Tela (St. Petersburg) **40**, 998–1001 (June 1998)

Investigation of the temperature behavior of electronic Raman scattering in $\text{Bi}_2\text{Sr}_2\text{CaCu}_2\text{O}_{8+x}$ superconducting crystals indicates the frequency of the mode whose spectral position is customarily used to derive the width of the superconducting gap to be only weakly temperature dependent. Measurements carried out under different resonance conditions can be interpreted as due to spatial dispersion of the superconducting gap. © 1998 American Institute of Physics. [S1063-7834(98)00906-X]

Debates about the superconducting gap started immediately after the discovery of high-temperature superconductivity. Among the various techniques employed in studies of the order parameter, which in the Bardeen–Cooper–Schrieffer model is identical with the superconducting gap, Raman spectroscopy occupies a well-deserved place. The use of Raman spectroscopy for detection of the superconducting gap was proposed theoretically in 1961.¹ The current revival of interest in this technique is reflected in the large number of publications. Most of the relevant papers are discussed in recent reviews dealing with theory² and experiment³ in this area. These efforts are beginning to produce a proper understanding of the mechanism of electronic Raman scattering in superconductors, although the problem of the symmetry and magnitude of the order parameter in high- T_c superconductors is still awaiting solution. The above-mentioned proper understanding of electronic Raman scattering, which is supported by many groups of researchers,^{2,3} includes 1) the absence of scattering threshold and 2) polarization dependence of the position of the peak associated with Cooper-pair breaking. Both these properties are presently regarded as a manifestation of superconducting-gap anisotropy.^{2,3} Note that isotropic s wave pairing can be excluded with a high degree of confidence. At the same time deciding between the anisotropic s or d pairing based on experimental data would be very difficult. Besides the symmetry of the order parameter, the temperature dependence of the superconducting gap likewise still remains unclear. Attempts at measuring the temperature dependence of the superconducting gap in $\text{Bi}_2\text{Sr}_2\text{CaCu}_2\text{O}_{8+x}$ (Bi-2212) by angle-resolved photoemission produced an interesting result, namely, that this temperature dependence is different for gaps measured along the CuO bonds and at an angle of 45° to them.⁴ Raman studies made on a similar crystal revealed deviations from the BCS model for the temperature dependence of the gap determined from the fully symmetric scattering component.⁵ Unfortunately, the energy resolution of the photoemission method is of the order of the superconducting gap itself, and the Raman spectra obtained in Ref. 5 contained the complete set of fully symmetric phonons, whose discrimination is an extremely ambiguous procedure. Moreover, in order to derive the temperature dependence, the spectra had to be multiplied or divided by a

factor determined from the intensity of one of the phonon species present under the assumption that this intensity is temperature independent.⁵

The present work reports a detailed study of the temperature dependence of electronic Raman spectra of a Bi-2212 crystal measured in B_{1g} symmetry. According to some theoretical models, it is this scattering component that reflects the symmetry and magnitude of the superconducting gap.^{2,3} Excitation with the He-Ne laser line permitted us to avoid phonon involvement and, thus, to exclude the ambiguous procedure of spectral deconvolution. Particular attention was paid to the signal/noise ratio in spectra and to their reproducibility.

The studies were made with a triple-grating spectrometer equipped with a multichannel detector. Excitation was by either an Ar⁺ or He-Ne laser (458- and 633-nm wavelength, respectively). The quasi-backscattering geometry was used with the laser beam striking the sample below the Brewster angle, which reduced the Rayleigh component to a minimum and permitted one to approach the laser line more closely. To avoid overheating the sample located in a cryostat, the power density never exceeded 1–5 W/cm². According to Stokes/anti-Stokes ratio measurements, this excluded overheating to within ≈ 10 K. The excitation point (the laser spot diameter was typically $\approx 150 \mu\text{m}$) was monitored with a high precision with the use of a microscope attachment, which enabled excitation in different measurements of the same region in the crystal to within $\approx 10 \mu\text{m}$. Electronic Raman spectra were obtained from freshly prepared ab planes of the crystal which, before placing into the cryostat were properly oriented using a Laue pattern. Magnetic measurements showed the sample to undergo the superconducting transition at $T_c = 89$ K, which evidences close to optimum doping and a nonstoichiometry coefficient $x \approx 0.15$.

When a crystal becomes superconducting, the electronic Raman spectrum undergoes intensity redistribution, which reflects the specific features of the superconducting state. This intensity redistribution is illustrated by Fig. 1, which displays B_{1g} spectra measured in $x'y'$ polarization in the normal and superconducting states under excitation with a $\lambda = 633$ -nm laser line. The depression of scattering at low frequencies with decreasing temperature is connected with

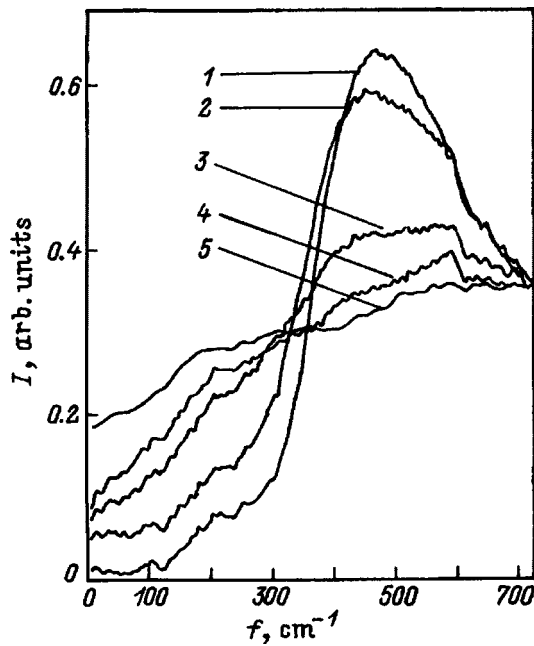


FIG. 1. Raman scattering spectra (B_{1g} symmetry) of Bi-2212 crystals obtained under excitation in the basal ab plane with a He-Ne laser at different temperatures, both above and below the superconducting point $T_c = 89$ K. T (K): 1 — 5, 2 — 55, 3 — 75, 4 — 90, 5 — 295.

the opening of the superconducting gap,¹⁻³ whereas the peak which is not observed in the normal state is assigned to the new scattering channel associated with Cooper-pair breaking². An analysis of the temperature behavior of the pair-breaking peak revealed that its integrated intensity grows with decreasing temperature, although its frequency is practically temperature independent. While locating a broad peak can be ambiguous, the point at which the superconducting spectra intercept the normal-state spectrum practically does not depend on temperature (see Fig. 1). Because the maximum can lie only to the right of this point, one can readily estimate the smallest possible gap at T_c as being only smaller by 25% than that detected at 5 K. In actual fact, the superconducting gap derived from the position of the pair-breaking peak maximum is wider, and the ratio $\Delta(T_c)/\Delta(T = 5 \text{ K})$ is smaller (see Fig. 2). In any case, our data indicate that the pair-breaking peak does not form in the low-frequency domain. The temperature dependence of integrated intensity (measured as the excess spectral weight at high frequencies when comparing a superconducting spectrum obtained at a given temperature with the normal-state spectrum) offers supportive evidence for the superconducting condensate being responsible for the pair-breaking peak, because the experimental points fit well to the temperature dependence of the superconducting condensate density in the two-liquid model. An analysis of the intensity redistribution shows that the growth in intensity at high frequencies for a given excitation is compensated by a depression of scattering at low energies. Such a behavior confirms a relation between the pair-breaking peak and formation of the superconducting gap and is explained by the shift toward higher energies of the states expelled from the gap region, which results in divergence of the density of states at the energy equal to the

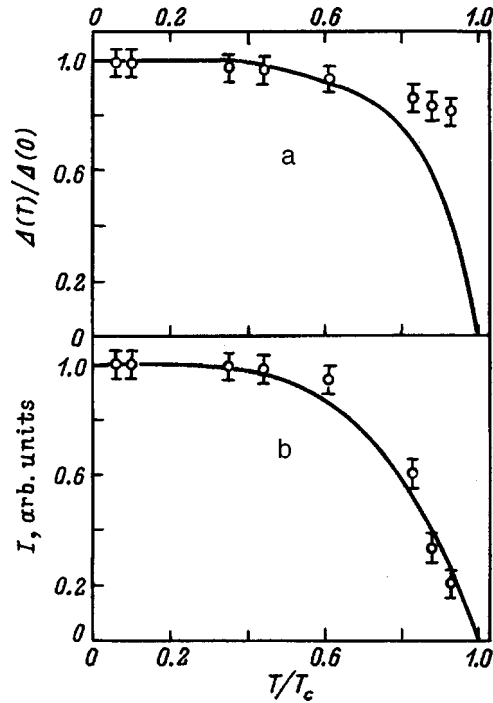


FIG. 2. Temperature dependence of the position of the maximum (a) and relative integrated intensity (b) of the pair-breaking peak observed in B_{1g} symmetry. Solid lines relate to (a) the temperature dependence of the superconducting gap (BCS model) and (b) superconducting condensate density (two-liquid model). Open circles - experiment.

superconducting gap. Note that the spectral weight “lost” at low frequencies in our experiments coincides, within experimental accuracy, with the excess weight appearing in the formation of the peak. This indicates that the sum rule in inelastic light scattering occurring at a given polarization and given resonance conditions is satisfied. On the other hand, the absence of a temperature dependence of the peak frequency gives one grounds to doubt whether this peak is a *measure* of the superconducting gap. Indeed, a comparison of experimental data with BCS predictions reveals serious discrepancies, particularly close to the critical temperature. This comparison is illustrated in Fig. 2 by the behavior of the superconducting gap observed in the given polarization under the assumption that 2Δ is the position of the pair-breaking peak maximum. The superconducting gap determines the Cooper-pair binding energy, and its independence of temperature implies that pairs have a finite binding energy directly at T_c . Moreover, a comparison of spectra obtained at room temperature and above the superconducting transition (90 K) suggests that the peak begins to form before the crystal has become superconducting. This effect exists apparently in other classes of high- T_c superconductors as well,⁶ but its detection is made difficult by the presence of strong phonon scattering which we avoided by making use of the resonant properties of scattering studied earlier⁷. The formation of the pair-breaking peak before the onset of superconductivity may evidence unusual properties of the normal state, although, considering its closeness to T_c , it appears more reasonable to attribute it to the fluctuation region which is broader here than in conventional superconductors.

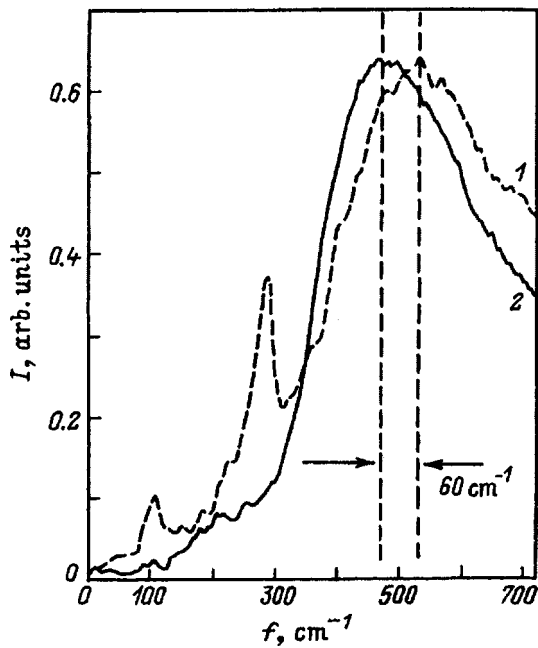


FIG. 3. Comparison of low-temperature Raman spectra ($T=5$ K) of a Bi-2212 crystal obtained under different laser excitations. For convenience, the spectra are normalized to match their maxima in intensity. λ (nm): 1 — 458, 2 — 633.

A new and quite unexpected observation is the existence of a scattering threshold observed in superconducting state, which is demonstrated by the low-temperature spectrum ($T=5$ K) in Fig. 1. The electronic Raman scattering intensity is zero within experimental accuracy, from the lowest detectable frequencies (≈ 10 cm^{-1}) to ≈ 100 cm^{-1} . For optimally doped Bi-2212 crystals, one usually observes in this polarization a power-law growth of intensity, $I \propto \omega^3$, in the low-energy part of the spectrum, which is believed by some authors^{2,3} to indicate d wave pairing.

To make possible comparison of our data with the results quoted by other researchers, we switched to another ($\lambda=458$ nm) excitation (most of the available data were obtained by using the Ar^+ laser blue lines for excitation). The results thus obtained are displayed in Fig. 3, and their comparison with earlier spectra³ measured for similar crystals shows them to be identical. The cubic dependence in the low-frequency domain, the pair-breaking peak position, and even the frequencies and relative intensities of the phonon modes coincide with a good enough accuracy. A comparison of two spectra taken in fully identical conditions, except for the laser wavelength, in Fig. 3 indicates that the change in excitation affects considerably the spectral response, with a change evident not only in the position of the peak maximum but in the low-frequency wing of the peak as well.

Although none of the current theories of electronic Raman scattering in superconductors include resonance terms, taking them into account would hardly improve the fit to the observed effect, because these terms are responsible for scattering intensity and not for the shape and position of a spectral mode.³ The explanation lies most likely in different optical penetration depths for different laser lines. As a result, the wave vector range probed in different resonance condi-

tions is different, and what we see is actually the same excitation but with a different wave vector.⁸ An estimate made based on available data⁹ shows that under red excitation ($\lambda=633$ nm) the penetration depth is 25–30% less than under the blue one ($\lambda=458$ nm), and that the wave vector range involved is, accordingly, larger in the same proportion. It appears pertinent to note here that in high- T_c superconductors the region in k space where the gap was determined is large compared to the Raman-probed wave-vector interval, because the coherence length is small. The observed dependence of the pair-breaking peak frequency on excitation wavelength can be understood (if one follows the generally accepted relation^{1–3} between the peak position and the width of the superconducting gap) as a dependence of the gap not only on the direction in k space^{2,3} (angular dependence) but on the absolute magnitude of the wave vector as well. And if the frequency dependence of scattering in this symmetry at low energies does indeed reflect the dominant kind of pairing (the existence of a threshold for s wave pairing and its absence and cubic growth for d pairing), it may be conjectured that in different layers of the Fermi sphere electrons are paired in different channels. Such an analysis could resolve the existing controversy, where different experiments,^{10,11} each apparently faultless, suggest different symmetries for the electron pairs responsible for superconductivity.

To conclude, a careful study of the temperature dependence of electronic Raman scattering spectra has revealed that the behavior of the frequency of the pair-breaking peak, whose position is usually employed to derive the superconducting gap width, differs strongly from BCS predictions. The temperature dependence of the intensity of this peak confirms that it can be associated with breaking of the Cooper pairs forming the superconducting condensate. A comparison of the positions of this peak and of its spectral shape obtained under different laser excitations suggests that while being anisotropic (the angular dependence), the superconducting gap depends also on the absolute magnitude of the wave vector, $|k - k_F|$, which results in spatial dispersion of the gap.

The author expresses gratitude to E. Ya. Sherman for fruitful discussions and to M. P. Kulakov for providing the single crystals.

¹A. A. Abrikosov and L. A. Afanas'ev, Zh. Éksp. Teor. Fiz. **40**, 262 (1961) [Sov. Phys. JETP **13**, 179 (1961)].

²T. P. Devereau and D. Einzel, Phys. Rev. B **51**, 16336 (1995).

³D. Einzel and R. Hackl, J. Raman Spectrosc. **27**, 307 (1996).

⁴R. J. Kelley, J. Ma, G. Margaritondo, and M. Onellion, Phys. Rev. Lett. **71**, 4051 (1993).

⁵M. Boekholt, M. Hobbmann, and G. Guntherodt, Physica C **175**, 127 (1991).

⁶F. Slakey, M. V. Klein, J. P. Rice, and D. M. Ginsberg, Phys. Rev. B **42**, 2643 (1990).

⁷O. V. Misochko and A. Kh. Arslanbekov, Mod. Phys. Lett. B **6**, 1137 (1992).

⁸O. V. Misochko and E. Ya. Sherman, Physica C **222**, 219 (1994).

⁹V. K. Kelly, P. Barboux, J. M. Tarascon, and D. E. Aspnes, Phys. Rev. B **40**, 6797 (1989).

¹⁰D. J. Van Harlingen, Rev. Mod. Phys. **67**, 515 (1995).

¹¹A. G. Sun, D. A. Gajewski, M. B. Maple, and R. C. Dynes, Phys. Rev. Lett. **72**, 2267 (1994).

SEMICONDUCTORS AND INSULATORS

Ground-state characteristics of an acceptor center in wide-gap semiconductors with a weak spin-orbit coupling

A. V. Malyshev, I. A. Merkulov, and A. V. Rodina

A. F. Ioffe Physicotechnical Institute, Russian Academy of Sciences, 194021 St. Petersburg, Russia
(Submitted October 16, 1997)

Fiz. Tverd. Tela (St. Petersburg) **40**, 1002–1009 (June 1998)

Spin-orbit splitting, strain-potential constants, and the g factor of the acceptor-center ground state described by a superposition of a Coulomb and a central-cell potential have been calculated for wide-band-gap semiconductors, such as GaN. Analytical expressions for these parameters, which depend only on the light- to heavy-hole mass ratio, have been obtained within the zero-range potential model. It is shown that the differences between these parameters for the limiting cases of purely Coulomb and zero-range potentials do not exceed 7%, thus permitting one to use for estimates simple analytical expressions. Calculation of the acceptor-center ground state made for the hexagonal modification of GaN suggests a strong anisotropy of the g factor, whereas measurements yield a practically isotropic value of g close to that of a free electron. This contradiction is removed if a spontaneous strain due to the Jahn-Teller effect appears perpendicular to the C_6 axis of the crystal near the acceptor center. © 1998 American Institute of Physics. [S1063-7834(98)01006-5]

It is well known that the ground state of the acceptor-bound hole in cubic semiconductors is fourfold-degenerate and has a total angular momentum of $3/2$.¹ In GaAs-type semiconductors the spin-orbit interaction energy is, as a rule, large compared to the acceptor binding energy, so that the bound-state wave function is dominated by contributions of the light- and heavy-hole subbands. The acceptor-state wave functions in k representation for this limiting case were found, for instance, in Refs. 2–4. For Si and a number of wide-band-gap semiconductors (GaN, AlN) the depth of acceptor states is comparable to or even exceeds the valence-band spin-orbit splitting Δ_{so} . For instance, for GaN, the band gap $E_G = 3.4$ eV (Ref. 5), the acceptor binding energy $E_a \geq 200$ meV (Ref. 6), and $\Delta_{so} = 12$ meV (Ref. 7). In this case the wave function of the acceptor-bound hole contains a noticeable contribution of the spin-orbit-split band states. In Ref. 2, calculation of the ground-state wave function of a Coulomb acceptor was made in spherical approximation for two limiting cases, namely, infinitely large and zero spin-orbit splitting. The objective of this work is to extend the method developed in Ref. 2 to the case where the spin-orbit interaction energy is finite but small compared to the binding energy of the acceptor-bound hole, and the attractive potential is a superposition of a long-range Coulomb and a short-range central-cell potential. Calculations will be carried out for wurtzite acceptor centers in gallium nitride. The hexagonal (noncubic) symmetry of this compound will be taken into account within the simplest model of valence-band rearrangement under an effective strain acting along the $[111]$ axis, which is the symmetry axis C_6 of a hexagonal crystal.¹

The paper will be organized as follows. In Section I we shall find acceptor-state wave functions in the absence of

spin-orbit interaction and strain. These functions will be used in Section II to calculate the spin-orbit coupling and strain potential constants for an acceptor-bound hole. In the limiting case considered here, these parameters determine uniquely the sublevel structure of the acceptor ground state. In Section III, the ground-state wave functions will be employed to calculate the g -factor tensor for an acceptor-bound hole. The symmetry considerations and the sign of the effective strain alone lead one to a conclusion that the \hat{g} tensor of this hexagonal crystal should be strongly anisotropic. Experimental measurements yield, however, a practically isotropic bound-hole g factor.⁶ This is attributed to a large spontaneous strain in the vicinity of the acceptor center, which is induced by the Jahn-Teller effect.

1. ACCEPTOR GROUND-STATE WAVE FUNCTIONS

For wurtzite crystals, similarly to diamond semiconductors, a hole in the vicinity of the Brillouin zone center may be approximately considered as a quasi-particle with an internal orbital momentum $l = 1$ and a spin $S = 1/2$.¹ The actual form of the wave functions and the effective masses of such quasi-particles depend on the relative magnitude of the kinetic energy

$$\hat{H}(\mathbf{k}) = \frac{\hbar^2}{2m_0} [(\gamma_1 + 4\gamma)k^2 - 6\gamma(\mathbf{k} \cdot \hat{\mathbf{I}})^2], \quad (1)$$

spin-orbit interaction energy

$$\hat{H}_{so} = -\frac{2}{3}\Delta_{so}(\hat{\mathbf{I}}\hat{\mathbf{S}}), \quad (2)$$

and the spin splitting energy of hole levels in a hexagonal crystal field, which may be considered as resulting from the action of an effective strain along the C_{6v} axis:

$$\hat{H}_d = -(a+2b)\text{Sp}(\hat{\varepsilon}^0) + 3b(\hat{I}_\alpha \hat{\varepsilon}_{\alpha\beta}^0 \hat{I}_\beta). \quad (3)$$

Here m_0 is the free-electron mass, \mathbf{k} is the hole wave vector, γ_1 and γ are the Luttinger parameters⁸, a and b are the strain potential constants (we use here the spherical model: $\gamma_2 = \gamma_3 = \gamma$; $b = d/\sqrt{3}$), and Δ_{so} is spin-orbit splitting energy of the valence band in the absence of crystal field. The effective strain tensor $\hat{\varepsilon}^0$ is chosen such that the spectrum of states thus obtained for a zero wave vector \mathbf{k} coincides with the real spectrum of the crystal. This can be most conveniently done by aligning the z axis with the six-fold axis and by assuming that the effective strain has only one nonzero component $\varepsilon_{zz}^0 = -\Delta_{cr}/3b$, where Δ_{cr} is the valence-band splitting for $\mathbf{k}=0$ in the absence of spin-orbit interaction. Real valence-band splittings near the zone center can be written as the difference between the eigenvalues of the Hamiltonian

$$\begin{aligned} \hat{H}_6(\mathbf{k}) = & \frac{\hbar^2}{2m_0} [(\gamma_1 + 4\gamma)k^2 - 6\gamma(\mathbf{k} \cdot \hat{\mathbf{I}})^2] - \frac{2}{3}\Delta_{so}(\hat{\mathbf{I}}\hat{\mathbf{S}}) \\ & - (a+2b)\text{Sp}(\hat{\varepsilon}^0) - \Delta_{cr}\hat{I}_z^2. \end{aligned} \quad (4)$$

For $\mathbf{k}=0$, these splittings are related to Δ_{so} and Δ_{cr} through¹

$$\begin{aligned} E_1^0 - E_{2,3}^0 = & -\frac{1}{2}[(\Delta_{cr} + \Delta_{so}) \\ & \mp \sqrt{(\Delta_{cr} + \Delta_{so})^2 - (8/3)\Delta_{cr}\Delta_{so}}]. \end{aligned} \quad (5)$$

Here E_1^0 is the energy of the Γ_9 term, and $E_{2,3}^0$ are those of the Γ_7 terms.

Consider a shallow acceptor level whose binding energy E_a is small compared to the gap width E_G ($E_a \ll E_G$) while being large compared to Δ_{so} and Δ_{cr} . Then, in the first stage of our calculations, we can neglect the crystal-field and spin-orbit splittings and find the ground-state wave functions of the acceptor center in terms of a three-band Hamiltonian $H(\mathbf{k})$ describing a doubly degenerate subband of heavy holes with a mass $m_h = m_0/(\gamma_1 - 2\gamma)$ and a light-hole subband with masses $m_l = m_0/(\gamma_1 + 4\gamma)$. After this, the spin-orbit and crystal-field splittings of the acceptor level can be found by perturbation theory.

Following Ref. 2, we shall look for the wave function of a localized hole in k representation. Neglecting spin-orbit interaction and strain, we write the Hamiltonian of such a hole in the form

$$\hat{H}_a(\mathbf{k}) = \hat{H}(\mathbf{k}) + \hat{V}(\mathbf{k}, \mathbf{k}'), \quad (6)$$

where $\hat{V}(\mathbf{k}, \mathbf{k}')$ is the integral potential-energy operator representing a superposition of a long-range Coulomb potential and a short-range central-cell potential, which is approximated by a zero-range potential. This operator is presented in explicit form, for instance, in Refs. 3 and 4.

Neglecting the spin \mathbf{S} , the total angular momentum of a localized hole \mathbf{F} is a sum of the angular momentum of internal orbital motion \mathbf{I} and of that of orbital motion around the impurity center \mathbf{L} ($\mathbf{F} = \mathbf{I} + \mathbf{L}$). The multiplicity of degeneracy

of the acceptor ground state coincides with that of states at the top of the valence band,¹ so that $F=I=1$. Under these conditions, the wave function of a magnetic sublevel with projection $F_z=M$ can be written²

$$\Psi_{FM}(\mathbf{k}) = [\hat{\Lambda}_h(\mathbf{k})f_h(\mathbf{k}) + \hat{\Lambda}_l(\mathbf{k})f_l(\mathbf{k})]u_M, \quad (7)$$

where u_M is the Bloch basis function of the top of the valence band corresponding to $I_z=M$, $\hat{\Lambda}_{h,l}(\mathbf{k})$ are projection operators acting on heavy- and light-hole states, which can be presented explicitly in the form

$$\Lambda_h(\mathbf{k}) = \frac{(\mathbf{k} \cdot \hat{\mathbf{I}})^2}{k^2}, \quad \Lambda_l(\mathbf{k}) = \hat{E} - \frac{(\mathbf{k} \cdot \hat{\mathbf{I}})^2}{k^2}, \quad (8)$$

where \hat{E} is a 3×3 identity matrix. In spherical approximation, functions $f_{h,l}(k)$ depend only on wave-vector modulus k and satisfy the normalization condition [the crystal volume is taken equal to $(2\pi)^3$]:

$$\frac{4\pi}{3} \int_0^\infty [2f_h^2(k) + f_l^2(k)]k^2 dk = 1. \quad (9)$$

The squared moduli $|f_{h,l}(k)|^2$ have the meaning of distribution functions of the acceptor ground state over valence-subband states and momenta. Determination of the explicit form of the wave function Ψ_{FM} , which is the eigenfunction of Hamiltonian (6), reduces to solution of coupled integral equations for $f_h(k)$ and $f_l(k)$:

$$\begin{aligned} \left[\frac{\hbar^2 k^2}{2m_h} + E_a \right] f_h(k) = & \frac{e^2}{6\pi^2 \kappa} \left[\int \frac{d^3 \mathbf{q}}{(\mathbf{k}-\mathbf{q})^2} f_h(q) \right. \\ & \times [2 + P_2(\cos \Theta)] + \int \frac{d^3 \mathbf{q}}{(\mathbf{k}-\mathbf{q})^2} f_l(q) \\ & \left. \times [1 - P_2(\cos \Theta)] \right] + A, \\ \left[\frac{\hbar^2 k^2}{2m_l} + E_a \right] f_l(k) = & \frac{e^2}{6\pi^2 \kappa} \left[2 \int \frac{d^3 \mathbf{q}}{(\mathbf{k}-\mathbf{q})^2} f_h(q) \right. \\ & \times [1 - P_2(\cos \Theta)] + \int \frac{d^3 \mathbf{q}}{(\mathbf{k}-\mathbf{q})^2} f_l(q) \\ & \left. \times [1 + 2P_2(\cos \Theta)] \right] + A, \end{aligned} \quad (10)$$

where e is the absolute value of electronic charge, κ is the dielectric permittivity of the medium, $P_2(\cos \Theta) = P_2(\mathbf{k}\mathbf{q}/kq)$ is the Legendre polynomial, and constant A describes the action of the short-range potential^{3,4}. For a Coulombic acceptor, $A=0$, and the set (10) coincides with the coupled equations obtained in Ref. 2. Solution of this set of equations yields the eigenenergy and wave functions of the Coulomb-acceptor ground state. If the attractive potential does not have a Coulomb component, system (10) describes the acceptor ground-state wave functions in the zero-range

potential model, and can be solved analytically⁹ to yield

$$f_h(k) = a_B^{3/2} \frac{N}{(ka_B)^2 + \varepsilon}, \quad f_l(k) = a_B^{3/2} \frac{N\beta}{(ka_B)^2 + \beta\varepsilon},$$

$$N = \frac{\varepsilon^{1/4}}{\pi} \sqrt{\frac{3}{2 + \beta\sqrt{\beta}}}, \quad (11)$$

where $\beta = m_l/m_h$, $\varepsilon = E_a/E_B$, $E_B = e^4 m_h / 2\kappa\hbar^2$, $a_B = \kappa\hbar^2 / e^2 m_h$, and $A = NE_B a_B^{3/2}$. In a general case, parameter A is determined from the normalization condition (9) for the given binding energy E_a (determined from experiment). Our method of numerical solution of this system and of calculation of constant A is described in detail in Refs. 3 and 4.

To facilitate further analysis, the wave function $\Psi_{FM}(\mathbf{k})$ can be conveniently expressed through eigenfunctions of the orbital momentum \mathbf{L} and angular momentum \mathbf{I} :

$$\Psi_{FM}(\mathbf{k}) = f_0(k) Y_{00}(\mathbf{k}/k) u_M$$

$$+ f_2(k) \sum_{m,\mu} \langle 2m1\mu || 211M \rangle Y_{2m}(\mathbf{k}/k) u_{\mu}, \quad (12)$$

where $Y_{00}(\mathbf{k}/k)$ and $Y_{2m}(\mathbf{k}/k)$ are eigenfunctions of the angular momentum operator (spherical functions), $\langle 2m1\mu || 211M \rangle$ is the Clebsch–Gordan coefficient,¹⁰ and $f_0(k)$ and $f_2(k)$ are wave function components corresponding to orbital momenta 0 and 2 and related to functions $f_{h,l}$ through

$$f_0(k) = \frac{\sqrt{4\pi}}{3} [2f_h(k) + f_l(k)],$$

$$f_2(k) = -\frac{\sqrt{8\pi}}{3} [f_h(k) - f_l(k)]. \quad (13)$$

2. SPIN-ORBIT SPLITTING AND STRAIN-POTENTIAL CONSTANTS FOR AN ACCEPTOR

Using Eqs. (12) and (13), one can readily find the matrix elements of the spin-orbit and deformation Hamiltonians coupling ground-state sublevels. The corresponding truncated Hamiltonians coincide in form with (2) and (3):

$$\hat{H}'_{so} = -\frac{2}{3} \tilde{\Delta}_{so} (\hat{\mathbf{F}}\hat{\mathbf{S}}), \quad (14)$$

$$\hat{H}'_d = -(a + 2\tilde{b}) \text{Sp}(\hat{\varepsilon}^0) + 3\tilde{b} (\hat{F}_\alpha \hat{\varepsilon}_{\alpha\beta}^0 \hat{F}_\beta)$$

$$= -(a + 2\tilde{b}) \text{Sp}(\hat{\varepsilon}^0) - \tilde{\Delta}_{cr} F_z^2, \quad (15)$$

with the renormalized spin-orbit interaction constant $\tilde{\Delta}_{so}$, crystal-field constant $\tilde{\Delta}_{cr} = -3\tilde{b}\varepsilon_{zz}^0$, and strain-potential constants \tilde{b} , \tilde{d} given by

$$x_{so} = \frac{\tilde{\Delta}_{so}}{\Delta_{so}} = \left[\langle f_0^2(k) \rangle - \frac{1}{2} \langle f_2^2(k) \rangle \right] = \frac{4\pi}{3} [\langle f_h^2(k) \rangle$$

$$+ 2\langle f_h(k)f_l(k) \rangle], \quad (16)$$

$$x_{cr} = \frac{\tilde{\Delta}_{cr}}{\Delta_{cr}} = \frac{\tilde{b}}{b} = \left[\langle f_0^2(k) \rangle + \frac{1}{10} \langle f_2^2(k) \rangle \right] = \frac{2}{5}$$

$$+ \frac{4\pi}{5} [\langle f_h^2(k) \rangle + 2\langle f_h(k)f_l(k) \rangle]. \quad (17)$$

Here the angular brackets denote integration in modulus of the wave vector: $\langle F(k) \rangle = \int_0^\infty F(k) k^2 dk$. Note that the acceptor constant a is not renormalized in this approximation and is equal to the band constant.

Since the strain-induced and spin-orbit splitting energies of the acceptor ground state are small compared to the distances to the nearest excited acceptor level, finding the corrections to acceptor energies and wave functions in the presence of these interactions reduces to determination of the eigenvalues and eigenfunctions of the Hamiltonian

$$\hat{H}' = \hat{H}'_{so} + \hat{H}'_d. \quad (18)$$

Thus Eq. (5), after substitution of the renormalized constants $\tilde{\Delta}_{so}$ and $\tilde{\Delta}_{cr}$, will yield the splittings of the ground-state sublevels of the acceptor-bound hole.

The strain-potential constants (17) and spin-orbit splitting constant (16) were calculated for a chosen acceptor using the wave functions $f_{h,l}(k)$ found numerically for the given binding energy (type of impurity) and semiconductor type by the technique described in Sec. 1. The dependence of the quantities x_{so} and x_{cr} on acceptor binding energy in GaN was calculated for the Luttinger parameters $\gamma_1 = 2.18$ and $\gamma = 0.85$, which were determined in spherical approximation in heavy-hole mass for two mutually perpendicular directions, namely, along the wurtzite axis, $z || C_{6v}$, $m_h^|| = 2.03$, and in the xy plane, $m_h^\perp = 0.33$ (Ref. 7). In spherical approximation, these quantities are related to the Luttinger parameters through $m_h^|| = 1/(\gamma_1 - 2\gamma)$ and $m_h^\perp = 1/(\gamma_1 + \gamma)$.¹ For the dielectric permittivity we used in the calculations $\kappa = 9.5$ (Ref. 12). The full set of the parameters used in the calculations is given in Table I.

For a purely Coulombic acceptor ($E_a = 199.4$ meV), $x_{so} = 0.67$, and $x_{cr} = 0.8$. As the contribution of the central-cell attractive potential increases (i.e., as the binding energy E_a increases), these quantities decrease monotonically to reach 0.65 and 0.79, respectively, for $E_a = 500$ meV. As E_a increases still more, they approach their lower limits, namely, $x_{so} = 0.63$ and $x_{cr} = 0.78$, which were found analytically in the zero-range potential model by means of the functions (11):

$$x_{so} = \frac{1 + \sqrt{\beta} + 4\beta}{(2 + \beta\sqrt{\beta})(1 + \sqrt{\beta})}, \quad (19)$$

TABLE I. GaN parameters used in the calculations.

$m_h^ $ (Ref. 7)	m_h^\perp (Ref. 7)	γ_1	γ	κ	\varkappa (Ref. 12)	Δ_{so} (Ref. 7)	Δ_{cr} (Ref. 7)
2.03	0.33	2.18	0.85	0.017	9.5	12	37.5

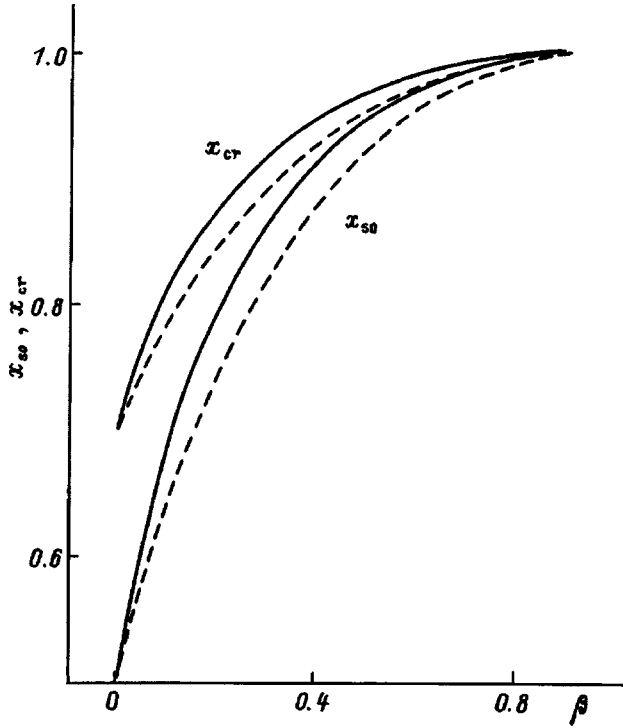


FIG. 1. Dependence of $x_{so} = \tilde{\Delta}_{so}/\Delta_{so}$ and $x_{cr} = \tilde{\Delta}_{cr}/\Delta_{cr} = \tilde{b}/b$ on the light/heavy hole-mass ratio $\beta = m_l/m_h$ for the two limiting cases of a Coulombic acceptor (solid lines) and an acceptor described by a zero-range potential (dashed lines).

$$x_{cr} = \frac{7 + 7\sqrt{\beta} + 12\beta + 2\beta\sqrt{\beta} + 2\beta^2}{5(2 + \beta\sqrt{\beta})(1 + \sqrt{\beta})}. \quad (20)$$

Expression (19) was derived earlier (Ref. 13). As evident from Eqs. (19) and (20), in the zero-range potential model the spin-orbit splitting and strain-potential constants do not depend on acceptor binding energy. The difference between these parameters of GaN for a Coulombic acceptor and a deep impurity center described by the same zero-range potential does not exceed 7%. Therefore Eqs. (19) and (20) can be used to estimate the spin-orbit splitting and strain-potential constants in semiconductors with substantially different Luttinger parameters.

This possibility is illustrated in Fig. 1 comparing the constants x_{so} and x_{cr} calculated for the two limiting cases of a Coulombic acceptor (solid lines) and an acceptor described by a zero-range potential (dashed lines) throughout the light-to-heavy-hole mass-ratio interval covered. The differences between these models are largest for the mass ratio $\beta \approx 0.1$ and are about 7% for x_{so} and 4% for x_{cr} .

Thus the analytical expressions (19) and (20) for an acceptor described by a zero-range potential yield a good estimate for the spin-orbit splitting and deformation potential constants of a Coulombic acceptor. For acceptors with a binding energy exceeding the Coulomb energy they describe x_{so} and x_{cr} with a still higher accuracy.

It should be pointed out that the relation $x_{so} < x_{cr}$ holds for all values of β . Thus, when calculating acceptor energy levels for crystals with $|\Delta_{so}| \ll |\Delta_{cr}|$ (for instance, GaN and AlN), one may also assume $|\tilde{\Delta}_{so}| \ll |\tilde{\Delta}_{cr}|$.

3. g FACTOR OF AN ACCEPTOR CENTER.

The above results can be used to calculate the acceptor-center g factor in the presence of uniform strain and spin-orbit interaction.

Consider the case of weak magnetic fields, i.e., assume the Zeeman splitting of magnetic sublevels to be much less than the crystal-field and spin-orbit splittings, and take into account the interaction with magnetic field by perturbation theory.

The Hamiltonian of an acceptor-bound hole in the presence of a magnetic field can be written

$$\hat{H}_a(\mathbf{k}, \mathbf{H}) = \hat{H}(\mathbf{p}, \mathbf{H}) + \hat{V}(\mathbf{k}, \mathbf{k}') + \hat{H}', \quad (21)$$

where in spherical approximation the operator

$$\hat{H}(\mathbf{p}, \mathbf{H}) = \hat{H}(\mathbf{p}/\hbar) - \mu_B(1 + 3\gamma + 3\kappa)(\hat{\mathbf{I}}\mathbf{H}) + \mu_B g_0(\mathbf{S}\mathbf{H}) \quad (22)$$

describes the behavior of a free hole with angular momentum $\mathbf{I} = 1$ in an external magnetic field,⁸ $\mathbf{p} = \hbar\mathbf{k} - (e/c)\mathbf{A}$ is the kinematic momentum of the hole, $\mathbf{A} = (1/2)[\mathbf{H} \times \hat{\mathbf{r}}]$ is the vector potential of the magnetic field, $\mu_B = e\hbar/2m_0c$ is the Bohr magneton, c is the velocity of light, $g_0 \approx 2$ is the free-electron g factor, κ is the Luttinger magnetic constant⁸, $\hat{H}(\mathbf{p}/\hbar)$ is the kinetic-energy operator (1), $\hat{V}(\mathbf{k}, \mathbf{k}')$ is the potential energy operator for interaction with the acceptor, and \hat{H}' is the sum of the Hamiltonians describing spin-orbit interaction and interaction with the strain field (18).

Isolating the perturbation linear in magnetic field as this was done in Ref. 14, we write the $\hat{H}(\mathbf{p}, \mathbf{H})$ Hamiltonian in the form

$$\hat{H}(\mathbf{p}, \mathbf{h}) = \hat{H}(\mathbf{k}) + H'_H, \quad (23)$$

$$\begin{aligned} \hat{H}'_H &= -\mu_B[(\gamma_1 + 4\gamma)(\hat{\mathbf{L}}\mathbf{H}) - 6\gamma(\mathbf{k}\hat{\mathbf{I}})([\hat{\mathbf{r}} \times \hat{\mathbf{I}}]\mathbf{H}) \\ &\quad + (1 + 3\gamma + 3\kappa)(\hat{\mathbf{I}}\mathbf{H}) - g_0(\hat{\mathbf{S}}\mathbf{H})] \\ &= -\mu_B(g_F \hat{\mathbf{F}} - g_0 \hat{\mathbf{S}})\mathbf{H}, \end{aligned} \quad (24)$$

where g_F is the acceptor g factor in the absence of spin-orbit interaction and external strain. The quantity g_F can be found by means of the acceptor wave functions Ψ_{FM} similar to the way this was done in Ref. 14. We obtain

$$g_F = (\gamma_1 + 4\gamma)\langle L_H \rangle - 6\gamma\langle N_H \rangle + (1 + 3\gamma + 3\kappa)\langle I_H \rangle, \quad (25)$$

where

$$\begin{aligned} \langle L_H \rangle &= \left\{ \frac{1}{2} - \frac{2\pi}{3} [4\langle f_h(k)f_l(k) \rangle - \langle f_l^2(k) \rangle] \right\}, \\ \langle N_H \rangle &= \left\{ 1 + \frac{4\pi}{3} [\langle f_h(k)f_l(k) \rangle - \langle f_l^2(k) \rangle \right. \\ &\quad \left. + \langle f_h'(k)k f_l(k) \rangle] \right\}, \\ \langle I_H \rangle &= \langle F_H \rangle - \langle L_H \rangle \equiv 1 - \langle L_H \rangle, \end{aligned} \quad (26)$$

with the prime on the function denoting the derivative with respect to the wave vector modulus k , and $\langle L_H \rangle$, $\langle N_H \rangle$, and

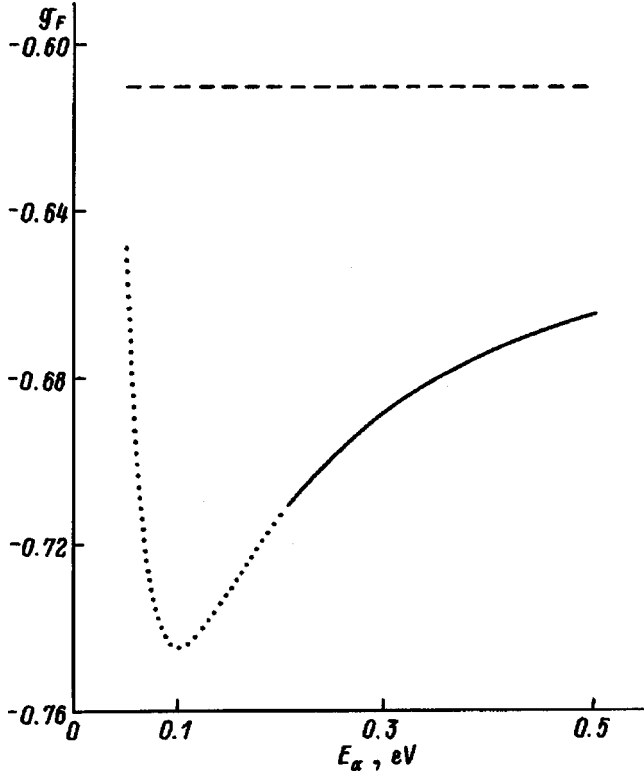


FIG. 2. Dependence of the acceptor ground-state g factor, g_F , on binding energy E_a in the absence of strain and spin-orbit interaction, calculated for GaN parameters in spherical approximation (solid line). The dashed line shows g_F for binding energies below the Coulombic acceptor energy ($E_a \leq 200$ meV). Dashed line: g_F in the zero-range potential model.

$\langle I_H \rangle$ standing for the averages of the projections of vectors $\hat{\mathbf{L}}, \hat{\mathbf{N}} = (\mathbf{k}\hat{\mathbf{I}})[\hat{\mathbf{r}} \times \hat{\mathbf{I}}]$, and $\hat{\mathbf{I}}$ on magnetic field. Figure 2 presents the dependence of g_F on the binding energy of the ground-state acceptor in GaN. The calculations used the value of the magnetic constant $\kappa = 0.015$ obtained from the relation

$$\kappa = \frac{5\gamma - \gamma_1 - 2}{3}.$$

This relation follows from a work¹⁵ where interaction with the nearest symmetry zones $\Gamma_2^-, \Gamma_{12}^-,$ and Γ_{15}^- was taken into account within \mathbf{kp} theory.

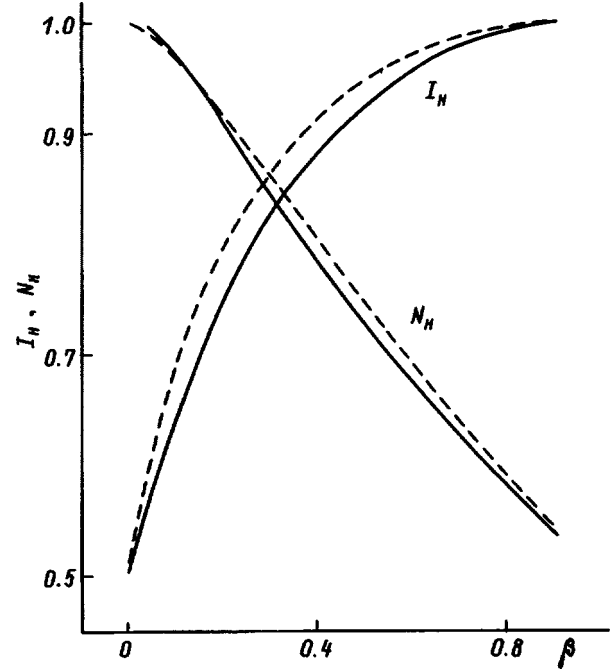


FIG. 3. Dependences of the average values $\langle I_H \rangle$ and $\langle N_H \rangle$ on the light/heavy hole-mass ratio $\beta = m_l/m_h = (\gamma_1 - 2\gamma)/(\gamma_1 + 4\gamma)$ for the two limiting cases of a Coulombic acceptor (solid lines) and an acceptor described by a zero-range potential (dashed lines).

As seen from Fig. 2, g_F depends only weakly on binding energy E_a and differs from the value $g_F = -0.61$ calculated within the zero-range potential model by not more than 15% for binding energies above the Coulomb acceptor energy ($E_a \geq 200$ meV).

Figure 3 displays the dependences of the average quantities $\langle I_H \rangle$ and $\langle N_H \rangle$ on the light- to heavy-hole mass ratio $\beta = m_l/m_h = (\gamma_1 - 2\gamma)/(\gamma_1 + 4\gamma)$, which permit one to obtain the value of g_F for arbitrary parameters $\gamma_1, \gamma,$ and κ . Interestingly, for small β the g factor of an acceptor-bound hole is negative, whereas that of a free hole, $g = 1 + 3\kappa$, is positive. A similar result was obtained^{16,17} for an acceptor center in GaAs.

The zero-range potential model yields an analytic expression for g_F . In this case, g_F depends only on the light-

TABLE II. g factor and energies of the acceptor ground-state sublevels in the presence of uniaxial strain ($\epsilon_{zz} \neq 0, \epsilon_{xx} = \epsilon_{yy} = 0$) for the case of weak spin-orbit coupling ($|\tilde{\Delta}_{so}| \ll |\tilde{b}\epsilon_{zz}|$).

E_n	$-(\tilde{a} + 2\tilde{b})\epsilon_{zz} + 3\tilde{b}\epsilon_{zz} - \frac{\tilde{\Delta}_{so}}{3}$	$-(\tilde{a} + 2\tilde{b})\epsilon_{zz} + 3\tilde{b}\epsilon_{zz} + \frac{\tilde{\Delta}_{so}}{3} + \frac{2\tilde{\Delta}_{so}^2}{27\tilde{b}\epsilon_{zz}}$	$-(\tilde{a} + 2\tilde{b})\epsilon_{zz} - \frac{2\tilde{\Delta}_{so}^2}{27\tilde{b}\epsilon_{zz}}$
g_{xx}	0	$\frac{V_{zz}^2}{2}g_0 + V_{zz}(2 - V_{zz})g_F$	$-g_0\left(1 - \frac{V_{zz}^2}{2}\right) + V_{zz}(2 - V_{zz})g_F$
g_{yy}	0	$-\frac{V_{zz}^2g_0 - V_{zz}}{2}(2 - V_{zz})g_F$	$-g_0\left(1 - \frac{V_{zz}^2}{2}\right) + V_{zz}(2 - V_{zz})g_F$
g_{zz}	$-g_0 + 2g_F$	$-g_0(1 - V_{zz}^2) - V_{zz}(2 - V_{zz})g_F$	$-g_0(1 - V_{zz}^2) + V_{zz}^2g_F$

Note: E_n are the split subband energies. The energies are reckoned from the acceptor level position in the absence of strain and spin-orbit coupling. We use the notation $V_{zz} = 2\tilde{\Delta}_{so}/9\tilde{b}\epsilon_{zz}$.

TABLE III. g factor and energies E_n of the acceptor ground-state sublevels in the presence of a weakly biaxial strain ($|\epsilon_{zz} - \epsilon_{xx}| \ll |\epsilon_{zz}| \neq 0$, $\epsilon_{yy} = 0$, $|\tilde{\Delta}_{so}| \ll |\tilde{b}\epsilon_{zz}|$).

E_n	$-(\tilde{a} + 2\tilde{b})(\epsilon_{zz} + \epsilon_{xx}) + 3\tilde{b}(\epsilon_{zz} + \epsilon_{xx})$	$-(\tilde{a} + 2\tilde{b})(\epsilon_{zz} + \epsilon_{xx}) + 3\tilde{b}\epsilon_{xx} + \frac{3}{2}\tilde{b}\epsilon_{zz}F_+$	$-(\tilde{a} + 2\tilde{b})(\epsilon_{zz} + \epsilon_{xx}) + 3\tilde{b}\epsilon_{xx} + \frac{3}{2}\tilde{b}\epsilon_{zz}F_-$
g_{xx}	$-g_0 - \left(V_{zz}V_- + \frac{V_{zz}V_+}{h}\right)g_F$	$-\frac{F_+^2 - V_{zz}^2}{F_+^2 + V_{zz}^2}g_0 - \frac{V_{zz}V_+}{h}g_F$	$-\frac{V_{zz}^2 - F_-^2}{V_{zz}^2 + F_-^2}g_0 + (V_{zz}V_-)g_F$
g_{yy}	$-g_0$	$-g_0 - \frac{4V_{zz}F_+}{F_+^2 + V_{zz}^2}g_F$	$-g_0 - \frac{4V_{zz}F_-}{F_-^2 + V_{zz}^2}g_F$
g_{zz}	$g_0 - \left(V_-F_- + \frac{V_+F_+}{h}\right)g_F$	$-\frac{F_+^2 - V_{zz}^2}{F_+^2 + V_{zz}^2}g_0 + \frac{V_+F_+}{h}g_F$	$-\frac{V_{zz}^2 - F_-^2}{V_{zz}^2 + F_-^2}g_0 - (V_-F_-)g_F$

Note: The energies are reckoned from the acceptor level position in the absence of strain and spin-orbit coupling. We use the notations $V_{\pm} = 2V_{zz}\sqrt{V_{zz}^2 + F_{\pm}^2}$, $F_{\pm} = 1 - h \pm \sqrt{(1-h)^2 + V_{zz}^2}$, $h = \epsilon_{xx}/\epsilon_{zz}$.

heavy-hole mass ratio and is independent of the binding energy

$$g_F = (\gamma_1 + 4\gamma) \frac{1 + \beta^{1/2} - 4\beta + \beta^{3/2} + \beta^2}{(1 + \beta^{1/2})(2 + \beta^{3/2})} - 6\gamma \frac{2(1 + 2\beta^{1/2} + \beta - \beta^{3/2})}{(1 + \beta^{1/2})^2(2 + \beta^{3/2})} + (1 + 3\gamma + 3\kappa) \frac{1 + \beta^{1/2} + 4\beta}{(1 + \beta^{1/2})(2 + \beta^{3/2})}. \quad (27)$$

In the presence of strain and for finite spin-orbit interaction, the six fold degenerate acceptor level splits into three sublevels, with each of them doubly degenerate in spin direction. The wave eigenfunctions of such sublevels are eigenfunctions of Hamiltonian H' (18), where, in a general case, we shall consider in place of the crystal strain tensor $\hat{\epsilon}^0$ an arbitrary strain tensor $\hat{\epsilon}$.

The behavior of a doubly degenerate hole sublevel in a magnetic field is described by a Hamiltonian like

$$\hat{H}_H = -\mu_B \frac{1}{2} \sum g_{ij}^{(n)} \hat{\sigma}_i H_j, \quad (28)$$

where $g_{ij}^{(n)}$ are components of the g -factor tensor, n labels the sublevels, σ_i are the Pauli matrices, and H_j are components of the magnetic field vector. By writing Hamiltonian H'_H (24) in the basis of wave eigenfunctions of a sublevel of interest and comparing it with Hamiltonian \hat{H}_H (28), one can determine all components of the g -factor tensor.

Table II lists expressions for the g factors of acceptor ground-state sublevels in the presence of axial strain (uniaxial: $\epsilon_{zz} \neq 0$, $\epsilon_{xx} = \epsilon_{yy} = 0$). For nonaxial strain (biaxial: $\epsilon_{zz} \neq \epsilon_{xx} \neq 0$, $\epsilon_{yy} = 0$), in the case of weak spin-orbit interaction of interest here ($|\tilde{\Delta}_{so}| \ll |\tilde{b}\epsilon_{zz}|$) one can obtain simple analytic expressions for components of tensor \hat{g} within two overlapping regions of $\epsilon_{zz} - \epsilon_{xx}$, namely, $|\epsilon_{zz} - \epsilon_{xx}| \ll |\epsilon_{zz}|$, and $|\tilde{\Delta}_{so}| \ll |\tilde{b}(\epsilon_{zz} - \epsilon_{xx})|, |\tilde{b}\epsilon_{xx}|$. The corresponding expressions for the components of the g tensor are presented in Tables III and IV. Note that the general case of triaxial strain ($\epsilon_{zz} \gg \epsilon_{xx} \gg \epsilon_{yy}$) reduces in the biaxial case considered here to a trivial isolation of hydrostatic strain, which does not affect the form of the acceptor-level wave function ($\tilde{\epsilon}_{\alpha\alpha} = \epsilon_{\alpha\alpha} - \epsilon_{yy}$).

In the uniaxial case (Table II) corresponding to an effective strain ϵ_{zz}^0 in GaN, the ground-state g factor ($J_z = F_z + S_z = \pm 3/2$) reaches the limit in anisotropy ($g_{zz} \neq 0, g_{xx}$

TABLE IV. g factor and energies E_n of the acceptor ground-state sublevels in the presence of a strongly biaxial strain ($|\tilde{\Delta}_{so}/\tilde{b}| \ll (|\epsilon_{zz} - \epsilon_{xx}|, |\epsilon_{zz}|, |\epsilon_{xx}|, \epsilon_{yy} = 0)$).

E_n	$-(\tilde{a} + 2\tilde{b})(\epsilon_{zz} + \epsilon_{xx}) + 3\tilde{b}(\epsilon_{zz} + \epsilon_{xx}) \left(1 + \frac{V_{xx}V_{zz}}{4}\right)$	$-(\tilde{a} + 2\tilde{b})(\epsilon_{zz} + \epsilon_{xx}) + 3\tilde{b}\epsilon_{xx} - \frac{3}{4}V_{zz}V_{xz}\tilde{b}(\epsilon_{xx} - 2\epsilon_{zz})$	$-(\tilde{a} + 2\tilde{b})(\epsilon_{zz} + \epsilon_{xx}) + 3\tilde{b}\epsilon_{zz} + \frac{3}{4}V_{xx}V_{xz}\tilde{b}(\epsilon_{zz} - 2\epsilon_{xx})$
g_{xx}	$-g_0 \left(1 - \frac{V_{xx}^2}{2}\right) - V_{zz}(2 + V_{xx})g_F$	$-g_0 \left(1 - \frac{V_{xz}^2}{2}\right) + V_{zz}(2 + V_{xz})g_F$	$-g_0 \left(1 - \frac{V_{xx}^2 + V_{xz}^2}{2}\right) + V_{xx}V_{xz}g_F$
g_{yy}	$-g_0 \left(1 - \frac{V_{xx}^2 + V_{zz}^2}{2}\right) + V_{xx}V_{zz}g_F$	$-g_0 \left(1 - \frac{V_{zz}^2}{2}\right) - V_{xz}(2 - V_{zz})g_F$	$-g_0 \left(1 - \frac{V_{xx}^2}{2}\right) + V_{xz}(2 - V_{xx})g_F$
g_{zz}	$-g_0 \left(1 - \frac{V_{zz}^2}{2}\right) - V_{xx}(2 + V_{zz})g_F$	$-g_0 \left(1 - \frac{V_{zz}^2 + V_{xz}^2}{2}\right) - V_{xz}V_{zz}g_F$	$-g_0 \left(1 - \frac{V_{xz}^2}{2}\right) + V_{xx}(2 - V_{xz})g_F$

Note: The energies are reckoned from the acceptor level position in the absence of strain and spin-orbit coupling. We use the notations $V_{xx} = 2\tilde{\Delta}_{so}/9\tilde{b}\epsilon_{xx}$, $V_{xz} = 2\tilde{\Delta}_{so}/9\tilde{b}(\epsilon_{xx} - \epsilon_{zz})$.

$=g_{yy}=0$). As seen from Table IV, in the case of biaxial strain and weak spin-orbit interaction, the g factor of all three sublevels is practically isotropic and approximately equal to that of the free electron.

The ground-state g factor of acceptors (Mg and Zn) in GaN was measured experimentally.⁶ It was shown that this g factor is close to g_0 , and that its anisotropy is small, which is at odds with the above simple theory, by which the acceptor ground-state g factor in GaN should be extremely anisotropic. This result can be explained qualitatively as due to the onset of spontaneous local strain in the plane perpendicular to the C_{6v} axis of wurtzite (i.e., as due to the Jahn–Teller effect). In this case the initial axial strain becomes nonaxial, which results, as seen from Table IV, in a practically isotropic g factor (the role of the Jahn–Teller effect in making the acceptor g factor in GaN isotropic was pointed out in Ref. 6). A comprehensive analysis of this spontaneous strain is beyond the scope of this paper.

We note in conclusion that the above theory becomes invalid for shallow acceptor centers whose binding energy is comparable to the spin-orbit or crystal-field splitting of the valence band. In particular, in the case of a high spin-orbit interaction energy nonaxial strain no more results in freezing of orbital motion of the hole, and its g factor should differ noticeably from that of the free electron.

The authors are grateful to Al. L. Efros, who turned our attention to this problem, as well as to P. G. Baranov and B. Meyer for fruitful discussions.

Support of the Russian Fund for Fundamental Research

(Grants 96-15-96392 and 95-02-04055) is gratefully acknowledged.

- ¹G. L. Bir and G. E. Pikus, *Symmetry and Strain-Induced Effects in Semiconductors* [Wiley, New York, 1974; Nauka, Moscow, 1972, 584 pp.].
- ²B. L. Gel'mont and A. V. Rodina, *Fiz. Tekh. Poluprovodn.* **25**, 2189 (1991) [*Sov. Phys. Semicond.* **25**, 1319 (1991)].
- ³A. V. Malyshev, I. A. Merkulov, and A. V. Rodina, *Phys. Rev. B* **55**, 4388 (1997).
- ⁴A. V. Malyshev, I. A. Merkulov, and A. V. Rodina, *Fiz. Tekh. Poluprovodn.* **30**, 159 (1996) [*Semiconductors* **30**, 91 (1996)].
- ⁵H. P. Maruska and J. J. Tietjen, *Appl. Phys. Lett.* **15**, 327 (1969).
- ⁶U. Kaufmann, M. Kunzer, C. Merz, I. Akasaki, and H. Amano, in *Mater. Res. Soc. Symp. Proc.*, Vol. 395 (1996).
- ⁷G. D. Chen, M. Smith, J. Y. Lin, H. X. Jiang, S.-H. Wei, M. Khan, and C. J. Sun, *Appl. Phys. Lett.* **68**, 2784 (1996).
- ⁸J. M. Luttinger, *Phys. Rev.* **102**, 1030 (1956).
- ⁹V. I. Perel' and I. N. Yassievich, *Zh. Éksp. Teor. Fiz.* **82**, 237 (1982) [*Sov. Phys. JETP* **55**, 143 (1982)].
- ¹⁰L. D. Landau and E. M. Lifshits, *Quantum Mechanics* [Pergamon Press, Oxford, 1974; Nauka, Moscow, 1989].
- ¹¹J. I. Pankove, S. Bloom, and G. Harbeke, *RCA Rev.* **36**, 163 (1975).
- ¹²Landolt-Börnstein, *Numerical Data and Functional Relationships in Science and Technology* (Springer, Berlin, 1982), Vol. 17a.
- ¹³I. V. Kostin, E. B. Osipov, and N. A. Osipova, *Fiz. Tekh. Poluprovodn.* **27**, 1743 (1993) [*Semiconductors* **27**, 962 (1993)].
- ¹⁴A. V. Malyshev and I. A. Merkulov, *Fiz. Tverd. Tela (St. Petersburg)* **39**, 58 (1997) [*Phys. Solid State* **39**, 49 (1997)].
- ¹⁵G. Dresselhaus, A. F. Kip, and C. Kittel, *Phys. Rev.* **98**, 368 (1955).
- ¹⁶R. I. Dzhioev, B. P. Zakharchenya, and V. G. Fleisher, *JETP Lett.* **17**, 174 (1973).
- ¹⁷B. L. Gel'mont and M. I. D'yakonov, *Fiz. Tekh. Poluprovodn.* **7**, 2013 (1973) [*Sov. Phys. Semicond.* **7**, 1345 (1973)].

Translated by G. Skrebtsov

Deep-level optical spectroscopy of ZnTe

A. V. Kvit, S. A. Medvedev, Yu. V. Klevkov, V. V. Zaitsev, E. E. Onishchenko,
A. V. Klovov, V. S. Bagaev, A. V. Tsikunov, A. V. Perestoronin, and M. V. Yakimov

P. N. Lebedev Physical Institute, Russian Academy of Sciences, 117924 Moscow, Russia

(Submitted September 17, 1997; resubmitted November 25, 1997)

Fiz. Tverd. Tela (St. Petersburg) **40**, 1010–1017 (June 1998)

The variation of the deep-level spectrum of stoichiometric ZnTe in the various stages of its purification and annealing in saturated Zn vapor has been studied by low-temperature photoluminescence and IR Fourier spectroscopy. The relation between the concentration of the main residual impurities with complex formation probability is analyzed. We have succeeded in observing for the first time *Z* center emission in ZnTe, as previously in CdTe and ZnSe. This center is shown to be a multicharged impurity in ZnTe. The activation energies of these levels have been determined. A comparison of the data obtained by chemical analysis with optical spectra has led to a conclusion that this center is associated with isolated oxygen present on the metalloid sublattice. While this emission exhibits the same specific features in a number of II–VI compounds (a high recombination rate, narrow emission lines, extremely weak electron-phonon coupling), the positions of the levels in the band gap and the characteristic charge state distinguish ZnTe from CdTe and ZnSe. As a rule, the *Z* center forms in a material in decomposition of various complexes (for instance, of the complex responsible for the 1.65-eV emission in ZnTe) and disappears when the material is doped leading to formation of the same complexes. An assumption is put forward that this center creates the main compensating deep levels and is an essential component of easily forming complexes with impurities. Its position in the lower half of the ZnTe band gap (in contrast to ZnSe and CdTe) makes preparation of the *n* material difficult. © 1998 American Institute of Physics. [S1063-7834(98)01106-X]

Despite certain differences in the fundamental characteristics of some wide-gap II–VI semiconductors (CdTe, ZnTe, ZnSe, CdSe, ZnS), one observes also similarities in the energies of impurity levels in these compounds. These tendencies are easily discernible for shallow impurities (acceptors and donors), whose energy position is described well by the effective-mass law. A comparison of the spectral positions and emission parameters of the deep states characteristic of these compounds reveals much in common. Indeed, one observes in all compounds (1) the so-called self-activation bands originating from complexes with impurities which act as shallow donors when isolated; (2) bands traditionally assigned to copper complex emission; and (3) some unidentified centers which are apparently also due to complexes. The deep centers due to complexes are characterized by strong electron-phonon coupling, which, as a rule, increases with binding energy. Starting with a certain center depth, individual *LO* phonon replicas become practically indistinguishable.

The most remarkable feature in photoluminescence and absorption spectra of ZnTe is a band near 630 nm with a very rich spectrum, which exhibits, besides a narrow zero-phonon line, emission involving phonons of various types. These lines are very well resolved, despite the high binding energy of this center. Comprehensive studies carried out in the 60s show convincingly that this radiative center is associated with an oxygen complex.^{1,2}

It is believed that ZnTe, in contrast to other II–VI com-

pounds, can have only *p* conduction. Although this effect is connected with the general problem of self-compensation or impurity compensation, the source of this compensation has not yet been convincingly established. By closely analyzing the problem of attaining *p* conduction in ZnSe, which was assumed during a long time to be an electronic material, one can hope, however, to realize *p*–*n* transitions in ZnTe-based compounds as well.

We started to look for the solution to this problem in the optical spectra of high-purity, close to stoichiometric II–VI compounds (with the so-called composition at the minimum vapor pressure point, P_{\min}). One can neglect here the concentration of native defects at the crystallization temperature. The properties of high-purity compounds of this composition are dominated by impurities. The spectra of high-purity II–VI compounds depend to a considerable extent on the method and conditions of their preparation. It is believed that dominant emission in the exciton spectral region is an indication of their purity. At the same time, in the presence of precipitates, impurity segregation centers, or impurity complex-formation centers, where impurities become optically inactive, the conclusion of high purity in such a material may turn out to be erroneous. This becomes clear only after doping II–VI compounds with shallow impurities. Therefore, in order to investigate the main properties of this group of compounds, we used the low-temperature methods of synthesis and purification developed by us, where the existence of a second phase is excluded, and the concentration

of native defects is certain to be less than that of impurities.

On the other hand, the low concentrations of residual impurities in a number of important elements in Groups I, III, V, and VII of the Periodic Table derived from chemical analyses, do not exclude the presence of some specific impurities (H, C, and O) in high concentrations. Analysis of these impurities meets with difficulties, so that in certification of the above materials they are usually disregarded. This relates in the first place to the isovalent oxygen impurity. Oxygen, similar to carbon, is the main residual impurity even in very pure II–VI compounds and is present in them in concentrations $>10^{17} \text{ cm}^{-3}$. Since oxygen is, in addition, an optically active element, which begins to manifest itself in emission and absorption spectra against the background of low concentrations of most residual impurities, one can follow its behavior in each purification stage from the dynamics of the spectra, and establish in this way its role in the formation of complexes with other impurities.

1. EXPERIMENT

The measurements of low-temperature photoluminescence of ZnTe were performed on cleaved faces of single-crystal grains up to 0.3 cm^2 in size, which were selected out of polycrystalline ingots directly after preparation of the compound and following each purification stage. A cw Ar ion laser ($\lambda \sim 487.8 \text{ nm}$) was used as excitation source. The excitation intensity was typically 5 W/cm^2 . IR transmittance measurements were carried out on a Bruker IFS-113v IR Fourier spectrometer. The spectra of transmittance were measured at 77 and 300 K, and those of photoluminescence, at 5 K.

The low-temperature synthesis in a direct reaction from preliminarily purified components and the three-stage purification of the compounds, by a technique modified slightly from that described in Ref. 3, were carried out to study the dynamics of low-temperature photoluminescence spectra. We believe that the composition of ZnTe does not change noticeably, since the vaporization and crystallization temperatures remained constant from one purification stage to another. The deposition rate of the congruently subliming compound at a vaporization temperature $\sim 780 \text{ }^\circ\text{C}$ was 12–15 g/h in any purification stage.

2. RESULTS AND DISCUSSION

Figure 1a shows a photoluminescence spectrum of polycrystalline ZnTe prepared from high-purity Zn and Te. Already in this initial stage the exciton region dominates in the spectrum. The intensity ratio of the acceptor-bound exciton line A^0X to the main shallow-acceptor line at 2.3318 eV (eA , where A is the acceptor with activation energy of 62.5 meV) is ten, and that to the oxygen-complex line at $\sim 1.985 \text{ eV}$, more than 1200 (Fig. 2a). Besides the oxygen complex, one observes here two deep-level transitions with a lower intensity, at 1.65 and 1.08 eV (Fig. 2).

The spectrum in the exciton region is typical of fairly pure ZnTe (Fig. 3). Besides the bound-exciton line and its

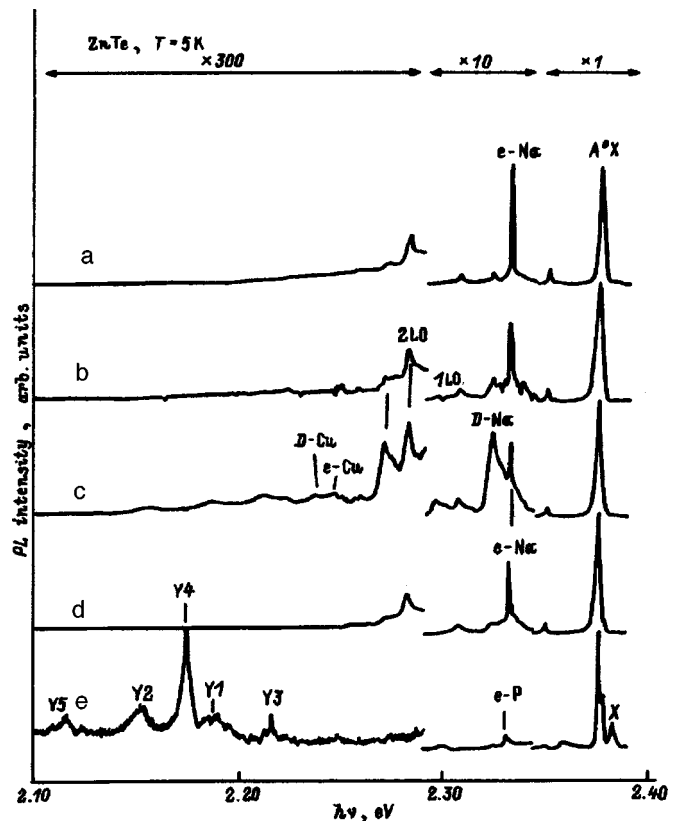


FIG. 1. Photoluminescence spectrum of polycrystalline ZnTe prepared from high-purity components Zn and Te. a — ZTS1, b — ZTO2, c — ZTO3H, d — ZTO3C, and e — ZTO3Zn.

phonon replicas, one can see also two lines at 2.3812 and 2.3827 eV, which correspond to the two free-exciton polariton branches.

The intensity ratios of various lines to the line of the exciton bound to a shallow neutral acceptor are listed in Table I for different ZnTe samples.

One readily sees that progressive purification of ZnTe results in an effective decrease in emission of both the oxygen complex and the shallow impurity. After the last purification stage, the characteristic oxygen-complex radiation with phonon replicas is practically not observed. There appears, however, another structureless band in the same region, which peaks at 1.87 eV. These bands originate apparently from complexes of different compositions.

The radiation from the deep traps at 1.65 and 1.08 eV behaves differently than that due to the oxygen complex (Table II).

These deep traps emit weak radiation. In the initial stages of purification, their integrated intensity is only one fifth of the oxygen complex intensity. Nevertheless, in the subsequent stages this ratio changes in favor of the 1.65- and 1.08-eV bands. We believe that this effect is due to fast decay of the oxygen complex in the course of ZnTe purification. It is known that the 1.65-eV band is due to a complex involving a donor, because its intensity increases noticeably, similar to that of the self-activated band in donor-doped materials.⁴ The band-intensity redistribution among the above complexes is apparently connected with decreasing

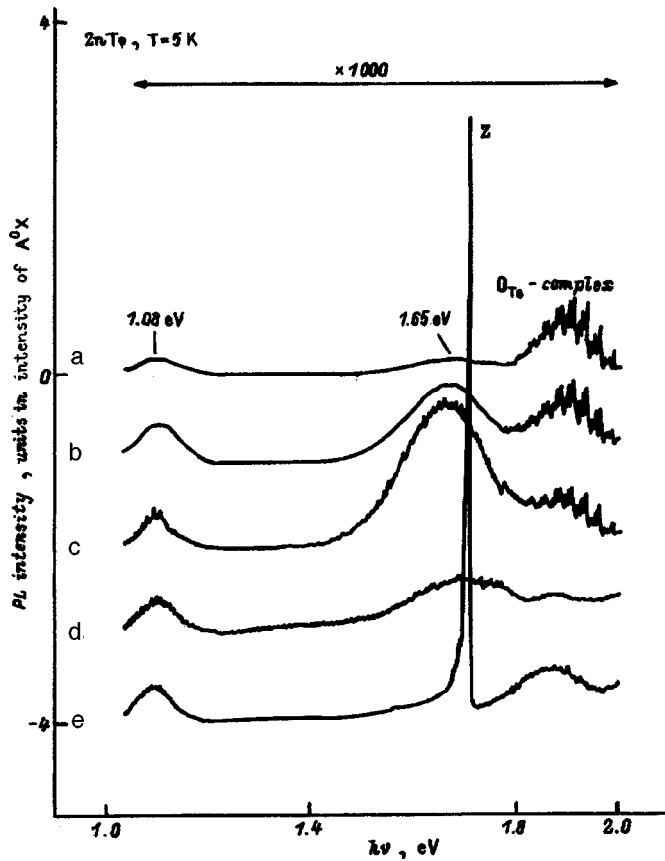


FIG. 2. Photoluminescence spectrum of deep radiative transitions in various purification stages and after annealing in Zn vapor. a — ZTS1, b — ZTO1, c — ZTO3H, d — ZTO3C, and e — ZTO3Zn.

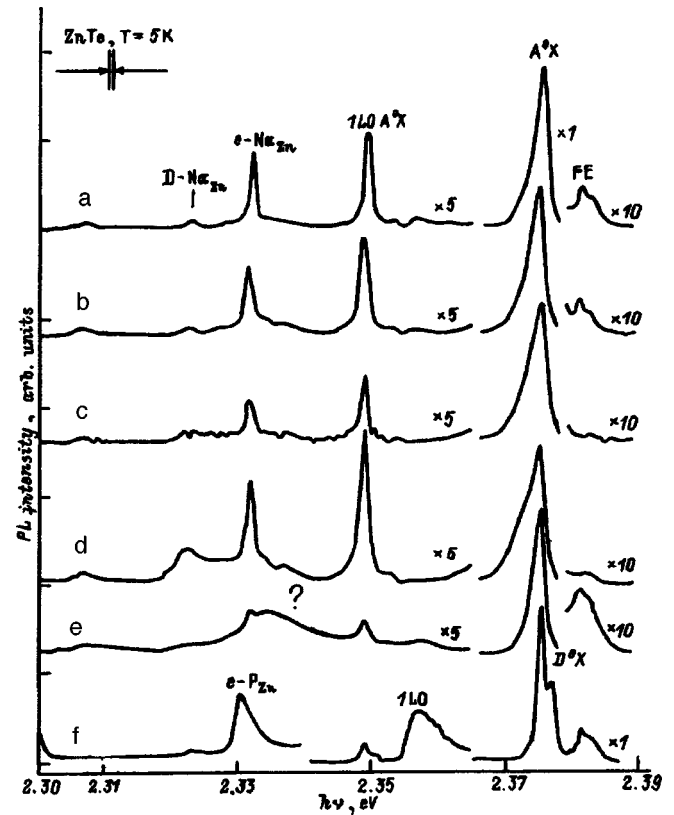


FIG. 3. Exciton spectrum of polycrystalline samples in various purification stages and following anneal in Zn vapor. a — ZTS1, b — ZTO1, c — ZTO2, d — ZTO3H, e — ZTO3C, and f — ZTO3Zn.

concentration of shallow acceptors and a relative increase in the fraction of donor impurities.

The appearance of isolated donor impurities itself is clearly seen from the appearance of bands due to donor recombination with various shallow acceptors (for instance, of the bands at 2.322 eV in ZTO3H or at 2.335 eV in ZTO3C in Fig. 1c and 1d). Moreover, if the starting materials ZTS1 and ZTO1 were very weakly compensated by shallow impurities (for which $N_A > N_{\text{deep}} \gg N_D$), then after the subsequent purification stages compensation by shallow impurities becomes stronger ($N_A \gg N_D > N_{\text{deep}}$). The extremely weak compensation by shallow donors in the first purification stages is indi-

cated by the presence of a fine structure in the donor-acceptor recombination line spectrum (one observes a large series of narrow lines in the interval 2.29–2.32 eV on the short-wavelength tail of the donor-acceptor recombination band at 2.283 eV, $E_A = 96$ meV). Additional donors make the line spectrum disappear, which can be explained by the random character of Coulomb interaction because of the spread in separations between a donor and a recombining donor-acceptor pair.

As purification continues and the complexes involving shallow acceptor impurities decay, new lines due to these impurities appear in photoluminescence spectra. All related

TABLE I. Intensity ratio of various bands to the main acceptor-bound exciton line (from low-temperature photoluminescence spectra).

Sample	Comment	$I(A^0X_{1LO})/ I(A^0X)$	$I(\text{FE})/ I(A^0X)$	$[I(O_{\text{comp}})/ I(A^0X)] \times 10^4$	$I(e\text{-Na})/ I(A^0X)$
ZTS1	After preparation	0.13	0.029	7.7	0.09
ZTO1	1st purification	0.13	0.031	5.9	0.08
ZTO2	2nd purification	0.24	0.008	?	0.06
ZTO3H	3rd purification, hot zone	0.11	0.005	3.6	0.06
ZTO3C	3rd purification, cold zone	0.025	0.055	0.9*	0.02
ZTO3Zn	ZTO3C sample annealed in Zn vapor for 72 h.	0.023	0.205	3.2*	0

*Ratio to the intensity of the structureless band peaking at 1.87 eV, with practically no oxygen-complex emission at ~1.9 eV observed.

TABLE II. Intensity ratio of deep-trap bands to the main acceptor-bound exciton line.

Sample	Comment	$[I(1.65 \text{ eV}) / I(A^0X)] \times 10^4$	$[I(1.08 \text{ eV}) / I(A^0X)] \times 10^4$
ZTS1	After preparation	~1.4	~1.8
ZTO1	1st purification	~6.8	~4.1
ZTO3H	3rd purification, hot zone	~1.4	~4.1
ZTO3H	3rd purification, cold zone	~4.5	~4.1
ZTO3c	sample annealed	<0.3	4.1
ZTO3Zn	in saturated Zn vapor for 72 h.		

transitions and their activation energies are listed in Table III.

A comparison of the data in Table III with available activation energies of shallow acceptors in ZnTe revealed a series of new lines appearing in later stages of purification. While the form and character of radiation of shallow acceptors are fairly typical of ZnTe, the new, relatively deep acceptors have a very small Huang–Rhys factor (Table III). And it is only one acceptor, with activation energy of 146 meV, that is characterized by strong electron-phonon coupling ($S \sim 0.8$). We believe that the shallow acceptor lines seen in low-temperature photoluminescence spectra also result from decay of deep impurity complexes. In particular, we identify the well-known oxygen complex at ~ 1.9 eV as $O_{Te}-A$, where A is a shallow acceptor. The quenching of this band should give rise to lines associated with single shallow acceptors, and it is this what is observed experimentally (Fig. 3). This may also account for the radiation of isolated O_{Te} . The high level of ZnTe purification from oxygen was deduced from both the quenching of the oxygen-complex band and the oxygen content in the remainder of the batch determined by mass-spectrometric analysis (LAMMA). As a rule, in the first stages of purification the

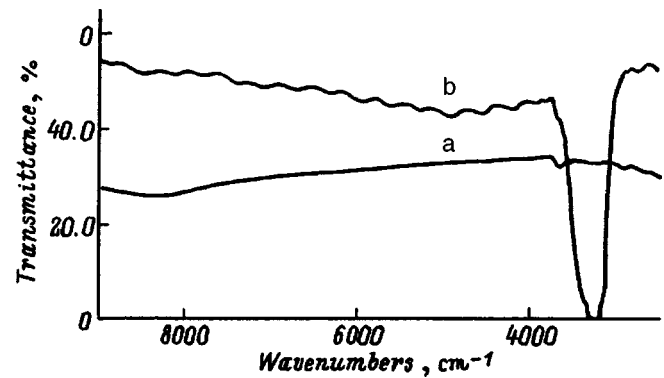


FIG. 4. IR transmittance spectra of polycrystalline ZnTe samples (a) before and (b) after anneal in Zn vapor.

batch was enriched in oxygen ($\sim 1\%$). In the last stage, the oxygen concentration in the batch was at the resolution level of the measurement technique used.

Z is a deep center in all II–VI compounds. In CdTe and ZnSe it forms levels in the upper half of the band gap. In CdTe, the Z center has several charge states, $+ / 0 / -$.⁸ It was shown^{8–10} that the Z center tends to form complexes with neighboring impurities. The manifestation of this center in photoluminescence spectra of CdTe is due to the decay of complexes as a result of decreasing concentration of residual impurities in the course of purification. This center is distinguished in the II–VI acceptors by (1) extremely weak electron-phonon interaction, (2) small halfwidths of the radiation lines (FWHM as small as 3 meV), and (3) a high radiative recombination rate. We expected the Z center to appear in ZnTe as well in a certain stage of purification of the material. It was not, however, detected in the course of purification either in photoluminescence spectra throughout the 1.0–2.4-eV range covered, or in near- and far-IR absorption (Fig. 4a).

TABLE III. Main acceptors in ZnTe and characteristic electron-phonon coupling constant.

Acceptor activation energy, meV	Emission lines, eV (recombination type)	Huang–Rhys factor S (arb. units)	Assignment
51	2.335 (<i>DA</i>)	0.04	Unknown
60.6	2.3335 (<i>eA</i>) 2.323 (<i>DA</i>)	0.04	Li_{Zn} (Ref. 5)
62.5	2.3318 (<i>eA</i>) 2.322 (<i>DA</i>)	0.04	Na_{Zn} (Ref. 5)
63.5	2.3308 (<i>eA</i>)	<0.01	P_{Te} (Ref. 5)
96	2.230 (<i>eA</i>) 2.283 (<i>DA</i>)	0.07	Unknown acceptor A_{Te} ;
146	2.248 (<i>eA</i>) 2.236 (<i>DA</i>)	0.8	Cu_{Zn} or self-activation band ⁶
177	2.217 (<i>eA</i>)	<0.1	Y3*
200	2.195 (<i>eA</i>) 2.184 (<i>DA</i>)	?	Y1 (Ref. 7)
220	2.174 (<i>eA</i>)	<0.005	Y4*
240	2.1545 (<i>eA</i>) 2.1465 (<i>DA</i>)	<0.01	Y2 (Ref. 7)
273	2.116 (<i>DA</i>)	<0.01	Y5*
692	1.702 (<i>eA</i>) 1.688 (<i>DA</i>)	<0.005	O_{Te} , $Z^{0/-}$

*This work.

The radiation of this center was observed only after annealing the high-purity material in Zn vapor at $T=680^\circ\text{C}$ for 72 h (Fig. 2). The two lines at 1.702 and 1.688 eV became the most pronounced features in the deep-center radiation region (FWHM ~ 4 meV). Such annealing produces strong redistribution of the impurities, which is evident both from transformation of the low-temperature photoluminescence and IR absorption spectra and from a change in the material's resistivity. The latter is apparently due to a change in chemical potential. While before the anneal the material had a resistivity of $\sim 10^3 \Omega \cdot \text{cm}$ (p type), after it the resistivity rose by several orders of magnitude, although no inversion of conduction type was observed. We assign this effect to Fermi level pinning by the Z center. Thus in contrast to CdTe and ZnSe, in ZnTe the levels of the Z center lie in the lower half of the band gap.

A comparison of photoluminescence spectra measured at different pumping levels permitted us to assign the 1.702-eV line to $e-Z^{0/-}$, and the line at 1.688 eV, to $D^{0/+}-Z^{0/-}$, which means that the Z center is seen in photoluminescence spectra of zinc telluride as a very deep acceptor (with a binding energy of 692 meV). Knowing the position of the Z center levels in CdTe, we expected to observe the radiation due to the second charge state ($Z^{0/+}$) in ZnTe, by analogy, in the intermediate or far IR range. Figure 4 presents an IR transmittance spectrum of ZnTe obtained at 80 K before and after annealing in Zn vapor. While before the anneal, as we have already mentioned, the transmittance spectra do not exhibit any features, after the anneal a new strong absorption band appears at ~ 0.41 eV (3300 cm^{-1}). The appearance of this absorption band only after annealing in Zn vapor, its energy position, the relatively narrow width, and the absence of phonon replicas in transmittance spectra gave us grounds to assign it to a manifestation of the second charge state of the Z center.

Why did we succeed in observing the emission and absorption of the Z center only after annealing the material in Zn vapor? To answer this question, one has to analyze the changes in optical spectra induced by the anneal. The anneal in Zn vapor resulted in a strong rearrangement of the electronic spectrum of impurity levels. First, as seen from low-temperature photoluminescence spectra, after the anneal there is practically no radiation due to the shallow acceptor Na_{Zn} (Fig. 1e). The line at 2.3318 eV ($e-\text{Na}_{\text{Zn}}$), which was clearly seen in all samples before the anneal (Fig. 1a–1d), disappears. We attribute this effect to expulsion of alkali metals from the Zn sublattice into interstices because of the enthalpy of formation of Na_{Zn} (Li_{Zn} , K_{Zn}) being smaller than that of Zn_{Zn} . In the region of shallow acceptor emission a band associated with P_{Te} appears. Its intensity is 20 times lower. It was not observed in the starting samples against the background of Na radiation. In addition to an intensity increase of free-exciton emission near the edge, one observes also at 2.3772 eV manifestation of an exciton bound to neutral donors (Fig. 1e). Note that, before the anneal, the radiation involving shallow donors was barely visible. Only extremely weak interimpurity DA recombination bands are seen. The onset of donor emission was apparently favored by the decay of the 1.65-eV complex containing these donors in

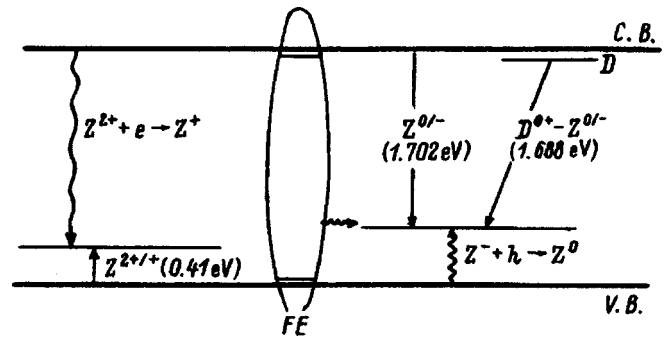


FIG. 5. Main transitions associated with the Z center. Solid lines identify the transitions seen in low-temperature photoluminescence and transmittance spectra. The wavy line refers to Coulombic trapping into charged states and free-exciton capture at the neutral Z center.

the course of annealing in Zn vapor. We believe that it is this anneal that accounts for the formation of single Z centers, i.e., the Z center was a part of the complex responsible for the 1.65-eV band. Our experiments on doping ZnTe with various donors showed that the band at 1.65 eV rises in intensity when Group III donors are used for this purpose. This is why we identify this complex as $Z-D(\text{III})_{\text{Zn}}$. The decay of the complex may be caused by enhanced diffusion of Group III donors or of the Z center and by an increase of their separation during the anneal in Zn vapor, when a concentration gradient of created vacancies (V_{Zn} , V_{Te}) sets in. Note an essential feature: one does not succeed in reproducing the appearance of the Z center in insufficiently pure or doped materials, as well as at high anneal temperatures.

This relation between the Z center formation in II–VI compounds and the decay of complexes^{8,9} is a convincing argument against the prevailing opinion that the 1.65-eV band originates from native defects (the A center $V_{\text{Zn}}-D$). Annealing in saturated Zn vapor should undoubtedly have destroyed the A center, and nothing should have been observed except the above-mentioned enhancement of shallow-donor radiation. On the other hand, one might expect the annealing in Zn vapor to give rise to increasing concentration of interstitial zinc, if one starts with the assumption that Frenkel defects predominate here. It is hardly possible, however, to speak about a substantial concentration of native defects in close to stoichiometric materials in conditions of low-temperature equilibrium growth. The strong relation with the purification effect suggests instead that this center originates from a dominant residual impurity. Only two impurities were present in noticeable concentrations in our experiments, O and C.

Figure 5 shows schematically the main transitions associated with the Z center. The solid lines identify the transitions seen in low-temperature photoluminescence and transmittance spectra. Note that the transmittance spectra do not exhibit any features close to 0.7 and 1.7 eV. Such features would correspond to ejection of an electron from the valence band to a neutral Z center, and to electron promotion from the Z^- center into the conduction band, respectively. Besides, neither in photoluminescence nor in transmittance spectra are there any lines around ~ 2.0 eV, which in the first case would signal electron capture by a charged Z^+ center,

TABLE IV. Main characteristics of the Z center in II–VI compounds.

Material	$Z^{2+/+}$	$Z^{0/+}$	$Z^{-/0}$	Huang–Rhys factor S (arb. units)	FWHM, meV
CdTe	$E_C - 1.2$ eV	$E_C - 0.246$ eV	$E_V + 1.4$ eV	0.001	3
ZnTe	$E_V + 0.41$ eV* $E_C - 1.98$ eV	$E_V + 1.36$ eV ?	$E_C - 0.206$ eV $E_V + 0.692$ eV	<0.005	4
ZnSe	$E_V + 0.41$ eV* ?	$E_C - 0.400$ eV $E_V + 2.38$ eV	$E_C - 1.702$ eV* ?	<0.01	~10

*This work, transmittance spectra

**This work, photoluminescence spectra.

and in the second, electron promotion from the neutral Z^0 center into the conduction band.

The fact that transmittance spectra measured in equilibrium conditions do not exhibit transitions associated with the initial neutral state Z^0 argues for the positive charge state of this center. As for transitions involving electron recombination at the neutral Z^0 center, they are possible only in non-equilibrium conditions, when photoluminescence spectra are taken.

Besides, measurements of the temperature dependence of luminescence quenching of this center apparently indicate that, for the ~ 1.7 -eV radiation to be observable, free excitons must be trapped by the Z center. The extremely fast extinction of this line with increasing temperature was totally unexpected by us. The thermal activation energy was found to be only ~ 10 meV. This value is very close to the free-exciton activation energy in ZnTe.

Our hypothesis reduces to the following: in order for the ~ 1.7 -eV band to appear in photoluminescence spectra, two electrons have to be trapped by a Z^{2+} center. The first electron is trapped from the conduction band under nonequilibrium excitation. The second nonequilibrium carrier is trapped with subsequent recombination as a result of binding and dissociation of free excitons at the positively charged Z center (Z^+). This effect is fairly typical of Z-center emission in the above-mentioned II-VI compounds. Remarkably, the excitation spectra of the Z center, for instance, in CdTe, exhibit a strong maximum in the free-exciton region.³

Another interesting feature is observed in the exciton part of the spectrum where, after ZnTe is annealed in zinc vapor, strong recombination channels appear at the Z center. One observes strong radiation only from the upper polariton branch of free excitons. Although the mechanism responsible for this behavior remains unclear to us, this effect is associated apparently with the capture and dissociation of free excitons at the Z center.

The above results permit a conclusion that the Z-center emission observed in ZnTe is similar to CdTe and ZnSe. The detection and study of the properties of this center in high-purity ZnTe crystals were performed by optical spectroscopy for the first time. The position of this center in the lower half of the ZnTe band gap produces difficulties in preparing samples of this material with electronic conduction. The Z

center is observed in photoluminescence and IR transmittance spectra only for high-purity material grown at a low temperature in close to stoichiometric conditions. While this radiation exhibits similar features in a number of II-VI compounds (high recombination rate, narrow emission lines, extremely weak electron-phonon coupling), the position of the levels in the band gap and the characteristic charge state distinguish ZnTe strongly from CdTe and ZnSe. The data on Z center emission are listed in Table IV. The Z center forms, as a rule, in materials after decay of various complexes and disappears when the material is doped with impurities forming the same complexes. We believe that this center produces the main compensating deep levels and is a very important impurity involved in complex formation. A comparison of chemical analysis data with optical spectra has led us to a conclusion that this center is due to the existence of oxygen in the metalloid sublattice, as an isolated isovalent impurity.

Support of the Russian Fund for Fundamental Research (Grants 95-02-3586a and 97-02-17747) is gratefully acknowledged.

¹J. L. Merz, Phys. Rev. **176**, 961 (1968).²V. S. Bagaev, V. V. Zaitsev, V. V. Kalinin, and E. E. Onishchenko, Fiz. Tverd. Tela (St. Petersburg) **38**, 1728 (1996) [Phys. Solid State **38**, 953 (1996)].³S. Medvedieff, Yu. Klevkov, A. Kvit, A. Perestoronin, V. Bagaev, A. Plotnikov, and A. Karuzskii, J. Cryst. Growth (in press).⁴Y. Hishida, T. Toda, and T. Yamaguchi, J. Cryst. Growth **117**, 396 (1992).⁵P. J. Dean, H. Venghaus, J. C. Pfister, B. Schaub, and J. Marine, J. Lumin. **16**, 363 (1978).⁶Y. Biao, M. Azoulay, M. A. George, A. Burger, W. E. Collins, E. Silberman, C.-H. Su, M. E. Volz, F. R. Szofran, and D. C. Gillies, J. Cryst. Growth **138**, 219 (1994).⁷A. Naumov, K. Wolf, T. Reisinger, H. Stanzl, and W. Gebhardt, J. Appl. Phys. **73**, 2581 (1993).⁸A. V. Kvit, Yu. V. Klevkov, S. R. Oktyabrsky, A. V. Tsikunov, and B. G. Zhurkin, Mater. Sci. Eng., B **26**, 1 (1994).⁹A. V. Kvit, Yu. V. Klevkov, S. R. Oktyabrsky, and B. G. Zhurkin, Semicond. Sci. Technol. **9**, 1805 (1994).¹⁰A. Gukasyan, A. Kvit, Yu. Llevkov, and S. Oktyabrsky, Solid State Commun. **97**, 897 (1996).

Formation of a nuclear spin polaron under optical orientation in GaAs-type semiconductors

I. A. Merkulov

A. F. Ioffe Physicotechnical Institute, Russian Academy of Sciences, 194021 St. Petersburg, Russia
(Submitted December 5, 1997)

Fiz. Tverd. Tela (St. Petersburg) **40**, 1018–1021 (June 1998)

A theory is developed for the formation of a nuclear spin polaron under optical cooling of nuclear spins in the vicinity of donor centers. It is shown that the polaron does not form above a certain limiting nuclear-spin temperature. For a shallow donor in GaAs, this temperature is about 10^{-7} K. The formation of a nuclear spin polaron should manifest itself in an anomalous increase of the spin relaxation time of the total spin of its component nuclei. © 1998 *American Institute of Physics*. [S1063-7834(98)01206-4]

Hyperfine interaction between conduction electrons and crystal-lattice nuclei in GaAs-type semiconductors opens a possibility for the creation of nuclear magnetic-polaron states, which can appear, for instance, around an electron localized at a donor center. The contact hyperfine electron interaction in these crystals is described by the scalar product of their spin with that of a lattice nucleus,¹ and it does not differ in form from the exchange coupling of conduction-band electrons to magnetic ions in a semimagnetic semiconductor, where magnetic polarons were studied both experimentally and theoretically.² As a result of the smallness of the hyperfine interaction parameter, however, the correlations between the spin of a donor-localized electron and the spins of the surrounding lattice nuclei are negligible, even at liquid-helium temperature. Polarized electrons are capable of polarizing noticeably the neighboring nuclei only at ultralow temperatures of the order of $10^{-6} - 10^{-7}$ K.

Such temperatures can be reached by optical cooling of the nuclear spin system under the conditions of optical orientation.^{1,3} At the lowest nuclear spin temperature T_N reached experimentally,⁴ of the order of 10^{-6} K, even a weak field of a few Oe can polarize noticeably the nuclear spins. In these conditions one succeeded in observing an anomalous enhancement of the low-frequency components of the nuclear spin correlator, which can be interpreted as a depression of nuclear polarization relaxation. Such a depression of spin relaxation accompanying magnetic polaron formation in semimagnetic semiconductors was pointed out in Ref. 5.

We are going to show that optical cooling of the nuclear spin system in a semiconductor by oriented electrons can indeed initiate formation of nuclear spin polarons, which should manifest itself, in particular, in a depression of spin relaxation of the nuclear spins making up the polaron.

In contrast to the case of semimagnetic semiconductors, formation of a nuclear spin polaron entails a very small change in carrier localization energy. The electron hopping time between donors is short compared to the characteristic times of electron interaction with nuclear spins, so that the polaron state is initiated by the mean field created at the

nuclei by a large number of electrons, whose spin distribution is determined by the lattice temperature. The nuclear magnetic polaron forms only if the product of the spin temperature of the nuclei by the electron temperature is less than a certain critical value, which depends on the parameters of the electron localization potential. Numerical estimates made for shallow Coulomb donors in GaAs suggest that this level can be reached by the optical cooling technique, but it is lower than the spin temperature reached experimentally.⁴ Thus despite the fact that nuclear spin relaxation can be depressed by formation of magnetic polaron states under optical orientation of carriers, experimental results⁴ do not lend themselves to explanation within the nuclear magnetic polaron model.

Section I develops a theoretical model of the nuclear spin polaron described by two spin temperatures in the approximation of short correlation times of the hyperfine field generated by a localized electron at the nuclei surrounding the donor. Section II analyzes the effect of hyperfine nuclear interaction with a localized electron on the rate of spin relaxation of the total nuclear spin.

1. NUCLEAR MAGNETIC POLARON

Let us estimate the possibility of formation of correlated states of electron spins (having the lattice temperature) and of the spins of the nuclei (cooled to a very low temperature) surrounding the donor centers. Taking the hyperfine contact interaction Hamiltonian

$$\hat{H}_{sf} = \sum_n a |\Psi(\mathbf{r}_n)|^2 (\hat{\mathbf{S}} \hat{\mathbf{I}}_n), \quad (1)$$

one can readily show that if the electrons can be characterized by an average spin $\langle \mathbf{S} \rangle$, the nuclear spins are acted upon by an average electron field

$$\mathbf{B}_e(\mathbf{r}_n) = a |\Psi(\mathbf{r}_n)|^2 \langle \mathbf{S} \rangle, \quad (2)$$

and that the average polarization of the nuclei surrounding a donor produces a nuclear field acting on a localized electron

$$\mathbf{B}_N = a \sum_n |\Psi(\mathbf{r}_n)|^2 \langle \mathbf{I}_n \rangle \approx aN \int \int \int |\Psi(\mathbf{r})|^2 \langle \mathbf{I}(\mathbf{r}) \rangle d^3r. \quad (3)$$

Here \mathbf{S} and Ψ are the spin operator and wave function of the impurity-bound electron, \mathbf{I}_n is the spin operator of a nucleus at point \mathbf{r}_n , a is the hyperfine interaction parameter, and N is the concentration of nuclei in the crystal lattice. [The electronic and nuclear fields chosen in accordance with Eqs. (2) and (3) have the dimension of energy, and we shall present their numerical values in units of thermal energy corresponding to one degree Kelvin.] When the nuclei are fully polarized, the nuclear field does not depend on the size of the electron localization region, and for gallium arsenide it is equivalent to a magnetic field of 5.29 T (Ref. 3) or

$$B_{N,\max} = \frac{3}{2} aN \approx k_B \cdot 1.6 \text{ K}, \quad (4)$$

where k_B is the Boltzmann constant.

Experiments are usually carried out at liquid-helium temperature (4.2 K). In these conditions, the electron spin-level splitting turns out to be less than the characteristic thermal energy even for the largest possible crystal-lattice nuclear polarization, so that the average electron spin in a nuclear field \mathbf{B}_N is given by the high-temperature expression

$$\langle \mathbf{S} \rangle \approx \frac{\beta_e \mathbf{B}_N}{4} \left[1 - \frac{1}{3} \left(\frac{\beta_e B_N}{2} \right)^2 \right], \quad (5)$$

where β_e is the inverse electron temperature.

An electron interacts simultaneously with approximately 10^5 nuclei located in the immediate vicinity of the donor center. Therefore the characteristic electron field is hundreds of thousands of times lower than $B_{N,\max}$. A noticeable nuclear polarization can be reached in this field only in a deeply cooled nuclear spin system of the semiconductor. Taking into account that all nuclei in GaAs have a spin of 3/2, we obtain within the high-temperature approximation

$$\langle \mathbf{I}_n \rangle \approx \frac{5}{4} \beta_N B_e(\mathbf{r}_n) \left[1 - \frac{17}{60} (\beta_N B_e(\mathbf{r}_n))^2 \right], \quad (6)$$

where β_N is the inverse spin temperature of the cooled nuclear system. As follows from Eqs. (6) and (2), in the vicinity of a donor center localized electrons with an average spin $\langle \mathbf{S} \rangle$ produce a cloud of nuclear polarization, whose total spin is approximately

$$\mathbf{I}_P \approx \frac{5}{4} \beta_N aN \langle \mathbf{S} \rangle. \quad (7)$$

Substituting (2) into (6), (6) into (3), and (3) into (5), one can readily obtain a self-consistent equation for the average spin of the localized electron in a nuclear polaron:

$$\langle \mathbf{S} \rangle \approx \varepsilon(\beta_e, \beta_N) [1 - \gamma(\beta_e, \beta_N) \langle S^2 \rangle] \langle \mathbf{S} \rangle, \quad (8)$$

where

$$\varepsilon(\beta_e, \beta_N) = \frac{5}{16} \beta_e \beta_N a^2 N \int \int \int |\Psi(\mathbf{r})|^4 d^3r,$$

$$\gamma(\beta_e, \beta_N) = \frac{4}{3} \varepsilon(\beta_e, \beta_N)^2 + \frac{17}{60} (\beta_N a)^2 \frac{\int \int \int |\Psi(\mathbf{r})|^8 d^3r}{\int \int \int |\Psi(\mathbf{r})|^4 d^3r}. \quad (9)$$

The nuclear magnetic polaron forms if $\varepsilon(\beta_e, \beta_N) > 1$, with the average spin projection of the localized electron on the nuclear field of the polaron given by the expression

$$\langle S \rangle = \sqrt{\frac{\varepsilon(\beta_e, \beta_N) - 1}{\gamma(\beta_e, \beta_N)}}. \quad (10)$$

Assuming the electrons to be localized at shallow, ground-state Coulombic donors with a Bohr radius $r_B = \hbar / \sqrt{2m'E}$ (m' is the electron effective mass, and E is the binding energy to the impurity center), we come to the following final expressions for the criterion of nuclear polaron formation

$$\varepsilon(\beta_e, \beta_N) = \frac{5\beta_e \beta_N B_{N,\max}^2}{6^3 N_B},$$

$$\gamma(\beta_e, \beta_N) = \frac{1}{3^5} \left(\frac{\beta_N B_{N,\max}}{N_B} \right)^2 \left[\frac{34}{5} + \left(\frac{5\beta_e B_{N,\max}}{12} \right)^2 \right], \quad (11)$$

and for its total spin

$$|I_P| = \frac{108 N_B}{\beta_N B_{N,\max}} \sqrt{\frac{(5\beta_e \beta_N B_{N,\max}^2 - 216 N_B) 15}{N_B [4896 + 125(\beta_e B_{N,\max})^2]}} = N_B j. \quad (12)$$

Here $N_B = (4/3)N\pi r_B^3$ is the characteristic number of the nuclei making up the polaron, and j is the average spin of one such nucleus in the hyperfine field of the electron in the polaron.

Substituting into Eqs. (11) and (12) the parameters corresponding to a typical experiment on a shallow hydrogenic donor center in crystalline gallium arsenide ($E_B = 5.59$ meV, $r_B = 95$ Å, $N_B = 1.6 \times 10^5$, $B_{N,\max} = 1.6$ K, and $T_e = \beta_e^{-1} \approx 4.2$ K), we establish that the nuclear spin polaron forms for $\beta_N \geq 1.1 \times 10^7$ K⁻¹.

The theory developed here is the simplest generalization of the theory² of the magnetic polaron state for equal spin temperatures of the electron and magnetic ions. As seen from Eq. (11), in the case of different spin temperatures, the magnetic-polaron state can form only for equal signs of β_N and β_e . By contrast, if the electron and nuclear spin temperatures are opposite in sign, no spontaneous self-ordering of the nuclear and electronic spins occurs, and the quasi-equilibrium electron spin $\langle \mathbf{S} \rangle$ appearing in the fluctuation field produces at nuclei an electronic field which tends to depress (rather than enhance) the initial deviation of nuclear polarization from zero.

Let us estimate now the nuclear spin temperature which can be reached in optical orientation experiments. To do this, consider the two-stage procedure used⁴ for deep cooling of the nuclear spin system in an n -type semiconductor. In the first stage one performs optical cooling in a strong magnetic

field (\mathbf{H}), in which the maximum attainable inverse nuclear spin temperature is related to the nonequilibrium photoelectron spin $\langle S_0 \rangle$ (or to the degree of optically induced circular polarization of luminescence $\rho = \langle S_0 \rangle$) through¹

$$\beta_N(H) = \frac{4Ik_B \langle \mathbf{H} \langle S_0 \rangle \rangle}{\mu_I H^2 + \xi H_L^2} \approx \frac{4Ik_B \rho}{\mu_I H}, \quad (13)$$

where H_L^2 is the mean squared random field generated by neighboring nuclear spins and acting on a nuclear spin I , μ_I is the nuclear magnetic moment, k_B is the Boltzmann constant, and ξ is a parameter depending on the coherence length of the electronic field. [For GaAs, $\xi=3$, and $H_L \approx 1.7$ G (Ref. 4)].

In the second stage, the pump light was turned off, and the external magnetic field was reduced adiabatically to zero. In these conditions, the nuclear spin temperature decreased to

$$\beta_N(0) = \beta_N(H) \sqrt{\frac{H^2 + H_L^2}{H_L^2}} \approx \frac{4Ik_B \rho}{\mu_I H_L}. \quad (14)$$

A comparison of this expression with the relations derived for the critical nuclear spin temperature (9) and (11) shows that in this case a nuclear magnetic polaron can form around equilibrium electrons localized at shallow hydrogenic donors in GaAs if in the first stage of experiment the following condition is met

$$\langle S_0 \rangle \geq \frac{54\mu_I H_L N_B}{5IB_{N,\max}^2 k_B}. \quad (15)$$

In gallium arsenide, the maximum optically-oriented electron spin is 0.25,¹ and the ratio μ_I/k_B varies from 3.5×10^{-8} K/G (for As nuclei) to 6.2×10^{-8} K/G (for the ⁷¹Ga isotope).⁶ Substituting into Eq. (15) the average value 5×10^{-8} K/G and the other parameters specified above we find

$$\langle S \rangle \beta_e \geq 0.05 \text{ K}^{-1}. \quad (16)$$

Under optical orientation conditions, $\langle S \rangle$ is less than 0.25. A comparison of this value with the estimate (16) shows that the nuclear spin polaron can form if the crystal temperature does not exceed 5 K.¹

For the nuclear spin polaron to form at liquid-helium temperature, the average oriented-electron spin should be not less than 0.2. In experiments,⁴ this quantity was approximately 0.025, i.e., it was not large enough for the polaron state to set in. In principle, however, polarons can form in experiments on optical cooling of the nuclear spin system of a semiconductor at a lower lattice temperature or for deeper impurity centers.

2. POLARIZATION RELAXATION OF THE TOTAL SPIN OF THE POLARON NUCLEI

The change in the electron binding energy induced by nuclear magnetic polaron formation is small and, therefore, the existence of the nuclear polaron can hardly be established from the Stokes luminescence shift. The formation of such a polaron could manifest itself in a change of the relaxation

rate of the total spin \mathbf{I}_Σ of the nuclei surrounding the donor center. Consider the changes in the behavior of \mathbf{I}_Σ resulting from hyperfine interaction of nuclei with a localized electron.

A rigorous quantitative calculation of the behavior of the spin of the nuclei in time is a very complex problem, because all characteristic times, namely, (i) the characteristic time of the random local field of neighboring nuclei which acts on nuclear spins and gives rise to nuclear spin relaxation and (ii) the nuclear spin precession period in this local field, are equal in order of magnitude. Therefore we shall make here only simple estimates based on the relaxation equation with a random field. This approach yields an asymptotically exact expression for the nuclear-polaron spin correlator.

Following Ref. 7, we shall describe the relaxation of deviations of the spin of the nuclei surrounding the donor center, $\mathbf{I}(\mathbf{r})$, from its equilibrium value with the equation

$$\frac{d\mathbf{I}(\mathbf{r})}{dt} = -\frac{1}{T_2}(\mathbf{I}(\mathbf{r}) - \mathbf{J}(\langle \mathbf{S}(\mathbf{I}(\mathbf{r})) \rangle)) + \mathbf{f}(t), \quad (17)$$

where $\mathbf{J}(\langle \mathbf{S}(\mathbf{I}(\mathbf{r})) \rangle)$ is the equilibrium nuclear spin in the hyperfine field of localized electrons, and $\mathbf{f}(t)$ is the random field responsible for the fluctuations of the nuclear spin about its equilibrium value,² and T_2 is the characteristic relaxation time of nuclear polarization, which coincides in order of magnitude with the random-field correlator decay time $\langle \mathbf{f}(0)\mathbf{f}(t) \rangle$.

Generally speaking, the spatial distribution of nuclear polarization $\mathbf{I}(\mathbf{r})$ is arbitrary. It can, however, be split into two components, one of which is proportional to $\Psi(\mathbf{r})^2$, and the other, when integrated with $\Psi(\mathbf{r})^2$, vanishes. The first component may be considered as a nucleus of the polaron state, whose spin relaxation is strongly affected by hyperfine interaction with the localized electron. At the same time the other component practically does not feel the hyperfine field of the localized electron.

In linear approximation, for the amplitude of the polaron state nucleus $\mathbf{J} = \epsilon \mathbf{I}_p$, so that Eq. (17) can be recast in the form

$$\frac{d\mathbf{I}_p}{dt} = -\frac{1}{T'_2} \mathbf{I}_p + \mathbf{f}(t), \quad (18)$$

where

$$T'_2 = \frac{T}{1 - \epsilon}. \quad (19)$$

For opposite signs of the electronic and nuclear spin temperatures $T'_2 < T_2$, and therefore a decrease of the nuclear spin temperature in absolute magnitude (increase of $|\epsilon|$) brings about a decrease of the characteristic relaxation time. As a result, high-frequency components begin to play a considerable role in the spectral expansion of the nuclear spin correlator.

If the spin temperatures of electrons and nuclei have the same sign, cooling of the nuclear spin system results in an increase of T'_2 and, hence, a decrease of the characteristic frequencies in nuclear spin correlator variation. At the critical point, the relaxation time found from Eq. (19) goes to infinity to become negative subsequently, which implies a

loss of stability of the state with $\mathbf{I}_P=0$. In this region of parameters, a magnetic polaron state sets in, and the linear approximation is not accurate enough to determine \mathbf{I}_P .

In the magnetic polaron state, the relaxation described by Eq. (17) follows a more complex pattern. As in the absence of the polaron, the average value of the nuclear spin \mathbf{I}_P relaxes to the level given by Eq. (12) with a characteristic time of the order of T_2 . At the same time relaxation of the nuclear spin in direction slows down considerably.

Indeed, if the average value of $J(I_P)$ is large compared to its fluctuations under the action of a random force ($\sqrt{5N_B/4}$), spin \mathbf{I}_P may be considered to move in a random manner over the sphere of radius $I_P=N_B j$ (12). In time T_2 the spin shifts a distance of the order of $\delta I_P \approx \sqrt{5N_B/4}$ or, which is the same, changes its direction through an angle $\delta\Theta \approx \sqrt{5/(4j^2N_B)}$. Thus in a time of the order of T_2 the projection of the total spin of the nuclei on its initial direction decreases by $I_P(\delta\Theta)^2/2$. Since for times longer than T_2 there are no correlations between the values of the force \mathbf{f} , subsequent steps in the relaxation process are directed in a random way. Therefore the dependence of the spin correlator on time can be written

$$G(t) = G(0) \exp[-t/\tilde{T}], \quad (20)$$

where

$$\tilde{T} \approx T_2 \frac{8j^2 N_B}{5}. \quad (21)$$

Since the donor center is surrounded by a very large number of nuclei (for GaAs, $N_B \approx 1.6 \times 10^5$), formation of a nuclear spin polaron may result in a giant increase of the nuclear spin relaxation time.

Note that the dependence of the random force \mathbf{f} in the relaxation equation (20) on time affects only the relaxation time \tilde{T} . This follows from the asymptotic character of the

expression, which is valid only for times considerably in excess of T_2 , when no individual features in the behavior of a random force affect the final result (for details, see, e.g., Ref. 8). Therefore the asymptotic expression is applicable only if the polaron spin is so large that the inequality $T_2 \ll \tilde{T}$ is met with a large margin.

The author expresses his sincere thanks to V. I. Perel', M. I. Dyakonov, B. P. Zakharchenya, K. V. Kavokin, and V. K. Kalevich for fruitful discussions.

Support of the Russian Fund for Fundamental Research (Grant 96-02-16941) and of the Volkswagen Stiftung is gratefully acknowledged.

¹This value exceeds by about a factor three the maximum critical temperature for another interesting nonlinear phenomenon, namely, the dynamic nuclear self-polarization.¹

²In the high-temperature approximation, the rms deviation of the total spin N_B of nuclei from its equilibrium value is $\sqrt{5N_B/4}$.

³M. I. Dyakonov and V. I. Perel', in *Optical Orientation*, Modern Problems in Condensed Matter Sciences, Vol. 8, edited by F. Meier and B. P. Zakharchenya [North-Holland, Amsterdam, 1984; Nauka, Leningrad, 1989, p. 17].

⁴P. A. Wolff, in *Semiconductors and Semimetals*, Vol. 25, edited by J. K. Furdyna and J. Kossut (Academic, London, 1988), p. 413.

⁵I. A. Merkulov and V. G. Fleisher, in *Optical Orientation*, Modern Problems in Condensed Matter Sciences, Vol. 8, edited by F. Meier and B. P. Zakharchenya [North-Holland, Amsterdam, 1984; Nauka, Leningrad, 1989, p. 137].

⁶V. K. Kalevich and V. G. Fleisher, *Izv. Akad. Nauk SSSR, Ser. Fiz.* **47**, 2294 (1983).

⁷I. A. Merkulov, D. R. Yakovlev, K. V. Kavokin, G. Mackh, W. Ossau, A. Waag, and G. Landwehr, *JETP Lett.* **62**, 335 (1995).

⁸A. Lösche, *Kerninduktion* [Deutscher Verlag der Wissenschaften, Berlin, 1957; IL, Moscow, 1963].

⁹L. D. Landau and E. M. Lifshits, *Statistical Physics* (Pergamon Press, Oxford, 1980) [Russian orig., Nauka, Moscow, 1976, Vol. 1, p. 394].

¹⁰Ya. B. Zel'dovich and A. D. Myshkis, *Fundamentals of Mathematical Physics* [in Russian], Nauka, Moscow, 1973, p. 223–245.

Translated by G. Skrebtsov

Absorption spectrum and excitons in thin films of the solid electrolyte $\text{RbCu}_4\text{Cl}_3\text{I}_2$

V. K. Miloslavskii, E. N. Kovalenko, and O. N. Yunakova

Khar'kov State University, 310077 Khar'kov, Ukraine

(Submitted June 11, 1997)

Fiz. Tverd. Tela (St. Petersburg) **40**, 1022–1026 (June 1998)

We have investigated the absorption spectrum of thin films of the superionic conductor $\text{RbCu}_4\text{Cl}_3\text{I}_2$ synthesized on NaCl crystalline substrates. It is shown that the electron and exciton excitations in the energy interval 3–6 eV are associated with optical transitions in the CuHal sublattice, and the edge of the fundamental band is controlled by optical transitions in the Cu(II)Hal sublattice. It is found that the large band gap of this compound ($E_g = 3.86$ eV) in comparison with those of CuCl and CuI is a result of the small number of Cu ions in the second coordination sphere. The temperature dependence of the spectral position and half-width of the low-temperature exciton band reveals features associated with the phase transitions $\gamma \rightarrow \beta$ ($T_{c1} = 170$ K) and $\beta \rightarrow \alpha$ ($T_{c2} = 220$ K) and with disordering of the cation sublattice attendant to the transition to the superionic state. © 1998 American Institute of Physics. [S1063-7834(98)01306-9]

The superionic conductor $\text{RbCu}_4\text{Cl}_3\text{I}_2$ crystallizes in a lattice isostructural with RbAg_4I_5 and has four molecules per unit cell with period 10.03 Å (Ref. 1); sixteen Cu^+ ions are distributed over 56 tetrahedral voids and are the majority current carriers in the ionic conductivity. The record high value of the ionic conductivity of this solid electrolyte at room temperature ($\sigma \approx 0.45 \Omega^{-1} \cdot \text{cm}^{-1}$) has stimulated a number of studies examining the electrical conductivity and other physical properties of this compound over a wide temperature range.^{2–6} In particular, the existence of two phase transitions has been established: $\gamma \rightarrow \beta$ ($T_{c1} = 170$ K) and $\beta \rightarrow \alpha$ ($T_{c2} = 220$ K), similar to those in RbAg_4I_5 , with the first of these corresponding to the transition from the insulator to the superionic phase. The phase transitions show up as salient points in the temperature dependence of the electrical conductivity,^{1,3} anomalies in the specific heat,⁶ and in the temperature dependence of the total luminescence intensity.⁷ The electronic absorption spectrum of $\text{RbCu}_4\text{Cl}_3\text{I}_2$, as far as we know, has not been studied. At the same time, studies in Refs. 8 and 9, carried out on similar compounds, established that the transition to the superionic state is accompanied by a significant change in the characteristics of the low-frequency exciton bands due to phase transitions and exciton scattering by Frenkel'-defect-created fluctuations in the internal electric field.

The aim of the present work is to examine the absorption spectrum of $\text{RbCu}_4\text{Cl}_3\text{I}_2$ thin films in the region of the fundamental band and in the temperature interval including the phase transitions. It is of great interest to examine the influence of the phase transitions on the main characteristics (spectral position, half-width, etc.) of the exciton bands of this compound.

1. EXPERIMENT

To prepare thin films of this compound we used a starting mixture of chemically pure powders of RbI, CuI, and

CuCl in the appropriate stoichiometric ratio. The compound was synthesized by melting the components of the mixture together in vacuum. Thin films were prepared by thermal vacuum deposition of the melt onto heated (to 100°C) crystalline substrates of NaCl. The choice of substrate and substrate temperature was dictated by the possibility of preparing structurally perfect films (epitaxial growth), and also by the possibility of examining their uv absorption spectra. The structural perfection of the films was monitored directly from the absorption spectra of the films at liquid-nitrogen temperatures. Deviations from stoichiometry or preparation of the films by evaporation of the mixture leads to smeared absorption spectra. At the same time, the absorption spectra of the films prepared by evaporation of the melt onto NaCl substrates reveal comparatively narrow exciton bands. Measurements of the transmission spectra in the energy interval 3–6 eV and temperature interval 90–293 K were carried out in a vacuum optical cryostat mated with an SF-46 spectrophotometer. Film thickness was determined by the Tolanski method (film deposited on a glass substrate).

To determine the parameters of the exciton bands, we subjected the absorption spectra to computer processing with allowance for Fresnel losses at the film–air and film–substrate boundaries as well as interference in the film. Details of the processing of the spectra are spelled out in Ref. 10. The exciton band was fitted by a symmetrically mixed Gaussian and Lorentzian contour.

2. MEASUREMENT RESULTS AND DISCUSSION

An exciton band with maximum at 3.785 eV can be distinguished clearly in the low-frequency edge of the intrinsic absorption band (Fig. 1a). Further along, against the background of the interband absorption, which grows with the photon energy, a series of steps can be observed whose spectral positions are listed in Table I. In the interval 5–6 eV wide

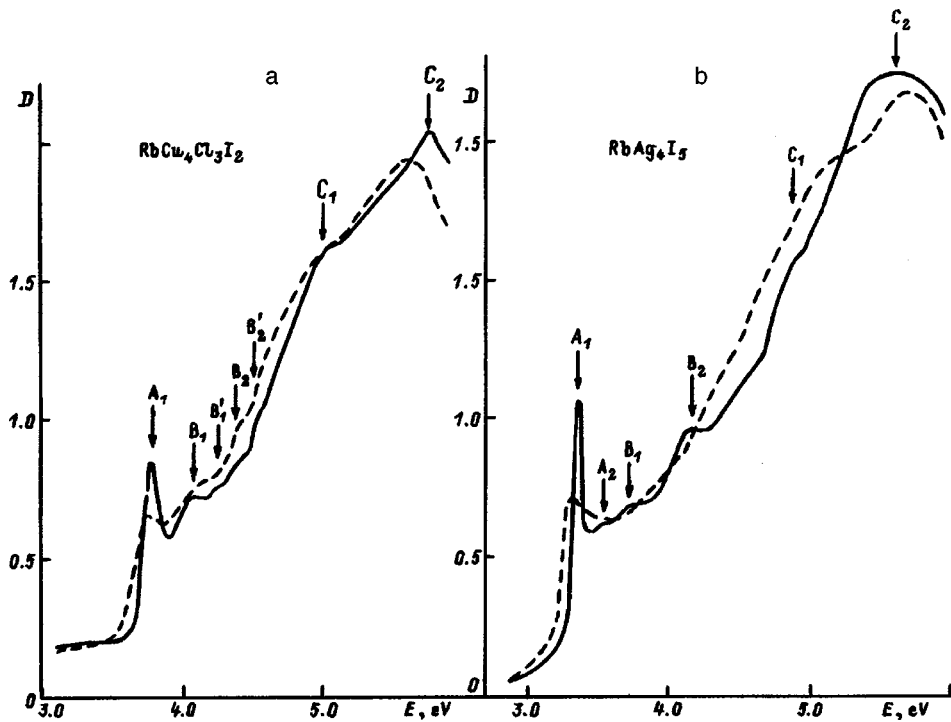


FIG. 1. Absorption spectrum of RbCu₄Cl₃I₂ (a) and RbAg₄I₅ (b) thin films at T=90 (solid curve) and 290 K (dashed curve).

C bands at 5.0 and 5.9 eV are observed, probably corresponding to interband transitions between the centers of the valence bands and the conduction band.

In order to interpret the absorption spectrum of RbCu₄Cl₃I₂ in the measured energy interval 3–6 eV, it is useful to compare the spectrum of this compound with the spectra of the similar binary compounds CuCl and CuI and the absorption spectrum of the isostructural compound RbAg₄I₅ (Ref. 11) (Fig. 1b). The binary compounds CuCl and CuI crystallize with a sphalerite lattice with a tetrahedral bond between the Cu⁺ and Hal⁻ ions. Interband absorption in these compounds in the energy interval 3–6 eV corresponds to transitions between the valence band formed by the 3d states of Cu and the 4p(5p) states of Cl(I), and the 3s(Cu) conduction band.¹² In the absorption edge the exciton bands Z_{1,2} and Z₃ are observed, providing evidence of spin-orbit splitting of the valence band. The interband absorption spectrum in CuI (CuCl) has a maximum at 4.8 eV (6.3 eV), corresponding to Λ₃–Λ₁ transitions between the band centers; between the exciton bands and the indicated maxima no features are observed in the CuCl and CuI spectra.

Since Cu⁺ ions in RbCu₄Cl₃I₂ are also located in tetrahedra consisting of Cl⁻ and I⁻ ions,¹ we believe that the absorption spectrum in this compound in the energy interval 3.5–6 eV also corresponds to exciton excitations in the Cu-

Hal sublattice and interband transitions between the valence band formed by the 3d states of Cu and the 4p(5p) states of Cl(I), and the 4s(Cu) conduction band. But in distinction to CuI and CuCl, the absorption spectrum of RbCu₄Cl₃I₂ has a more complicated structure and the low-frequency A₁ band is shifted by 0.6 eV toward higher frequencies relative to the mean position of the exciton bands in CuI and CuCl.

At the same time, the structure of the spectrum of this compound is similar in many respects to the structure of the absorption spectrum of RbAg₄I₅ (Fig. 1b). In the ternary compound, as in RbCu₄Cl₃I₂, is observed a series of bands against the interband absorption background, i.e., the spectrum of RbAg₄I₅ is more complicated than that of the similar compound γ AgI (Ref. 13), and the low-frequency exciton band in RbAg₄I₅ at 3.4 eV is shifted relative to the corresponding band in γ AgI (2.92 eV) by 0.42 eV toward higher frequencies.

The similarity of the spectra of these two compounds is a reflection of the similarity of their crystal lattices. It follows from the data of Ref. 1 that the sixteen Cu ions are distributed nonuniformly among the tetrahedral voids and divide into three groups: Cu(II), Cu(III), and Cu(C). Groups II and III contain 8.14 and 7.06 ions distributed among 24 sites, and group C, 1.06 ions distributed among eight sites. Analogous groups exist in α RbAg₄I₅ which contain 9.38, 5.5, and 0.88 Ag ions in the groups Ag(II), Ag(III), and Ag(C), respectively. In the binary compounds CuCl and CuI the Cu ions occupy half of the tetrahedral voids, i.e., the number of Cu ions in the second-coordination sphere, M, is equal to 12. The presence of different groups in the CuHal and AgI sublattices of the superionic conductors can probably be explained by the more complicated character of the electronic spectrum of these compounds. The shift of the exciton A₁ bands toward higher frequencies relative to the

TABLE I. Positions of the steps (in eV) in the absorption spectra of the films.

Compound	E _{A₁}	E _{A'₁}	E _{B₁}	E _{B'₁}	E _{B₂}	E _{B'₂}	E _{C₁}	E _{C₂}
RbAg ₄ Cl ₃ I ₂	3.735	3.795	4.05	4.24	4.36	4.52	5.04	5.72
RbAg ₄ I ₅	3.345		3.74		4.1		4.5	
CuI	3.056 (Z _{1,2})		3.709 (Z ₃)					
CuCl	3.23 (Z ₃)		3.29 (Z _{1,2})					

corresponding bands in CuCl, CuI, and γ AgI is evidence of a contraction of the allowed v and c bands, adjoining the band gap. The contraction of these bands is probably connected with a smaller value of M in the second-ordination sphere in $\text{RbCu}_4\text{Cl}_3\text{I}_2$ and RbAg_4I_5 .

To estimate the total width of the resolved bands adjoining the band gap, it is necessary to know the width of the band gap E_g and the energy of the optical transition between the band centers E_0 since

$$\Delta E = \Delta E_v + \Delta E_c = 2(E_0 - E_g). \quad (1)$$

To determine E_g in $\text{RbCu}_4\text{Cl}_3\text{I}_2$, we separated the A_1 band from the interband absorption edge. Estimating from the inflection point $D(E)$ gives $E_g = 3.86 \pm 0.02$ eV. For CuCl and CuI $E_g = 3.40$ and 3.11 eV, respectively.¹² Since each Cu ion in groups II and III is surrounded by a Cl ion and an I ion,¹ the value of E_g found above is comparable with the mean value $\bar{E}_g = 3.25$ eV for the hypothetical solid solution $\text{Cu}(\text{ClI})_{0.5}$ (solid solutions of CuCl and CuI do not exist); for this same (hypothetical) compound $\bar{E}_0 = 0.5(6.3 + 4.8)\text{eV} = 5.55$ eV. If we assume that E_0 is the same for $\text{RbCu}_4\text{Cl}_3\text{I}_2$ and $\text{Cu}(\text{ClI})_{0.5}$, then on the basis of Eq. (1) $\Delta E_1 = 3.38$ eV and $\Delta E_2 = 4.1$ eV, respectively.

In the tight-binding approximation the total width of the allowed bands is proportional to the sum of the resonance integrals J_c and J_v , constructed in terms of the wave functions of the neighboring equivalent ions for the states in the conduction band and the valence band, and to the coordination number M . If J_c and J_v are equal for the two compounds, then

$$(\Delta E_1 / \Delta E_2) = (M_1 / M_2). \quad (2)$$

Using the values of ΔE found above and the coordination number $M_2 = 12$ for $\text{Cu}(\text{ClI})_{0.5}$, we find $M_1 = 8.8$. This quantity exceeds the value $M_1 = 8.14$ determined from the x-ray diffraction data¹ for the group Cu(II). However, if we allow for the error in the determination of the latter quantity (0.48, Ref. 1), the errors in the determination of ΔE from the spectroscopic estimates of E_g and E_0 , and the possible difference in the values of M_1 for the insulator (γ) phase and the superionic (α) phase, we can conclude that there is satisfactory agreement between the values of M_1 found by these two methods. Similar values of M_1 (9.2 and 9.4) were also obtained for RbAg_4I_5 (Ref. 14). From the above estimates of ΔE_1 and M_1 we can draw the following conclusions: 1) the increase in E_g in the investigated compound in comparison with E_g in CuCl and CuI is explained by the lower value of the coordination number M ; 2) the absorption edge in $\text{RbCu}_4\text{Cl}_3\text{I}_2$ corresponds to electron and exciton excitations in the sublattice containing the Cu(II) ions; 3) a similar estimate of M_1 was obtained for the sublattice containing the Cu(III) ions. Taking into account the energy interval between the A_1 and B_1 exciton bands (0.29 eV), we find that the B_1 band adjoins the edge of the interband transitions situated at 4.15 eV. Hence $\Delta E_1 = 2.8$ eV, and on the basis of relation (2) $M_1 = 7.3$, which is close to $M_1 = 7.06$ from Ref. 1.

Interpretation of the higher-frequency features of the $\text{RbCu}_4\text{Cl}_3\text{I}_2$ spectrum is hindered. Note that the number of features in the spectrum of this compound is larger than that

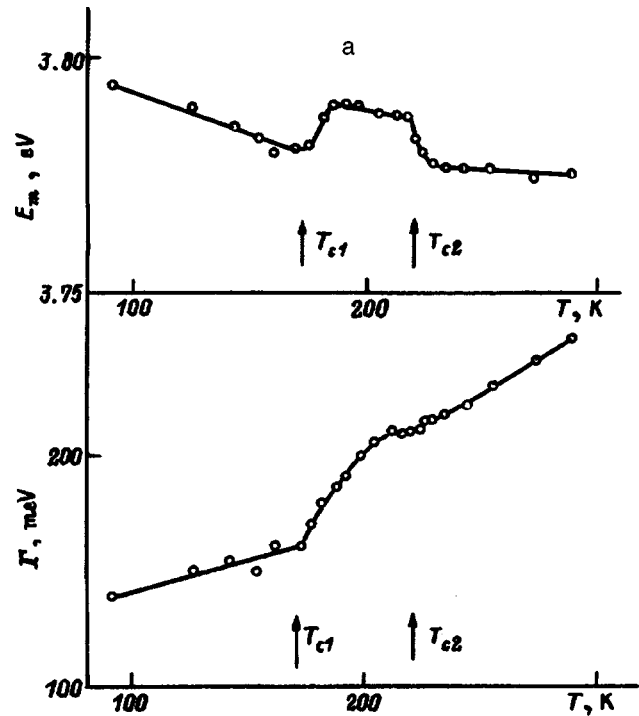


FIG. 2. Temperature dependence of the spectral position E_m (a) and half-width Γ (b) of the A_1 -exciton band in $\text{RbCu}_4\text{Cl}_3\text{I}_2$.

of RbAg_4I_5 . A possible reason for this is the lowered symmetry of the tetrahedra in the Cu(II) and Cu(III) groups [the $(\text{CuCl}_2\text{I}_2)^{3-}$ tetrahedra], leading to additional splitting of the states in the valence band.

To examine the temperature dependence of the parameters of the low-frequency A_1 band, we measured the absorption spectrum in the region 3.5–4.0 eV more carefully at 21 points in the temperature range 90–290 K. Computer processing of the $D(E)$ spectra allowed us to determine the spectral position E_m and half-width Γ of the band, and also its oscillator strength and the Gaussian fraction of the total contour. Measurements at liquid-nitrogen temperatures (Fig. 1a) show that the A_1 band is non-elementary and consists of two overlapping bands: a band at 3.795 eV and a weaker band at 3.735 eV. However, when the temperature is raised the bands do not resolve; for this reason the A_1 band is fitted by one symmetric contour. It follows from the processing results (Fig. 2a) that a low-frequency band shift is observed in the temperature interval 90–170 K, whose magnitude $dE_m/dT = 2.5 \times 10^{-4}$ eV/K is typical in order of magnitude for many similar compounds and is due to the exciton-phonon interaction. In the region of the $\gamma \rightarrow \beta$ transition ($T_{c1} = 170$ K) in a small temperature interval centered at 15 K a high-frequency shift of the A_1 band equal to 14 meV is observed. An analogous shift in the region of the $\gamma \rightarrow \beta$ transition is observed in RbAg_4I_5 (8 meV, Ref. 11; 15 meV, Ref. 9) and in KAg_4I_5 (14 meV, Ref. 14). As was shown in Refs. 11 and 14, the shift of the A_1 band is connected with an increase in the volume of the unit cell during a first-order phase transition. Obviously, the shift for $\text{RbCu}_4\text{Cl}_3\text{I}_2$ is also evidence of a first-order phase transition at 170 K, accompanied by an expansion of the unit cell in the β phase. In the

region of the $\beta \rightarrow \alpha$ transition ($T_{c2} = 220$ K), on the contrary, the band is observed to shift by 12 meV toward lower frequencies. In the temperature interval 230–290 K the shift of the exciton band is insignificant.

Phase transitions also configure the complicated dependence $\Gamma(T)$ of the A_1 band. In the temperature interval 90–170 K (the γ phase) the half-width grows according to a linear law with $d\Gamma/dT = 2.2 \times 10^{-4}$ eV/K. In the temperature interval 170–200 K an abrupt growth of Γ from 160 to 200 meV is observed ($d\Gamma/dT = 1.33 \times 10^{-3}$ eV/K). The increase in Γ accompanying the transition to the β phase is probably connected with the generation of a large number of Frenkel' defects accompanied by disordering of the Cu cation sublattice. This lattice disordering, as was shown in Ref. 15, leads to fluctuations of the internal electric field and to additional scattering of excitons by the field fluctuations. The expansion of the lattice accompanying the $\gamma \rightarrow \beta$ transition probably facilitates the generation of Frenkel' defects since the probability of passage of the Cu ions through the faces of the tetrahedra grows in this case. In the temperature interval 200–230 K the value of $d\Gamma/dT$ is decreased, which correlates with the low-frequency shift of E_m at T_{c2} and is probably connected with the decrease in the volume of the unit cell accompanying the $\beta \rightarrow \alpha$ first-order phase transition. However, to connect this shift with the change in the volume of the unit cell requires additional dilatometric data.

For $T > T_{c2}$ (the α phase) the half-width grows approximately according to a linear law, but the value of $d\Gamma/dT = 6 \times 10^{-4}$ eV/K is significantly larger than in the region of the γ phase. We link growth of Γ in the region of the α phase with thermal generation of Frenkel' defects, i.e., in addition to the phonon component of $\Gamma(T)$ there is a component $\Gamma_F(T)$ due to scattering of excitons by Coulomb fluctuations. The exciton band in the region of the α phase has a Gaussian shape; therefore the total half-width in this temperature interval is equal to $\Gamma = (\Gamma_{ph}^2 + \Gamma_F^2)^{1/2}$, where Γ_{ph} is the contribution to the half-width due to the exciton–phonon interaction. The Frenkel' defect concentration obeys the Arrhenius law

$$n_F = N \exp(-U_F/kT). \quad (3)$$

Assuming a linear dependence of Γ_{ph} over the entire temperature interval, with $d\Gamma_{ph}/dT = 2.5 \times 10^{-4}$ eV/K, and assuming Γ_F to be proportional to the defect concentration n_F , it is possible, after separating Γ_F from the total half-width, to determine the activation energy U_F of the Frenkel' defects in the α phase from relation (3). Processing of the functional dependence $\ln\Gamma_F(T^{-1})$ gives $U_F = 0.065$ eV.

Note that some correlation exists between the temperature dependence of the half width $\Gamma(T)$ and the temperature

dependence of the conductivity $\sigma(T)$. In the region $T \approx T_{c1}$ a jump in $\sigma(T)$ is observed; in the region of the β phase the electrical conductivity grows exponentially with activation energy $U = 0.18$ eV; and in the region of the α phase the quantity U falls to 0.15 eV (Ref. 1). However, there is a substantial difference between the two dependences $\Gamma(T)$ and $\sigma(T)$. On the one hand, this difference is governed by the contribution to $\Gamma(T)$ from broadening due to the exciton–phonon interaction and from inhomogeneous broadening. On the other hand, the activation energy of the electrical conductivity has an additional term governing the activation growth of the mobility of the Cu ions. The latter probably explains the lower value of U_F in comparison with the value of U found from $\sigma(T)$ in the region of the α phase.

To summarize, the above analysis of the absorption spectra of $\text{RbCu}_4\text{Cl}_3\text{I}_2$ thin films shows that the edge of the fundamental band corresponds to electron and exciton excitations in the Cu(II)Hal sublattice of this compound. The lower number of Cu ions in the second coordination sphere explains the increase in the width of the band gap in this compound in comparison with its value in CuCl and CuI . The temperature dependence of the spectral position and half-width of the low-frequency exciton band reveal features associated with the first-order phase transitions $\gamma \rightarrow \beta$ and $\beta \rightarrow \alpha$ and with disordering of the cation sublattice attendant to the transition from the insulator phase to the superionic phase.

¹ S. Geller, J. R. Akridge, and S. A. Wilber, *Phys. Rev. B* **19**, 5396 (1979).

² E. S. Nimon, A. L. L'vov *et al.*, **20**, 4, 670 (1984).

³ Zong-yuan Zhao, Li-guan Chen *et al.*, *Acta Phys. Sin.* **33**, 11, 1556 (1984).

⁴ H. Looser and D. Brinkmann, *Solid State Ionics* **17**, 4, 277 (1985).

⁵ F. M. Mustafaev, A. S. Abbasov, and I. Ya. Aliev, *Izv. Akad. Nauk SSSR, Neorg. Mater.* **25**, 11, 1820 (1989).

⁶ T. Atake, H. Kawaji *et al.*, *Solid State Ionics* 53–56, Pt. 2c, 1260 (1992).

⁷ M. M. Afanas'ev, G. B. Venus, O. G. Gromov *et al.*, *Fiz. Tverd. Tela (Leningrad)* **26**, 2956 (1984) [*Sov. Phys. Solid State* **26**, 1785 (1984)].

⁸ I. Kh. Akopyan, D. N. Gromov *et al.*, *Fiz. Tverd. Tela (Leningrad)* **26**, 2628 (1984) [*Sov. Phys. Solid State* **26**, 1593 (1984)].

⁹ I. Kh. Akopyan, *Elektrokhimiya* **26**, 11, 1495 (1990).

¹⁰ V. K. Miloslavskii, O. N. Yunakova, and Sun' Tsya-Lin', *Opt. Spektrosk.* **78**, 436 (1995) [*Opt. Spectrosc.* **78**, 391 (1995)].

¹¹ V. K. Miloslavsky, O. N. Yunakova, and Sun Tsya-Lin, *Funct. Mater.* **1**, 1, 51 (1994).

¹² A. Goldmann, *Phys. Status Solidi B* **81**, 1, 9 (1977).

¹³ R. Galbadakh and V. K. Miloslavskii, *Ukr. Fiz. Zh.* **39**, 2, 167 (1994).

¹⁴ V. K. Miloslavskii and Sun' Tsya-Lin', *Funct. Mater.* **2**, 4, 438 (1995).

¹⁵ I. Kh. Akopyan, V. N. Bondarev, D. N. Gromov, A. B. Kuklov, and B. V. Novikov, *Fiz. Tverd. Tela (Leningrad)* **29**, 2263 (1987) [*Sov. Phys. Solid State* **29**, 1305 (1987)].

Induced impurity photoconductivity in crystals of Si- and Ge-sillenites

T. V. Panchenko

Dnepropetrovsk State University, 320625 Dnepropetrovsk, Ukraine

(Submitted June 30, 1997)

Fiz. Tverd. Tela (St. Petersburg) **40**, 1027–1029 (June 1998)

The spectral distribution of the uv-induced photoconductivity intensity and relaxation in $\text{Bi}_{12}\text{SiO}_{20}$ and $\text{Bi}_{12}\text{GeO}_{20}$ crystals both undoped and doped with Al, Ga, Cr, Cu, Mn, and V is investigated in the optical range 0.5–3.5 eV in the temperature ranges 85–95 K and 285–295 K. It is shown that in the short-wavelength region 2.2–3.5 eV it is controlled by multicenter recombination in which both “fast” and “slow” recombination participate. © 1998 *American Institute of Physics*. [S1063-7834(98)01406-3]

Crystals of the sillenites $\text{Bi}_{12}\text{MO}_{20}$ (BMO), where $M = \text{Si, Ge, Ti}$, are a complex object of study for investigation of nonequilibrium processes in connection with their rich spectra of local states of the forbidden band. The induced impurity photoconductivity (IIP) provides useful information about the electronic energy-level diagrams. It has been observed in pure in crystals of $\text{Bi}_{12}\text{SiO}_{20}$ (BSO), $\text{Bi}_{12}\text{GeO}_{20}$ (BGO), and also in crystals of BSO doped with Cr, Mn, and Ni,^{1–5} and is characterized by an increase in the photoconductivity by 1–2 orders of magnitude with a “red limit” $h\nu_f \leq 2.1$ eV. The transition to the IIP state is accompanied by growth of the drift mobility of the photocarriers,² and a modification of the current–brightness characteristics³ and relaxation kinetics.^{4,5} These effects cannot be explained within the framework of a simple model¹ linking induced impurity photoconductivity with the filling of donor levels at the expense of the annihilation (by light with $h\nu > 2.1$ eV) of acceptor levels without an account of the recombination mechanism. Multicenter recombination in BMO crystals is indicated by thermal activation and photoconductivity quenching effects, which are well described with the help of s centers of “fast” recombination and r centers of “slow” recombination.^{6–9}

The present paper reports results of a study of induced impurity photoconductivity in BSO and BGO crystals at the temperatures $T_1 = 285–295$ K and $T_2 = 85–95$ K, corresponding to the mechanisms of fast and slow recombination.^{8,9}

We investigated nominally pure crystals of BSO and BGO, and BSO and BGO crystals doped with Al, Ga, Cr, V, Cu, and Mn, grown by the Czochralski method. The impurity content of the doped crystals was 6×10^{-3} (Cr), 3×10^{-2} (Mn), 5×10^{-2} (V), 3×10^{-1} (Cu), 4×10^{-2} (Ga), and 6×10^{-3} wt.% (Al). The samples were prepared in the form of polished wafers of thickness 0.3–0.7 mm with large (001) faces on which Ag electrodes were deposited, burnt-in in vacuum. All the samples were heated in darkness to 700 K before the measurements.

We investigated the spectral distribution of the steady-state and induced photoconductivity ($\Delta\sigma^{\text{ph}}(h\nu)$) in the range $h\nu = 0.5–3.5$ eV and also relaxation of the induced impurity photoconductivity. An SPM-2 monochromator was used,

with resolving power better than or equal to 0.02 eV. As the light source we used a 400-watt incandescent lamp, whose light was modulated with a frequency of 12 Hz. The dependences $\Delta\sigma^{\text{ph}}(h\nu)$ were normalized to the instrument photon flux distribution function $N(h\nu)$. The measurements were performed in sequence from low to high values of $h\nu$ to avoid uncontrollable IIP. The constant field regime $E = 100–200$ V·cm^{−1} and the synchronous detection technique were used. IIP was excited by a mercury lamp emitting in the band $h\nu \approx 3.4$ eV (interband excitation).

IIP was observed (in contrast to Refs. 1–3 and in line with Refs. 4 and 5) over the entire spectral range. The gain in the induced impurity photoconductivity in the Cr, Mn, Cu, and V doped crystals purchased by lowering the temperature was especially pronounced (Fig. 1).

To analyze the induced impurity photoconductivity, we distinguish two regions: the long-wavelength region $\Delta h\nu_1 = 0.5–2$ eV (the impurity absorption region) and the short-wavelength region $\Delta h\nu_2 = 2.2–3.5$ eV (the absorption “shoulder” due to intrinsic defects, adjoining the fundamental absorption edge).

In the region $\Delta h\nu_1$, induced impurity photoconductivity is observed which is typical of broad-band semiconductors and due to filling of the impurity levels. At T_1 it is the largest in BSO : Cu and BSO : Ga crystals. Lowering the temperature to $T_2 \approx 85–95$ K leads to an increase in the IIP, and this increase is most significant for BGO : Mn (Fig. 1). The optical activation energies E_a^{Op} , found from the thresholds of the impurity photoelectric effects, are listed in Table I. Relaxation of the photocurrent has one “fast” and two “slow” components with characteristic relaxation times: $\tau_1 = 0.2$ s, $\tau_2 = 62$ s, and $\tau_3 = 120$ s, which points to the participation of sticking levels, whose parameters were determined in Refs. 8 and 9.

In the short-wavelength region $\Delta h\nu_2$ the IIP mechanism is more complicated. In BSO and BGO crystals uv illumination causes the photosensitivity to decrease in the band with $h\nu_{\text{max}} = 2.48$ eV and causes it to grow significantly in the region near ($h\nu \sim 3.3$ eV), where the bands with $h\nu_{\text{max}} = 3$ and 3.1 eV separate (lowering the temperature to T_2 shifts them toward larger $h\nu$). A similar IIP intensity distribution is observed in BSO : Cu and BSO : V crystals. In BGO : Mn,

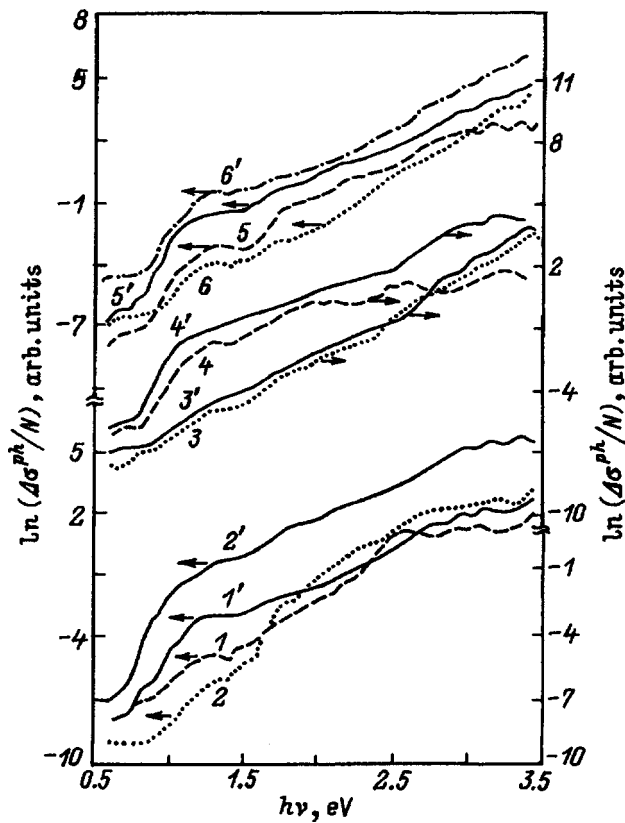


FIG. 1. Spectral distribution of the steady-state (1-6) and induced (1'-6') photoconductivity of BSO (1, 1'), BSO:Cu (2, 2'), BGO:Al (3, 3'), BSO:V (4, 4'), BSO:Cr (5, 5'), and BGO:Mn (6, 6') crystals. $T=90$ K.

BSO:Cr, BGO:Al, and BSO:Ga crystals it is nearly exponential and is observed in a narrower near-edge band (Fig. 2). Taking into account that Al and Ga ions almost completely, and Cr and Mn ions partly (in their role as acceptors), compensate the optical absorption and photosensitivity of BMO in the shoulder region,¹⁰⁻¹² we conclude that the IIP spectral intensity distribution depends on the degree of compensation.

A steady-state photocurrent is set up under the action of a rectangular light pulse in the band with $h\nu_{\max}=2.48$ eV, obeying the ordinary law $I_{\max}(1-t/\tau)$, where τ has the components $\tau_1=2.5$ s, $\tau_2=18.5$ s, and $\tau_3=60$ s, which also characterize its exponential falloff (Fig. 3). In the IIP state

TABLE I. Optical activation energy E_a^{Op} (in eV) of the impurity levels of BSO and BGO.

BSO	BGO:Al	BSO:Ga	BGO:Mn	BSO:Cr	BSO:Cu	BSO:V
0.79	0.84	0.86	0.84	0.74	0.72	0.86
1.02	1.52	1.24	1.0	1.13	0.83	1.0
1.5	2.45*	1.24	1.36	1.37	1.23	1.32
1.92	2.6*	2.2	1.52	1.48	1.5	1.43
2.22	3.0	3.13	1.92	1.93	1.9	1.52
2.45*	3.19		2.18*	2.45	2.26	1.89
2.6*	3.39		2.48*	2.55	2.52	2.23
2.86			2.55*	2.87	2.89	2.8
3.03			3.04	3.02	3.07	3.02
3.2				3.26	3.23	3.27

*Photosensitivity bands whose intensities fall under uv illumination.

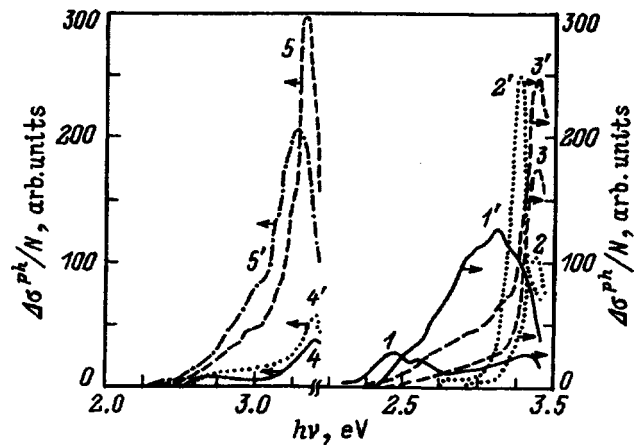


FIG. 2. Short-wavelength spectral distribution of the intensity of the steady-state (1-5) and induced (1'-5') photoconductivity of BSO (1, 1'), BSO:Ga (2, 2'), BSO:Cr (3, 3'), BSO:Cu (4, 4'), and BGO:Mn (5, 5') crystals. $T=290$ K.

the photoresponse relaxation mechanism varies: it acquires a "spikelike" character, whereby the setting up of the photocurrent can be described by the expression $I=\{A/(\tau^{-1}-B)\} \times \{\exp(-Bt)-\exp(-t/\tau)\}$, where τ varies within the limits 1-370 s and $A, B=\text{const}$. After the spike the photocurrent does not fall to zero, but settles to $I_0=0.7I_{\max}$. After the light is switched off, the IIP falls significantly more slowly than the steady-state photoconductivity (Fig. 3). The spikelike character of the relaxation is evidence of optical recharging of impurity centers. According to Ref. 11, the absorption and photosensitivity in the region $\Delta h\nu_2$ are due to nonstoichiometry defects: Bi^{3+} and Bi^{5+} ions in the roles of acceptors and donors, replacing Si^{4+} ions at the sites of the Si-sublattice. Therefore transitions of the type $\text{Bi}_{\text{Si}}^{5+} + 2e \rightarrow \text{Bi}_{\text{Si}}^{3+}$ are a possible recharging mechanism.

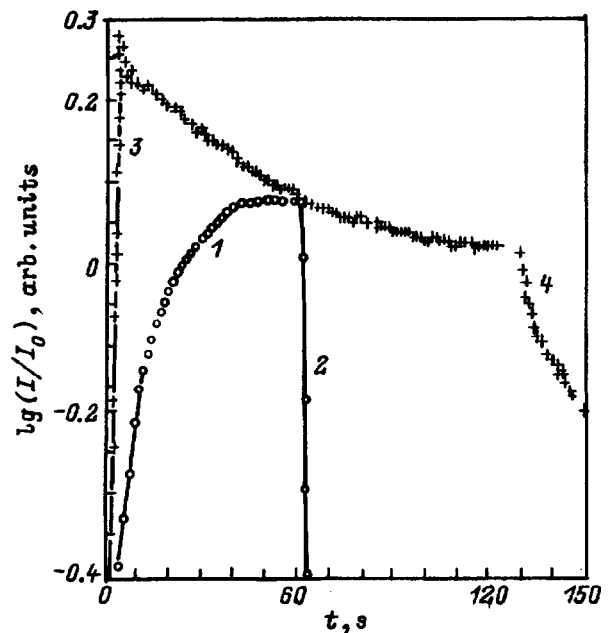


FIG. 3. Relaxation curves of the steady-state (1, 2) and induced (3, 4) photoconductivity of BSO crystals for excitation by a rectangular light pulse of duration 60 (1, 2) and 130 s (3, 4). $T=290$ K.

The effect of temperature on the IIP reduces to the following. Near T_1 the total IIP ($\int \Delta \sigma^{\text{ph}}(h\nu) d(h\nu)$) is the greatest for BSO, BGO, BSO:Ga, and BGO:Al crystals (group *A*), and at T_2 , for crystals of BSO:Cu, BGO:Mn, BSO:V, and BSO:Cr (group *B*, Fig. 2). This situation is completely determined by the effect of temperature quenching of the photoconductivity. In Ref. 9 it was shown that near T_1 the strongest (in comparison with the undoped crystals) quenching of the photoconductivity takes place in crystals of group *B*, for example, in crystals doped with Cr or Cu, while at T_2 photoconductivity is quenched in crystals of group *A*.

Thus, the following mechanism of IIP may be proposed: uv illumination causes a photochemical conversion of deep impurity centers of donor type ($\text{Bi}_{\text{Si}}^{5+}$, for example) into "sensitizing" r centers of slow recombination of acceptor type (possibly $\text{Bi}_{\text{Si}}^{3+}$). This causes IIP due to an increase of the lifetime of the photocarriers, which depends nonlinearly on the degree of participation of the r carriers in the recombination processes. Strong temperature quenching of photoconductivity points to switching from r centers of slow recombination to s centers of fast recombination, weakening the IIP effect. It was shown in Ref. 8 that the spectral range of the photoconductivity controlled by the r and s recombination centers has a red limit ≈ 2.1 eV, which corresponds to the considered spectral region.

I am grateful to Z. Z. Yanchuk for assistance with the experiments.

- ¹A. Ya. Volosov, V. Kh. Kostyuk, A. Yu. Kudzin, and G. Kh. Sokolyanskiĭ, *Fiz. Tverd. Tela (Leningrad)* **23**, 2187 (1981) [*Sov. Phys. Solid State* **23**, 1281 (1981)].
- ²V. Kh. Kostyuk, A. Yu. Kudzin, and G. Kh. Sokolyanskiĭ, *Fiz. Tverd. Tela (Leningrad)* **22**, 8, 2454 (1980) [*Sov. Phys. Solid State* **22**, 1429 (1980)].
- ³V. P. Avramenko, A. Yu. Kudzin, and G. Kh. Sokolyanskiĭ, *Fiz. Tverd. Tela (Leningrad)* **26**, 2, 485 (1984) [*Sov. Phys. Solid State* **26**, 290 (1984)].
- ⁴I. A. Karpovich, E. E. Kolosov, E. I. Leonov, V. M. Orlov, and M. V. Shilova, *Izv. Akad. Nauk SSSR, Neorg. Mater.* **21**, 6, 965 (1985).
- ⁵M. V. Shilova, V. M. Orlov, E. I. Leonov, E. E. Kolosov, and I. A. Karpovich, *Izv. Akad. Nauk SSSR, Neorg. Mater.* **22**, 1, 103 (1986).
- ⁶I. S. Zakharov, I. A. Petukhov, V. M. Skorikov, and M. G. Kisteneva, *Izv. Vuzov. Fizika*, **6**, 85 (1985).
- ⁷I. S. Zakharov, *Fiz. Tverd. Tela (Leningrad)* **27**, 1062 (1985) [*Sov. Phys. Solid State* **27**, 643 (1985)].
- ⁸T. V. Panchenko and Z. Z. Yanchuk, *Fiz. Tverd. Tela (St. Petersburg)* **38**, 2018 (1996) [*Phys. Solid State* **38**, 1113 (1996)].
- ⁹T. V. Panchenko and Z. Z. Yanchuk, *Fiz. Tverd. Tela (St. Petersburg)* **38**, 3042 (1996) [*Phys. Solid State* **38**, 1663 (1996)].
- ¹⁰T. V. Panchenko and N. A. Truseeva, *Ukr. Fiz. Zh.* **29**, 8, 1186 (1984).
- ¹¹T. V. Panchenko, V. Kh. Kostyuk, and S. Yu. Kopylova, *Fiz. Tverd. Tela (St. Petersburg)* **38**, 155 (1996) [*Phys. Solid State* **38**, 84 (1996)].
- ¹²T. V. Panchenko, A. Yu. Kudzin, and V. Kh. Kostyuk, *Izv. Akad. Nauk SSSR, Neorg. Mater.* **19**, 7, 1144 (1983).

Translated by Paul F. Schippnick

Excitation of intrinsic defects in ionic crystals by high-power optical and electron beams

V. I. Baryshnikov and T. A. Kolesnikova

Scientific-Research Institute of Applied Physics, Irkutsk State University, 664003 Irkutsk, Russia

(Submitted July 8, 1997)

Fiz. Tverd. Tela (St. Petersburg) **40**, 1030–1035 (June 1998)

The efficiency of excitation and recharging of intrinsic defects by hot charge carriers has been investigated in ionic crystals acted on by high-power optical and electron beams. The interaction cross sections of hot electrons and holes with intrinsic lattice sites and F_n -type defects ($n=1,2$) are shown to be commensurate. It is also shown that the potential of the intracrystalline field in the vicinity of F and F_2 centers is nearly regular. © 1998 American Institute of Physics. [S1063-7834(98)01506-8]

In the interaction of ionizing radiation with crystalline materials, ionization of inner shells of ions or atoms results in the creation of an avalanche of fast electrons. This process continues until the energy of the electrons is lower than the ionization potential of the inner shells of the ions or atoms making up the crystal structure.¹ The electrons then ionize by impact only the outer (valence) shells, and the electrons of the valence band are kicked up into the conduction band. Thus are created free (hot) electrons (e) and holes (h). When the energy of the free electrons reaches the ionization threshold of the valence shell of the ions or atoms of the material (W_i), the process of creation of hot (band) electrons and holes ceases. As they relax, the hot electrons and holes interact with point defects of the crystal lattice and excite their luminescence via electron-hole and exciton mechanisms. Analysis of the experimental studies on this subject^{2,3} indicates that the exciton mechanism is significantly out-paced by the electron-hole mechanism. Studies of the temperature dependence of the radioluminescence yield (η) have shown that the main contribution to the excitation of impurity and intrinsic defects comes from the recombination process with participation of hot holes and electrons.⁴ η is determined by the concentration N and the excitation efficiency of the defects during migration of the electrons and holes (η_m) (Ref. 5)

$$\eta = \frac{\eta_g \eta_m \eta_c N h \nu}{W}, \quad (1)$$

where η_g is the efficiency of generation of hot electrons and holes, η_c is the intracenter luminescence, N is the concentration of defects, and W is the energy of the fast electrons. The concentration of the recombination-excited defects (N^*) during migration of the band electrons and holes is determined by N and the probability of their capture by a luminescence center (P)

$$N_a^* = PN, \quad P = R\sigma_d n \text{ (Ref. 5)}, \quad R\sigma = \eta_m, \quad (2)$$

where n is the concentration of hot electrons and holes, R is their mean free path in an unactivated crystal, on which their energy drops below W_i and is dissipated down to W_g , σ_d is

the capture (interaction) cross section of electrons or holes for (with) a luminescence center. From the data of Ref. 6, R in alkali-halide crystals lies in the range $(60-1200)a$, where a is the lattice constant. The value of R can be found from relation (2) on the basis of the rough estimate $\sigma_d = \pi a^2/4$ (Ref. 5). Hot electrons and holes give back energy to the lattice, in the process creating acoustical and optical phonons. In one collision with a regular ion they lose an amount of energy equal to $W_f \sim 0.01$ eV (Ref. 7). Hence $R \approx (W_i - W_g)/W_f$ for the band electrons and holes in ionic crystals is equal to $(\sim 800-1500)a$ and, as was mentioned in Ref. 7, it is a characteristic of the material. It follows from relations (2) and Refs. 6 and 7 that, at the stage of hot electron and hole migration, the efficiency of recombination excitation of defects is controlled mainly by σ_d .

Intrinsic defects (color centers) of F and F_2 type are the working centers of tunable lasers and under intense optical excitation have a high emissivity.^{8,9} The available methods of coloring crystals allow one to create quite high concentrations of F and F_2 color centers.¹⁰ However, the question of the efficiency of excitation of radioluminescence of F and F_2 centers remains open. Reference 11 notes the high probability of recombination of hot electrons and holes with F_2 centers in LiF. This result cannot be taken as convincing since the measurements of the kinetics of the M band were made without taking the strong overlap of the absorption bands of the F_2 and F_3^+ color centers into account. In this case, the parallel process of capture of band electrons by the F_3^+ centers, which is unavoidable due to the Coulomb interaction, levels the result of recombination of hot electrons and holes with the F_2 centers and does not allow a reliable estimate of the capture cross section σ_{F_2} . For other crystals, data are also lacking on the efficiency of radiation-excited luminescence of F and F_2 centers. It is well known that the probability of recombination of electrons and holes with isoelectronic built-in impurity defects is governed by the structure of the outer s and p shells of the intrinsic and activator ions.¹² But the impurity defects and F centers differ fundamentally both in their nature and in their electronic structure. Thus, directed studies of the characteristics of crystals determining the mag-

nitude of the interaction cross section of the hot electrons and holes with F -type defects are of great interest.

1. THEORY OF THE METHOD

The efficiency of interaction of hot charge carriers with lattice defects is given by $A_r = \sigma(R_e + R_h)$, where, according to the data of Ref. 5, $R_e \approx R_h$. To investigate R_e and σ , it is convenient to use the one-electron approximation, which considers the motion of a single electron in the self-consistent field of the crystal created by the nuclei and the remaining electrons. The Schrödinger equation for the electron wave function in the self-consistent field takes the form¹³

$$-\frac{\hbar}{2m}\Delta^2\psi(\mathbf{r}) + U(\mathbf{r})\psi(\mathbf{r}) = W\psi(\mathbf{r}), \quad (3)$$

where $U(\mathbf{r})$ is the self-consistent potential satisfying the periodicity condition $U(\mathbf{r}+a) = U(\mathbf{r})$, a is the lattice constant (length of the unit cell), and W is the energy.

For a crystal consisting of N unit cells, the wave function ψ is the approximation solution of Eq. (3), where $p = \hbar k$ is the quasimomentum of the electron

$$\psi_{pj}(\mathbf{r}) = \frac{1}{\sqrt{N}} u_{pj}(\mathbf{r}) \exp \frac{i}{\hbar} \mathbf{p} \cdot \mathbf{r}, \quad (4)$$

where $u(\mathbf{r}+a) = u(\mathbf{r})$.

The equation of the periodic function $u_{pj}(r)$ is obtained from Eqs. (3) and (4)

$$\left[U(r) + \frac{p^2}{2m} - W_{pj} \right] u_{pj} = \frac{\hbar}{2m} \Delta^2 u_{pj} + \frac{i\hbar}{m} \Delta u_{pj}. \quad (5)$$

The Bloch theorem states that the mean velocity for states of the form (4) is equal to the derivative of the energy with respect to the quasimomentum $v_{pj} = \Delta_p W_{pj}$ (Ref. 13), i.e., in the field $U(\mathbf{r})$ of an ideal crystal lattice the state ψ_{pj} corresponds to nondecaying directed motion of the electron. For strict periodicity of the crystal field the electron migrates without scattering. Proceeding from this, the finite mean free path of the hot charge carriers is associated with deviations from regularity of the crystal field in the vicinity of the intrinsic or impurity defects or with phonon fluctuations of the lattice.¹³ Then, in "ideal" crystals, the interaction cross section of the hot electrons with the regular lattice sites (σ) tends to zero.

Thus, in the region of permissible values of the electron velocity v the cross section σ allows us to estimate the parameters of the perturbing defect potential $U^*(\mathbf{r})$. The interaction cross section potential of the conduction band electrons with the defect lattice sites $\sigma(v)$ determines the transition probability of the impurity ions or F centers to an excited state. Hence, for the region of permissible values of the velocity of the hot electrons the number of excited defects (N^*) is given by

$$N^* = N_d n_e \int_{v_{\min}}^{v_{\max}} \sigma(v) F(v) v dv, \quad (6)$$

where N_d is the concentration of activator ions or F centers in the ground state, $F(v)$ is the velocity distribution function of the electrons, and n_e is their number per unit volume. The integral is equal to the probability of ionization (excitation) of an impurity ion or F_n center ($n=1,2$) per unit time. The minimum ionization energy ($W_{i_{\min}}$) is determined by the position of the ground state of the impurity ion relative to the bottom of the conduction band. This value was obtained experimentally.¹⁴ Hence, from the equation $v_s = \sqrt{2W_{i_{\min}}/m_e}$, we shall calculate the minimum velocity of the band electrons taking part in the process of excitation of impurity and intrinsic defects. Then, from the threshold ionization energy of the inner shells of the ions of the material ($W_i \sim 2W_g$), we shall find the maximum velocity of the band electrons $v_{i_{\max}} = \sqrt{4W_g/m_e}$. Employing Eq. (4), we construct an analytical expression for the cathodoluminescence (CL) yield

$$\eta = \frac{N_d n_e \int_{v_{\min}}^{v_{\max}} \sigma_a(v) F(v) v dv}{(N - N_d) n_e \int_{v_{\min}}^{v_{\max}} \sigma(v) F(v) v dv}, \quad (7)$$

where N is the total ion concentration. The velocity interval $[v_{\min}, v_{\max}]$ of the conduction band electrons corresponds to the following dispersion law in the crystal for the Bloch functions:

$$v_{pj} = \int_V \psi_{pj}^*(\mathbf{r}) \left(-\frac{i\hbar}{m} \nabla \right) \psi_{pj}(\mathbf{r}) d^3\mathbf{r}. \quad (8)$$

Therefore, in the interval $[v_{\min}, v_{\max}]$, where the ionization of the ions is complex, $\sigma_a(v)$ and $\sigma(v)$ are essentially independent of the velocity of the free charge carriers and depend only on the properties of the material. Simplifying expression (7), we obtain an expression for σ_d/σ

$$\frac{\sigma_d}{\sigma} = \eta \frac{N - N_d}{N_d}. \quad (9)$$

Thus, the plan of the experiment is to measure the cathodoluminescence yield η of the defects, to determine the efficiency of their recombinational excitation (σ_d/σ) from the known defect concentration N_d and then, using the Bloch criterion,¹³ to estimate the function $U^*(\mathbf{r})$ on its periodicity.

2. EXPERIMENTAL METHOD

As our object for study we chose the well-known compounds LiF, MgF₂, and Al₂O₃ with color centers. Pre-induced F and F_2 color centers were excited by high-power nanosecond electron beams (250 keV, 0.5–2.0 kA/cm², 1 ns, 0.1–12.5 Hz) and optical pulses: a nanosecond pulse (0.1–5.0 MW/cm², 180–700 nm, 15 ns, 0.1–12.5 Hz) and a microsecond pulse (0.01–0.5 MW/cm², 180–700 nm, 0.3–10 μ s, 0.1–12.5 Hz) from xenon lamps and a 4 ω : YAG: Nd laser (0.1–5.0 MW/cm²). Excitation in the absorption bands of the F and F_2 color centers was by light pulses passing through an intense MDR-4 monochromator and sets of standard light filters.

In the case of electron bombardment of the crystals, we investigated conversion and excitation of defects with nano-

second resolution. Toward this end, we synchronized the xenon lamps with the electron accelerator (accuracy 2 ns) by means of a controllable delay device (from 5 ns to 1 s). The weakly divergent light beam formed by this telescopic system of lamps was the probe beam in the measurement channel of electron-induced short-lived absorption or clearing. But at the same time, light from the lamp synchronously excites photoluminescence (PL) of the initial and induced defects. Therefore, in the recording channel of the spectral kinetic CL parameters the given delay time also determines the growth and decay kinetics of the photoluminescence spectra. In the measured spectral region in this arrangement transitory absorption (clearing) reveals the dynamics of creation and destruction of centers, the intensity and kinetics of the cathodoluminescence spectra allow one to assess the nature and concentration of the excited centers, while the photoluminescence determines the change in the number of centers in the ground state and their type.

In the recording channel we used VMS-1 and MDR-1 grating monochromators, a high-speed photomultiplier (31ELU-FM) with small-inductance capacitors in all the dynode circuits, allowing the photomultiplier to convert the optical signal (200–400 nm) efficiently without distortion and to amplify the photocurrent pulses on a 50-Ω load in a time interval from 1 ns to 50 μs. For the wavelength range 400–1100 nm, we used a high-speed (1 ns) *p-i-n*-photodiode (SI722-01, Hamamatsu) and a μPC1651G×3 operational amplifier (0–1200 MHz) with controllable gain in the range 10–60 dB.

3. RESULTS AND DISCUSSION

The efficiency of radiative excitation of F_2 color centers was investigated on precolored LiF crystals. To create the F_2 color centers, we used a coloring regime that was optimized in electron energy, current density, and bombardment/irradiation time. The basis of this regime consisted of electron beam bombardment (250 keV, 1.0–2.0 kA/cm², 1 ns) with an interval between pulses of 120–180 s exceeding the lifetime of the anion vacancies (10–60 s), and total bombardment cycle (20–30 min) less than the lifetime of the F_2^+ centers (6 h). Such a regime makes it possible to achieve a high value of the optical absorption coefficient with a very low efficiency of formation of other *F*-aggregate centers (Fig. 1).¹⁵ Under the action of high-power electron bombardment and irradiation by filtered radiation from a pulsed lamp in the LiF *M* band, only an insignificant change in the photoluminescence intensity of the F_2 centers was detected ($\Delta I_{F_2} < 0.1\%$) (Fig. 2). Therefore, allowing for the high efficiency of nanosecond growth in the absorption of the F_3 color centers and synchronous decrease in the amplitude of photoluminescence of the F_3^+ color centers (Fig. 2), the ns-degradation of the *M* band (absorption by F_2 and F_3^+ centers) can be ascribed to recharging: $F_3^+ + e \rightarrow F_3$. Consequently, hot charge carriers (*e* and *h*) in LiF have small interaction cross sections with F_2 centers (σ_{F_2}). It follows from a comparison of the cathodoluminescence yield of the F_2 centers, ΔI_{F_2} , and the concentration of the F_2 centers that σ_{F_2} is comparable to the interaction cross section of the hot

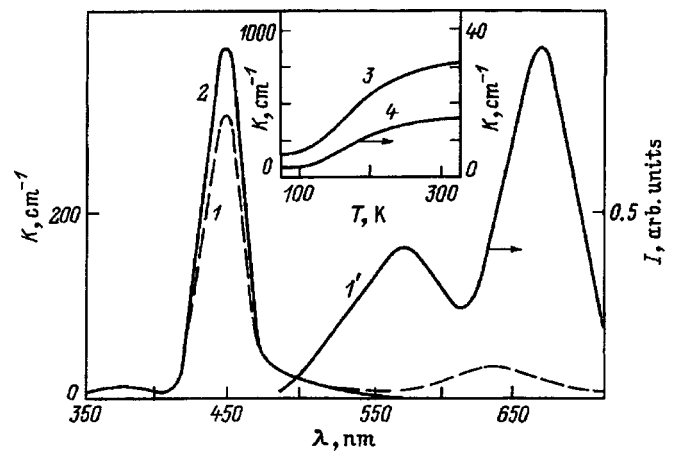


FIG. 1. Absorption spectra (*I*, 2) and photoluminescence spectrum (*I'*) of LiF crystals. *I* — 5 min after electron bombardment, 2 — 12 h after electron bombardment. *I'* — excitation by an ns-Xe lamp to the *M* band (420–475 nm). Inset: temperature dependence of the accumulation of F^+ (3) and F_2^+ (4) centers.

electrons and holes with regular lattice sites (σ). But then it is necessary to explain the nanosecond component in the creation of the F_2^+ color centers (Fig. 2). Under electron bombardment, the ns-growth of the F_2^+ color centers de-

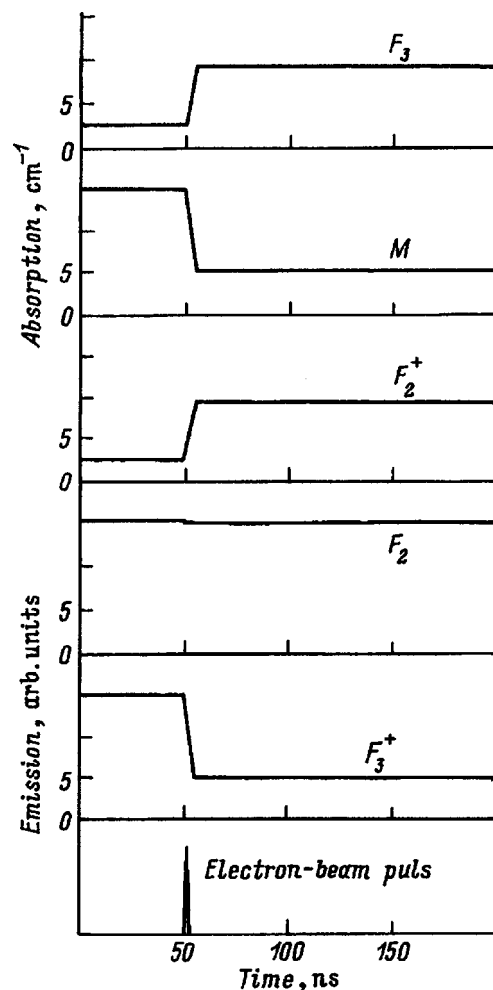
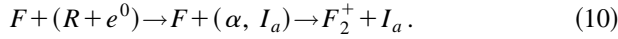


FIG. 2. Kinetics of conversion of color centers in LiF. $T = 300$ K.

pends linearly on the initial concentration of the F centers, the temperature dependence of the formation efficiency of the F and F_2^+ color centers are described by a single trend (Fig. 1), and the formation of F centers proceeds via the exciton mechanism.¹⁶ Hence it follows that the nanosecond component in the formation of the F_2^+ color centers is due to a process that involves excitons



We may next ask about the magnitude of the interaction cross section of the induced electrons and holes with the F centers (σ_F). The answer to this question is complicated because efficient creation of new F centers under the action of an electron pulse in LiF takes place during times < 1 ns. As a result, it is impossible to separate out the component of the interaction of the initial F centers with the induced electrons and holes. To address this problem, let us consider the regularities of the interaction of hot electrons and holes with F centers in Al_2O_3 , where the exciton mechanism of defect formation is not manifested.¹⁷

F and F^+ color centers are created in Al_2O_3 single crystals by an impact mechanism with a threshold displacement energy of O^{2-} equal to ~ 70 eV (Ref. 17). Therefore, upon bombardment (2 kA/cm^2 , 1 ns) of Al_2O_3 crystals by electrons with energies below the formation threshold of stable F and F^+ color centers ($W_e < W_0 \sim 390$ keV), only a high concentration ($n = 10^{20} \text{ cm}^{-3}$) of hot charge carriers (electrons and holes) is formed. Here the induced short-lived $F^{2+}O^{2-}$ defects have only an insignificant effect on the concentration of hot electrons and holes (n), which exceeds their concentration by three orders of magnitude.¹⁸ Stable F centers in

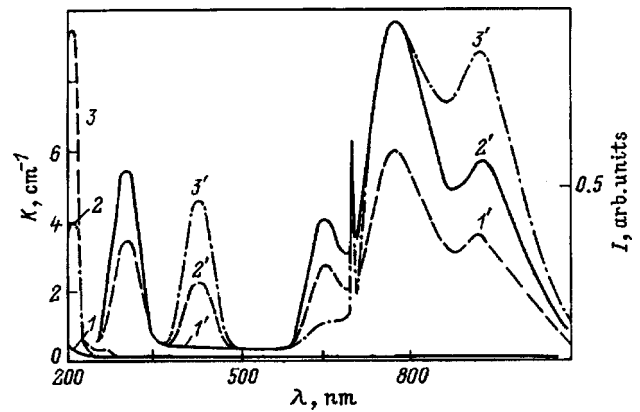


FIG. 3. Absorption (1–3) and cathodoluminescence spectra (1'–3') of Al_2O_3 : Ti, Cr, V crystals. 1 — original, 2 — additively colored, 3 — neutron colored. $T = 300$ K.

Al_2O_3 were pre-induced by two methods: thermochemically in Al vapors at $2000^\circ C$ and by neutron bombardment (fluence $\sim 10^{15} \text{ n/cm}^2$). At the synthesis stage, the rare-earth impurity Cr^{3+} (luminescence at 694 nm, 3 ms) and the transition-element impurities Ti^{3+} (780 nm, 3 μs), V^{3+} (920 nm, 4 μs), and $V^{4+}O^-$ (650 nm, 800 ns) with concentrations equal to 10^{-3} wt.% were implanted isoelectronically in the samples. Figure 3 plots the absorption spectra of Al_2O_3 . It can be seen that the concentration of stable F centers (absorption at 206 nm, emission at 420 nm, $\tau = 36$ ms) exceeds the concentration of the impurity centers by two orders of magnitude. However, in the cathodoluminescence spectra the intensity of the impurity defects exceeds

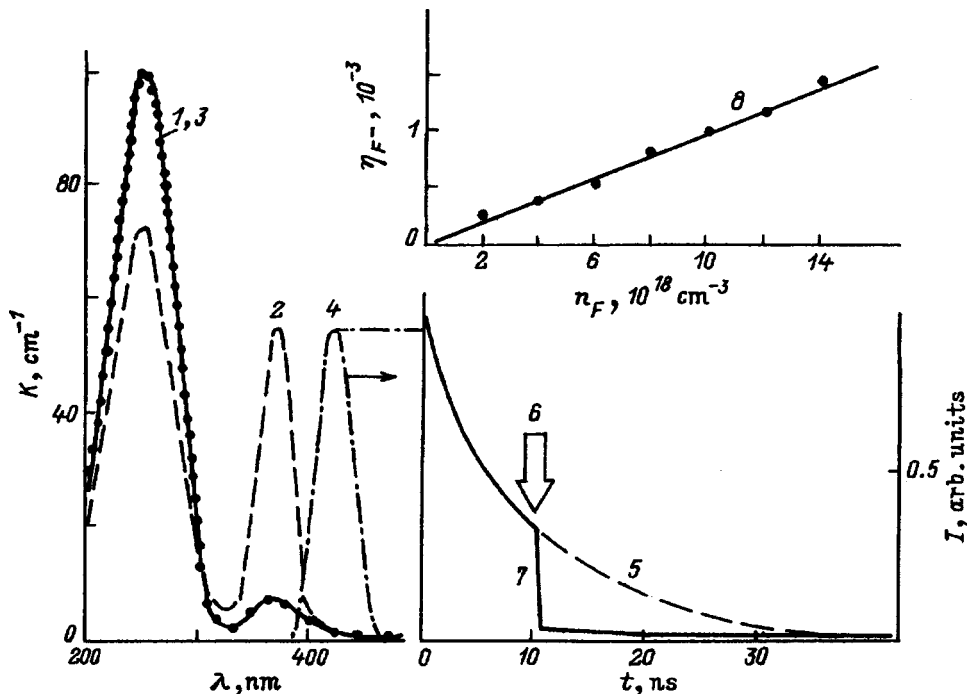


FIG. 4. Absorption spectra (1–3) and photoluminescence spectrum (4) of MgF_2 crystals: 1 — electron colored, 2 — the same after 4ω : YAG: Nd laser irradiation at 78 K, 3 — after irradiation by a single electron-beam pulse at 78 K. 5, 7 — kinetics of photoluminescence decay for excitation in the 420-nm band, 6 — moment at which the electron-beam pulse acts, 8 — dependence of the cathodoluminescence yield of the F^- centers on the concentration of the F centers.

the emission level of the F centers by a factor of 2–4 (Fig. 3).

Such an unexpected result is direct evidence that the interaction efficiency of hot electrons and holes with charge-neutral impurity defects (σ_a) is almost 2.5 orders of magnitude higher than with the F centers ($\sigma_a \gg \sigma_F$). For Al_2O_3 it was shown in Ref. 11 that $\sigma_a \gg \sigma$ stands in the same ratio. Consequently, for Al_2O_3 the value of σ_F is commensurate with the value of σ .

A similar trend in the interaction of the hot charge carriers with the F centers appears in MgF_2 crystals. F centers were pre-induced by electron bombardment. Under the action of a laser pulse (4ω : YAG: Nd, 266 nm, 10 ns), after a time $\tau < 5$ ns at 78 K, absorption into the F band was observed having its maximum at 370 nm (Fig. 4). It was established that the absorption band at 370 nm and the emission band at 420 nm in MgF_2 are due to F^- centers.¹⁹ Subsequent bombardment by a nanosecond electron pulse at 78 K clears the 370-nm band to its original level within < 1 ns and synchronously re-establishes the initial concentration of the F centers (Fig. 4). Rapid direct and reverse recharging of the F and F^- centers at 78 K is possible only with participation of the band electrons, with two-step photoionization of the F centers [$2h\nu \rightarrow F \rightarrow V_a + e$, $F + e \rightarrow (F^-)^* \rightarrow F^- + h\nu_{F^-}$], and hot holes, with reconstruction of the F centers during electron bombardment ($F^- + h \rightarrow F$). The concluding phase of the reaction of photoionization of the F centers is confirmed by the fact that the intensity of the accompanying photoluminescence of the F^- color centers at 420 nm depends directly on the absorption coefficient of the F band (Fig. 4). The cathodoluminescence intensity of the F^- color centers (emission at 420 nm) also depends linearly on the initial concentration of the F centers (Fig. 4). Therefore, the excited F^- centers are also formed under electron bombardment due to recombination of hot electrons with F centers (Fig. 4). During electron bombardment or F illumination of MgF_2 crystals the CL and PL yield of F^- centers was $\sim 0.1\%$. Here the initial concentration of F centers was 10^{19} cm^{-3} . Consequently, in MgF_2 crystals the interaction cross section of the hot electrons with the F centers does not go beyond the limits of σ .

According to Eq. (4), omitting the phonon fluctuations of the lattice, the electrons with velocities $v < v_{\text{max}}$ have an insignificant interaction cross section with the regular lattice sites. As experiments have shown in Al_2O_3 , σ_a exceeds σ by more than two orders of magnitude (Fig. 3). This means that the potential U^* in the vicinity of the impurity centers, formed mainly by the s and p subgroups of the inner shell of the impurity ions, loses its regularity as a function of $r+a$

$$U(r) \neq U^*(r+a). \quad (11)$$

Thus, Bloch's rule is violated, and the mean electron velocity function $v_{pi} = \Delta_p(W_0 - W^*)_{pi}$ becomes even. In this case, as

the results of experiments testify (Fig. 3), the band electrons and holes efficiently transfer energy to the impurity atoms. If the s and p subgroups of the inner shells of the activator and ions of the host material are similar in structure (e.g., $\text{Ce}:\text{LaF}_3$), then according to Ref. 11 and relation (9) we have $\sigma_a \sim \sigma$. Here nearly coherent motion of the hot charge carriers is conserved according to Bloch's rule.

The interaction cross section of the hot charge carriers with F -type intrinsic defects is commensurate with σ . Therefore, according to Bloch's theorem in the region of the F and F_2 color centers, the criterion of coherent motion of the hot electrons and holes $v_{pi} = \Delta_p W_{pi}$ is also fulfilled. Thus, in the vicinity of the F_n centers ($n=1,2$) of ionic crystals the field potential is nearly regular: $U(r) \approx U^*(r+a)$.

This work was carried out with the support of the Russian Fund for Fundamental Research (Grant No. 96-02-16319-a).

¹C. Gout and F. Pradal, J. Phys. Chem. Solids **29**, 581 (1968).

²B. N. Gorbachev, É. R. Il'mas, Ch. B. Lushchik, and T. I. Savikhina, Tr. IFA Akad. Nauk ÉSSR **34**, 30 (1966).

³Cj. B. Lushchik and T. A. Soovik, Tr. IFA Akad. Nauk ÉSSR **34**, 68 (1966).

⁴G. A. Mikhail'chenko, Doctoral Dissertation [in Russian], Leningrad (1970), 430 pp.

⁵É. D. Aluker, D. Yu. Lysis, and S. A. Chernov, *Electronic Excitations and Radio Luminescence of Alkali-Halide Crystals* [in Russian], Zinatne, Riga, 1979, 251 pp.

⁶É. D. Aluker and S. A. Chernov, *Radiation Physics* [in Russian], Zinatne, Riga, 1973, p. 9.

⁷D. I. Vašburd (Ed.), *High-Energy Solid State Electronics* [in Russian], Nauka, Novosibirsk, 1982, 225 pp.

⁸Yu. A. Gusev, S. N. Konoplin, and S. I. Marennikov, *Kvantovaya Elektron.* **4**, 2046 (1977) [sic].

⁹B. Henderson, *Opt. Lett.* **6**, 737 (1981).

¹⁰E. F. Martynovich, V. I. Baryshnikov, V. A. Grigorov, and L. I. Shchepina, *Kvantovay Elektron.* **15**, 47 (1988) [*Sov. J. Quantum Electron.* **18**, 26 (1988)].

¹¹B. P. Aduv and D. I. Vašburd, *Fiz. Tverd. Tela (Leningrad)* **23**, 1869 (1981) [*Sov. Phys. Solid State* **23**, 1093 (1981)].

¹²V. I. Baryshnikov, T. A. Kolesnikova, and I. Kvapil, *Fiz. Tverd. Tela (St. Petersburg)* **36**, 2788 (1994) [*Phys. Solid State* **36**, 1524 (1994)].

¹³Yu. A. Il'inskiĭ and L. V. Keldysh, *Interaction of Electromagnetic Radiation with Matter* [in Russian], Izdat. MGU, Moscow State Univ. Press, Moscow, 1989, 300 pp.

¹⁴V. I. Baryshnikov, N. Sarukura, and Y. Segawa, *Solid State Lasers, SPIE Proc.*, V. 2772, p. 74 (1995).

¹⁵V. I. Baryshnikov and G. A. Kolesnikova, *Opt. Spektrosk.* **77**, 57 (1994) [*Opt. Spectrosc.* **77**, 47 (1994)].

¹⁶Ch. B. Lushchik E. A. Vasil'chenko, and A. Ch. Lushchik, Tr. IFA Akad. Nauk ÉSSR **51**, 7 (1980).

¹⁷G. P. Pells and D. C. Phillips, *J. Nucl. Mater.* **80**, 207 (1979).

¹⁸V. I. Baryshnikov, L. I. Shchepina, T. A. Kolesnikova, and E. F. Martynovich, *Fiz. Tverd. Tela (Leningrad)* **32**, 1888 (1990) [*Sov. Phys. Solid State* **32**, 1103 (1990)].

¹⁹V. I. Baryshnikov, T. A. Kolesnikova, L. I. Shchepina, S. V. Dorokhov, and G. V. Sotserdotova, *Opt. Spektrosk.* **66**, 217 (1989) [sic].

Non-Markovian shape of the magnetic resonance line

É. Kh. Khalvashi and M. V. Chkhartishvili

Batumi Polytechnical Institute, Georgian Technical University, 384500 Batumi, Georgia
(Submitted August 11, 1997)

Fiz. Tverd. Tela (St. Petersburg) **40**, 1036–1037 (June 1998)

On the basis of a magnetic resonance theory in the memory function formalism developed by one of the authors, we have investigated quantitatively the shape of the absorption line under classical conditions of magnetic resonance in solids. We have found that the theoretical curves provide a good description of the plateau-like shape of the experimental lines, but have somewhat wider wings. In addition, they are nontrivial (non-Gaussian and non-Lorentzian), as follows from the non-Markovian theory of line shapes, and behave “in the Provotorov fashion” with increase in the amplitude of the variable field (the Gaussian line shape transforms into a Lorentzian line shape). © 1998 American Institute of Physics. [S1063-7834(98)01606-2]

The Markovian stage of development of research on the shape of the magnetic resonance line in solids can be logically considered to have taken shape with the appearance of the ground-breaking theory of Provotorov, which, in particular, explained the experimental fact of the narrowing of the magnetic resonance line in solids with increase in the amplitude of the external variable magnetic field ω_1 (transformation of the line shape from Gaussian into Lorentzian).^{1,2}

The theory of the shape of the magnetic resonance line in the formalism of the memory function (non-Markovian theory) was developed in the work of Lado, Memory, and Parker (LMP), which explained the experimental fact associated with the nontriviality (non-Gaussian-ness and non-Lorentzian-ness) of the shape of the magnetic resonance line in solids.^{3–5} The theory of Provotorov takes as relevant the integrals of motion, that is, the diagonal operators of the Zeeman spin and secular dipole–dipole spin interactions H^z and H^d , respectively. The LMP theory, on the other hand, takes the nondiagonal operator I^x (the x -component of the total spin).

In the non-Markovian theory of magnetic resonance developed within the framework of the well-known method of memory functions, in which both the diagonal operators H^z and H^d and the nondiagonal operators I^x and I^y are taken as relevant, equations are obtained combining the non-Markovian equations of Provotorov and the non-Markovian Bloch equations.⁶¹ The steady-state solution of these equations, in particular, gives an expression for the y component of the total spin, from which it is possible to obtain the following expression for the shape of the magnetic resonance line:

$$G(\Delta, S) = 2g(\Delta)[(4\pi)^2\Delta^2g^2(\Delta) + (1 - 4\pi\Delta g'(\Delta))^2 + \pi M^{1/2}g(\Delta)S(1 + \varepsilon/2)]^{-1}, \quad (1)$$

where $\Delta = \omega_0 - \omega$, ω , and ω_0 are the frequencies of the Zeeman splitting and the external magnetic field²⁾ respectively, $S = \omega_1^2 M_2^{1/2} T_1$ is the Bloch saturation factor, M_2 is the second moment of the resonance line, T_1 is the spin–lattice

relaxation time of the Zeeman energy (the corresponding relaxation term was introduced phenomenologically), the two functions $g(\Delta)$ and $g'(\Delta)$, appearing as a result of unification of the memory functions, are the cosine and sine Fourier transforms of the correlation function

$$g(t) = \text{Tr} I^x(t) I^x / \text{Tr} (I^x)^2, \quad \varepsilon = \text{Tr} (H^z)^2 / \text{Tr} (H^d)^2.$$

Reference 6 introduced a qualitative analysis of the expression for the shape of the magnetic resonance line, from which it is clear that the proposed non-Markovian theory explains the above-mentioned experimental facts described by the theories of Provotorov and LMP from different points of view, in a unified approach. However, it is not clear, within what saturation limits (the quantity S) this is better realized.

The present paper examines quantitatively the non-Markovian shape of the magnetic resonance line on the basis of expression (1).

Toward this end, it is first necessary to approximate the functions $g(\Delta)$ and $g'(\Delta)$. Since in our case the memory functions (there are 16 of them in the equations of Ref. 6) are expressed in terms of $g(t)$, while in the non-Markovian approach to the question of the line shape a Gaussian approximation is applied, as a rule, to the memory functions,^{3–5,7} it is natural to represent $g(t)$ in the form of a Gaussian. In addition, in the classical Markovian theory of magnetic resonance $g(t)$ represents the line shape and, in the case of solids, the Gaussian approximation is specifically used for it. If we now note that

$$\varepsilon = \Delta^2/d^2 = \Delta^2/\text{Tr} (H^d)^2/\text{Tr} (I^z)^2 \approx \Delta^2/\omega_{\text{loc}}^2 \approx \Delta^2/M_2,$$

where ω_{loc} is the frequency of the local magnetic field acting on the spin from the direction of its neighbors,² and we have introduced the notation $\Delta/(2M_2)^{1/2} = x$ and $G(x, S)M_2^{1/2} = f(x, S)$, then for the shape of the magnetic resonance absorption line we obtain the following expression, convenient for calculation:

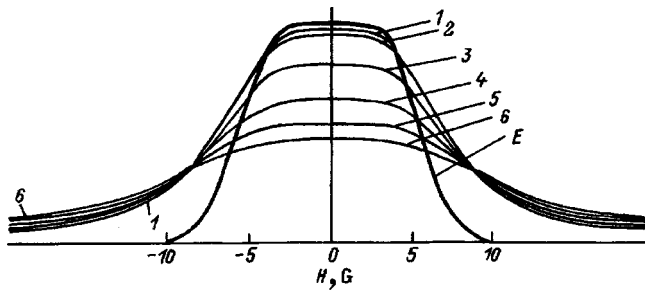


FIG. 1. The curve E describes the absorption signal of ^{19}F nuclei in CaF_2 in an external constant magnetic field parallel to the $[100]$ axis. Curves 1–6 correspond to resonance lines calculated according to Eq. (2) for $S_1=0.001$, $S_2=0.01$, $S_3=0.1$, $S_4=0.3$, $S_5=0.6$, and $S_6=0.9$.

$$f(x, S) = [16\pi^3 x^2 \exp(-x^2) + (1 - 8\pi x D(x))^2 + \pi(\pi/2)^{1/2} S(1+x^2)]^{-1}, \quad (2)$$

where $D(x) = \exp(-x^2) \int_0^x \exp(y^2) dy$ is the Dawson function, which has a ‘‘bell shape’’ with maximum value 0.54 (to simplify the calculations we take its arithmetic mean to be ≈ 0.27).⁸ Also, we carry out the standard normalization of function (2)

$$A \int_{-\infty}^{\infty} f(x, S) dx = 1, \quad (3)$$

where A is the normalization factor, defined for each value of S , varying within the limits from 0.001 to 10. Computer calculation of the integral in Eq. (3) was performed approximately by the simplex method. Since the resonance peak is located for the most part within the limits from -2 to 2 , the limits of integration were replaced by just these values. Then, for the above-indicated values of S using the corresponding normalization factor we performed computer calculations of Eq. (2). Curves 1–6 in Fig. 1 plot the resonance lines for six values of S . The fat line, labelled by the letter E , reproduces the experimental resonance curve.⁴

It can be seen that the theoretical curves give a good description of the plateaulike peak of the experimental curve. Closest in slope to curve E are the unsaturated theoretical resonance lines with the values S_1 and S_2 , whereas with further increase of the amplitude of the variable field ω_1

(curves 3–6) the theoretical lines ‘‘settle down’’ somewhat, the slope decreases and the height of the ‘‘pedestal’’ increases. Obviously, the theoretical curves have the nontrivial form characteristic of the LMP theory (in order not to crowd the figure we have not plotted the Gaussian and Lorentzian lines). Also, it is easy to trace out the ‘‘Provotorov’’ dependence on ω_1 . Indeed, it can be seen that the more Gaussian-like curve 1 transforms into the more Lorentzian-like curve 6 with increase of the amplitude of the variable magnetic field ω_1 .

To summarize, the proposed unsaturated theoretical curves describe approximately the experimental line at its peak. In this regard they bear a nontrivial relation to the LMP theory and behave in the ‘‘Provotorov’’ fashion with increase of ω_1 .

We are grateful to staff-members of the computing center of our institute I. Didmanidze, T. Teliya, and R. Kokoladze for their programming assistance and their constant help in this effort.

¹The non-Markovian Bloch equations were introduced in Ref. 7 by replacing the relaxation terms of the transverse components of the total spin with the corresponding memory integrals.

²The interaction of the spins with the external magnetic field, $\omega_1 I^x$, is assumed to be a small perturbation in comparison with the remaining terms of the Hamiltonian of the problem $H^z = \Delta I^z$ and H^d , where I^z is the z component of the total spin.

¹B. N. Provotorov, Zh. Éksp. Teor. Fiz. **41**, 1582 (1961) [Sov. Phys. JETP **14**, 1126 (1961)].

²M. Goldman, *Spin Temperature and Nuclear Magnetic Resonance in Solids* (Clarendon Press, Oxford, 1970; Moscow, 1972, p. 342).

³F. Lado, G. D. Memory, and G. W. Parker, Phys. Rev. B **4**, 1406 (1971).

⁴A. Abragam and M. Goldman, *Nuclear Magnetism: Order and Disorder* (Clarendon Press, Oxford, 1982; Moscow, 1984, Vol. 1, p. 300; Vol. 2, p. 360).

⁵U. Haeberlen, *High Resolution NMR in Solids; Selective Averaging*, Advances in Magnetic Resonance (Academic Press, New York, 1973); M. Mehring, *High Resolution NMR Spectroscopy in Solids* (Springer-Verlag, Berlin, 1976; Moscow, 1980, p. 504).

⁶É. Kh. Khalvashi, Zh. Éksp. Teor. Fiz. **110**, 703 (1996) [JETP **83**, 369 (1996)].

⁷L. L. Buishvili, M. D. Zviadadze, É. Kh. Khalvashi, Zh. Éksp. Teor. Fiz. **91**, 310 (1986) [Sov. Phys. JETP **64**, 181 (1986)].

⁸U. Gauci, in *Handbook of Special Functions* [in Russian], Moscow, 1979, p. 830.

Electrically controlled diffraction of light by reflection holograms in an LiNbO₃ crystal

M. P. Petrov, A. V. Shamraï, and V. M. Petrov

A. F. Ioffe Physicotechnical Institute, Russian Academy of Sciences, 194021 St. Petersburg, Russia

(Submitted November 11, 1997)

Fiz. Tverd. Tela (St. Petersburg) **40**, 1038–1041 (June 1998)

A theoretical and experimental investigation is made of the electrical selectivity of reflection volume holograms recorded in a LiNbO₃ crystal using a near-optimum geometry. An analysis is made of the factors limiting electrical multiplexing. © 1998 American Institute of Physics. [S1063-7834(98)01706-7]

It is known that diffraction by volume holograms satisfies the Bragg conditions

$$|\mathbf{K}_g| = 2 \frac{2\pi}{\lambda} n_a \sin \theta_0 = \frac{2\pi}{\Lambda}. \quad (1)$$

Here \mathbf{K}_g is the wave vector of the hologram, λ is the wavelength of light, θ_0 is the Bragg angle inside the material in which the hologram is recorded, n_a is the average refractive index, and Λ is the spatial period of the recorded grating.

It can be seen from the conditions (1) that the refractive index n_a is an independent variable like θ_0 or λ . Thus, by varying any independent variable, we can control the diffraction conditions. It is well-known that volume holograms exhibit high angular and spectral selectivity. It was shown in Refs. 1 and 2 that a small change in the refractive index Δn_a is equivalent to a small change $\Delta \lambda$ in the wavelength of light, and consequently the refractive index selectivity is equivalent to the spectral selectivity. Volume holograms exhibit maximum spectral selectivity in a reflection recording geometry. Thus, control of diffraction by varying the refractive index is most effective in reflection holograms. As a result of the electrooptic effect in photorefractive crystals, the refractive index can be varied by applying a static electric field.

The first studies^{3–5} concerned with the electrical control of diffraction conditions at reflection holograms in LiNbO₃ were published in 1978. Electrical multiplexing of six holograms was demonstrated experimentally but no detailed theoretical analysis was made. This effect is now attracting renewed interest following the progress achieved in the development of holographic memory systems^{6,7} and also because photorefractive materials can now be used to fabricate narrow-band holographic filters.^{8,9} A general theoretical analysis has now been made of the electrical selectivity of volume holograms.^{1,2} A more detailed investigation has been made using transmission geometry. Experimental and theoretical data on the electrical multiplexing of reflection holograms in an LiNbO₃ crystal were presented in Ref. 10. However, the selected experimental geometry cannot be used to multiplex more than two holograms since, in the longitudinal electrooptic effect, the external electric field required to switch from one hologram to another is determined by the half-wave voltage.

The aim of the present paper is to make a detailed theoretical and experimental study of the electrical selectivity of reflection holograms using a photorefractive LiNbO₃ crystal in the geometry of the transverse electrooptic effect.

1. THEORETICAL ANALYSIS

As in Ref. 11, we write an expression for the diffraction efficiency of a reflection hologram as a function of the change in the refractive index n_a

$$\eta = \frac{1}{(\xi_r/\nu_r)^2 + [1 - (\xi_r/\nu_r)^2] \coth^2 [\nu_r^2 - \xi_r^2]^{1/2}}, \quad (2)$$

where

$$\xi_r = \beta T \frac{\Delta n_a}{n_a} \sin \theta_0, \quad \nu_r = \frac{\pi n_1 T}{\lambda \sin \theta_0}, \quad \beta = 2\pi n_a/\lambda,$$

T is the thickness of the hologram and n_1 is the amplitude of the refractive index of the grating.

Although an LiNbO₃ crystal is uniaxial, for the natural modes we can use this expression for an isotropic medium. Then Δn_a should be replaced by Δn_o (the change in the ordinary refractive index) or Δn_e (the change in the extraordinary refractive index). Note that because of the anisotropy of the electrooptic effect, these changes in the natural refractive indices induced by an external electric field depend on the crystal orientation. This theoretical analysis showed that the largest change in the refractive index is observed for the extraordinary wave when the \mathbf{C} optic axis and the external electric field \mathbf{E} form the angle $90^\circ - \alpha \approx 39^\circ$. However, the most efficient holographic recording is observed when the optic axis is parallel to the wave vector of the hologram $\mathbf{C} \parallel \mathbf{K}_g$ (Refs. 12 and 13).

For our investigations we selected a compromise geometry (Fig. 1b): $\alpha = 45^\circ$. This orientation gives almost maximum sensitivity to the external electric field with a fairly high diffraction efficiency. In this geometry we obtain for the extraordinary wave

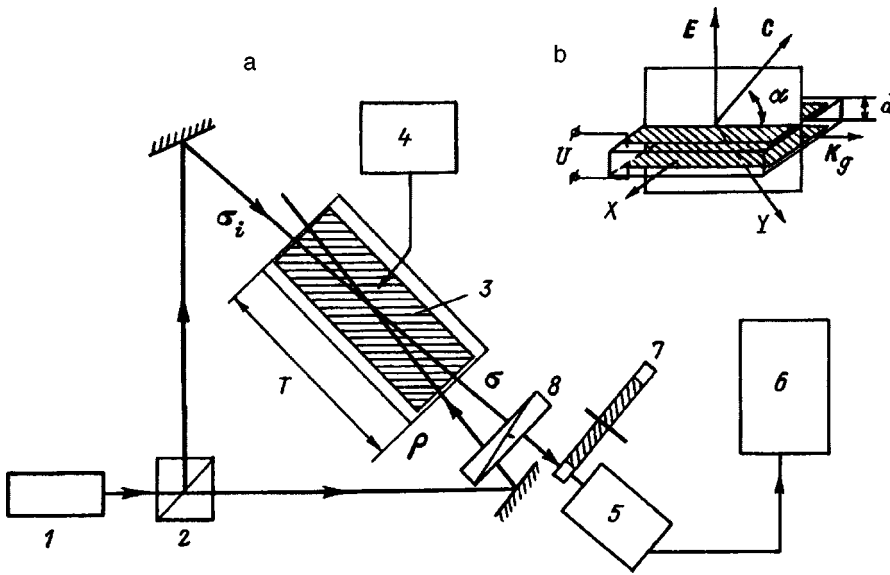


FIG. 1. Experimental setup to investigate electrical selectivity: a) 1 — He-Ne laser, 2 — beam splitter, 3 — LiNbO₃ crystal (showing upper electrode), 4 — controllable high-voltage source, 5 — photodetector, 6 — narrow-band amplifier, 7 — rotating chopper, 8 — polarizer, ρ and σ_i are the wave vectors of the recording beams, and σ is the wave vector of the reconstructed beam. b) Orientation of LiNbO₃ crystal.

$$\xi_r = 2 \frac{\pi T}{\lambda} \left(\frac{n_e n_0}{\sqrt{n_0^2 + n_e^2}} \right)^3 \sin \theta_0$$

$$\times \left(r_{51} + \frac{r_{33}}{2} + \frac{r_{13}}{2} + \frac{r_{22}}{2} \right) E = 2 \Delta n_e \pi \frac{T}{\lambda} \sin \theta_0,$$

$$\nu_r = \frac{\pi}{\lambda} \frac{T}{\sin \theta_0} \frac{\delta D}{2\sqrt{2} |\mathbf{K}_g| n_e}$$

$$\times \left(\frac{r_{13} n_0^4}{\varepsilon_{33}} + \frac{r_{33} n_e^4}{\varepsilon_{33}} + \frac{r_{22} n_0^4}{\varepsilon_{11}} - 2 \frac{r_{51} n_0^2 n_e^2}{\varepsilon_{11}} \right), \quad (3)$$

and for the ordinary wave

$$\xi_r = \frac{\pi n_0^3 T}{\sqrt{2} \lambda} \sin \theta_0 (r_{13} + r_{22}) E = 2 \Delta n_0 \pi \frac{T}{\lambda} \sin \theta_0,$$

$$\nu_r = \frac{\pi}{\lambda} \frac{T}{\sin \theta_0} \frac{\delta D}{2\sqrt{2} |\mathbf{K}_g| n_0} \left(\frac{r_{13}}{\varepsilon_{33}} - \frac{r_{22}}{\varepsilon_{11}} \right) n_0^4. \quad (4)$$

Here E is the applied electric field, r_{ij} is the electrooptic coefficient, ε_{ij} is the component of the permittivity tensor, and δD is the amplitude of the space charge grating.

Thus, we obtained the relationship between the diffraction efficiency and the external electric field, which illustrates the electrical selectivity of a reflection hologram.

Note that in this theoretical analysis, apart from the electrooptic effect we neglected any other effects associated with the external electric field since estimates show that these have a negligible influence in our case.¹⁰

2. EXPERIMENTAL DATA

For the experiments we used an LiNbO₃ crystal doped with Fe²⁺. The concentration of Fe²⁺ ions was approximately 0.05 mol.%. The orientation of the sample is shown in Fig. 1b. The dimension in the direction of propagation of the light (T) was 1 cm. Electrodes were deposited on the upper and lower surfaces of the sample of thickness $d = 3.3$ mm using silver paste.

The optical part of the experimental apparatus consisted of a system conventionally used to record reflection holograms (Fig. 1a). After the recording process, one of the recording beams was shut off and the intensity of the diffracted light was recorded. Thus, the relationship between the diffraction efficiency and the external electric field was obtained experimentally.

The experimental and theoretical curves are compared in Fig. 2. As was predicted theoretically, the electrical selectivity was higher for the extraordinary polarization of the readout beam ($\Delta n_0 / \Delta n_e \approx 0.2$). Good agreement is observed between the theoretical and experimental data except for the region where the theoretical curves approach zero. At the points where the theoretical diffraction efficiency vanishes ($\xi_r \approx \pi$), a value of the order of $0.05 \eta_{\max}$ was obtained experimentally. This difference between theory and experiment (subsequently called the background signal) is the main factor limiting the electrical multiplexing in our experiments, i.e., the number of holograms which can be recorded and reconstructed independently for different external electric fields.

For an extraordinary readout beam we have $\xi_r \approx \pi$ in an external electric field $E_{\min} = 1560 \text{ V} \cdot \text{cm}^{-1}$, if the hologram

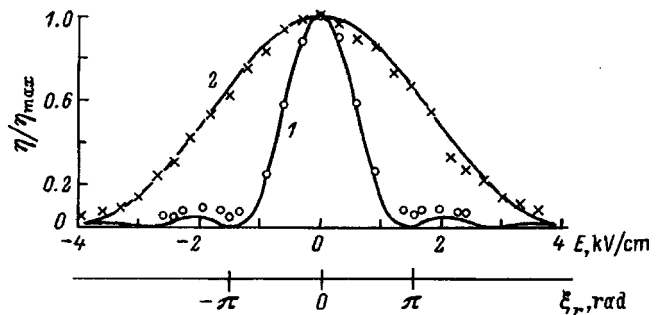


FIG. 2. Comparison between theoretical (solid curves) and experimental dependences of the diffraction efficiency on the applied electric field: 1 — extraordinary polarization, 2 — ordinary polarization. The ξ_r axis is given for the extraordinary polarization.

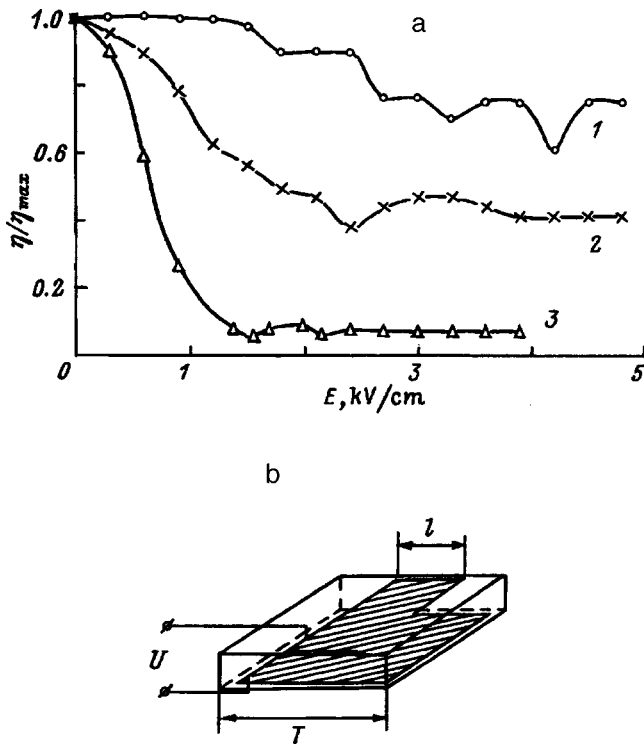


FIG. 3. Experimental curves obtained for upper electrodes of different length l (mm): 1 — 2, 2 — 4, and 3 — 10 ($l=T$); b) Electrode configuration to create electric field nonuniformity.

was recorded without the field. However, the electric breakdown field in air is $E^{BD}=30 \text{ V}\cdot\text{cm}^{-1}$. If each successive hologram is recorded at that external electric field for which the previous hologram had the minimum diffraction efficiency (which gives the minimum crosstalk), we can electrically multiplex no more than $M_E^{BD}=2E^{BD}/E_{\min}\approx 40$ holograms.

However, the upper limit for electrical multiplexing is given by the ratio

$$M_E = \eta_{\max} / \eta_{\xi=\pi} \approx 20.$$

One of the main factors responsible for the background signal is the simultaneous penetration of two natural modes through the input polarizer, since the zeros of the diffraction efficiency for the extraordinary and ordinary beams are observed for different external electric fields. As an example, the background signal increases 4.3 times if the polarizer is removed completely.

Other postulated sources of the background signal are the nonuniform electric field inside the crystal, the nonuniform temperature distribution, and also scattered light.

The simplest method of creating a fairly nonuniform applied electric field involves changing the electrode configuration, as shown in Fig. 3. The experiments show that as the size of the upper electrode is reduced (and thus the nonuniformity of the electric field inside the crystal increases), the electrical selectivity deteriorates and the background signal increases.

Figure 4 shows experimental curves for various cross sections of the readout beam. A LiNbO_3 crystal is a photoconductor so that nonuniform illumination produces a non-

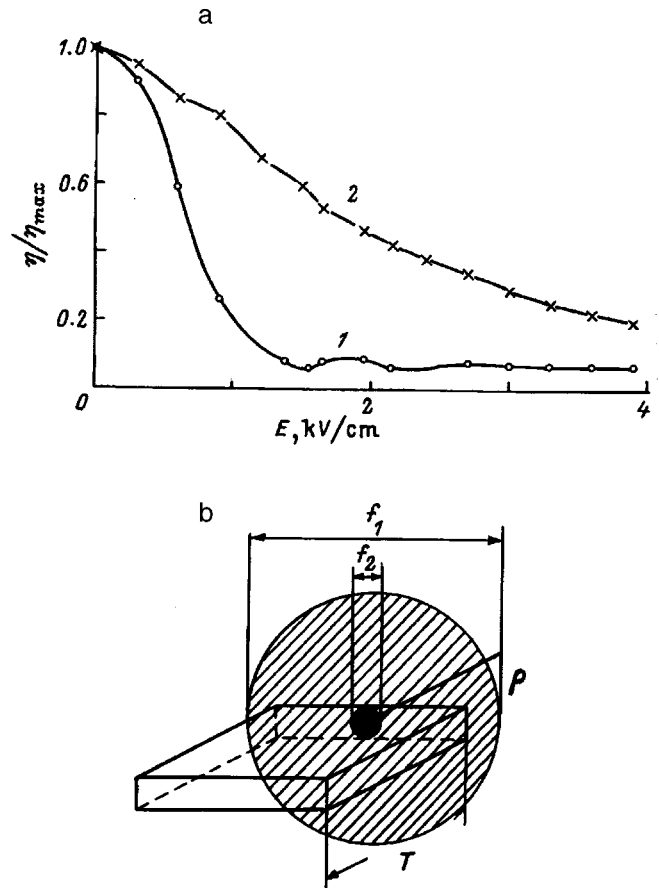


FIG. 4. a) Experimental curves for a readout beam with different cross-sectional diameters: 1 — $f_1=17 \text{ mm}$, 2 — $f_2=3 \text{ mm}$; b) Cases of a readout beam with large and small cross-sectional diameters.

uniform electric field and also a temperature nonuniformity, which explains the poor electrical selectivity and the high background signal when the cross section of the readout beam is smaller than the transverse dimension of the sample.

In our final experiment we achieved electrical multiplexing of two holograms. Figure 5 gives the experimental dependence of the diffraction efficiency on the external electric field when two holograms are recorded at different electric fields.

To sum up, experimental and theoretical investigations have been made of the electrically controlled diffraction of light by holograms recorded in a LiNbO_3 crystal using a reflection geometry and the transverse electrooptic effect. The orientation of the crystal was near-optimum. Excellent

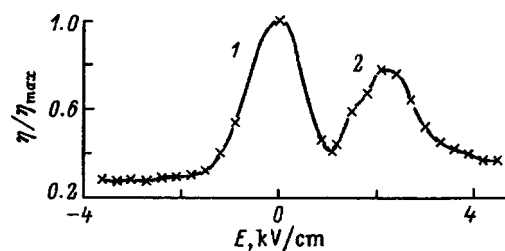


FIG. 5. Diffraction efficiency versus applied electric field for two holograms recorded at different voltages.

agreement is observed between the theoretical and experimental results. In our experiments, the maximum number of holograms which can be recorded and reconstructed independently is $M_E \approx 20$ and is limited by the background noise. The nonuniformity of the electric field and the nonuniformity of the readout beam intensity substantially reduce the electrical selectivity and are sources of the background noise.

This work was supported by the European Office of Aerospace Research and Development (Contract F61708-96-W308).

¹A. Kewitsch, M. Segev, A. Yariv, and R. R. Neurgaonkar, *Opt. Lett.* **18**, 534 (1993).

²R. de Vre, M. Jeganathan, J. P. Wilde, and L. Hesselink, *J. Opt. Soc. Am. B* **12**, 600 (1995).

³A. A. Kamshilin, M. P. Petrov, S. I. Stepanov, and A. V. Khomenko, *Avtometriya* **1**, 16 (1978).

⁴M. P. Petrov, S. I. Stepanov, and A. A. Kamshilin, *Ferroelectrics* **21**, 631 (1978).

⁵M. P. Petrov, S. I. Stepanov, and A. A. Kamshilin, *Opt. Commun.* **29**, 44 (1979).

⁶J. H. Hong, I. McMichael, T. Y. Chang, W. Christian, and E. Gi Paek, *Opt. Eng. (Bellingham)* **34**, 2193 (1995).

⁷L. Hesselink and M. C. Bashaw, *Opt. Quantum Electron.* **25**, S611 (1993).

⁸K. Sayano, F. Zhao, S. T. Hendow, and N. V. Kukhtarev, Post-deadline paper presented at CLEO '96, Anaheim, CA, 1996.

⁹G. A. Rakuljic and V. Leyva, *Opt. Lett.* **18**, 459 (1993).

¹⁰J. V. Alvarez-Bravo, R. Muller, and L. Arizmendi, *Europhys. Lett.* **31**, 443 (1995).

¹¹H. W. Kogelnik, *Bell Syst. Tech. J.* **48**, 2909 (1969).

¹²A. K. Mikaélyan, É. Kh. Gulanyan, E. I. Dmitrieva, and I. R. Dorosh, *Kvantovaya Élektron. (Moscow)* **5**, 440 (1978) [*Sov. J. Quantum Electron.* **8**, 257 (1978)].

¹³É. Kh. Gulanyan, I. R. Dorosh, and A. I. Zhmurko, *Vopr. Radioélektron. Ser. Obshchetekhn.* **8**, 95 (1979).

Translated by R. M. Durham

Total quantum-current yield in the soft x-ray region

V. N. Shchemelev and E. P. Savinov

Scientific-Research Institute of Physics, St. Petersburg State University, 198904 Petrodvoretsk, Russia
(Submitted November 21, 1997)

Fiz. Tverd. Tela (St. Petersburg) **40**, 1042–1046 (June 1998)

The emission of slow secondary electrons excited in efficient photocathodes by fast internal x-ray electrons upon absorption of x-ray photons having energies in the range 1–10 keV is analyzed. Analytical expressions are derived for the quantum current yield of the x-ray photoelectric effect for a “point” model and a “non-point” model of energy exchange of fast internal x-ray electrons. We present some estimates for its parameters in a CsI photocathode. © 1998 American Institute of Physics. [S1063-7834(98)01806-1]

As is well known, when various materials are irradiated by x rays, x-ray electron emission arises. This electron emission, known as the x-ray photoelectric effect, is a physical phenomenon consisting of a series of complex processes taking place in the material of the photocathode–emitter when it is irradiated by x rays.¹

When x radiation of intensity I_0 falls upon a flat photocathode at a grazing angle φ , part of this radiation, equal to $I_0 R(\varphi)$, is reflected [$R(\varphi)$ is the reflection coefficient of the flat photocathode surface], and part, equal to $[1 - R(\varphi)]I_0$, after being refracted, passes into the photocathode and propagates within it, in the process being absorbed exponentially.

Throughout the entire penetration distance of the radiation into the photocathode, as a result of absorption of the x-ray photons by the inner shells of the atoms in the solid, fast (with large kinetic energy) photo- and Auger electrons appear, and also the so-called fluorescence electrons which are formed upon absorption in the photocathode of the fluorescence electrons. These electrons are usually called primaries, or internal x-ray electrons. As they propagate, these fast, primary electrons traverse some distance l in the photocathode (the mean free path of the electron^{2–4}). Within this distance the primary electron loses its initial kinetic energy to ionization of atoms of the medium in a cascade of inelastic electron–electron collisions, creating in the process some number of true secondary electrons which have energies much less than that of the primary, but sufficient to overcome the energy barrier at the surface of the photocathode and escape into the vacuum. The slow electrons created in this way are usually called “secondaries.” Note that the energies of these secondary electrons are small,⁵ their motion is of a diffusive nature and can be characterized by some diffusion length L , which is sometimes called the mean free path of the slow, secondary electrons. If, as the secondary electron approaches the photocathode–vacuum interface, the normal component of its total energy exceeds the energy barrier at the photocathode surface, then such an electron can escape into the vacuum outside the photocathode.

As is well known, the total-current quantum yield K_C , to within a factor of the electron charge, is the ratio of the total current emitted by the photocathode to the number of x-ray

photons incident on the photocathode per second. Strictly speaking, the total-current quantum yield K_C is the sum of the quantum yield of the internal x-ray electrons⁶ and the quantum yield of the secondary electrons. However, since for efficient photocathodes in the x-ray region of the spectrum the quantum yield of the internal x-ray electrons is much less than the quantum yield of the secondary electrons, in what follows, for efficient photocathodes, we shall consider the quantum yield of the slow, secondary electrons created by the fast primary electrons to be the total-current quantum yield.

The expression for the quantum yield of the x-ray photoelectric effect in the total electron current K_C is obtained as follows. First we consider the simple “point” model, which is based on the one-dimensional theory of diffusion of slow, secondary electrons inside the photocathode toward the vacuum surface of the photocathode surface and then, taking the mean free path of the fast, primary electrons into account, we derive a general expression for the quantum yield.

The “point” model assumes that inside a solid at the point at which an x-ray photon is absorbed there appear fast, primary electrons which dissipate their energy in the immediate vicinity of this point, forming some number of slow, secondary electrons. The appearance of these secondary electrons can be described with the help of the generation function $G_0(x)$ (the x axis is directed into the photocathode, perpendicular to its surface, and $x=0$ at the vacuum surface of the photocathode).

The probability of absorbing an x-ray photon in a layer of thickness dx at a depth x from the photocathode surface, obviously, is given by

$$[1 - R(\varphi)]\mu' \exp(-\mu'x)dx,$$

where $\mu' = \mu/\sin\varphi'$, μ is the linear absorption coefficient, and φ' is the refraction angle of the incident x ray.⁷

The number of secondary electrons generated in the layer dx at the depth x apparently equals

$$G_0(x)dx = [1 - R(\varphi)] \frac{h\nu}{\varepsilon} \mu' \exp(-\mu'x)dx, \quad (1)$$

where $h\nu$ is the energy of a photon of the x radiation incident on the flat photocathode at a grazing angle φ , and ε is some

mean energy needed to created one secondary electron capable of escaping from the photocathode to the vacuum. The quantity $n_0 = h\nu/\varepsilon$ is the number of the “batch” or “swarm” of electrons that is formed at the point at which a photon is absorbed.

If we assume, as is customary, that the probability of escape from the photocathode of the slow, secondary electrons is described by the function

$$P(x) = B \exp\left(-\frac{x}{L}\right), \tag{2}$$

where B is the escape probability of the electron from the surface of the photocathode at $x=0$, then the number of electrons escaping from a very thick photocathode per unit time, i.e., the total-current quantum yield for the “point” model (K_{CPM}), is equal to

$$K_{CPM} = [1 - R(\varphi)] \int_0^\infty G_0(x) P(x) dx = [1 - R(\varphi)] \frac{h\nu}{\varepsilon} B \frac{\mu' L}{1 + \mu' L}. \tag{3}$$

1. ACCOUNT OF THE MEAN FREE PATH OF A FAST X-RAY ELECTRON

Obviously, even for efficient photocathodes, using the “point” model to calculate the total-current quantum yield K_C is to a certain degree a convenient approximation. It is clear that in reality the “point” model is not always and not completely justified by experiment. Therefore, it makes sense to treat the phenomenon of x-ray electron photoemission by assuming that in the formation of slow, secondary electrons a primary, internal x-ray electron traverses some completely determined distance l (Refs. 2–4).

For simplicity we assume that radiation losses are absent in the photocathode upon absorption of an x-ray photon and, consequently, the sum of the energies of all the primary, internal x-ray electrons E_j is equal to the energy of this photon $\sum_j E_j = h\nu$.

Slow, secondary electrons appear over the entire path l_j of motion of the fast, internal x-ray electrons in the photocathode. The mean free path l_j is determined by the electron energy E_j and the photocathode material.²⁻⁴

We seek an expression for K_C for some concrete value of the mean free path l of a fast electron having initial energy E . We assume that, for motion of primary, internal x-ray electrons, the diffusion model⁶ is valid and that the slow, secondary electrons appear over the entire mean free path of the electron with constant linear density: $\rho = n_0/V$, where $n_0 = h\nu/\varepsilon$, and $V = \frac{4}{3}\pi l^3$ is the volume of generation of secondary electrons, determined by the mean free path of the primary x-ray electron.

Figure 1 presents a schematic depiction of the geometrical conditions for calculating K_C . The radius of the sphere of propagation of the fast electron is equal to its mean free path l . The quantity x' is the distance from the point at which an x-ray photon is absorbed to the vacuum surface of

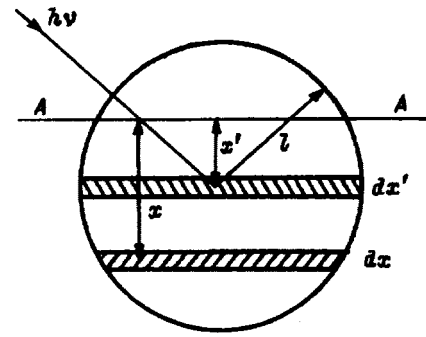


FIG. 1. Diagram of the calculation of x-ray emission of secondary electrons created by fast primary electrons.

the photocathode (AA'), x is the distance to this same surface (AA') from the layer dx , where the appearance of secondary electrons is considered.

The quantity $F(x')dx' = \mu' \exp(-\mu'x')dx'$ is the probability of formation of a fast, primary electron in the layer dx' at the depth x' upon absorption of an x-ray photon. Thus, the number of secondary electrons created per unit time in the layer dx at the depth x is equal to

$$dn^{(2)} = F(x')dx' \rho \pi [l^2 - (x - x')^2] dx. \tag{4}$$

To find the total number of secondary electrons $G(x)dx$ appearing in the layer dx at the depth x upon absorption of an x-ray photon, both above and below the layer dx (Fig. 1), we need to integrate the expression $dn^{(2)}$ over all dx' . Here the value of $G(x)dx$ will be different at different values of x .

For $x \leq l$ the function $G(x)dx \equiv G_1(x)dx$ can be represented in the form

$$G_1(x)dx = \int_0^{x+l} dn^{(2)} = \frac{3}{4} \frac{n_0}{l^3} \left[(l^2 - x^2) \exp(\mu'x) + \frac{2}{\mu'} \times \left(x - \frac{1}{\mu'} \right) \exp(\mu'x) + \frac{2}{\mu'} \exp(-\mu'l) \left(l + \frac{1}{\mu'} \right) \right] \times \exp(-\mu'x) dx = B_1(x) \exp(-\mu'x) dx. \tag{5}$$

For $x \geq l$ it has the form

$$G_2(x)dx = \int_{x-l}^{x+l} dn^{(2)} = \frac{3n_0}{l^2 \mu'} \left[\cosh(\mu'l) - \frac{\sinh(\mu'l)}{\mu'l} \right] \times \exp(-\mu'x) dx = B_2 \exp(-\mu'x) dx. \tag{6}$$

It can be seen that the generation function $G(x)$ has a quite complicated form, and for $x \leq l$ the factor B_1 depends on x , while for $x \geq l$ B_2 it does not depend on x .

For a semi-infinite photocathode the expression for the total-current quantum yield of the slow, secondary electrons formed by the fast, primary electrons with energy E and mean free path l can be written as follows:

$$K_C = \int_0^\infty G(x) P(x) dx, \tag{7}$$

where $P(x)$ is the escape probability of the secondary electrons from the depth x . If we assume that $P(x)$ is correctly

represented by an expression of the form (2), then we obtain the following expression for the total-current quantum yield for a photocathode of large depth:

$$K_C = [1 - R(\varphi)] \left\{ \int_0^l B_1(x) B \exp \left[- \left(\mu' + \frac{1}{L} \right) x \right] dx + \int_l^\infty B_2 B \exp \left[- \left(\mu' + \frac{1}{L} \right) x \right] dx \right\} = [1 - R(\varphi)] \times \left\{ \frac{3}{2} B \frac{E}{\varepsilon} \frac{1}{1 + b/a} \left[\frac{1}{a^3} \left(\frac{1}{2} a^2 + (a + 1) \exp(-a) - 1 \right) + \frac{1}{b^3} \left(\frac{1}{2} b^2 + (b + 1) \exp(-b) - 1 \right) \right] \right\}, \quad (8)$$

where $a = \mu' l$ and $b = l/L$. We have introduced the notation

$$\frac{1}{a^3} \left(\frac{1}{2} a^2 + (a + 1) \exp(-a) - 1 \right) = f(a) = f(\mu' l),$$

$$\frac{1}{b^3} \left(\frac{1}{2} b^2 + (b + 1) \exp(-b) - 1 \right) = f(b) = f\left(\frac{l}{L}\right).$$

Thus, expression (8) for K_C can be represented by

$$K_C = [1 - R(\varphi)] \left\{ \frac{3}{2} B \frac{E}{\varepsilon} \frac{1}{1 + b/a} (f(a) + f(b)) \right\}. \quad (8a)$$

The total-current quantum yield taking into account all groups of primary electrons arising upon the absorption of an x-ray photon is expressed by

$$K_C = [1 - R(\varphi)] \left\{ \sum_{j=1}^M \frac{3}{2} B \frac{E_j}{\varepsilon} P_j \frac{\mu' L}{1 + \mu' L} [f(a_j) + f(b_j)] \right\} = K_{CPM} \left\{ \sum_j \frac{3}{2} \frac{E_j}{h\nu} P_j [f(a_j) + f(b_j)] \right\}, \quad (9)$$

where E_j is the energy of a fast x-ray electron of the given group, P_j is the probability of appearance of this group, M is the number of groups of fast electrons, $a_j = \mu' l_j$, $b_j = l_j/L$, l_j is the mean free path of a fast electron, and K_{CPM} is the total current quantum yield of the slow, secondary electrons for the ‘‘point’’ model without allowing for the finite mean free path of the fast x-ray electrons.

We will represent the summand in Eq. (9) as ΔK_j ; then the general expression for the total-current quantum yield can be written in the form

$$K_C = K_{CPM} \sum_{j=1}^M \Delta K_j = K_{CPM} \Delta K, \quad (10)$$

where $\Delta K = \sum_{j=1}^M \Delta K_j$ is a function describing the transformation of the energy of the fast x-ray electrons into the energy of slow electrons.

If a fast electron has escaped from the photocathode without loss of energy, then for it $\Delta K = 0$; if, however, the fast electron loses all its energy to formation of slow, secondary electrons, then $\Delta K = 1$. Thus, the numerical value of ΔK will be found within the limits $0 < \Delta K \leq 1$.

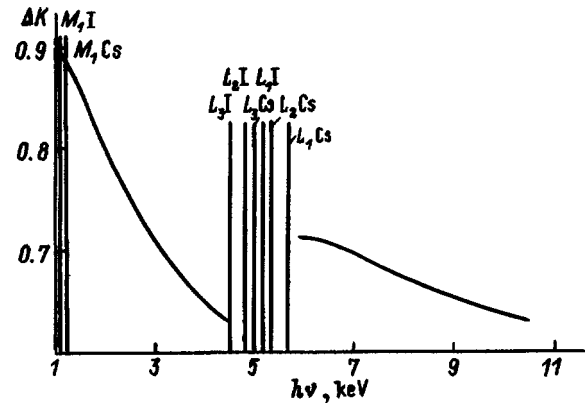


FIG. 2. Spectral dependence of ΔK for a CsI photocathode. $L = 300 \text{ \AA}$, $C = 6$.

2. X-RAY PHOTOEMISSION FOR A CsI PHOTOCATHODE

Analysis of the equations derived above applied to the case of an efficient CsI photocathode shows that the quantity L —the diffusion length of the slow electrons—appears in the formulas for K_C . The dependence of the escape depth of the secondary electrons L on their energy was calculated in Ref. 8 for a CsI photocathode for the secondary electrons scattering off optical and acoustical phonons. The calculations show that for $E \approx 2 \text{ eV}$ and larger, the escape depth of the slow electrons does not depend on their energy and is equal to approximately $L \approx 300 \text{ \AA}$. References 9 and 10 adopted the value $l = 200 - 250 \text{ \AA}$ for the diffusion length of the slow electrons in CsI. We will use these values of L in our calculations of K_C for a CsI photocathode.

As follows from Eq. (10), the total-current quantum yield K_C with the mean free path of the fast x-ray electrons taken into account is given by expression (3) corrected by some additive function ΔK , which describes the transformation of the energy of the fast electrons into the energy of slow electrons. As can be seen from expression (8), the quantity ΔK depends on two parameters: $a_j = \mu' l_j$ and $b_j = l_j/L$, in which appear the quantities l_j and L and the linear absorption coefficient of x radiation μ' , referred to the normal to the photocathode surface. Since the numerical value of μ' is well known,^{7,11} but the quantities l_j and L derived by various authors¹⁰ have a large spread, it is very important to examine the effect of the numerical values of L and l_j on the magnitude of ΔK .

The length l_j for CsI can be calculated according to

$$l_j = C \cdot 10^{-6} \frac{A_{Cs} + A_I}{\rho(Z_{Cs} + Z_I)} E_j^{1.4}, \quad (11)$$

where A_{Cs} and A_I are the atomic weights of Cs and I ($A_{Cs} = 132.9$, $A_I = 126.9$), Z_{Cs} and Z_I are the atomic numbers of Cs and I ($Z_{Cs} = 55$, $Z_I = 53$), ρ is the density of CsI ($\rho_{CsI} = 4.5 \text{ g/cm}^3$), E_j is the energy of the fast electrons (keV), and $C = \text{const}$.

For a CsI photocathode the calculations of ΔK as a function of l_j and L show that when l_j and L vary by 100% (i.e., by a factor of 2), ΔK varies by only $\approx 6\%$.

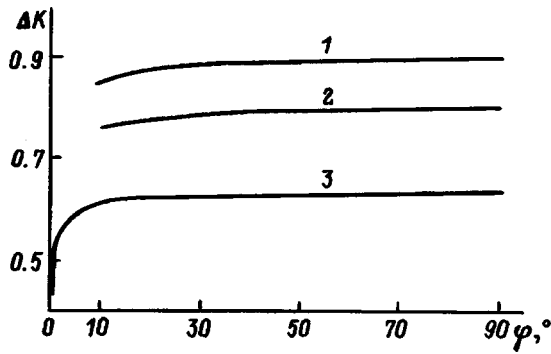


FIG. 3. Angular dependence of ΔK for a CsI photocathode. $h\nu=1.04$ (1), 2.01 (2), 10.5 keV (3).

For a CsI photocathode with $L=300 \text{ \AA}$ and $C=6$ we calculated the spectral dependence of ΔK (Fig. 2). The calculations show that the numerical values of ΔK for different photon energies differ substantially, one from the other, and in the region of the L -absorption edges of the Cs and I atoms the value of ΔK undergoes a series of jumps. This has to do with the fact, that as the energy of the incident x-ray photon decreases, the value of ΔK will change due to changes in both $\mu(h\nu)$ and $l_j(h\nu)$.

Calculation of the angular dependence of $\Delta K(\varphi)$ for three photon energies ($h\nu=1.04, 2.01,$ and 10.5 keV) shows (Fig. 3) that ΔK is essentially independent of the grazing angle φ in the region $10\text{--}90^\circ$. However, at angles $\varphi < 10^\circ$ ΔK decreases quite abruptly as the grazing angle is decreased. This decrease is especially marked for radiation with lower photon energies, for which refraction is noticeable in this angular range. Therefore, in the calculation of K_C , it is especially important to take ΔK into account at small grazing angles.

Note that for CsI photocathodes an experimental determination of the spectral dependence of the total-current quantum yield K_C^e (Refs. 12 and 13) and a knowledge of the value of μ' (Refs. 7 and 11) and L (Refs. 8–10) allows one to estimate the main parameters of the x-ray photoelectric effect, specifically B and ε . Table I shows the spectral dependence of $K_C^e, \mu, \Delta K,$ and ε/B , where these values were calculated separately for each photon energy shown. It is clear from the table that the last quantity remains practically constant for the photon energies shown. Its mean value is 14.8 eV. Thus, the value 14.8 eV is an upper bound on the numerical value of ε if $B=1$. As is well known, the lower bound on ε can be estimated as follows:

TABLE I. Spectral dependence of $\Delta K, \mu, K_C^e,$ and ε/B for a CsI photocathode. The angle $\varphi=90^\circ$.

Line	$h\nu, \text{keV}$	$\Delta K, \%$	μ, cm^{-1}	$K_C^e, \frac{\text{electron}}{\text{photon}}$	$\varepsilon/B, \text{eV}$
Cr $K\alpha$	5.41	67.2	3500	2.60	14.71
Cr $K\beta$	5.95	71.3	3000	2.54	15.0
Co $K\alpha$	6.92	69.9	2000	2.00	14.92
Co $K\beta$	7.65	68.2	1600	1.70	14.71
Cu $K\alpha$	8.04	67.3	1400	1.54	14.78
Cu $K\beta$	8.90	65.5	1100	1.24	15.54

$$\varepsilon = E_g + \chi + E_{\text{kin}},$$

where E_g is the width of the band gap of CsI, χ is the electron affinity, and E_{kin} is the kinetic energy of the escaping secondaries. For a CsI photocathode $E_g \approx 6.2 \text{ eV}, \chi \approx 0.2 \text{ eV},$ and $E_{\text{kin}} \approx 1.6 \text{ eV}$ (Refs. 5 and 9). Consequently, $\varepsilon \approx 8 \text{ eV}$. Thus, the numerical value of ε can vary within the limits $8 \leq \varepsilon \leq 14.8 \text{ eV}$. The numerical value of B will then vary within the limits $0.54 \leq B \leq 1$.

From other literature sources,⁸ as a lower bound on ε for CsI we can take the value $\varepsilon \approx 1.7E_g = 10.54 \text{ eV}$, which does not contradict the condition $(\varepsilon/B)_{\text{av}} = 14.8 \text{ eV}$, and the value of ε in this case will vary within the limits $10.54 \leq \varepsilon \leq 14.8 \text{ eV}$. The value of B will then vary within the limits $0.71 \leq B \leq 1$.

¹M. A. Rumsh, Report in Pursuit of the Learned Degree of Doctor of Phys.–Math. Sciences [in Russian], Izdat. LGU, Leningrad State Univ. Press, Leningrad, 1962.
²E. A. Burke, IEEE Trans. Nucl. Sci. **NS-24**, 2505 (1977).
³T. Tabata, R. Ito, S. Okabe, Nucl. Instrum. Methods **103**, 85 (1972).
⁴I. M. Bronshtein and A. N. Protsenko, Fiz. Tverd. Tela (Leningrad) **7** (1965) [sic].
⁵J. L. Llacer and E. L. Garvin, J. Appl. Phys. **40**, 2766 (1969).
⁶V. N. Shchemelev, E. P. Savinov, and V. V. Shchemelev, Fiz. Tverd. Tela (St. Petersburg) **39**, 1665 (1997) [Phys. Solid State **39**, 1487 (1997)].
⁷B. L. Henke, P. Lee, T. J. Tanaka, et al., At. Data Nucl. Data Tables **27**, 1, 1 (1982).
⁸E. Nymmiste, Author's Abstract of Candidacy Dissertation [in Russian], Tartu, 1991, 15 pp.
⁹B. L. Henke, J. P. Knauer, and K. Premaratne, J. Appl. Phys. **52**, 1509 (1981).
¹⁰G. W. Fraser, Nucl. Instrum. Methods **206**, 265 (1983).
¹¹O. S. Marenkov and N. I. Komyak, Handbook of Photon Interaction Coefficients in X-ray Radiometric Analysis [in Russian], Energoatomizdat, 1988, 224 pp.
¹²A. M. Prokhorov, V. K. Chevokin, and V. N. Shchemelev, Tr. FIAN **155**, 212 (1985).
¹³J. E. Lees, G. W. Fraser, S. E. Pearce, J. F. Pearson, V. N. Shchemelev, A. P. Pavlov, and A. S. Shulakov, Nucl. Instrum. Methods Phys. Res. A **381**, 453 (1996).

Translated by Paul F. Schippnick

Quadrupole and paramagnetic interactions of ^{27}Al nuclei in mixed yttrium-dysprosium-aluminum garnets $\text{Y}_{3-x}\text{Dy}_x\text{Al}_5\text{O}_{12}$

A. A. Vorob'ev, N. A. Grigor'eva, S. N. Ivanov, V. S. Kasperovich, E. N. Khazanov, and E. V. Charnaya

Institute of Physics, St. Petersburg State University, 198904 Petrodvorets, Russia
(Submitted December 19, 1997)

Fiz. Tverd. Tela (St. Petersburg) **40**, 1047–1051 (June 1998)

An ^{27}Al NMR study of mixed yttrium-dysprosium-aluminum garnets $\text{Y}_{3-x}\text{Dy}_x\text{Al}_5\text{O}_{12}$ is reported for $x=0, 0.15, 0.50, 0.64,$ and 1.00 . The quadrupole coupling parameters for the a and d aluminum sites have been determined. The spectra have been theoretically calculated with inclusion of the paramagnetic shift induced by Dy^{3+} ions. An analysis of the NMR line shape has permitted a conclusion that there is no substitutional order in the mixed crystals under study. © 1998 American Institute of Physics. [S1063-7834(98)01906-6]

Single-crystal solid solutions based on the yttrium-aluminum garnet $\text{Y}_{3-x}\text{Re}_x\text{Al}_5\text{O}_{12}$ (where Re stands for rare-earth elements and lutetium) are widely used in present-day laser technology and acousto-electronics.¹ Yttrium-dysprosium-aluminum garnets $\text{Y}_{3-x}\text{Dy}_x\text{Al}_5\text{O}_{12}$ enjoy particularly wide recognition. These crystals were studied by different methods, including the acoustic² and heat pulse^{3,4} techniques, and optical spectroscopy⁵.

Despite the practical importance of $\text{Y}_{3-x}\text{Dy}_x\text{Al}_5\text{O}_{12}$ mixed garnets, however, the magnitude and distribution of their crystal fields remain unclear. These problems can be clarified by nuclear magnetic resonance (NMR), which is capable of determining the microstructure of solid materials with a high sensitivity. NMR was employed by us previously in studies of mixed garnets of different compositions, as well as of mixed aluminates.^{3,6–9} These studies permitted us to find concentration dependences of the crystal-field distribution and to investigate the extent of substitutional rare-earth ordering on the yttrium sublattice. These relations were found^{3,6–9} to be closely connected to the properties of these compounds essential for applications.

This work reports an ^{27}Al NMR study of $\text{Y}_{3-x}\text{Dy}_x\text{Al}_5\text{O}_{12}$ crystals for $x=0, 0.15, 0.50, 0.64,$ and 1.00 . The available information relates only to ^{27}Al NMR data for nominally pure yttrium-aluminum, $\text{Y}_3\text{Al}_5\text{O}_{12}$ (Refs. 3, 6, 9, and 10), and dysprosium-aluminum, $\text{Dy}_3\text{Al}_5\text{O}_{12}$,¹¹ garnets, which corresponds to $x=0$ and 3. Our measurements were carried out on a RYa-2301 NMR spectrometer in magnetic fields of 0.6 and 1 T at room temperature. The samples were parallelepipeds cut along the crystallographic axes a, b, c . The main measurements were performed with the sample rotated about axis c with the dc magnetic field in the (a, b) plane. The sample position was fixed by the angle θ between the magnetic induction vector and the crystallographic axis a .

It is known that the garnets under study have cubic symmetry, space group $Ia\bar{3}c$.¹² One unit cell of the garnet contains 40 aluminum ions, of which 16 are octahedrally (a site), and 24, tetrahedrally (d site), coordinated by oxygen

ions.¹² The oxygen octahedra and tetrahedra are distorted so that the crystal field at the aluminum ions is axially symmetric with the axes directed along the cubic axes a, b, c (d sites) and along the cube body diagonals (a sites). As a result, the Al nuclei in this crystal occupy, in a general case, three magnetically nonequivalent d positions, and four magnetically nonequivalent a positions. ^{27}Al nuclei possess a quadrupole moment, because the spin of the aluminum nuclei is $5/2$. Interaction of the quadrupole moment of the ^{27}Al nucleus with electric crystal-field gradients in garnets splits the NMR line, with the shifts of the components being described in second-order perturbation theory by the following relations¹⁴

$$\begin{aligned} \nu_{\pm\frac{5}{2}, \pm\frac{3}{2}} &= \nu_0 \pm (3 \cos^2 \phi - 1) \frac{3e^2qQ}{20h} \\ &+ \frac{1}{4\nu_0} \sin^2 \phi (33 \cos^2 \phi - 1) \left(\frac{3e^2qQ}{20h} \right)^2, \\ \nu_{\pm\frac{3}{2}, \pm\frac{1}{2}} &= \nu_0 \pm (3 \cos^2 \phi - 1) \frac{3e^2qQ}{40h} \\ &+ \frac{1}{16\nu_0} \sin^2 \phi (5 - 21 \cos^2 \phi) \left(\frac{3e^2qQ}{20h} \right)^2, \\ \nu_{\frac{1}{2}, -\frac{1}{2}} &= \nu_0 + \frac{1}{2\nu_0} \sin^2 \phi (1 - 9 \cos^2 \phi) \left(\frac{3e^2qQ}{20h} \right)^2, \end{aligned} \quad (1)$$

where Q is the quadrupole nuclear moment, e is the electronic charge, eq is the zz component of the electric-field gradient (EFG) tensor, ϕ is the angle between the principal EFG axis and the external magnetic field, and ν_0 is the Larmor frequency. Equations (1) were written with due account of the fact that the asymmetry parameter for garnets is zero. As follows from Eqs. (1), the ^{27}Al NMR spectrum of an yttrium-aluminum garnet sample ($x=0$) oriented arbitrarily in the magnetic field consists of 20 lines for the a sites and of 15 lines for the d sites, which correspond to the $\pm 5/2 \leftrightarrow \pm 3/2$, $\pm 3/2 \leftrightarrow \pm 1/2$, and $1/2 \leftrightarrow -1/2$ transitions and are split by first- and second-order quadrupole shifts [proportional to

TABLE I. Quadrupole coupling constants and lattice parameters for mixed yttrium-dysprosium-aluminum garnets studied in this work, and for pure dysprosium-aluminum garnet.

	<i>x</i>					
	0	0.15	0.50	0.64	1.00	3.00
$\frac{e^2qQ}{h}(d)$, kHz	6020±20*	6020±10	6000±10	5910±15	5850±15	5873±20**
$\frac{e^2qQ}{h}(a)$, kHz	630±6*	630±10	630±10	630±15	600±10	447±30**
Lattice constant, Å	12.008	12.010	12.014	12.015	12.019	12.041

*Data from Ref. 10

**Data from Ref. 11.

e^2qQ/h and $(e^2qQ/h)^2$, respectively]. Since the second-order shift for ^{27}Al in an *a* position is, however, considerably smaller than the NMR linewidth, all the four lines produced in the $1/2 \leftrightarrow -1/2$ transitions merge into one.^{6,9}

If part of the Y^{3+} ions are replaced by Dy^{3+} paramagnetic ions, the resonant frequencies of ^{27}Al nuclei undergo a paramagnetic shift,¹⁴ which depends on the number of dysprosium ions in the nearest-neighbor environment of aluminum ions. Because the separation between the nearest-neighbor aluminum and dysprosium ions is larger than the extent of the Dy^{3+} wave functions, the paramagnetic shift is dominated by dipole-dipole interaction.¹⁵ In this case the paramagnetic shift can be written

$$\Delta\nu_p = \frac{\gamma}{2\pi} \sum_i \frac{\langle\mu_i\rangle(1-3\cos^2\chi_i)}{r_i^3}, \quad (2)$$

where γ is the gyromagnetic ratio of ^{27}Al nuclei, $\langle\mu_i\rangle$ is the average magnetic moment of Dy^{3+} ions, index *i* labels Dy^{3+} ions surrounding ^{27}Al , r_i is the distance between a ^{27}Al nucleus and the *i*th dysprosium ion, and χ_i is the angle between vector \mathbf{r}_i and external magnetic field \mathbf{B}_0 .

For room temperature, the average dipole moment of Dy^{3+} can be calculated from¹⁵

$$\langle\mu_i\rangle = \frac{\mu_B^2 g^2 J(J+1)B_0}{3kT}, \quad (3)$$

where g is the Landé factor, μ_B is the Bohr magneton, J is the total angular momentum of the Dy^{3+} ion, k is the Boltzmann constant, and T is the temperature. The average magnetic moment of Dy^{3+} , $\langle\mu_i\rangle$, calculated in this way coincides with the experimental value obtained¹¹ for nominally pure dysprosium-aluminum garnet.

The quadrupole coupling parameters e^2qQ/h found in this work for the yttrium-aluminum garnet ($x=0$) from the dependence of NMR spectra on angle θ for the *a* and *d* positions coincide fully with the values quoted in Refs. 6 and 9 and agree within experimental error with other data¹⁰. These values are listed in Table I.

In mixed garnets, the combined action of quadrupole and paramagnetic shifts should result in a very complex pattern of NMR spectra.

Spectral assignments should take into account that, as follows from x-ray diffraction data, the Y^{3+} and Dy^{3+} ions in mixed yttrium-dysprosium-aluminum garnets are not fully

mutually ordered to produce a superlattice. As a result, for any solid-solution concentration there exists a certain probability of finding different numbers of Dy^{3+} ions in the nearest-neighbor environment of an Al^{3+} ion. For a fully disordered solid solution, this probability is given by the binomial distribution⁷

$$\frac{p!}{(p-n)!} \frac{x^n(1-x)^{p-n}}{n!}, \quad (4)$$

where p is the number of positions occupied by Y^{3+} and Dy^{3+} ions in the nearest-neighbor environment of aluminum.

Partial ordering in the substitution of Dy^{3+} ions for Y^{3+} may change considerably the probability distribution in the local environment of an Al ion.^{7,16}

To illustrate the effect of paramagnetic coupling on the ^{27}Al NMR spectrum, Fig. 1 shows angular dependences of the NMR line component shifts corresponding to the central $1/2 \leftrightarrow -1/2$ transition for aluminum *d* positions, which were calculated by us using the measured quadrupole constant

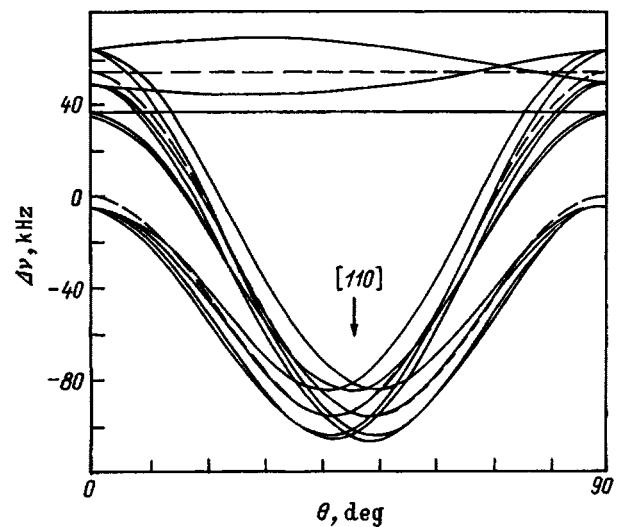


FIG. 1. Theoretical dependence of the *d*-site ^{27}Al NMR components corresponding to $1/2 \leftrightarrow -1/2$ transitions calculated, with inclusion of the second-order quadrupole shift and of the paramagnetic shift for $x=0.15$, for the case with one Dy^{3+} ion present in the nearest environment of aluminum. Dashed lines are orientation dependences calculated without inclusion of the paramagnetic shift. External magnetic field induction $B_0=0.678$ T. The degeneracy multiplicity for individual components is not given.

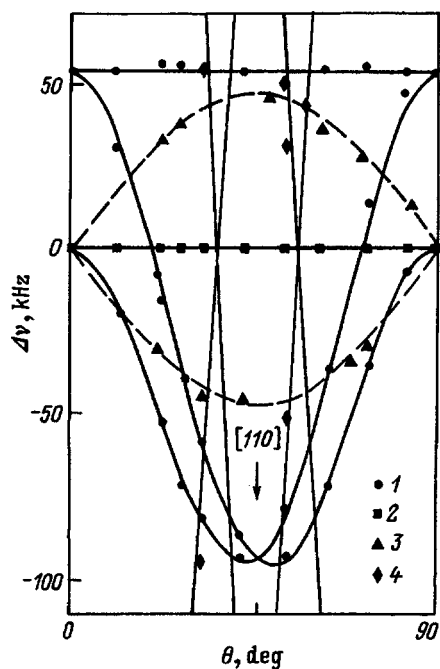


FIG. 2. Experimental angular dependence of ^{27}Al NMR central-transition components obtained in a field $B_0=0.678$ T for a $x=0.15$ sample. 1 — d components corresponding to the $1/2 \leftrightarrow -1/2$ transition; 2 — a component corresponding to the $1/2 \leftrightarrow -1/2$ transition; 3 — a components corresponding to the $\pm 3/2 \leftrightarrow \pm 1/2$ transition; 4 — d satellites corresponding to the $\pm 3/2 \leftrightarrow \pm 1/2$ transition. Solid lines display theoretical relations calculated neglecting the paramagnetic shifts.

(see below) for a concentration $x=0.15$ for the case of one of the six yttrium ions in the nearest environment of aluminum replaced by dysprosium ions. Similar dependences were obtained by us for all the concentrations studied here and for different numbers of dysprosium ions surrounding aluminum ions, for both d and a positions. It should be pointed out, however, that not all theoretically possible NMR line components will be observable experimentally against the background because of their low intensity and of the superposition of various components. The assignment of different components is favored by the fact that the paramagnetic shift, according to Eq. (2), is directly proportional to the external magnetic field, whereas the first-order quadrupole shift is field independent, and the second-order shift varies inversely with the external field [see Eqs. (1)].

An experimental angular study of the positions of the NMR d components corresponding to the central transition made for $x>0$ samples established reliably only the line components whose shift decreased 1.67 times with the external field induction increased from 0.6 to 1 T, which shows the second-order quadrupole shift to be dominant. Figure 2 presents for a particular case of $x=0.15$ angular dependences of the observed central components scanned in the (ab) plane. The above reasoning suggests that these components are due primarily to ^{27}Al nuclei surrounded only by yttrium ions. There is also a contribution due to aluminum nuclei for which the paramagnetic shift is small because of geometric factors and does not exceed the linewidths of the central d components; note that for the crystals under study they varied from 7 kHz ($x=0.15$) to 19.5 kHz ($x=1$) in a field of

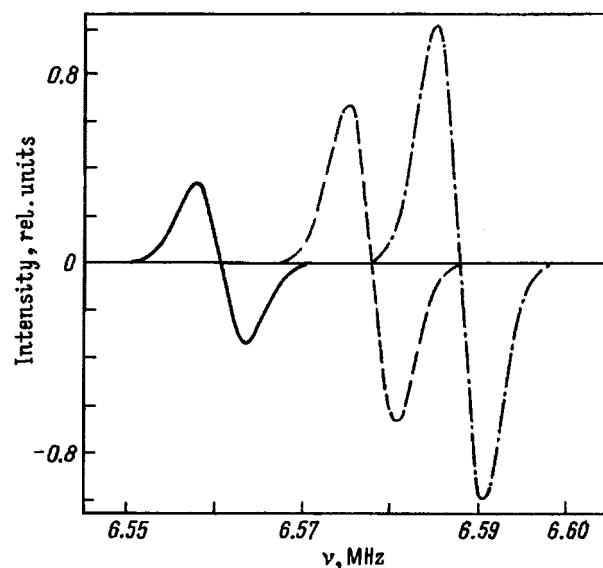


FIG. 3. Spin packets contributing to the central a component of ^{27}Al NMR spectrum, which correspond to one Dy^{3+} ion in the closest environment of aluminum ions in a positions. $\mathbf{B}_0 \parallel [110]$. External field induction $B_0 = 0.593$ T. The lattice parameters correspond to $x=0.15$.

0.6 T. A comprehensive analysis of the paramagnetic shifts (see, e.g., Fig. 1) showed, however, that the role played by these components is small, and that their total contribution does not exceed 5% even for the maximum dysprosium concentrations used.

It thus follows that the observed shifts of the central d components can be used to calculate the quadrupole coupling constant. The values of $(e^2qQ/h)(d)$ thus found are listed in Table I. The lattice constants of the mixed crystals used in the calculation were derived from x-ray diffraction measurements. These lattice constants satisfy Vegard's law¹⁷ which establishes a linear dependence of many parameters of mixed crystals on concentration. In a similar way, the angular dependence of the a satellites, whose positions were primarily determined by the first-order quadrupole shift, was used to calculate the values of $(e^2qQ/h)(a)$, which are likewise given in Table I. We readily see that the quadrupole constants for both aluminum positions vary monotonically with dysprosium concentration. Note that the quadrupole constant for the d position of Al varies stronger than predicted by Vegard's law. At the same time for the a position this variation is noticeably weaker.

While paramagnetic coupling practically does not affect the positions of visible d components and of a satellites, it influences considerably the shape of the central a component corresponding to the $1/2 \leftrightarrow -1/2$ transitions. Note that the central a component is a set of individual spin packets, which are related not only to the number of paramagnetic Dy^{3+} ions surrounding Al nuclei, but, as follows from Eq. (2), to actual dysprosium ion positions. This permits one to derive from an analysis of the line shape of the central a component information on the mutual arrangement of Y^{3+} and Dy^{3+} ions on the rare-earth garnet sublattice and, hence, on the presence or absence of partial substitutional order.¹⁸ As an illustration, Fig. 3 presents spin packets originating

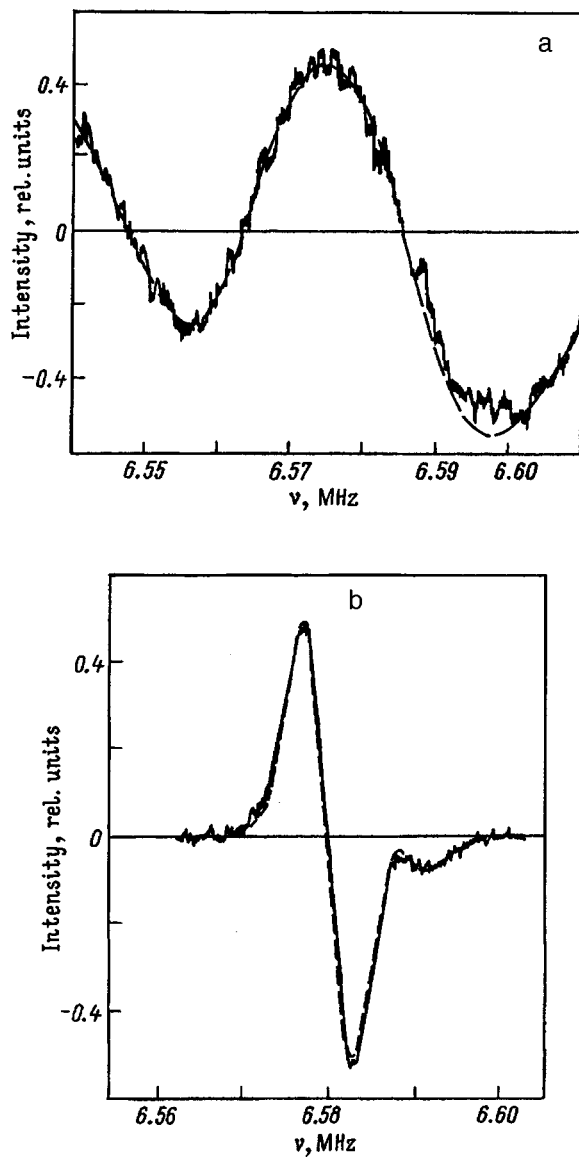


FIG. 4. Theoretical (dashed) and experimental (solid line, ten accumulations) derivatives of the ^{27}Al NMR central component corresponding to a aluminum positions with $\mathbf{B}_0 \parallel [110]$. (a) $x=1.00$ and (b) $x=0.15$. External field induction $B_0=0.593$ T.

from one Dy^{3+} ion occupying six different sites in the octahedral environment of aluminum for a crystal orientation where the external field is parallel to the $[110]$ crystallographic direction. We analyzed the shape of the central a component in the same orientation for all the mixed garnets studied, because in this geometry the d and the other a components are located at maximum distances from the central a component. The intensity of individual spin packets was calculated using Eq. (4) for a completely disordered solid solution. The line shapes calculated with Eq. (4) were found to be in an excellent agreement with experiment for all

samples. For illustration, Fig. 4 presents the calculated and experimental line shapes for the central a component for a mixed garnet with $x=1.00$ and 0.15 . These results permit a conclusion that mixed yttrium-dysprosium-aluminum garnets are disordered solid solutions in contrast, for instance, to mixed yttrium-lutetium-aluminum garnets^{3,6}. It should be pointed out that this conclusion is in accord with the studies of mixed yttrium-dysprosium-aluminum garnets made^{3,4} by the heat pulse technique. The assumption of the absence of ordering in our yttrium-dysprosium-aluminum garnets is in accord also with the monotonic variation of the quadrupole coupling constants with dysprosium concentration (see Table I). At the same time in mixed yttrium-lutetium-aluminum garnets one observed⁶ a sharp minimum in $(e^2qQ/h)(d)$ at a concentration $x=0.75$, where structural ordering was found^{3,6} to occur in these solid solutions.

Support of the Russian Fundamental Research Foundation (Grants 96-02-19523 and 97-02-16810) and of State Committee for Higher Education (Grant 95-0-7.1-160) is gratefully acknowledged.

- ¹A. A. Kaminskiĭ, L. K. Aminov, and V. L. Ermolaev, *Physics and Spectroscopy of Laser Crystals* [in Russian], Nauka, Moscow, 1986, 272 pp.
- ²S. N. Ivanov, V. V. Medved', and A. N. Makletsov, *Fiz. Tverd. Tela (Leningrad)* **26**, 1832 (1984) [*Sov. Phys. Solid State* **26**, 1108 (1984)].
- ³P. Yu. Efitsenko, E. N. Khazanov, S. N. Ivanov, V. V. Medved, and E. V. Charnaya, *Phys. Lett. A* **147**, 135 (1990).
- ⁴S. N. Ivanov, A. V. Taranov, and E. N. Khazanov, *Zh. Éksp. Teor. Fiz.* **89**, 1824 (1985) [*Sov. Phys. JETP* **62**, 1051 (1985)].
- ⁵Yu. K. Voron'ko, S. B. Gessen, and A. B. Kudryavtsev, *Trudy IOFAN* **29**, 3 (1991).
- ⁶P. Yu. Efitsenko, V. S. Kasperovich, A. A. Kuleshov, and E. V. Charnaya, *Fiz. Tverd. Tela (Leningrad)* **31**, No. 9, 170 (1989) [*Sov. Phys. Solid State* **31**, 1572 (1989)].
- ⁷E. V. Charnaya, N. A. Grigoreva, S. N. Ivanov, V. S. Kasperovich, E. N. Khazanov, and A. V. Taranov, *Phys. Status Solidi A* **147**, 313 (1995).
- ⁸L. S. Vorotilova, S. N. Ivanov, V. S. Kasperovich, E. V. Charnaya, and E. N. Khazanov, *Fiz. Tverd. Tela (Leningrad)* **34**, 2911 (1992) [*Sov. Phys. Solid State* **34**, 1560 (1992)].
- ⁹N. A. Grigor'eva, S. N. Ivanov, V. S. Kasperovich, E. N. Khazanov, and E. V. Charnaya, *Fiz. Tverd. Tela (St. Petersburg)* **37**, 3360 (1995) [*Phys. Solid State* **37**, 1846 (1995)].
- ¹⁰D. T. Edmonds and A. J. Lindop, *J. Appl. Phys.* **39**, 1008 (1968).
- ¹¹K. C. Brog, W. H. Jones, Jr., and C. M. Verber, *Phys. Lett.* **20**, 258 (1966).
- ¹²G. Menzer, *Z. Kristallogr.* **69**, 300 (1928).
- ¹³V. S. Grechishkin, *Nuclear Quadrupole Interactions in Solids* [in Russian], Nauka, Moscow, 1973, 262 pp.
- ¹⁴A. Abragam, *The Principles of Nuclear Magnetism* [Clarendon, Oxford, 1961; IL, Moscow, 1963, 552 pp.].
- ¹⁵J. S. Smart, *Effective Field Theories of Magnetism* [Saunders, Philadelphia, 1966, 393 pp.].
- ¹⁶J. Ziman, *Models of Disorder: The Theoretical Physics of Homogeneously Disordered Systems* [Cambridge University Press, Cambridge, 1979; Mir, Moscow, 1982, 592 pp.].
- ¹⁷L. Vegard, *Z. Phys.* **17**, 558 (1921).
- ¹⁸E. V. Charnaya, N. A. Grigor'eva, and V. S. Kasperovich, *Abstracts European Experimental NMR Conference (Paris, 1996)*, p. 298.

Translated by G. Skrebtsov

Spectral migration and decay characteristics of triplet excitations in glassy benzophenone

V. I. Mel'nik

Institute of Physics, Ukraine Academy of Sciences, 252022 Kiev, Ukraine

(Submitted December 19, 1997)

Fiz. Tverd. Tela (St. Petersburg) **40**, 1052–1055 (June 1998)

Spectral and kinetic properties of triplet excitons in thin films of glassy benzophenone were studied at temperatures between 4.2 and 220 K. The influence of the film thickness on the lifetime and nature of their phosphorescence decay was observed and discussed. It was shown that studies of spectral diffusion in thin glassy films of benzophenone must take into account the dependence of the emission lifetime on the recording wavelength and the influence of the excitation intensity on the phosphorescence decay process, among other factors. The hypothesis is put forward that the characteristics of the temperature transformations of the spectra (displacements, changes in band half-widths) are related to phase transitions and relaxation processes in the glassy benzophenone. © 1998 American Institute of Physics. [S1063-7834(98)02006-1]

One of the characteristic properties of disordered condensed systems is the inhomogeneous broadening of their spectral bands, which generally obey a Gaussian distribution. At fairly low temperatures, when kT is considerably smaller than the inhomogeneous broadening σ , energy relaxation of the photoexcitation given by this distribution will take place until thermal activation counteracts the energy losses and dynamic equilibrium is established.

Various recently published studies have investigated spectral diffusion and relaxation of triplet excitations in amorphous and glassy structures of organic molecular compounds,^{1–6} with the most interesting results being obtained by Bässler and coworkers.^{1–3} Time-resolved spectroscopic techniques at temperatures between 4.2 and 120 K were used to make detailed studies of the spectral and kinetic properties of thin amorphous films of various organic compounds (anthraquinone, benzophenone, phenanthrene). Triplet energy transfer processes in these systems were described by Monte Carlo computer modeling as well as by analytic theory.⁷ An arbitrary volume possessing cubic symmetry, consisting of $40 \times 40 \times 40$ sites, was considered. It was assumed that the spread of energy states obeys a Gaussian distribution and the probability of excitation jumps (transfer) from a particular site to 124 nearest-neighbor sites was calculated.

The rate constant for transfer of triplet excitation from one site to another is caused by exchange interaction and is expressed in the form¹

$$W_{ij} \sim \exp(-2\gamma r_{ij}) \exp[(\varepsilon_j - \varepsilon_i)/kT], \quad \varepsilon_j > \varepsilon_i,$$

$$W_{ij} \sim \exp(-2\gamma r_{ij}), \quad \varepsilon_i \leq \varepsilon_j,$$

where γ is the overlap parameter of the wave functions, r_{ij} is the distance between two sites which have exchanged energy, and ε_i is the energy of the i th state.

An important characteristic in the analyses of random exciton motion in amorphous systems having energy disor-

der at temperatures, when $\sigma/kT \gg 1$, is the asymmetry of the “down”–“up” transition probabilities. At low temperatures, where thermally activated up jumps are inhibited, an ensemble of excitations distributed statistically within an inhomogeneously broadened band with time will become concentrated near the long-wavelength edge of the density-of-states curve. Predicted results include red shifts of the time-resolved phosphorescence spectra, changes in the half-widths of the spectral bands, and a reduction in the lifetime of the triplet excitations. Since the number of lower-energy vacant levels to which a stray excitation may jump will decrease with time, the efficiency of excitation transfer should also decrease with time, which will slow the red shift. Some of these effects have been observed experimentally.^{1,8} It has also been shown^{1,2} that the nonequilibrium transfer of triplet excitations is described by a time-dependent, ensemble-averaged rate constant for energy transfer $W(t) \sim (t/t_0)^{\alpha-1}$, where $\alpha^{-1} = (\sigma/kT)^2 + 1$ is the time-dependent dispersion parameter. It has thus been demonstrated that triplet energy transfer processes in disordered condensed media exhibit dispersion (time-dependent) behavior.

Despite the fundamental importance of these results, it is the author's view that the studies made in Refs. 1–3 disregarded various important factors such as the influence of the thickness of thin films on the triplet energy transfer process, and the dependence of the phosphorescence lifetime on the recording wavelength and the intensity of the exciting light. In addition, the wider temperature range (4.2–220 K) in the present study allowed observation of various spectral and kinetic characteristics of glassy benzophenone and yielded the hypothesis that these are related to phase changes in the benzophenone. Thus, the present study considers the influence of these factors on the decay kinetics of triplet excitations in thin films of glassy benzophenone and we discuss possible mechanisms for the effects caused by them.

Figure 1 shows temperature dependences of the phos-

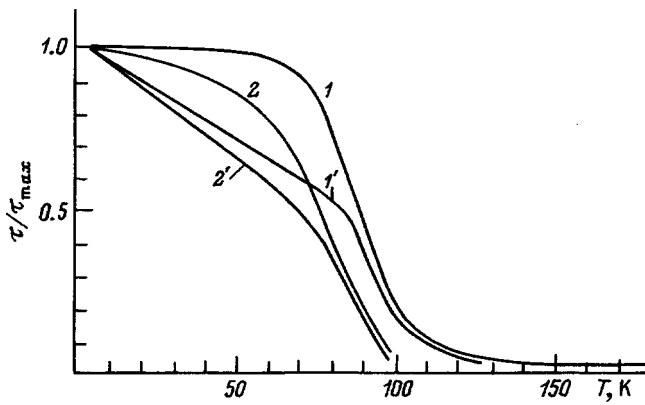


FIG. 1. Temperature dependence of the lifetime of triplet excitations in glassy benzophenone films: 1, 1' — film thickness 3 μm, measured at band maximum, 2, 2' — film thickness 0.5 μm, measured at $h/2$ point.

phorescence lifetime τ of glassy benzophenone films of different thickness. An analysis of the experimental results indicates that as the films become thinner and the temperature increases, which enhances the efficiency of triplet excitation migration in glassy benzophenone,⁹ the dimensions of the samples have an appreciable influence. It was shown that, for the particular case where the film thickness and temperature are such that the diffusive displacement length l of the triplet excitons is of comparable order of magnitude to the film thickness ($l = \sqrt{D\tau}$, where D and τ are the temperature-dependent diffusion coefficient and triplet-excitation lifetime), the lifetime τ decreases abruptly as a result of additional quenching at the surface of the samples. For the studies presented here, this effect became noticeable for film thickness of 1 μm or less, at temperatures $T \geq 50$ K.

Figure 1 also gives the lifetime τ as a function of the wavelength used to record the decay (the measurements were made at the maximum of the 0-0 band and at its short-wavelength edge at the point corresponding to the half-width of this band — $h/2$). In particular, at $T = 60$ K for benzophenone films 3 μm thick, the value of τ at the band maximum was 4600 μs and at the $h/2$ point, it was 2500 μs whereas for the 0.5 μm thick film, these values were 3700 and 2300 μs, respectively. This substantial reduction in τ for the shorter-wavelength radiation within the inhomogeneously broadened phosphorescence band was caused by the spectral

diffusion effect. In the shorter-wavelength range the phosphorescence decays as a result of spontaneous decay and as a result of a red shift (“drift”) of the emission spectrum away from the recording wavelength. Ultimately, the phosphorescence lifetime observed at a particular wavelength is shortened.

Since the probability of the $S_1^* \rightsquigarrow T_0$ intercombination transition in benzophenone is close to one, there is always a relatively high concentration of triplet excitations. Thus, the spectral and luminescence properties of benzophenone are extremely sensitive to the intensity of the exciting light. Note that at $T = 60$ K for a 3 μm thick film at an excitation power of ~100 W (LGI-21 laser, the excitation intensity was controlled using neutral and mesh filters), exponential decay was observed with $\tau = 2500$ μs (measured at the $h/2$ point). At an excitation power of ~1000 W, the decay of τ (1600 μs) differed from exponential as a consequence of nonlinear effects caused by triplet-triplet annihilation.¹⁰

The phosphorescence spectra of glassy benzophenone (both steady-state and time-resolved), at temperatures between 4.2 and 220 K, comprise a series of broad, inhomogeneously broadened bands with a 1640 cm^{-1} dominant vibrational mode typical of the benzophenone molecule. When the temperature is increased to 100 K, the spectrum is shifted by 370 cm^{-1} in the long-wavelength direction. Interestingly, when the temperature is increased further to 220 K, the spectrum is shifted back by the same amount, so that at 4.2 and 220 K the positions of the spectra on the energy scale are the same. At the same time, the position of the phosphorescence spectra of naphthalene impurities in the benzophenone remained constant over the entire temperature range studied.

Figure 2 gives temperature dependences of the steady-state phosphorescence spectra of glassy benzophenone and the half-widths of their first short-wavelength bands. It is noticeable that an abrupt increase in the half-widths of the spectral bands and a change in the direction of the spectral shift are observed in the same temperature range. A unique “phase transition” takes place in glassy benzophenone in this spectral range.

A graph of $\ln(\sigma - \sigma_0)$ versus $1/T$ was plotted with a correction for the residual half-width σ_0 ($\sigma_0 = 392 \text{ cm}^{-1}$ at $T = 4.2$ K) and the potential barrier ($E = 0.60$ kcal/mol) impeding the hindered molecular rotation and flip was deter-

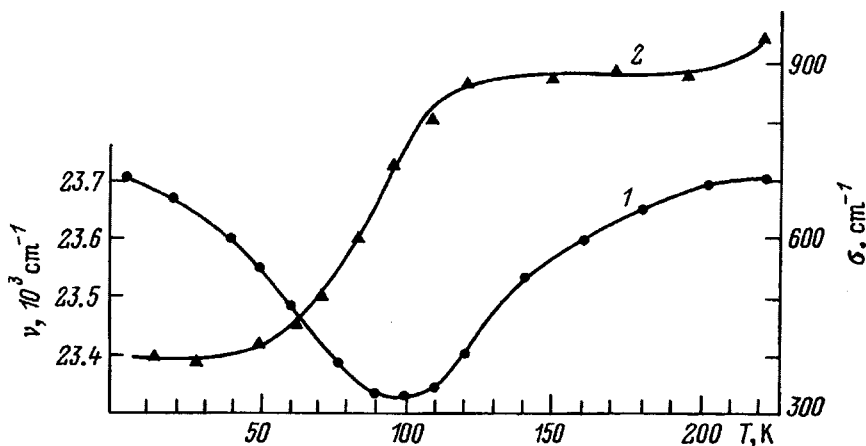


FIG. 2. Temperature dependences of the phosphorescence spectra (1) of glassy benzophenone and of the half-widths of their first short-wavelength bands (2).

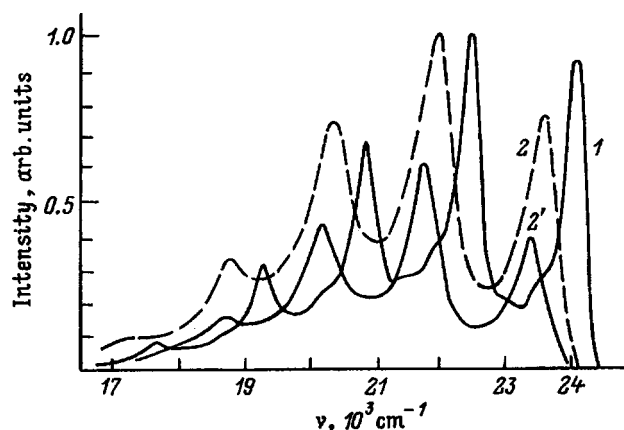


FIG. 3. Phosphorescence spectra of polycrystalline (1) and glassy (2, 2') benzophenone for delay times of 0.1 μs (1, 2) and 5 ms (2').

mined. The linear behavior of this dependence indicates that a thermal activation process takes place in this temperature range, accompanied by an increase in the band width in the phosphorescence spectrum. In this case, it is difficult to specify precisely which degrees of freedom of the molecular motion responsible for the relaxation and phase transitions, are "frozen out."

It was shown in Ref. 11 that molecular glasses exhibit two universal types of relaxation caused by the presence of two regions with a different ordering (loose and close-packed). According to one model,¹² the structure of glass is made up of two subsystems: groups (clusters) of close-packed molecules interspersed by layers with a relatively loose structure. Thus, it may be postulated that the phosphorescence spectrum of naphthalene impurity molecules located in regions of loose structure, where short-range order is conserved over a wide range of temperature, should not undergo appreciable shifts in this temperature range, as was observed experimentally. The temperature jump of the half-widths of the spectral bands is probably caused by relaxation motion of the molecules associated with the ordering in the structure of an amorphous substance. In terms of the concepts of two-level systems,¹³ this ordering may be interpreted as the transition of an amorphous system from one potential well to another.

Figure 3 shows phosphorescence spectra of polycrystalline and glassy benzophenone obtained for various delay times after the exciting laser pulse. The position of the phosphorescence spectrum of the polycrystal with the purely electronic transition frequency $\nu_{0-0} = 24\,053\text{ cm}^{-1}$ did not depend on the delay time and was the same as the spectrum under cw excitation. The emission spectrum of the glassy benzophenone is shifted toward the red and for a delay time of 5 ms this shift was 200 cm^{-1} . In general, the observed magnitude and direction of the shift are the result of the interaction between two competing processes. On the one hand, energy transfer will lead to a red shift while the dispersion of the excited-state lifetime caused by its decrease in the long-wavelength range produces a blue shift. Thus, in the present case the dominant mechanism is that caused by energy transfer within the inhomogeneously broadened band of

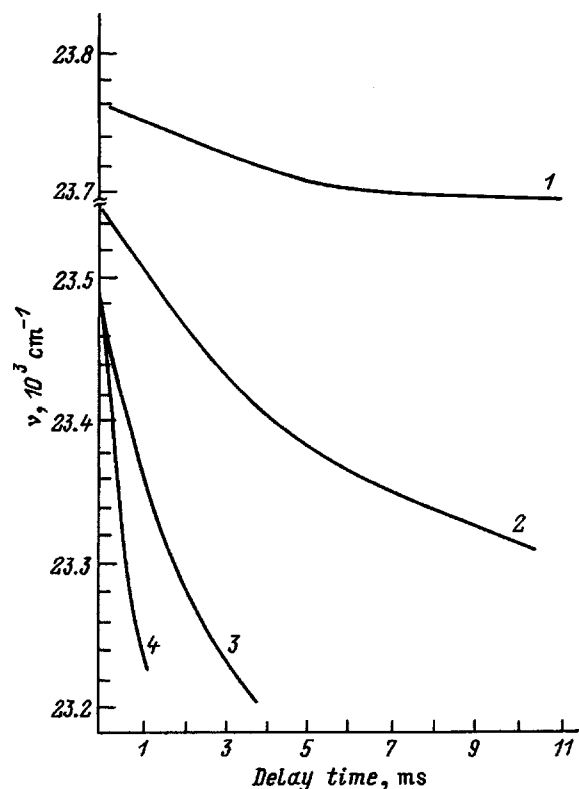


FIG. 4. Time dependences of the phosphorescence spectra at various temperatures, T (K): 1 — 4.2, 2 — 77, 3 — 100, and 4 — 120.

the phosphorescence spectrum of glassy benzophenone.

Figure 4 gives results of measurements of the shift of the phosphorescence spectra of glassy benzophenone as a function of the delay time τ_d . Attention is drawn to two factors. As the temperature increases, the rate of displacement of the spectra on the energy scale increases sharply. This can be attributed to the fact that the diffusion coefficient of triplet excitons in glassy benzophenone increases exponentially with temperature.⁹ In addition, for each temperature a slowing of the long-wavelength shift is observed with increasing τ_d , which is consistent with similar experimental results obtained for other materials.⁸

To conclude, the most important result in the author's view is that the decay of triplet excitations in thin benzophenone films depends on temperature, since this means that phenomena associated with the surface effect can be taken into account.

With regard to the possible phase changes taking place in glassy benzophenone at various temperatures, it would be interesting to establish a correlation between the spectroscopic and thermodynamic data (specific heat, entropy), although very little such data is available in the literature on benzophenone at present.

The author would like to thank K. I. Nelipovich for assistance with the experimental measurements.

¹R. Richert and H. Bässler, J. Chem. Phys. **84**, 3567 (1986).

²R. Richert and H. Bässler, Chem. Phys. Lett. **118**, 235 (1985).

³R. Richert, H. Bässler, B. Ries, B. Movaghar, and M. Grünewald, Philos. Mag. Lett. **59**, 95 (1989).

- ⁴S. A. Bagnich and A. V. Dorokhin, Zh. Prikl. Spektrosk. **54**, 919 (1991).
⁵S. A. Bagnich and A. V. Dorokhin, Fiz. Tverd. Tela (Leningrad) **33**, 1382 (1991) [Sov. Phys. Solid State **33**, 779 (1991)].
⁶I. A. Levitskiĭ and Yu. V. Rubinov, Khim. Fiz. **11**, 1224 (1992).
⁷M. Grünewald, B. Pohlman, B. Movaghar, and D. Wurtz, Philos. Mag. B **49**, 341 (1984).
⁸G. B. Talapatra, D. N. Rao, and P. N. Prasad, J. Phys. Chem. **88**, 4636 (1984).
⁹V. I. Mel'nik, K. I. Nelipovich, A. N. Faïdysh, and M. T. Shpak, Zh. Prikl. Spektrosk. **34**, 1078 (1981).
¹⁰P. Avakian and R. E. Merrefield, Phys. Rev. Lett. **13**, 541 (1964).
¹¹G. P. Johari, Philos. Mag. **46**, 549 (1982).
¹²S. A. Dzyuba and Yu. D. Tsvetkov, Zh. Strukt. Khim. **28**, 15 (1987).
¹³W. A. Philips, Rep. Prog. Phys. **50**, 1657 (1987).

Translated by R. M. Durham

MAGNETISM AND FERROELECTRICITY

Multiple nuclear spin echo in thin polycrystalline ferromagnetic films

V. O. Golub, V. V. Kotov, and A. N. Pogorelyĭ

Institute of Magnetism, Ukraine Academy of Sciences, 252142 Kiev, Ukraine

(Submitted November 17, 1997)

Fiz. Tverd. Tela (St. Petersburg) **40**, 1056–1061 (June 1998)

The formation of multiple nuclear spin echo signals has been studied in thin ferromagnetic polycrystalline films of 3d-metals and their alloys with induced anisotropy at temperatures between 2.2 and 300 K using two-pulse and three-pulse excitation. A method is proposed for the experimental determination of the contributions made by different mechanisms to the formation of spin-echo signals in magnets with strongly inhomogeneous Zeeman and quadrupole interactions. It is shown that in ferromagnets with a high rf field gain at the nucleus, the frequency modulation mechanism has a substantial influence in observations of nuclear spin-echo signals at nuclei with a high magnetic moment, even at liquid-helium temperatures.

© 1998 American Institute of Physics. [S1063-7834(98)02106-6]

Most experimental investigations of nuclear magnetic resonance in magnets use pulsed techniques. The main signals observed are the two-pulse and three-pulse (stimulated) echo. In some cases however, auxiliary signals appear in addition to the main echo signals (see, for example, Refs. 1–4) and this effect has been called multiple echo. Toward the end of the seventies, various reasons were identified for the appearance of these multiple echo signals: analyses were made of the influence of indirect interaction of nuclear spins via the electronic subsystem^{2,3,5} and of multiphoton cascade transitions for nuclei with the spin $I > 1/2$ (Refs. 1 and 6–8).

Since the inhomogeneity $\Delta\omega$ of the hyperfine fields at the nuclei in real magnets is microscopic and this inhomogeneity considerably exceeds the Suhl–Nakamura broadening, the influence of the indirect interaction between the nuclear spins via the electronic subsystem depends strongly on the relation between $\Delta\omega$ and the dynamic frequency shift

$$\omega_p = D \frac{m_z}{m_0}, \quad (1)$$

which characterizes the magnitude of this interaction,⁹ where D is the dynamic frequency shift parameter, m_z is the longitudinal component of the nuclear magnetization, and m_0 is the equilibrium nuclear magnetization.

1) $\omega_p \ll \Delta\omega$. The system of nuclear spins may be considered to be a set of noninteracting oscillators and a formal approach may be used: the resulting spin-echo signal, being amplified by the electronic subsystem, acts as an exciting pulse, which leads to the appearance of additional echo signals (echo-pulse mechanism^{2,3}). The relative amplitude and number of these signals is proportional to D . This approach can also be extended to the case $I > 1/2$ (this situation is analyzed in Ref. 10).

2) $\omega_p > \Delta\omega$. In this case, the motion of the nuclear spins will be strongly correlated. The equation describing the motion of the nuclear magnetization becomes nonlinear which

leads to the appearance of additional echo signals (frequency modulation mechanism⁵). The number and amplitude of these echo signals depends on ω_p .

3) The case $\omega_p \approx \Delta\omega$ has been studied very little.

The multiple nuclear-spin-echo technique can provide unique information on the crystal and magnetic structures of a substance. However, its use to investigate a wide range of inhomogeneous magnets (including thin polycrystalline magnetic films) is severely impeded by the fact that power and frequency dependences cannot be used because of the substantial spread of the hyperfine fields and rf field gains at the nuclei. Thus, an investigation of the formation of multiple echo in inhomogeneous magnets remains a real problem.

1. INVESTIGATED SAMPLES

The main samples investigated in this study were polycrystalline Fe, Co, FeCo, and Fe₂₀Ni₈₀ films with induced magnetic anisotropy. These materials were selected for the following reasons: 1) the NMR signal is strong over the entire temperature range studied (between 2.2 and 300 K); 2) no phase transitions and related effects, which could impede the interpretation of the results, occur in this temperature range; 3) a large volume of reference literature is available on the magnetic and crystalline properties of these samples; 4) multiphoton effects may be investigated for nuclei with $I > 1/2$ ($I = 3/2$ for Ni⁶¹, $I = 7/2$ for Co⁵⁹); 5) numerical calculations can be made of various NMR parameters such as the rf field gain η at the nucleus and the dynamic frequency-shift parameter D .

The main conclusions were checked in films of other magnets. Powders of these and other materials were also used in control experiments.

All the films studied here were fabricated by condensation of metal vapor on cold or heated mica substrates. During deposition, a pressure of 10^{-6} Torr was maintained in the

TABLE I. Parameters of films used in this study.

Film	Nucleus	<i>I</i>	μ_B	μ_e	n_n , %	$\omega_0/2\pi$, MHz	H_n , kOe	H_A , Oe	$DT/2\pi$ MHz-K		δQ , MHz
			(Nuclear magneton)	(Bohr magneton)					Theor.	Exp.	
Fe	Fe ⁵⁷	1/2	0.09	2.22	95	47	332	10	0.039	0.02	—
Fe ₂₀ Ni ₈₀	Ni ⁶¹	3/2	0.75	0.75	65	58	154	4	1.3	1	0.6
Co (fcc)	Co ⁵⁹	7/2	4.65	1.72	~50	213	211	30	15	3.5 (77 K)	0.4
										12 (300 K)	
FeCo	Co ⁵⁹	7/2	4.65	2.42	50	284	284	40	22	15	1

chamber. The rate of deposition was regulated by varying the current of the electron beam gun and in most cases was 0.5–0.6 mm/s. In order to produce uniaxial anisotropy, a magnetic field of the order of 70 Oe was applied in the plane of the substrate. The parameters of some of the films used are presented in Table I. For the temperature measurements the resonator containing the sample was placed in a helium cryostat. In order to vary the coefficient of coupling between the nuclear and electronic subsystems, a magnetic field of 0–200 Oe generated by Helmholtz coils was applied to the sample, parallel or perpendicular to the easy magnetization axis.

2. TWO-PULSE METHOD

It has been noted that the Zeeman and quadrupole interactions in our samples are strongly inhomogeneous, which makes it almost impossible to study the characteristics of the formation of multiple spin echo signals from the NMR spectra. The appreciable inhomogeneity of the anisotropy field (and thus η) also makes it very difficult to use the power characteristics. In this case, as we have already shown,¹¹ good results are obtained by studying the dependences of the echo signal amplitude on the time interval τ between the exciting pulses.¹¹

It was shown in Ref. 11 that, at high temperatures for nuclei with the spin $I > 1/2$, even echo signals (appearing at times $t = 2n\tau$, $2n \leq 2I$, where n is a natural number) decay rapidly to zero with a time constant inversely proportional to the inhomogeneity of the quadrupole interaction δQ . The values of δQ for our films determined using these relations are given in Table I. It should be noted that for all the samples, this time constant was almost independent of temperature.

As the temperature decreases, the dependence of the intensity of the even echo signals E_{2n} on τ reveals a second section where the decay time constant increases with decreasing temperature, as is observed for the usual ‘‘Hahn’’ echo. The appearance of this second section cannot be explained merely by considering multiphoton cascade transitions.¹¹ The contribution of this section increases with decreasing temperature. At relatively high temperatures, when D is much smaller than the width of the spectrum of excited nuclei $2\pi/\tau_e$ (where τ_e is the duration of the first echo), the formation of even echo signals should evidently be described by the ‘‘echo pulse’’ theory.^{2,3,10} Then, according to Ref. 3, under optimum conditions for excitation of the

second echo signal (for $\tau \gg 1/\delta Q$ and neglecting relaxation processes), the ratio of the amplitudes of the first and second echo signals is

$$E_2/E_1 = D\tau_e. \tag{2}$$

Thus, E_2/E_1 should increase as the echo pulse spectrum decreases (τ_e increases). Figure 1 gives E_2/E_1 as a function of τ_e in Fe₂₀Ni₈₀ films with Ni⁶¹ nuclei at $T = 77$ K. The experimental results are accurately described by Eq. (2) within experimental error. Similar results were achieved for FeCo (Co⁵⁹ nuclei) and Co (Co⁵⁹) films in the fcc and hcp phases (the ratio of the phases in the film was ~50/50) at $T = 77$ and 300 K and for Fe films (enriched in Fe⁵⁷) at $T = 4.2$ K (control measurements for nuclei with spin $I = 1/2$).

The experimentally determined values of the parameter D

$$D = \frac{1}{\tau_e} \frac{E_2}{E_1} \tag{3}$$

were compared with those calculated theoretically for real film parameters. The calculations were made using the relation

$$D = \omega_0 \eta \frac{\mu_n(I+1)}{3\mu_e} \frac{\hbar \omega_0}{k_B T} n_n, \tag{4}$$

where ω_0 is the NMR frequency, $\eta = H_n/H_A$, μ_n is the nuclear magnetic moment, μ_e is the magnetic moment per atom, k_B is the Boltzmann constant, and n_n is the concentration of nuclei of a particular species in the sample. The results are given in Table I.

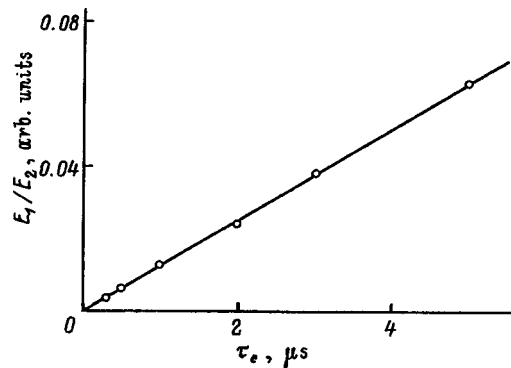


FIG. 1. Ratio of the amplitudes of the second and first echo signals versus duration of the first echo in an Fe₂₀Ni₈₀ film at $T = 77$ K.

It can be seen that, whereas good agreement between theory and experiment is observed for Fe₂₀Ni₈₀ films, for Fe and FeCo films the agreement is slightly poorer, and for Co films a substantial difference is observed between the results of the measurements at different temperatures: whereas at room temperature, the experimentally determined value of D is close to the theoretical one, at $T=77$ K these differ substantially. This is because in cobalt films, η decreases with decreasing temperature. Effects of this nature were described in Ref. 12 and were attributed to a magnetostrictive contribution (in our theoretical calculations this contribution was neglected). In our films the spin echo signal remained almost constant at temperatures between 77 and 300 K and only began to increase with decreasing temperature at liquid-nitrogen temperatures, as predicted by the theory. Thus, the theoretical estimate given in Table I is not completely accurate: for $T=77$ K the value of η should be reduced by a factor of 4 which corresponds to $DT/2\pi=5$ MHz·K (this agrees fairly well with the experiment). A Permalloy film has a nonmagnetostrictive composition and the usual Hahn echo signal increases in inverse proportion to the temperature, i.e., η does not vary. In Fe and FeCo films the gain also varies slightly with temperature, although this variation is substantially less than that in Co films.

The temperature dependence of the gain is related to the film fabrication technology.¹² We selected Co samples for which η depends negligibly on temperature and the parameter D is close to the theoretical value.

The dependence of E_2/E_1 on η was also investigated. To reduce η , a static magnetic field was applied parallel to the easy magnetization axis and, to increase η , the field was applied perpendicular to the axis, as was done in studies of NMR and FMR frequency matching.^{13,14} The ratio of the amplitudes of the second and first echo increased with increasing $\eta(D)$, as predicted by Eq. (2). Similar results were obtained for two-layer Co/FeNi films for Co⁵⁹ nuclei in which the interaction between the cobalt and Permalloy layers creates an effective anisotropy, whose magnitude depends on the thickness of the layers and decreases as the ratio of the cobalt layer thickness to the Permalloy thickness decreases.¹⁵

On the basis of this reasoning, it may be considered that the formation of even echo signals at relatively high temperatures is described fairly accurately by the echo-pulse theory.^{2,3} For Fe and Fe₂₀Ni₈₀ films this is a good approximation down to the lowest temperatures reached in our experiments (~ 2.2 K), which is completely consistent with the theory since for these films we have $D \ll \Delta\omega$. However, for Co and FeCo films, the value of D at liquid-helium temperatures becomes comparable with the inhomogeneity of the Zeeman interaction (see Table I) so that some characteristics may appear in the formation of echo signals.

Whereas at high temperature (low values of D), the maximum number of additional echo signals is observed under near-optimum conditions for the excitation of the first echo signal, for $D \sim \Delta\omega$ the maximum number is observed when the power of the exciting pulses is much lower than that needed to obtain the maximum amplitude of the usual echo.

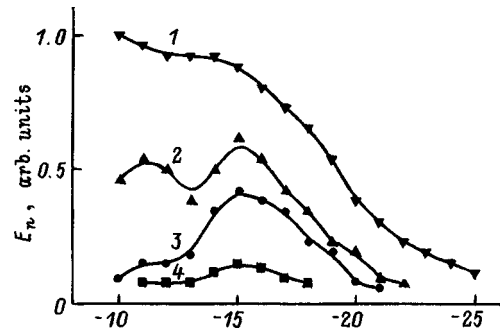


FIG. 2. Amplitude of echo signals versus power of the exciting pulses P for the first (1), fourth (2), eighth (3), and seventeenth (4) echoes in an FeCo film for the Co⁵⁹ nuclei: $T=2.2$ K, $\omega_0/2\pi=288$ MHz.

Figure 2 gives the amplitudes of several additional echo signals E_n as a function of the exciting pulse power in an FeCo film at $T=2.2$ K. The dependences of the amplitude of the echo signals (appearing at times $t=n\tau$) with small n have two peaks (at high and low power) whereas for signals with large n , only one peak is observed at low power. As n decreases, the relative magnitude of the peak increases at high powers.

To explain the reasons for this behavior, we shall again use the dependences of the echo-signal amplitude on the time interval between the exciting pulses. Figure 3 shows these curves for low exciting pulse powers. The amplitude of all the echo signals initially increases with increasing τ and then decays as usual. As the power of the exciting pulses increases, the ascending section has a “shelf,” followed by a gently sloping descending section: the curve $E_n(\tau)$ approaches exponential. The same behavior is observed with increasing temperature. Similar effects were observed in Ref. 13 in studies of relaxation processes in the NMR and FMR frequency matching region for the usual echo signal in nonmagnetostrictive FeNiCo films (according to our calculations, when an external magnetic field $H=2H_A$ is applied perpendicular to the easy magnetization axis of the film, we have $DT/2\pi \approx 10$ MHz·K).

At low pulse powers the number of echo signals may be substantially in excess of $2I$ (the number of echo signals formed as a result of multiphoton cascade transitions in these samples¹¹). For example, in FeCo films ($2I=7$) at $T=2.2$ K, more than twenty echo signals were observed, while in Co

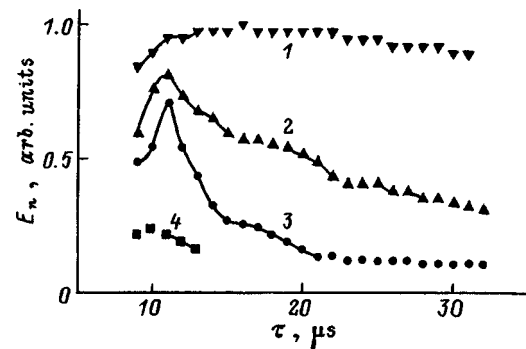


FIG. 3. Amplitude of echo signals versus time interval between exciting pulses. The notation is the same as in Fig. 2; $P=-16$ dB.

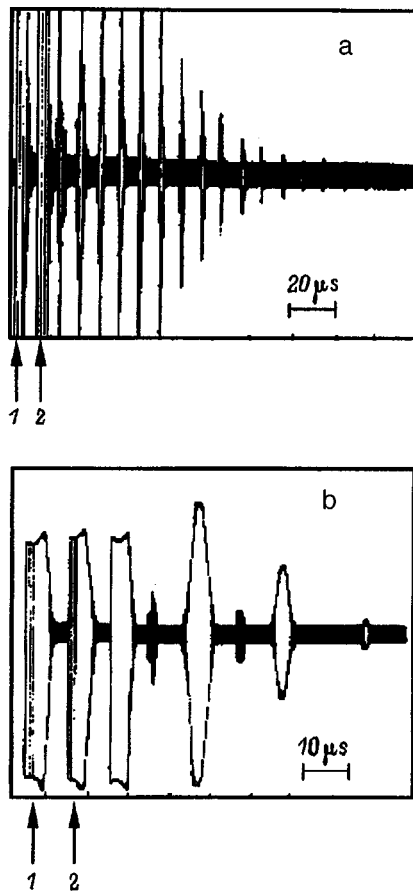


FIG. 4. Oscilloscope trace of echo signals in a cobalt film (fcc phase) for Co^{59} nuclei at low (a) and high (b) exciting pulse powers; 1 and 2 — first and second exciting pulses, respectively; $T=2.2$ K, $\omega_0/2\pi=212$ MHz, single trigger.

films with a weak dependence $\eta(T)$ up to thirty signals were observed (see also Ref. 4). In this case, the amplitudes of the echo signals depend monotonically on n . As the pulse power increases, this dependence becomes nonmonotonic and in some cases (for nuclei with $I > 1/2$ and moderate values of D), the amplitudes of the even echo signals become smaller than those of the directly following odd signals (Fig. 4).

We shall analyze these results. At low exciting pulse powers when the longitudinal component of the nuclear magnetization m_z varies little, the dynamic frequency shift has a maximum ($\omega_p \approx D$, see Eq. (1)). Since the dynamic frequency shift parameter in Co and FeCo films at liquid-helium temperatures is of the order of the width of the spectrum of excited nuclei, a strong correlation should be observed in the motion of the nuclear spins. This hypothesis is confirmed by the time and power dependences. According to Ref. 5, at high values of ω_p the amplitudes of the echo signals should initially increase with increasing τ and the number of these signals should increase with increasing D (the system becomes increasingly nonlinear). This is observed experimentally. As D increases, the power of the exciting pulses needed to form echo signals decreases, which is also fully consistent with Ref. 5. By increasing the exciting pulse power, we can increase the deviation of the nuclear magnetization from the equilibrium position, thereby reducing ω_p

(Ref. 9). This reduces the influence of the frequency modulation mechanism.⁵ Meanwhile, echo signals appear as a result of multiphoton cascade transitions, which by acting as refocusing pulses, lead to the formation of additional echo signals, and so on. This explains the appearance of a second peak on the power dependence (Fig. 2).

Thus, over a wide range of temperature, several mechanisms are involved in the formation of multiple nuclear spin-echo signals, which gives rise to complex time and power dependences. It should be noted that similar effects may also be observed in bulk samples as a result of the high rf-field gain at the nucleus in domain walls. Such experiments were carried out as part of the present study but, since they are too difficult to interpret because it is impossible to estimate the real η distribution in the samples and to make numerical calculations of the main parameters, the results are not given here.

We shall now summarize some of the main results obtained in this section. It has been demonstrated experimentally that different mechanisms influence the formation of multiple nuclear spin-echo signals in thin ferromagnetic films. At high temperatures the main contribution to their formation is made by multiphoton cascade transitions for nuclei with $I > 1/2$. As the temperature decreases, the formation of echo signals by the refocusing action of the echo pulses begins to play an important role. Finally at low temperatures, the frequency modulation mechanism comes into play. It was shown that this mechanism must be taken into account at liquid-helium temperatures when NMR experiments are carried out using nuclei with a large magnetic moment in weakly anisotropic thin ferromagnetic films. This has hardly ever been done before.

3. THREE-PULSE EXCITATION. NONSTANDARD PULSE CONFIGURATION

Particular attention will be paid in this section to the formation of multiple nuclear spin echo signals in a non-standard time configuration of exciting pulses with $\tau_{12} \gg \tau_{23}$, where τ_{12} and τ_{23} are the time intervals between the first and second, and between the second and third exciting pulses, respectively. Of particular interest are the echo signals formed directly ahead of the stimulated echo which appears at the time $t = \tau_{12}$ after the third exciting pulse. As we showed in Ref. 16, these signals are formed as a result of multiphoton transitions with a reduction in the eigenvalues of the nuclear spin operator I_z . In addition, various characteristic features are observed in the formation of these echo signals.

The formation of multiple echo signals directly ahead of the stimulated echo cannot be attributed to any combinations of radio pulses and echo signals, i.e., the echo pulse mechanism cannot be responsible for their formation. For the same reason, these additional echo signals cannot be obtained at nuclei with spin $I = 1/2$. If the nuclear spin is $I > 1/2$, these signals may appear, as was shown in Ref. 16. In principle, these echo signals, acting as refocusing pulses, may influence the formation of the following echo signals. However, it is easy to show that, for signals appearing at times $t = \tau_{12}$

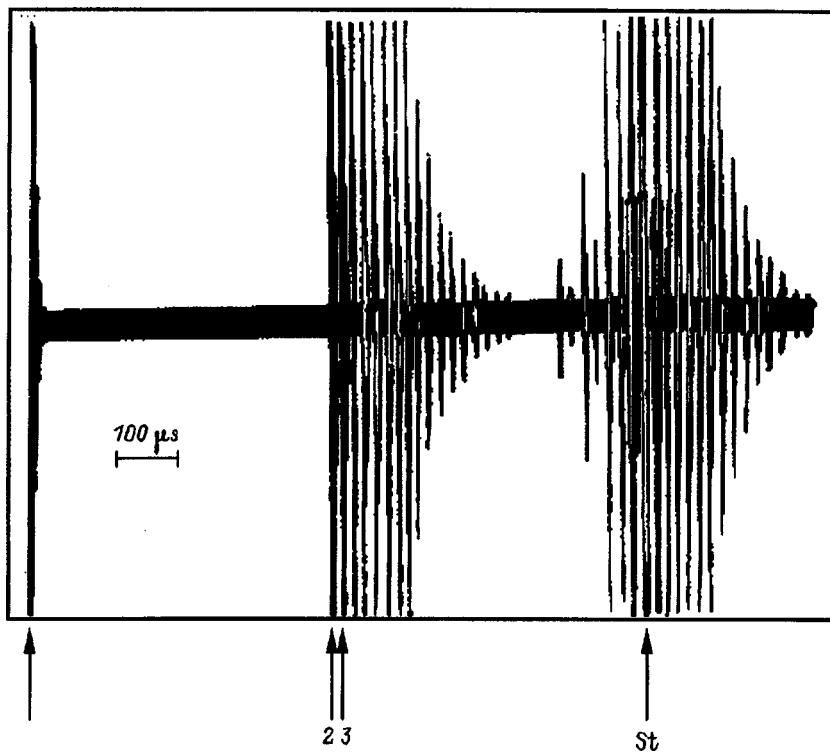


FIG. 5. Oscilloscope trace of echo signals in FeCo film for Co^{59} nuclei with a nonstandard time configuration of exciting pulses: 1–3 — first, second, and third exciting pulses, respectively, St — stimulated echo, $T=2.2$ K, $\omega_0/2\pi=288$ MHz, single trigger.

$-n\tau_{23}$, this influence is small (although noticeable).

The formation of these signals cannot be explained using the frequency modulation mechanism. This can be easily demonstrated experimentally. Films of FeCo were cooled to $T=2.2$ K. A static magnetic field $H \approx H_A$ was applied perpendicular to the easy magnetization axis to increase the rf field gain at the nucleus (and thus, the dynamic frequency shift). The number of echo signals directly preceding the stimulated echo never exceeded $2I=7$ (Co^{59} nucleus) whereas up to fifteen echo signals were observed after the stimulated echo (Fig. 5). Both the power and time dependences showed that the main mechanism for the formation of all the echo signals, apart from those directly preceding the stimulated echo, was the frequency modulation mechanism.⁵ However, as before, the echo signals formed directly ahead of the stimulated echo were only formed as a result of multiphoton transitions. For $\tau_{23} \gg 1/\delta Q$ the amplitude of the signals observed at time $t = \tau_{12} - 2n\tau_{23}$ was smaller than those observed at times $t = \tau_{12} - (2n+1)\tau_{23}$ (gaps in the series). For all the other signals no gaps were observed in this case.

Thus, this study is an experimental attempt to classify the contributions made by the various mechanisms for the excitation of nuclear spin echo in magnetics with strongly inhomogeneous Zeeman and quadrupole interactions according to the temperature, time, and power dependences of the echo signal amplitude under two-pulse and three-pulse excitation (including the nonstandard configuration of exciting pulses proposed by us earlier¹⁶). We reiterate some of the main results.

The temperature-independent decay of the amplitude of even echo signals under two-pulse and three-pulse excitation is determined by the inhomogeneity of the quadrupole interaction. The appearance of residual echo signals when the

interval between the exciting pulses is much greater than $1/\delta Q$ is caused by the interaction of nuclear spins via the electronic subsystem. By using the echo-pulse formalism, we determined the dynamic frequency shift parameter fairly accurately in different samples (see the agreement between the calculated and experimental data given in Table I). The disagreement between some of the calculated and experimental values can be attributed to the difficulty of making accurate calculations of the rf-field gain at the nucleus.

It has been shown experimentally for the first time that in ferromagnetic substances with a high rf field gain at the nucleus, the formation of spin echo signals from nuclei with a large magnetic moment is strongly influenced by frequency modulation, even at liquid-helium temperatures⁵ (i.e., the dynamic frequency shift parameter becomes comparable to the NMR line width). An exception are the multiple echo signals observed directly preceding the stimulated echo using a nonstandard time configuration of exciting pulses, whose formation is attributed to multiphoton transitions, even when the frequency modulation mechanism makes the main contribution to the formation of the other echo signals.⁵

¹ I. Solomon, Phys. Rev. **110**, 61 (1950).

² C. W. Searle, J. Davis, A. Hirai, and K. Fukuda, Phys. Rev. Lett. **27**, 1380 (1971).

³ M. P. Petrov, V. V. Moskalev, and G. A. Smolenskii, Pis'ma Zh. Éksp. Teor. Fiz. **15**(3), 32 (1972) [sic].

⁴ A. N. Pogorelyi and V. V. Kotov, Fiz. Tverd. Tela (Leningrad) **22**, 1013 (1980) [Sov. Phys. Solid State **22**, 591 (1980)].

⁵ A. S. Borovik-Romanov, Yu. M. Bun'kov, B. S. Dumes, M. I. Kurkin, M. P. Petrov, and V. P. Chekmarev, Usp. Fiz. Nauk **142**, 537 (1984) [Sov. Phys. Usp. **27**, 235 (1984)].

⁶ H. Abe, H. Yasuoka, and A. Hirai, J. Phys. Soc. Jpn. **21**, 77 (1966).

⁷ G. N. Abelyashev, V. N. Berzhanskiĭ, N. A. Sergeev, and Yu. V. Fedotov, Zh. Eksp. Teor. Fiz. **94**(1), 227 (1988) [Sov. Phys. JETP **67**, 127 (1988)].

- ⁸ V. I. Tsifrinovich, Zh. Éksp. Teor. Fiz. **94**(7), 208 (1988) [Sov. Phys. JETP **67**, 1413 (1988)].
- ⁹ P. G. de Gennes, P. A. Pincus, F. Hartmann-Boutron, and J. M. Winter, Phys. Rev. **129**, 1105 (1963).
- ¹⁰ V. I. Tsifrinovich, Fiz. Met. Metalloved. **2**, 16 (1990).
- ¹¹ V. O. Golub, V. V. Kotov, A. N. Pogorelyĭ, and Yu. A. Pod'elets, Fiz. Tverd. Tela (Leningrad) **31**, 48 (1989) [Sov. Phys. Solid State **31**, 1864 (1989)].
- ¹² A. N. Pogorelyĭ, N. A. Lesnik, and N. A. Belous, Fiz. Tverd. Tela (Leningrad) **15**, 345 (1973) [Sov. Phys. Solid State **15**, 255 (1973)].
- ¹³ A. N. Pogorelyĭ and V. V. Kotov, Pis'ma Zh. Éksp. Teor. Fiz. **21**, 472 (1971) [sic].
- ¹⁴ V. K. Mal'tsev, A. E. Reĭngardt, and V. I. Tsifrinovich, Fiz. Tverd. Tela (Leningrad) **24**, 3 (1982) [Sov. Phys. Solid State **24**, 1 (1982)].
- ¹⁵ N. A. Lesnik and V. O. Golub, Metallofizika **14**, 9, 85 (1992).
- ¹⁶ V. V. Kotov, Yu. A. Pod'elets, V. I. Chernetskii, and V. O. Golub, Fiz. Tverd. Tela (Leningrad) **32**, 1108 (1990) [Sov. Phys. Solid State **32**, 650 (1990)].

Translated by R. M. Durham

Magnetic properties of solidified ferrocolloids

A. F. Pshenichnikov and V. V. Mekhonoshin

Institute of Continuum Mechanics, Urals Branch of the Russian Academy of Sciences, 614013 Perm, Russia
(Submitted October 7, 1997; resubmitted December 18, 1997)

Fiz. Tverd. Tela (St. Petersburg) **40**, 1062–1067 (June 1998)

Experimental and theoretical investigations are made of the magnetization of solidified dielectric colloids prepared using single-domain magnetite particles with randomly oriented axes of easy magnetization. A method is proposed to calculate the magnetization curves with allowance for blocking of the magnetic moments of particles and magnetic-dipole interparticle interactions. It is shown that magnetic colloids with an extremely low remanent magnetization (a few tens of amps per meter) may be obtained. © 1998 American Institute of Physics.

[S1063-7834(98)02206-0]

The magnetic properties of ensembles of single-domain particles distributed in a solid matrix have been studied experimentally and theoretically by many authors.^{1–5} The theoretical model used in Refs. 1 and 2 is based on dividing all the colloid particles into two groups (superparamagnetic and “magnetically hard” particles) depending on the Néel relaxation time τ_N . By fitting the particle size distribution parameters and the effective anisotropy constant, the authors^{1,2} succeeded in obtaining a good description of the experimental magnetization curves for cobalt and magnetite colloids at low temperatures but the assumptions made were not justified. Here we present new results of an experimental investigation of solidified magnetite colloids. The experimental data were analyzed using the theoretical model from Refs. 1 and 2 into which we introduced significant refinements and corrections, mainly resulting from the need to allow for interparticle magnetic-dipole interactions and the magnetic anisotropy of superparamagnetic particles.

1. EXPERIMENTAL DETAILS AND MAGNETIZATION CURVES

The samples were prepared using colloidal magnetite obtained by a standard chemical deposition technique. The entire volume of the magnetite was divided into several parts, each being used to prepare a single sample. This ensured that all the samples had the same disperse composition and only differed in terms of the magnetic phase concentration and the base (particle carrier). The carriers were undecane (in this case, an ordinary magnetic liquid was obtained), 3-phenyl-methane (melting point 364 K), and epoxy resin. Oleic acid was used as the stabilizer. The undecane-based magnetic liquid functioned as a standard against which the solidified ferrocolloids were compared to assess the role of the rotational degrees of freedom of the particles. All the samples were solidified in the absence of any external magnetic field so that the easy magnetization axes were randomly oriented.

The magnetization curves of the samples were measured with a permeameter at a frequency of 0.04 Hz in fields up to 500 kA/m using a technique described in Ref. 6. The satura-

tion magnetization was determined by a standard method, by extrapolating the experimental curve $M(1/H)$ to the ordinate. Since the solidified colloid contains particles with a “blocked” magnetic moment, they have a nonzero remanent magnetization M_r , whose magnitude, however, is small compared with the saturation magnetization. This means that the remanent magnetization cannot be determined directly from the magnetization curve. Thus, this remanent magnetization was measured with a F191 microweber meter in additional experiments. In this case, the measuring coil was placed inside a long solenoid oriented along the field lines of the Earth’s magnetic field, which was compensated by the solenoid field. The particle size distribution was determined by means of a magnetogranulometric analysis of the magnetic liquid.⁷ The mean diameter of the particle magnetic nucleus $\langle x \rangle = 8.1$ nm and the relative width of the particle size distribution $\Delta = 0.37$ were typical of magnetite colloids.

A total of thirteen samples of solidified colloids were investigated with saturation magnetizations between 15 and 99 kA/m and initial susceptibilities between 0.7 and 8.4 units. In all cases, the remanent magnetization of the colloids did not exceed 0.07% of the saturation magnetization. By way of example, Fig. 1 presents the magnetization curve of a concentrated epoxy-resin-based ferrocolloid. The curve appears to be hysteresis-free although this is only so because the selected scale of the image and the very low remanent magnetization which is simply not resolved in Fig. 1. The finite width of the hysteresis loop only becomes clearly visible when the scale is enlarged several thousand-fold, as in the inset showing the initial section of the magnetization curve.

Figure 2 shows the relative difference between the reduced magnetizations of a magnetic liquid (I_l) and a solidified ferrocolloid (I_s) with saturation magnetizations of 67 and 61 kA/m, respectively. The reduced magnetization is taken to be that relative to the saturation magnetization. This method of comparing the data has the obvious advantages that curves for samples with different concentrations of the magnetic phase may be shown on the same scale and small differences in the concentrations have little influence on the form of the curve. As was to be expected, the magnetization

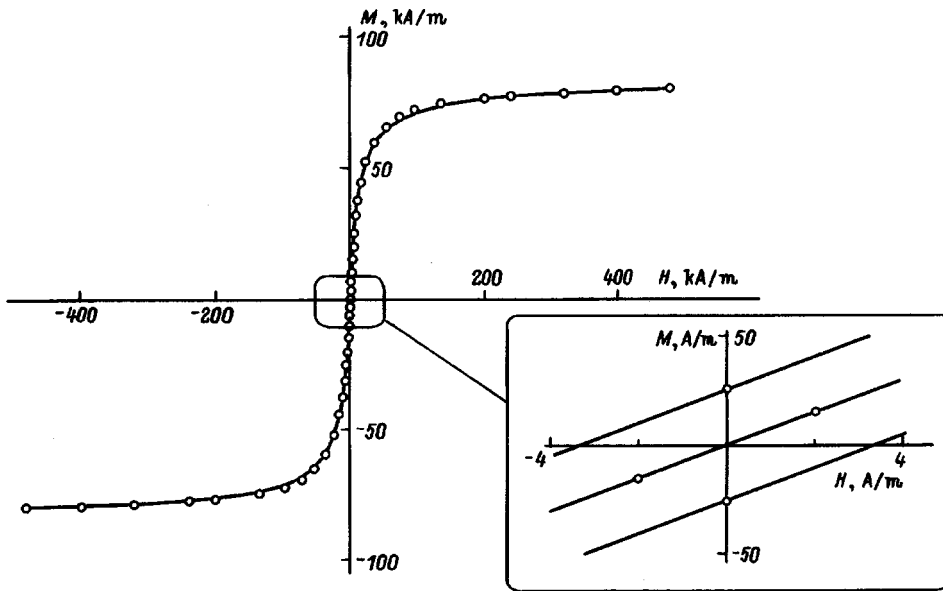


FIG. 1. Magnetization curves of a solidified ferrocolloid: circles — experimental values, curves — calculations using Eqs. (2)–(7).

of the solidified ferrocolloid is substantially lower than that of the liquid and the largest difference (up to 50%) is observed in weak fields. This difference may be explained qualitatively by the blocking of the rotational degrees of freedom of the particles. In the magnetic liquid, a substantial contribution (tens of percent) to the initial susceptibility is made by large particles with a Brownian mechanism for the relaxation of magnetization, which involves rotational diffusion of the particles in the viscous carrier liquid. As the ferrocolloid solidifies, some of the particles (for which τ_N is shorter than the measurement time) remain superparamagnetic and make the same contribution to the magnetization as before while the others are converted to a discharge of “magnetically hard” particles and do not respond to a weak external field. As the field strength increases, this effect diminishes but the magnetic anisotropy begins to influence the behavior of the superparamagnetic particles. For this reason, the magnetization of the solidified ferrocolloid still remains substantially lower than that of the liquid (other conditions being equal) and the difference only decreases to a few percent in strong fields.

2. CALCULATION MODEL

We introduced the following modifications to the theoretical model described in Refs. 1 and 2.

1) The magnetization of superparamagnetic particles was calculated with allowance for the energy of anisotropy, as in Ref. 8. The low remanent magnetization and therefore the small deviation of the system from equilibrium justify the use of equilibrium statistics (Gibbs distribution).

2) Allowance was made for the fluctuations of the magnetic moments of magnetically hard particles. The particle magnetic moment is located in a deep potential well and cannot overcome the potential barrier within the measurement time. Nevertheless, its orientation is not rigidly defined: it can undergo fluctuations near the minimum of the potential energy.

3) The effective-field approximation was used to allow for magnetic-dipole interparticle interactions.

Since shape anisotropy predominates, the total magnetic anisotropy of magnetite nanoparticles is usually assumed to be uniaxial. In this case, the energy of a particle with the volume V , which depends on the orientation of the magnetic moment, is given by⁹

$$U = -KV(\mathbf{en})^2 - \mu_0 M_S V H(\mathbf{eh}), \tag{1}$$

where \mathbf{e} , \mathbf{n} , \mathbf{h} are unit vectors in the direction of the magnetic moment, the axis of easy magnetization, and the external field \mathbf{H} , respectively, K is the effective anisotropy constant, M_S is the saturation magnetization of the particle material, and $\mu_0 = 4\pi \times 10^{-7}$ H/m. In fields $H < 2K/\mu_0 M_S = H_A$, where H_A is the effective anisotropy field, the magnetic moment has two orientations \mathbf{e}_1 and \mathbf{e}_2 corresponding to the minima of the function (1) and the orientation \mathbf{e}_3 , corresponding to the saddle point separating these minima. We

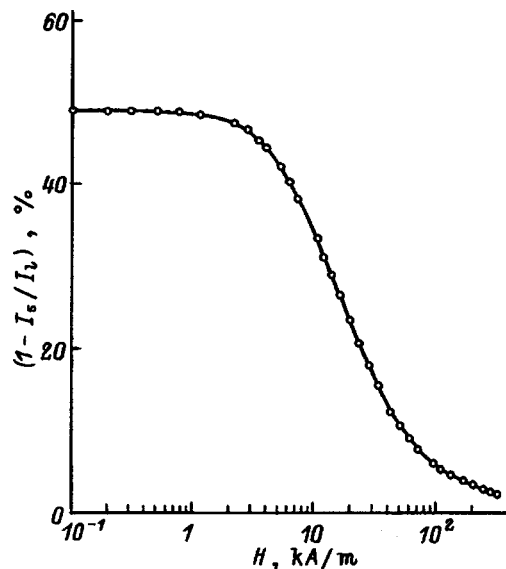


FIG. 2. Difference between the normalized magnetizations of a magnetic liquid and a solidified ferrocolloid.

shall denote by $\Delta U_2 = U(\mathbf{e}_3) - U(\mathbf{e}_2)$ the energy barrier which must be overcome by the magnetic moment for a particle to be transferred from the metastable state \mathbf{e}_2 to the energetically favorable position \mathbf{e}_1 . If $(\mathbf{e}_1 \mathbf{h}) > (\mathbf{e}_2 \mathbf{h})$, the magnetic moment must overcome an even higher barrier $\Delta U_1 = U(\mathbf{e}_3) - U(\mathbf{e}_1)$ for a return transition.

The magnetic reversal of a fixed single-domain particle is characterized by a relaxation time which in the Néel model¹⁰ is given by $\tau_N = \tau_0 \exp\{\delta U/kT\}$, where τ_0 is a characteristic time of the order of 1 ms (the Larmor precession period of the magnetic moment), k is the Boltzmann constant, and T is the temperature. Equating the magnetization measurement time τ to the Néel relaxation time, we obtain the following approximate criterion to find the maximum barrier height to be overcome by the particle magnetic moment: $\Delta U^*/kT = \ln(\tau/\tau_0)$.

For convenience in the following calculations, all the colloid particles are divided into three groups according to the size of the magnetic nucleus.

1) Superparamagnetic particles — particles for which $\Delta U_1 < kT \ln(\tau/\tau_0)$ and the distribution of magnetic moments over different orientations can be considered to be equilibrium. The condition $\Delta U_1 = kT \ln(\tau/\tau_0)$, solved for the particle size, determines the critical particle diameter d_1 from which the particle ceases to be superparamagnetic.

2) Magnetically hard particles in the lowest-energy state \mathbf{e}_1 , satisfying the condition $\Delta U_2 < kT \ln(\tau/\tau_0) < \Delta U_1$. For these particles the potential barrier ΔU_2 is below the critical value, the particles cannot be confined for long in the local minimum \mathbf{e}_2 , and are transferred to the principal minimum \mathbf{e}_1 . They cannot be transferred back to \mathbf{e}_2 since the time taken for this transition is greater than the measurement time. The condition $\Delta U_2 = kT \ln(\tau/\tau_0)$, solved for the particle size, determines the second critical diameter d_2 from which the particle may be blocked in the metastable state \mathbf{e}_2 .

3) Magnetically hard particles with maximum anisotropy energies situated either in the principal (\mathbf{e}_1) or local (\mathbf{e}_2) minima. The magnetic moments of these particles cannot overcome the energy barrier separating positions \mathbf{e}_2 and \mathbf{e}_1 , in either direction. For these particles we have $\Delta U_2 > kT \ln(\tau/\tau_0)$.

The particle classification used means that the Gibbs distribution can be applied separately to each group. In this case, the nonequilibrium of the system as a whole is only observed in particle transitions between groups and potential minima. Since the potential barriers ΔU_1 and ΔU_2 depend on the external field, the fractions of particles in a particular group are not constant and vary with the field strength. The classification of the particles into groups is clearly arbitrary, and the boundaries between the groups are blurred because of the indeterminacy of the magnetization measurement time τ and the approximate nature of the superparamagnetism condition $\tau_N < \tau$. However, the blurring of the boundaries is small and the critical diameters are determined fairly reliably because of the logarithmically weak dependence of the height of the appropriate potential barriers on τ . It can also be shown that additional difficulties with calculations of the magnetization should arise in weak fields when $\Delta U_1 \approx \Delta U_2$ and the second group cannot be accurately identified. In

practice, no significant problems arise since, as the external field decreases, the number of particles in the second group and thus, their contribution to the magnetization of the system, rapidly tend to zero. In this case, the presence or absence of the second group does not influence the magnetization. For this reason, the formal classification of the particles into three groups was retained in weak fields but only so that the calculation algorithm was not made more complex.

The contribution of superparamagnetic particles with fixed-direction easy axes to the magnetization of a ferrocolloid may be expressed in the form⁶

$$M_1(\mathbf{n}, \mathbf{H}) = \frac{ckT}{\mu_0} \int_0^{d_1} f(x) \frac{\partial}{\partial H} \ln Z(\mathbf{n}, \mathbf{H}) dx,$$

$$Z(\mathbf{n}, \mathbf{H}) = \int \exp\{\xi(\mathbf{e}\mathbf{h}) + \sigma(\mathbf{e}\mathbf{n})^2\} d\mathbf{e}, \quad (2)$$

where c is the particle number density, Z is the configurational partition function, $\sigma = KV/kT$, $\xi = \mu_0 m(x)H/kT$ is the Langevin parameter, $m(x) = M_s \pi x^3/6$ is the particle magnetic moment, x is the diameter of a sphere the same size as the particle, and $f(x)$ is the particle size distribution function. A two-parameter Γ distribution which accurately approximates the disperse composition of the magnetite particles⁸ is then used as $f(x)$

$$f(x) = \frac{x^s \exp(-x/x_0)}{x_0^{s+1} \Gamma(s+1)}, \quad (3)$$

where s and x_0 are the distribution parameters.

The contribution to the magnetization M_2 from the second group of particles may be obtained as in the previous case, except that the vicinity of the vector \mathbf{e}_1 is used as the region of integration to calculate the partition function. Thermal fluctuations of the magnetic moments of particles in the principal potential minimum are then automatically taken into account. The third group of particles can be either in state \mathbf{e}_1 or in state \mathbf{e}_2 but the populations of these states will differ and will depend on the prehistory of the sample. In particular, as we move along the upper curve of the hysteresis loop, the relative fractions of particles in the groups are $p_1 = 1, p_2 = 0$. The magnetization M_3 of the third group is a linear combination of the contributions of particles blocked in these two states. We obtain the total magnetization of the system by summing the contributions of all the fractions and averaging the result over the orientations of the easy axes, assuming that these are distributed isotropically

$$M_0(\mathbf{H}) = \frac{1}{4\pi} \int (M_1(\mathbf{n}, \mathbf{H}) + M_2(\mathbf{n}, \mathbf{H}) + M_3(\mathbf{n}, \mathbf{H})) d\mathbf{n}. \quad (4)$$

In weak fields, the magnetization depends linearly on the field strength so that the initial susceptibility $\partial M/\partial H$, according to Eq. (4), will be given by

$$\chi_0 = \frac{\mu_0 c}{3kT} \int_0^{d_2} m^2(x) f(x) dx + \left. \frac{\partial M_3}{\partial H} \right|_{H=0}. \quad (5)$$

It is known that the equilibrium magnetization of magnetic liquids is strongly influenced by magnetic dipole interparticle interactions. In concentrated solutions allowance for these interactions doubles or trebles the initial susceptibility.^{7,8,11} Solidified magnetite colloids are only slightly nonequilibrium: in our experiments the contribution to the magnetization of particles with blocked moments does not exceed 1% (see, for example, Fig. 1). Thus, theoretical models developed for magnetic liquids which can quite satisfactorily describe the effects associated with magnetic-dipole interactions, can naturally be applied to these colloids.^{7,8,12} We subsequently use a modified median-field variant⁸ which is convenient for the calculations and gives a high accuracy. In this approximation, the magnetic-dipole interactions between particles distributed in a solid matrix are taken into account by replacing the field strength in Eq. (4) by its effective value

$$H_e = H + M_0/3, \quad (6)$$

where M_0 is the magnetization in the single-particle approximation determined from Eq. (4). Formally speaking, expression (6) used by us for the effective field is merely an expansion of H_e as a power series of the concentration constrained to a linear dependence: M_0 is strictly proportional to the particle number density. In this respect, it differs qualitatively from the effective Weiss field for which the correction to the external field is proportional to the magnetization M and increases with concentration more rapidly than linearly. The application of the Weiss model to magnetic liquids would inevitably result in spontaneous "ferromagnetic" ordering of the magnetic moments of all the particles. Although such predictions were made in various studies, known experimental data unambiguously indicate that this ordering does not occur in large (compared with the particle size) volumes. In the effective-field approximation we have

$$M(\mathbf{H}) = \frac{1}{4\pi} \int (M_1(\mathbf{n}, \mathbf{H}_e) + M_2(\mathbf{n}, \mathbf{H}_e) + M_3(\mathbf{n}, \mathbf{H}_e)) d\mathbf{n}, \quad (7)$$

and in the weak-field limit ($\xi \rightarrow 0$)

$$\chi = \chi_0(1 + \chi_0/3), \quad (8)$$

where χ_0 is the susceptibility in the single-particle approximation calculated using Eq. (5). It can be seen from Eq. (8) that χ_0 may be considered to be a dimensionless parameter which determines the degree of influence of magnetic-dipole interparticle interactions on the magnetization of ferrocolloids in a weak field. This influence is small for $\chi_0 \ll 1$ and doubles the magnetization for $\chi_0 = 3$.

3. RESULTS OF CALCULATIONS AND COMPARISON WITH EXPERIMENT

We calculated the magnetization of solidified ferrocolloids using Eqs. (2)–(7) for the particle size distribution parameters determined in experiments using a magnetic liquid for $\tau = 100$ s at room temperature 293 K. The other parameters were varied to assess the role of different factors in the

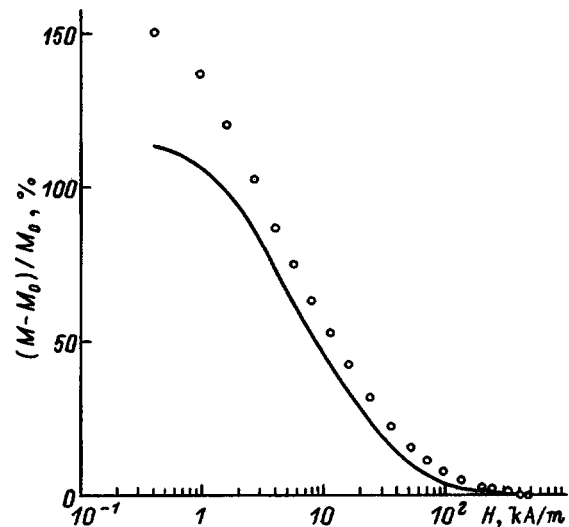


FIG. 3. Influence of magnetic-dipole interparticle interactions on the magnetization of a solidified ferrocolloid. Solid curve — calculations using Eqs. (2)–(7), circles — experimental values.

formation of the magnetic properties of ferrocolloids. The only fitting parameter was the effective anisotropy constant which was determined from the condition that the calculated remanent magnetization agrees with that measured experimentally. Since the disperse composition of the particles in the samples was the same, the spread of magnetic anisotropy constants was small. The value of K was varied between 14.3 and 16.6 kJ/m³. The existence of magnetic anisotropy and the loss of rotational degrees of freedom by superparamagnetic particles reduces their contribution to the magnetization of the solid colloid compared with Langevin theory. The relative decrease in magnetization is around 10–16% and reaches a maximum in fields of approximately the same order of magnitude as the anisotropy field.

Allowance for the thermal fluctuations of blocked magnetic moments yields corrections of around 1–2%, which can be neglected without appreciable detriment. This implies that the directions of the blocked magnetic moments can be accurately assumed to be the same as the directions corresponding to the potential energy minima. The role of the blocking itself (i.e., the departure of the system from equilibrium) is already significant. In weak fields the corresponding reduction in magnetization is 10–40%. In moderate fields the blocking effect and the influence of anisotropy on the behavior of superparamagnetic particles are added and give a total reduction in the magnetization of a solidified ferrocolloid compared with the liquid, shown in Fig. 2.

The influence of interparticle interactions on the magnetization of a ferrocolloid ($M_\infty = 83$ kA/m) is shown in Fig. 3, where M_0 is the magnetization in the single-particle approximation. This influence is measured quantitatively as the relative increase in magnetization when interparticle interactions are "switched on." Since in real experiments the interparticle interactions cannot be "switched off," the magnetization M_0 was calculated from the concentration of the magnetic phase in the sample as a quantity strictly proportional to this concentration. The coefficient of proportionality,

which depends on the field strength, was determined from the results of measurements for a weakly concentrated colloid, i.e., for the weakest influence of interparticle interactions on the magnetization. It may be assumed that the calculated results agree satisfactorily with the experimental data and indicate that the effective field model (6) can be applied to solidified ferrocolloids. It can be seen that in weak fields and concentrated colloids the influence of these interparticle interactions approximately doubles the magnetization. Although this effect is slightly weaker in solidified colloids compared with magnetic liquids, it is still fairly strong and clearly cannot be disregarded.

One of the consequences of interparticle interactions is a nonlinear dependence of the susceptibility on the concentration of the magnetic phase. Since the single-particle susceptibility χ_0 is proportional to the particle number density, in the selected theoretical model the concentration dependence of the initial susceptibility should be described by a parabola (8). A comparison between Eq. (8) and the experimental data for different samples revealed good agreement, provided that the coefficient of proportionality between the volume fraction of the magnetic phase and the single-particle susceptibility χ_0 is determined using data for the ferrocolloid having the lowest concentration.

In summation, we have made experimental and theoretical investigations of dielectric ferrocolloids with single-domain magnetite particles distributed in a solid matrix. These systems typically exhibit randomly oriented axes of easy magnetization and a broad particle-size distribution with an average magnetic-nucleus diameter of 7–9 nm. Particular attention was focused on the various factors strongly influencing the properties of the system. A theoretical model was proposed to describe the properties of a system of single-domain particles with allowance for these factors and a comparison was made with the experimental data.

It was found that interparticle magnetic-dipole interactions have the strongest influence on the magnetization of the system. These interactions approximately double the initial susceptibility and their influence on the superparamagnetic particle fraction may be described quite accurately using a

modified effective-field model with simultaneous renormalization of the effective-anisotropy constant. Magnetic anisotropy of the coarsely dispersed particle fraction is observed in weak fields as a result of the blocking of magnetic moments in the local potential minimum. This blocking leads to very slight hysteresis and reduces the magnetization by several tens of percent compared with the equilibrium value. The remanent magnetization of concentrated ferrocolloids is a few tens of amperes per meter and is three orders of magnitude lower than that in strong fields. Magnetic anisotropy of the finely dispersed fraction is observed in moderate fields comparable with the anisotropy field and reduces the magnetization by approximately 10–20% compared with the Langevin value. The thermal fluctuations of the blocked magnetic moments negligibly influence the magnetization of the system.

The authors would like to thank K. I. Morozov and V. I. Stepanov for discussions of the results and useful comments.

This work was supported financially by the Russian Fund for Fundamental Research (Project No. 97-03-32119).

¹R. W. Chantrell, J. Popplewell, and S. W. Charles, *J. Magn. Magn. Mater.* **15–18**, 1123 (1980).

²A. Tari, J. Popplewell, and S. W. Charles, *J. Magn. Magn. Mater.* **15–18**, 1125 (1980).

³K. O'Grady and R. W. Chantrell, in *Studies of Magnetic Properties of Fine Particles and their Relevance to Materials Science* (Elsevier, Amsterdam, 1992), p. 93.

⁴M. Hanson, V. Johansson, M. S. Pedersen, and S. Mørup, *J. Phys.: Condens. Matter* **7**, 9269 (1995).

⁵J. L. Dormann, in *Studies of Magnetic Properties of Fine Particles and their Relevance to Materials Science* (Elsevier, Amsterdam, 1992), p. 115.

⁶A. F. Pshenichnikov, A. V. Lebedev, and K. I. Morozov, *Magn. Gidrodin.* **1**, 37 (1987).

⁷A. F. Pshenichnikov, V. V. Mekhonoshin, and A. V. Lebedev, *J. Magn. Magn. Mater.* **161**, 94 (1996).

⁸Yu. L. Raïkher, *Dokl. Akad. Nauk SSSR* **279**, 354 (1984) [*Sov. Phys. Dokl.* **29**, 944 (1984)].

⁹M. I. Shliomis, *Usp. Fiz. Nauk* **112**, 427 (1974) [*Sov. Phys. Usp.* **17**, 153 (1974)].

¹⁰L. Néel, *Ann. Geophys.* **5**, 99 (1949).

¹¹A. F. Pshenichnikov, *J. Magn. Magn. Mater.* **145**, 319 (1995).

¹²K. I. Morozov, *Izv. Akad. Nauk SSSR, Ser. Fiz.* **51**, 1073 (1987).

Translated by R. M. Durham

Suppression of the domain structure in uniaxial ferromagnetic films with a superconducting coating

Yu. I. Bespyatykh, V. Vasilevskii*, É. G. Lökk, and V. D. Kharitonov

Institute of Radio Engineering and Electronics, Russian Academy of Sciences, 141120 Fryazino, Moscow Province, Russia

(Submitted December 23, 1997)

Fiz. Tverd. Tela (St. Petersburg) **40**, 1068–1074 (June 1998)

Specific models of domain walls are used to investigate conditions for the single-domain state and quasi-single-domain states in structures with magnetic materials having a quality factor higher than one. It is shown that the critical thickness of the magnetic film in a tangentially magnetized system decreases monotonically as the magnetizing field increases from zero to the transition from the collinear to the homogeneous angular phase and then increases monotonically with increasing external field. In a thin isolated magnetic film, the size of the domains increases exponentially with decreasing thickness. This dependence is logarithmic near the transition to the single-domain state for a film coated on two sides and obeys a power law for a film coated on one side. The establishment of a single-domain state and characteristic features in the asymptotic behavior of the domain structure in magnetic films with and without coatings can be attributed to differences in the asymptotic behavior of the field of a single domain wall. © 1998 American Institute of Physics. [S1063-7834(98)02306-5]

1. It is known that ferrites in weak static magnetic fields are in an inhomogeneous magnetic state.¹ Exceptions to this are small particles and quasi-one-dimensional samples (so-called “whiskers”) which are single-domain for any homogeneous external magnetic field.² The existence of a domain structure in a magnetic substance is frequently a harmful factor. For example, the existence of domains leads to noise accompanying magnetic reversal and causes increased damping of spin waves as a result of their scattering by domain walls. The suppression of domains in fairly large magnetic samples can be used to improve a row of devices which use ferrites.

The present paper analyzes the conditions for the establishment of a single-domain state in uniaxial ferromagnetic films coated either on one or on two sides with a type-II superconductor, assuming that the coupling between the magnetic subsystem and the conduction electrons of the superconductor is electromagnetic.

2. We shall examine the conditions for the suppression of magnetic domains in two types of layered systems: a) a symmetric system and b) an asymmetric system. The symmetric system is a thin uniaxial ferromagnetic film coated on two sides with a thick superconducting layer and the asymmetric system is a thin ferromagnetic film on a thick superconducting substrate. We shall subsequently consider systems with superconductors characterized by a large Ginzburg–Landau parameter $\kappa = \lambda/\xi \gg 1$ (λ is the London depth of penetration of the magnetic field and ξ is the correlation radius). We shall also assume that the Abrikosov vortices in the superconductor are securely anchored at pinning centers and their displacements make a small contribution to the magnetic susceptibility. The magnetic film possesses magnetic anisotropy of the “easy axis” type with the constant $\beta = 4\pi Q > 0$, where Q is the quality factor of the ma-

terial. The anisotropy axis \mathbf{n}_a is perpendicular to the developed surface of the film. The system is located in a tangential external magnetic field \mathbf{H}_e , where $H_e \ll H_{c2}$ (H_{c2} is the upper critical field for the superconductor). The geometry of the symmetric and asymmetric systems is shown in Figs. 1a and 1b, respectively.

The ground state of the system in a given external magnetic field \mathbf{H}_e corresponds to the minimum of the Gibbs potential G

$$G = \int_{V_f} dv \left\{ -\mathbf{H}_e \mathbf{M} - \frac{1}{2} \mathbf{H}_D \mathbf{M} - 2\pi Q M_y^2 + \frac{\alpha}{2} (\nabla \mathbf{M})^2 \right\}, \quad (1)$$

where \mathbf{M} is the magnetization, \mathbf{H}_D is the dipole magnetic field, α is the inhomogeneous exchange constant of the ferromagnetic, and integration is performed over the volume of the magnetic film V_f . Expression (1) has the same form as the Gibbs potential of an insulated uniaxial ferromagnetic film, although the dipole field in Eq. (1) also includes the field generated by the magnetic moments of the ferromagnetic and the field of the screening Meissner currents in the superconductor.

The magnetic field \mathbf{H} in the superconductor is described by the London equation

$$\mathbf{H} + \lambda^2 \text{curl curl } \mathbf{H} = 0, \quad (2)$$

and the scalar potential Ψ of the dipole field $\mathbf{H}_D = \mathbf{H} - \mathbf{H}_e = \text{grad} \Psi$ is described by the Laplace equation in vacuum

$$\nabla^2 \Psi = 0, \quad (3)$$

and by the Poisson equation in the ferromagnetic film

$$\nabla^2 \Psi = -4\pi \text{div } \mathbf{M}. \quad (4)$$

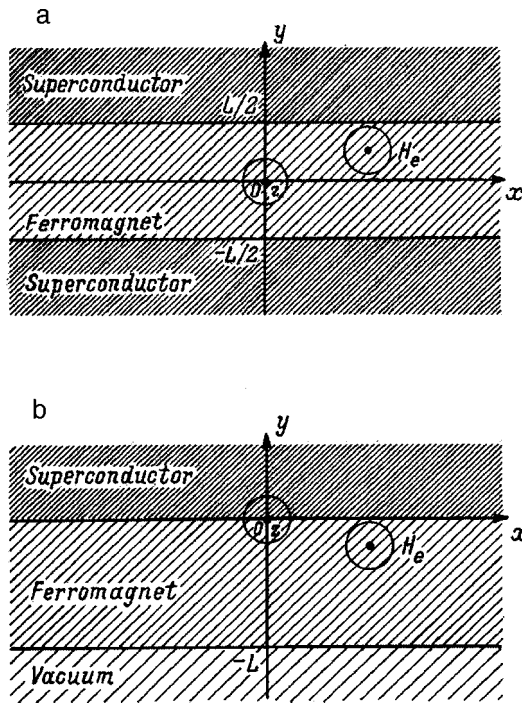


FIG. 1. Ferromagnetic film with superconducting coating on two sides (a) and on one side (b).

Equations (2)–(4) together with the conditions for continuity of the tangential components of the magnetic field \mathbf{H} and the normal component of the magnetic induction $\mathbf{B} = \mathbf{H} + 4\pi\mathbf{M}$ at the interfaces between the media can be used to calculate the magnetic field and the induction in the system if the distribution of the magnetization in the ferromagnetic film is known.

Since the system is homogeneous along the coordinates x and z , it is convenient to convert to the Fourier transforms of the magnetization \mathbf{M} and the field \mathbf{H} using the relations

$$\mathbf{M}(\mathbf{r}) = \int \frac{d\mathbf{k}}{4\pi^2} \mathbf{M}_{\mathbf{k}}(y) e^{i\mathbf{k}\mathbf{r}}, \quad \mathbf{M}_{\mathbf{k}}(y) = \int d\mathbf{r} \mathbf{M}(\mathbf{r}) e^{-i\mathbf{k}\mathbf{r}}. \tag{5}$$

We also introduce the dimensionless quantities $g = [4\pi M_0^2 (\alpha/4\pi)^{3/2}]^{-1} G$, $\mathbf{m} = \mathbf{M}/M_0$, $m_x = \sin\theta \cos\phi$, $m_y = \sin\theta \sin\phi$, $m_z = \cos\theta$, $\mathbf{h} = \mathbf{H}_e / (4\pi M_0)$, $\mathbf{h} = \mathbf{h}_\perp \mathbf{n}_y + \mathbf{h}_\parallel$, $(\mathbf{h}_\perp \mathbf{n}_y) = 0$, $\mathbf{h}_D = \mathbf{H}_D / (4\pi M_0)$, $\psi = (4\pi/\alpha)^{1/2} (4\pi M_0)^{-1} \Psi$, and we normalize all the spatial scales to $(\alpha/4\pi)^{1/2}$ (we keep their notation as before, so that this should not give rise to any confusion).

The Fourier transform of the normalized potential $\psi_{\mathbf{k}}$ in the magnetic for the symmetric (a) and asymmetric (b) systems is

$$\psi_{\mathbf{k}} = A \sinh ky + B \cosh ky + \frac{1}{2} \int_{-L/2}^{+L/2} dy' \left[i \frac{\mathbf{k}}{k} \mathbf{m}'_{\mathbf{k}} - m_{\mathbf{k}}^{y'} \operatorname{sgn}(y-y') \right] e^{-k|y-y'|}, \tag{6a}$$

$$A = \frac{(\tau-k)}{2(\tau \cosh kL/2 + k \sinh kL/2)} e^{-kL/2} \times \int_{-L/2}^{+L/2} dy' \left(i \frac{\mathbf{k}}{k} \mathbf{m}'_{\mathbf{k}} \sinh ky' - m_{\mathbf{k}}^{y'} \cosh ky' \right),$$

$$B = \frac{(\tau-k)}{2(\tau \sinh kL/2 + k \cosh kL/2)} e^{-kL/2} \times \int_{-L/2}^{+L/2} dy' \left(i \frac{\mathbf{k}}{k} \mathbf{m}'_{\mathbf{k}} \cosh ky' - m_{\mathbf{k}}^{y'} \sinh ky' \right),$$

$$\psi_{\mathbf{k}} = \frac{1}{2} \int_{-L/2}^{+L/2} dy' \left\{ \left[i \frac{\mathbf{k}}{k} \mathbf{m}'_{\mathbf{k}} - m_{\mathbf{k}}^{y'} \operatorname{sgn}(y-y') \right] e^{-k|y-y'|} + \frac{(\tau-k)}{\tau+k} \left(i \frac{\mathbf{k}}{k} \mathbf{m}'_{\mathbf{k}} - m_{\mathbf{k}}^{y'} \right) e^{-k(y+y')} \right\}, \tag{6b}$$

where $\mathbf{m}_{\mathbf{k}} \equiv \mathbf{m}_{\mathbf{k}}(y)$, $\mathbf{m}'_{\mathbf{k}} \equiv \mathbf{m}_{\mathbf{k}}(y')$, $\tau^2 = k^2 + \lambda^{-2}$. If in Eq. (6a) the normal component of the magnetization $m^y(y)$ is symmetric and the tangential components $m^{x,z}(y)$ are anti-symmetric functions of y , then $B=0$, otherwise $A=0$. Using the expressions for the potential of the dipole field (6), we find the Gibbs potential of system (1). We shall not give this expression here because for an asymmetric system this was given previously in Ref. 3 and for a symmetric system, it is cumbersome.

3. The ground state of insulated thin single-domain ferromagnetic films depends strongly on the quality factor Q . For magnetic materials with a quality factor $Q > 1$ in weak external fields no single-domain state is established. From a certain thickness, the equilibrium period of the domain structure increases monotonically as the thickness of the magnetic film decreases.⁴ An analysis of the single-domain state in systems containing these materials presents considerable difficulties since an essentially nonlinear problem must be solved for the range of magnetizing fields in which domain walls are formed. On the other hand, for isolated magnets with a quality factor $Q < 1$, there is a critical thickness from which the domain structure becomes energetically unfavorable and the ground state of the film will be homogeneous.⁵ In this case, the conditions for the single-domain state in isolated films as well as films with a superconducting coating can be investigated comparatively easily since this involves analyzing the spectrum of small excitations in the system.^{6,7} Here we analyze a magnet with the quality factor $Q > 1$.

As the thickness of a ferromagnet with the quality factor $Q > 1$ decreases to the critical value, the period of the domain structure becomes infinite but the thickness and structure of the domain walls vary negligibly. Thus, the condition for the existence of the single-domain state is the same as the condition that the total domain-wall energy is zero. An accurate solution of these problems involves cumbersome numerical calculations and thus models of domain walls and domain structures are generally used in conjunction with variational methods.

We shall first analyze some characteristics of the domain structure of uniaxial ferromagnetic films near the thickness L_c for the transition to the single-domain state. Since in this

case, the period of the domains is large, we shall call this state of the film quasi-single-domain. Here we merely give the results for a stripe structure: the main qualitative behavior is also conserved for grids of bubble domains.

We shall assume that the magnetization is uniform in each domain and over the thickness of the magnetic film. We shall also assume that the domain walls are parallel to the y axis, the magnetization is distributed symmetrically relative to the origin, the azimuthal angle for the direction of magnetization is $\phi \equiv \pi/2$, and the dependence of the polar angle $\theta = \theta(x)$ within the half-period of the domain structure $0 \leq x \leq D/2$ is described by the piecewise-linear function

$$\theta(x) = \begin{cases} \theta^+ & \text{for } x \leq D^+/2, \\ (\theta^- - \theta^+)x/\Delta + \theta^+ & \text{for } D^+/2 \leq x \leq D^+/2 + \Delta, \\ \theta^- & \text{for } x \geq D^+/2 + \Delta. \end{cases} \quad (7)$$

Here D^\pm and θ^\pm are the dimensions of the domains and their polar angles, respectively, and Δ is the width of the domain wall. We shall subsequently assume that θ^\pm are the same as the polar angles for the directions of magnetization in uniform angular phases, and we shall determine these using the equation

$$h_\perp \sin \theta^\pm - h_\parallel \cos \theta^\pm + \frac{\tilde{Q}}{2} \sin 2\theta^\pm = 0, \quad \tilde{Q} = Q - 1. \quad (8)$$

The values of D , D^+ , and Δ are independent parameters of the model and their values are obtained from the condition for a minimum Gibbs potential. Then, the volume-averaged local contributions to the Gibbs energy subtracting the energy of the uniform angular phase with $\theta = \tilde{\theta}^-$, have the form

$$\begin{aligned} g_Z &= [h_\parallel (\sin \theta^- - \sin \theta^+) + h_\perp (\cos \theta^- - \cos \theta^+)]Y \\ &+ \left[h_\parallel \left(\sin \theta^- + \frac{\cos \theta^- - \cos \theta^+}{\theta^- - \theta^+} \right) \right. \\ &\left. + h_\perp \left(\cos \theta^- - \frac{\sin \theta^- - \sin \theta^+}{\theta^- - \theta^+} \right) \right] Z, \\ g_a &= \frac{\tilde{Q}}{4} \left[(\cos 2\theta^- - \cos 2\theta^+)Y \right. \\ &\left. + \left(\cos 2\theta^- - \frac{\sin 2\theta^- - \sin 2\theta^+}{2(\theta^- - \theta^+)} \right) Z \right], \\ g_{ex} &= \frac{(\theta^- - \theta^+)^2 k^2}{2\pi^2} \frac{1}{Z}, \end{aligned} \quad (9)$$

where $k = 2\pi/D$, $Y = D^+/D$, $Z = 2\Delta/D$, g_Z is the Zeeman energy, g_{ex} is the exchange energy, and g_a is the anisotropy energy. The local component of the dipole energy is included in the anisotropy energy (9) by replacing the quality factor Q with \tilde{Q} . The nonlocal component of the dipole energy for the symmetric (a) and asymmetric (b) systems is given by

$$g_D = -\frac{1}{4} \sum_{n=1}^{\infty} \left[1 - \frac{2\tau_n \sinh k_n L/2}{k_n L (k_n \sinh k_n L/2 + \tau_n \cosh k_n L/2)} \right] A_n^2, \quad (10a)$$

$$\begin{aligned} g_D &= -\frac{1}{4} \sum_{n=1}^{\infty} \left\{ 1 - \frac{1}{k_n L} \left[1 - e^{-k_n L} \right. \right. \\ &\left. \left. + \frac{(\tau_n - k_n)}{2(\tau_n + k_n)} (1 - e^{-k_n L})^2 \right] \right\} A_n^2, \end{aligned} \quad (10b)$$

where $k_n = kn$, $\tau_n^2 = k_n^2 + \lambda^{-2}$, A_n are the coefficients in the Fourier series expansion of the function $\cos \theta(x)$

$$\begin{aligned} \cos \theta(x) &= A_0 + \sum_{n=1}^{\infty} A_n \cos k_n x, \\ A_0 &= \begin{cases} \cos \theta^- - (\cos \theta^- - \cos \theta^+)Y \\ - \left(\cos \theta^- - \frac{\sin \theta^- - \sin \theta^+}{\theta^- - \theta^+} \right) Z, \end{cases} \\ A_n &= \frac{2}{\pi n [1 - \pi^2 n^2 Z^2 / (\theta^- - \theta^+)^2]} \left\{ \left[-\cos \theta^- \sin \pi n Z \right. \right. \\ &\left. \left. + \frac{\pi n Z}{(\theta^- - \theta^+)} (\sin \theta^- \cos \pi n Z - \sin \theta^+) \right] \cos \pi n Y \right. \\ &\left. + \left[\cos \theta^+ - \cos \theta^- \cos \pi n Z \right. \right. \\ &\left. \left. - \frac{\pi n Z}{(\theta^- - \theta^+)} \sin \theta^- \sin \pi n Z \right] \sin \pi n Y \right\}. \end{aligned} \quad (11)$$

We shall now compare the quasi-single-domain states of uniaxial ferromagnetic films with and without a superconducting coating, for a tangential external magnetic field not exceeding that for a transition from the collinear to the homogeneous angular phase. For an isolated magnetic film with strong magnetic anisotropy ($\Delta \ll L$) (we subsequently take strong or weak anisotropy to mean the effective anisotropy, which includes the influence of the magnetizing field) where $kL \ll 1$, we have

$$\begin{aligned} g_D &\cong \frac{\cos^2 \theta^+}{\pi^2} kL \left[\ln(kL) - \frac{3}{2} - \ln 2 - \frac{(kL)^2}{72} \right] + o(k^4 L^4), \\ \Delta^2 &\cong \frac{(\pi - 2\theta^+)}{2} \left\{ \frac{\tilde{Q}}{4} \cos 2\theta^+ + h_\parallel \left[\sin \theta^+ - \frac{\cos \theta^+}{(\pi - 2\theta^+)} \right] \right\}^{-1}, \\ k &\cong \frac{1}{L} \exp \left[-\frac{\pi(\pi - 2\theta^+)^2}{\Delta L \cos^2 \theta^+} \right]. \end{aligned} \quad (12)$$

From this it can be seen that as the thickness of the magnetic film decreases, the size of the domains increases exponentially while the width of the domain walls remains almost the same.

Under the same conditions for a film coated on two sides with an ideal superconductor ($\lambda=0$), the dipole energy is transformed to give

$$g_D = -\frac{8kL \cos^2 \theta^+}{\pi^4} \sum_{n=1}^{\infty} \frac{1}{(2n-1)^3} \tanh \frac{\pi^2(2n-1)}{2kL}. \tag{13}$$

Using Eq. (13), we can determine the critical thickness L_c and the relation between k and L for films of near-critical thickness

$$L_c \cong \frac{\pi(\pi-2\theta^+)^2}{I\Delta \cos^2 \theta^+},$$

$$\frac{L-L_c}{L_c} \cong \frac{16\pi^2}{7\zeta(3)} \frac{1}{(kL)} \exp\left(-\frac{\pi^2}{kL_c}\right), \tag{14}$$

where

$$I = \int_0^{\infty} \frac{dx}{x^2} \left(1 - \frac{\tanh x}{x}\right) \cong 0.82.$$

It can be seen from Eq. (14) that the dependence of the reciprocal period of the domain structure k on the film thickness L near the transition to the single-domain state is logarithmic. If the London depth for the superconducting material is large ($\lambda \gg L$), we have

$$g_D \cong \frac{kL}{\pi^2} \cos^2 \theta^+ (\ln l + C - 3/2), \quad l = L/2\lambda, \tag{15}$$

and the dependence $L_c(\lambda)$ is expressed in the parametric form

$$\begin{cases} L_c \cong -\frac{\pi(\pi-2\theta^+)^2}{\Delta \cos^2 \theta^+ (\ln t + C - 3/2)}, \\ \lambda = L_c/2t, \end{cases} \tag{16}$$

where C is the Euler constant. In this case, the value of k depends logarithmically on $L-L_c$. This dependence is a consequence of the exponential decay of the magnetic induction and the tangential component of the domain-wall magnetic field with increasing distance from this wall as a result of the magnetic charge field being screened by currents near the surface of the superconducting coating. The screening radius increases monotonically from a value of the order of L for an ideal superconductor to a value of the order of λ for a superconductor with $\lambda \gg \Lambda$.

For a magnetic film with an ideal superconducting coating on one side ($\lambda=0$), we have

$$g_D \cong -2 \frac{\cos^2 \theta^+}{\pi^2} kL \left[\ln 2 - \frac{(kL)^2}{12} \right] + o(k^4 L^4), \tag{17}$$

so that

$$L_c \cong \frac{\pi(\pi-2\theta^+)^2}{2 \ln 2} \frac{1}{\Delta \cos^2 \theta^+},$$

$$(kL_c)^2 \cong 4 \ln 2 \frac{(L-L_c)}{L_c}. \tag{18}$$

For $\lambda \gg L$ expressions (15)–(16) are valid if 3/2 is replaced by 2. The domain-wall width in Eqs. (14), (16), and (18) is described by formula (12).

For magnetic films with a superconducting coating, the principal term in the expansion of the dipole energy in powers of the small parameter kL is proportional to kL and the derivative of the dipole energy with respect to k exhibits no divergence for $kL \rightarrow 0$. The differences in the expressions for the dipole energy and in the dependences $k(L)$ are attributed to differences in the asymptotic behavior of the induction and the domain-wall field at large distances from it. For an insulated magnetic film the field of a domain wall centered at the point $x=0$ for $x \rightarrow \infty$ is given by

$$h_D^x \cong -\frac{2}{\pi} \cos \theta^+ \frac{y}{x^2}, \quad b_D^y = h_D^y + m^y \cong \frac{2}{\pi} \cos \theta^+ \frac{1}{x}. \tag{19}$$

The induction component b_D^y decays slowly with increasing x which leads to the appearance of $\ln kL$ in the expression for the dipole energy (12).

For a film coated on one side we have

$$h_D^x \cong -\frac{8}{\pi l} \cos \theta^+ \frac{1}{x^2},$$

$$b_D^y \cong \frac{8}{\pi l} \cos \theta^+ \frac{(1+l)(1-ly)}{x^3}, \tag{20}$$

so that b_D^y decays rapidly with increasing x and the derivative of the dipole energy with respect to k exhibits no divergence for $kL \rightarrow 0$. For a film coated on two sides, it has been noted that these value decay exponentially with increasing distance from the domain wall.

Using the expressions for the Gibbs energy (9) and (10), we also analyzed the quasi-single-domain states and the critical thickness of uniaxial ferromagnetic films with a superconducting coating in an external magnetic field directed at an angle to the plane of the film. Without giving all the calculated results, we note that as the normal component of the external field $H_e^y \mathbf{n}_y$ increases, the region of absolute stability of the angular phase with the magnetization component $M^y H_e^y > 0$ increases.

4. Quite clearly, the specific type of domain structure is not important for determining the critical thickness, and this thickness may be obtained from the condition that the total energies of an insulated domain wall and the homogeneous angular phase are the same.

We shall calculate the critical thickness of a uniaxial ferromagnet with the quality factor $Q > 1$ in a tangential external magnetic field \mathbf{H}_e , assuming the following distribution of magnetization in the domain wall:

$$m^y = \cos \theta_0 \tanh(x/\Delta),$$

$$m^z = [1 - \cos^2 \theta_0 \tanh^2(x/\Delta)]^{1/2}, \tag{21}$$

where Δ is the width of the domain wall and $\theta_0 = \arcsin h/\tilde{Q}$. As above, we shall use normalized variables and we shall also introduce the notation $\nu = kL/2$, ρ

$=\pi\Delta/L$, $\varepsilon = \tau L/2$, $\tilde{g} = G/(4M_0^2 L^2)$. Then, per unit length of the domain wall, we have the Zeeman energy

$$\tilde{g}_z = \tilde{Q}\rho \sin \theta_0 [(2\theta_0 - \pi)\cos \theta_0 - 2 \sin \theta_0 \ln \sin \theta_0], \quad (22)$$

the anisotropy energy, including the local component of the dipole energy

$$\tilde{g}_a = \tilde{Q}\rho \cos^2 \theta_0, \quad (23)$$

the exchange energy

$$\tilde{g}_{ex} = \frac{\pi^2}{\rho L^2} \left(1 - \frac{\sin^2 \theta_0}{\cos \theta_0} \arctan \cos \theta_0 \right), \quad (24)$$

and the energy of the dipole field in the symmetric

$$\begin{aligned} \tilde{g}_D &= -\rho^2 \cos^2 \theta_0 \\ &\times \int_0^\infty \frac{d\nu}{\sinh^2(\rho\nu)} \left[1 - \frac{\varepsilon \sinh \nu}{\nu(\varepsilon \cosh \nu + \nu \sinh \nu)} \right], \end{aligned} \quad (25a)$$

and asymmetric systems

$$\begin{aligned} \tilde{g}_D &= -\rho^2 \cos^2 \theta_0 \int_0^\infty \frac{d\nu}{\sinh^2(\rho\nu)} \left\{ 1 - \frac{1}{2\nu} (1 - e^{-2\nu}) \right. \\ &\times \left. \left(1 + \frac{(\varepsilon - \nu)}{2(\varepsilon + \nu)} (1 - e^{-2\nu}) \right) \right\}. \end{aligned} \quad (25b)$$

Analytic expressions for the critical thickness L_c can only be obtained for systems with an ideal superconductor ($\lambda=0$) and strong $\rho \ll 1$ or weak $\rho \gg 1$ anisotropy of the film, and also for systems for which the depth of penetration of the field in the superconductor is large $\lambda \gg L, \Delta$.

For a symmetric system with an ideal superconducting coating and strong anisotropy $\rho \ll 1$, we have

$$\tilde{g}_D \cong -\frac{7\zeta(3)}{\pi^2} \cos^2 \theta_0 \cong -0.853 \cos^2 \theta_0, \quad (26)$$

$$L_c \cong \frac{2\pi^2}{7\zeta(3)\cos^2 \theta_0} \sqrt{RS\tilde{Q}}, \quad (27)$$

$$\rho_c \cong \sqrt{S/(R\tilde{Q}L_c^2)}, \quad (28)$$

where

$$\begin{aligned} R &= \sin \theta_0 [(2\theta_0 - \pi)\cos \theta_0 - 2 \sin \theta_0 \ln \sin \theta_0] \\ &+ \cos^2 \theta_0, \end{aligned} \quad (29)$$

$$S = \pi^2 \left(1 - \frac{\sin^2 \theta_0}{\cos \theta_0} \arctan \cos \theta_0 \right). \quad (30)$$

Note that Eqs. (26)–(28) are valid for weak external fields although, as the external field increases and the point of transition from the collinear to the homogeneous angular phase is approached, the domain wall becomes broader and the approximation $\rho \ll 1$ ceases to hold.

For weak anisotropy $\rho \gg 1$ we obtain

$$\tilde{g}_D \cong -\frac{a}{\rho} + \frac{b}{3\rho^3}, \quad a \cong \frac{\pi^2}{18} \cos^2 \theta_0, \quad b \cong \frac{\pi^4}{75} \cos^2 \theta_0, \quad (31)$$

$$L_c^2 \cong S/a, \quad \rho_c^4 \cong b/(3R\tilde{Q}). \quad (32)$$

It can be seen from Eqs. (29)–(32) that the critical thickness decreases monotonically with increasing external field from $L_c^2 \cong 18$ for $h=0$ to $L_c^2 \cong 15/\pi^2$ for $h=\tilde{Q}$. It can also be seen from expressions (27) and (32) that the critical thickness decreases with increasing magnetizing field (in the range of validity of these expressions) and its maximum corresponds to zero field. This behavior is caused by a reduction in the effective magnetic anisotropy in the yz plane and a decrease in the domain scattering field as the point of transition from the homogeneous angular to the collinear phase is approached.

For an asymmetric system with an ideal superconducting substrate ($\lambda=0$) and strong magnetic anisotropy $\rho \ll 1$ we have

$$\tilde{g}_D \cong -2 \ln 2 \cos^2 \theta_0, \quad (33)$$

$$L_c \cong \frac{1}{\ln 2 \cos \theta_0^2} \sqrt{RS\tilde{Q}}, \quad (34)$$

$$\rho_c \cong \sqrt{S/(R\tilde{Q}L_c^2)}, \quad (35)$$

and for weak anisotropy $\rho \gg 1$

$$\tilde{g}_D \cong -\frac{a}{\rho} + \frac{b}{2\rho^2}, \quad a \cong \frac{\pi^2}{9} \cos^2 \theta_0,$$

$$b \cong \frac{3\zeta(3)}{2} \cos^2 \theta_0, \quad (36)$$

$$L_c^2 \cong S/a, \quad \rho_c^3 \cong b/(4R\tilde{Q}). \quad (37)$$

In the opposite case, where the depth of penetration of the field in the superconductor is large $\lambda \gg L, \Delta$, for a symmetric system with strong anisotropy $\rho \ll 1$, we have

$$\tilde{g}_D \cong \cos^2 \theta_0 [\ln(L/\lambda) + C - 3/2], \quad (38)$$

and $L_c(\lambda)$ and $\rho_c(\lambda)$ are functions of the parameter t , which varies in the range $0 < t \ll 1$

$$\begin{cases} L_c \cong \rho_c^{-1} (S/R\tilde{Q})^{1/2}, \\ \rho_c \cong \cos^2 \theta_0 (-\ln t + 3/2 - C) (2R\tilde{Q})^{-1}, \\ \lambda = L_c/(2t). \end{cases} \quad (39)$$

If the anisotropy is weak $\rho \gg 1$, then

$$\tilde{g}_D \cong -[\ln(\lambda/\rho L) + 1] \cos^2 \theta_0 \quad (40)$$

and the critical parameters are

$$\begin{aligned} \rho_c &\cong [\cos^2 \theta_0 / (4R\tilde{Q})] \ln(4\lambda^2 R\tilde{Q}/S), \\ L &\cong (\rho_c^2 R\tilde{Q}/S)^{-1/2}. \end{aligned} \quad (41)$$

For an asymmetric system with strong $\rho \ll 1$ and weak anisotropy $\rho \gg 1$, $\rho L/\lambda \ll 1$, the dipole energy and the critical

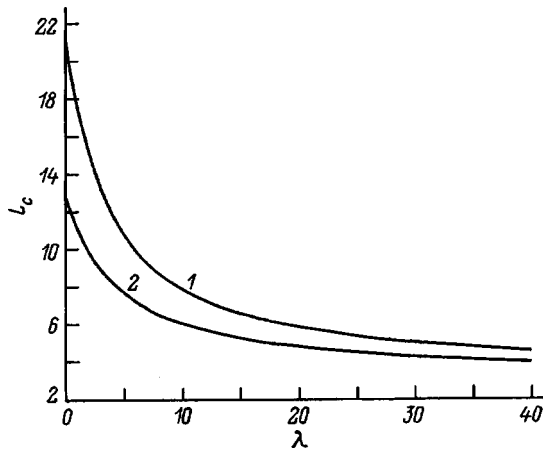


FIG. 2. Critical thickness L_c versus London depth λ for $h=0$ and the quality factor $\tilde{Q}=7$. 1 — coating on two sides, and 2 — on one side.

values L_c and ρ_c are described by formulas (38), (39), and (40), (41), respectively, if λ is replaced by $\lambda\sqrt{e}$.

The domain-wall model (21) can be used to make fairly accurate calculations of the critical thickness for a magnetic film with strong anisotropy in weak fields. However, this model cannot be used for fields close to the transition from the angular to the collinear phase $h=\tilde{Q}$ since the distribution of the magnetization over the thickness of the magnetic becomes highly nonuniform. Calculations of the critical thickness for weak anisotropy $0 < \tilde{Q} \ll 1$ are qualitative.

If the tangential external field is larger than the field for the transition from the collinear to the angular phase $h > \tilde{Q}$, an isolated domain wall does not exist and the critical thickness, as for films with $\tilde{Q} < 0$, may be calculated from a linearized system of equations.⁷ By analyzing the spectrum of weak perturbations in the system (the discriminants of the systems of linear equations (5) and (15) from Ref. 7), we can easily find the critical film thickness for the case $\lambda \gg 1$, $L \ll 1$. For typical type II superconductors and ferrites we find $\lambda \sim 10^{-4}$ cm, $\alpha/4\pi \sim 10^{-10} - 10^{-11}$ cm², so that this case is of the greatest interest. The dependence $L_c(h)$ for a symmetric system is given by

$$\begin{cases} L_c(k) \cong 4(k^2 + \lambda^{-2})^{3/2} / (k^2 + 2\lambda^{-2}), \\ h(k) \cong \tilde{Q} + k^4 / (k^2 + 2\lambda^{-2}), \end{cases} \quad (42)$$

where k is a parameter equal to the wave number of the critical mode. The equivalent dependence for an asymmetric system is written as follows:

$$\begin{cases} L_c(k) \cong 2\tau(k + \tau) / (2\tau - k), \\ h(k) \cong \tilde{Q} + k^3(2\tau - k). \end{cases} \quad (43)$$

It follows from Eqs. (42) and (43) that the critical thickness and the wave number of the critical mode increase monotonically with increasing external field. The minimum critical thickness L_c^* corresponding to the external field $h = \tilde{Q}$ agrees with that obtained in Ref. 7.

Equations (22)–(25) were used for a numerical analysis of the critical parameters. Figures 2 and 3 give the critical thickness L_c of magnetic film coated on one and two sides as

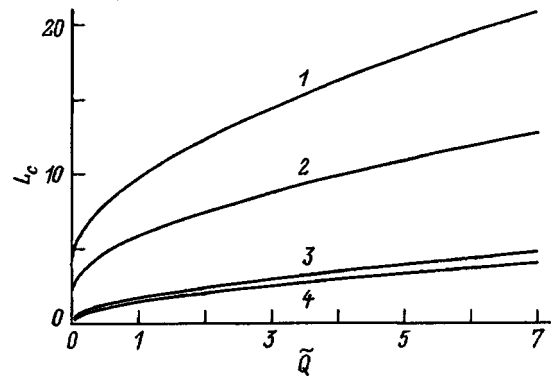


FIG. 3. Critical thickness L_c versus quality factor \tilde{Q} for $h=0$ and $\lambda=0$ (1, 2) and 35.5 (3, 4): 1, 3 — coating on two sides, 2, 4 — coating on one side.

a function of the London depth λ and \tilde{Q} . It can be seen from Fig. 2 that for small λ the critical thickness L_c varies rapidly with λ , and for large λ varies logarithmically as given by expression (39). An increase in L_c with increasing \tilde{Q} (Fig. 3) is caused by an increase in the scattering field and the domain-wall energy. Figure 4 gives the critical thickness L_c as a function of the magnetizing field h . Over a wide range of fields, the critical thickness L_c is almost constant but it decreases rapidly as the field tends toward that for the transition from the angular to the collinear phase. This is caused by an increase in the width of the domain wall and an associated decrease in the scattering field. The minimum critical thickness L_c^* for the calculation parameters is very accurately described by formulas (42) and (43). The discontinuity of the curves for $h = \tilde{Q}$ occurred because for the range of fields $h > \tilde{Q}$ the results are accurate, whereas for the range $h < \tilde{Q}$ a highly flawed model was used.

An analysis of the results presented in this section suggests that in these approximations the transition over thickness from a homogeneous to a domain state in uniaxial ferromagnetics with the quality factor $Q > 1$ is a second-order phase transition for fields $H_e > \tilde{Q}$ and a first-order phase tran-

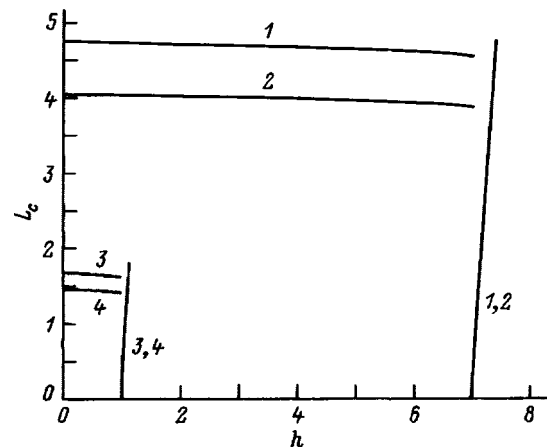


FIG. 4. Critical thickness L_c versus tangential magnetizing field h for $\lambda = 35.5$ and values of the quality factor $\tilde{Q}=7$ (1, 2) and 1 (3, 4): 1, 3 — coating on two sides, 2, 4 — coating on one side.

sition for $H_e < \tilde{Q}$. The line describing the loss of stability of the inhomogeneous state for $H_e < \tilde{Q}$ is the same as the first-order phase transition line (these lines may differ if more complex domain structure models are used). The line describing the loss of stability of the angular phase is not shown in Fig. 4.

5. We shall assess the validity of these results for the case where the external field is zero and no pinning is observed in the superconducting material. Vortices occur in the superconductor when the tangential dipole field H_D^* at the surface of the superconductor exceeds the lower critical field H_{c1} . However, the magnetic flux structure only varies substantially if the characteristic size of the region Λ in which vortices exist is considerably greater than the London penetration depth of the field in the superconductor $\Delta \gg \lambda$ and the thickness of the magnetic film $\Lambda \gg L$ (for $L \gg \Delta$) or the width of the domain wall $\Lambda \gg \Delta$ (for $\Delta \gg L$). For a symmetric system these conditions are equivalent to the inequality

$$h_{c1} = H_{c1} / (4\pi M_0) \ll h_D^* = |h_D^*[y = L_c/2, x = \max(\lambda, L_c, \Delta_c)]|. \quad (44)$$

For $\lambda \ll L_c \ll \Delta_c$ the field decreases rapidly with increasing wall width $h_D^* \cong h_D^*(y = L_c/2, x = 0) \cong (\pi/2\rho_c)$, so that vortices cannot appear in the superconductor. If $\lambda \ll \Delta_c \ll L_c$, then we have $h_D^* \cong -(2/\pi)\ln\rho_c$. Then vortices generally appear in the superconductor and the critical thickness may be substan-

tially less than that obtained here. For $\lambda \gg \Delta_c \gg L_c$ the field is exponentially small $h_D^* \cong (8/\pi)\rho_c \exp(-\pi/\rho_c L_c)$, so that no vortex structure exists. The case $\lambda \gg L_c \gg \Delta_c$ is of little interest since the critical thickness L_c for large λ is small and the inequality $L_c \gg \Delta_c$ is rarely satisfied. Under conditions where inequality (44) is satisfied, a stricter approach is required to describe the mixed state of a superconductor and this should form the subject of a special analysis.

This work was supported by the Russian Fund for Fundamental Research (Grant 96-02-17283a).

*Polytechnic Institute, 26-600 Radom, Poland

¹L. D. Landau and E. M. Lifshitz, *Electrodynamics of Continuous Media*, transl. of 1st Russ. ed. [Pergamon Press, Oxford, 1960; Russ. original, Nauka, Moscow, 1982, 620 pp.].

²S. V. Vonsovskii, *Magnetism*, Vols. 1 and 2 [Wiley, New York, 1974; Russ. original, Nauka, Moscow, 1972, 1032 pp.].

³Yu. I. Bespyatykh, V. Vasilevskii, M. Gaidek, A. D. Simonov, and V. D. Kharitonov, *Fiz. Tverd. Tela* (St. Petersburg) **35**, 2983 (1993) [Phys. Solid State **35**, 1466 (1993)].

⁴N. M. Salanskii and M. Sh. Erukhimov, *Physical Properties and Applications of Magnetic Films* [in Russian], Nauka, Novosibirsk (1975), 224 pp.

⁵A. Holz and H. Kronmuller, *Phys. Status Solidi* **31**, 787 (1969).

⁶V. G. Bar'yakhtar and B. A. Ivanov, *Zh. Éksp. Teor. Fiz.* **72**, 1504 (1977) [Sov. Phys. JETP **45**, 789 (1974)].

⁷Yu. I. Bespyatykh, V. Vasilevskii, M. Gaidek, A. D. Simonov, and V. D. Kharitonov, *Fiz. Tverd. Tela* (St. Petersburg) **36**, 586 (1994) [Phys. Solid State **36**, 323 (1994)].

Translated by R. M. Durham

Temperature dependences of the high-field magnetization of dilute frustrated ferrimagnetic spinels

N. N. Efimova and S. R. Kufferina

Kharkov State University, 310077 Kharkov, Ukraine

(Submitted August 4, 1997; resubmitted December 29, 1997)

Fiz. Tverd. Tela (St. Petersburg) **40**, 1075–1079 (June 1998)

Results are presented of an investigation of the magnetic properties of dilute frustrated ferrimagnetic spinels $\text{Li}_{0.5}\text{Fe}_{2.5-x}\text{Ga}_x\text{O}_4$ ($x=0.8-1.2$), which characterize the main parameters of the ferrimagnetic state and provide evidence of local violation of collinear spin ordering and frustrations. In particular, measurements were made of the concentration dependences of the magnetic moment $n_0(x)$ and the Curie point $T_c(x)$, the magnetization isotherms $\sigma_T(H)$ at $T=4.2$ K and $H \leq 10$ kOe, and also the low- and high-field magnetization polytherms $\sigma_H(T)$. It was established that for $x \geq 0.8$ in fields exceeding the technical saturation field $H_s \sim 2$ kOe, the temperature dependences of the high-field magnetization $\sigma_H(T)$ between 4.2 and 230 K cannot be described by the Bloch $T^{3/2}$ law whereas this law is satisfied for undiluted Li spinel ($x=0$). Over the entire temperature range (4.2–230 K) the experimental curves $\sigma_H(T)$ may be approximated by $\sigma_H(T) = \sigma_0(1 - AT^{3/2} - BT^{5/2})$ for $x=0.8-1.0$ and $\sigma_H(T) = \sigma_0[1 - CT^{3/2}\exp(\mu(H-H_0)/k_B T)]$ for $x=1.1, 1.2$, where $\mu H_0 \sim 15$ K is the internal field produced by competition between exchange interactions and frustrations. © 1998 American Institute of Physics. [S1063-7834(98)02406-X]

Here we report results of investigating the magnetic properties of dilute two-sublattice ferrimagnetic spinels $\text{Li}_{0.5}\text{Fe}_{2.5-x}\text{Ga}_x\text{O}_4$ ($x=0.8-1.2$) with only one species of magnetic ions — Fe^{3+} . Particular attention is paid to identifying the temperature dependences of the high-field magnetization σ_H , i.e., the magnetization in fields greater than the technical saturation field $H > H_s$ and in particular, to the possibility of describing these dependences by the Bloch $T^{3/2}$ law, which is satisfied for collinear ferromagnets and ferrimagnets up to temperatures $\sim 0.8T_c$ (Refs. 1 and 2).

For these concentrations of nonmagnetic Ga^{3+} ions, Li–Ga spinels are weakly frustrated Heisenberg ferrimagnets. For $x=0.8, 0.9$ the ferrimagnetic state exists over the entire temperature range between $T=4.2$ K and T_c (Curie point) while the range $x=1.0-1.2$ corresponds to the reentrant region of the $x-T$ diagram.³ In zero or weak magnetic fields two transitions take place successively with decreasing temperature: paramagnetic to ferrimagnetic at the Curie point T_c and ferrimagnetic to ferrimagnetic spin glass at the freezing point $T_f < T_c$. For $x=1.0-1.2$ the values of T_f are 10–12 K (Ref. 4).

The influence of competition between exchange interactions and frustrations on the spectrum of magnetic perturbations was initially examined mainly in the context of disordered spin glass states.⁵ Although the situation has recently changed and increasing interest has been shown directly in studying various models of frustrated magnetics,^{6,7} the most promising systems for experimental investigations are those in which a change in the concentration of components is accompanied by a transition to the spin glass state.

1. SAMPLES AND MEASUREMENT METHOD

Polycrystalline samples of $\text{Li}_{0.5}\text{Fe}_{2.5-x}\text{Ga}_x\text{O}_4$ ($x=0.8-1.2$) spinels were synthesized by a solid-phase reaction, as in Ref. 3. The single-phase state was checked by x-ray diffraction.

In order to avoid any confusion, it should be noted that, unlike Ref. 4, we used samples with $x=0.9$, which do not exhibit any transition to the ferrimagnetic spin-glass state.

The magnetic properties were investigated using methods and apparatus similar to those used in Refs. 3 and 4. The low-field magnetization polytherms in the temperature ranges 4.2–200 K, 77–300 K and 300–950 K were measured by an induction technique using three ballistic magnetometers with sensitivities of 10^{-3} , 10^{-2} and 10^{-2} $\text{G} \cdot \text{cm}^3 \cdot \text{g}^{-1}$, respectively. The $\sigma_T(H)$ isotherms in fields up to 10 kOe and also the high-field magnetization polytherms $\sigma_H(T)$ were measured in the range $4.2 \leq T \leq 230$ K using a ballistic magnetometer. For the measurements of $\sigma_H(T)$ the temperature step was 3–5 K. The temperature was measured using a TSU-2 carbon resistance thermometer.

2. EXPERIMENTAL RESULTS AND DISCUSSION

1) Influence of diamagnetic dilution on magnetic properties.

The influence of diamagnetic dilution on the macroscopic parameters of the ferrimagnetic state is illustrated in Fig. 1, which gives the concentration dependences of the Curie point $T_c(x)$ and the magnetic moment at $T=4.2$ K — $n_0(x)$. The values of T_c were determined by two methods: by the Belov–Arrott method¹ and by extrapolating to the T axis the high-temperature sections of the curves $\sigma_H(T)$ cor-

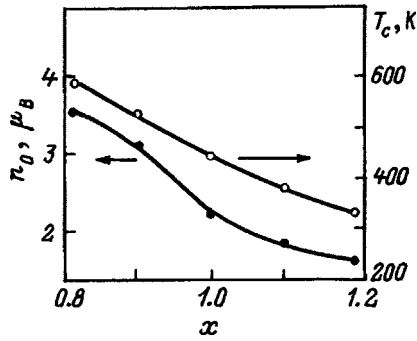


FIG. 1. Concentration dependences of the Curie point $T_c(x)$ and the magnetic moment $n_0(x)$ of $\text{Li}_{0.5}\text{Fe}_{2.5-x}\text{Ga}_x\text{O}_4$ spinels.

responding to the maximum of the derivative $(\partial\sigma/\partial T)$ (Fig. 2). The values of T_c agreed within the experimental error of both methods (± 2 K).

Table I gives information on the cation distribution calculated using the values of n_0 (Fig. 1), as in Ref. 8. Results of an investigation of the magnetization $\sigma_T(H)$, similar to those plotted in Fig. 3 for $T=4.2$ K, served as the basis for using this approximation. For $x=0.8-1.1$ saturation is achieved at $H=H_x \sim 2$ kOe. The low-temperature paraprocess, which is an indication of spin ordering noncollinearity,¹ is only observed for $M > M_s$ in samples with $X=1.2$.

However, for $x=0.8$, nonmagnetic Ga^{3+} ions have already replaced 32 mol.% of the Fe^{3+} ions and in weak fields or $H=0$, the macroscopically collinear ferrimagnetic structure has local violations — spin canting near magnetic vacancies (Ga^{3+}) (Refs. 3 and 9). Qualitative confirmation of the existence of regions of local noncollinearity may be provided by the results plotted in Fig. 2, which gives the low-field magnetization polytherms $\sigma_H(T)$ obtained for different sample prehistories: ZFC — precooling to $T=4.2$ K in the absence of a field, and FC — cooling with $H \neq 0$. It can be seen that in all cases, except for $X=0$ (nonsubstituted Li spinel), the profile of the polytherms is irreversible: $\sigma_{\text{ZFC}}(T, H) \neq \sigma_{\text{FC}}(T, H)$. The absence of this effect for Li spinel indicates that it is not related to the characteristics of the polycrystalline structure of the samples. In fields of

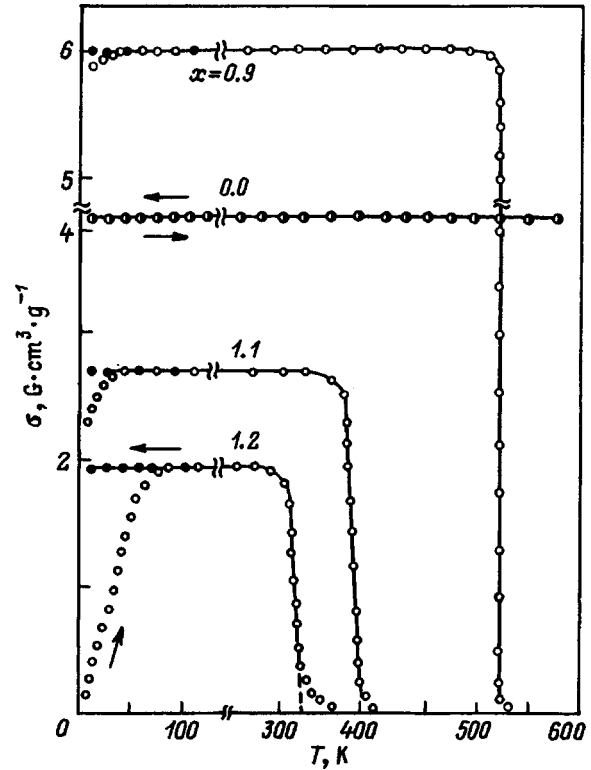


FIG. 2. Low-field magnetization polytherms $\sigma_H(T)$ of dilute $\text{Li}_{0.5}\text{Fe}_{2.5-x}\text{Ga}_x\text{O}_4$ ($x=0.0, 0.9, 1.1,$ and 1.2) spinels; $H=50$ Oe.

~ 1 Oe irreversible effects are observed at temperatures between approximately 4.2 and 100 K, whereas for $H > 100$ Oe, they are only observed for $x=1.2$ at low temperatures. On the whole, the irreversibility effects observed over the entire range of concentrations $x=0.8-1.2$ (taking into account their dependence on $x, T,$ and H) are quite consistent with the model for the formation of ferrimagnetic spin-glass states,⁹ which assumes that regions of local noncollinearity are formed at the preceding stage of concentration ($T=0$) or temperature ($T > T_f$).

Since the existence of frustrations is associated with regions of local noncollinearity, the presence ($x \geq 1.0$) or absence ($x = 0.8, 0.9$) of low-temperature ferrimagnetic spin-glass states and also the behavior in weak and strong fields

TABLE I. Cation distribution in a system of dilute $\text{Li}_{0.5}\text{Fe}_{2.5-x}\text{Ga}_x\text{O}_4$ spinels ($x=0.8-1.2$), the coefficients A in the Bloch magnetization law (1), A_a and B in the Dyson expansion (2), the coefficient C , and the gap Δ (3). N_A and N_B are the numbers of magnetic ions (Fe^{3+}) in the tetrahedral and octahedral sublattices.

	x						Note
	0	0.8	0.9	1.0	1.1	1.2	
$N_A \pm 0.05$	1	0.49	0.52	0.50	0.51	0.47	
$N_B \pm 0.05$	1.5	1.21	1.08	1.00	0.89	0.83	
$A_{\text{LT}} \cdot 10^5, \text{K}^{-3/2}$		10.0 ± 0.7	10.0 ± 0.7	18.1 ± 1.2	17.4 ± 1.4		
$A_{\text{HT}} \cdot 10^5, \text{K}^{-3/2}$		7.0 ± 0.7	7.0 ± 0.7	10.0 ± 1.2	9.5 ± 1.4	15.50 ± 1.4	(1)
$A \cdot 10^5, \text{K}^{-3/2}$	1.4 ± 0.10	8.00 ± 0.11	8.00 ± 0.11	13.00 ± 0.32	13.00 ± 0.30	15.00 ± 0.13	(1)
$\langle\langle\chi^2\rangle\rangle$		0.202	0.198	0.293	0.396	0.197	
$A_2 \cdot 10^5, \text{K}^{-3/2}$		11.03 ± 0.36	11.7 ± 0.43	19.76 ± 0.71	17.84 ± 1.12	17.6 ± 0.66	(2)
$B \cdot 10^7, \text{K}^{-5/2}$		1.58 ± 0.20	1.69 ± 0.24	4.18 ± 0.41	2.71 ± 0.63	1.15 ± 0.31	
$\langle\langle\chi^2\rangle\rangle$		0.071	0.072	0.060	0.154	0.141	
$C \cdot 10^5, \text{K}^{-3/2}$		8.00 ± 0.75	8.00 ± 0.64	12.00 ± 2.00	12.00 ± 0.46	14.00 ± 0.12	(3)
Δ, K		-9.4 ± 27.3	-16.2 ± 29.6	-5.80 ± 12.02	-15.20 ± 0.13	-14.80 ± 1.23	
$\langle\langle\chi^2\rangle\rangle$		0.178	0.176	0.259	0.378	0.168	

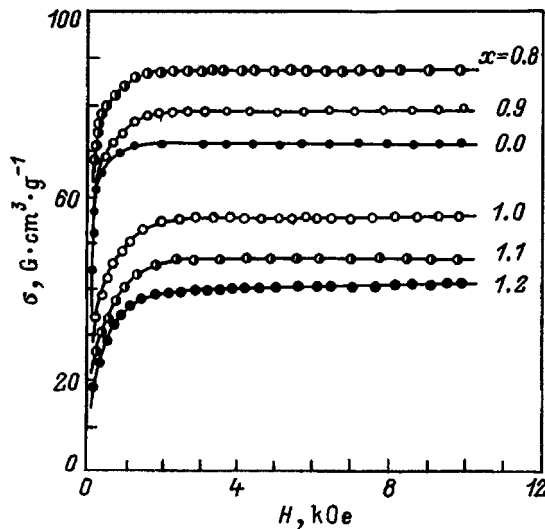


FIG. 3. Magnetization isotherms $\sigma_T(H)$ of Li-Ga-spinels with $x=0.0$ and $0.8-1.2$ at $T=4.2$ K.

(Figs. 2 and 3) can be used to classify the samples into groups having roughly the same level of frustrations. In ascending order, this classification will be: 1) $x=0.8, 0.9$; 2) $x=1.0, 1.1$; 3) $x=1.2$.

2) Temperature dependences of the high-field magnetization.

Figure 4 gives the experimental curves $\sigma_H(T)$ measured at $H=5$ kOe. Also plotted for comparison is the curve for nonsubstituted Li spinel ($x=0$).

In Fig. 5 the experimental results $\sigma_H(T)$ are plotted using the coordinates $\sigma_H(T^{3/2})$. These results clearly show that for $x=0.8-1.0$ the dependences $\sigma_H(T^{3/2})$ are accurately approximated by two linear sections which blend smoothly into each other. The change in profile is observed at $T \sim 100$ K, i.e., in that region of temperature where, according to the results of the low-field studies, effects associated with perturbed exchange begin to appear: $\chi'(T)$ decreases (Ref. 4) and the profile of the polytherms becomes irreversible (see Part 1 of this section). When $T \rightarrow 0$ K for samples with x

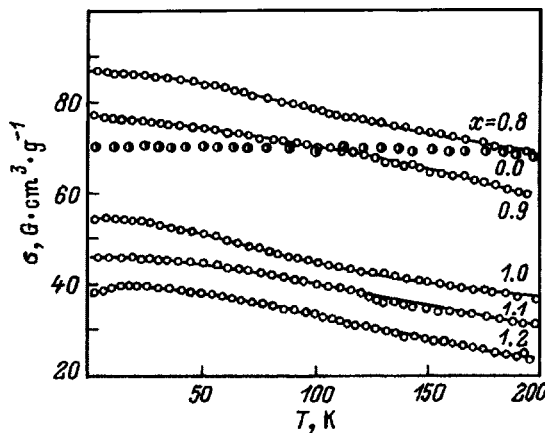


FIG. 4. High-field magnetization polytherms in the field $H > H_s$ ($H=5$ kOe) for $\text{Li}_{0.5}\text{Fe}_{2.5-x}\text{Ga}_x\text{O}_4$ spinels ($x=0.0, 0.8-1.2$). Solid curves — calculated using Eq. (2) ($x=0.8-1.0$) and Eq. (4) ($x=1.1, 1.2$).

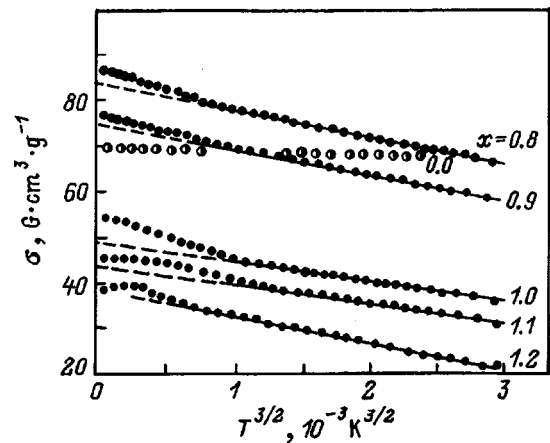


FIG. 5. Polytherms from Fig. 4 plotted as σ versus $T^{3/2}$.

$=1.1$ and 1.2 , for which the curves $\sigma_H(T)$ have a plateau (at $T < 30$ K) or a slightly broadened peak (at $T < 50$ K), respectively, the $T^{3/2}$ law is clearly not satisfied. However, at higher temperatures, as can be seen from Fig. 5, two linear sections with different slopes can also be identified for $x=1.1$ ($T > 30$ K) whereas for $x=1.2$, there is only one linear section, near $T > 50$ K.

The slope of the curves $\sigma_H(T^{3/2})$ is determined by the coefficient A in the Bloch law

$$\sigma_s(T) = \sigma_{s0}(1 - AT^{3/2}), \tag{1}$$

where σ_{s0} and $\sigma_s(T)$ are the spontaneous magnetization at $T=0$ and $T > 0$ K. In our case, σ_s and σ_{s0} were taken to be the values of $\sigma_H(T)$ at $H=5$ kOe and σ_{s0} , obtained by extrapolating the curves $\sigma_H(T^{3/2})$ to 0 K, respectively.

Table I gives the values of the coefficients A from Eq. (1) determined from the low- ($T < 100$ K) and high-temperature ($T > 100$ K) sections of the curves $\sigma_H(T^{3/2})$ (A_{LT} and A_{HT} , respectively). For comparison this coefficient is also given for nonsubstituted Li spinel and also for the case where Eq. (1) with $A = \text{const}$ is used over the entire temperature range. These data show that the samples can be classified into the same groups as before (see Part 1 of this section).

The concentration dependences of the coefficients A_{LT} and A_{HT} considered separately are quite regular.¹⁰ A change in A with temperature, i.e., $A_{LT} \neq A_{HT}$, would be justified, for instance, in the presence of a phase transition. However, in the appropriate temperature range we did not observe any typical characteristics of the low-field dynamic susceptibility, whereas for $T = T_c$ and $T = T_f$ the curves $\chi'(T)$ have characteristic peaks.^{4,11} The characteristic behavior of $\sigma_H(T^{3/2})$ for these samples also cannot be explained in terms of the temperature dependence of D as a result of spin wave interaction with two-level systems,¹² since this mechanism presupposes that $D(T)$ has a plateau or peak in the range $T_c < T < T_f$ and that D decreases appreciably for $T \rightarrow T_f$. This behavior is clearly not consistent with the experimental results. Thus, there are no convincing physical reasons for the approximation of the experimental curves $\sigma_H(T)$ by two linear sections $\sigma_H(T^{3/2})$. Thus, after using a mathematical treatment of the experimental curves $\sigma_H(T)$, we examined

the possibility of describing these using the same functional dependences over the entire temperature range.

3) Choice of approximating functions.

Assuming that the spin-wave approximation is satisfied for the curves $\sigma_H(T)$, we used the Dyson expansion¹³

$$\sigma_s(T) = \sigma_{s0}(1 - A 2T^{3/2} - BT^{5/2}), \quad (2)$$

and also various approximations to allow for a gap in the spin-wave spectrum.¹⁴ The functional approximations to which we paid particular attention were initially selected taking into account the values of the correlation coefficient R and also the physical nature of the calculation parameters, especially the gap Δ . Ultimately, for the analysis, we only retained the Bloch law (1), the Dyson expansion (2), and relation (3), which assumes the gap Δ in the spin-wave spectrum

$$\sigma_s(T) = \sigma_0[1 - CT^{3/2} \exp(-\Delta/k_B T)], \quad (3)$$

where k_B is the Boltzmann constant. Correlations coefficients $R > 0.99$ were obtained in all these cases. The “ χ^2 ” criterion was subsequently analyzed as the reliability criterion. A comparison of the data presented in Table I (taking into account the χ^2 criterion and thus the error in the determination of Δ) shows that preference should be given to the Dyson equation (2) for $x=0.8-1.0$, where χ^2 has a minimum and the error in the determination of Δ considerably exceeds this value. For $x=1.1$ and 1.2 , the situation is more complex: the values of χ^2 corresponding to the approximating functions (2) and (3) are similar for $x=1.2$ whereas, for $x=1.1$, they differ more than twofold. However, although the approximation of the experimental curves $\sigma_H(T)$ by the Dyson equation gives $R=0.99$ and the lowest values of χ^2 , it clearly does not “work” at low temperatures. At the same time, these sections of the curves $\sigma_H(T)$ up to $T=4.2$ K are accurately described by Eq. (3). The curves $\sigma_H(T)$ calculated using Eq. (2) for $x=0.8$ and using Eq. (3) for $x=1.1$ and 1.2 are shown by the solid lines in Fig. 3. Thus, if the experimental curves $\sigma_H(T)$ are to be described by a single functional dependence over the entire temperature range ($T=4.2-230$ K), Eq. (3) would be preferable for samples with $x=1.1$ and 1.2 , bearing in mind the low-temperature behavior, and Eq. (2) would be preferable for $x=0.8-1.0$.

Negative values were obtained for the gap parameter Δ , similar to the values of the freezing points T_f (see above). This agrees with the results of Refs. 15–17 where a gap of the type $\Delta = \mu(H - H_0)$ was considered in the excitation spectrum. Since in our experiments $H=5$ kOe, $\mu=5\mu_B$ for Fe^{3+} and $\mu H \sim 0.3$ K, the gap is almost completely determined by the internal field, i.e., $\Delta = -\mu H_0$. This type of gap is formed because disordering of the spins and frustration is conducive to the appearance of excitations in the magnetic subsystem, whereas the magnetic field suppresses these.¹⁷ Note that this type of gap was obtained independently of the calculated results¹⁴ using experimental data obtained by studying the specific heat in strong magnetic fields for reentrant and spin-glass samples of (Eu–Sr)S (Refs. 15 and 16).

Thus, the present results are broadly consistent with available data obtained for other frustrated systems.^{15–19}

In summation, the results of an investigation of the magnetic properties of dilute $\text{Li}_{0.5}\text{Fe}_{2.5-x}\text{Ga}_x\text{O}_4$ ($x=0.8-1.2$) spinels have shown that this range of concentrations of non-magnetic Ga^{3+} ions can be subdivided into regions having different degrees of saturation of the frustration. This factor not only determines the type of low-temperature states in zero magnetic field (ferrimagnet or ferrimagnetic spin glass) but also determines the temperature behavior of the high-field magnetization $\sigma_H(T)$ in fields exceeding the technical saturation field of the ferrimagnet.

It has been established that the curves $\sigma_H(T)$ for these frustrated ferrimagnets at temperatures between 4.2 and 230 K do not obey the Bloch $T^{3/2}$ law which is satisfied in the absence of frustrations (nonsubstituted Li spinel). If the collinear ferrimagnetic ordering is restored by application of an external field $H > H_s$, the curves $\sigma_H(T)$ may be described using the Dyson approximation, Eq. (2), which includes the terms $T^{3/2}$ and $T^{5/2}$. In this case the role of the $T^{5/2}$ term increases with increasing temperature. If local violations of the collinear ferrimagnetic structure and frustrations are conserved in the field $H > H_s$, the curves $\sigma_H(T)$ may also be described using the spin-wave approximation but with a gap $\Delta = \mu(H - H_0)$ in the excitation spectrum.

¹ K. P. Belov, *Ferrites in Strong Magnetic Fields* [in Russian], Nauka, Moscow, 1972, 200 pp.

² S. J. Poon and J. Durand, *Phys. Rev. B* **16**, 316 (1977).

³ N. N. Efimova, Yu. A. Popkov, and N. V. Tkachenko, *Zh. Éksp. Teor. Fiz.* **90**, 1413 (1986) [*Sov. Phys. JETP* **63**, 627 (1986)]; *Fiz. Nizk. Temp.* **16**, 1565 (1990) [*Sov. J. Low Temp. Phys.* **16**, 881 (1990)].

⁴ N. N. Efimova, Yu. A. Popkov, S. R. Kuferina, M. Khalibi, V. A. Pervakov, V. I. Ovcharenko, and N. Yu. Tyutryumova, *Fiz. Nizk. Temp.* **20**, 564 (1994) [*sic*].

⁵ K. Binder and A. P. Young, *Rev. Mod. Phys.* **58**, 801 (1986).

⁶ M. Benakli, H. Zheng, and M. Gabay, *Phys. Rev. B* **55**, 278 (1997).

⁷ A. E. Feiguin, C. J. Gazza, A. E. Trumper, and H. A. Ceccato, *Phys. Rev. B* **52**, 15 043 (1995).

⁸ D. J. Hudson, CERN Report [Geneva, 1964; Mir, Moscow, 1970, 296 pp.] (unpublished).

⁹ J. Villain, *Z. Phys. B* **33**, 31 (1979).

¹⁰ Yu. A. Izyumov and M. V. Medvedev, *Magnetically Ordered Crystals Containing Impurities* [Consultants Bureau, New York, 1973; Russ. original, Nauka, Moscow, 1970, 271 pp.].

¹¹ N. N. Efimova, Yu. A. Popkov, G. A. Takzei, A. B. Surzhenko, and A. M. Dvoeglazov, *Fiz. Tverd. Tela (St. Petersburg)* **36**, 490 (1994) [*Phys. Solid State* **36**, 271 (1994)].

¹² I. Ya. Korenblit and E. F. Shender, *Phys. Rev. B* **33**, 624 (1986).

¹³ Yu. A. Izyumov and R. P. Ozerov, *Magnetic Neutron Diffraction* [Plenum Press, New York, 1970; Russ. original, Nauka, Moscow, 1966, 532 pp.].

¹⁴ A. I. Akhiezer, V. G. Bar'yakhtar, and S. V. Peletminskii, *Spin Waves* [North-Holland, Amsterdam, 1968; Russ. original, Nauka, Moscow, 1967, 368 pp.].

¹⁵ H. v. Löhneysen, R. Berg, G. V. Lekomte, and W. Zinn, *Phys. Rev. B* **31**, 2920 (1985).

¹⁶ J. Woznitza, H. v. Löhneysen, W. Zinn, and U. Krey, *Phys. Rev. B* **33**, 3436 (1986).

¹⁷ U. Krey *J. Phys. (France) Lett.* **46**, Z-845 (1985).

¹⁸ G. Gavoille and J. Hubsch, *J. Phys. C* **49**, 1159 (1988).

¹⁹ P. L. Paulose and V. Nagarajan, *Phys. Rev. B* **54**, 14 934 (1996).

Dimer state in the two-dimensional anisotropic alternated-exchange Heisenberg model

S. S. Aplesnin

*L. V. Kirenskiĭ Institute of Physics, Siberian Branch of the Russian Academy of Sciences,
660036 Krasnoyarsk, Russia*

(Submitted January 2, 1998)

Fiz. Tverd. Tela (St. Petersburg) **40**, 1080–1085 (June 1998)

An analysis is made of the two-dimensional Heisenberg model with $S=1/2$, anisotropic exchange interaction between nearest neighbors, and alternating exchange in two directions, [100] and [010] (corresponding to condensation of the (π, π) mode) and in one direction [100] (corresponding to condensation of the $(\pi, 0)$ mode). The quantum Monte Carlo method is used to calculate the thermodynamic characteristics and the spin correlation functions which are used as the basis to determine the boundary of stability of an anisotropic antiferromagnetic with respect to alternation of exchange $\delta=(1-J^{x,y}/J^z)^{0.4}$ in the (π, π) model and $\delta=(1-J^{x,y}/J^z)^{0.31}$ in the $(\pi, 0)$ model. In the $(\pi, 0)$ model a disordered quantum state exists in the range $(1-J^{x,y}/J^z)^{0.31} < \delta < (0.3-0.35)$. The energy $(E-0.68)=0.36\delta^{1.80(6)}$ and $0.21\delta^{2.0(5)}$, the energy gap between the ground and excited states $H_c(\delta)=1.96\delta^{2.1(1)}$, $1.8(1)$ $(\delta-0.35(3))^{0.67(2)}$ were determined as a function of the alternation of exchange in the (π, π) - and $(\pi, 0)$ models, respectively. © 1998 American Institute of Physics. [S1063-7834(98)02506-4]

Dimerization of the lattice caused by electron–phonon interaction and leading to a spin–Peierls transition in one-dimensional systems has been analyzed in detail in the literature.^{1,2} Following the discovery of high-temperature superconductors, the Peierls instability was investigated using the two-dimensional half-filled Hubbard model.^{3,4} In the strong-attraction limit $(U/t) \gg 1$ of the adiabatic approximation, an exact diagonalization method⁵ was used to analyze the alternating-exchange model which corresponds to the (π, π) - and $(\pi, 0)$ phonon modes. According to these calculations, dimerization takes place in the [100] direction.

The region of stability of antiferromagnetic ordering with respect to exchange alternation was calculated by numerically solving a system of equations for the spin operators in the Schwinger representation using a 40×40 lattice⁶ in the inhomogeneous Hartree–Fock approximation.^{7,8} In all cases, the long-range antiferromagnetic order disappears for a critical dimerization of the lattice, which corresponds to a 50% change in volume, when the alternation is $\sim 0.5J$. For quasi-two-dimensional magnets CuGeO_3 (Ref. 9) and $\text{Cs}_3\text{Cr}_2\text{Br}_9$ (Ref. 10), in which a transition takes place to the dimer state, these estimates are not realistic. Possibly because of these high estimates of exchange alternation, interest in studies of two-dimensional alternating exchange models has declined.

Three problems are solved here. The first involves determining which phonon mode, (π, π) or $(\pi, 0)$, gives the largest magnetic energy per alternated bond. The second involves studying the stability of the antiferromagnetic ordering relative to exchange alternation as a function of the volume anisotropy. The third involves identifying whether a disordered quantum state exists or whether the antiferromagnet is converted directly to the dimer state as the exchange

alternation parameter increases. A quantum Monte Carlo method based on a trajectory algorithm is used to solve these problems.¹¹ The basic idea of the algorithm is to transform the quantum D -dimensional problem to a classical $D+1$ -dimensional one by introducing “time” cutoffs in the imaginary time space $0 < \tau < 1/T$ and implementing a Monte Carlo procedure in the “imaginary time–coordinate” space.

MODEL AND GROUND STATE OF THE TWO-DIMENSIONAL HEISENBERG MODEL WITH ALTERNATING EXCHANGE

We consider a two-dimensional lattice with the spins $S=1/2$ localized at lattice sites. Exchange alternation will be considered using two models. In the first case, alternation takes place in one of the directions of the lattice (for example, [100]) and according to the notation used in Ref. 5, is caused by condensation of the $(\pi, 0)$ phonon mode. In the second case, alternation takes place in two directions and is caused by condensation of the (π, π) mode, i.e., $J_{l,l+1}=J_0 + \delta$, $J_{l+1,l+2}=J_0 - \delta$ (Fig. 1). This exchange inhomogeneity may be caused by distortion of the lattice $J_{l,l+1}^c - J_{l+1,l+2}^c = \lambda'(u_l - u_{l+1})$, where u is the displacement of an atom from the equilibrium position, or by anharmonicity of the vibrations. The Hamiltonian in the $(\pi, 0)$ model has the form

$$H = -\frac{1}{2} \sum_{i,j=1}^L \{J_{i,j}^{z(010)} S_i^z S_j^z + J_{i,j}^{x,y(010)} (S_i^+ S_j^- + S_i^- S_j^+) / 2\} \\ \times \frac{1}{2} \sum_{i,j=1}^L \{J_{i,j}^{z(100)} + (-1)^j \delta^z\} S_i^z S_j^z + (J_{i,j}^{x,y(100)} \\ + (-1)^j \delta^{x,y}) (S_i^+ S_j^- + S_i^- S_j^+) / 2\} - \sum_{i=1}^N h^z S_i^z,$$

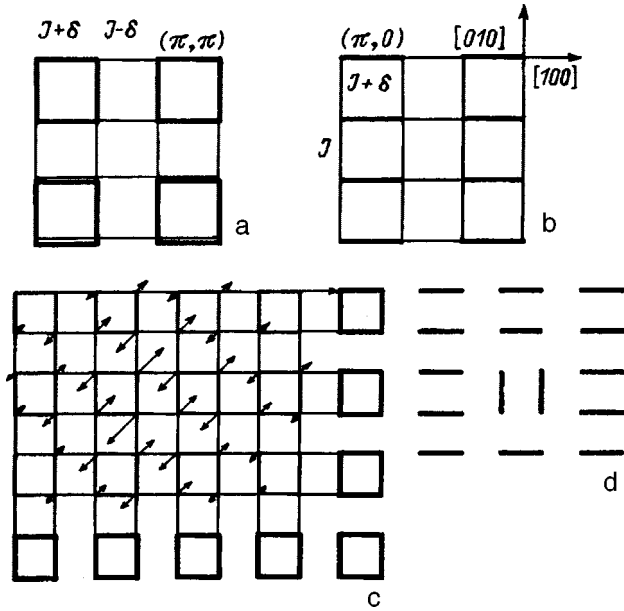


FIG. 1. Distribution of bonds on the lattice in two models: (π, π) (a) and $(\pi, 0)$ (b), the arrows indicate a soliton (c), and the line segments corresponds to spin pairs in the singlet state — dimers (d).

and in the (π, π) model

$$H = -\frac{1}{2} \sum_{i,j=1}^L \{ (J_{i,j}^z + (-1)^j \delta^z) S_i^z S_j^z + (J_{i,j}^{x,y} + (-1)^j \delta^{x,y}) \times (S_i^+ S_j^- + S_i^- S_j^+) / 2 \} - \sum_{i=1}^N h^z S_i^z,$$

where $J^{z,x,y} < 0$ is the anisotropic interaction, $J^z > J^{x,y}$, $\Delta = 1 - J^{x,y}/J^z$, $\delta^{z(x)}$ is the exchange alternation parameter, $H = h^z/J$ is the external magnetic field, and L is the linear dimension of the lattice ($N = L \times L$) (Fig. 1a).

The algorithm and Monte Carlo method were described in detail in Ref. 12. The Hamiltonian is divided into clusters of four spins per square whose commutation is taken into account using the Trotter equation. Here periodic boundary conditions in the Trotter direction and along the lattice are used in the Monte Carlo procedure. The linear dimension of the lattice is $L = 40, 48, 64$ and $m = 16, 24, 32$. The number of Monte Carlo steps per spin varied between 3000 and 10 000. One Monte Carlo step is determined by the flip of all spins on a $L \times L \times 4m$ lattice.

We shall determine the order parameter of the dimers from the four-spin correlation function $\langle S_0^z S_1^z S_r^z S_{r+1}^z \rangle$ whose dependence on distance is oscillatory and has a difference between the minimum and the maximum of $\langle S_0^z S_1^z S_r^z S_{r+1}^z \rangle - \langle S_0^z S_1^z S_{r+1}^z S_{r+2}^z \rangle$. We calculate the pairwise spin-spin correlation functions for the longitudinal and transverse components of the spins, between which a relation must be satisfied at distance $r = 1$ to establish a singlet state.

We determine the region of stability of the antiferromagnetic and dimer states from the spin-spin correlation functions, the dimerization parameter, and the correlation radius calculated for three temperatures $T/J = 0.1, 0.15,$ and 0.2 as a function of the exchange alternation parameter for various

values of the exchange anisotropy $\Delta = 0, 0.01, 0.05, 0.1, 0.15, 0.2, 0.25, 0.3, 0.4,$ and 0.5 . The critical exchange alternation δ_c for which the long-range antiferromagnetic order disappears, is determined from the spin-spin correlation functions $\langle S_0^z S_r^z \rangle \rightarrow 0$ at the distance $r = L/2$ calculated for different lattice dimensions.

Figure 2 gives the spin correlation functions for three values of the exchange anisotropy parameter $\Delta = 0, 0.05, 0.25$, calculated using the two models of exchange alternation. The exchange alternation corresponding to the point of inflection of the dimerization parameter $q(\delta)$ and the formation of a dimer state coincides with the critical value δ_c for which antiferromagnetic order is impaired in both the (π, π) and $(\pi, 0)$ models for the exchange anisotropy $\Delta > 0.02$. For the isotropic Heisenberg model, the dependence $q(\delta)$ is linear and passes through the origin for (π, π) dimerization (Fig. 2b) and intercepts the δ axis at $\delta_c \approx 0.3$ for $(\pi, 0)$ (Fig. 2a). The spin correlation functions between the nearest neighbors along the longitudinal and transverse components of the spin do not vary significantly as the exchange alternation increases for (π, π) and $(\pi, 0)$ dimerization in the $[100]$ direction since an isotropic two-dimensional antiferromagnet is in the singlet state.^{13,14} In an anisotropic antiferromagnet in the direction of exchange alternation the correlation function along the transverse components increases, which also indicates dimer formation, whereas in the $[010]$ direction in the $(\pi, 0)$ direction, $\langle S_0^+ S_1^- \rangle$ decreases with increasing δ .

The correlation radius in the dimer state diverges following a power law as the critical value δ_c is approached (Figs. 2c and 2d). For (π, π) dimerization the relation $\xi = 1/(\delta - \delta_c)^\beta$ is satisfied, where the exponent decreases with increasing exchange anisotropy. In the isotropic case, the correlation radius is well approximated by $\xi = 1/\delta^2$ ⁽¹⁵⁾ in the (π, π) model and by $\xi = 4.5/(\delta - 0.33(3))^{0.70(4)}$ in the $(\pi, 0)$ model with the critical value $\delta_c = 0.33(3)$. The corresponding interpolated dependences are given by the dashed lines in Figs. 2c and 2d, and to within the calculation error of $\sim 10\%$ do not depend on the lattice dimensions as shown in the figure for $L = 48$ and 64 . The calculated dependences $q(\delta)$, $\xi(\delta)$, and $\langle S_0^{z,+} S_1^{z,-} \rangle(\delta)$ indicate that alternation of exchange in two directions in the two-dimensional Heisenberg model is accompanied by the formation of a dimer state and an anisotropic antiferromagnetic is converted to the dimer state at a certain critical value of the exchange alternation parameter. A correlation in terms of longitudinal spin components exists between the dimers in a region of dimensions $\sim \xi^2$, shown in Fig. 1c. In the $(\pi, 0)$ model an ordered dimer state is formed at the critical value $\delta_c = 0.3-0.35$. The energy of an isolated dimer is $E/J = 3/2(1 + \delta)$. When two dimers commute in the $[010]$ direction, as shown in Fig. 1d, the energy is reduced by $\Delta E/J = 3\delta$. If this energy is lower than the triplet excitation energy $\Delta E/J = 1$, then for $\delta < \delta_c = 1/3$ no ordered dimer state exists. In the $(\pi, 0)$ model the correlation radius is anisotropic and has a maximum in the $[100]$ direction.

The energy calculated by the Monte Carlo method for the two models, (π, π) and $(\pi, 0)$, and different exchange anisotropies is accurately fitted by the power dependence $(E - E(0)) = A\delta^\alpha$, where the exponent α increases with in-

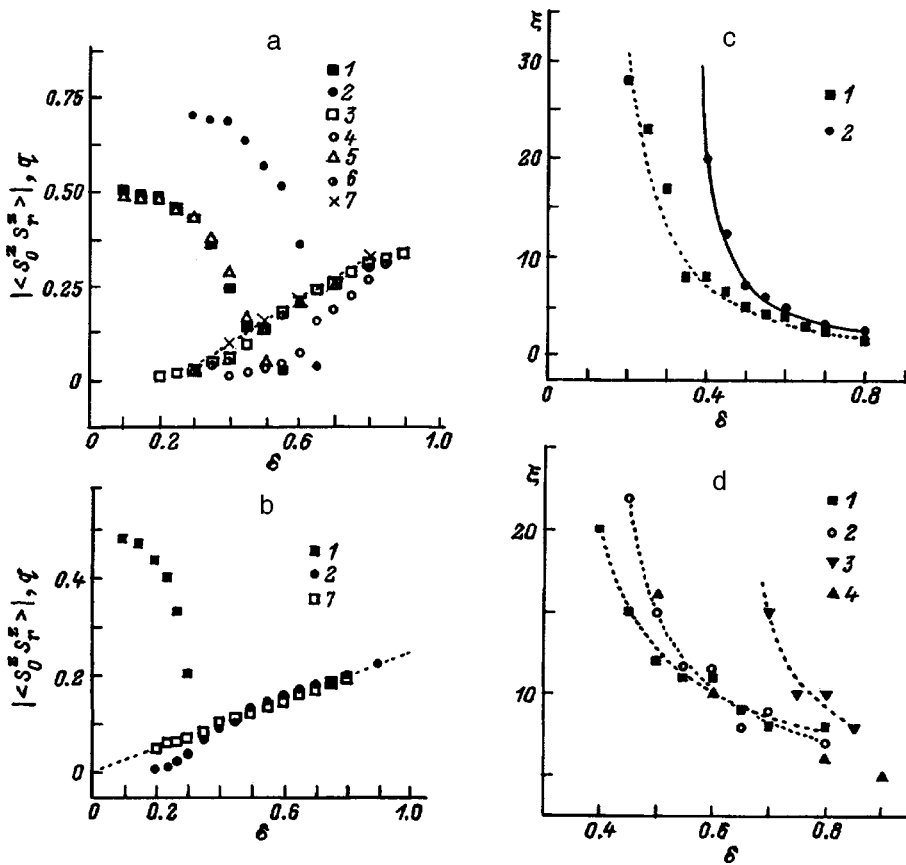


FIG. 2. Correlation function at the distance $r=22$ (5, 6), 30 (1), the dimerization parameter q (2–4, 7) for the exchange anisotropy $\Delta=0$ (7), 0.05 (1–3, 5), 0.25 (4, 6) on a lattice $L=64$ (1, 2, 7), 48 (3, 5, 6), and the correlation radius ξ for $\Delta=0$ (1), 0.05 (2, 4), 0.25 (3) on 64×64 (1, 2) and 48×48 (3, 4) lattices as a function of the exchange alternation in the $(\pi, 0)$ (a, c) and (π, π) (b, d) models.

creasing exchange anisotropy. In the isotropic limit in the (π, π) and $(\pi, 0)$ models, the interpolated dependences respectively have the form $(E - 0.68) = 0.36\delta^{1.80(6)}$ and $0.21\delta^{2.0(5)}$. For $\delta \approx 0.50(4)$ the energies calculated using the two dimerization models and normalized to the number of alternated bonds are the same. For $\delta < 0.50(4)$, the dimer state energy normalized to the number of alternated bonds has a higher absolute value in the (π, π) model compared to the $(\pi, 0)$ model, and for $\delta > 0.50(4)$ we find $E(\pi, \pi) < E(\pi, 0)$. In a spin-Peierls transition, the increase in the magnetic energy achieved by dimerization should exceed the energy loss in the elastic system $0.36\delta^{1.80(6)} \geq Ku^2/2$ or $\lambda^{1.8} \geq 1.4Ku^{0.2}$, where λ is the spin-phonon interaction constant, K is the modulus of elasticity, $u = |u_i - u_j|$ is the change in the distance between nearest neighbors, i.e., as a result of interaction between the elastic and magnetic subsystems for $\delta < 0.5J$, dimerization of the magnetic structure takes place preferentially in two directions. For large spin-phonon interaction constants, dimers may be formed along one of the translation vectors of the lattice. Calculations made for small lattices⁵ indicate that $(\pi, 0)$ dimerization predominates. This may be caused by the finite dimensions of the 4×4 lattice. For example, the linear dimension of the lattice is equal to the correlation radius for $\delta = 0.7$, and for this exchange alternation the Monte Carlo calculations give $(\pi, 0)$ dimerization.

The boundary of stability of long-range antiferromagnetic order is accurately approximated by the power dependence $\delta = (1 - J^{x,y}/J^z)^{0.4}$ in the (π, π) model and $\delta = (1 - J^{x,y}/J^z)^{0.31}$ in the $(\pi, 0)$ model a dis-

ordered quantum state exists in the range of parameters $\delta < \delta_c = 0.27 - 0.33$ and $\Delta \leq 0.02$.

2. DETERMINATION OF THE SEQUENCE OF DIMER STATE-QUANTUM DISORDERED STATE-PARAMAGNETIC TRANSITIONS

Calculations of the specific heat and susceptibility as a function of temperature reveal two critical regions and two characteristic transition temperatures: T_{c1} and T_{c2} . Below T_{c1} the temperature dependence of the specific heat and the susceptibility is accurately approximated by an exponential dependence which indicates that there is an energy gap in the excitation spectrum. In the range $T_{c1} < T < T_{c2}$ the behavior of $C(T)$ obeys a power law. At low temperatures $T < T_{c1}$ an ordered dimer state is conserved in both models. The dimerization parameter q , the correlation radius, and the correlation functions along the longitudinal spin components at distance $r=1$ depend fairly weakly on temperature for $T < T_{c1}$ (Fig. 3). This is because the excitations are spinons (a concept introduced by Anderson¹³), i.e., the dimer breaks down into two spins separated by a certain distance. This type of excitation may be represented as a soliton, as shown in Fig. 1c. At T_{c1} soliton percolation occurs and in the range $T_{c1} < T < T_{c2}$ a soliton gas forms. With increasing temperature, the soliton density increases, the average distance between them decreases, and the correlation radius is therefore reduced. Near T_{c2} the temperature dependence of the correlation radius $\xi(T)$ may change from exponential to a power

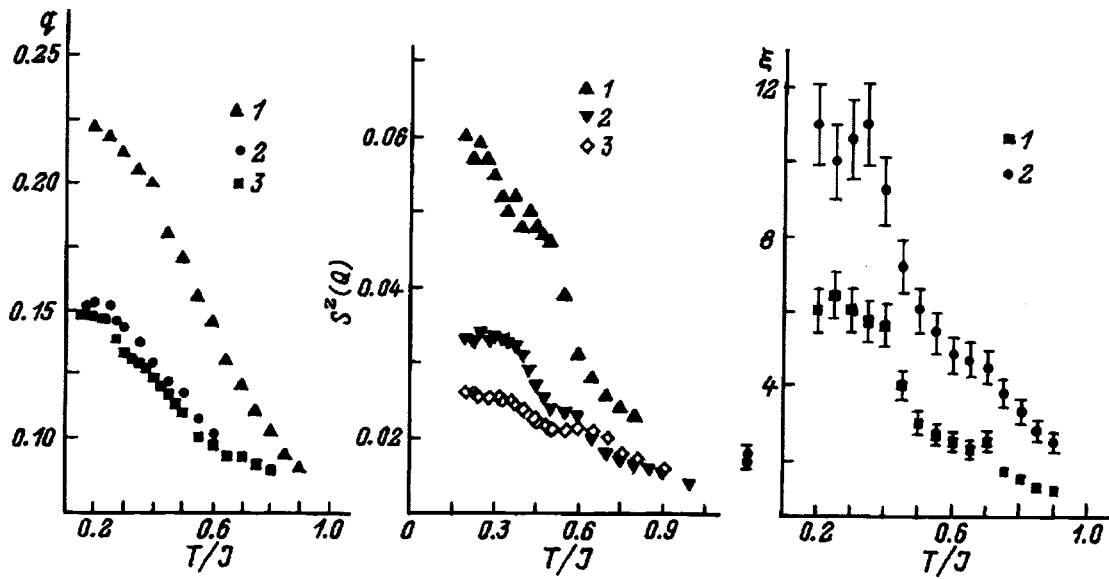


FIG. 3. Temperature dependences of the dimerization parameter q in the [100] direction, the correlation radius ξ in the [010] direction for $\Delta=0.05$, $\delta=0.65$ (1), $\Delta=0.0$, $\delta=0.5$ (2, 3) for $L=64$ (1, 2), 48 (3) and the static magnetic structure factor $S^z(Q)$ for $Q=\pi$ in the [010] (1, 3), and [100] (1, 2) direction for $\Delta=0.05$, $\delta=0.65$ (2, 3), and $\Delta=0.0$, $\delta=0.35$ (1) in the dimer state for the $(\pi, 0)$ model.

dependence (Fig. 3). The correlation function $\langle S_0^{z+} S_1^{z-} \rangle$, and the static magnetic structure factor $S^z(Q)$ at $Q=\pi$ have two points of inflection caused by a transition from the dimer state to a disordered quantum state having short range dimer order and topological excitations (solitons) (QD) and by a

quantum disorder-paramagnetic (QD-PM) transition. For $\delta=0.3$ in the $(\pi, 0)$ model, $S^z(Q)$ has a single point of inflection at T_{c2} (Fig. 3).

The dependence of the DS-QD transition temperature is accurately described by the power law $T_{c1}=0.7(\delta$

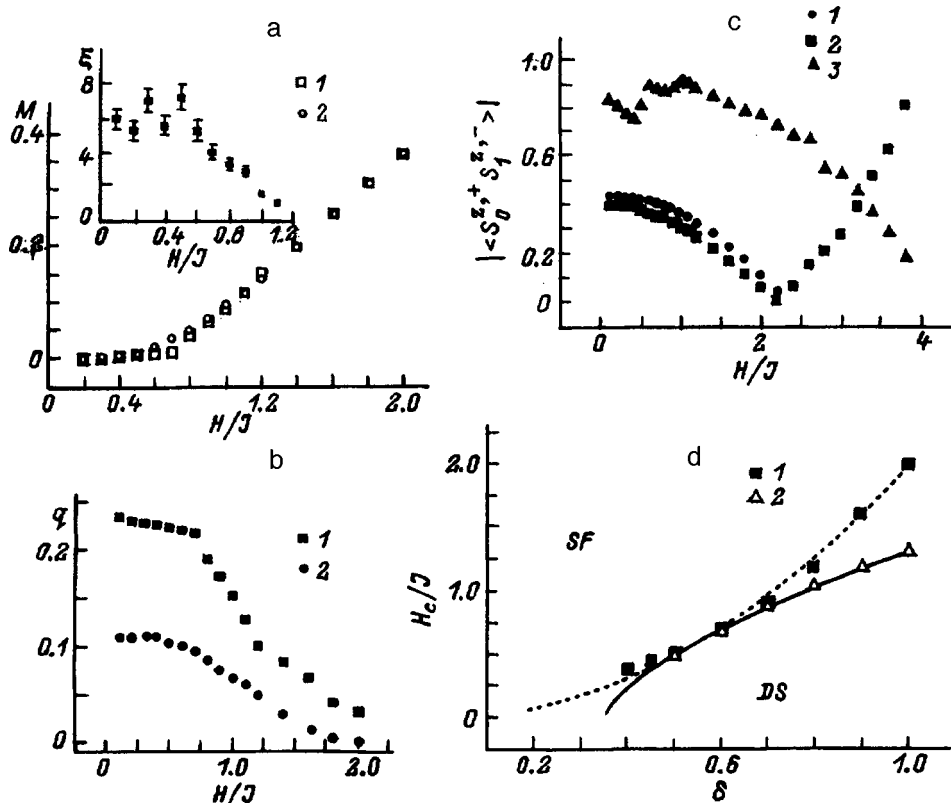


FIG. 4. Magnetization M (a), correlation radius ξ (inset), dimerization parameter q (b), and spin-spin correlation function at $r=1$ along the longitudinal (z) (1, 2) and transverse (+, -) (3) components of the spin $\langle S_0^{z+} S_1^{z-} \rangle$ in the $(\pi, 0)$ model, $\Delta=0.05$, $\delta=0.65$ (1) and in the (π, π) model, $\Delta=0.0$, $\delta=0.45$ (2, 3) (c) as a function of the external field. d — Phase diagram of the dimer state (DS), the spin flip phase (SF) on the field-exchange alternation plane in the (π, π) (1) and $(\pi, 0)$ (2) models for isotropic exchange $\Delta=0$.

$-\delta_c)^{0.50(4)}$ in the $(\pi,0)$ model, where the parameter δ_c shows good agreement with the critical values of exchange alternation in the isotropic case $\delta_c=0.33(2)$. For (π,π) alternation of exchange $T_{c1}(\delta)=1.10(7)\delta^{2.0(7)}$.

The energy gap between the ground and excited states is determined from the dependence of the magnetization on the external magnetic field perpendicular to the lattice plane. For example, for the critical field H_c the magnetization is $M \neq 0$, and the correlation radius and dimerization parameter decrease abruptly with increasing field in both models (Fig. 4). The correlation functions for the transverse components vary negligibly. Here we can also identify a range of fields $H_c < H < H^*$, in which an inhomogeneous magnetic state exists which disappears when $\xi \rightarrow 0$. The dependence $M(H)$ is linear in this range of fields. In fields $H > H^*$ a classical spin flip state is formed. Figure 4 gives the critical fields as a function of the exchange alternation for the two models in the isotropic case. In the (π,π) and $(\pi,0)$ models these dependences are power laws $H_c=1.96\delta^{2.0(1)}$ and $H_c=1.8(1)(\delta-0.35(3))^{0.67(2)}$, respectively. When exchange alternates in two directions, the ratio $H_c/T_{c1} \cong 1.78$ does not depend on the exchange alternation and in the $(\pi,0)$ model a dependence on δ is observed which can be approximately estimated as $H_c/T_{c1} \sim (\delta-0.34)^{0.17}$. Thus, this is related to the anisotropy of the correlation radius. As δ increases, the magnetic quasi-one-dimensionality increases and the density of states of the singlet and triplet excitations becomes redistributed, which is observed as a temperature shift of the maximum specific heat and susceptibility. In the two-dimensional Heisenberg model we find $T_{C_{\max}}/T_{\chi_{\max}} \approx 0.5$, and in the one-dimensional model $T_{C_{\max}}/T_{\chi_{\max}} \approx 0.76$. In the range $\delta \approx 0.5$, where the dimer state energies in the two models are the same, the energy gaps are also the same.

Thus, asymptotic dependences on the exchange alternation of the energies $(E-0.68)=0.36\delta^{1.80(6)}$ and $0.21\delta^{2.0(5)}$,

and the energy gap between the ground and triplet states $H_c(\delta)=1.96\delta^{2.0(1)}$ and $1.8(1)(\delta-0.35(3))^{0.67(2)}$ were obtained for exchange alternation along two translation vectors or along one of these. The boundaries of stability of an anisotropic antiferromagnet relative to exchange alternation $\delta=(1-J^{x,y}/J^z)^{0.4}$ in the (π,π) model and $\delta=(1-J^{x,y}/J^z)^{0.31}$ in the $(\pi,0)$ model were determined. The energy per alternated bond has a higher absolute value in the (π,π) model compared to the $(\pi,0)$ model for $\delta < 0.5$. When exchange alternates along one of the translation vectors, an anisotropic antiferromagnet with the anisotropy $\Delta < 0.02$ is transferred to the dimer state via a disordered quantum state. This state exists at temperatures between DS and PM.

¹L. N. Bulaevskii, A. I. Buzdin, and D. I. Khomskii, *Solid State Commun.* **27**, 5 (1978).

²M. C. Cross and D. S. Fisher, *Phys. Rev. B* **19**, 402 (1979).

³S. A. Kivelson, D. S. Rokhsar, and J. P. Sethna, *Phys. Rev. B* **35**, 8865 (1987).

⁴J. E. Hirsch, *Phys. Rev. B* **35**, 8726 (1987).

⁵S. Tang and J. E. Hirsch, *Phys. Rev. B* **37**, 9546 (1988).

⁶A. Feiguin, C. J. Gazza, A. E. Trumper, and H. A. Ceccatto, *J. Phys. Condens. Matter* **6**, L503 (1994).

⁷K. Yonemitsu, A. R. Bishop, and J. Lorenzana, *Phys. Rev. B* **47**, 8065 (1993).

⁸N. Read and S. Sachdev, *Phys. Rev. B* **42**, 4568 (1990).

⁹M. Nishi, O. Fujita, and J. Akimitsu. *Tech. Rep. ISSP Ser. A* **2759**, 1 (1993).

¹⁰J. R. Fletcher, S. S. Kazmi, K. J. Maxwell, and J. R. Owers-Bradley, *Physica B* **165-166**, 173 (1990).

¹¹H. Raedt and A. Lagendijk, *Phys. Rep.* **127**, 233 (1985).

¹²S. S. Aplesnin, *Fiz. Tverd. Tela (St. Petersburg)* **38**, 1868 (1996) [*Phys. Solid State* **38**, 1031 (1996)].

¹³P. W. Anderson, *Mater. Res. Bull.* **8**, 153 (1973).

¹⁴P. de Vries and H. De Raedt, *Phys. Rev. B* **47**, 7929 (1993).

Translated by R. M. Durham

Unusual electromechanical effects in glycine

V. V. Lemanov and S. N. Popov

A. F. Ioffe Physicotechnical Institute, Russian Academy of Sciences, 194021 St. Petersburg, Russia
(Submitted February 2, 1998)

Fiz. Tverd. Tela (St. Petersburg) **40**, 1086–1089 (June 1998)

Unusual piezoresponse signals have been observed in glycine aminoacid powder at a frequency near 10 MHz, which exhibited a regular pattern in time determined by a periodic phase variation in the elastic vibrations of individual powder particles. This phenomenon results from the formation of spatial structures in glycine powder under the action of a strong rf field.

© 1998 American Institute of Physics. [S1063-7834(98)02606-9]

Glycine, $\text{NH}_2\text{CH}_2\text{COOH}$, is the simplest of the 20 protein aminoacids. Crystalline glycine exists in three modifications, viz. α , with point group C_{2h} , β , with point group C_2 , and γ , with C_3 symmetry.¹⁻⁴ Thus α glycine crystals are centrosymmetric and do not exhibit piezoeffect, whereas the β and γ glycines have polar symmetry groups, i.e., are piezoelectrics, pyroelectrics, and can in principle, be ferroelectrics as well.

The objective of this work was to study the electromechanical effects associated with piezoelectric excitation of elastic vibrations in glycine powder. A Model IS-2 nuclear quadrupole resonance spectrometer was used. The signals were measured with an AI-1024 multichannel analyzer.

The glass ampoule about 1.5 cm^3 in volume containing glycine powder was placed into the capacitor of a circuit (Fig. 1) fed by 1–6- μs long rf pulses ($\sim 10 \text{ MHz}$), with a pulse repetition frequency of 40 Hz. The maximum voltage amplitude across the circuit was 6 kV, which corresponded to a field of about 5 kV/cm in the sample.

In such experiments, each rf pulse is accompanied in a piezoelectric powder sample by the so-called ringing, whose duration is determined by the damping time of elastic vibrations in the powder. The glycine powder was found to exhibit

a very specific piezoresponse (Fig. 2c) different from the conventional ringing (Fig. 2b). The piezoresponse rf signal produced in glycine powder exhibits a regular amplitude

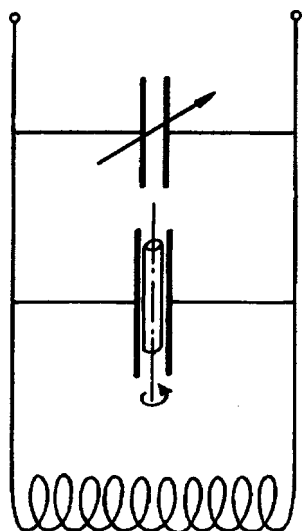


FIG. 1. Capacitor with sample in the oscillator circuit.

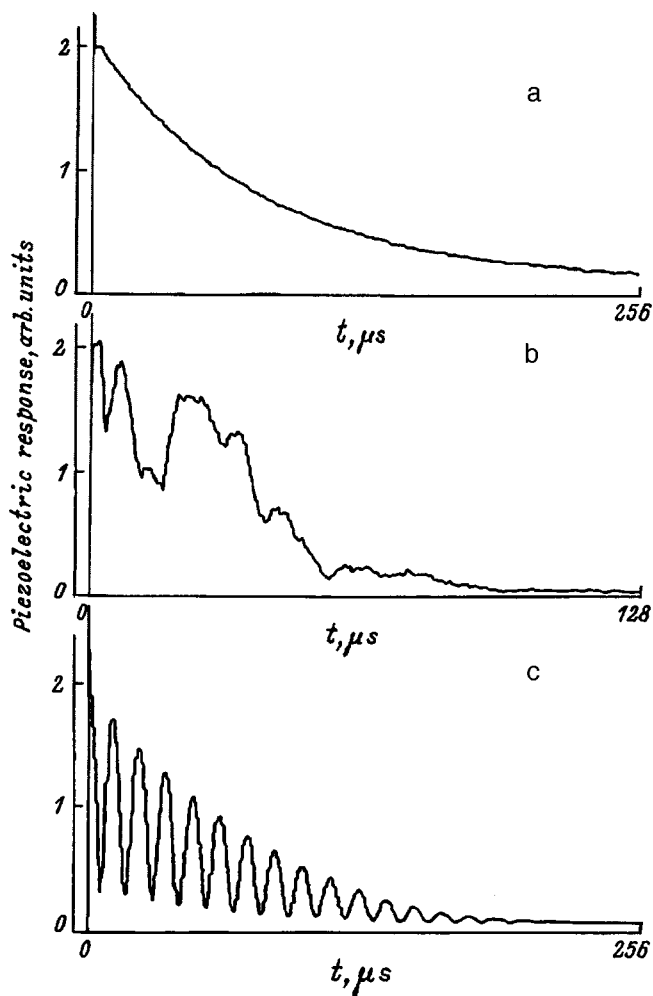


FIG. 2. Piezoresponse signals of a powder sample (the ringing of powder after termination of a short rf pulse). (a) idealized signal of a sample consisting of particles identical in size, shape, and orientation; (b) signal obtained on *L* alanine powder, a signal typical of conventional piezopowder samples. RF pulse length 4.5 μs , carrier frequency 9.52 MHz; (c) signal from a glycine powder. Pulse duration 4.1 μs , carrier frequency 10.41 MHz. Modulation period $T = 12 \mu\text{s}$.

modulation, whose period remains constant up to complete damping of the signal. Consider in more detail the excitation and detection of the piezoresponse signals. Let the capacitor of the circuit contain one powder particle. Inverse piezoeffect induced by the electric field of the rf pulse excites elastic vibrations in the particle of the same frequency (about 10 MHz in our case), with the excitation being most efficient under resonance, where the particle size is equal to one half the wavelength of the elastic vibrations. After termination of the rf pulse, the particle continues to vibrate during the time determined by the damping time of elastic vibrations in the given material. For soft crystals like glycine, the more or less typical damping rate for a 10-MHz frequency is of the order of 0.1 dB/ μ s, which yields a particle damping time of the order of 100 μ s (the time in which the vibration amplitude decreases 2.7 times). The elastic vibrations of the particle are converted by direct piezoeffect to an electric signal of the same frequency, which is detected by the measurement system. The resultant signal visualized on the oscillograph screen will be an exponentially decaying videosignal about 100 μ s long (Fig. 2a). In actual fact, the sample consists of a very large number of particles (10^5 – 10^6), but assuming them to be of the same size, shape, and oriented similarly relative to the electric field, all particles will vibrate in phase, so that the detected signal will have the same shape as that due to one particle. A real powder sample contains particles differing in size, shape, and orientation, and this should affect the shape of the detected signal. After termination of the rf pulse, the elastic vibrations of the particles will start to spread in phase, and the vibrations will assume opposite phase in a time $T=1/(2\Delta f)$, where Δf is the oscillator frequency band, which depends on pulse length and is about 500 kHz in our case. This is the minimum dephasing time, because the maximum difference in particle vibration frequencies is Δf . The dephasing time for particle vibrations with a smaller frequency difference will be longer (up to the damping time). All this should result in irregular signal variations. Such irregular piezoresponse signals are observed in powders of the conventional piezoelectrics SiO_2 , $\text{Bi}_{12}\text{SiO}_{20}$, KDP, and others. Figure 2b illustrates a piezoresponse signal obtained from a powder sample of another aminoacid, *L* alanine, $\text{NH}_2\text{CHCH}_3\text{COOH}$ (symmetry group D_2). The signal is indeed seen to have an irregular structure.

Figure 2c presents a piezoresponse signal of glycine powder. One clearly sees a regular structure, namely, periodic oscillations in signal amplitude with a period of about 12 μ s superimposed on the overall exponential decay of signal amplitude with a time constant of about 60 μ s. Experiments show that the oscillation period may differ from about 5 to 50 μ s (Figs. 3 and 4). These signals were obtained for a powder of the 70–100 μ m fraction separated by passing it through calibrated screens, but the starting, unscreened powder produced signals of approximately the same shape. It is essential that in order for such a regular signal to appear, one had to subject the sample sometimes to a very short (and difficult to control) action of the rf pulse. It was also found that if the powder in the ampoule was packed fairly densely, it was virtually impossible to produce such regular signals.

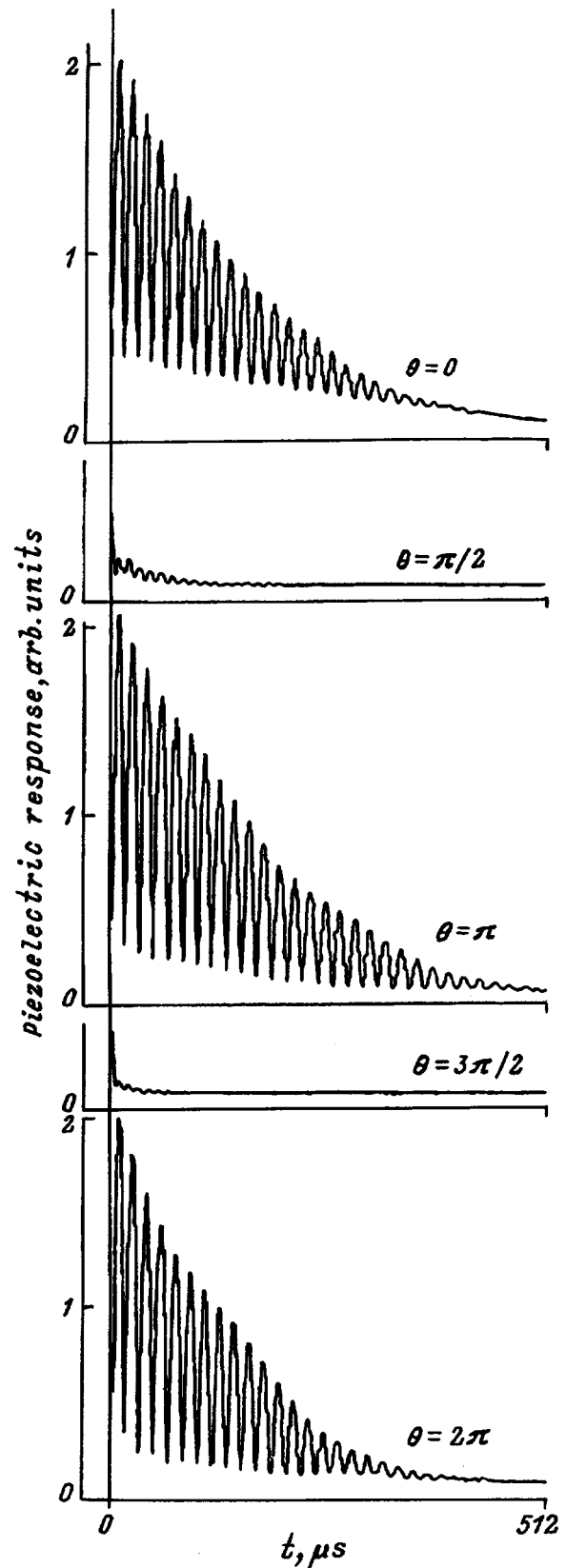


FIG. 3. Angular dependence of glycine-powder piezoresponse signal. Pulse duration 6.4 μ s, carrier frequency 9.45 MHz. Modulation period $T=17 \mu$ s.

This suggested that strong rf pulses create some ordered spatial structures in the powder, and it is these structures that are responsible for signals with a regular behavior in time. To check this assumption, the following experiment was carried

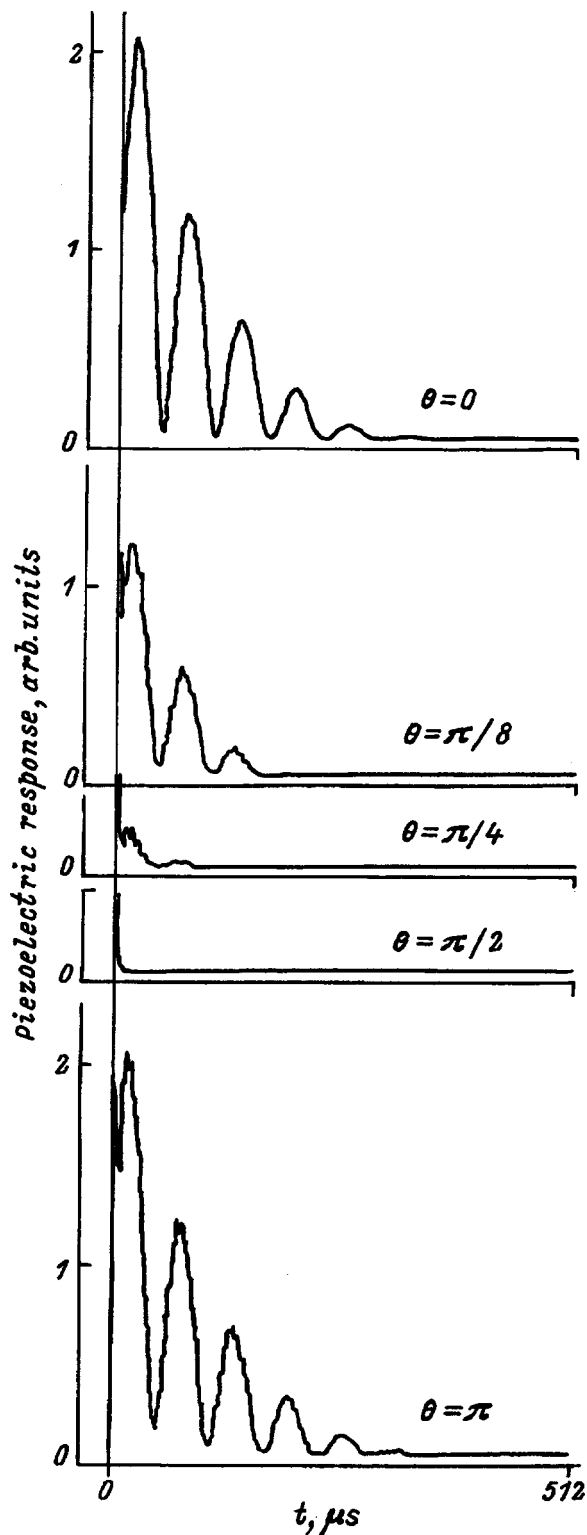


FIG. 4. Angular dependence of glycine-powder piezoresponse signal. Pulse duration $4.4 \mu\text{s}$, carrier frequency 9.693 MHz . Modulation period $T=60 \mu\text{s}$.

out. After a regular signal has been detected (Fig. 3, $\theta=0$), the ampoule with the powder was turned about its vertical axis (Fig. 1) perpendicular to the direction of the rf electric field in the capacitor. As seen from Fig. 3, the signal practically disappeared after rotation through the angles $\theta=\pi/2$ and $3\pi/2$ with respect to the original position, whereas when

turned through $\theta=\pi$ and 2π the signal recovered to approximately the same level. It should be stressed that the orientation of the ampoule is determined by its original position relative to the rf electric field; indeed, after shaking the ampoule (i.e., destroying the structure) in the $\theta=\pi/2$ position, one could obtain a strong signal in this position again and observe subsequently the same pattern of signal variation with the angle θ , as in Fig. 3, but with a shift in θ by $\pi/2$.

Figure 4 presents a piezoresponse signal of the same sample for a somewhat different carrier frequency and pulse duration. While the signal modulation period is in this case longer than that in Fig. 3, the angular relation remains the same.

The angular pattern of the signal in Figs. 3 and 4 supports the hypothesis that a strong rf field induces the formation of some spatial structures in a powder, and that it is these structures that are responsible for the observed regular signals.

Let us discuss now the results obtained. Because the piezoeffect is observed in a glycine powder, the modification involved is either β or γ . According to published data, the β phase is unstable in air, i.e., our powder contains apparently the γ phase as well (it doesn't matter for our further reasoning whether the phase involved is β or γ , the only important thing is the existence of the piezoeffect). Note that glycine single crystals grown from an aqueous solution of the same powder do not exhibit the piezoelectric effect, which means that they consist of the α centrosymmetric modification with point group C_{2h} .⁵ All this permits an assumption that the starting glycine powder is a mixture of two phases, the nonpiezoelectric α and piezoelectric β or γ (or both).

In this case the following mechanism of the unusual electromechanical effects in glycine can be proposed. The strong electric field of the rf pulse produces alignment of the piezoelectric (polar) phase particles in such a way that their symmetry axes become parallel to the electric field direction, i.e., perpendicular to the plane capacitor plates. This alignment can be related to interaction of the electric field both with the spontaneous electric polarization directed along the symmetry axis and with the polarization induced by the electric field along this axis. The interaction of polarized particles results in particles of the nonpiezoelectric phase sticking to the piezoelectric ones. Water molecules adsorbed on the surface of particles (glycine is fairly hygroscopic) can also play a certain role in these sticking processes. As a result, the sample acquires a structure made up of field-oriented particles of the piezoelectric phase with nonpiezoelectric particles stuck to them. This structure turns out to be fairly stable; indeed, when the ampoule with the powder is turned, the structure turns with it; application of electric field does not result in rearrangement of the previously formed structure; and the structure breaks down only under mechanical action (shaking of the ampoule).

Now how can this structure produce a regular signal? A piezoelectric particle with particles of the nonpiezoelectric phase (this can also be only one such particle) stuck to it may be considered as a system of weakly coupled oscillators. Elastic vibrations are excited by an rf pulse only in the pi-

ezoparticle (and it is this particle that produces the piezoelectric response), and they are transmitted through the weak coupling to the other particle(s). The energy flux between the particles will be determined by the vibration phase difference $\Delta\varphi$ and will be proportional to $\sin\Delta\varphi = \sin(\Delta\omega t)$, where $\Delta\omega$ is the difference between the resonant frequencies of the piezo- and nonpiezoparticles. There are many analogs of such weakly coupled systems, from mechanical pendulums to Josephson junctions. For particles of the same size, the difference in frequencies will be determined only by that in the velocity of elastic waves, $\Delta\omega/\omega = \Delta v/v$. The time in which the phase difference changes by π is $T = \pi/\Delta\omega = 1/[2f(\Delta v/v)]$. Assuming the relative difference in velocities between the piezoelectric and nonpiezoelectric phases to be 0.5% (a more or less typical value for second-order phase transitions, or transitions of first order not very far from the

tricritical point), we obtain $T = 10\mu\text{s}$ for $f = 10\text{ MHz}$, which agrees in order of magnitude with the experiment. Since the relative changes in velocity depend also on the orientation of nonpiezoelectric particles, the period of oscillations T may vary within a certain range.

The proposed mechanism for the formation of regular piezoelectric response signals in glycine powder is naturally hypothetical and requires substantiation.

¹R. Marsh, *Acta Crystallogr.* **11**, 654 (1958).

²Y. Iitaka, *Acta Crystallogr.* **11**, 225 (1958).

³Y. Iitaka, *Acta Crystallogr.* **13**, 35 (1960).

⁴Y. Iitaka, *Acta Crystallogr.* **14**, 1 (1961).

⁵D. Vasilescu, R. Cornillon, and G. Mallet, *Nature* **225**, 635 (1970).

Translated by G. Skrebtsov

Acoustic properties of betaine phosphite in the vicinity of phase transitions

E. V. Balashova and V. V. Lemanov

A. F. Ioffe Physicotechnical Institute, Russian Academy of Sciences, 194021 St. Petersburg, Russia

J. Albers and A. Klöpperpieper

Universität des Saarlandes, D-66041 Saarbrücken, Germany

(Submitted October 30, 1997)

Fiz. Tverd. Tela (St. Petersburg) **40**, 1090–1096 (June 1998)

A study is reported of acoustic anomalies in the vicinity of the antiferrodistortive and ferroelectric phase transitions in nominally pure betaine phosphite crystals and a crystal with 3% betaine phosphate impurity. The observed anomalies in the velocity and damping rate of longitudinal acoustic waves propagating along different crystallographic axes are interpreted within Landau theory. It is shown that the phase transitions in these crystals are characterized by a relatively weak correlation of the order parameter to strain and by a considerable contribution to the acoustic anomalies of an interaction higher in order than striction. © 1998 American Institute of Physics. [S1063-7834(98)02706-3]

Betaine phosphite (BPI), $(\text{CH}_3)_3\text{NCH}_2\text{COO}\cdot\text{H}_3\text{PO}_3$, belongs to a broad class of complex ferroelectric crystals based on the betaine aminoacid $(\text{CH}_3)_3\text{N}^+\text{CH}_2\text{COO}^-$.^{1,2} These crystals contain quasi-one-dimensional chains extended along the monoclinic b axis and consisting of inorganic HPO_3 tetrahedra linked through hydrogen bonds. The betaine molecules are bonded also by hydrogen to each of the inorganic groups in the chains and are oriented almost perpendicular to the latter. BPI crystals exhibit a high-temperature structural phase transition at $T_{c1}=355$ K associated with a change in space group $P2_1/m(Z=2)\rightarrow P2_1/c(Z=4)$,^{2,3} and a ferroelectric transition $P2_1/c\rightarrow P2_1$ at a temperature T_{c2} , which is extremely sensitive to the presence of very small amounts of impurities (PO_4^{3-}) or crystal defects ($224 < T_{c2} < 208$ K, Refs. 2–4). Spontaneous polarization appears along the monoclinic axis b oriented along the chains. The high-temperature phase transition is assigned to ordering of betaine molecules³ and rotations of the HPO_3 groups,⁵ whereas the transition to ferroelectric state is ascribed to proton ordering in hydrogen bonds.^{4,6} Additional anomalies in dielectric susceptibility were also observed at $T_{c3}=177$ K and $T_{c4}=140$ K.^{1,7} It was conjectured that these dielectric anomalies are connected with a very slow motion of PO_3 groups and betaine molecules in the MHz frequency range.⁷

From the purely crystallographic standpoint, ferroelectric BPI crystals are similar to the antiferroelectric betaine phosphate (BP), $(\text{CH}_3)_3\text{NCH}_2\text{COO}\cdot\text{H}_3\text{PO}_4$. Both these crystals have the same space group in the paraelectric phase and a similar quasi-one-dimensional chain structure. It is of interest in this connection to study cooperative phenomena in ferroelectric-BPI–antiferroelectric-BP solid solutions. A phase diagram of this system based on measurements of the dielectric constants and pyroelectric coefficients, as well as on x-ray diffraction data, was constructed.⁸ One of the directions pursued in investigating such compounds is studying their acoustic properties in the vicinity of the phase transitions. Acoustic studies, which permit one to determine also

dynamic features of the relation between a polar or nonpolar order parameter and strain, may contribute to understanding the cooperative phenomena in these solid solutions throughout the concentration range of interest.

This work reports a study of acoustic anomalies in the vicinity of phase transitions in a nominally pure BPI crystal and in a BPI crystal containing 3% BP [BPI(97)BP(3)]. The velocity and damping rate 15-MHz longitudinal acoustic waves were measured by the echo pulse technique. The accuracy of the velocity and damping rate determination was approximately 10^{-4} and 0.1 dB/ μs , respectively. LiNbO_3 piezotransducers were used to excite the acoustic waves. Measurements close to the phase transitions were carried out with the temperature varied at a rate of 0.25 K/min. The acoustic wave power was about 1 W/cm².

Figures 1 and 2 display the temperature dependences of the velocity and damping rate of longitudinal acoustic waves propagated along the monoclinic axis b (Y) in BPI crystals, and along the b (Y) and a (X) axes in BPI(97)BP(3) crystals, measured in the region of the antiferrodistortive phase transition at T_{c1} . We readily see that the high-temperature phase transition occurs in both crystals at practically the same temperature, and that the velocity anomalies in the vicinity of the transition are also practically equal. At the transition point one observes a clearly pronounced change in the slope of the temperature dependence of velocity. Note also some differences in the temperature behavior of velocity in the high-temperature phase for $T > T_{c1}$ along different crystallographic directions; indeed, while one observes an increase of velocity along the monoclinic axis Y with decreasing temperature, the velocity of the longitudinal acoustic wave along the X axis is practically temperature independent.

We shall use Landau theory to describe the anomalies in the acoustic properties of the crystal at a phase transition.

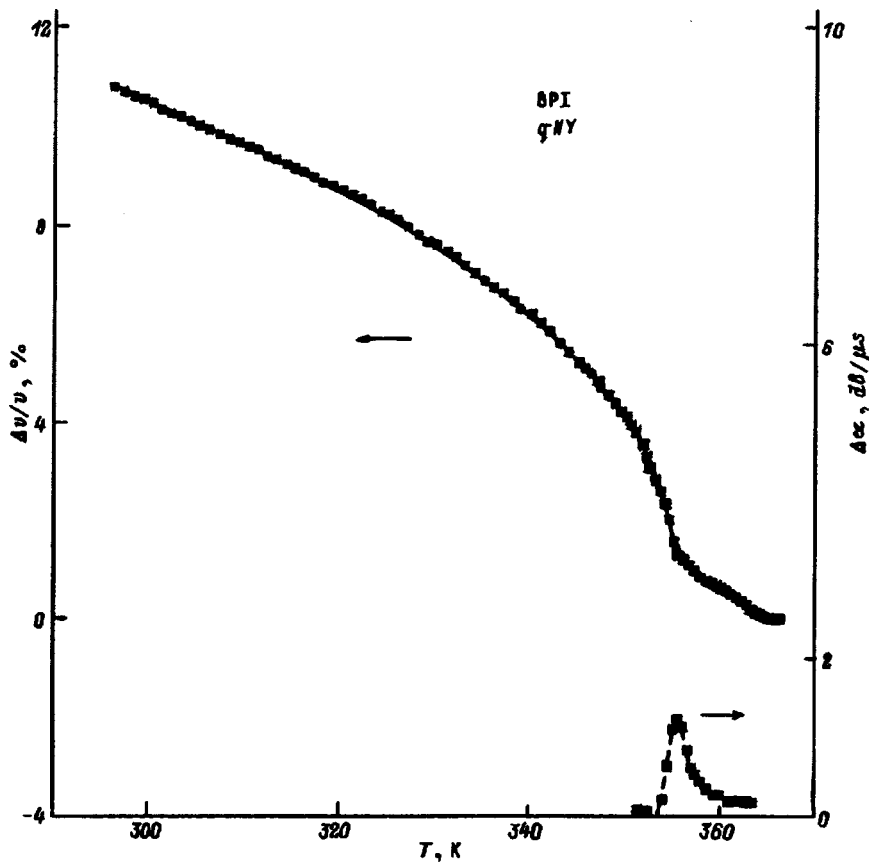


FIG. 1. Temperature dependences of the velocity and damping rate of longitudinal acoustic waves propagating along the Y axis in the vicinity of the antiferrodistortive phase transition (T_{c1}) in a BPI crystal [solid line – a plot of Eq. (3) with the parameters listed in Table I].

The thermodynamic potential will be written in its usual form

$$F = \frac{1}{2} \alpha Q^2 + \frac{1}{4} \beta Q^4 + \frac{1}{6} \gamma Q^6 + dQ^2 S + gQ^2 S^2 + \frac{1}{2} c_0 S^2 + \dots, \quad (1)$$

where Q is the order parameter, S is the strain, $\alpha = \lambda(T - T_{c1})$, and $\beta > 0$. The absence of noticeable negative jumps in velocity at T_{c1} indicates that the contribution of interaction energy quadratic in the order parameter and linear in strain, $dQ^2 S$, is small, and that the temperature dependence of the longitudinal velocity is dominated by the interaction energy quadratic in the order parameter and strain, $gQ^2 S^2$. This interaction provides a purely static contribution to the temperature dependence of the elastic constant

$$c = c_0 + 2gQ_0^2, \quad (2)$$

where Q_0 is the equilibrium value of the order parameter. Taking into account only the interaction energy of the form $gQ^2 S^2$, we use Eqs. (1) and (2) to obtain an expression for the change in the acoustic wave velocity in the region of the phase transition

$$\Delta v/v = \frac{g\beta}{2c_0\gamma} \left[\left(\frac{T_{c1} - T + \Delta T}{\Delta T} \right)^{1/2} - 1 \right], \quad T < T_{c1}, \quad (3)$$

where $\Delta T = \beta^2/4\gamma\lambda$ is a parameter determining the closeness of the phase transition to the tricritical point.

The experimental data were used to calculate using Eq. (3) the thermodynamic potential constants for BPI and BPI(97)BP(3) crystals, which are given in Table I. The small values of the ΔT parameters obtained for both crystals indi-

cate that the phase transitions at $T = T_{c1}$ are very close to the tricritical point, which is in accord with dielectric studies^{2,8}. Note the very large contribution of the interaction energy $gQ^2 S^2$ to the temperature dependence of the elastic constants. In principle, this interaction should not contribute to damping of the acoustic wave. The small damping rate peaks seen in the region of T_{c1} in both crystals (Fig. 1) can be attributed to a contribution of both a weak striction interaction of the order parameter with strain and to fluctuations in the order parameter, or to defects.

Since BP and BPI crystals undergo the same symmetry changes, $P2_1/m(Z=2) \rightarrow P2_1/c(Z=4)$, in their high-temperature transition,^{2,3} it appears of interest to compare the acoustic properties of these compounds, which reflect specific features of structural transformations in these materials connected with ordering of betaine molecules at T_{c1} . The acoustic anomalies in BP crystals observed at T_{c1} were studied by the resonance technique,⁹ and in deuterated betaine phosphate (DBP), by ultrasonic^{10,11}. These studies permit a conclusion that, for longitudinal waves propagating along the monoclinic axis b in BP and DBP, the acoustic anomalies are practically the same and are characterized by a considerable negative jump in velocity of about 8% due to striction, as well as by a large contribution of the term biquadratic in the order parameter and strain. Table I presents, for comparison, the thermodynamic potential constants quoted for the phase transition at T_{c1} in Refs. 10 and 11. The acoustic anomalies in the vicinity of the high-temperature transition in BPI differ radically from those in BP and DBP in a considerably

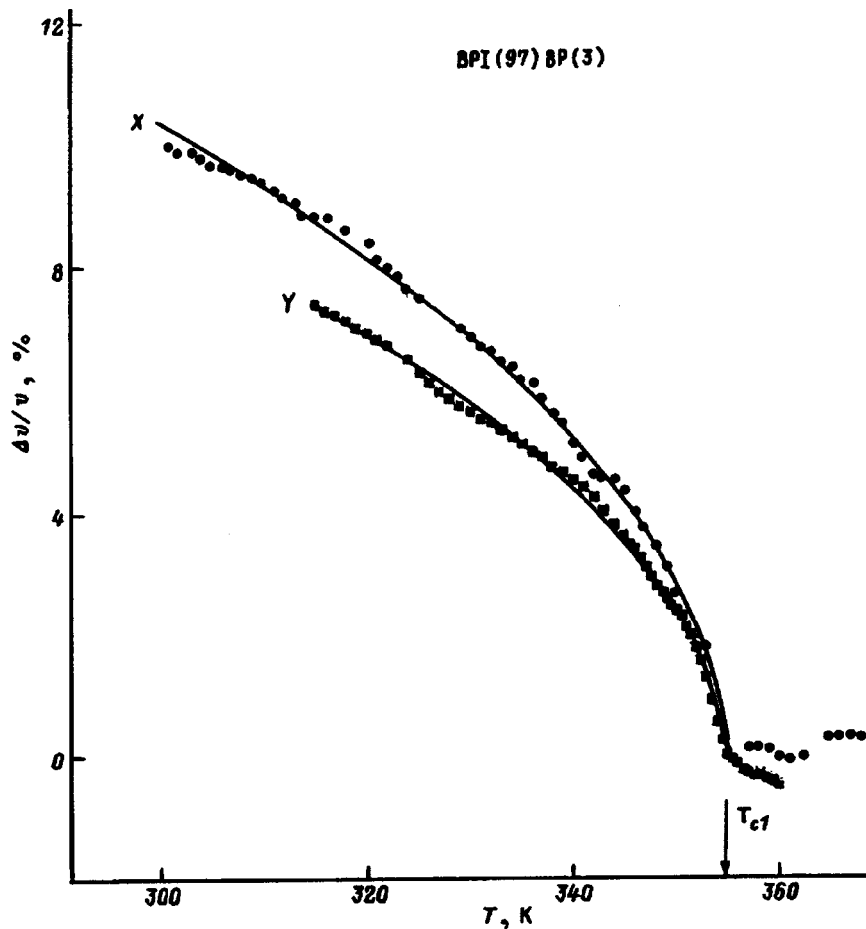


FIG. 2. Temperature dependences of the velocity of longitudinal acoustic waves propagating along the Y and X axes in the vicinity of the antiferrodistortive phase transition (T_{c1}) in a BPI(97)BP(3) crystal [solid line — a plot of Eq. (3) with the parameters listed in Table I].

smaller contribution of striction energy to interaction of the order parameter with strain, and in a substantially closer phase transition temperature to the tricritical point. Actually, for $T < T_{c1}$ the change in velocity in BPI is related to the temperature behavior of the square of the order parameter, which is determined by the degree of betaine molecule ordering. Experiments showed that adding BP to BPI affects noticeably neither the phase-transition temperature T_{c1} (in contrast to the ferroelectric transition point T_{c2}) nor the behavior of the velocity anomaly at T_{c2} . The qualitative differences between the acoustic anomalies observed at T_{c1} in BP and BPI crystals are apparently associated with the substantial changes in the structure of betaine molecule bonding to the PO_4 and HPO_3 tetrahedra, respectively (as a result of the absence of one oxygen in the tetrahedron and of its substitution by a proton in BPI, only one of the two hydrogen bonds coupling the betaine molecule to the inorganic group in BP remains).

TABLE I. Thermodynamic potential coefficients derived from acoustic measurements in DBP and BPI crystals.

Crystal	T_{c1} , K	Direction	ΔT , K	$d^2/\beta c_0$	$gB/\gamma c_0$
DBP90	365	Y	10	0.07	0.17
BPI	355	Y	0.13	<0.001	0.011
BPI(3%BP)	355	Y	0.16	<0.001	0.009
BPI(3%BP)	355	X	0.16	<0.001	0.013

Figure 3 plots temperature dependences of the velocity of longitudinal acoustic waves propagating along the three crystallographic directions X , Y , and Z in BPI(97)BP(3) in the vicinity of the ferroelectric transition. Acoustic measurements were paralleled by studies of the dielectric permittivity ϵ_b and of $\tan\delta$. Figure 4 displays temperature dependences of ϵ' and ϵ'' measured at a frequency of 1 kHz along the Y axis. A slightly diffuse maximum in dielectric permittivity is observed around 180 K, which is approximately 40 K below the ferroelectric transition point in nominally pure BPI. This shift of T_{c2} is in agreement with the phase diagram of the BP–BPI system.⁸ As seen from Fig. 3, the velocities of longitudinal acoustic waves exhibit anomalies in the same temperature region. Note that while the velocity decreases along directions perpendicular to the spontaneous polarization axis (X and Y) in the phase transition region, propagation along the spontaneous polarization axis [monoclinic axis b (Y)] is accompanied only by a change in slope of the temperature dependence of velocity.

While the temperature dependence of dielectric permittivity in the BPI(97)BP(3) crystal in the vicinity of the ferroelectric transition can be analyzed in terms of the quasi-one-dimensional Ising model, the experimental data can be described with approximately the same accuracy by the Curie-Weiss law in both the paraelectric and ferroelectric phase, with exception of a few degrees above and below the maximum in dielectric permittivity (T_m). The Curie-Weiss

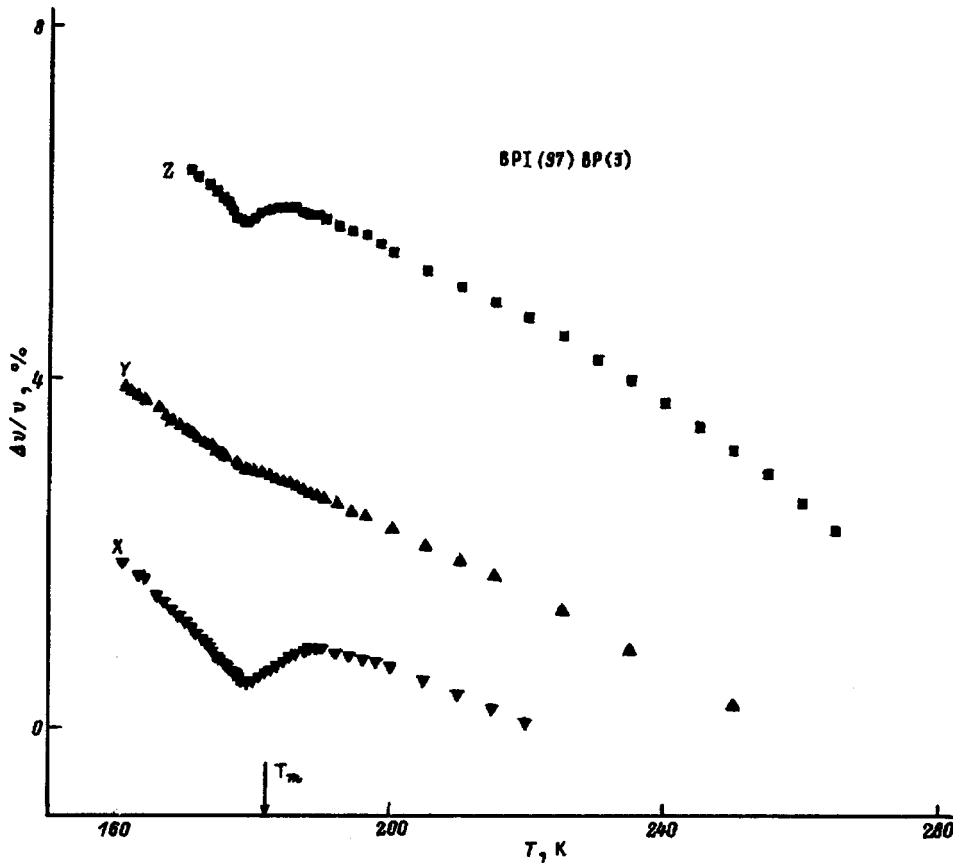


FIG. 3. Temperature dependences of the velocity of longitudinal acoustic waves propagating along the X, Y and Z axes in the vicinity of the ferroelectric phase transition (T_{c2}) in a BPI(97)BP(3) crystal.

constant thus determined turns out to practically coincide with that calculated^{4,12} for pure BPI. Besides, the ratio of the slopes of the inverse dielectric permittivity in the ferro- and paraelectric phases is found to be close to four, which implies closeness of the phase transition to the tricritical point.

The temperature behavior of the velocity of a longitudinal wave propagating along the X and Z axes is shown graphically in Fig. 3. It is characterized by a fairly smooth decrease of the velocity in the vicinity of the ferroelectric transition and its strong increase with decreasing temperature to the level in excess of the value in the paraphase. The temperature of the maximum in dielectric permittivity T_m is identified by arrows. Leaving aside the region of diffuseness, estimate some parameters of the acoustic anomalies by means of Landau theory in the temperature range where the Curie-Weiss law for dielectric permittivity is approximately satisfied. We shall use the thermodynamic potential in the form similar to (1) for $Q \equiv P$, where P is polarization, $\alpha = \lambda(T - T_{c2})$, and $\beta > 0$. Taking into account spontaneous deformation results in renormalization of the coefficient of P^4 in the thermodynamic potential: $\beta^* = \beta - 2d^2/c_0$. The squared order parameter can now be written

$$P^2 = -\frac{\beta^*}{2\gamma} \left[1 - \left(\frac{T_{c2} - T + \Delta T}{\Delta T} \right)^{1/2} \right], \quad (4)$$

where $\Delta T = \beta^*/4\gamma\lambda$.

Using the Landau-Khalatnikov equation and the equation of motion for elastic displacements, we obtain from Eq.

(1) the following expressions for the velocity and damping rate of acoustic waves, which are due to the electrostriction coupling of the order parameter and strain

$$\Delta v/v = \left[1 - \frac{1}{(1 + \omega^2 \tau^2)} \left[1 + \left(\frac{T_{c2} - T + \Delta T}{\Delta T_1} \right)^{1/2} \right]^{-1} \right]^{1/2} - 1, \quad T < T_{c2}, \quad (5)$$

$$\alpha = \frac{1}{2} \frac{\omega^2 \tau}{(1 + \omega^2 \tau^2) \left[1 + \left(\frac{T_{c2} - T + \Delta T}{\Delta T_1} \right)^{1/2} \right]^{-1}}, \quad T < T_{c2}, \quad (6)$$

where $\Delta T_1 = d^4/\gamma\lambda c_0^2$ is a parameter determining the coupling strength between polarization and strain, ω is the circular frequency of the acoustic wave, and $\tau = L^{-1}(\partial^2 F/\partial P^2)_0^{-1}$ is the order-parameter relaxation time (L is a transport coefficient).

The temperature dependence of τ can be written

$$\tau = \tau_0 \left[\left(\frac{T_{c2} - T + \Delta T}{\Delta T_1} \right)^{1/2} - \left(\frac{\Delta T}{\Delta T_1} \right)^{1/2} \right]^{-1} \times \left[1 + \left(\frac{T_{c2} - T + \Delta T}{\Delta T_1} \right)^{1/2} \right]^{-1}, \quad (7)$$

where $\tau_0 = \gamma/L(\beta - \beta^*)^2$.

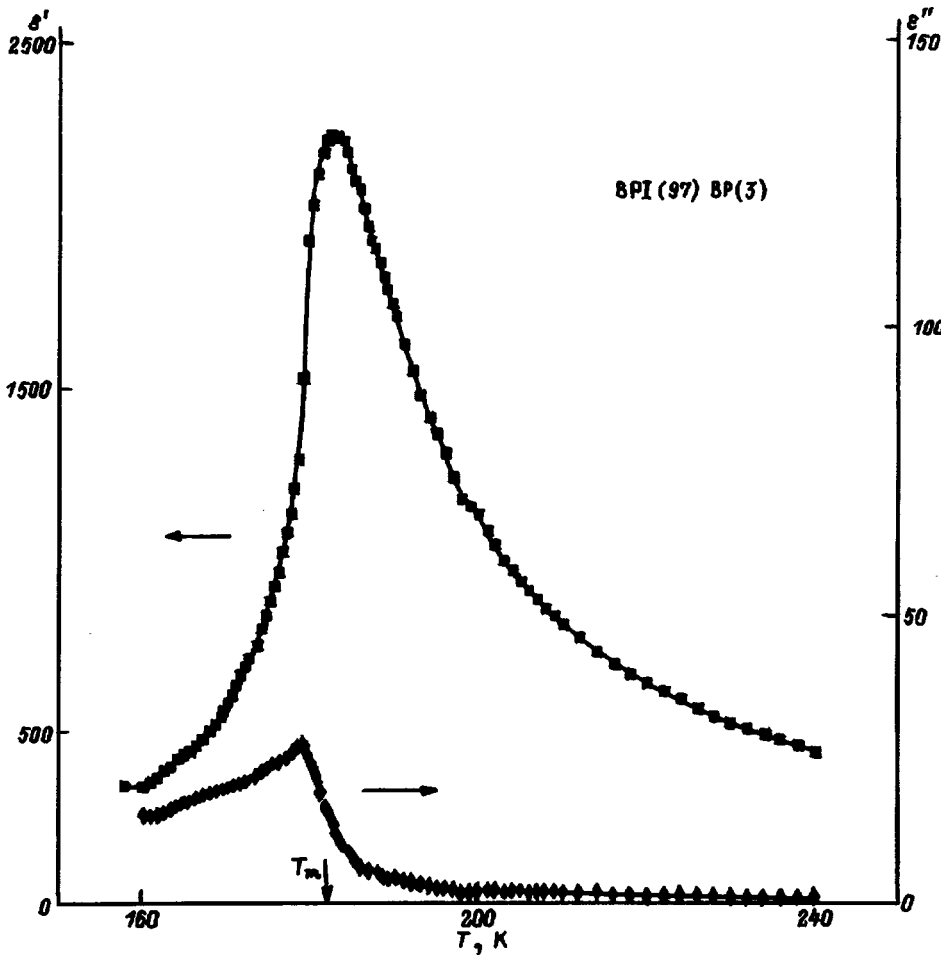


FIG. 4. Temperature dependences of the imaginary and real parts of dielectric permittivity in the vicinity of the ferroelectric transition (T_{c2}) in a BPI(97)BP(3) crystal.

To compare the relaxation times for different crystals and for different phase transitions, one can conveniently determine from Eq. (7) the relaxation time for $T=0$ K in the form

$$\tau_0^* = \tau_0 \left[\left(\frac{T_{c2} + \Delta T}{\Delta T_1} \right)^{1/2} - \left(\frac{\Delta T}{\Delta T_1} \right)^{1/2} \right]^{-1} \times \left[1 + \left(\frac{T_{c2} + \Delta T}{\Delta T_1} \right)^{1/2} \right]^{-1}. \quad (8)$$

Taking into account additionally in Eq. (5) the static contribution to the change in velocity due to the interaction of the order parameter with strain in the form gP^2S^2 , we come to the following expression for the change in velocity

$$\Delta v/v = \left[1 - \frac{1}{1 + \omega^2 \tau^2} \left[1 + \left(\frac{T_{c2} - T + \Delta T}{\Delta T_1} \right)^{1/2} \right]^{-1} \right]^{-1} - 1 + \frac{g\beta^*}{2c_0\gamma} \left[\left(\frac{T_{c2} - T + \Delta T}{\Delta T} \right)^{1/2} - 1 \right]. \quad (9)$$

Using Eqs. (6) and (9) and the experimental data, we estimated ΔT , ΔT_1 , τ_0^* , and the combination of the constants $g\beta^*/c_0\gamma$. Figure 5 plots the calculated temperature dependence of the velocity along the X axis obtained from Eq. (9) for the polarization relaxation times $\tau_0^* \cong 10^{-10}$ s, $\Delta T = 1.6 \times 10^{-2}$, $\Delta T_1 = 5.2 \times 10^{-3}$, and $g\beta^*/c_0\gamma = 5.6 \times 10^{-4}$. The small value of parameter ΔT indicates that the

phase transition is close to the tricritical point. This conclusion agrees with dielectric measurements, which yield a ratio of the slopes of the inverse dielectric permittivity in the ferro- and paraphase close to four. The order-parameter relaxation times derived from the velocity and damping rate anomalies coincide. As for the parameter ΔT_1 describing the coupling strength of the order parameter and strain, its value derived from the velocity anomaly exceeds by a factor of two–three that extracted from the damping rate anomaly. In both cases the ΔT_1 parameter is fairly small. This means that noticeable changes in velocity should be observed within a narrow temperature interval close to the phase transition from the side of the ordered phase. As already mentioned, however, the absence of a clearly pronounced negative jump in velocity at T_{c2} and the decrease of velocity above the temperature of the maximum in dielectric permittivity, i.e., actually in the paraphase, distinguishes radically the velocity anomaly from the classical thermodynamic behavior for crystals which do not exhibit piezoeffect in the paraphase, and requires invoking additional mechanisms. The specific features of BPI structure, characterized by the existence of quasi-one-dimensional chains, imply an essential role of fluctuations in the order parameter, which can become particularly strongly manifest in such low-dimension systems. On the other hand, the presence of BP, capable of creating very strong local fields with HPO_3 replaced by the PO_4 group,¹³ can, in principle, give rise to specific features in

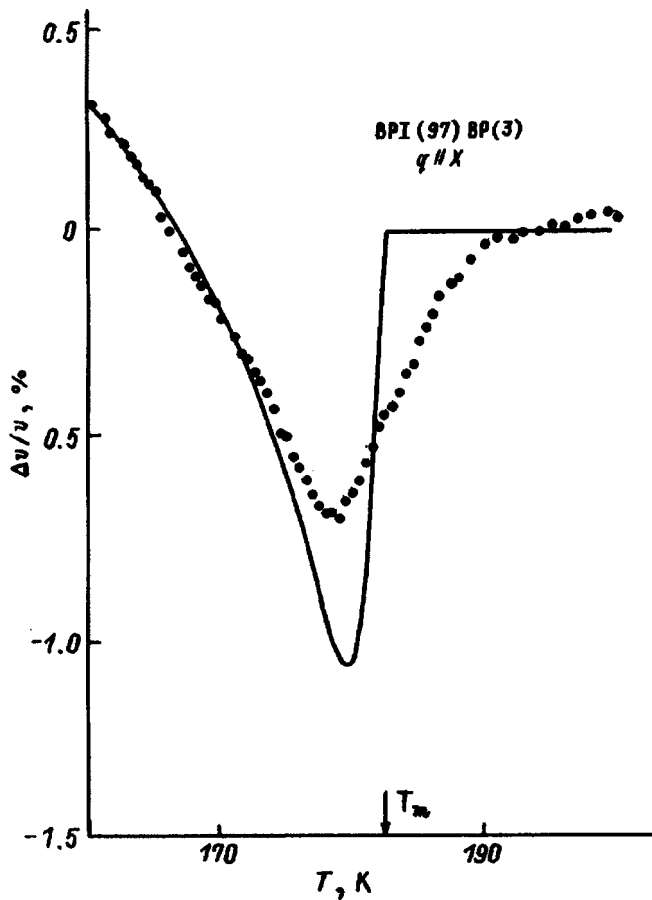


FIG. 5. Temperature dependences of the velocity of longitudinal acoustic waves propagating along the X axis in the vicinity of the ferroelectric phase transition (T_{c2}) in a BPI(97)BP(3) crystal [solid line — a plot of Eq. (9) with the parameters given in text].

acoustic anomalies. Besides, the available experimental data also give grounds to assume the existence of internal electric fields in BPI crystals,¹² which can affect the acoustic anomalies in the ferroelectric phase transition.

As seen from Fig. 3, propagation of longitudinal acoustic waves along the monoclinic axis (Y) is not accompanied by a decrease of velocity at the ferroelectric transition. At the maximum of dielectric permittivity one observes only a plateau in the temperature dependence of velocity, and a slight change in the slope because of a gQ^2S^2 -type biquadratic relation. No damping rate peak is evident either. The absence of a negative jump in velocity and of a maximum in damping rate due to the striction energy dQ^2S for longitudinal acoustic waves propagating along the spontaneous polarization axis (Y) results from the suppression of these anomalies by long-range dipole interaction¹⁴ in a uniaxial ferroelectric.

Support of the Russian Fund for Fundamental Research (Grant 96-02-17857) is gratefully acknowledged.

¹J. Albers, *Ferroelectrics* **78**, 3 (1988).

²J. Albers, A. Klöpperpieper, H. J. Rother, and S. Haussühl, *Ferroelectrics* **81**, 27 (1988).

³I. Fehst, M. Paasch, S. L. Hutton, M. Braune, R. Böhmer, A. Loidl, M. Dörfel, T. H. Narz, S. Haussühl, and G. J. McIntyre, *Ferroelectrics* **138**, 1 (1993).

⁴R. Sobestrianskas, J. Grigas, Z. Czaplá, and S. Dacko, *Phys. Status Solidi A* **136**, 223 (1993).

⁵A. Pöpl, G. Völkel, H. Metz, and A. Klöpperpieper, *Phys. Status Solidi B* **184**, 471 (1994).

⁶H. Bauch, R. Böttcher, and G. Völkel, *Phys. Status Solidi B* **178**, K39 (1993).

⁷H. Bauch, J. Banys, R. Böttcher, C. Klimm, A. Klöpperpieper, and G. Völkel, *Phys. Status Solidi B* **187**, K81 (1995).

⁸M. L. Santos, J. M. Kiat, A. Almeida, M. R. Chaves, A. Klöpperpieper, and J. Albers, *Phys. Status Solidi B* **189**, 371 (1995).

⁹M. Maeda, *J. Phys. Soc. Jpn.* **57**, 3059 (1988).

¹⁰J. Albers, E. V. Balashova, A. Klöpperpieper, V. V. Lemanov, H. E. Müser, and A. B. Sherman, *Ferroelectrics* **108**, 357 (1990).

¹¹J. Albers, E. V. Balashova, A. Klöpperpieper, V. V. Lemanov, H. E. Müser, and A. B. Sherman, *Ferroelectrics* (in press).

¹²R. Cach, S. Dacko, and Z. Czaplá, *Phys. Status Solidi A* **148**, 585 (1995).

¹³H. Bauch, G. Völkel, R. Böttcher, A. Pöpl, H. Schäfer, J. Banys, and A. Klöpperpieper, *Phys. Rev. B* **54**, 9162 (1996).

¹⁴S. Ya. Geguzina and M. A. Krivoglaз, *Fiz. Tverd. Tela (Leningrad)* **9**, 3095 (1967) [*Sov. Phys. Solid State* **9**, 2441 (1967)].

Translated by G. Skrebtsov